Nuclear Computations under Uncertainty

New methods to infer and propagate nuclear data uncertainty across Monte Carlo simulations

by

Pablo Ducru

Master of Management Science, Tsinghua University (2020)
Diplôme de l'École polytechnique (2016)

Submitted to the Center for Computational Science & Engineering
and Department of Nuclear Science & Engineering
in partial fulfillment of the requirements for the degree of

Doctor of Philosophy
in
Computational Nuclear Science & Engineering
at the
MASSACHUSETTS INSTITUTE OF TECHNOLOGY
June 2021

Author .....
Center for Computational Science & Engineering
and Department of Nuclear Science & Engineering

Certified by .....
Benoit Forget
Associate Department Head, Department of Nuclear Science & Engineering
Professor of Nuclear Science & Engineering
Thesis Supervisor

Certified by .....
Kord Smith
Korea Electric Power Company (KEPCO)
Professor of the Practice of Nuclear Science & Engineering
Thesis Supervisor

Certified by .....
Vladimir Sobes
Assistant Professor, Department of Nuclear Engineering
The University of Tennessee, Knoxville
Thesis Reader

Accepted by .....
Ju Li
Battelle Energy Alliance Professor of Nuclear Science & Engineering
and Professor of Materials Science & Engineering

Accepted by .....
Nicolas Hadjiconstantinou
Co-Director, Center for Computational Science & Engineering
Professor of Mechanical Engineering

Nuclear Computations under Uncertainty

New methods to infer and propagate nuclear data uncertainty across Monte Carlo simulations

by

Pablo Ducru

Submitted to the Center for Computational Science & Engineering
and Department of Nuclear Science & Engineering
on June 4, 2021, in partial fulfillment of the
requirements for the degree of

Doctor of Philosophy
in
Computational Nuclear Science & Engineering

Abstract

This thesis introduces new methods to efficiently infer and propagate nuclear data uncertainty across Monte Carlo simulations of nuclear technologies. The main contributions come in two areas: 1. novel statistical methods and machine learning algorithms (Embedded Monte Carlo); 2. new mathematical parametrizations of the quantum physics models of nuclear interactions and their uncertainties (Stochastic Windowed Multipole Cross Sections).

1. Embedded Monte Carlo infers the uncertainty in nuclear codes inputs (reactor geometry, nuclear data, etc.) from samples of noisy outputs (e.g. experimental observations), and in turn propagates this uncertainty back to the simulation outputs (reactor power, reaction rates, flux, multiplication factor, etc.), without ever converging any single Monte Carlo reactor simulation. Such embedding of the uncertainty within the Nested Monte Carlo computations vastly outperforms previous methods (10–100 times less runs), and is achieved by approximating the input parameters Bayesian posterior via variational inference, and reconstructing the outputs distribution via moments estimators. We validate the Embedded Monte Carlo method on a new analytic benchmark for neutron slowdown we derived.

2. Stochastic Windowed Multipole Cross Sections is an alternative way to parametrize nuclear interactions and their uncertainties (equivalent to R-matrix theory), whereby one can sample on-the-fly uncertain nuclear cross sections and analytically compute their thermal Doppler broadening. This drastically reduces the memory footprint of nuclear data (at least 1,000-fold), without incurring additional computational costs.

These contributions are documented in nine peer-reviewed journal articles (eight published and one under review) and seven conference articles (six published and one under review), constituting the core of this thesis.

Thesis Supervisor: Benoit Forget
Title: Associate Department Head, Department of Nuclear Science & Engineering
Professor of Nuclear Science & Engineering

I am just the messenger...

Acknowledgments

The highest forms of understanding we can achieve are laughter and human compassion.
- Richard Feynman

Life has been so plentiful over the past six years that acknowledgments are a perilous task. Boring the reader with a long list of names is a poor way of giving back. Then, there is the terrifying fear of forgetting someone we hold dear, regretting it forever. So, at the end of these acknowledgements, I leave you with an interesting story, some teachings, and a life lesson: "The Tale of Greg Sanchez, the man who built his freedom alone".

A lot of people contributed to making this thesis possible.

First and foremost, I am deeply grateful to Professor Benoit Forget, who had the generosity and audaciousness to support me in all my meanderings and adventures throughout my time at MIT: ranging from my Schwarzman Scholarship at Tsinghua University in China, to the MIT Sandbox startup project in the shrimp farms of northern Mexico, or the breathtaking views of the Pajarito Plateau at Los Alamos National Laboratory, as well as my stints with Professor Vladimir Sobes, first at Oak Ridge National Laboratory, and then at University of Tennessee, Knoxville. Thank you to Erin and Tommy for welcoming me inside your family.

Most of these findings were achieved with the challenging and active collaboration of Professor Vladimir Sobes, in whom I found a life-long friend and mentor. Thank you, Vlad and Julia, for welcoming me in your life as a family member, making me run in the morning, getting us rescued at Myrtle Beach, and taking me flying over the Smokey mountains. What a ride we had together.

To all those whom believed in me along the way — at MIT — Jinane Abounadi; Kimberly Benard; Richard Lester; Ju Li; Alison Hynd — at Tsinghua University — Steve Schwarzman; Pan Qingzhong (David); Julia Zupko; Richard Robinson; Barry Nalebuff — at École Polytechnique — Yves Bréchet; Gilles Auffret; Alain Gachet; Yves Demay; Frank Carré; François Gélébart — and beyond — Isabelle and Philippe Morin; Stéphane Chaouat; Daniel Payan; Lourdes Melgar; Adrián Katzew; Nadia Boukhetaia; and all the others. Thank you for your mentorship, and for being a constant source of inspiration.

To all the MIT staff, and in particular the NSE one: Brandy Baker; Lisa Magnano Bleheen; Peter Brenton; Kate Nelson; Sylvia Hiestand; Ian Murray; to name but a few – without your indispensable help and support, I, just as many students (and

professors), would never have made it through MIT – you are the ones whom hold MIT together.

Thank you to all my article co-authors and close collaborators, without whom this work would not have been possible: Abdulla Alhajri, Colin Josey, Isaac Meyer, Jingang Liang, Karia Dibert, Mark Paris, Gerald Hale, Professor Joshua Tenenmbaum, and of course Professors Kord Smith, Benoit Forget, and Vladimir Sobes. You have been at the core of my research and thus of my life for these past years.

To all the people who welcomed me into their work and research, thank you for betting on our collective creativity: Professor Ramesh Raskar on an MIT Media Lab study of corporate interdisciplinary research institutes; Alain Gachet on a fabulous adventure in water and natural resources exploration, from radars and satellites all the way the the NASA's "Space Technology Hall of Fame"; Professor Jacopo Buongiorno on the offshore nuclear power plants (which I still believe could provide developing countries with a zero-carbon pathway to industrialization); Giancarlo Lenci and Rami Abi-Akl for our Sfumato average; Jingang Liang, XingJie Peng, and ShiChang Liu on regularized vector-fitting for nuclear cross sections; Andrew Holcomb, Goran Arbanas, Marco Pigni, and Dorothea Wiarda for the Generalized Reich-Moore formalism; Professors Vladimir Sobes and Barry Ganapol for Abdulla Alhajri's neutron slowdown analytic benchmark; Professor Ju Li on electrochemical-hydrodynamics; Professor Scott Kemp on nuclear weapon detection; Professor Kenneth Strzepek on water rights; and may others.

To all my teammates with whom we worked hard in all these MIT and Harvard projects: Arturo Chavez-Gehrig and Michael Sandford for our great "The Beetles" team for The Economist NRG competition; Nestor Sepulveda and Diego Maturana for our amazing trading in Professor Christopher Knittel electricity market; Diego Ariza Munoz on Professor Henry Weil's strategic opportunities in the Energy sector; Zhaoyuan Liu on population Monte Carlo machine learning; Conleigh Byers on our study of the Lib-Dems network of bills in the UK Parliament; and many others.

Of course, to all my Nuclear Science and Engineering (NSE) classmates — Nestor Sepulveda; Geoffrey Haratyk; Jake Jurewicz; Pierre Guenoun; Alexandre Cooper; Ruaridh Macdonald; Alexandre Guion; Lucio Milanese; TD McDonald; Jayson Vavrek; Reid Tanaka; Juan Ruiz Ruiz; and many more. In particular, to the Computational Reactor Physics Group (CRPG) — Zhaoyuan Liu; Miriam Kreher; Guillaume Giudicelli; Sterling Harper; Shikhar Kumar; and all the others.

To my fellow students of the NSE student board and ANS MIT Chapter, and beyond: Cody Dennett; Juan Ruiz Ruiz; Lucas Rush; Patrick White; Jayson Vavrek; Paolo Minelli; Nestor Sepulveda; Karen Dawson; Geoffrey Haratyk; Guillaume Giudicelli; Reid Tanaka; Adam Kuang. Thank you for committing some of your time to helping the department and the students, from serious matters, to the bonfire of New Hampshire where we started the tradition of the Atomic Retreat.

To my friends of the MIT Energy club — Libby, Pedro, Julia, and the others — the MIT Judo Club — Fil; Kiri; Ted; and all the other warriors — the MIT Rowing Club, the MIT Sailing Club, the MIT Ski Team, the MIT Rugby team, and the MIT TPP people who welcomed me so warmly in fabulous trips together.

To my flatmates at 18 Amory street: Alix de Monts; Ola (Alexandra) Kalinowska; Korbinian Riener; Kemal Armada; Olivier Cornes; Cosima du Pasquier; Humberto Ramirez; Stanislas Chaillou; Alice Sommer; Jonathon Hazell; Mark York; Jérôme Michon; Nils Pasquero; Stuart Russell; Fil Twarowski. What a memorable household we forged together.

Professors who change the course of one's life often go unsung. Let me here right this wrong — at École Jeannine Manuel (EJM) — Jérôme Giovendo; Jocelyn Huchette; Alain Javello; George Jewsbury — at Lycée Louis-le-Grand — Aléxis Fagebaume; Jean-Pierre Lecardonnel; Frédéric Turiel; Paul Watson — at École Polytechnique — Frank Carré; Michel Gonin; Pere Roca i Cabarrocas; Jean-Eric Wegrowe; Florent Gusdorf — at Tsinghua University — Pan Qingzhong (David); Julia Zupko; Barry Naughton; Gao Xiqing; Todd Henshaw; Michael Powers; Barry Nalebuff; Djoomart Otorbaev — at MIT — Joshua Tenenbaum; César Hidalgo; Rebecca Saxe; Tomaso Poggio; Christopher Knittel; Dimitris Bertsimas; Dennis Whyte (specially for teaching me Craps at Las Vegas); Michael Short; Scott Kemp; Paola Cappellaro; and Noah Feldman (at Harvard Law School). Thank you all for your immense teachings, which have been instrumental in shaping who I am and how I look at the world.

To all my friends — from MIT, École Polytechnique, Lycée Louis le Grand, École Jeannine Manuel, Schwarzman Scholars, and beyond — whom I admire and look up to, even when I do not see you as often as I wish I did: Mark York; Grégoire Jacquot; Jonathon Hazell; Filip Twarowski; Robert Mahari; Haofeng Xu; Vladimir Sobes; Geoffrey Haratyk; Nestor Sepulverda; Nils Pasquero; Alice Sommer; Khahlil Louisy; Alexander Hayman; Johannes Norheim; Elena Jacobson; Jérôme Michon; Rami Abi Alk; Juan Ruiz Ruiz; Pierre Guenoun; Estienne Granet; Nicolas Lobato-Dauzier; Sébastien Boyer; Martin Averseng; Lucas David; William Legrand; Isabelle Albertalli; Louis Virey; Pierre Lecointre; Lætitia Jubin; Johan Amar; Sophie Marbach; Jonathan Raiman; Elisabetta Pietrostefani; Kevin Machefert; Charles Cheval; Dimitri Tran Tien; Adrien Payan; Adedotun Adejare; Jennifer Almodovar; Theodore Breyer; Kai Cash; Abdourahamane Diallo; Guanhua Feng (Roger); Dominic Feroze; Hector Fuentes; Bita Ghassemi; Shubhojit Ghose; Paul Greenbaum; William Haynes; Felipe Flores; Neil Jain; Atoka Jo; Harnidh Kaur; Seyoung Lee; Chubing Li; Jesse Marks; Conor McGylnn; Farid Nemri; Toure Owen; Pedro Robledo; Kathia Salazar; Jieying Shi; Christopher Sperrazza; Kiran Sridhar; Himakeerth Tammineedi; Zachary Tan; Darren Touch; Taylor Wong; Fangzhou Xu; Christopher Yeh; Zhou Yu; and all the others...

À Alix, à ta spontanéité, ta façon cash et unique d'aborder et de tester le monde, ton rapport pratique aux choses, pour toutes ces aventures vécues. Merci pour tes valeurs, ta ténacité, ton courage, ton amitié, et ton amour fidèle.

À ma famille française: Solange et Josef Strachwitz; Christine, Frédérick, et Alexandra Bolzan — et leurs merveilleux Elliot, Gabriel, Benjamin, et Olivier — aux Ducrus — Olivier, Cécile et Barthélémy, Laurent et Gaëtane, Sophie et Max, et leurs adorables petits — et aux Morcourts, Thibaut, Geoffroy, et leur magnifiques familles.

A toda mi famillia Mexicana, gracias por seguir mostrando el ejemplo y transmitiendo esta irresistible llamada de la tribu Clouthier. ¡Qué alegria, orgullo, valores, ánimo, coraje, energía, felicidad, e intensidad de vivir!

À ma famille, Amaya, maman, papa: VFQVA.

- Pablo

The Take of Greg Sanchez, the man who built his freedom alone

In the summer of 2017, I drove across America to the deserts of New Mexico, to work at the theoretical division of Los Alamos National Laboratory. Finding rent in the towns of Los Alamos or Santa Fee quite expensive, I looked north to the town of Española, much to the fear and dismay of my supervisors Mark Paris and Gerry Hale as it was the national epicenter of the opioids epidemic. I ended up living in the nearby Native American Pueblo of Ohkay Owingeh, where Greg Sanchez lent me a room in his magnificent adobe house. In Tano, "Ohkay Owingeh" means "place of the strong people", and Greg Sanchez was a prodigious force of nature. Standing straight with a profound sense of dignity and pride in his Native American origins, Greg was a strong man with long black hair falling straight behind his shoulders, and a deep look in his eyes. He showed me around the house, explaining with pride the traditional adobe construction which let sunlight in during winter and provided shade during summer. He showed me the view of the Rio Colorado and the Sangre de Cristo mountains, and I saw a shinny light in his dark eyes. "Greg, what a magnificent house! It looks both traditional and new, did you acquire it recently?" I asked. "No, I build it myself", replied this man of few words. "You mean, you designed it?" I questioned. "No, I built it with my own two hands". "Impressive! I exclaimed in admiration, what do you do for a living?". And Greg replied: "I am a nuclear weapons designer". I was shocked and in awe. Greg had spend two years of his life designing nuclear weapons during the day, and then his two-storey home during the night, driving after work to lay every adobe brick one by one, all by himself. "I did it for my wife and my two daughters" he smiled pointing to their pictures on the wall. I opened the freezer, and it was full of brown meat. "What is it?" I asked. "There is a good hunting season, Greg noted, I go to the mountain to hunt the Elk, bring one back, and cut it so we have natural, healthy meat". I could sense the pride he

took in his self-reliance. He had actually gone even further: he had bought the lands between his house and the Rio Colorado, and a tractor, and started farming the land, ploughing the earth in the evenings and the weekends, to achieve food sufficiency. It was a Herculean task. Greg had build his freedom with his own two hands, all to provide for his wife and his two daughters. And it showed: Greg, the house, and the scenery, were majestic.
I stopped for a moment to contemplate it all, feeling very lucky and humbled. “Greg, it is an honor for me to live this summer in your house you built for your family. Are you off all together for the summer?”. He looked at the horizon, calm, proud, and somber, like a fearless warrior facing death. “No, my wife found it too isolated here. She left to the city with the girls”...

This tragic tale is a cautionary lesson for each one of us in pursuit of freedom. And also for the nuclear industry as a whole: building prodigious things that people might not want. Sharing this life story is my way here of giving back, and saying thank you.

Contents

List of Figures

List of Tables

Chapter 1

Introduction | Executive summary

Imagination is more important than knowledge.
- Albert Einstein

Nuclear computations are amongst the world's most challenging, and still today require the world's top supercomputers. Advances in nuclear computations therefore impact the broader field of high performance computer science and engineering.

Both the Monte Carlo method and supercomputers emerged from the Manhattan Project, to develop atomic weapons. Both have been necessary to their stewardship ever since nuclear tests were banned by international treaties. Civil nuclear power also heavily relies on nuclear computations in order to meet stringent regulatory requirements. To design future advanced nuclear technologies — for zero-carbon energy, medical applications, or weapons stewardship — we must be able to simulate nuclear reactors to high predictive fidelity and with trustworthy confidence intervals.

By developing a series of new mathematical, physical, and computational methods — both in statistical inference and machine learning (*Embedded Monte Carlo*) as well as in nuclear physics and data models (*windowed multipole stochastic cross sections*) — our work holds the promise of greatly advancing the accuracy and efficiency of such intensive computations.

1.1 The problems

The most accurate nuclear simulators are Monte Carlo particle transport codes. They compute the random walks of nuclear particles across a reactor, and average their outcomes. Yet, quantifying the uncertainty of these outputs has been a major computational challenge. The two inputs of Monte Carlo codes are the reactor geometry, and the nuclear physics properties of materials. In particular, elemental nuclear reaction rates – for instance the probability of a fission occurring when a neutron hits a uranium ^{235}U nucleus – are represented with energy-dependent cross sections,

parametrized by nuclear data. Since we know these cross sections in part from experimental measurements, nuclear data therefore comes with uncertainties. Propagating this nuclear data uncertainty across Monte Carlo simulations, from fundamental nuclear physics to nuclear reactor power, is amongst the hardest uncertainty to compute in the field. So is the converse problem: inferring back an uncertainty distribution of nuclear data from integral reactor experiments.

Currently, the two state-of-the-art uncertainty methods are: Nested Monte Carlo (NMC); and Sensitivity Analysis (SA).

- Nested Monte Carlo (NMC) samples nuclear data from its uncertainty distribution, and for each runs a Monte Carlo nuclear reactor simulation, yielding a histogram of outputs (e.g. reactor power). However, these nested Monte Carlo computations are forbiddingly costly, as we must converge thousands of different reactor simulations for the outputs. But even sampling the input possible nuclear cross sections from their uncertainty distribution presently represents a gargantuan computational and memory burden. That is because of the way we account for temperature effects, in particular Doppler broadening, which is the averaging of cross sections over the thermal motion of the target atoms. Doppler broadening is of critical importance in neutron transport applications, as it ensures the stability of many nuclear reactors (negative thermal reactivity feedback). Currently, Doppler broadening to any desired temperature is performed by interpolating between pre-computed Doppler broadened cross sections at different reference temperatures. This costly process itself must them be repeated myriad times if we want to generate uncertain cross section inputs.

- Sensitivity Analysis (SA) considers small perturbations in nuclear data inputs, and propagates them to the outputs of the nuclear reactor simulations. However, computing the sensitivities of the outputs to the inputs – say the derivatives of reactor power to nuclear data – is costly and difficult (requiring to solve the adjoint problem and store many derivatives), while accounting for the effects of temperature Doppler broadening on the sensitivities is currently out-of-reach. Also, sensitivity analysis is only valid to first order, even though some nuclear data uncertainties are large enough to propagate non-linearly. It is possible to develop higher-order sensitivity methods, but at an impractically higher computational and memory cost. Furthermore, sensitivity analysis can only quantify the effects of input perturbations on one given output at a time.

1.2 Our solutions

In this work, we developed new *Embedded Monte Carlo* statistical methods to infer and propagate inputs uncertainty across intractable ensemble-average stochastic simulations. Embedded Monte Carlo is based on variational Bayesian inference and moments propagation in Nested Monte Carlo computations. For nuclear reactor physics, Embedded Monte Carlo constitutes a breakthrough compared to the present state-of-the-art uncertainty propagation methods (sensitivity analysis and Nested Monte

Carlo): it can propagate nuclear data uncertainty non-linearly across a complex transport simulation to all the integral outputs at once with only twice the number of neutrons of a single Monte Carlo run without uncertainty propagation, versus 1000 times for fast-TMC (an efficient NMC scheme) or 10 times for sensitivity analysis per any given output quantity (because of sensitivity estimations). Embedded Monte Carlo can also non-linearly infer nuclear data uncertainty across integral experiments, which can only be achieved presently with linear Bayesian update for Gaussian sensitivity analysis, or costly point-by-point Bayesian update on the NMC histogram.

However, to successfully apply Embedded Monte Carlo to nuclear reactor computations, we must be able to efficiently sample and Doppler broaden possible nuclear cross sections from their uncertainty distribution, and for each simulate corresponding particle random walks.
We reduced this memory burden by developing an optimal Doppler broadening interpolation method (Kernel reconstruction quadrature) which cuts the number of pre-computed cross sections at reference temperatures ten times over the present state-of-the-art.
Nonetheless, to reap the full benefits of Embedded Monte Carlo, we must be able to sample stochastic nuclear cross sections at any temperature on-the-fly, that is without any interpolations nor pre-computations stored in memory. Two capabilities are needed for this: 1. Generate on-the-fly stochastic cross sections from their nuclear data uncertainty distribution at zero Kelvin; 2. Doppler broaden them to any temperature on-the-fly. We achieve both by developing a new mathematical formulation of the quantum physics models for nuclear interactions — the *windowed multipole representation* of R-matrix cross sections — which changes the parameter space of nuclear data, replacing traditional resonance parameters with windowed multipole parameters.

The multipole representation of nuclear cross sections was introduced by R. Hwang at the end of the 20th century, with the promise of enabling on-the-fly Doppler broadening. Yet it suffered from a set of drawbacks: the formalism was only valid for neutron particles without threshold; there was no analytic way to perform Doppler broadening at low-energies; and converting nuclear resonance parameters data to multipoles was complex and numerically unstable. We solved all these issues by fully establishing the *windowed multipole representation* as an alternative physical parametrization of nuclear cross sections (R-matrix theory), encompassing charged particles and thresholds, thereby providing the foundations for a standard nuclear data *Windowed Multipole Library*. We showed Hwang's numerical instabilities were caused by spurious pole parameters, and derived the correct number of poles, proving unexpected cancellations. We also established methods to directly convert nuclear data and its uncertainty into windowed multipole parameters and their corresponding covariances. We moreover derived a method to Doppler broaden windowed multipole cross sections at low-energies. In the process, we were also able to establish arbitrary order temperature derivatives of cross sections, which could prove a boon for thermal feedback multi-physics coupling computations. Finally, we derived a neutron slowdown benchmark which, for the first time, analytically solves the neutron slowdown problem across overlapping resonances, using multipole cross sections. We validate

our new Embedded Monte Carlo method on this analytic benchmark, comparing its results to Total Monte Carlo and first-order Bayesian sensitivity analysis.

By enabling the on-the-fly sampling of uncertain nuclear cross sections and their analytical Doppler broadening, the Windowed Multipole Library cuts 1,000 times over the memory requirements of cross section Doppler broadening, at virtually no additional processing cost, in turn compounded over the 1000-10,000 samples of uncertain nuclear cross sections required to run Nested Monte Carlo (while Doppler broadened uncertainty quantification remains out-of-reach of previous sensitivity analysis). Thus, compared to Nested Monte Carlo, using the Windowed Multipole representation for Embedded Monte Carlo uncertainty quantification achieves the same accuracy on the reconstructed outputs distribution with 10–100 times less neutrons (and thus processor cost), and 200,000–2,000,000 times less memory: a game-changer for modern supercomputers.

As such, we here introduce a versatile suite of novel physics, statistics, algorithms, benchmarks, and methods, which can be deployed to perform on-the-fly non-linear uncertainty propagation and inference across nuclear Monte Carlo computations: a breakthrough in the field.

1.3 The claims

This thesis establishes novel statistical methods and algorithms, combined with new mathematical representations of nuclear physics models, which enable us to infer and propagate nuclear data uncertainty across Monte Carlo simulations of nuclear technologies. The main contributions come in seven areas:

1. Establishing Embedded Monte Carlo, a suite of new statistical methods and algorithms to perform approximate Bayesian inference of nuclear data uncertainty across nuclear transport computations. This Embedded Variational Inference is performed by a stochastic approximation algorithm that minimizes the information loss when constraining the Bayesian posterior to a given parametric family [132, 133].

2. Conversely, Embedded Monte Carlo can then also perform approximate non-linear forward propagation of nuclear data uncertainty across nuclear transport computations. This Embedded Forward Propagation is achieved by constructing unbiased estimators of the nested moments, and reconstructing the distribution of outputs accordingly [132, 133]. Given a fixed number of total simulations, we established the optimal inner-loop-to-outer-loop trade-off between converging the mean and the variance of the distribution (figure 3-4).

3. Generalizing the windowed multipole formalism to all R-matrix cross sections [130], in the process discovering many new mathematical and physical properties in R-matrix theory [125, 127], including: Mittag-Leffler expansions of

the outgoing wavefunction and its reduced logarithmic derivative; generalization of the alternative (Brune) parametrization to the Reich-Moore formalism; existence of shadow alternative (Brune) poles; analytic continuation properties (poles cancellations, generalized unitarity, evanescent closure of cross sections below threshold); radioactive parameters properties (number and location on the energy-wavenumber multi-sheeted Riemann surface, poles and residue widths channel radii invariance properties); generalized Reich-Moore formalism (converting complex Reich-Moore resonance energies to equivalent real R-matrix formalism); windowed multipole formalism (analytic continuation and residues estimation by contour integrals around the radioactive poles).

4. Establishing new methods to convert resonance parameters and their covariance matrices into windowed multipoles with their multipole covariances [130].

5. Deriving new methods to Doppler broaden windowed multipole cross sections, in the wake obtaining their temperature derivatives to arbitrary order [197, 130].

6. Establishing an optimal quadrature *kernel reconstruction* method for Doppler broadening interpolation of point-wise nuclear cross sections [124].

7. Deriving an analytic benchmark for neutron slowdown [298, 53], with which the Embedded Monte Carlo methods were validated [132, 132].

These contributions are documented in 9 peer-reviewed journal articles – 8 of which are published [298, 53, 130, 125, 127, 262, 124, 197], and 1 still under review [132] – as well as 7 conference papers [133, 129, 60, 222, 123, 131, 128] (one still under review [133]). Together, their results constitute the core of this thesis.

Chapter 2

Background: Monte Carlo particle transport & nuclear data uncertainty

All models are wrong, but some are useful.
- George Box

Ever since nuclear weapon tests were banned [19, 20, 15, 47, 233, 213, 40], and stringent regulatory constraints on nuclear power made prototype development prohibitive, the entire nuclear field – from weapon stewardship [39, 44, 204], fission or fusion electric power generation [312, 37, 310], to medical [224, 226] and space [247, 297] applications, or scientific investigations such as materials damage [17, 248] – has had to rely on nuclear computations to design and innovate.

One of the greatest challenges for these simulations has been the accurate quantification and efficient computation of uncertainties (both on inputs and outputs) [237, 14, 174, 46]. This doctoral thesis introduces a series of novel tools — from nuclear physics formalism to applied mathematics methods and statistical inference algorithms — which, when combined, can systematically quantify uncertainties in nuclear simulations with equal or superior accuracy than previous state-of-the-art methods, while outperforming them on computational efficiency by several orders of magnitude.

2.1 Monte Carlo particle transport: nuclear simulations

The Monte Carlo method — ubiquitous in modern science [211, 240, 170] — was born at Los Alamos National Laboratory during the Manhattan project for the sole initial

purpose of simulating nuclear weapons [241, 239]. Monte Carlo particle transport codes are extremely computationally intensive, which is their major drawback. So much so that they have pioneered and been at the forefront of the high-performance computing field [141, 176, 7, 229], and, still today, US Department of Energy National Laboratories [18] — specially the nuclear weapons stewardship ones of Los Alamos (LANL) [16], Lawrence Livermore (LLNL) [13], and Sandia (SNL) [27], but also broader scientific and R&D laboratories such as Oak Ridge (ORNL) [22], Argone (ANL) [3], or Brookhaven (BNL) [4] — possess the world largest supercomputers [35, 38, 9, 33, 29, 30, 36], dedicated to solving the particle transport problem for weapon stewardship programs [1, 142, 204, 277] (figure 2-1).

(a) Weapons simulations.

(b) "Trinity" supercomputer, LANL.

Figure 2-1: Nuclear computations have been necessary for the stewardship of nuclear weapons stockpiles ever since tests were banned [7]. This spearheaded both the Monte Carlo method [241, 239], and the high-performance computing field [229]. Today's top world supercomputers are dedicated to nuclear computations [142] in National Laboratories [18]: here the "Trinity" supercomputer [36] at Los Alamos National Laboratory [16].

Monte Carlo particle transport codes are the "gold standard" for such high-fidelity predictive simulations of nuclear technologies. As such, in addition to their initial nuclear weapons stewardship mission, they are used in many scientific investigations requiring the modelling of transported nuclear particles (radiation), ranging from science research (astronomy, climate, and medical sciences), to computer-assisted design for companies proposing new nuclear technologies with novel geometries and physical regimes (figure 2-2).

Given how mission-critical the outputs of nuclear Monte Carlo codes can be, it is of paramount importance to properly quantify their uncertainty. Since they are stochastic, Monte Carlo codes introduce *statistical uncertainty* to their results, which is reduced by simulating the random walks of ever more particles. In addition to this, one must also account for the *epistemic uncertainty* introduced by our incomplete knowledge of the simulated phenomena and of the code inputs. Monte Carlo particle transport codes take two inputs: (a) the reactor geometry (spacial configuration and materials); and (b) the quantum physics properties of individual nuclear interactions,

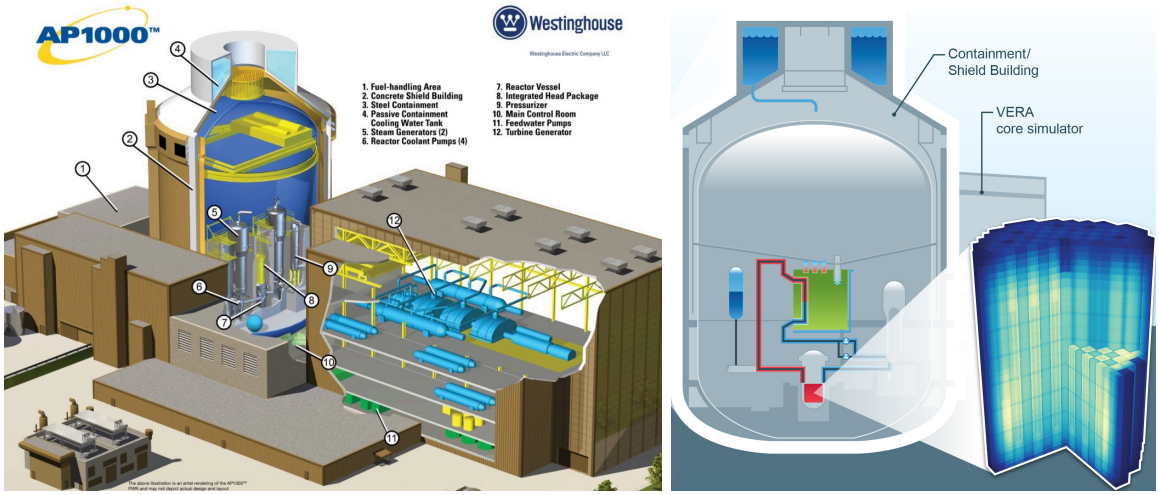

(a) Westinghouse AP-1000 reactor (2018). (b) Monte Carlo core simulation (2014).

Figure 2-2: Nuclear reactor simulations: help design nuclear technologies by computing the power distribution of reactor cores (and other reaction rates). Here a simulation of the Westinghouse AP-1000 [2] pressurized light water reactor [6], performed in 2014 by CASL [5].

parametrized by so-called *nuclear data* (figure 2-3).

Monte Carlo particle transport codes — such as MCNP [138], FLUKA [69], Geant4 [58], TRIPOLI-4 [91], Serpent [219], OpenMC [287], the SCALE suite [28](KENO, TSUNAMI, etc.) or Shift [257], etc. — simulate the outcomes of a myriad of nuclear particles (neutrons, photons, protons, decay products, etc.) transported across the geometry of the system, where they interact, scatter, and react with the nuclei of the core. This random walk spans the space, momentum (velocity or frequencies and therefore energy and angles), and time dimensions, and as such constitutes a considerable computational challenge.

In the case of commercial nuclear power reactors (figure 2-2), neutrons are typically born at high energy from fission reactions. As they collide (scattering) with nuclei across the geometry of the core, they change energy: mostly slowing down until they reach thermal equilibrium. Along the way, they can occasionally be absorbed to yield other nuclear reactions (fission, photon-emission γ-capture, α, β or other decays, fusion, etc.). Many such reactions release energy, which is subsequently deposited in the core and impacts material temperatures. Some reactions produce more neutrons than they consume (notably fission of uranium ^{235}U produces 2.5 neutrons on average while plutonium ^{239}Pu yields 2.88), so that if they happen in the right quantity they can sustain a chain-reaction, a state called *criticality*, which can dampen out, stabilize, or run-away. In this branching process, the mean number of new neutrons produced by each born neutron is called the multiplication factor k_{eff}. The chain reaction is maintained (criticality) when $k_{\text{eff}} = 1$, whereas $k_{\text{eff}} < 1$ (subcriticality) entails a the chain reaction cannot be sustained, and $k_{\text{eff}} > 1$ (supercriticality) an exponentially increasing chain reaction. The outputs of Monte Carlo nuclear simulations are thus

the different particle densities and fluxes, and their resulting reaction rates, output power, and multiplication factor (figure 2-2). The inputs are: (i) the geometry of the system, and; (ii) the outcomes of individual nuclear reactions, parametrized by nuclear cross section data (figure 2-3).

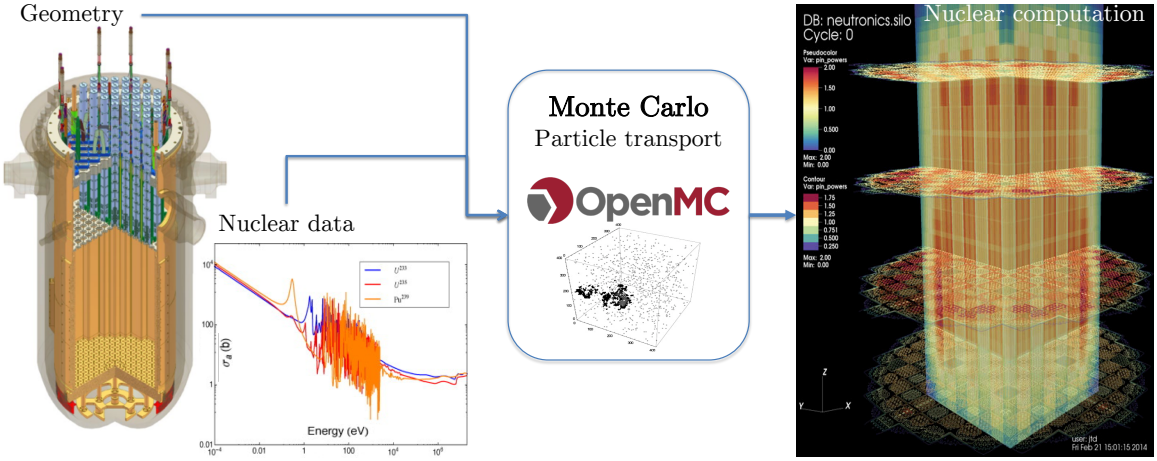

Figure 2-3: Nuclear computations take two inputs: (i) geometry; and (ii) cross sections. These are fed into a Monte Carlo particle transport code (or alternatively a deterministic reactor physics code), such as MCNP [138] or OpenMC [287], which in turns outputs the reaction rates in the nuclear core. Here shown is the full core 3D Monte Carlo simulation of the AP1000 first startup cycle produced by VERA in 2014 [31], developed by CASL.

2.2 Nuclear data & cross sections: Parametrizing quantum interactions

When two nuclear bodies collide and interact, different (probabilistic) outcomes are possible: they can bounce back (scattering) with a transfer of kinetic energy; they can form a new compound nucleus which is often less stable and thus decays, releasing a photon, an alpha particle, or even breaks up into two large stabler nuclides (fission) while releasing extra neutrons. If the compound nucleus is more stable (fusion) the extra energy is released in the form of highly energetic particles (often neutrons or protons). The rates at which all these different outcomes occur when the two bodies interact are quantified by nuclear *cross sections*. Nuclear cross sections depend on the relative energy of the collision, and exhibit quantum resonances, as can be seen in figure 2-4 for uranium ^{238}U and ^{235}U. A general quantum physics theory, called *R-matrix theory* [200, 79, 214, 120], models such interactions and parametrizes this energy dependence with a set of *resonance parameters*, together called *nuclear data*. Nuclear data thus constitutes our collective knowledge of nuclear interactions, which nations document in standard *Evaluated Nuclear Data Libraries*: ENDF [87] (USA), JEFF [267] (Europe), JENDL [293] (Japan), CENDL [153] (China), BROND [80] (Russia), TENDL [207, 209] (TALYS).

Throughout this thesis, we will symbolically denote nuclear cross sections at zero Kelvin (no temperature effects) as $\sigma_0(E)$, and the resonance parameters (and all

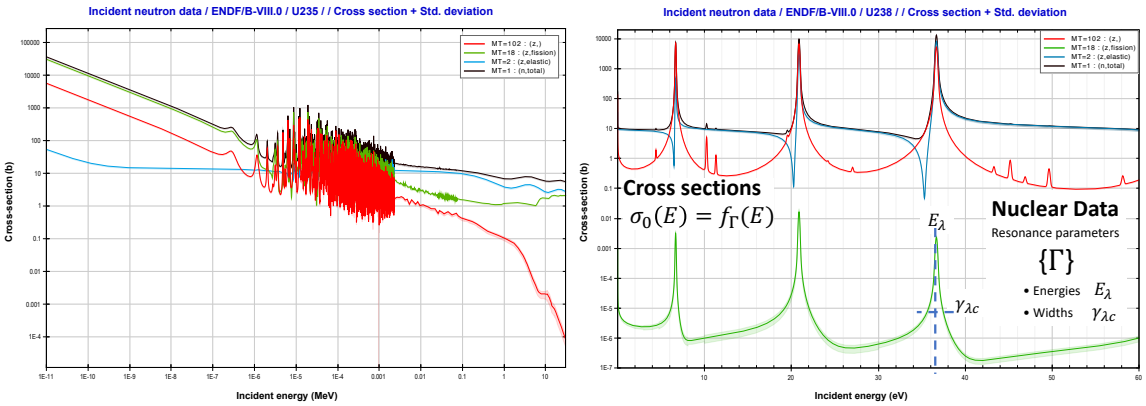

(a) ^{235}U nuclear cross section (wide energy range).

(b) ^{238}U first resonances (3 s-waves and 8 p-waves).

Figure 2-4: Nuclear cross sections quantify the ratios of different outcomes occurring from a nuclear integration, which depend on the energy of the colliding bodies. This energy dependence of cross sections is parametrized by nuclear data, which describe the quantum resonances (energies E_λ and widths $\gamma_{\lambda c}$) as well as the threshold reactions. (a) Several energy ranges for ^{235}U: low/thermal energy; resolved resonance; unresolved resonance; and high-energy/optical model. (b) First resonances of ^{238}U, data from JANIS [11]. Natural uranium is composed of about $\sim 99.3\%$ of ^{238}U and $\sim 0.7\%$ of ^{235}U. Only the latter has a large fission cross section at low energies, hence the need for enrichment.

nuclear data) as $\{\Gamma\}$, so that R-matrix theory formally describes nuclear cross sections as a parametric function of energy (represented in figure 2-4):

$$\sigma_0(E) = f_\Gamma(E) \tag{2.1}$$

2.3 The inference problem: Nuclear data evaluations and inputs uncertainty

Nuclear data is a convenient way of parametrizing nuclear cross sections, but we cannot measure resonance parameters directly. Only cross sections are observable. To construct the nuclear data libraries, an *evaluation* process must thus be undertaken, whereby resonance parameters are inferred from experimental data.

Nations conduct experimental campaigns to collect nuclear cross section measurements at different energies. Such setups are called *differential experiments*, in that they are an attempt to directly measure nuclear cross sections at an atomic level. Pulsating beams of particles (photons, neutrons, protons, alpha particles, etc.) are projected against target nuclei, and the different reaction outcomes (scattering, capture, fission, fusion, alpha or beta decay, etc.) are measured along with their experimental uncertainty. The energy of the incoming pulsed beam is selected (to a given accuracy), for instance the velocity of non-relativistic neutron particles (and there-

fore their kinetic energy) is resolved by chopping the time-of-flight between the source and the target, with longer distance allowing for higher accuracy [94]. As such, these differential experiments for nuclear data evaluations require large, expensive facilities such as the GELINA [103] one shown in figure 2-5.

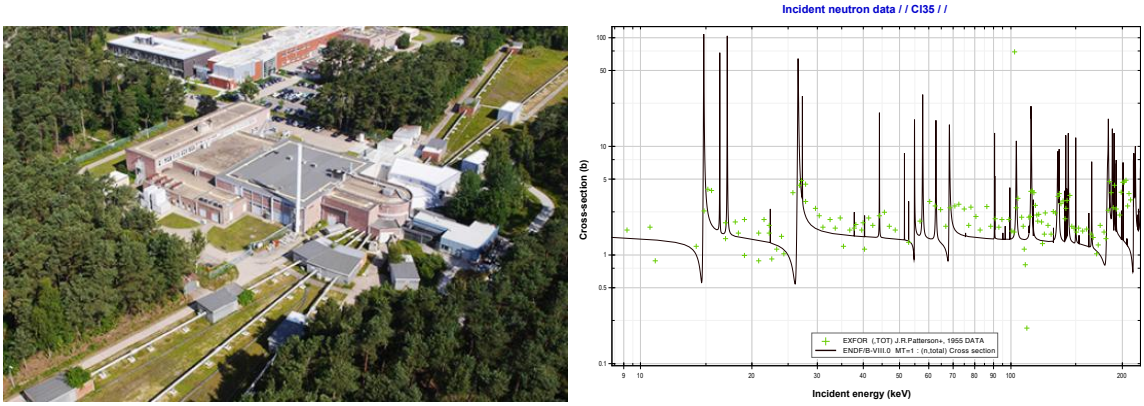

(a) GELINA differential experiment facility. (b) ^{35}Cl total cross section measurements

Figure 2-5: Evaluations of nuclear data: differential experiments measure cross sections, from which evaluators infer resonance parameters. (a) European GELINA neutron differential experiments facility [103]. (b) Chlorine ^{35}Cl total cross section experimental measurement points, and the resulting evaluated cross section plotted from the inferred resonance parameters.

Having collected the differential experiments measurements, evaluators must in turn interpret these results under the prism of the information we have on the experimental setup, and on our knowledge of nuclear physics interactions — the R-matrix theoretical quantum models of nuclear interactions parametrized by nuclear data — in order to infer the values of the nuclear data (their uncertainty) that most faithfully reproduce the experimental observations.
The observed cross section measurements are thus fitted with R-matrix codes [45, 309] — such as EDA [164, 166] (Los Alamos National Laboratory LANL), SAMMY [26, 217] (Oak Ridge National Laboratory ORNL), RAC [107] (China), CONRAD [106] (France), AZURE [63], etc. — to infer the corresponding resonance parameters $\left\{\Gamma\right\}$ nuclear data. Because measurements invariably introduce epistemic experimental uncertainties (both energy and cross section resolution), $\sigma(E_i \pm \Delta E_i) \pm \epsilon_i$, these translate — through R-matrix cross section parametrization (2.1) — into a distribution of input resonance parameters $\left\{\Gamma\right\}$. Traditionally, the latter has been represented as a multivariate normal distribution, $\mathcal{N}\left(\Gamma, \mathbb{V}\mathrm{ar}\left(\Gamma\right)\right)$, whose mean is the estimated true value of the resonance parameters, and whose covariance matrix quantifies our uncertainty on that estimate (figure 2-6 illustrates the uncertain cross section measurements and the corresponding covariances). Evaluated nuclear data libraries therefore document both the mean and the covariance matrix of their resonance parameters. Presently, two methods compete to infer nuclear data and its uncertainty from differential experiments: stochastic inference; and sensitivity inference.

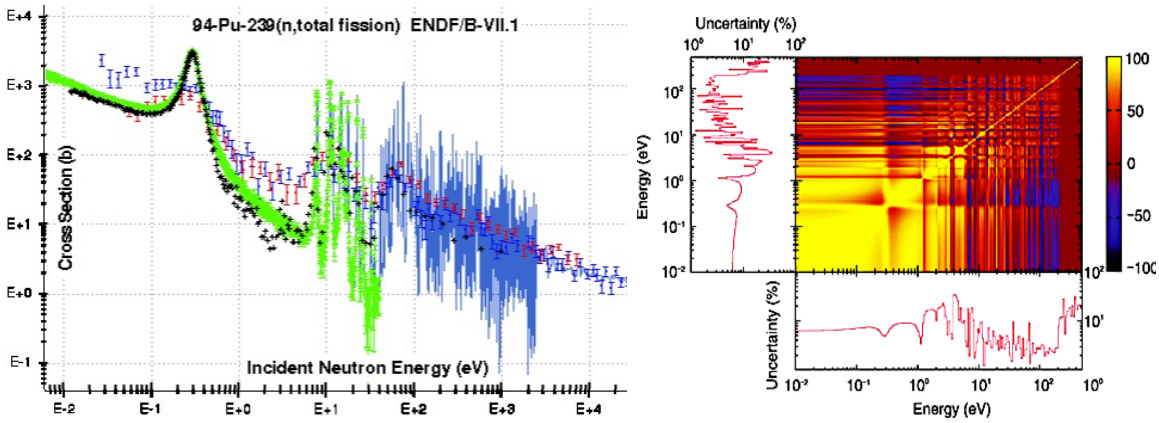

(a) ^{239}Pu neutron-induced fission (cross section measurements with uncertainties).

(b) Uncertainty covariance matrix

Figure 2-6: Nuclear data uncertainty. Uncertainty in nuclear cross section measurements from differential experiments (a) translate into an uncertainty distribution of nuclear data resonance parameters $\{\Gamma\}$, traditionally represented as a covariance matrix (b).

2.3.1 Stochastic inference: Bayesian Monte Carlo histogram

Stochastic inference is the direct numerical point-wise Bayesian inference of nuclear data, yielding a histogram of resonance parameters. As such, it is the most straightforward way to infer the uncertainty distribution of nuclear data from experimental observations. Formally, it can be expressed as follows.

Consider a set of input parameters, denoted X in general, in this case these are the nuclear data resonance parameters $X = \{\Gamma\}$. We denote $Z(X)$ the observable quantity, for a nuclear data evaluation this would be the cross sections measured in a differential experiment, parametrized as (2.1) from R-matrix theory $Z(X) = \sigma(E) = f_{X=\Gamma}(E)$. The differential experiments provide us with a data-set $D \triangleq \{Z_i\}$ of noisy observations — measurements of $Z(X)$ cross sections at different energies with their experimental uncertainty as in figure 2-6(a) — from which we seek to infer a new distribution of input parameters $X|D$ (nuclear data), starting from a given prior distribution $p(X|\theta)$. We can do this directly by computing the likelihood $p(D|X)$ of observing D for each possible input values X, and then numerically estimate the Bayesian posterior $p(X|D)$ histogram using Laplace's VI$^{\text{th}}$ principle of inference [215]:

$$p(X|D) = \frac{p(D|X)p(X|\theta)}{p(D|\theta)} \tag{2.2}$$

For any given input parameters value X, computing $p(D|X)$ — that is the probability that inputs X produced observables D given their uncertainty — requires calculating $Z(X)$ and comparing it to the experimental measurements Z_i. In a differential experiment evaluation, the observable $Z(X)$ may be a direct cross section point $Z(X) = \sigma(E)$, of which we know the parametrization from R-matrix theory (2.1), or a ratio of such cross sections, all in a well-defined and simple geometry at a

known temperature and controlled environment. Evaluators can therefore accurately model the experimental setup and directly compute, for any given set of nuclear data parameters X, the corresponding observables $Z(X)$, and thereafter perform Bayesian inference (2.2) numerically, building a histogram of posterior resonance parameters $X|D$. Note that this requires a correct accounting of the measurements $D = \{Z_i\}$ uncertainties, itself a tricky problem requiring models of the experimental setup and the detectors resolution profiles. Also, an issue common to any Bayesian inference is that of specifying an appropriate prior distribution $p(X|\theta)$.

This stochastic inference method has been called *Unified Monte Carlo* [100, 101] or *Bayesian Monte Carlo* [70, 205, 206] in the nuclear data evaluation field, and the TENDL nuclear data library is built in this fashion, using the TALYS code [70, 208, 207, 205, 206, 209]. Stochastic inference has the major advantage of being the exact and direct application of Bayes rule (2.2). It can therefore account for any type of input and output distributions, and thus go beyond the simple use of multivariate normal distributions and their covariance matrices. There is indeed a push in the nuclear data evaluation community towards the use of other uncertainty distributions, such as lognormals, as some nuclear data parameters must be positive, or exhibit skewed Bayesian posterior histograms.

Yet, though conceptually simple, stochastic inference is not the norm for nuclear data evaluations: the most widespread approach to date is *sensitivity inference* hereafter explained in section 2.3.2. This may in part be due to the following drawbacks:

- As most Monte Carlo methods, stochastic inference can be computationally expensive.

- In stochastic inference, the posterior distribution comes out in the form of a point-wise histogram. Storing this information, and sampling from the uncertainty distribution, therefore becomes a challenge of its own. Some approaches have consisted in fitting the posterior distribution with a well-known parametric family which is both simple to store and to sample from [100, 194]. Alternative "brute-force" approaches have also been proposed [101, 205], to sample directly from the histogram (Markov-chain Monte Carlo (MCMC) [240], Metropolis-Hastings [170], etc.). But these are cumbersome and unfeasible in practice, they are also somewhat of an overkill considering that the posterior histograms are often well fitted by simple distributions (lognormal or normal). Moreover, the precise posterior also depends on the uncertainty distribution of the measurements, which themselves can also be somewhat arbitrarily set (usually normal, exponential, Poisson, or log-normal). As such, nuclear data uncertainty is a good illustration of George Box's adage: "All models are wrong, but some are useful.".

Regardless of which method was used to perform the nuclear data evaluation — stochastic inference (here explained in section 2.3.1) or sensitivity inference (hereafter explained in section 2.3.2) — we obtain a Bayesian posterior distribution of nuclear data (usually described as a multivariate normal distribution of resonance parameters Γ with its mean vector and covariance matrix). Figure 2-7 shows how sampling from

this nuclear data uncertainty distribution in turn generates stochastic cross sections, through functional parametrization (2.1). The distributions of these stochastic cross sections balance the different uncertainty profiles from various measurements.

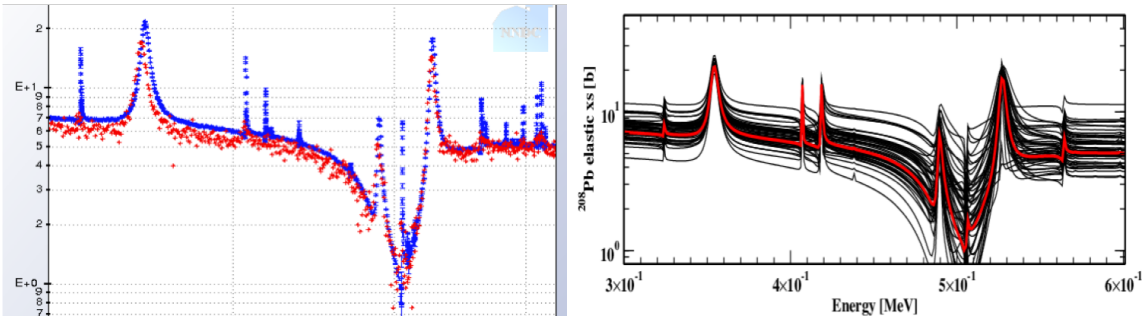

(a) ^{208}Pb cross section measurements (differential experiments)

(b) Stochastic cross sections (^{208}Pb)

Figure 2-7: Stochastic cross sections. Uncertainty in nuclear cross section measurements from differential experiments (a) translates into a distribution of resonance parameters $\{\Gamma\}$. Sampling from this nuclear data uncertainty distribution generates stochastic nuclear cross sections (b). In red (b), the ^{208}Pb cross section calculated with the mean resonance parameters.

2.3.2 Sensitivity inference: linear Bayesian Sensitivity Analysis (SA)

The bread-and-butter way to perform nuclear data evaluations is *sensitivity inference*, which is the use of *Sensitivity Analysis* (SA) to infer uncertainty, and simply consists of linearizing the input-to-output relations around the mean values (1$^{\text{st}}$-order Taylor expansion), so as to use conjugate-prior relations to perform Bayesian inference (2.2) analytically (assuming some conditions on the noisy measurements).

Formally, sensitivity analysis (SA) therefore assumes the uncertainty is small, and performs a Taylor expansion around the mean input parameters $X_0 \triangleq \mathbb{E}[X]$, so as to see the 1$^{\text{st}}$-order effects of small input parameters perturbations on the outputs:

$$\begin{aligned} Z(X) &\simeq Z(X_0) + \left.\frac{\partial Z}{\partial X}\right|_{X_0}^{\mathsf{T}} \cdot (X - X_0) \\ &= \langle \boldsymbol{a} | X \rangle + b \end{aligned} \tag{2.3}$$

with

$$\begin{aligned} \boldsymbol{a} &\triangleq \left.\frac{\partial Z}{\partial X}\right|_{X_0} \\ b &\triangleq Z(X_0) - \left.\frac{\partial Z}{\partial X}\right|_{X_0}^{\mathsf{T}} \cdot X_0 \end{aligned} \tag{2.4}$$

This linear approximation (2.3) of the $Z(X)$ relation allows to easily translate various

uncertainty distributions of inputs X into distributions of outputs $Z(X)$ through affine transform (2.3).

This is crucial to perform sensitivity inference, whereby we are provided with a data-set of N_D noisy empirical observations $D = \left\{Z_i\right\}_{i\in[\![1,N_D]\!]}$ of the observable $Z(X)$, and seek to infer a posterior uncertainty distribution on the inputs $X|D$, starting from a given prior $X|\theta$ (say corresponding to our present knowledge), using Laplace's VI$^{\text{th}}$ principle of inference (2.2). A key quantity in this step is the likelihood $p(D|X)$ that the input parameter values X yielded measurements $\left\{Z_i\right\}_{i\in[\![1,N_D]\!]}$. This likelihood naturally depends on the type of noisy observations D. Sensitivity inference can only infer nuclear data uncertainty by assuming Gaussian additive noise for the measurements

$$Z_i = Z(X) + \epsilon_i \tag{2.5}$$

where the noise ϵ_i is normally distributed and heteroskedastic, that is each measurement Z_i has a different known variance Σ_i (the square of the standard deviation) specific to the experimental setup in question, so that the samples from the uncertain measurements are normally distributed as $Z_i \sim \mathcal{N}\left(Z(X), \Sigma_i\right)$, entailing the data likelihood (with $|\cdot|$ denoting the pseudo-determinant):

$$p(D|X) = \prod_{i=1}^{N_D} \left|\frac{\Sigma_i^{-1}}{2\pi}\right|^{\frac{1}{2}} \mathrm{e}^{-\frac{1}{2}\Sigma_i^{-1}\left(Z_i - Z(X)\right)^2} \tag{2.6}$$

Importantly, all the noisy observations Z_i come from the same X parameters. Note that in practice many experimental quantities can be re-cast into this additive noise model (2.5): for instance, for a product of noisy positive variables, a logarithmic change of variables will transform the measurements into this form (2.5).

By linearizing the $Z(X)$ relation (2.3), and assuming additive noise (2.5) with Gaussian data likelihood (2.6), sensitivity analysis can then perform Bayesian inference (2.2) analytically from a multivariate normal conjugate prior distribution, $X|\theta \sim \mathcal{N}\left(\boldsymbol{\mu}_0, \boldsymbol{\Sigma}_0\right)$, yielding a normal Bayesian posterior $X|D \sim \mathcal{N}\left(\boldsymbol{\mu}_D, \boldsymbol{\Sigma}_D\right)$ with the well-known conjugacy relations:

$$\boldsymbol{\Sigma}_D^{-1} = \boldsymbol{\Sigma}_0^{-1} + \boldsymbol{a}\left[\sum_{k=1}^{d} \Sigma_i^{-1}\right]\boldsymbol{a}^{\mathsf{T}} \tag{2.7}$$

$$\boldsymbol{\mu}_D = \boldsymbol{\Sigma}_D\left[\boldsymbol{\Sigma}_0^{-1}\boldsymbol{\mu}_0 + \boldsymbol{a}\left[\sum_{k=1}^{d} \Sigma_i^{-1}\left(Z_i - b\right)\right]\right] \tag{2.8}$$

This linear sensitivity inference is the standard industry practice in the nuclear data field: most evaluation codes, such as SAMMY [26, 217], EDA [164, 166], or CONRAD [106], perform nuclear data evaluations using this 1$^{\text{st}}$-order Bayesian update (2.8), assuming a multivariate normal input X and linearizing $Z(X)$ as (2.3) [43, 282, 162]. Most often, the observable $Z(X)$ corresponds to a differential experiment, where the $Z(X)$ relation is simple enough to obtain analytical expressions for the output of mean inputs $Z(X_0)$ and their sensitivities $\left.\frac{\partial Z}{\partial X}\right|_{X_0}$.

The main advantage of the sensitivity inference method over the stochastic one is that it is simple, producing multivariate normal uncertainty distributions of nuclear data, under the reasonable hypotheses of small perturbations (uncertainty is small) and Gaussian noisy measurements (2.5). To these intrinsic limitations of the sensitivity inference method (which can therefore not capture non-linear lognormal behavior for instance), we can add the complications arising from the non-trivial task of calculating the mean values $Z(X_0)$ and their sensitivities $\frac{\partial Z}{\partial X}\Big|_{X_0}$. Though this is in practice often possible for differential experiments, it is a significant challenge for integral experiments as we explain in section 2.5.2.

2.4 The propagation problem: Monte Carlo codes output uncertainty

Section 2.3 explained the inference problem: how uncertainty in nuclear cross section measurements translates into a distribution of nuclear data resonance parameters Γ, which in turn generates stochastic nuclear cross sections (figure 2-7). This section 2.4 addresses the propagation problem: how these stochastic cross sections, input to the Monte Carlo particle transport codes that simulate nuclear reactors (figure 2-3), entail a distribution of outputs, as represented in figure 2-8. In other words, uncertainties in the input parameters of nuclear computations (nuclear data and geometry) entail uncertainties in the simulated outputs (reaction rates, flux, power, multiplication factor). And in particular, the uncertainty in our knowledge of nuclear physics (nuclear data) propagates across simulations to generate a distribution of outputs, as shown in figure 2-8.

For certain military applications, such as weapons stewardship programs, where nuclear particle transport computations are indispensable, accurately quantifying the range of possible outputs from the simulations — i.e. the output uncertainty distribution — is critically important. The same can also be said for numerous civilian applications, from nuclear medical imaging [81, 275], radiation and criticality safety, as well as for designing future advanced nuclear reactors [12, 21, 24, 25, 10, 41, 42]. For the latter, the nuclear data uncertainty can be a limiting factor. For instance, the Terrapower [34] new molten salt fast spectrum nuclear reactor design (MSR) [8, 114, 32, 301] was calculated to have a considerable 5000 p.c.m. difference in the beginning-of-life k_{eff}, solely due to the changes in the neutron-proton (n, p) cross section evaluations of chlorine ^{35}Cl between the ENDF 7.0 and the 7.1. libraries [68, 311, 312, 12]. Nuclear data uncertainty can also be significant in pressurized water reactors (PWR) calculations: for the PWR full core Martin-Hoogenboom benchmark [178, 177, 179], Total Monte Carlo (and fast-TMC) propagation of uranium ^{235}U, ^{238}U, plutonium ^{239}Pu, and the hydrogen H in water H_2O uncertainties [284, 285], translates into a significant reactor output power uncertainty ranging between 1% and 5%, as shown in figure 2-9. All these instances are testimony to the importance of propagating nuclear data uncertainty across nuclear computations, just as quantifying uncertainty from geometry or material factors [83], or from multi-physics coupling

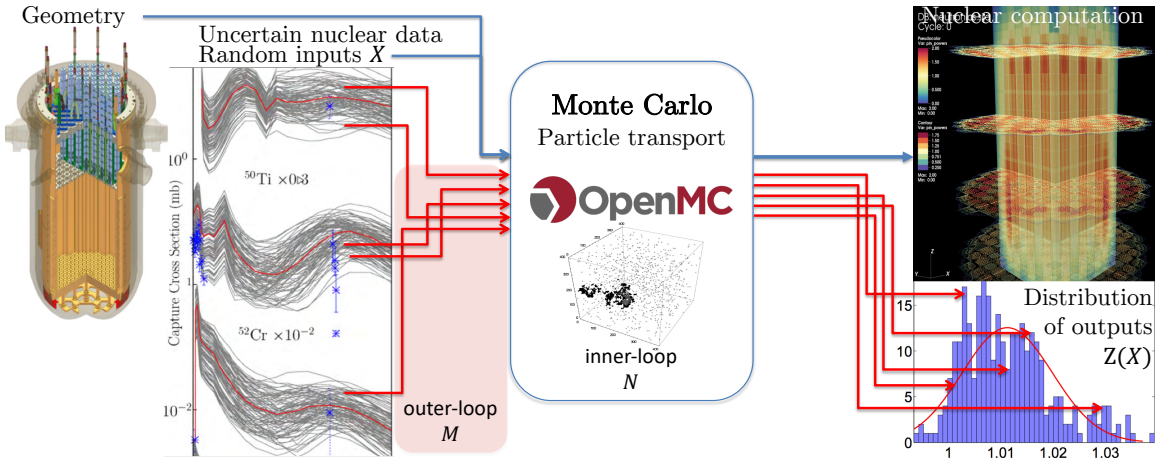

Figure 2-8: Uncertainty propagation: Nested Monte Carlo computations. Uncertain nuclear data inputs propagate across nuclear computations, yielding a distribution of outputs. Directly computing this histogram of outputs requires nesting Monte Carlo simulations: that is sampling many stochastic cross sections (outer-loop of M samples), and for each running a nuclear particle transport Monte Carlo simulation of the reactor core (inner-loop taking N particles to converge), thereby computing a point-wise distribution of outputs. This direct *Nested Monte Carlo* [274] method has been called *Total Monte Carlo* [283, 285] in the nuclear data field.

[329].

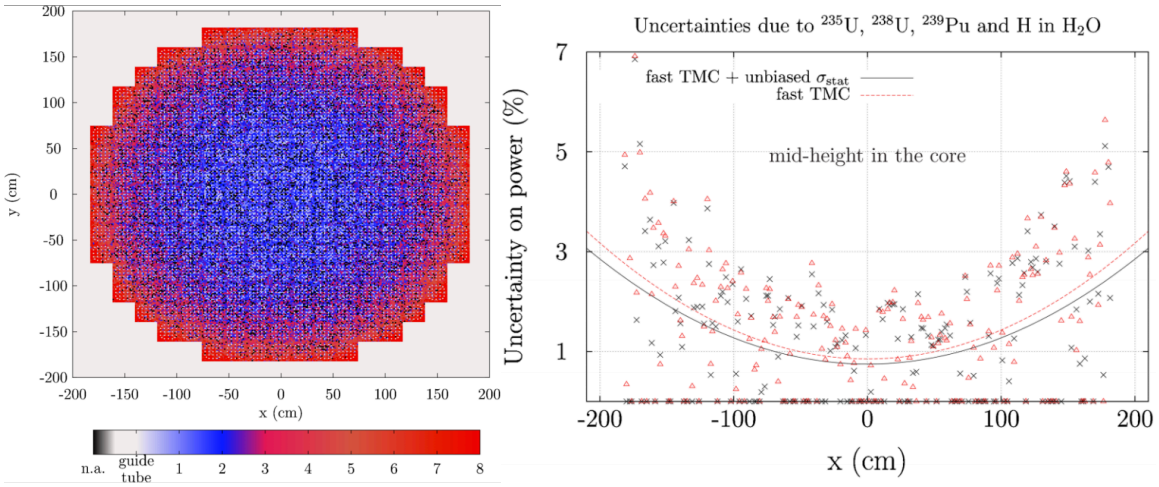

Figure 2-9: Output power uncertainty from nuclear data propagation. Propagating nuclear data uncertainties across the Martin-Hoogenboom pressurized water reactor core benchmark [178, 177, 179] yields 1-5% uncertainty in output power, using the Total Monte Carlo and fast-TMC approach [284, 285].

Just as for the inference problem (section 2.3), the same two main methods compete to solve this propagation problem (amongst many hybrids [330, 140]): stochastic propagation (Nested Monte Carlo (NMC) simulations which are called Total Monte Carlo (TMC) in the field); and sensitivity propagation (Sensitivity Analysis (SA)).

2.4.1 Stochastic propagation: Nested Monte Carlo (NMC)

Stochastic propagation consists of nesting Monte Carlo simulations [274], that is running an outer-loop Monte Carlo on the nuclear data uncertainty, and for each sampled nuclear data value, run a full Monte Carlo particle transport problem to compute its corresponding output observable quantities (multiplication factor k_{eff}, power, flux, reaction rates, etc.), as illustrated in figure 2-8.

This Nested Monte Carlo scheme, called *Total Monte Carlo* in the nuclear data field [283, 285, 284, 172, 55], is therefore conceptually simple in practice: let X be the input parameters to the Monte Carlo particle transport problem (nuclear data or geometry), and denote $Y|X$ the particle transport stochastic process ($Y|X$ is then any tallied quantity). Inputs X have an uncertainty distribution $p(X)$, from which we sample M nuclear data sets X_m (outer-loop). For any such sample X_m of possible input parameters, one then runs N different simulations of the stochastic process $Y_n|X_m$ (inner-loop), averaging them to approximate the conditional means $Z(X)$ with $\widehat{Z}(X_m) \triangleq \frac{1}{N}\sum_{n=1}^{N} Y_n|X_m$.
Propagating the distribution of inputs X to that of outputs $Z(X)$ is then a matter of repeating this process M times over an *outer-loop* of different X_m samples, thereby constructing the point-wise histogram of outputs $p(\widehat{Z}(X_m))$. The latter will converge to the distribution of outputs $p(Z(X))$ as both N and M increase, with an asymptotic convergence rate of $\mathcal{O}\left(\frac{1}{\sqrt{N\times M}}\right)$.

The major drawback of TMC is that it is tremendously expensive computation-wise, precisely because both M and N must be large to converge. Methods such as fast-TMC [285] and half-Monte Carlo [136] have been proposed to address this high computational cost, resting on the principle that in practice one only needs to converge the inner-loop outputs (say reaction rate and k_{eff} tallies) to within the uncertainty we have from the outer-loop (nuclear data outputs distribution), thereby diminishing the number of runs dedicated to the inner-loop. Another major drawback of this Nested Monte Carlo approach is sampling the inputs X_m, which can be impractical to generate and prohibitive to store when pre-computation is needed, as we explain in section 2.6. This is why the vast majority of nuclear data uncertainty propagations are performed using *sensitivity propagation* (SA).

2.4.2 Sensitivity propagation: linearized Sensitivity Analysis (SA)

Sensitivity propagation is the standard in dusty practice for uncertainty propagation in the nuclear data field [89, 203, 90, 265, 259, 294]. Just as for sensitivity inference (section 2.3.2), it consists of assuming the uncertainty in the inputs parameters are small, 1$^{\text{st}}$-order perturbations, and linearize the input-outputs relationship (Taylor expansion) to propagate the inputs uncertainty to the outputs using the simple affine relation (2.3).

The key to this Sensitivity Analysis (SA) is thus to compute the output of the mean inputs, $Z(X_0)$, and the Jacobian derivatives $\left.\frac{\partial Z}{\partial X}\right|_{X_0}$, which are called *sensitivities*.

Once these are obtained, forward propagating the distribution of inputs $p(X)$ to the outputs simply consists in applying an affine transform (2.3), which for the first two moments yields:

- for the mean:

$$\begin{aligned} \mathbb{E}_X\left[Z(X)\right] &\simeq Z(X_0) \\ &= \langle \boldsymbol{a} | X_0 \rangle + b \end{aligned} \tag{2.9}$$

- for the variance:

$$\begin{aligned} \mathbb{V}\mathrm{ar}_X\left[Z(X)\right] &\simeq \left.\frac{\partial Z}{\partial X}\right|_{X_0}^{\mathsf{T}} \mathbb{V}\mathrm{ar}\left[X\right] \left.\frac{\partial Z}{\partial X}\right|_{X_0} \\ &= \boldsymbol{a}^{\mathsf{T}} \mathbb{V}\mathrm{ar}\left[X\right] \boldsymbol{a} \end{aligned} \tag{2.10}$$

For instance, if the input distribution is a multivariate normal with mean vector $\boldsymbol{\mu}_X = X_0$ and covariance matrix $\boldsymbol{\Sigma}_X$, that is $X \sim \mathcal{N}\left(\boldsymbol{\mu}_X, \boldsymbol{\Sigma}_X\right)$, then the distribution of output is also normal, $Z(X) \sim \mathcal{N}\left(\mu_Z, \Sigma_Z\right)$, with the well-known:

$$\begin{aligned} \mu_Z &= Z(\boldsymbol{\mu}_X) \\ &= \boldsymbol{a}^{\mathsf{T}} \cdot \boldsymbol{\mu}_X + b \end{aligned} \tag{2.11}$$

$$\begin{aligned} \Sigma_Z &= \left.\frac{\partial Z}{\partial X}\right|_{X_0}^{\mathsf{T}} \boldsymbol{\Sigma}_X \left.\frac{\partial Z}{\partial X}\right|_{X_0} \\ &= \boldsymbol{a}^{\mathsf{T}} \boldsymbol{\Sigma}_X \boldsymbol{a} \end{aligned} \tag{2.12}$$

In solving the propagation problem to 1$^{\text{st}}$ order, the sensitivity analysis method is both simple and informative, as it answers the physically interesting question of what perturbations in the inputs X are the outputs $Z(X)$ particularly sensitive to. Nonetheless, in addition to the fact that sensitivity analysis is only a linear approximation (intrinsically incapable of translating higher-order non-linear effects), the computation of the sensitivities $\left.\frac{\partial Z}{\partial X}\right|_{X_0}$ are the main drawback of the method (along with its intrinsic limitation to 1$^{\text{st}}$-order linear regime). The latter are indeed difficult to estimate in Monte Carlo transport solvers, increasing about 2-to-10 times over the computational cost of a single $Z(X_0)$ calculation (accounting for the cost of computing the adjoint flux necessary for a critical reactor computation) [89, 203, 90, 265, 263].

2.5 Propagation & inference: Integral experiment evaluations

Section 2.4 described the problem of propagating nuclear data inputs across a Monte Carlo particle transport calculation. We here consider the inverse problem (figure 2-10): if we dispose of (noisy) observations from *integral experiments* — resulting from the transport of particles across a geometry (say the output power, or measured reac-

tion rates of a given nuclear reactor) — can we infer an updated knowledge of nuclear data and our uncertainty on it (elemental nuclear quantum physics interactions)?

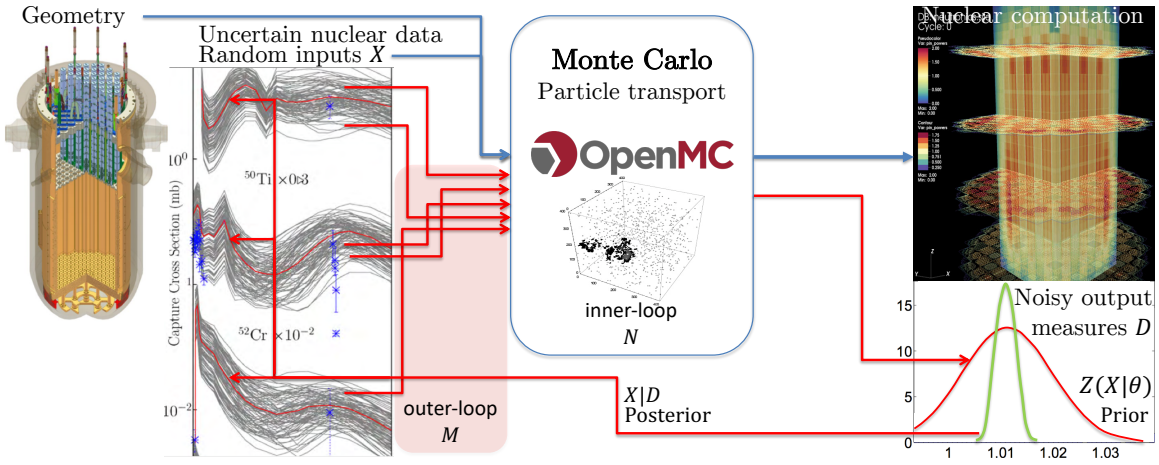

Figure 2-10: Propagation and inference from integral experiments: Prior uncertainty distribution of nuclear data inputs $X|\theta$ propagates across nuclear particle transport Monte Carlo computations, yielding a prior distribution of outputs $Z(X|\theta)$ (computed by nesting Monte Carlo simulations [274] called Total Monte Carlo [283, 285]). We then observe noisy measurements D of the outputs $Z(X)$ (reactor power), and perform Bayesian inference (2.2) on the histogram of outputs, to obtain a posterior distribution of inputs $X|D$ (nuclear data).

Integral experiments consist of large-scale setups, for instance a measure of the conditions which bring a given nuclear reactor mock-up to a sustained chain reaction (*criticality*). Extracting nuclear data (a nuclear physics quantity) from such an integral measure of the multiplication factor (a human-scale quantity) is difficult: one must first forward propagate the prior nuclear data uncertainty, which requires translating resonance parameters values into nuclear cross sections (using R-matrix theory), and then compute how these stochastic cross section propagate through a large scale Monte Carlo particle transport problem with a more complex geometry. In the most simple of cases, this large-scale experimental setup could be a plutonium or uranium sphere brought to criticality. More generally, this means a full experimental reactor mock-up, with corresponding materials and geometry affecting the transport of particles. Such joint inference therefore couples the uncertainty on all the nuclear data values in question (different materials and isotopes).

The common practice in the field has been to use integral experiments mainly for validation of nuclear data and codes, and adjustments to nuclear data are typically made to accurately match a set of experiments. The ability to infer and propagate nuclear data uncertainty across nuclear simulations can then in turn be used to perform computer-assisted design of nuclear experiments especially sensitive to the regions of high uncertainty, thereby providing a tool for efficiently narrowing down nuclear data uncertainty with future experiments.

Because it is in general not possible to invert the function linking output measurements to nuclear data, in order to infer nuclear data uncertainty we must first

be able to translate a given distribution of nuclear data inputs into a distribution of observable outputs from the system: that is to forward propagate the nuclear data uncertainty across the nuclear simulation of the integral experiment. Then, the same two methods compete to infer uncertainty across integral experiments: *stochastic inference*, and *sensitivity inference*.

2.5.1 Stochastic inference: Bayesian Nested Monte Carlo histogram

Just as for differential experiments, stochastic inference takes noisy measurements of the observed outputs (for instance nuclear reactor power or multiplication factor), and computes the point-wise histogram Bayesian posterior. However, for integral experiments this first requires solving the Monte Carlo particle transport problem for each sampled prior nuclear data, as illustrated in figure 2-11. Upon nesting these Monte Carlo simulations [274] — that is a Total Monte Carlo [283] (fast-TMC in practice [285]) forward propagation of uncertainty — the Bayesian update to infer the posterior nuclear data uncertainty distribution $p(X|D)$ is then calculated point-wide on the histogram (see figure 2-11). As for Total Monte Carlo, this is immensely computationally intensive.

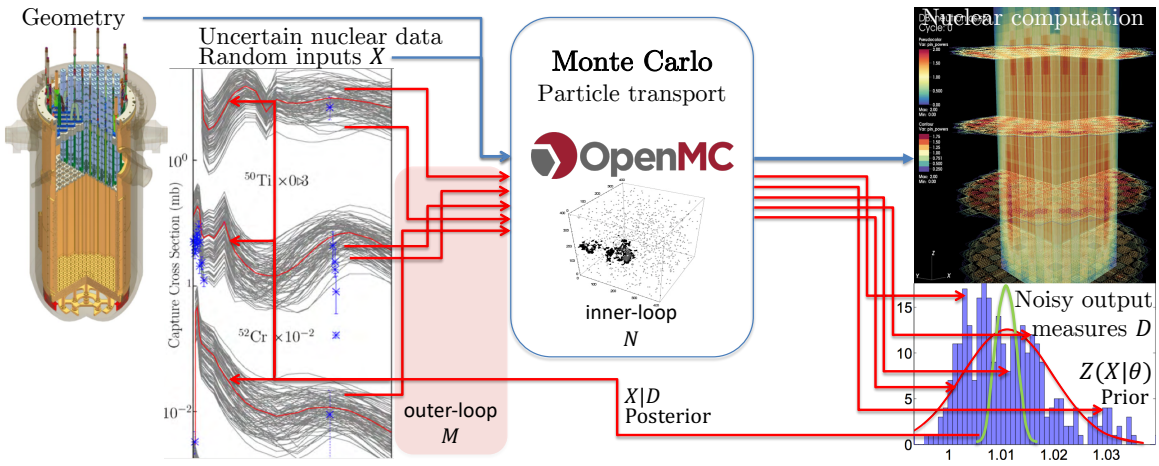

Figure 2-11: Nested Monte Carlo propagation and inference in integral experiments: Prior uncertainty distribution of nuclear data inputs $X|\theta$ is propagated across the Monte Carlo particle transport simulation using the Nested Monte Carlo method [274] (called Total Monte Carlo [283] or fast-TMC [285]), yielding a point-wise histogram of prior output estimates $\widehat{Z}(X_m|\theta)$ (computed by nesting Monte Carlo simulations [274] called Total Monte Carlo [283, 285]). We then observe noisy measurements D of the outputs $Z(X)$ (reactor power), and perform histogram-wise Bayesian inference (2.2), to obtain a posterior distribution of inputs $X|D$ (nuclear data).

The forward propagation is performed by sampling the outer-loop M inputs X_m (nuclear data samples) from their prior uncertainty distribution $p(X|\theta)$. Provided with a data-set D of noisy observations, and having converged the inner-loop, one can in turn compute the likelihood $p(D|X_m)$ of observing the measurements for each

sampled nuclear data set X_m, and numerically perform the Bayesian inference update (2.2) on this histogram (figure 2-11). This stochastic integral inference method [295, 281], which combines "unified Monte Carlo" [100, 101] and "Total Monte Carlo" [283, 285], has been used in various occasions [272], such as for the TENDL [207, 209] nuclear data library [173, 295, 272, 281, 54].

2.5.2 Sensitivity inference: linear Bayesian Monte Carlo Sensitivity Analysis (SA)

When using sensitivity analysis to infer nuclear data uncertainty from integral experiments, the method is the same as for differential experiments: using the conjugate prior relations (2.7) and (2.8) to calculate the Bayesian posterior mean and variance of the multivariate normal nuclear data uncertainty distribution, as explained in section 2.3.2. Such integral sensitivity analysis inference have been performed for evaluations in various nuclear data libraries [315], with integrated frameworks such as MOCABA [175, 281].

Unlike for differential experiments, though, is the way the output of mean inputs $Z(X_0)$ (reaction rates and multiplication factor computed from the prior mean nuclear data resonance parameters X_0) and their sensitivities $\frac{\partial Z}{\partial X}\Big|_{X_0}$ are obtained: a full Monte Carlo particle transport code must now be converged to compute them, which is the sensitivity propagation step described in section 2.4.2. In particular, computing the sensitivities $\frac{\partial Z}{\partial X}\Big|_{X_0}$ and the adjoint flux (necessary to compute the perturbed eigenvalue multiplication factor δk_{eff}) can be numerically challenging, and on average multiplies the cost of the Monte Carlo particle transport run by a factor of two to ten, depending on the method implemented [89, 203, 90, 265, 263].

This is all the more true if we wish to account for the temperature effects on the sensitivities, in particular Doppler broadening (c.f. section 2.6): this is so computationally expensive as to be out-of-reach of present reactor physics computational methods [53, 52, 263]. This hurdle posed by temperature treatments and Doppler broadening leads us to the *sampling problem* of generating nuclear cross section inputs to Monte Carlo particle transport, hereafter discussed in section 2.6.

2.6 The sampling problem: Temperature exacts massive memory cost on stochastic cross sections

Temperature agitates things up. As temperature rises, nuclei vibrate, so that a particle that was going to collide with a target nucleus at a given relative speed if it were at rest now finds it vibrating, thereby lowering or increasing the relative speed (or energy) at which their interaction occurs. The resulting effective cross section is therefore the average of the zero Kelvin cross section (target at rest) over all the possible relative energies at which the target and the particle interact (thermal vibration).

This has the effect of "broadening" the effective cross section resonances, as shown in figure 2-12, because particles that were hitting the targets at peak resonance energies find themselves off due to the vibrations, and conversely particles that were close to the peak find that the vibrations can bring them to the peak resonance energy.

This *Doppler broadening* phenomenon — that is the averaging of cross sections over the thermal motion of the target atoms — is of critical importance in neutron transport applications, as it ensures the stability of many nuclear reactors (negative thermal reactivity feedback caused by increased absorption from Doppler broadening). Accurately accounting for this temperature effect is therefore of paramount importance.

Yet, Doppler broadening is also a major computational hurdle to generating stochastic nuclear cross sections for uncertainty propagation, because present methods rely on memory-intensive pre-processing and storing, and this access to memory is a prominent bottleneck for modern-day supercomputers (which have plenty of processing power).

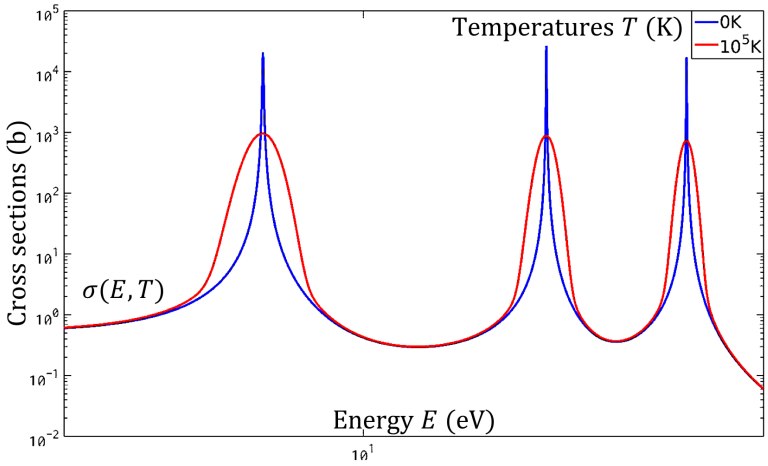

Figure 2-12: Doppler broadening of nuclear cross sections: temperature vibrations of the target nuclei entail the effective cross section is the result of the zero Kelvin one (at rest) averaged over the statistical distribution of the relative velocities with the target nucleus. This Doppler broadening of cross sections can increase absorption as temperature rises, guaranteeing the thermal stability of numerous nuclear power reactors (negative thermal reactivity feedback). Here the three first s-wave resonances of uranium ^{238}U at zero Kelin (blue) and Doppler broadened at 100,000 Kelvin (red line).

2.6.1 The temperature problem: Doppler broadening & Solbrig's kernel

In the semi-classical model of non-relativistic massive particles (i.e. not photons), Doppler broadening of nuclear cross section assumes an isotropic Maxwellian distribution of velocities for the target nuclei (that is a Boltzmann distribution of energies), in what is called the *Solbrig kernel* [300], where the cross section $\sigma_T(E)$ at temperature T and energy E (in the laboratory coordinates) is related to the cross section

$\sigma(E)$ at temperature T_0 as:

$$E\sigma_T(E) = \int_0^\infty \frac{\sigma(E')E'^{\frac{1}{2}}}{2\beta\sqrt{\pi}} \left[\mathrm{e}^{-\left(\frac{\sqrt{E'}-\sqrt{E}}{\beta}\right)^2} - \mathrm{e}^{-\left(\frac{\sqrt{E'}+\sqrt{E}}{\beta}\right)^2} \right] \mathrm{d}E' \tag{2.13}$$

where β is the square root temperature energy parameter:

$$\beta \triangleq \sqrt{\frac{k_{\mathbb{B}}(T - T_0)}{A}} \tag{2.14}$$

A designating the atomic mass number, and $k_{\mathbb{B}}$ the universal Boltzmann constant. Changing variables to $z = \sqrt{E}$, $x = \sqrt{E'}$, and denoting $\mathcal{K}_\beta^{\mathbb{D}}$ the Doppler broadening kernel, yields:

$$\begin{aligned} z^2\sigma_T(z) &= \int_0^\infty x^2 \sigma_{T_0}(x) \cdot \mathcal{K}_\beta^{\mathbb{D}}(z,x)\mathrm{d}x \\ \text{where: } \mathcal{K}_\beta^{\mathbb{D}}(z,x) &\triangleq \frac{1}{\beta\sqrt{\pi}} \left[\mathrm{e}^{-\left(\frac{z-x}{\beta}\right)^2} - \mathrm{e}^{-\left(\frac{z+x}{\beta}\right)^2} \right] \end{aligned} \tag{2.15}$$

2.6.2 Previous state-of-the-art temperature cross section interpolations methods

Computing the Solbrig kernel integral (E.136) is a major challenge of nuclear reactor physics. The traditional way of computing the Doppler broadened cross section at any temperature $\sigma_T(E)$ has been to pre-tabulate and store the exact point-wise cross sections $\sigma_{T_j}(E)$ (usually using the SIGMA1 algorithm of [118]) for several reference temperatures $\left\{T_j\right\}$, and then interpolate between these points to obtain $\sigma_T(E)$ [111, 313, 261]. This requires two grids, for energy (about 100,000 points for uranium 235), and temperature (about 100 different temperatures to interpolate on the range from 300K to 3000K using traditional log-log interpolation [314]), amounting to a considerable memory footprint for storing these pre-computed quantities.

Methods to minimize this memory footprint and perform Doppler broadening (E.136) *on-the-fly* — that is without pre-computations stored in memory yet at a reasonable cost (running SIGMA1 [118] on-the-fly in prohibitive) — have therefore been actively sought after, either from advanced interpolation and quadrature methods (such as the MCNP temperature curve-fit method [326]), new Fourier transform methods [145], or Monte Carlo target motion sampling rejection schemes such as SERPENT [316, 317, 288].

2.6.3 Computational pathway: pre-processing nuclear data libraries

Doppler broadening has been a major computational bottleneck, significantly burdening the pathway of nuclear computations. Nuclear data libraries (say ENDF [104, 87]) must be processed by codes (such as NJOY [228]) in order to:

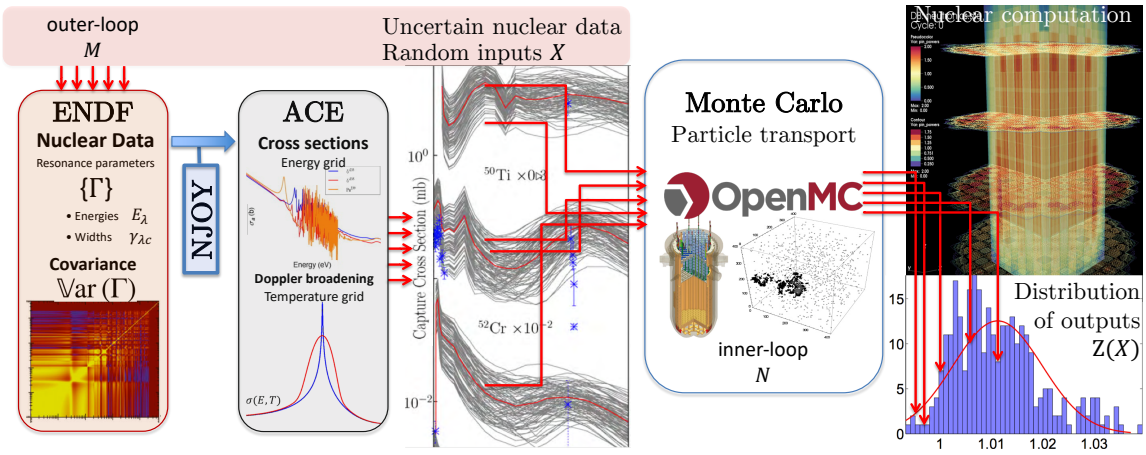

Figure 2-13: The sampling problem: pre-computing Doppler broadened cross sections entails generating stochastic cross sections is extremely memory-intensive. Resonance parameters from nuclear data libraries are processed into point-wise cross sections on an energy and temperature grid (using NJOY code). The operation must be repeated thousands of times to generate stochastic cross sections callable at any energy or temperature.

1. Translate resonance parameters $\{\Gamma\}$ into point-wise nuclear cross sections on an energy grid (about 100,000 points for uranium ^{238}U) at zero Kelvin (no temperature vibrations) using R-matrix theory models (2.1),

2. Transform the zero Kelvin cross sections to the temperature of the experiment, thereby accounting for the effects atomic vibrations have on nuclear cross sections (crystalline structure for low energies, Doppler broadening for higher energies). In NJOY [228], Doppler broadening is performed from the point-wise cross section using algorithm SIGMA1 [118], generating Doppler broadened cross sections at given reference temperatures, from which to interpolate. The classic log-log interpolation requires 100 reference temperatures to achieve a 0.1% accuracy when interpolating between 300K and 3000K [314], while the latest state-of-the-art curve-fit method of MCNP requires pre-storing some 12 coefficients for different temperatures [326], and our Kernel reconstruction optimal quadrature [124] only 10 reference temperaturess (see chapter 4 section 4.1).

Once processed by NJOY [228], these cross sections are reported point-wise (in energy and temperature grids) in ACE files [228], which are the input files to nuclear Monte Carlo particle transport codes (as shown in figure 2-13). For an order of magnitude, the ENDF library (about 400 isotopes) thus processed for OpenMC [23, 287] has a 500MB memory footprint per temperature point, on a 6 reference temperature grid, for a total of 3GB of data (for the resolved resonance range region). To be able to fully treat temperatures ranging from 300K to 3000K using standard log-log interpolation (100 reference temperatures), this should rise to 50GB of data per input file, while 10 references temperatures if using our *Kernel reconstruction method* (see section 4.1 or article [124]) would yield 5GB of data. Note that SERPENT [316, 317, 288]

having an on-the-fly rejection sampling method brings this down to 500MB. Orders of magnitude comparisons between these memory and speed performance of different Doppler broadening methods are compared in table 2.1, where we included our optimal quadrature Doppler kernel reconstruction method and the windowed multipole representation Doppler broadening from chapter 4.

Table 2.1: Doppler broadening methods memory and speed footprint comparisons for a 0.1% interpolation accuracy from 300K to 3000K: traditional log-log interpolation [314]; optimal quadrature Doppler kernel reconstruction [124]; rejection sampling [316, 317, 288]; windowed multipole [130, 197].

	Method	Memory	Speed
Traditional log-log interpolation	point-wise $\sigma(E,T)$ 100 temperatures	ref.	ref.
Kernel reconstruction	point-wise $\sigma(E,T)$ 10 temperatures	10 $\times$ less	same
Rejection sampling	point-wise $\sigma(E,T_0)$ 1 temperature 0K	100 $\times$ less	2 $\times$ slower
Windowed multipole	Windowed multipoles $\left\{\Pi\right\}$ Library	1000 $\times$ less	same

In addition to the cumbersome computational pathway the pre-processing of nuclear data libraries requires, in great part due to Doppler broadening (figure 2-13), the ACE files end up having a sizeable memory footprint. They become intractable once we seek to propagate (or infer) nuclear data across Monte Carlo particle transport codes. For sensitivity propagation, it is currently prohibitively costly to account for temperature effects on uncertainty (Doppler broadening the sensitivities to resonance parameters). For stochastic propagation, the need to generate stochastic nuclear cross sections at any given temperature and energy entails the entire pre-processing operation must be repeated thousands of times over (M times) to perform the outer-loop (figure 2-13). Since $M \simeq 10^3 - 10^4$ (specially for high-dimensionality of input parameter space), this multiplies the point-wise memory requirements by as much, putting the worst-case log-log method at 50-500TB of input data for generating stochastic cross sections. While this would be cut to 5-50TB for the Kernel reconstruction method, or 0.5-5TB for the point-wise rejection sampling method. This huge memory burden is particularly harmful when dealing with supercomputers, where access to memory is a greater bottleneck than processing power. In other words, sampling stochastic nuclear cross sections at any temperature and energy is currently a considerable memory burden.

We have hitherto identified three major challenges when it comes to quantify nuclear data uncertainty in integral experiments: the sampling problem; the propagation problem; and the inference problem. Our thesis proposes new methods to address, and partially solve, all three of them.

Inferring and propagating nuclear data uncertainty across Monte Carlo simulations

To summarize, nuclear data uncertainty is documented in nuclear data libraries (such as ENDF). These propagate across Monte Carlo particle transport simulations to generate a distribution of possible outputs (reactor power, multiplication factor, etc.). Conversely, if we measure these observables (reactor power, multiplication factor, etc.) in a real-world integral experiment, we can then simulate the experiment with a Monte Carlo particle transport code, and infer updated values of nuclear data and its uncertainty. For both these tasks (inference and propagation) there are presently two methods in the field: Sensitivity Analysis (SA), and stochastic Nested Monte Carlo (NMC). The main drawbacks of SA is that it is linear, and it can only propagate uncertainty to one output at the time (because of the need to compute the adjoint flux). It is also presently too costly for SA to compute the temperature effects on uncertainty. The main drawbacks of NMC is that it is extremely computationally intensive, and yields point-wise histogram distributions which are difficult to store and to sample from. Moreover, sampling the stochastic nuclear cross sections for NMC also exacts a heavy memory toll because of the pre-computed Doppler broadening.

In this thesis, we develop new methods to address these three problems: sampling, propagation, and inference.
Chapter 3 presents our new *Embedded Monte Carlo* methods to propagate and infer nuclear data uncertainty across Monte Carlo particle transport simulations. Embedded Monte Carlo avoids the major computational burden of NMC by performing approximate (but fair) propagation and inference using new statistical estimators. This brings down the cost of propagating and inferring nuclear data across Monte Carlo particle transport simulations to about the same as one single reactor simulation without uncertainty quantification.
Chapter 4 finds a solution to the sampling problem in a new formalism for nuclear data parameters, called the *windowed multipole representation*, which enables us to sample parameters and compute the corresponding Doppler broadened stochastic nuclear cross section on-the-fly (without pre-computation), thereby drastically cutting the memory footprint.

2.7 On transport and uncertainty

We close our background chapter on a few remarks regarding particle and Boltzmann transport codes, and on our models of nuclear data uncertainty.

2.7.1 Deterministic versus probabilistic transport solvers

Consider the neutrons and photons bouncing around in the sun, or any other nuclear reactor. The geometry and the physics of the system – such as the outcomes of nuclear collisions – can be described by a set of input parameters X. Given X, the average energy released by nuclear reactions along the stochastic branching process $Y|X$ determines the output power (that is the average number of times an atom is split in nuclear fission or atoms combining in nuclear fusion). This process can be formally expressed as follows. Let X denote the set of input parameters to any given nuclear transport computation (for instance X could be nuclear data or geometry). A Monte Carlo code will simulate the individual random walks, denoted $Y|X$, of the different nuclear particles, tallying their reactions and histories, and averaging them out so as to estimate the expectation value of any given outcome

$$Z(X) \triangleq \mathbb{E}_Y [Y|X] \tag{2.16}$$

whereby any output observable $Z(X)$ is the *ensemble average* over the stochastic process $Y|X$. For instance, $Z(X)$ can be any reaction rate $R_i(E)$ at given energy E (for non-relativistic neutrons this is the kinetic energy $E = \frac{1}{2}m_n v^2$ of the neutron of mass m_n going at speed v), where $i \in \{\text{fis}, \gamma, \text{fus}, \text{tot}\}$ indicates fission, γ-capture, fusion, or any other reaction of interest, including the total reaction rate $R_{\text{tot}}(E)$ from which we derive the particle flux $\phi(E) = \frac{R_{\text{tot}}(E)}{\Sigma_{\text{tot}}(E)}$ (where $\Sigma_{\text{tot}}(E)$ denotes the total cross section at energy E). In the case of a criticality calculation, $Z(X)$ can also be the multiplication factor $Z(X) = k_{\text{eff}}$. This direct Monte Carlo modeling of the particles is a statistical mechanics approach to the problem of particle transport [102, 227].

There also exists a continuous, classical mechanics approach to this problem. In the limit where the number of particles is very large, all quantities tend to their ensemble average (2.16). This expectation value is then subject to a partial differential equation called the *Boltzmann transport equation* [82], which is directly linked to the statistical interpretation of the Fokker–Planck equation or Kolmogorov's forward equation. *Deterministic codes* take this classical mechanics approach, and discretize the energy and space dimensions to numerically integrate the Boltzmann transport partial differential equation, that is the mean behavior of the particles along their overall trajectories. Such deterministic solvers using various methods such as the *method of characteristics*, or the S_N and P_N methods with homogenization and diffusion equivalence [72, 171, 279, 99].

Though they are only valid in the limit of very large number of particles [303, 320, 121, 192, 264], deterministic codes are much more computationally efficient than Monte Carlo particle transport codes, and as such they are the bread-and-butter of the commercial nuclear power industry. They also require a lot of pre-processing and careful neutron preservation during the order reduction process (energy group cross section condensation, spacial homogenization) as well as the integration of their different computational stages (pin-cell, assembly, full-core). This necessitates a long suite of tailored procedures, such as spatial self-shielding (Dancoff factors), energy self-shielding (Livoulant-Jeanpierre resonance mixture models), and other equiva-

lence methods including SPH factors, discontinuity factors, transport correction, etc. [72, 171, 279, 99]. Such fine-tuning of deterministic codes has made them very efficient at modelling standard commercial nuclear reactors, but it has also made them heavily reactor-specific, performing poorly away from these standard well-known configurations. In a way, they are over-specialized: their fine-tuning requires experimental data that cannot easily be gathered for novel or future designs. In a nutshell, deterministic codes, and in particular their pre-tuned inputs, are not always best equipped to deliver the predictive performance and high-fidelity level of simulations required for certain applications.

2.7.2 Modeling nuclear data uncertainty: a plea in favor of distributions

The first principle is that you must not fool yourself
— and you are the easiest person to fool
- Richard Feynman

A final note on the present uncertainty methods in nuclear data. Currently, all methods assume there exists a true value of nuclear parameters X, and consider that the noisy measurements D induce an uncertainty distribution $p(X|D)$ on this true value X, modeled as the mean of $p(X|D)$. This viewpoint warrants that the more experiments we do, the more we narrow our uncertainty on the value of X, as can be seen from the ever-smaller covariance matrices induced by Bayesian update (2.8).

Though this doctoral thesis follows and improves on this general practice in the field, it is our personal belief that this viewpoint is not necessarily the best way to account for and model our uncertainty in nuclear data parameters X. Actually, it is a secret of Polichinelle that the uncertainty inferred from differential experiments – by equation (2.8) – translates into minuscule uncertainties on $Z(X)$, so small that the evaluators manually increase the nuclear data uncertainty to better match that of their differential experiment setup. Yet, when propagated across nuclear transport simulations to integral experiments, these manually enlarged uncertainties predict outputs $Z(X)$ with very large uncertainties, deemed nonphysical considering the accuracy we have on the integral observable $Z(X)$ (say the multiplication factor k_{eff}).

Our opinion is that if two measurements give discrepant values to alleged high accuracy, this should actually increase our uncertainty on the knowledge of X, and not decrease it. Such behavior could readily be achieved by modelling nuclear data as a random variable X (and not a fixed value), and seek to infer its distribution $p(X|D)$ from the (noisy) data D. This is very different from assuming the true value is the mean of $p(X|D)$, which is updated with more experiments as (2.7), and that our uncertainty on this mean narrows down with more experiments as (2.8). Rather, we advocate for an approach that models nuclear data as a random variable X with a

parametric distribution $p(X;\alpha_X)$, which could for instance be a multivariate normal with mean and covariance parameters $\alpha_X \triangleq \{\boldsymbol{\mu}_X, \boldsymbol{\Sigma}_X\}$. We would then seek to infer these parameters α_X of the X distribution (say both the mean and variance) from the experimental observations D, so that if two different experiments produce significantly different results, this would translate into a larger variance for the nuclear data random variable X, thereby increasing our uncertainty on it.

So as to fall in line with the present canon of the field, the subsequent methods presented in this doctoral thesis do not implement this *nuclear data distribution* approach, even though we believe it to be the correct one despite commanding disregard for the orthodoxy that there can only exist one true value of nuclear data (and not a distribution of it). Nonetheless, we reckon the Embedded Monte Carlo method hereafter exposed could be generalized to encompass this perspective, for instance by means of the following procedure: starting from a hyperparameter priors distribution $p(\alpha_X|\theta)$ on the α_X family (if need be a Jeffrey prior), one could then perform Bayesian inference

$$p(\alpha_X|D) = \frac{p(D|\alpha_X)p(\alpha_X|\theta)}{p(D|\theta)} \tag{2.17}$$

where the likelihood is now an integral on all the possible parameter values from the distribution:

$$p(D|\alpha_X) = \int p(D|x) \cdot p\left(x|\alpha_X\right) \mathrm{d}x$$

If the (noisy) observations $D \triangleq \{Z_i\}_{[\![1,N_D]\!]}$ are all independent Gaussians, and assuming the input parameters are a multivariate normal distribution $X \sim \mathcal{N}\left(\boldsymbol{\mu}_X, \boldsymbol{\Sigma}_X\right)$, the likelihood therefore becomes

$$\begin{aligned} p(D|\alpha_X) &= \int \prod_{i=1}^{N_D} p(Z_i|x) \cdot p\left(x|\alpha_X\right) \mathrm{d}x \\ &= \left|\frac{\boldsymbol{\Sigma}_X^{-1}}{2\pi}\right|^{\frac{1}{2}} \cdot \left(\prod_{i=1}^{N_D} \left|\frac{\Sigma_i^{-1}}{2\pi}\right|^{\frac{1}{2}}\right) \cdot \int \mathrm{e}^{-\frac{1}{2}\left[(x-\boldsymbol{\mu}_X)^{\intercal}\boldsymbol{\Sigma}_X^{-1}(x-\boldsymbol{\mu}_X)+\sum\limits_{i=1}^{N_D}\Sigma_i^{-1}\left(Z_i-Z(x)\right)^2\right]} \mathrm{d}x \end{aligned}$$

which, upon invoking some proper assumptions — for instance on the nature of the noise or by locally linearizing $Z(X)$ — may be possible to incorporate into the general Embedded Monte Carlo framework hereafter exposed.

Chapter 3

Embedded Monte Carlo

It is better to be approximately right than precisely wrong.
- Warren Buffet

When seeking to propagate nuclear data uncertainty across Monte Carlo particle transport codes, and conversely infer updated nuclear data values from integral experiments, there currently exists two main methods: sensitivity analysis (SA); and Nested Monte Carlo (NMC). We identified in chapter 2 their various shortcomings, primarily: linear regime and computing the sensitivities with temperature dependence (for SA); gargantuan computational cost (for NMC).

We developed a novel suite of methods, called *Embedded Monte Carlo*, to infer and propagate nuclear data uncertainty across intractable Nested Monte Carlo computations. Embedded Monte Carlo samples different possible nuclear data values from their uncertainty distribution, and is able to converge towards accurate uncertainty estimates for both inference and propagation, despite running only a few non-converged nuclear simulations for each possible nuclear data sample (thereby considerably cutting computational cost). This solves most problems of the prior state-of-the-art Total Monte Carlo and Sensitivity Analysis methods, though bringing about many convergence problems of its own. All the results we here present are published in [133] and [132].

3.1 Embedded Forward propagation

Embedded Forward Propagation (EFP) is a novel suit of algorithms, which we established in [133, 132], to propagate input parameters X distributions to output *ensemble averages* (2.16) (conditional means)

$$Z(X) \triangleq \mathbb{E}_Y [Y|X]$$

The stochastic process $Y|X$ is considered intractable in that computing samples $Y|X$ is feasible, but converging their means $Z(X)$ for many different values of X is not, rendering Nested Monte Carlo [274] prohibitive in practice (called *Total Monte Carlo* in the nuclear data field [283, 285]). Embedded Forward Propagation (EFP) estimates the moments of the outputs $Z(X)$ distribution, at an asymptotic rate of $\mathcal{O}\left(\frac{1}{\sqrt{M}}\right)$ for M input samples X_m (possible nuclear data values from their uncertainty distribution): the same as it would take to compute any single output $Z(X)$. The corresponding distribution of outputs $p(Z(X))$ is then best reconstructed according to some pre-specified family or principle (such as maximum entropy): this excludes fat-tailed distributions (for which the moments are ill defined and cannot be used for reconstruction). Importantly, we established theoretical results for the optimal ratio of inner-loop N to outer-loop M runs, given a total $M \times N$ budget of $Y|X$ simulations.

3.1.1 Embedded Forward Propagation (EFP) synthesis

- Key hypotheses: the distribution of outputs $Z(X|D)$ must belong to a family which is fully parametrizable with its moments (for instance Normal or Lognormal).

- Advantages:

  - Converges at a $\mathcal{O}\left(\frac{1}{\sqrt{M}}\right)$ rate, proportional to the cost of any one Monte Carlo simulation without uncertainty, whereas Total Monte Carlo requires $\mathcal{O}\left(\frac{1}{\sqrt{N \times M}}\right)$ to converge.
  - Can perform non-linear forward propagation, while Sensitivity Analysis (SA) can only perform 1^{st} order linear propagation.
  - EFP can propagate inputs $X|D$ uncertainty to any tally, whereas in particle transport problems SA can only (linearly) propagate uncertainty to one tally at a time (because it needs to compute the sensitivities and the adjoint flux).

- Drawbacks:

  - Looses the point-wise mapping of inputs $X|D$ (nuclear data) to simulation outputs $Z(X|D)$ (tallies such as the multiplication factor).
  - EFP is not exact (but good approximation of outputs distribution through moments reconstruction).
  - Cannot reconstruct fat-tailed distributions.
  - For Monte Carlo particle simulations, EFP does not give the sensitivities (which can be of interest for informing design).
  - The convergence is severely hindered if the output $Z(X|D)$ is not an integral quantity (as is for case for any Monte Carlo computation).

For validation and illustration purposes, we designed an Embedded Monte Carlo toy-problem with multivariate normal parameters $X|\theta$ and Gaussian noisy data (appendix C in [132] transcribed *verbatim* here in appendix A.3), demonstrating the reconstruction capabilities of the EFP algorithm in figure 3-1.

3.1.2 General theory (EFP)

Theorem 1. *Embedded Forward Propagation.*
Let $p(X)$ be a known distribution of input parameters X, which we seek to propagate to the output ensemble averages $Z(X) \triangleq \mathbb{E}_Y[Y|X]$. Considering $p(Z)$ intractable, we approximate it with a parametric family of distributions $p_\zeta(Z)$. If $p_\zeta(Z)$ can be fully reconstructed with a finite amount of propagated moments (which are assumed to exist),

$$\langle Z^k \rangle \triangleq \mathbb{E}_X\left[Z^k(X)\right] \tag{3.1}$$

we can then sample M elements from the $p(X)$ distribution and find the best approximation $p_{\zeta_\star}(Z)$ at an asymptotic converge rate of $\mathcal{O}\left(\frac{1}{\sqrt{M}}\right)$.
In particular, if log-likelihood $\ell_\zeta(Z) \triangleq \ln p_\zeta(Z)$ is polynomial of degree d, knowledge of its first $2d-1$ moments suffices to reconstruct all the polynomial coefficients, through system (A.3) of theorem 4. Similarly, if $p_\zeta(Z)$ is log-normal, knowledge of its first 2 moments yields $\zeta_\star$ through (3.6).

Proof. The "best approximate" Embedded Forward Propagation (EFP) distribution $p_{\zeta_\star}(Z)$ can be defined in various ways. If we choose the principle of minimum discrimination information, we can seek to minimize the Kullback-Leibler divergence [212]:

$$\mathbb{Z}[\zeta] \triangleq \int \ln\left(\frac{p_\zeta(z)}{p(z|D)}\right) p(z|D)\mathrm{d}z = \int \Big(\ell_\zeta(z) - \ell(z|D)\Big) p(z|D)\mathrm{d}z$$

whose gradient can be expressed as expectation value:

$$\frac{\partial \mathbb{Z}}{\partial \zeta}[\zeta] = \int \frac{\partial \ell_\zeta(Z)}{\partial \zeta} p(z|D)\mathrm{d}z = \mathbb{E}_{Z|D}\left[\frac{\partial \ell_\zeta(Z)}{\partial \zeta}\right] \tag{3.2}$$

Optimal meta-parameters $\zeta_\star$ will then annul this gradient:

$$\frac{\partial \mathbb{Z}}{\partial \zeta}[\zeta_\star] = 0 \tag{3.3}$$

Approximating $Z|D$ with parametric distribution $p_\zeta(Z)$ belonging to the polynomial log-likelihood class, we then have:

$$\ell_\zeta(Z) = \sum_{k=1}^{d} b_k[\zeta] \cdot Z(X)^k$$

so that the Jacobians are:

$$\frac{\partial \ell_\zeta(Z)}{\partial \zeta} = \sum_{k=1}^{d} \frac{\partial b_k}{\partial \zeta}[\zeta] \cdot Z(X)^k \tag{3.4}$$

Conversely, if the Jacobians are polynomials in $Z(X)$, then the log-likelihood is polynomial. Akin to our EVI method (theorem 3), we can use the mean-power property (3.28) to construct unbiased estimators

$$\widehat{\frac{\partial \mathbb{Z}}{\partial \zeta}}[\zeta] = \sum_{k=1}^{d} \frac{\partial b_k}{\partial \zeta}[\zeta] \cdot \widehat{Z^k}(X)$$

and undertake an approximate forward-propagation by annulling gradient (3.3) with a fixed-point stochastic optimization algorithm [280, 269]:

$$\begin{aligned} \zeta_{t+1} &= \zeta_t - \gamma_t \cdot \widehat{\frac{\partial \mathbb{Z}}{\partial \zeta}}[\zeta_t] \\ \gamma_t &= \frac{c}{t^\alpha} \text{ , with } 0 < \alpha < 1 \text{ , and } 0 < c \\ \overline{\zeta_T} &\triangleq \frac{1}{T}\sum_{t=0}^{T} \zeta_t \end{aligned} \tag{3.5}$$

Actually, plugging (3.4) into (3.2) shows this approach consists in calculating the (3.1) propagated moments $\langle Z^k \rangle$ and finding the polynomial of which these moments are the roots

$$\frac{\partial \mathbb{Z}}{\partial \zeta}[\zeta_\star] = \sum_{k=1}^{d} \frac{\partial b_k}{\partial \zeta}[\zeta_\star] \cdot \langle Z^k \rangle = 0$$

(note that the negative dominant coefficient condition of theorem 4 can be enforced by searching for $b_d = -c_d^2$). This can be a more complicated problem than directly converging the first $2d-1$ moments $\langle Z^k \rangle$, $k \in [\![1, 2d-1]\!]$, and reconstructing $p_\zeta(Z)$ directly using the linear system (A.3) and normalization condition (A.5) of theorem 4.

The class of distributions that can be fully reconstructed with their moments is broader than the polynomial log-likelihood class. Indeed, the moments problem has a long history [105, 234, 302, 210], and there are many metrics and methods that can be used to approximate distributions using empirical estimates of their moments, from orthogonal polynomial decomposition to the principle of maximum entropy [260]. Consequently, rather than performing stochastic optimization (3.5), which restricts us to the polynomial log-likelihood class in the framework of the minimum discrimination information principle, we can simply estimate the moments of the output mean (3.1), with which we can reconstruct other distributions accordingly. □

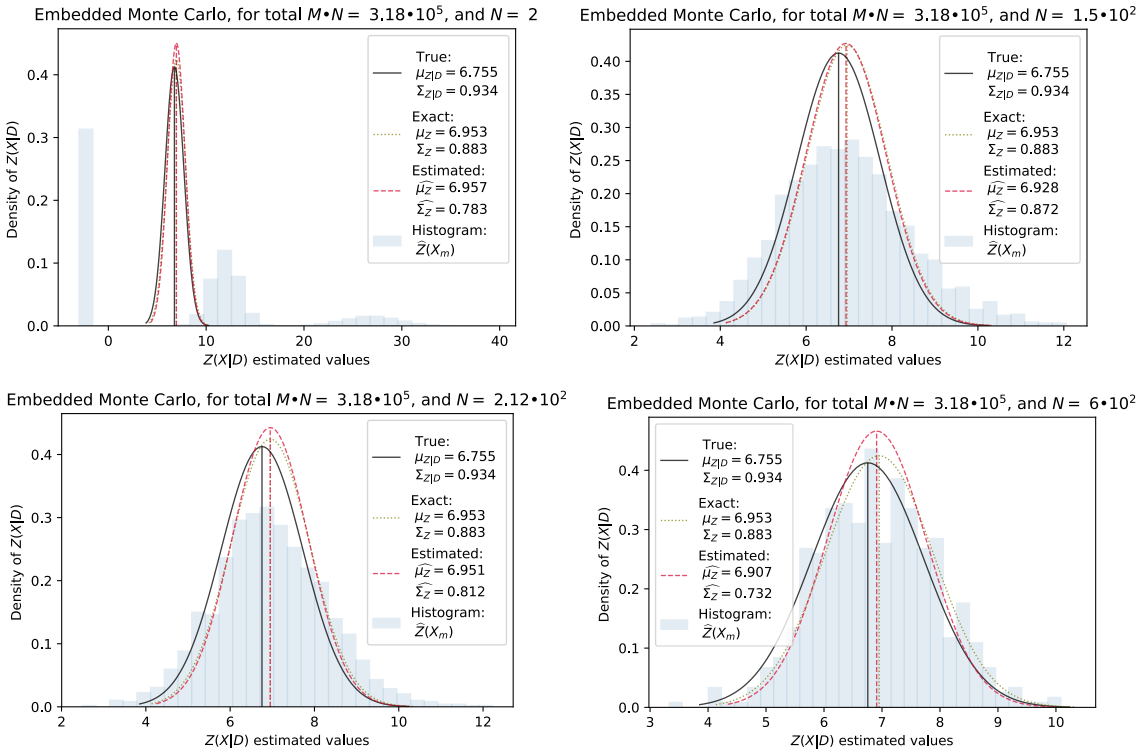

Figure 3-1: Embedded Forward Propagation (EFP) (theorem 1). Inferred parameters distribution from figure 3-5 (EVI) are propagated to the ensemble average using EFP theorem 1. The reconstructed distribution from EFP moments estimation (with $\mathcal{O}\left(\frac{1}{M}\right)$ simulations) matches the Nested Monte Carlo histogram (point-wise propagation with $\mathcal{O}\left(\frac{1}{M \times N}\right)$ simulations). Results from the analytic toy-problem of appendix C in [132], for different levels of inner-loop convergence (given a fixed budget of total runs): minimal convergence (optimal for mean), optimal trade-off, optimal variance convergence, over-converged.

3.1.3 Practical considerations (EFP)

In practice, theorem 1 consists in estimating the forward propagated moments (3.1) – with asymptotic converge rate of $\mathcal{O}\left(\frac{1}{\sqrt{M}}\right)$ – and then approximating the distribution of output means $Z(X|D)$ accordingly. This restricts the Embedded Forward Propagated method to ensemble averages $Z(X)$ that do not have fat-tail distributions, in the sense that the moments of $p(Z(X))$ must exist (note that Embedded Variational Inference (EVI) does not need such requirement to approximately infer posterior distribution $X|D$).

Having estimated the output moments, reconstructing the distribution of ensemble averages $Z(X)$ can be performed in various ways. For instance, under the principle of maximum entropy, the log-normal distribution can consistently (but with bias) be

reconstructed as:

$$\begin{aligned} \mu &\simeq \ln \widehat{\langle Z \rangle} - \frac{1}{2}\sigma^2 \\ \sigma^2 &\simeq \ln\left(1 + \frac{\widehat{\langle \Delta^2 Z \rangle}}{\widehat{\langle Z \rangle}^2}\right) \end{aligned} \tag{3.6}$$

where we plugged-in the unbiased estimators of the outputs mean $\langle Z \rangle \triangleq \mathbb{E}_X\left[Z(X)\right]$ and variance $\langle \Delta^2 Z \rangle \triangleq \mathbb{E}_X\left[Z(X)^2\right] - \mathbb{E}_X\left[Z(X)\right]^2$. If we instead approximate $Z(X|D)$ with a polynomial log-likelihood distribution, we can still estimate the forward propagated moments (3.1), and use theorem 4 (Appendix A.1) to find the best meta-parameters $\zeta_\star$.

The key to Embedded Forward Propagation (EFP) is therefore to construct unbiased estimators of these moments (3.1). This can be achieved using the mean-power property (3.28) – akin to (3.36) – but this time with the inner-loop estimators (instead of actual independent samples of $Z(X_m)$), yielding:

$$\widehat{\langle Z \rangle}^2 \triangleq \frac{2}{M(M-1)} \sum_{m=1}^{M} \sum_{m'=1}^{m-1} \widehat{Z}(X_m) \cdot \widehat{Z}(X_{m'}) \tag{3.7}$$

Note that the estimators of the outer-loop (ensemble average) are complicated by the inner-loop stochastic process $Y|X$, which introduces additional moments and estimators of its own. The latter must be cancelled out in order to construct unbiased estimators of the outer-loop moments. For instance, the variance $\langle \Delta^2 Z \rangle$ of the output means $Z(X|D)$ distribution can be unbiasedly estimated as:

$$\widehat{\langle \Delta^2 Z \rangle} \triangleq \widehat{\langle Z^2 \rangle} - \widehat{\langle Z \rangle}^2 \tag{3.8}$$

where $\widehat{\langle Z^2 \rangle}$ can be computed using (3.36) or (3.40) as:

$$\widehat{\langle Z^2 \rangle} \triangleq \frac{1}{M} \sum_{m=1}^{M} \widehat{Z^2}(X_m) \tag{3.9}$$

Interestingly, an equivalent estimator to (3.8) can be computed by tallying the stochastic process variance $\widehat{\Sigma_Y}(X)$ from (3.39) and computing:

$$\widehat{\langle Z \rangle} \triangleq \frac{1}{M} \sum_{m=1}^{M} \widehat{Z}(X_m) \tag{3.10}$$

$$\widehat{\langle \sigma^2_{\widehat{Z}} \rangle} \triangleq \frac{1}{M-1} \sum_{m=1}^{M} \left(\widehat{Z}(X_m) - \widehat{\langle Z \rangle}\right)^2 \tag{3.11}$$

$$\widehat{\langle \Sigma_Y \rangle} \triangleq \frac{1}{M} \sum_{m=1}^{M} \widehat{\Sigma_Y}(X_m) \tag{3.12}$$

$$\widehat{\langle \Delta^2 Z \rangle} \triangleq \widehat{\langle \sigma^2_{\widehat{Z}} \rangle} - \frac{\widehat{\langle \Sigma_Y \rangle}}{N} \tag{3.13}$$

Note that this latter form (3.13) is equivalent to

$$\widehat{\langle \Delta^2 Z \rangle} = \frac{1}{M} \sum_{m=1}^{M} \left[\hat{Z}(X_m)^2 - \frac{\hat{Z}(X_m)}{M-1} \sum_{\substack{k=1 \\ k \neq m}}^{M} \hat{Z}(X_k) - \widehat{\Sigma_Y}(X_m) \right] \tag{3.14}$$

but expression (3.13) is much more computationally efficient when M is large, as it is computed in $\mathcal{O}(2 \times M)$ operations, rather than the $\mathcal{O}\left(\frac{M \times (M-1)}{2}\right)$ needed to compute (3.7) or (3.14).

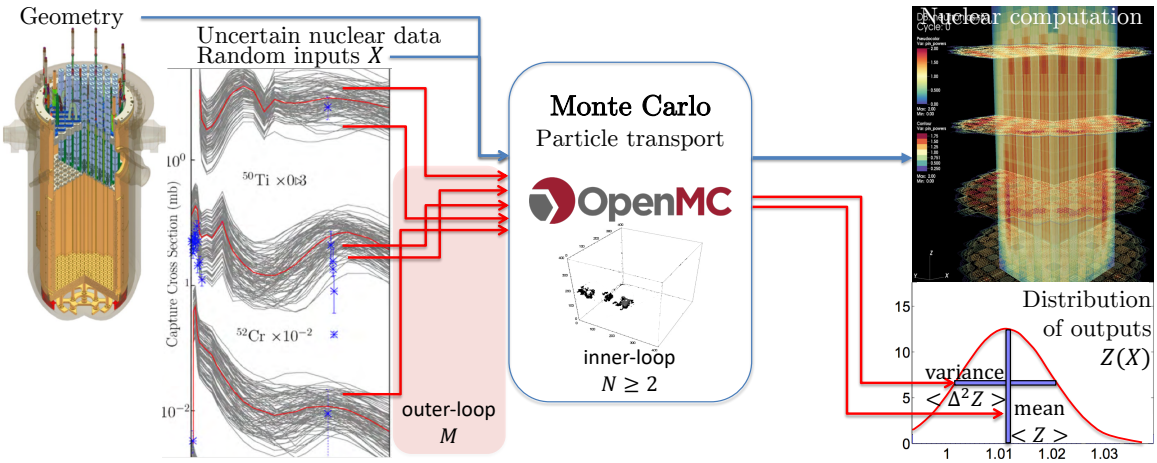

Figure 3-2: Embedded Forward Propagation: given a distribution of inputs X, EFP converges the moments of the corresponding outputs $Z(X)$ distribution, at a asymptotic rate of $\mathcal{O}\left(\frac{1}{\sqrt{M}}\right)$, without ever converging the inner-loop (only two particle counts for the tallied quantities suffice for the reactor simulation). The output distribution $p(Z(X))$ is then reconstructed from its moments.

Propagating nuclear data uncertainty across Monte Carlo particle transport computations

For context, let use the example of critical integral experiments modelled with a Monte Carlo particle transport code, with uncertain resonance parameters (inputs X). We seek to propagate this uncertainty to the multiplication factor k_{eff} (outputs $Z(X)$). We thus sample thousands of resonance parameters (outer-loop M), and for each previous methods had to process an ACE file of point-wise Doppler broadened stochastic cross sections, to give as inputs to our particle transport code (figure 2-13). For each resonance parameter sample, Nested Monte Carlo (NMC) — called Total Monte Carlo (TMC) or fast-TMC — converges a full nuclear reactor simulation using N neutrons (inner-loop) to obtain the corresponding multiplication factor k_{eff}. The histogram of these M converged outputs k_{eff} is the propagated uncertainty (figure 2-8). TMC converges at an overall rate of $\mathcal{O}\left(\frac{1}{\sqrt{M \times N}}\right)$.

Our EFP method calculates the mean and variance of the k_{eff} histogram by running only two neutrons per resonance parameter sample, that is without having to converge the inner-loop (any $N \geq 2$ works). We then use these mean and variance to reconstruct the distribution of k_{eff}, say by assuming it is a normal or a lognormal distribution.
EFP converges at an overall rate of $\mathcal{O}\left(\frac{1}{\sqrt{M}}\right)$. There is however a trade-off between converging the mean and the variance of the k_{eff} distribution: given a total number of neutrons $L = M \times N$, the optimal number of neutrons per simulation is the ratio of the variance of the inner-loop to the outer-loop (3.20).

Combining EFP with windowed multipole parameters would enable on-the-fly sampling of stochastic nuclear cross sections, thereby drastically cutting the memory footprint (figure 3-3).

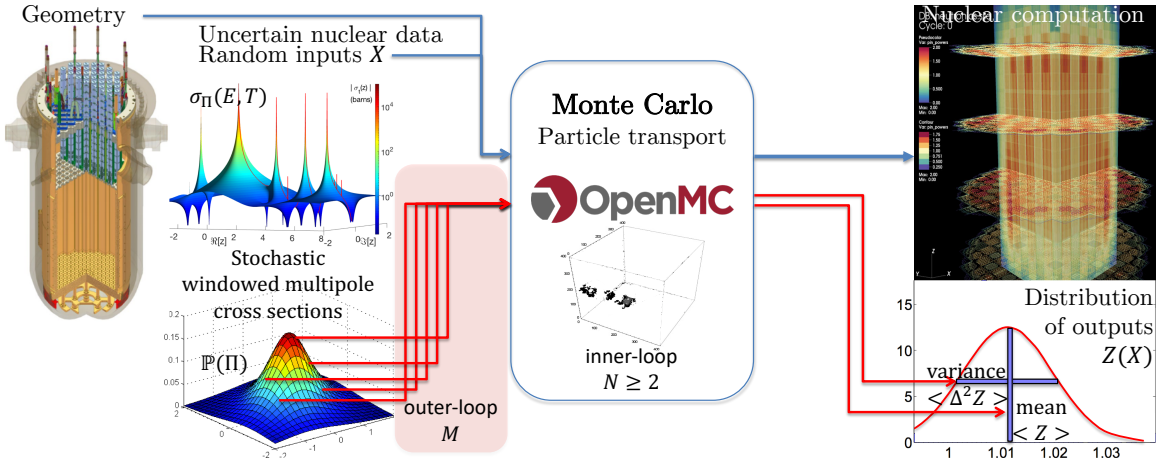

Figure 3-3: Embedded Forward Propagation: using a windowed multipole library where one can sample windowed multipoles from their uncertainty distribution (multipole covariance matrices) would enable us to run EFP with on-the-fly generation of stochastic cross sections, thereby drastically cutting the memory footprint of the sampling problem.

3.1.4 Mean versus variance convergence trade-off (EFP)

Mean $\langle Z \rangle$ and variance $\langle \Delta^2 Z \rangle$ unbiased estimators (3.10) and (3.13) show it is possible to estimate the first two moments of the distribution of ensemble average $Z(X)$ without ever converging the mean of the inner-loop stochastic process $Y|X$ (a phenomenon [156] also studied). Indeed, $N = 2$ suffices to construct unbiased estimator (3.39), which is defined as long as $N \geq 2$. Therefore, for each input parameter X_m, one can run only two independent tallies $Y_1|X_m$ and $Y_2|X_m$ and accurately converge the mean $\langle Z \rangle$ and variance $\langle \Delta^2 Z \rangle$ of the distribution of ensemble averages $Z(X)$. In essence, this is possible because we have reduced the entire point-wise output distribution $p(Z(X))$ to two quantities: mean $\langle Z \rangle$ and variance $\langle \Delta^2 Z \rangle$. Nonetheless, running

only $N = 2$ stochastic processes for each X_m sample may not be the optimal choice in terms of convergence speed. Indeed, we here establish in theorem 2 that there exists a trade-off between converging the output mean $\langle Z \rangle$, for which we show the optimum (3.16) is $N_{\text{mean}} = 1$, and converging the output variance $\langle \Delta^2 Z \rangle$, for which we show the optimal N_{var} is (3.19).

Theorem 2. *Embedded Forward Propagation:*
Mean versus variance convergence trade-off.

The output average estimator converges in law to the mean of the ensemble average, with the following asymptotic distribution:

$$\widehat{\langle Z \rangle} \underset{M \to \infty}{\overset{\mathbb{L}\text{aw}}{\longrightarrow}} \mathcal{N}\left(\langle Z \rangle, \frac{\langle \Delta^2 Z \rangle}{M} + \frac{\langle \Sigma_Y \rangle}{MN} \right) \tag{3.15}$$

Given a fixed total amount L of stochastic process $Y|X$ simulations, $L \triangleq M \times N$, the optimal convergence rate (variance reduction) for the mean is therefore achieved for:

$$N_{\text{mean}} = 1 \tag{3.16}$$

Nonetheless, to construct unbiased estimators of this convergence rate (3.15), we must have at least $M \geq 2$ and $N \geq 2$.

Meanwhile, the unbiased output variance estimator converges in law to the variance of the ensemble average, with the following asymptotic distribution:

$$\widehat{\langle \Delta^2 Z \rangle} \underset{M \to \infty}{\overset{\mathbb{L}\text{aw}}{\longrightarrow}} \mathcal{N}\left(\langle \Delta^2 Z \rangle, \frac{\langle \Delta^4 Z \rangle - \langle \Delta^2 Z \rangle^2}{M} + \frac{4\langle \Delta^2 Z \; \Sigma_Y \rangle + 2\frac{\langle \Sigma_Y^2 \rangle}{N-1}}{MN} \right) \tag{3.17}$$

where we denote $\langle \cdot \rangle \triangleq \mathbb{E}_X [\cdot]$ the expectation value over the input parameters, so that $\langle \Delta^2 Z \; \Sigma_Y \rangle \triangleq \mathbb{E}_X \left[\left(Z(X) - \langle Z \rangle \right)^2 \cdot \Sigma_Y(X) \right]$ is the expectation value of the product between the stochastic process $Y|X$ variance $\Sigma_Y(X)$ and the squared centered output (ensemble average) variable $\Delta^2 Z(X) \triangleq \left(Z(X) - \langle Z \rangle \right)^2$, while the the fourth central moment of the outer ensemble average is

$$\langle \Delta^4 Z \rangle \triangleq \mathbb{E}_X \left[\left(Z(X) - \langle Z \rangle \right)^4 \right] \tag{3.18}$$

Given a fixed total amount L of stochastic process $Y|X$ simulations, $L \triangleq M \times N$, the optimal convergence rate (variance reduction) for the variance is therefore achieved for the integer that best approaches

$$N_{\text{var}} \underset{\mathbb{N}}{\simeq} 1 + \sqrt{\frac{2\langle \Sigma_Y^2 \rangle}{\langle \Delta^4 Z \rangle - \langle \Delta^2 Z \rangle^2}} \tag{3.19}$$

Moreover, to construct unbiased estimators of the convergence rate (3.17), we must

have at least $M \geq 4$ *and* $N \geq 4$.

Proof. The proof follows that of the convergence rate for traditional mean and variance estimators from the central limit theorem on random variable $Z(X)$, but is complicated by the fact that the latter is the ensemble average of stochastic process $Y|X$ (that is the conditional expectation value $Z(X) = \mathbb{E}_Y[Y|X]$), which adds internal loop variance Σ_Y components. The full derivations are reported in [132], *verbatim* transcribed here in appendix A.2. □

Theorem 2 warrants a few remarkable properties:

- The third $\mu_Y^3(X)$ and fourth $\mu_Y^4(X)$ central moments cancel out of (3.17), so that neither the skewness nor the kurtosis of the inner-loop stochastic process $Y|X$ affect the asymptotic convergence rate of the ensemble average variance estimator $\widehat{\langle \Delta^2 Z \rangle}$. Nonetheless, they do affect our unbiased estimation of this convergence rate.

- The cross term $\langle \Delta^2 Z \, \Sigma_Y \rangle$ between inner and outer loops does not appear in the optimal variance reduction number N_{var} of inner-loop simulations (3.20) .

- For fixed inner loop and outer loop variances Σ_Y and $\langle \Delta^2 Z \rangle$, fat tails (leptokurtic) ensemble average $Z(X)$ output distributions require smaller inner-loop convergence N_{var}. Conversely, thin tails $p(Z(X))$ distributions (platykurtic) require larger inner-loop convergence.

- For a normal (Laplace-Gaussian) distribution of ensemble averages $Z(X)$, or any other mesokurtic distribution, well-known property $\langle \Delta^4 Z \rangle = 3\langle \Delta^2 Z \rangle^2$ entails that the optimal N_{var} from (3.19) becomes the interpretable and intuitive ratio of the inner and outer loop variances, plus one:

$$\underset{\text{normal}}{N_{\text{var}}} \underset{\mathbb{N}}{\simeq} 1 + \frac{\sqrt{\langle \Sigma_Y^2 \rangle}}{\langle \Delta^2 Z \rangle} \tag{3.20}$$

Theorem 2, which generalizes the results of [156], shows there exists an inherent conflict between accurately estimating the ensemble average mean $\langle Z \rangle$ (which increases linearly with internal-loop N convergence), versus the ensemble average variance $\langle \Delta^2 Z \rangle$ (which first decreases and then increases as a hyperbola in N), as illustrated by figure 3-4. The optimal trade-off in convergence rate acceleration (variance reduction) will depend on the estimated distribution, and the goal we seek to achieve. If the goal is to best reconstruct the distribution $p(Z(X))$, then the optimal trade-off will be determined by how its moments parametrize it (assuming as in theorem 1 that the distribution can be fully parametrized by its moments).

In the case of the normal distribution (Laplace-Gaussian), this optimal trade-off between mean and variance convergence rates is achieved by the integer that best approaches:

$$\underset{\text{normal}}{N_{\text{trade-off}}} \underset{\mathbb{N}}{\simeq} 1 + \frac{1}{\sqrt{2}} \frac{\sqrt{\langle \Sigma_Y^2 \rangle}}{\langle \Delta^2 Z \rangle} = \frac{N_{\text{var}}}{\sqrt{2}} + \left(1 - \frac{1}{\sqrt{2}}\right) \tag{3.21}$$

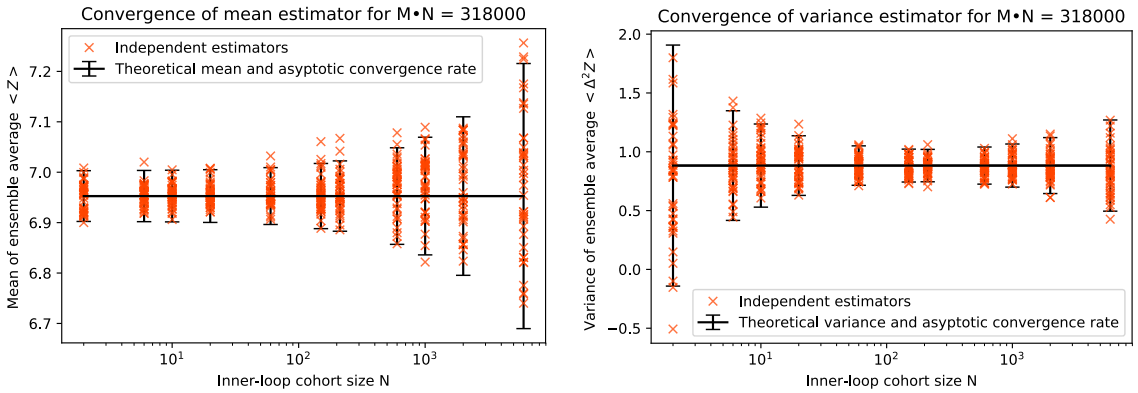

Figure 3-4: Mean versus variance trade-off (EFP) (theorem 2). Asymptotic convergence rates of theorem 2 have competing behaviors: linear increase (3.15) for the mean $\langle Z \rangle$; hyperbolic decrease then increase (3.17) for the variance $\langle \Delta^2 Z \rangle$. For analytic toy-problem of appendix C in [132], the optimal convergence rates are: $N_{\text{mean}} = 1$ for the mean; $N_{\text{var}} = 212$ for the variance; and $N_{\substack{\text{trade-off} \\ \text{normal}}} = 150$ for trade-off (3.21). Independent estimators (20 different random seeds) are plotted against the theoretical exact values and a convergence interval with $2\sigma \triangleq 2\sqrt{\langle \Delta^2 Z \rangle}$, covering $\simeq 95.45\%$ of the asymptotic estimators distribution.

which is about 70% of the optimal variance convergence number (3.20): $N_{\text{trade-off}} \simeq 70\% N_{\text{var}}$. Figure 3-4 shows this optimal normal distribution trade-off (3.21), compared to the variance optimal point (3.20). Result (3.21) can be established by considering a fixed "budget" number $L = M \times N$ of total stochastic process $Y|X$ simulations, so that convergence rates (3.15) and (3.17) of theorem 2 can be re-written as

$$\frac{\widehat{\langle Z \rangle} - \langle Z \rangle}{\sqrt{\langle \Delta^2 Z \rangle}} \xrightarrow[M \to \infty]{\mathbb{L}\text{aw}} \mathcal{N}\left(0, \frac{1}{L} \underbrace{\left[N + \frac{\langle \Sigma_Y \rangle}{\langle \Delta^2 Z \rangle} \right]}_{\triangleq v_N}\right)$$

$$\frac{\widehat{\langle \Delta^2 Z \rangle} - \langle \Delta^2 Z \rangle}{\langle \Delta^2 Z \rangle} \xrightarrow[M \to \infty]{\mathbb{L}\text{aw}} \mathcal{N}\left(0, \frac{2}{L} \underbrace{\left[N \frac{\left(\frac{\langle \Delta^4 Z \rangle}{\langle \Delta^2 Z \rangle^2} - 1 \right)}{2} + 2 \frac{\langle \Delta^2 Z \, \Sigma_Y \rangle}{\langle \Delta^2 Z \rangle^2} + \frac{1}{N-1} \frac{\langle \Sigma_Y^2 \rangle}{\langle \Delta^2 Z \rangle^2} \right]}_{\triangleq w_N}\right)$$

In other words, for outputs mean μ and variance σ^2, we respectively have estimators convergence $\widehat{\mu} \xrightarrow[M \to \infty]{\mathbb{L}\text{aw}} \mu \pm \frac{v_N}{L}\sigma$, and $\widehat{\sigma^2} \to \sigma^2(1 \pm \frac{2w_N}{L})$. The latter's first-order Taylor expansion yields $\sqrt{\widehat{\sigma^2}} \xrightarrow[M \to \infty]{\mathbb{L}\text{aw}} \sigma(1 \pm \frac{w_N}{L})$.

For the Laplace-Gaussian (normal) distribution, quantiles covering p percent of the probability are expressed as multiples of the standard deviation from the mean: $\mu \pm q_p \sigma$ (with well-known $q_{95\%} \simeq 1.96$ and $q_{99.9\%} \simeq 3.29$). Therefore, if both the mean and the variance are known to a given accuracy, plugging-in mean and standard

deviation estimators $\widehat{\mu}$, $\widehat{\sigma}$ into the normal distribution quantiles expression entails: $\widehat{\mu} \pm q_p \widehat{\sigma} = \mu \pm q_p \sigma \pm \left(\frac{v_N + w_N}{L}\right) \sigma$. Therefore, the inner-loop N value which most accurately describes a normal distribution of outputs $Z(X)$ is that which minimizes $v_N + w_N$. By differentiating this quantity with respect to N, one readily finds the optimal trade-off between mean and variance convergence rates is (3.21).

Additional schemes are possible for further variance reduction. In particular Multi-Level Monte Carlo [109, 155] could be well suited to our ensemble average (2.16), depending on the specific stochastic process $Y|X$ being computed. Though [155] explains how to use the Multi-Level Monte Carlo framework for nested simulation (section 9 p.57), the method nonetheless solely focuses on the expectation value of the mean $\langle Z \rangle$, and not the variance $\langle \Delta^2 Z \rangle$ nor higher moments, which Embedded Monte Carlo uses to reconstruct the distribution of ensemble averages (theorem 1).

3.2 Embedded Variational Inference

Embedded Variational Inference (EVI) is a set of new algorithms, which we established in [133, 132], to infer input parameters X distributions from uncertain output observations $D \triangleq \left\{ Z_i \right\}$, when the outputs are *ensemble averages* (2.16) (conditional means)

$$Z(X) \triangleq \mathbb{E}_Y \left[Y|X \right]$$

over an intractable stochastic process $Y|X$: for a Monte Carlo particle transport problem $Z(X)$ would be any output from the nuclear simulation (reaction rates, flux, multiplication factor, etc.), while $Y|X$ would be the individual tallies of each particle (neutron or photon for reactor physics) along their random walk (stochastic process $Y|X$). Computing samples $Y|X$ is feasible, but converging their means $Z(X)$ for many different values of X is not, so nesting Monte Carlo estimators [274] is intractable (called *Total Monte Carlo* in the nuclear data field [283, 285]). Using an iterative stochastic approximation algorithm with T iterations, Embedded Variational Inference finds the best Bayesian posterior $X|D$ (2.2)

$$p(X|D) = \frac{p(D|X) p(X|\theta)}{p(D|\theta)}$$

approximation within a parametric family (by minimizing discrimination information), at an asymptotic rate of $\mathcal{O}\left(\frac{1}{\sqrt{T}}\right)$. This stochastic optimization is made possible under the condition that the data D uncertainty has a polynomial log-likelihood

$$\ell \left(D|X \right) \triangleq \ln p \left(D|X \right) \in \mathbb{R} \left[X \right] \tag{3.22}$$

which is the case for data $D = \left\{ Z_i \right\}_{i \in [\![1, N_D]\!]}$ with standard additive Gaussian noise

$$Z_i = Z(X) + \epsilon_i$$

where ϵ_i are drawn at random from the Gaussian uncertainty measurements (which can be heteroskedastic). We can then embed the uncertainty and never converge any single output $Z(X)$, each of which would converge at a rate of $\mathcal{O}\left(\frac{1}{\sqrt{T}}\right)$.

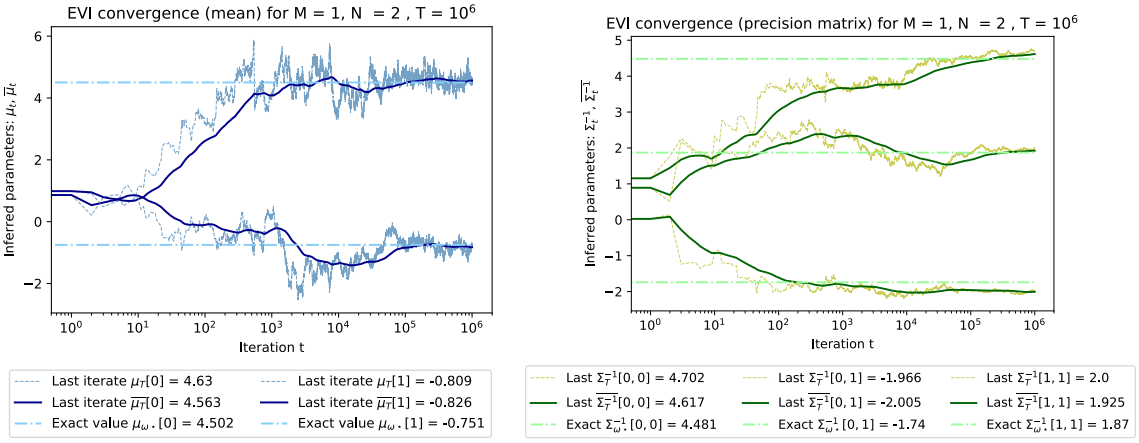

Figure 3-5: Embedded Variational Inference (EVI) (theorem 3). Given data-set D of $N_D = 5$ noisy observations of ensemble average $Z(X)$, the posterior inputs $X|D$ distribution is approximated with a parametric family $p_\omega(X)$, within which stochastic approximation EVI algorithm (3.30) converges towards the best meta-parameters $\omega_\star$. In this case, $\omega = \left\{\boldsymbol{\mu}, \boldsymbol{\Sigma}^{-1}\right\}$ are the mean and variance (precision matrix) parameters of the multivariate normal distribution from the analytic toy-problem of appendix C of [132].

3.2.1 Embedded Variational Inference (EVI) synthesis

- Key hypotheses: Noise must be of polynomial log-likelihood class (normal noise works). The true Bayesian posterior is approximated with an uncertainty distribution belonging to a pre-specified parametric family: for instance, EVI finds the "best multivariate normal posterior" approximation.
- Advantages:
  - Converges at a $\mathcal{O}\left(\frac{1}{\sqrt{T}}\right)$ rate, proportional to the cost of any one Monte Carlo simulation without uncertainty, whereas Total Monte Carlo requires $\mathcal{O}\left(\frac{1}{\sqrt{N \times M}}\right)$ to converge.
  - EVI can perform non-linear Bayesian inference, while Sensitivity Analysis (SA) can only do 1^{st} order linear approximation.
- Drawbacks:
  - The noise must be of polynomial log-likelihood, this excludes fat-tailed noise (though many non-heavy-tailed distributions with a local or compact support can be well approximated with polynomial log-likelihood distributions).

– Not exact in that one must pre-specify the parametric family of the approximate posterior (meta-optimization can be carried out to find best posterior family).

– Very sensitive to learning rates (more research needed to accelerate convergence).

– For nuclear transport problems, convergence is severely hindered if $Z(X)$ is not an integral quantity: as is the case with any Monte Carlo computation, local tallies in energy and space are much harder to converge.

For validation and illustration purposes, we designed an Embedded Variational Inference toy-problem with Gaussian noisy data and multivariate normal parameters $X|\theta$ (Appendix C in [132] here transcribed *verbatim* in appendix A.3), demonstrating the convergence of the EVI algorithm in figure 3-5.

3.2.2 General theory (EVI)

Theorem 3 lays the theoretical foundations of EVI Monte Carlo. We denote $\ell(X)$ the log-likelihood of any given random variable X of density $p(X)$ (distribution if discrete):

$$\ell(X) \triangleq \ln p(X) \tag{3.23}$$

Theorem 3. *Embedded Variational Inference.*
Let $p(X|D)$ be the true posterior inputs distribution from Bayesian inference (2.2). Let $p_\omega(X)$ denote a parametric family of probability distributions, with which we seek to approximate $p(X|D)$:

$$p_\omega(X) \approx p(X|D) = \frac{p(D|X)p(X|\theta)}{p(D|\theta)} \tag{3.24}$$

The information lost by approximating $p(X|D)$ with $p_\omega(X)$ is represented by the Kullback-Leibler divergence [212]:

$$\mathbb{K}[\omega] \triangleq \int p_\omega(x) \ln\left(\frac{p_\omega(x)}{p(x|D)}\right) \mathrm{d}x \tag{3.25}$$

We search for the member $p_{\omega\star}(X)$ of the family that minimizes this information loss cost function (3.25), that is the optimal meta-parameters [78]:

$$\omega_\star \triangleq \arg\min_\omega \mathbb{K}[\omega] \tag{3.26}$$

If the noisy data-set $D \triangleq \{Z_i\}$ is such that its log-likelihood $\ell(D|X)$ is a polynomial of degree d in $Z(X)$, i.e.

$$\ell(D|X) = \sum_{k=1}^{d} a_k^D Z(X)^k \tag{3.27}$$

where the $a_k^D \in \mathbb{R}$ coefficients depend on data-set D and its noise distribution, then the general mean-power property

$$\mathbb{E}_Y\left[Y|X\right]^d = \prod_{i=1}^{d} \mathbb{E}_{Y_i}\left[Y_i|X\right] = \mathbb{E}_{\prod_{i=1}^{d} Y_i}\left[\prod_{i=1}^{d} Y_i|X\right] \tag{3.28}$$

entails one can construct an unbiased Embedded Variational Inference estimator (EVI estimator)

$$\widehat{\frac{\partial \mathbb{K}}{\partial \omega}}\left[\omega\right] \triangleq \left[1 + \ell_\omega(X) - \widehat{\ell(D|X)} - \ell(X|\theta)\right]\frac{\partial \ell_\omega(X)}{\partial \omega} \tag{3.29}$$

so that in the following iterative stochastic approximation Robbins-Monro algorithm for Embedded Variational Inference

$$\begin{aligned} \omega_{t+1} &= \omega_t - \gamma_t \cdot \widehat{\frac{\partial \mathbb{K}}{\partial \omega}}\left[\omega_t\right] \\ \gamma_t &= \frac{c}{t^\alpha} \ , \ with \ 0 < \alpha < 1 \ , \ and \ 0 < c \\ \overline{\omega_T} &\triangleq \frac{1}{T}\sum_{t=0}^{T} \omega_t \end{aligned} \tag{3.30}$$

the Polyak-Ruppert average $\overline{\omega_T}$ will converge to the optimum meta-parameters $\omega_\star$ at an asymptotic rate of $\mathcal{O}\left(\frac{1}{\sqrt{T}}\right)$.

Proof. The Kullback-Leibler divergence (3.25) is a way of accounting for the information lost by approximating $p(X|D)$ with $p_\omega(X)$. Though not a metric, it satisfies $\mathbb{K}\left[\omega\right] \geq 0$, and is null if, and only if, $p_\omega(X) \overset{\text{a.e.}}{=} p(X|D)$ almost everywhere. Since $\int p_\omega(x)\mathrm{d}x = 1$, we can integrate $\ell(D|\theta)$ out of our cost function $\mathbb{K}\left[\omega\right]$ and express it as:

$$\mathbb{K}\left[\omega\right] = \ell(D|\theta) + \int p_\omega(x)\Big[\ell_\omega(x) - \ell(D|x) - \ell(x|\theta)\Big]\mathrm{d}x \tag{3.31}$$

We can choose parametric families differentiable in ω, so that after noticing $\frac{\partial p_\omega(X)}{\partial \omega} = p_\omega(X)\frac{\partial \ell_\omega(X)}{\partial \omega}$, the differential $\frac{\partial \mathbb{K}}{\partial \omega}$ can be expressed as the following expectation value over the unknown distribution $p_\omega(X)$:

$$\frac{\partial \mathbb{K}}{\partial \omega} = \mathbb{E}_{X|\omega}\left[\left[1 + \ell_\omega(X) - \ell(D|X) - \ell(X|\theta)\right]\frac{\partial \ell_\omega(X)}{\partial \omega}\right] \tag{3.32}$$

EVI seeks to find the meta-parameters $\omega_\star$ that minimize the $\mathbb{K}\left[\omega\right]$ cost-function (3.33) in our intractable Nested Monte Carlo case. Thus, optimal meta-parameter $\omega_\star$ will satisfy the necessary condition :

$$\frac{\partial \mathbb{K}}{\partial \omega}\left[\omega_\star\right] = 0 \tag{3.33}$$

We suppose that the noisy data-set $D \triangleq \{Z_i\}$ has a polynomial log-likelihood (3.27). Crucially, we can always construct unbiased estimators of the output raw

moments $\widehat{Z^k}(X)$ (i.e. such that $\mathbb{E}_Y\left[\widehat{Z^k}(X)\right] = Z(X)^k$), thanks to the general mean-power property (3.28) [274]:

$$\mathbb{E}_Y\left[Y|X\right]^d = \prod_{i=1}^{d}\mathbb{E}_{Y_i}\left[Y_i|X\right] = \mathbb{E}_{\prod_{i=1}^{d}Y_i}\left[\prod_{i=1}^{d}Y_i|X\right]$$

we can thus build an unbiased data-log-likelihood estimator:

$$\widehat{\ell(D|X)} \triangleq \sum_{i=1}^{d} a_i^D \widehat{Z^k}(X) \tag{3.34}$$

such that $\mathbb{E}_Y\left[\widehat{\ell(D|X)}\right] = \ell(D|X)$. We then use this $\widehat{\ell(D|X)}$ from (3.34) to establish the EVI estimator (3.29), which satisfies the following unbiased nested estimator property:

$$\mathbb{E}_{X|\omega}\left[\mathbb{E}_Y\left[\widehat{\frac{\partial\mathbb{K}}{\partial\omega}}\left[\omega\right]\right]\right] = \frac{\partial\mathbb{K}}{\partial\omega}\left[\omega\right] \tag{3.35}$$

This property is the keystone of the EVI method, as it enables us to solve the fixed-point problem (3.33) by means of stochastic optimization methods, such as the Robbins-Monro algorithm [280], and subsequent Polyak–Ruppert averaging [269], which guarantee the convergence of the the EVI iterations (3.30) at its asymptotic rate of $\mathcal{O}\left(\frac{1}{\sqrt{T}}\right)$. □

For generality, our EVI algorithm (3.30) here uses the generic learning rates $\{\gamma_t\}$ and Polyak-Ruppert averaging $\overline{\omega_T}$ of the Robbins-Monro algorithm. In practice, the choice of sequence $\{\gamma_t\}$ can dramatically impact the convergence of the EVI algorithm. With knowledge of the Hessian or numerical approximations of higher derivatives, it is possible take a stochastic gradient descent approach and tailor the learning rates to accelerate convergence. Though of high practical importance, the design of such learning rates sequences $\{\gamma_t\}$ is problem-specific and beyond the scope of this article.

3.2.3 Practical considerations (EVI)

To understand the scope of theorem 3, we have to understand what type of noise falls within the polynomial log-likelihood class. For instance, this encompasses any additive noise (2.5) where densities of ϵ_i are the exponential of polynomials of degree d. In practice, the particularly important case of Gaussian noise falls in this category with a second order polynomial $d = 2$. Note that, remarkably, EVI makes no assumption on the distribution of ensemble averages $p(Z(X))$ in theorem 3: that is EVI can still perform variational Bayesian inference across the intractable ensemble average $Z(X)$, even if the latter has a fat-tails distribution with infinite moments.

For each iteration step t of algorithm (3.30), M independent realizations of the parameter X_m are drawn from the $p_{\omega_t}(X)$ distribution. For each X_m, we simulate a cohort of N independent stochastic processes $Y_n|X_m$. Hence, the total amount of

samples is: $T \times M \times N$. For each X_m, we build unbiased estimators of $Z^d(X_m)$ by using the mean-power property (3.28). For instance, separating the pairs $n' \neq n$, $d = 2$ yields:

$$\widehat{Z^2}(X_m) \triangleq \frac{2}{N(N-1)} \sum_{n=1}^{N} \sum_{n'=1}^{n-1} \left(Y_n \cdot Y_{n'}\right) | X_m \tag{3.36}$$

However, the latter estimator has complexity of $\mathcal{O}\left(N^2\right)$, and in general such a $\widehat{Z^d}(X_m)$ would have complexity $\mathcal{O}\left(N^d\right)$. Using central moments estimators, and their relationship to raw moments (Binomial expansion), one can compute the same estimator with a $\mathcal{O}\left(d \times N\right)$ complexity. In the $d = 2$ case, this yields:

$$\widehat{Z}(X_m) \triangleq \frac{1}{N} \sum_{n=1}^{N} Y_n | X_m \tag{3.37}$$

$$\widehat{m_Y^2}(X_m) \triangleq \frac{1}{N} \sum_{n=1}^{N} Y_n^2 | X_m \tag{3.38}$$

$$\widehat{\Sigma_Y}(X_m) \triangleq \frac{1}{N-1} \sum_{n=1}^{N} \left(Y_n | X_m - \widehat{Z}(X_m)\right)^2 \tag{3.39}$$

$$\widehat{Z^2}(X_m) \triangleq \widehat{m_Y^2}(X_m) - \widehat{\Sigma_Y}(X_m) \tag{3.40}$$

Crucially, to construct an unbiased estimate of the d-th power $Z^d(X_m)$, we need to simulate at least $N = d$ different stochastic processes $Y_n | X_m$ for each value X_m. That means that the minimum complexity to construct an unbiased estimator $\widehat{Z^d}(X_m)$ is $\mathcal{O}\left(d \times d\right)$.

Remarkably, $M = 1$ suffices to compute the EVI estimator (3.29), though averaging over M-batches (3.41) can in some cases yield faster convergence rates:

$$\widehat{\frac{\partial \mathbb{K}}{\partial \omega}}[\omega_t] \triangleq \frac{1}{M} \sum_{m=1}^{M} \left[1 + \ell_{\omega_t}(X_m) - \ell(X_m|\theta) - \ell\widehat{(D|X_m)}\right] \frac{\partial \ell_{\omega_t}}{\partial \omega}(X_m) \tag{3.41}$$

Therefore, the minimum complexity to compute T iterations of the EVI algorithm is $\mathcal{O}\left(T \times d \times d\right)$, with an asymptotic convergence rate of $\mathcal{O}\left(\frac{1}{\sqrt{T}}\right)$. In contrast, converging a single output $Z(X_m)$ for one given X_m parameter value using estimator (3.37) has an asymptotic convergence rate of $\mathcal{O}\left(\frac{1}{\sqrt{N}}\right)$. This means that converging the mean $Z(X)$ or finding Bayesian posterior $X|D$ using the Embedded Variational Inference method is of the same order of computational complexity.

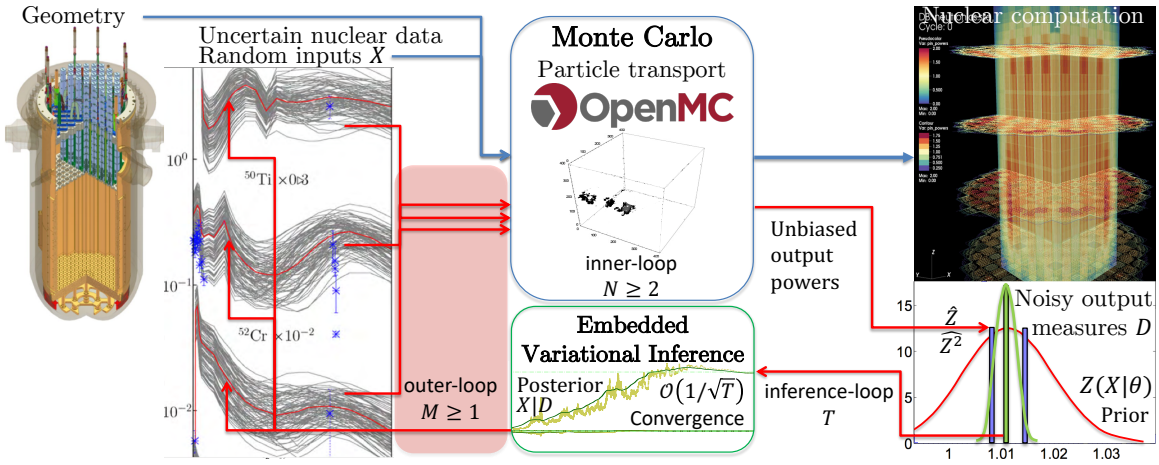

Figure 3-6: Embedded Variational Inference from integral experiments: given experimental observations D, EVI converges towards the best approximation of Bayesian posterior nuclear data uncertainty $X|D$ at a asymptotic rate of $\mathcal{O}\left(\frac{1}{\sqrt{T}}\right)$, without ever converging any inner-loop (reactor simulations). This is possible by building the unbiased estimators of the raw moments $\widehat{Z}(X)$ and $\widehat{Z^2}(X)$, and comparing them to the polynomial log-likelihood uncertainty profile of the measurement data D.

Inferring nuclear data uncertainty from integral experiments

Using our previous example, we now measure real-world k_{eff} values from the critical integral experiment. We assume these measures D have a Gaussian uncertainty, and seek to infer updated values of resonance parameters.
NMC would require sampling M sets of resonance parameters and for each run N neutrons to perform a histogram-wise Bayesian update (figure 2-10), converging overall at a rate of $\mathcal{O}\left(\frac{1}{\sqrt{M \times N}}\right)$.
If we model the resonance parameters with a multivariate normal (or any other parametric distribution, say Lognormal), then our EVI method can take the noisy data D and infer the updated resonance parameters distribution by the following iterative procedure (figure 3-6):

- sample a set of resonance parameters from their present uncertainty distribution
- run at least two neutrons in Monte Carlo (similar trade-off as in EFP)
- compare with noisy data D and update the uncertainty distribution of resonance parameters
- repeat T times

EVI converges at an overall rate of $\mathcal{O}\left(\frac{1}{\sqrt{T}}\right)$.
Combining EVI with windowed multipole parameters would enable the sampling of stochastic nuclear cross sections on-the-fly and directly update the windowed multipoles and their covariances during the EVI iterations (figure 3-7), thereby eliminating the sampling and processing computational bottleneck.

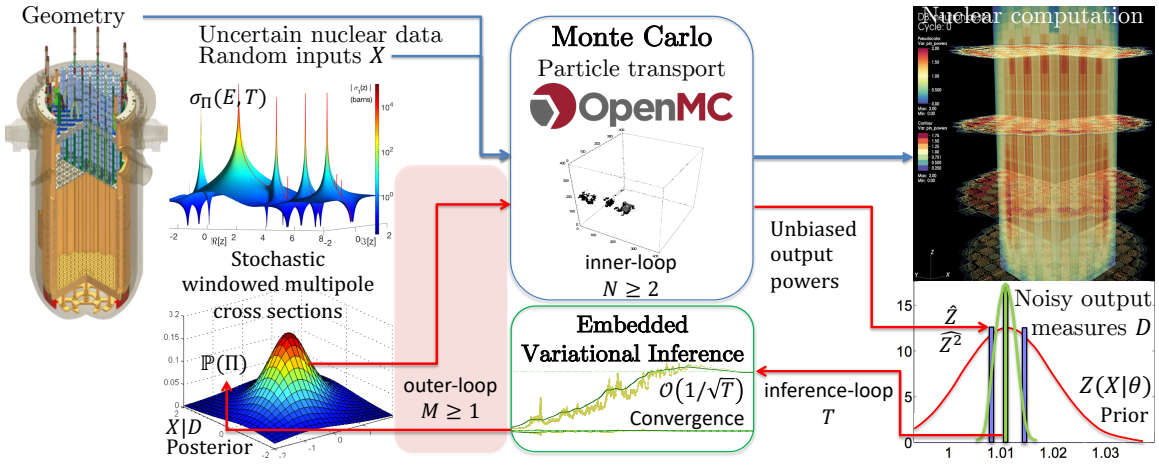

Figure 3-7: Embedded Variational Inference from integral experiments: from a multivariate normal uncertainty distribution of windowed multipoles, we could generate on-the-fly stochastic cross sections, drastically reducing the memory cost of sampling during the EVI algorithm, all the while directly inferring updated windowed multipoles and their covariances from integral experiments data at an asymptotic rate of $\mathcal{O}\left(\frac{1}{\sqrt{T}}\right)$.

3.2.4 Meta-optimization (EVI)

Solving problem (3.33) means finding the $\omega_\star$ parameters such that $\frac{\partial \mathbb{K}}{\partial \omega}[\omega_\star] = 0$. Note that this will only find the "best" approximate posterior (in the KL divergence sense) within the parametric family $p_\omega(X)$. A meta-optimization over different parametric families can be carried out to find the one with the lowest minimum KL divergence $\mathbb{K}[\omega_\star]$, that is the "closest fit" family: $0 \leq \mathbb{K}[\omega_\star] \leq \mathbb{K}[\omega'_\star]$. Though the $\ell(D|\theta)$ normalization term in (3.31) is usually intractable, the latter meta-optimization can still be carried out by using the KL divergence property $\mathbb{K}[\omega] \geq 0$ and comparing for different families their optimal lower-bound for the normalization:

$$\ell(D|\theta) \geq -\int p_{\omega_\star}(X)\Big[\ell_{\omega_\star}(X) - \ell(D|X) - \ell(X|\theta)\Big]\mathrm{d}x \tag{3.42}$$

3.2.5 Gaussian noise data & multivariate normal parameters (EVI)

In practice, an important EVI case is finding the best approximate multivariate normal parameters posterior $X|D$, inferred from noisy data D with Gaussian noise — for nuclear computations this would mean modeling the nuclear data uncertainty as a multivariate normal distribution (as it is traditionally modelled) and assume Gaussian noise on the observations. That is parametric family $p_\omega(X) \sim \mathcal{N}(\boldsymbol{\mu}_\omega, \boldsymbol{\Sigma}_\omega)$ with

$$p_\omega(X) = \left|\frac{\boldsymbol{\Sigma}_\omega^{-1}}{2\pi}\right|^{\frac{1}{2}} \mathrm{e}^{-\frac{1}{2}(X-\boldsymbol{\mu}_\omega)^\intercal \boldsymbol{\Sigma}_\omega^{-1}(X-\boldsymbol{\mu}_\omega)} \tag{3.43}$$

where $|\cdot|$ denotes the pseudo-determinant. When searching for meta-parameters $\omega_\star$ that solve problem (3.26), the log-likelihood and its derivatives are then

$$\begin{aligned}
\ell_\omega(X) &= \frac{1}{2}\left[\ln\left|\frac{\boldsymbol{\Sigma}_\omega^{-1}}{2\pi}\right| - (X-\boldsymbol{\mu}_\omega)^\mathsf{T}\boldsymbol{\Sigma}_\omega^{-1}(X-\boldsymbol{\mu}_\omega)\right] \\
\frac{\partial \ell_\omega(X)}{\partial \boldsymbol{\mu}_\omega} &= \boldsymbol{\Sigma}_\omega^{-1}(X-\boldsymbol{\mu}_\omega) \\
\frac{\partial \ell_\omega(X)}{\partial \boldsymbol{\Sigma}_\omega^{-1}} &= \frac{1}{2}\left[\boldsymbol{\Sigma}_\omega - (X-\boldsymbol{\mu}_\omega)(X-\boldsymbol{\mu}_\omega)^\mathsf{T}\right]
\end{aligned} \tag{3.44}$$

For numerical stability purposes, we consider the precision matrix $\boldsymbol{\Sigma}_\omega^{-1}$ (inverse covariance), and enforce its positive semi-definite properties by decomposing it as a Gram matrix:

$$\boldsymbol{\Sigma}_\omega^{-1} \triangleq \boldsymbol{S}_\omega^\mathsf{T}\boldsymbol{S}_\omega \tag{3.45}$$

In searching for $\boldsymbol{S}_\omega$, Jacobian (3.44) thus becomes:

$$\frac{\partial \ell_\omega(X)}{\partial \boldsymbol{S}_\omega} = \boldsymbol{S}_\omega^{-\mathsf{T}} - \boldsymbol{S}_\omega(X-\boldsymbol{\mu}_\omega)(X-\boldsymbol{\mu}_\omega)^\mathsf{T} \tag{3.46}$$

The prior density is

$$p(X|\theta) = \left|\frac{\boldsymbol{\Sigma}_0^{-1}}{2\pi}\right|^{\frac{1}{2}} \mathrm{e}^{-\frac{1}{2}(X-\boldsymbol{\mu}_0)^\mathsf{T}\boldsymbol{\Sigma}_0^{-1}(X-\boldsymbol{\mu}_0)} \tag{3.47}$$

so that the prior log-likelihood takes the form:

$$\ell(X|\theta) = \frac{1}{2}\left[\ln\left|\frac{\boldsymbol{\Sigma}_0^{-1}}{2\pi}\right| - (X-\boldsymbol{\mu}_0)^\mathsf{T}\boldsymbol{\Sigma}_0^{-1}(X-\boldsymbol{\mu}_0)\right] \tag{3.48}$$

In data set D of empirical observations (2.5), the Gaussian noise ϵ_i, each with different (heteroscedastic) variance Σ_i (the square of the standard deviation), entails likelihood:

$$p(D|X) = \prod_{i=1}^{N_D}\left|\frac{\Sigma_i^{-1}}{2\pi}\right|^{\frac{1}{2}} \mathrm{e}^{-\frac{1}{2}\Sigma_i^{-1}\left(Z_i - Z(X)\right)^2} \tag{3.49}$$

so that its log-likelihood is

$$\ell(D|X) = \frac{1}{2}\sum_{i=1}^{N_D}\left[\ln\left|\frac{\Sigma_i^{-1}}{2\pi}\right| - \Sigma_i^{-1}\Big(Z_i - Z(X)\Big)^2\right] \tag{3.50}$$

crucially, this satisfies the necessary polynomial log-likelihood condition (3.27) for the EVI method to work. Here $\ell(D|X)$ is a polynomial of degree $d=2$ (Gaussian case):

$$\ell(D|X) = a^D Z(X)^2 + b^D Z(X) + c^D \tag{3.51}$$

with

$$
\begin{aligned}
a^D &\triangleq -\frac{1}{2}\sum_{i=1}^{N_D}\Sigma_i^{-1} \\
b^D &\triangleq \sum_{i=1}^{N_D}\Sigma_i^{-1}Z_i \\
c^D &\triangleq \frac{1}{2}\sum_{i=1}^{N_D}\left[\ln\left|\frac{\Sigma_i^{-1}}{2\pi}\right| - \Sigma_i^{-1}Z_i^2\right]
\end{aligned}
\tag{3.52}
$$

We can thus plug-in (3.37) and (3.40) into (3.51) to build the unbiased data-log-likelihood estimator (3.34):

$$
\widehat{\ell(D|X)} = a^D\widehat{Z^2}(X) + b^D\widehat{Z}(X) + c^D \tag{3.53}
$$

combining (3.44), (3.46), and (3.53) yields the EVI estimators (3.41) for each EVI step (3.30)

$$
\begin{aligned}
\widehat{\frac{\partial\mathbb{K}}{\partial\boldsymbol{\mu}}}[\omega_t] &= \frac{1}{M}\sum_{m=1}^{M}\left[1+\ell_{\omega_t}(X_m)-\ell(X_m|\theta)-\widehat{\ell(D|X_m)}\right]\frac{\partial\ell_{\omega_t}}{\partial\boldsymbol{\mu}}(X_m) \\
\widehat{\frac{\partial\mathbb{K}}{\partial\boldsymbol{S}}}[\omega_t] &= \frac{1}{M}\sum_{m=1}^{M}\left[1+\ell_{\omega_t}(X_m)-\ell(X_m|\theta)-\widehat{\ell(D|X_m)}\right]\frac{\partial\ell_{\omega_t}}{\partial\boldsymbol{S}}(X_m)
\end{aligned}
\tag{3.54}
$$

3.3 Embedded Monte Carlo application: particle random walk under uncertain nuclear data

We demonstrate our new Embedded Monte Carlo methods on the stochastic process which gave birth to the Monte Carlo method: the complex random walk of nuclear particles [241, 239]. For this, we developed an analytic benchmark for neutron particle transport [298, 53]. This benchmark aims at resolving the energy variable, and as such it consists of an ideal neutron slowdown, complicated by overlapping nuclear resonances. It is remarkable in that it is the first explicit resolution of overlapping resonances in neutron transport, without a resonance model nor numeric brute-force [325, 221, 154, 108, 278], just analytic solutions using the multipole formalism we established in [130].

3.3.1 Analytic neutron slowdown benchmark

The critical neutron slowdown analytic benchmark [298, 53] is a simple eigenvalue problem (criticality calculation) for which we were able to derive closed-form solutions for the flux, despite there being overlapping resonances (from ^{238}U and ^{239}Pu).

Setup and key hypotheses

The three main hypotheses of the analytic benchmark are:

- Infinite homogeneous medium: no spatial or angular variables, only energy.
- Hydrogen-only scattering: scattering neutrons can uniformly go from their initial kinetic energy down to zero.
- Uniform fission: when a fission occurs, neutrons are equally likely to be born at any energy from $E_0 = 0$ to a cutoff E_∞, past which none are born.
- Steady-state (for multiplication factor k_{eff} eigenvalue calculation), or time Laplace transform for α-eigenvalue calculation.

The specific configuration is that of the first resonance of both ^{238}U and ^{239}Pu nuclear cross sections, here reported in figure 3-8. This is an idealized system simple enough for us to derive analytic solutions, yet complicated enough that the overlapping resonances pose a challenge to standard resonance self-shielding models. In this setup, the analytic benchmark studies the multiplication factor k_{eff}-eigenproblem:

$$\Sigma_t(E)\psi_k(E) - \int_E^{E_\infty} \mathrm{d}E' \frac{\Sigma_s(E')}{E'}\psi_k(E') = \frac{\chi(E)}{k_{\text{eff}}} \int_{E_0}^{E_\infty} \mathrm{d}E' \nu\Sigma_f(E')\psi_k(E'). \tag{3.55}$$

Key results and new achievements

The key results of the analytic benchmark are four-fold: (i) analytic resolution of the flux $\psi_k(E)$ and reaction rate $R_k(E)$; (ii) numerical resolution of the multiplication factor k_{eff}; (iii) resolution of α versus k_{eff} eigenvalue problems; and (iv) arbitrary order derivatives of the flux and eigenvalues to any parameter (nuclear data). We here succinctly summarize these findings, and refer to the benchmark articles for further detail [298, 53].

- (i) Analytic resolution of the flux and reaction rate.
  This is achieved by considering the *total reaction rate*:

  $$R_k(E) \triangleq \Sigma_t(E)\psi_k(E) \tag{3.56}$$

  and introducing the *downscattering ratio*:

  $$\mathsf{D_S}(E) \triangleq \frac{\Sigma_s(E)}{E\Sigma_t(E)} \tag{3.57}$$

  and the *fission production ratio*:

  $$\mathsf{f}_\nu(E) \triangleq \frac{\nu\Sigma_f(E)}{\Sigma_t(E)}, \tag{3.58}$$

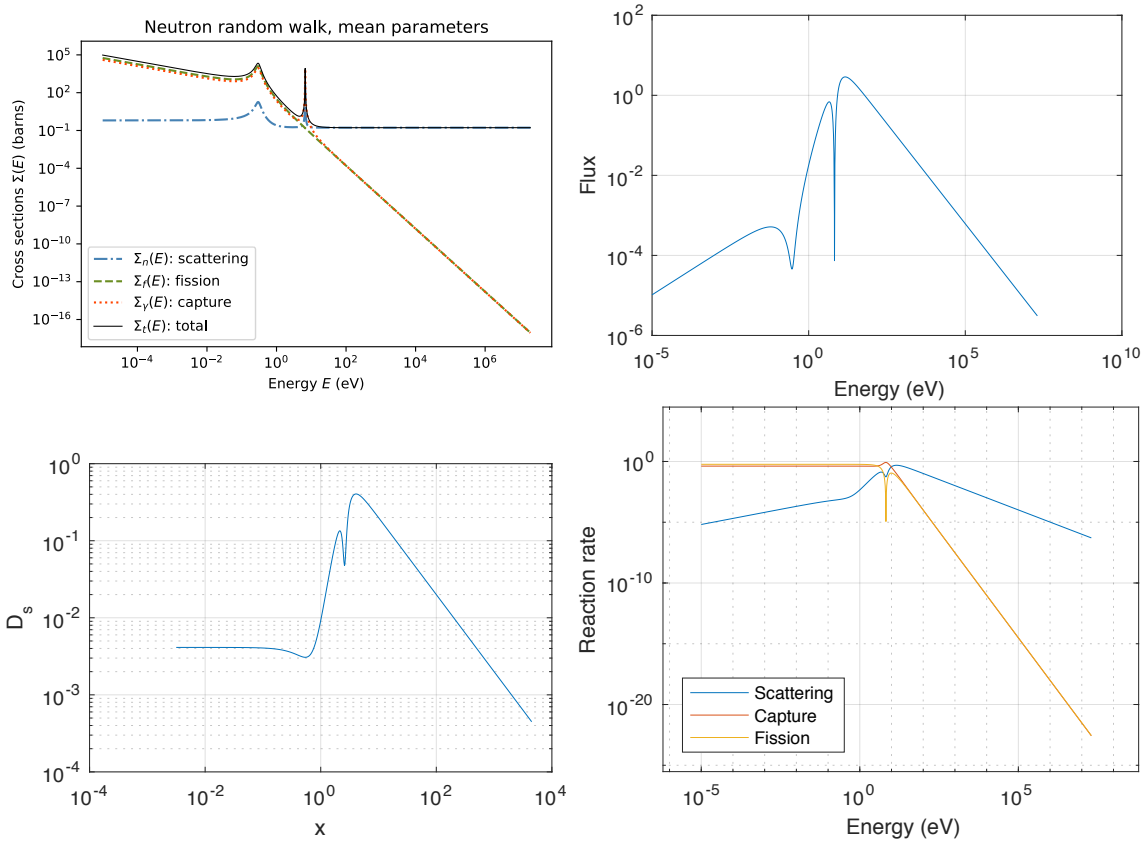

Figure 3-8: Analytic Benchmark for Neutron Slowdown [298, 53]: Neutrons are born from fission uniformly from 10^{-5} to 2×10^7 (eV). They slow down by scattering on hydrogen, and in the process encounter the two first resonances of uranium U^{238} and plutonium Pu^{239}. These cross sections are the inputs of the random walk, parametrized by nuclear data X (resonance parameters). When the mean parameters $X = \mu_0$ are chosen, the multiplication factor $k_{\text{eff}} \triangleq Z(X) \triangleq \mathbb{E}_Y[Y|X]$ equals one: $k_{\text{eff}} = 1$.

so that the Boltzmann transport slowing-down k_{eff}-eigenproblem (3.55) is simply re-cast as follows:

$$R_k(E) = \int_E^{E_\infty} \mathsf{D}_\mathsf{S} R_k \mathrm{d}E + \frac{\chi(E)}{k_{\text{eff}}} \int_0^{E_\infty} \mathsf{f}_\nu R_k \mathrm{d}E. \tag{3.59}$$

where we define the total neutron production by fission as

$$F_k \triangleq \int_0^{E_\infty} \mathsf{f}_\nu R_k \mathrm{d}E, \tag{3.60}$$

In the case of zero Kelvin nuclear cross sections, we established their windowed multipole representation (see publication [130] or chapter 4), which is their local meromorphic pole expansion. This means that we can also perform a partial

fraction decomposition of the downscattering ratio in $z \triangleq \sqrt{E}$ space:

$$\mathsf{D_S}(z) \triangleq \frac{2\Sigma_s(z)}{z\Sigma_t(z)} = \sum_{n=1}^{N_p} \frac{a_n}{z - b_n} \tag{3.61}$$

For neutral massive (not photons) particles, we proved the latter is a (complex valued) rational function of degree -1, with $N_p = 2N_L + 1$ poles, where N_L is the number of radioactive poles (E.42), which we demonstrated in [125]:

$$N_p \triangleq 2(2N_\lambda + \sum_c \ell_c) + 1. \tag{3.62}$$

We were then able to derive a closed-form expression for the reaction rate:

$$R_k(E) = \chi_0 \frac{F_k}{k_{\text{eff}}} \prod_{n=1}^{N_p} \left(\frac{\sqrt{E_\infty} - b_n}{\sqrt{E} - b_n} \right)^{a_n}. \tag{3.63}$$

This reaction rate, and the corresponding flux, is reported in figure 3-8. Though this result is only valid for zero Kelvin R-matrix reaction cross sections, it is to our knowledge the first-ever explicit resolution of nuclear resonance self-shielding. Strikingly, no assumptions were made on the overlap of nuclear resonances, a traditionally unsolved challenge in nuclear reactor physics [154, 278, 325, 108, 221].

- (ii) Numerical resolution of the multiplication factor k_{eff}.

Though the analytic benchmark provides closed-form expression (3.63) for the reaction rate (and therefore the flux), it only provides with an integral expression for the multiplication factor, which must them be computed numerically:

$$k_{\text{eff}} = \frac{\chi(E_\infty) \int_{E_0}^{E_\infty} \mathrm{d}E' \nu\Sigma_f(E')\psi_k(E')}{\Sigma_t(E_\infty)\psi_k(E_\infty)}. \tag{3.64}$$

- (iii) Resolution of α versus k_{eff} eigenvalue problems.
The analytic benchmark also studies the discrepancy between solving the k_{eff}-eigenproblem (3.55) and the α-eigenproblem:

$$\left[\frac{\alpha}{v} + \Sigma_t(E)\right] \psi_\alpha(E) - \int_E^{E_\infty} \mathrm{d}E' \frac{\Sigma_s(E')}{E'} \psi_\alpha(E') = \chi(E) \int_{E_0}^{E_\infty} \mathrm{d}E' \nu\Sigma_f(E')\psi_\alpha(E') \tag{3.65}$$

It establishes the remarkable closed-formula discrepancy between the α and the

k_{eff} reaction rates near-criticality ($k = 1$):

$$\frac{R_{\alpha,\Sigma} - R_{k,\Sigma}}{R_{k,\Sigma}}(E) \underset{|\alpha|\ll 1}{\simeq} \alpha \left[\sum_{n=1}^{N_p} \frac{\partial a_n}{\partial \alpha} \ln\left(\frac{\sqrt{E_\infty} - b_n}{\sqrt{E} - b_n} \right) + a_n \frac{\partial b_n}{\partial \alpha} \left[\frac{1}{\sqrt{E} - b_n} - \frac{1}{\sqrt{E_\infty} - b_n} \right] \right] \tag{3.66}$$

where the $\frac{\partial a_n}{\partial \alpha}$ and $\frac{\partial b_n}{\partial \alpha}$ are obtained by partial fraction decomposition (or contour integration) of

$$\frac{\partial \mathsf{D_S}^\alpha}{\partial \alpha}(z) = \sum_{n=1}^{N_p} \left[\frac{\frac{\partial a_n^\alpha}{\partial \alpha}}{z - b_n} + \frac{a_n \frac{\partial b_n^\alpha}{\partial \alpha}}{(z - b_n)^2} \right]. \tag{3.67}$$

where

$$\mathsf{D_S}^\alpha(z) \triangleq \frac{2\Sigma_s(z)}{z\Sigma_t^\alpha(z)} \tag{3.68}$$

and

$$\Sigma_t^\alpha(E) \triangleq \frac{\alpha}{v} + \Sigma_t(E) \tag{3.69}$$

- (iv) Arbitrary order derivatives of the flux and eigenvalues to any parameter: Using a similar approach to that for the study of the discrepancy between k_{eff} and α eigenvalue problems, we established general perturbation theory solutions for the flux and eigenvalues. The reasoning goes as follows: we decompose the Boltzmann transport problem into fission source and transport terms

$$T\psi = \lambda F\psi \tag{3.70}$$

Where $\lambda \triangleq 1/k$, and the operators are defined as:

$$T\psi \triangleq \Sigma_T(E)\psi(E) - \int_E^{E_\infty} \frac{\Sigma_s(E')}{E'}\psi(E')dE' \tag{3.71}$$

and

$$F\psi \triangleq \chi(E) \int_{E_0}^{E_\infty} \nu\Sigma_f(E')\psi(E')dE' \tag{3.72}$$

Taking the n-th derivative (denoted (n) superscript) of the transport eigenproblem (3.77) with respect to any arbitrary parameter X, we obtain a lower-triangular system:

$$\sum_{k=0}^{n} \binom{n}{k} T^{(k)}\psi^{(n-k)} = \sum_{k=0}^{n}\sum_{j=0}^{k} \binom{n}{k}\binom{k}{j} \lambda^{(j)} F^{(k-j)}\psi^{(n-k)} \tag{3.73}$$

with unknowns $\psi^{(k)}$, $\lambda^{(k)}$, while operators T, and F, and all their higher order derivatives, are known. Being lower-triangular, the system can be rewritten as:

$$T\psi^{(n)} = \lambda^{(n)} F\psi + C_n \tag{3.74}$$

with

$$C_n \triangleq \sum_{j=0}^{n-1} \lambda^{(j)} F^{(n-j)} \psi + \sum_{k=1}^{n-1} \sum_{j=0}^{k} \binom{n}{k} \binom{k}{j} \lambda^{(j)} F^{(k-j)} \psi^{(n-k)} - \sum_{k=1}^{n} \binom{n}{k} T^{(k)} \psi^{(n-k)} \tag{3.75}$$

Using the Fredholm alternative [57, 56] then allows us to solve for $\lambda^{(n)}$ as:

$$\lambda^{(n)} = -\frac{< C_n, \phi >}{< F\psi, \phi >} \tag{3.76}$$

where ϕ is the adjoint flux, solution to the adjoint transport eigenproblem:

$$T^{\dagger}\phi = \lambda^{\dagger} F^{\dagger} \phi \tag{3.77}$$

Such $\lambda^{(n)}$ guarantees the derivative transport equation (3.74) can be inverted (Fredholm alternative), from which the derivative flux $\psi^{(n)}$ can be found.

3.3.2 Prior nuclear data uncertainty and sensitivities

We now deploy our Embedded Monte Carlo method on the hereupon introduced analytic benchmark, as a proof-of-concept application to nuclear particle transport. The input parameters X of the benchmark are the resonance parameters of the first quantum resonance of both the ^{238}U and the ^{239}Pu nuclear cross sections. The resonance parameters X uncertainty is modeled as a multivariate normal distribution $X|\theta \sim \mathcal{N}(\mu_0, \Sigma_0)$, the mean vector μ_0 and covariance matrix Σ_0 which are documented in the standard nuclear data libraries that compose our collective knowledge of nuclear physics (ENDF [88]). The benchmark multiplication factor is $k_{\text{eff}}^0 = 1.0$ when computed with the mean resonance parameters $\boldsymbol{\mu}_0$.

In order to make evident the non-linear effects (and to reduce the computational cost of converging the Embedded Monte Carlo estimators), we here focus only on the capture widths resonance parameters X (plutonium ^{239}Pu and uranium ^{238}U respectively), and use their scaled-up uncertainty (fictitious large covariance matrix) from the analytic benchmark [298, 53] as the prior uncertainty distribution, which has an uncertainty of about 7% for the plutonium capture width and 105% for the uranium one:

$$\boldsymbol{\mu}_0 = \begin{bmatrix} 0.03982423 \\ 0.022711 \end{bmatrix}, \boldsymbol{\Sigma}_0 = \mathbf{diag}\left(\begin{bmatrix} 7.91779341 \times 10^{-6} \\ 5.69933580 \times 10^{-4} \end{bmatrix} \right) \tag{3.78}$$

Sampling resonance energies X from this prior uncertainty $X|\theta \sim \mathcal{N}(\boldsymbol{\mu}_0, \boldsymbol{\Sigma}_0)$ yields the stochastic cross sections in figure 3-9. These propagate to a distribution of multiplication factors $Z(X|\theta) = k_{\text{eff}}|\theta$, we report as the blue histogram in figure 3-9 (obtained using a Nested Monte Carlo "brute force" computation). We superimposed the two noisy measurements of k_{eff} which constitute the two data-points from which Embedded Variational Inference will infer and propagate back the uncertainty. These noisy measurements were generated numerically from $k_{\text{eff}} = 1 + \epsilon_i$, with the noise ϵ_i

being sampled from heteroskedastic centered Gaussians with uncertainties ranging around 2500 p.c.m., representing two experimental results as could be obtained from an integral experiment.

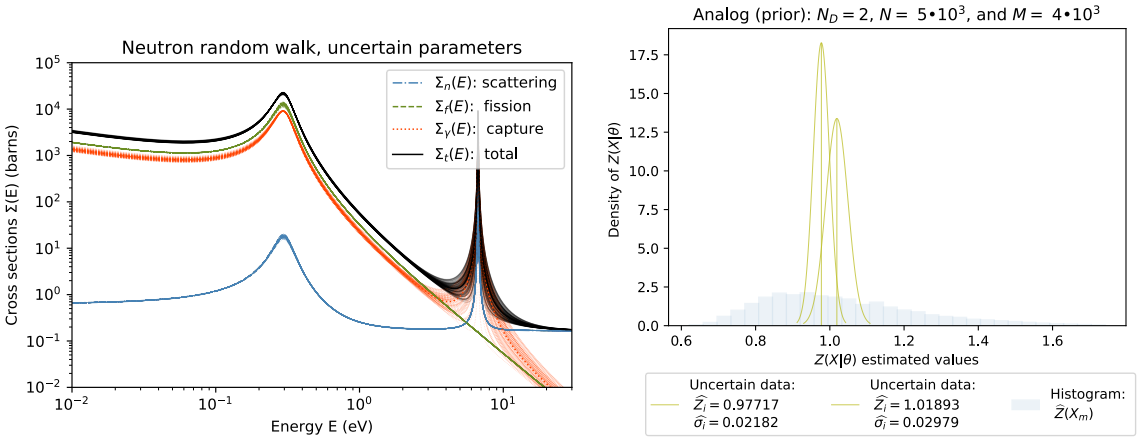

Figure 3-9: Prior distributions. The prior distribution of inputs $X|\theta$ (stochastic nuclear cross sections) propagates across the particles Monte Carlo random walk $Y|X$, yielding a distribution of outputs $Z(X|\theta)$ (blue histogram). Two noisy output measurements $D = \{Z_i\}$ are provided (green normal distributions) to perform Bayesian inference.

Importantly, the analytic benchmark [53] also provides the Jacobians $\frac{\partial Z}{\partial X}$ (sensitivities), by which *sensitivity analysis* (SA) first-order propagation and inference can be performed by linearizing the ensemble average relation through its Taylor expansion (2.3), linear forward propagation using the well-known variance relation (2.10) (called "sandwich rule" in the nuclear data field), and linear Bayesian inference (2.7) and (2.8) assuming Gaussian additive noisy data (2.5)

For the analytic benchmark, the multiplication factor k_{eff} sensitivities to the capture resonance width parameters are [53]:

$$\left.\frac{\partial Z}{\partial X}\right|_{X_0} = \frac{\partial k_{\text{eff}}}{\partial \mu_0} = \begin{bmatrix} -8.23992305 \\ -10.39643732 \end{bmatrix} \tag{3.79}$$

3.3.3 Prior uncertainty forward propagation

Sensitivities (3.79) enable us to compare linear (sensitivity analysis) to non-linear (Embedded Monte Carlo) inference and propagation, and in turn to the direct "brute-force" Nested Monte Carlo simulations (Total Monte Carlo). To first order (sensitivity analysis), the uncertainty (3.78) linearly propagates to the multiplication factor $k^0_{\text{eff}} \triangleq Z(X)$ as a normal distribution with mean 1 and standard deviation of $\sigma_{k^0_{\text{eff}}} = 24928$ p.c.m.. Figure 3-10 compares this distribution to those obtained from Embedded Forward Propagation (for both log-normal and normal reconstruction) and from Nested Monte Carlo. We coded two Monte Carlo implementations of the nuclear stochastic process $Y|X$ that we label: analog; and continuous. The analog case is a

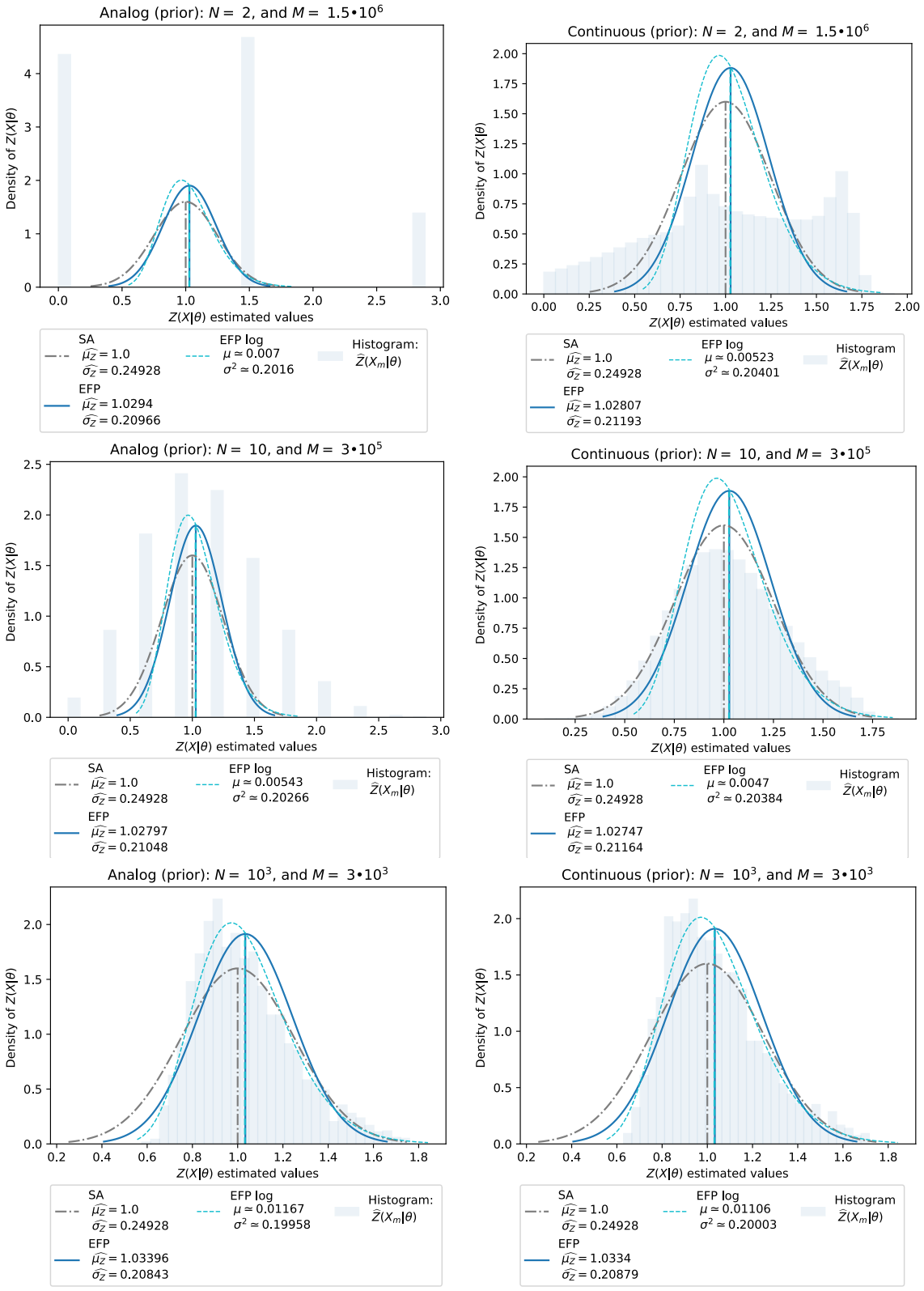

Figure 3-10: Embedded Forward Propagation: Analytic benchmark prior uncertainty. For analog and continuous Monte Carlo codes, prior inputs $X|\theta$ uncertainty distribution is forward propagated to the output multiplication factor $Z(X|\theta) = k_{\text{eff}}|\theta$ using: linearized sensitivity analysis SA; Embedded Forward Propagation EFP; and Nested Monte Carlo. According to the maximum entropy principle, since $k_{\text{eff}} > 0$, log-normal EFP reconstructs better than normal.

simple Bernoulli process, whereby each neutron either gets captured or fissions at the end of its slowdown, and thus contributes either 0 or ν to the output multiplication factor $k_{\text{eff}} \triangleq Z(X)$. In contrast, the implementation named continuous tallies the ratio of fission to capture, thereby contributing the corresponding fraction of ν to the multiplication factor. This reduces the variance of $Z(X)$, and therefore acts like a convergence accelerator. Figure 3-10 shows how the log-normal Embedded Monte Carlo fits the prior uncertainty distribution of multiplication factors $k^0_{\text{eff}} \triangleq Z(X|\theta)$ more accurately. Since the multiplication factor is a positive quantity, one can interpret the better log-normal fit as an instance of the maximum entropy principle.

For the prior uncertainty forward propagation, one can estimate the optimal trade-off between inner-loop N (number of particles per run) and outer-loop M (number of different nuclear data samples) theorem 2, and using subsequent (3.20) and (3.21) for order of magnitude reckonings. In the analog case $k_{\text{eff}} = \nu p$ — where p is the Bernoulli parameter that is the likelihood that a neutron that is born will fission, producing ν neutrons in the wake — so the variance of the inner-loop Bernoulli process is $\Sigma_Y = (\nu - k_{\text{eff}})^2 p + k^2_{\text{eff}}(1-p)$. Since $k^0_{\text{eff}} = 1$, it yields a corresponding inner-loop variance of 1.88, so we approximate $\langle \Sigma^2_Y \rangle \approx 3.5$ in (3.20). The outer-loop variance is $\langle \Delta^2 Z \rangle = \sigma^2_{k^0_{\text{eff}}} \approx 6.2 \times 10^{-2}$, so that the optimal EFP ratio would be on the order of $N \approx 40$ neutrons per run.

3.3.4 Inference from one noisy data-point

We then generate one noisy observation $D = \left\{ Z_i \right\}$ of outputs $Z(X)$, with $Z_i = Z(X) + \epsilon_i$, drawn at random yielding $Z_i = 0.97717 \pm 0.04364$ (standard deviation $\sigma_i = 0.02182$), and proceed to infer updated input parameters $X|D$ using Embedded Variational Inference (theorem 3). The EVI estimators (3.41) were computed with the analog Monte Carlo tallies at minimum convergence, that is for each iteration step t, only one sample of the resonance parameters is drawn ($M = 1$), for which only two neutrons are run ($N = 2$) each contributing either 0 or ν to the $Z(X) = k_{\text{eff}}$ estimator (3.37). It is likely that a continuous Monte Carlo simulation with a more optimized ratio of outer-loop M to inner-loop N estimators would accelerate convergence (such as in theorem 2), yet we deliberately chose the estimators as binary (analog) and non-converged to show the EVI algorithm works even under exacting circumstances. The initial guesses were set at the prior values $\theta = \{\boldsymbol{\mu}_0, \boldsymbol{\Sigma}_0\}$, which is a difficult starting point as one of the covariance matrix entry is expected to diminish by two orders of magnitude. All EFP propagations were computed with a total of three million particle runs ($M \times N = 3 \times 10^6$), while all EVI inferences were performed with three million iterations ($T = 3 \times 10^6$ and $T \times M \times N = 6 \times 10^6$). For a single observation ($N_D = 1$), the learning rate sequences of EVI algorithm (3.30) for the mean and the Gramm root matrix in (3.54), were respectively set to (3.80) — chosen empirically for their fast initial narrowing down towards the correct orders of magnitude given our computational constraint of 10^7 neutrons total budget:

$$\gamma_{t\boldsymbol{\mu}} = \frac{10^{-8}}{(t+1)^{1/2}} \cdot \boldsymbol{\mu}_0 \quad , \quad \gamma_{t\boldsymbol{S}} = \frac{5 \times 10^{-2}}{(t+1)^{1/8}} \tag{3.80}$$

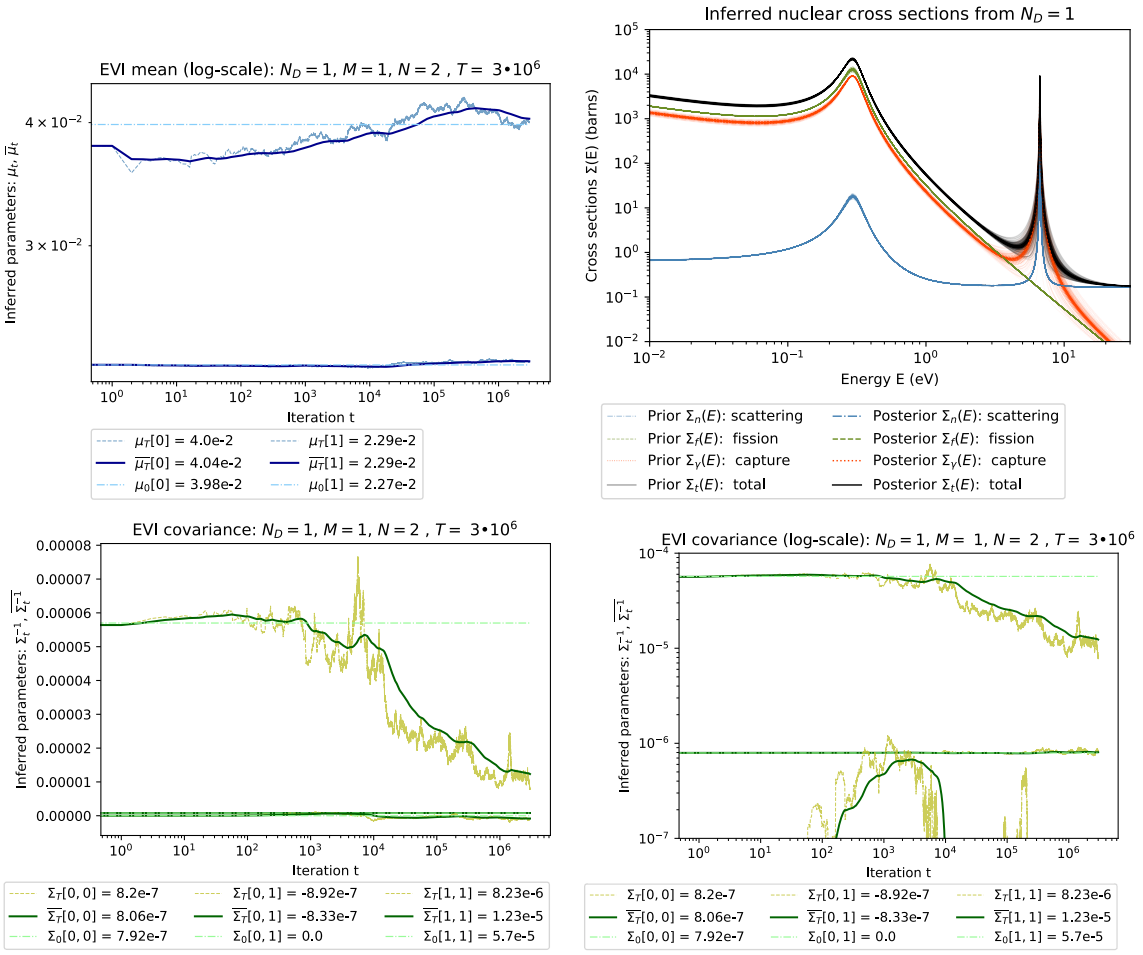

Figure 3-11: Embedded Variational Inference: one-point learning. Given one ($N_D = 1$) noisy observation D of multiplication factor outputs $k_{\text{eff}} \triangleq Z(X)$, Embedded Variational Inference algorithm (3) infers Bayesian posterior inputs $X|D$ across the analytic benchmark with a convergence rate of $\mathcal{O}\left(\frac{1}{\sqrt{T}}\right)$.

Figure 3-11 shows the $\mathcal{O}\left(\frac{1}{\sqrt{T}}\right)$ convergence of EVI algorithm (3.30), and stochastic cross sections from the updated uncertainty distribution. The updated parameters from Embedded Variational Inference are:

$$\boldsymbol{\mu}_{X|D}^{\text{EVI}} = \begin{bmatrix} 0.04036485 \\ 0.02290588 \end{bmatrix}, \boldsymbol{\Sigma}_{X|D}^{\text{EVI}} = \begin{bmatrix} 8.05708972 \times 10^{-7} & -8.32966704 \times 10^{-7} \\ -8.32966704 \times 10^{-7} & 1.23386885 \times 10^{-5} \end{bmatrix} \tag{3.81}$$

compared to those from first-order linearized sensitivity analysis:

$$\boldsymbol{\mu}_{X|D}^{\text{SA}} = \begin{bmatrix} 0.03984802 \\ 0.02487164 \end{bmatrix}, \boldsymbol{\Sigma}_{X|D}^{\text{SA}} = \begin{bmatrix} 7.84981490 \times 10^{-6} & -6.17380691 \times 10^{-6} \\ -6.17380691 \times 10^{-6} & 9.22847964 \times 10^{-6} \end{bmatrix} \tag{3.82}$$

We then propagate these inferred inputs $X|D$ to outputs $Z(X|D)$. Figure 3-12 compares the resulting $Z(X|D)$ distributions obtained from linear sensitivity analysis (SA); Embedded Monte Carlo (EFP); and Nested Monte Carlo. Note that the SA distribution is almost identical to the data-point $D = Z_i$ uncertainty, while the EVI uncertainty is larger. Perhaps three million EVI iterations did not fully converge the inferred parameters distribution $X|D$. Nonetheless, the EFP can accurately re-

construct the fully converged Nested Monte Carlo distribution, even for minimal estimators ($N = 2$). As previously, we consider the optimal EFP ratio of inner-loop N to outer-loop M, which theorem 2 links to the ratio of their variances (and kurtoses). We again use (3.20) and (3.21) as rough approximations, and estimate the optimal number of particles for analog EFP (Bernoulli binary process). The outer-loop is now determined by the data D uncertainty, in the order of 2000 p.c.m, so the optimal inner-loop number is closer to $N \approx 6000$. Thus, with more accurate data D, it is harder to resolve the Monte Carlo estimators, and it becomes more beneficial to converge the inner-loop variance. The continuous implementation of our Monte Carlo code will lower this optimal inner-loop number.

3.3.5 Inference from two noisy data-points

We generate a second noisy observation $Z_i = Z(X) + \epsilon_i$ of outputs $Z(X)$, drawn at random yielding $Z_i = 1.01893 \pm 0.05958$ (standard deviation $\sigma_i = 0.02979$). We then study the entire inference and propagation process with now two data-points $N_D = 2$, starting from the previously inferred parameters $X|D$ from one data-point. All runs were again carried out with three million particles, and identical learning rates (3.80) but for a doubling of the precision matrix one $\gamma_{t_{\boldsymbol{S}}} = \frac{10^{-1}}{(t+1)^{1/8}}$, yielding the following parameters distributions, inferred from two point $N_D = 2$ using EVI and SA respectively:

$$\boldsymbol{\mu}_{X|D}^{\text{EVI}} = \begin{bmatrix} 0.04105095 \\ 0.02281541 \end{bmatrix}, \boldsymbol{\Sigma}_{X|D}^{\text{EVI}} = \begin{bmatrix} 7.33049849 \times 10^{-7} & -6.88597475 \times 10^{-7} \\ -6.88597475 \times 10^{-7} & 5.99878688 \times 10^{-6} \end{bmatrix} \tag{3.83}$$

$$\boldsymbol{\mu}_{X|D}^{\text{SA}} = \begin{bmatrix} 0.03983285 \\ 0.02349389 \end{bmatrix}, \boldsymbol{\Sigma}_{X|D}^{\text{SA}} = \begin{bmatrix} 7.84963386 \times 10^{-6} & -6.19024919 \times 10^{-6} \\ -6.19024919 \times 10^{-6} & 7.73519189e \times 10^{-6} \end{bmatrix} \tag{3.84}$$

Figure 3-13 shows the EVI convergence towards the inferred parameters $X|D$, and the corresponding uncertain nuclear cross sections. Note that the elements of covariance matrices inferred from EVI were often smaller than those obtained from SA, yet would still yield larger uncertainties when propagated to $Z(X|D)$. This shows how much correlations in the covariance matrix and the sensitivities can influence the uncertainty of the outcome.

Finally, we then forward propagate these again to the multiplication factor outputs $Z(X|D) = k_{\text{eff}}|D$, and report the corresponding distributions in figure 3-14. There, one can see how the inferred parameters means are now in between the two data-points uncertainty distributions, correspondingly weighted as in sensitivity analysis (2.8). Embedded Monte Carlo closely matches the Nested Monte Carlo simulations, even with vastly under-converged inner-loops. Since fast-TMC is based on converging the inner-loop (reactor simulations) to within the outer-loop uncertainty (from nuclear data), that entails an order of magnitude of 10 to 100 times less neutrons needed to converge an Embedded Monte Carlo calculation, depending on the optimal trade-off number (3.21), which is of the order of $N \approx 6000$ for nuclear data uncertainty translating into 2000 p.c.m (outer-loop) for an analog (binary) Monte Carlo particle

transport close to criticality. Strikingly, computations with only two neutrons per resonance parameters, in analog Monte Carlo transport simulations yielding binary Bernoulli tallies, suffice to accurately propagate and infer the input data uncertainty across the complex stochastic process.

This analytic benchmark case is just an illustration of the potential applications of the Embedded Monte Carlo method to nuclear computations. More generally, Embedded Monte Carlo could be used to propagate and infer uncertainty from any random inputs in geometry (pebble-bed, structural uncertainty, etc. [216]), or nuclear physics (nuclear data, nuclear models, etc.).

3.4 Embedded conclusion

Given a set of input parameters X, you dispose of a simulator capable of generating occurrences of an intractable stochastic process $Y|X$, in the sense that simulations of $Y|X$ are costly. You are provided with a data set $D \triangleq \{Z_i\}$ of noisy observations of the stochastic process ensemble average $Z(X) \triangleq \mathbb{E}_Y[Y|X]$ (conditional mean). We here establish novel *Embedded Monte Carlo* methods to approximate the updated Bayesian inference distribution of the parameters $X|D$, and propagate it to the outputs $Z(X|D)$. Such Embedded Monte Carlo Bayesian inference works under the general hypotheses that the log-likelihood of the data, $\ln(p(D|X))$, is polynomial (which is the case for Gaussian noise). With appropriate learning rates, the *Embedded Variational Inference* algorithm (an iterative stochastic optimization) converges to the best posterior $X|D$ distribution approximation within a parametric family (as of the principle of minimum discrimination information), at the same asymptotic rate $\mathcal{O}\left(\frac{1}{\sqrt{T}}\right)$ as it takes to converge any one output value $Z(X)$. *Embedded Forward Propagation* can then propagate this inferred uncertainty distribution of inputs $X|D$ to the outputs $Z(X|D)$, at the same asymptotic rate $\mathcal{O}\left(\frac{1}{\sqrt{M}}\right)$. This is possible assuming the moments of the ensemble averages distribution $p(Z(X|D))$ exist (non-heavy-tails) and can well reconstruct the distribution (moments problem). We verify all the methods on a toy problem with step-by-step analytic solutions from multivariate normal conjugate priors. We then apply Embedded Monte Carlo to the stochastic process at the origins of the Monte Carlo method: the random walk of nuclear particles. We show how Embedded Monte Carlo enables Bayesian inference and uncertainty propagation of nuclear data across the intractable branching process of neutron fission chain reactions, without ever having to converge any one simulation: a breakthrough in the field.

Much research is further needed in order to determine systematic methods to chose learning rate sequences appropriate to given applications, as well as on how to scale up to many input parameters X, as our empirical experience was that the algorithms become ever more unstable as more and more parameters are added for inference.

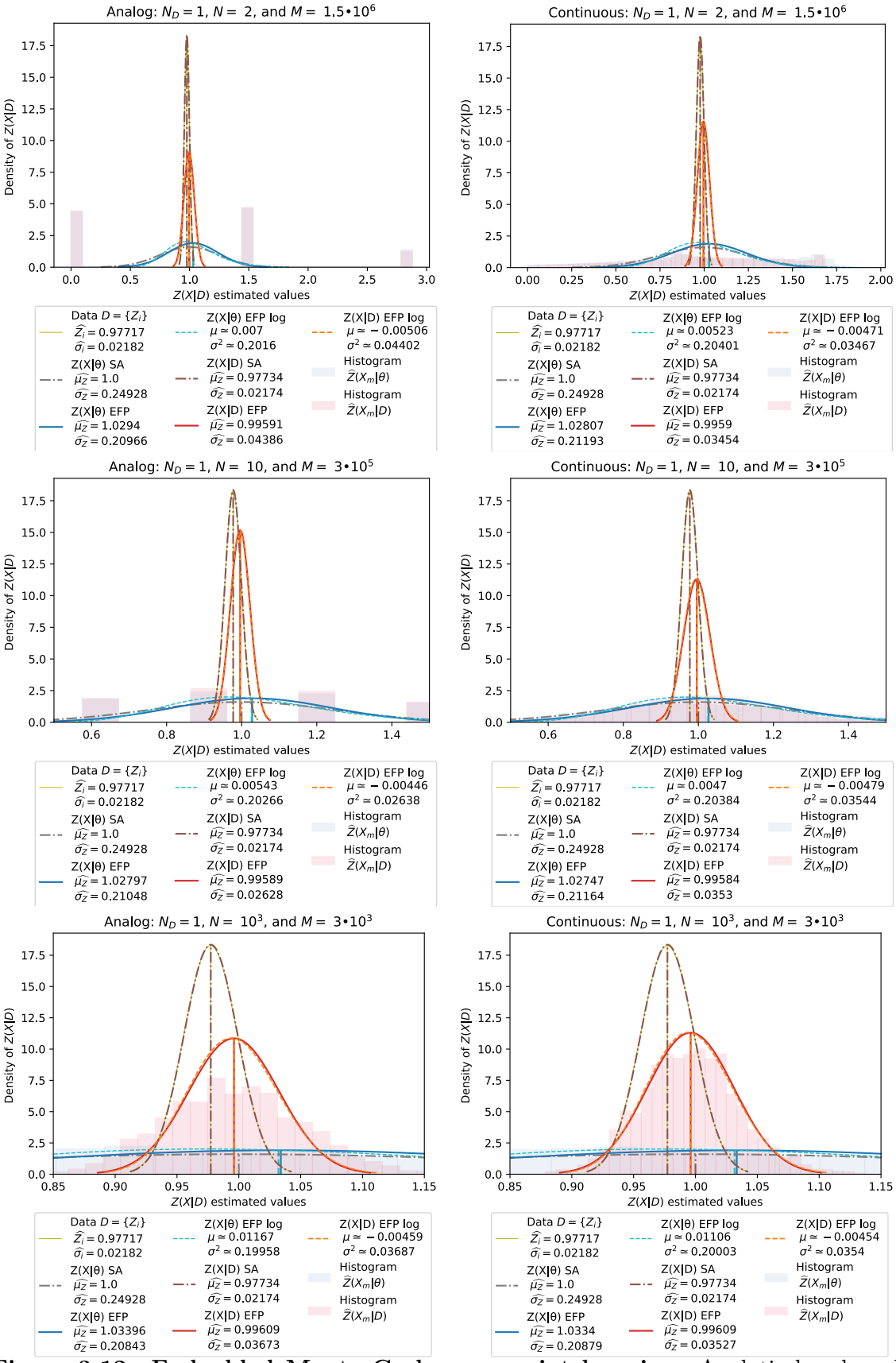

Figure 3-12: Embedded Monte Carlo: one-point learning. Analytic benchmark one-point inferred resonance parameters $X|D$ (EVI theorem 3 with $N_D = 1$), forward propagated to multiplication factor outputs $Z(X|D) = k_{\text{eff}}|D$ using SA, EFP, and Nested Monte Carlo, for analog and continuous neutron transport codes.

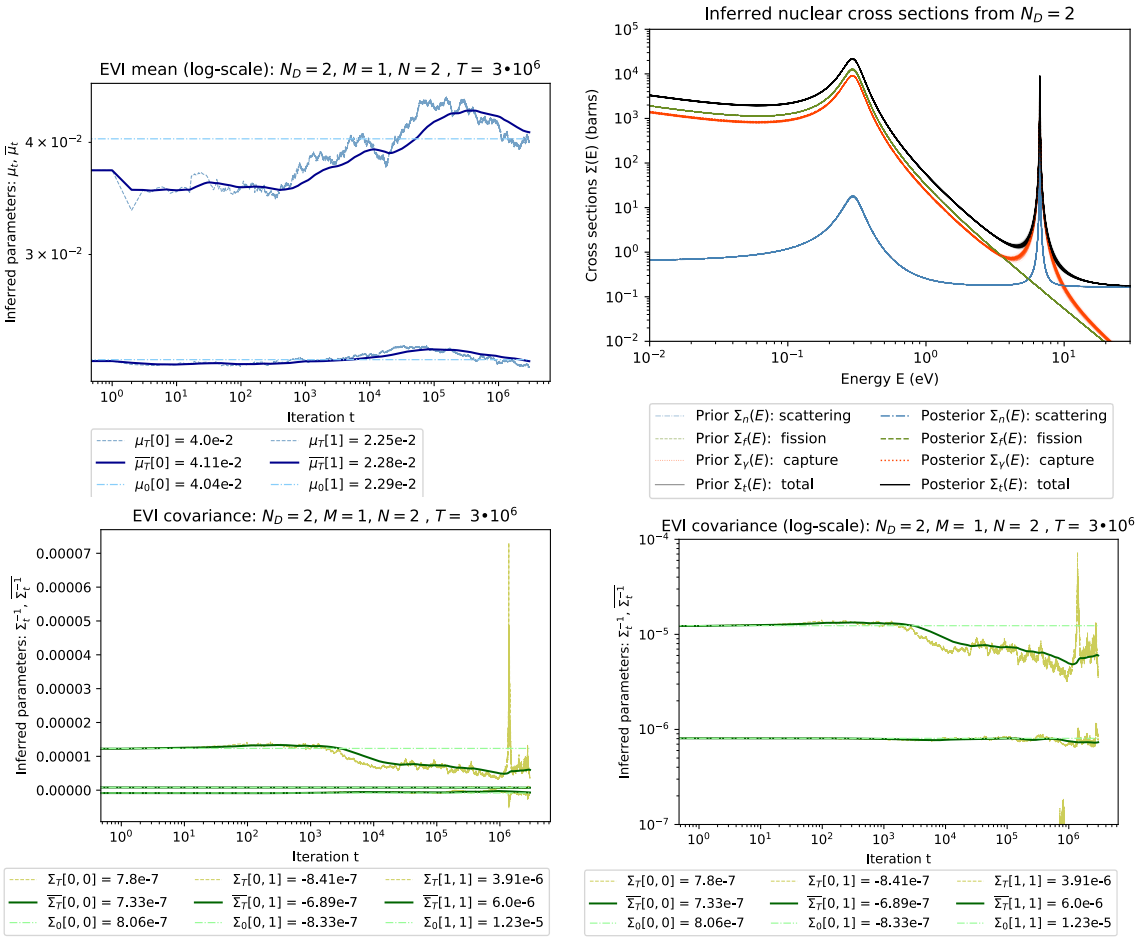

Figure 3-13: Embedded Variational Inference: Analytic benchmark two-points posterior uncertainty. Given two ($N_D = 2$) noisy observations D of outputs (multiplication factor $k_{\text{eff}} \triangleq Z(X)$), Embedded Variational Inference algorithm (3) infers Bayesian posterior inputs $X|D$ with a convergence rate of $\mathcal{O}\left(\frac{1}{\sqrt{T}}\right)$.

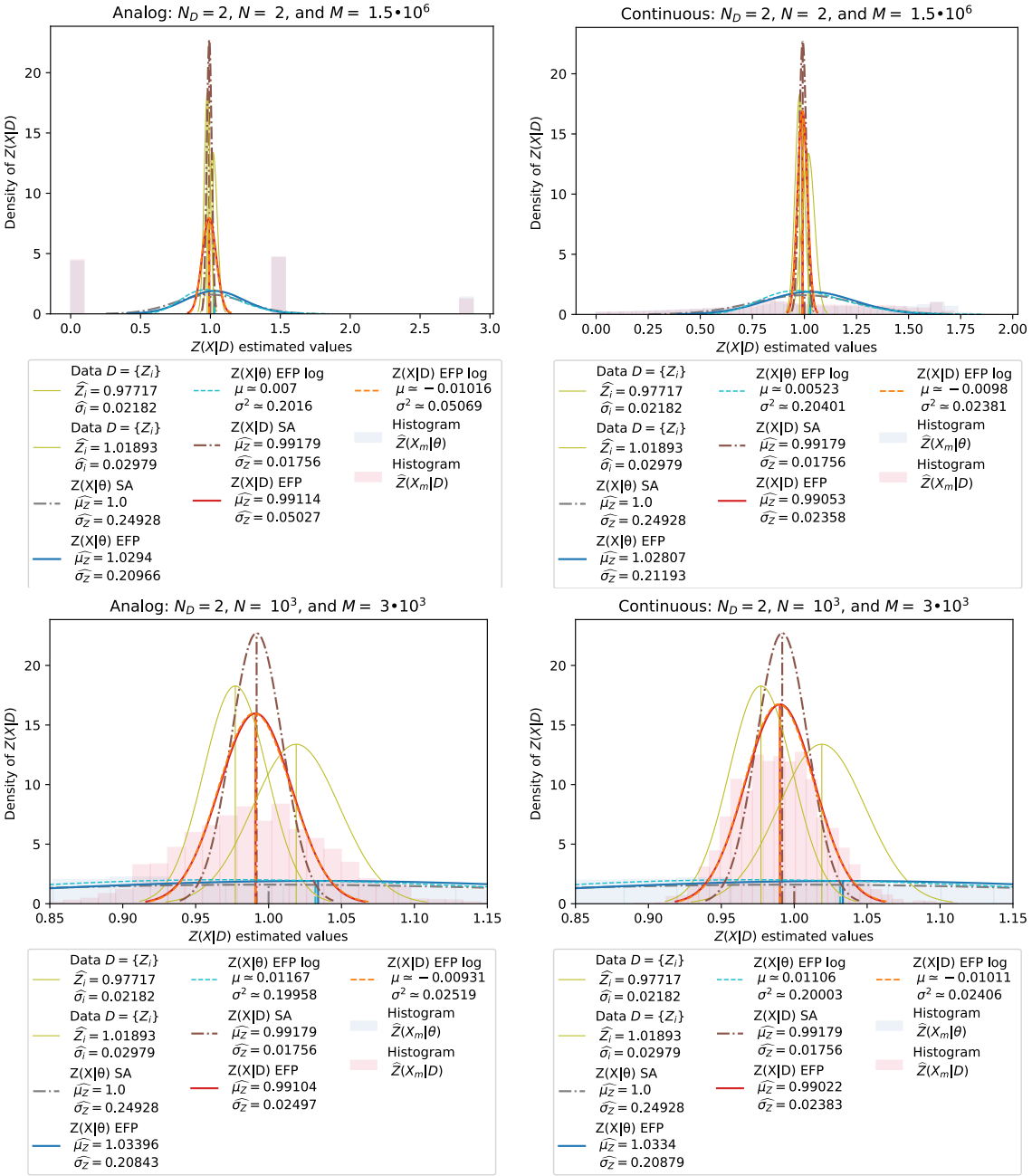

Figure 3-14: Embedded Monte Carlo: two-points learning. Analytic benchmark two-points inferred resonance parameters $X|D$ (EVI theorem 3 with $N_D = 2$), forward propagated to multiplication factor outputs $Z(X|D) = k_{\text{eff}}|D$ using SA, EFP, and Nested Monte Carlo, for analog and continuous neutron transport codes.

Chapter 4

Windowed Multipole Stochastic Cross Sections

Dans la vie, rien n'est à craindre, tout est à comprendre.
C'est maintenant le moment de comprendre davantage, afin de craindre moins.
- Marie Skłodowska-Curie

The analytic benchmark example demonstrates how the new Embedded Monte Carlo statistics can be used to both: (a) propagate uncertainty in nuclear data to the outputs of nuclear simulations (Embedded Forward Propagation); and (b) take empirical uncertainty from experimental observations of outputs, and combine them to a simulation of the experiment in question, in order to infer an updated distribution for the nuclear data (Embedded Variational Inference). Both are achieved at a drastically reduced computational cost compared to Total Monte Carlo (TMC), and rely on the capability of running few neutrons (as few as two) on many different possible nuclear physics landscapes, that is Embedded Monte Carlo rests on being able to readily sample nuclear cross sections from their uncertainty distributions.

While sampling nuclear data from their uncertainty distribution is fairly straightforward, it is in practice difficult to translate this into their corresponding nuclear cross sections (input to the nuclear simulation). This is because nuclear cross sections must undergo a processing step to account for temperature effects, in particular *Doppler broadening*. This difficulty was not present in the analytic benchmark problem because it is a zero-kelvin problem, but in practice standard nuclear libraries such as ENDF undergo a thorough pre-processing step to generate the cross sections at the correct temperatures (using codes such as NJOY [228]), storing the resulting point-wise nuclear cross sections into ACE files counting some 100,000 points for each actinide at each reference temperature, over a grid of some 100 reference temperatures: a considerable memory footprint. At present, generating millions of such ACE files would therefore be necessary to run an Embedded Monte Carlo scheme, and this

would be prohibitively costly (see section 2.6).

In order to efficiently use the Embedded Monte Carlo methods, we therefore need to be able to generate Doppler-broadened stochastic nuclear cross sections on-the-fly, meaning without any large pre-computations stored in memory, just as it was the case in the analytic benchmark. To achieve this, our team at MIT — in collaboration with research groups at Los Alamos and Oak Ridge national laboratories, as well as at University of Tennessee Knoxville — has developed a new *windowed multipole library*. This library parametrizes the same nuclear cross sections in a different mathematical representation — with *windowed multipole parameters* — which enables to sample windowed multipole parameters, and subsequently compute the corresponding Doppler broadened cross sections, on-the-fly and efficiently.

We introduced the temperature Doppler broadening problem in section 2.6, and how various methods have been recently proposed to perform Doppler broadening on-the-fly (section 2.6.2), ranging from temperature curve-fits [326], to rejection-sampling [316, 317, 288], or Fourier transform [145], and pseudo-materials [111, 313, 261]. Before moving-on to explain how we can perform Doppler broadening on-the-fly using the windowed multipole representation (section 4.2), let us first here briefly recall a *optimal quadrature kernel reconstruction* method we developed that is, to the best of our knowledge, the best performer in temperature interpolation for Doppler broadening.

4.1 Doppler kernel reconstruction optimal quadrature

In our article [124] (transcribed *verbatim* in appendix F), we developed a new optimal quadrature method for temperature interpolation — called *Doppler kernel reconstruction* — which outperforms ten-times-over the previous best-performing state-of-the-art "curve fit" interpolation method [326], in that with only 10 reference temperatures $\left\{T_i\right\}$ it achieves better than 0.1% interpolation accuracy (maximum relative error i.e. L_0-norm) for the Doppler broadened ^{238}U cross section over the energy range of $[10^{-5}\text{eV}, 20\,\text{keV}]$, and range of temperature $[300\,\text{K}, 3000\,\text{K}]$ — which are typical nuclear reactor conditions — when with the same 10 reference temperatures the current state-of-the-art "curve fit" method [326] achieves only a 1% interpolation accuracy, as we show in figure 4-1 (which is FIG. 4 from [124]).

Our Kernel reconstruction optimal quadrature method is thoroughly established in [124], and summarized in [123]. We here succinctly synthesize its essential steps for implementation purposes.

Kernel reconstruction approximates the exact cross section $\sigma_T^{(exact)}(E)$ at any energy E with a linear combination of pre-tabulated cross sections at reference temperatures $\left\{T_i\right\}$:

$$\sigma_T^{(exact)}(E) \approx \sigma_T^{(approx)}(E) = \sum_{j=1}^{N} c_j(T)\ \sigma_{T_j}(E) \tag{4.1}$$

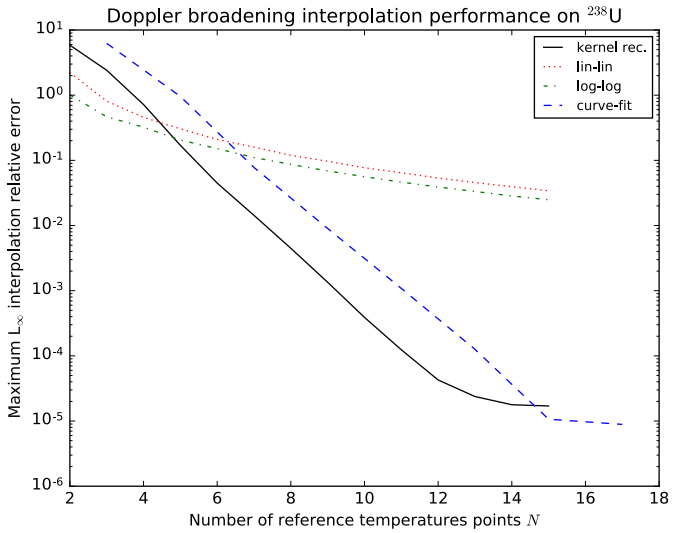

Figure 4-1: Kernel reconstruction optimal quadrature for Doppler broadening temperature interpolation. Maximum relative errors over energy $[10^{-5}\text{eV}, 20\,\text{keV}]$ and temperature $[300\,\text{K}, 3000\,\text{K}]$ ranges. Performance of optimal quadrature Doppler kernel reconstruction method (kernel rec. [124]) compared to linear interpolation (lin-lin), logarithmic interpolation (log-log), and the MCNP curve fit (curve-fit [326]) method. Kernel reconstruction is ten times more accurate than the MCNP curve-fit method. $N = 10$ optimal reference temperatures suffice to achieve 0.1% relative error.

the interpolation coefficients c_j of the quadrature are then obtained by solving minimization problem:

$$c_j(T) = \underset{c_j}{\operatorname{argmin}} \left\| \mathcal{K}_T^{\mathbb{D}} - \sum_j c_j \mathcal{K}_{T_j}^{\mathbb{D}} \right\|_{\mathrm{L}_2} \tag{4.2}$$

We managed to cast the latter as the Gram matrix inversion problem

$$\begin{bmatrix} \frac{\sqrt{T_1 T_1}}{\left(\frac{T_1+T_1}{2}\right)} & \cdots & \frac{\sqrt{T_1 T_N}}{\left(\frac{T_1+T_N}{2}\right)} \\ \vdots & \ddots & \vdots \\ \frac{\sqrt{T_1 T_N}}{\left(\frac{T_1+T_N}{2}\right)} & \cdots & \frac{\sqrt{T_N T_N}}{\left(\frac{T_N+T_N}{2}\right)} \end{bmatrix} \cdot \begin{bmatrix} c_1 \\ \vdots \\ c_N \end{bmatrix} = \begin{bmatrix} \frac{\sqrt{T_1 T}}{\left(\frac{T_1+T}{2}\right)} \\ \vdots \\ \frac{\sqrt{T_N T}}{\left(\frac{T_N+T}{2}\right)} \end{bmatrix} \tag{4.3}$$

which we were able to solve algebraically as

$$c_j(T) = \frac{\sqrt{T_j T}}{\left(\frac{T_j+T}{2}\right)} \prod_{i \neq j} \left(\frac{T - T_i}{T + T_i}\right) \left(\frac{T_j + T_i}{T_j - T_i}\right) \tag{4.4}$$

A remarkable property of the Doppler kernel reconstruction quadrature method is that the coefficients $\left\{c_j(T)\right\}$, readily calculable through (4.4), do not depend on any isotope-specific cross sections: they only depend on the reference temperatures $\left\{T_j\right\}$.

Having found the optimal linear coefficients (4.4), we can then optimize the grid of reference temperatures $\left\{T_j\right\}$ by solving the following min-max L_∞ problem over a range of temperatures of interest $T \in [T_{min}, T_{max}]$:

$$T_j = \underset{T_j}{\operatorname{argmin}} \left(\max_{T \in [T_{min}, T_{max}]} \left(\frac{\Delta\epsilon}{\epsilon} \right)_{\mathbb{D}} \right) \tag{4.5}$$

where $\left(\frac{\Delta\epsilon}{\epsilon}\right)_{\mathbb{D}}$ is the relative distance between the exact Doppler kernel at temperature T and the linear combination of reference temperature kernels:

$$\begin{aligned} \left(\frac{\Delta\epsilon}{\epsilon} \right)_{\mathbb{D}} &\equiv \frac{\left\| \mathcal{K}_T^{\mathbb{D}} - \sum_{j=1}^{N} c_j \mathcal{K}_{T_j}^{\mathbb{D}} \right\|_{\mathrm{L}_2}}{\left\| \mathcal{K}_T^{\mathbb{D}} \right\|_{\mathrm{L}_2}} \\ &= \sqrt{1 - 2 \sum_i c_i \frac{\sqrt{T_i T}}{\left(\frac{T_i + T}{2}\right)} + \sum_i \sum_j c_i c_j \frac{\sqrt{T_i T_j}}{\left(\frac{T_i + T_j}{2}\right)}} \end{aligned} \tag{4.6}$$

This optimal temperature grid for Doppler kernel reconstruction performs better than linearly interpolating between other traditional temperature meshes (such as linear, logarithmic spaced, etc.), as we document in figure -7 (FIG. E.7 of [124]). The optimal

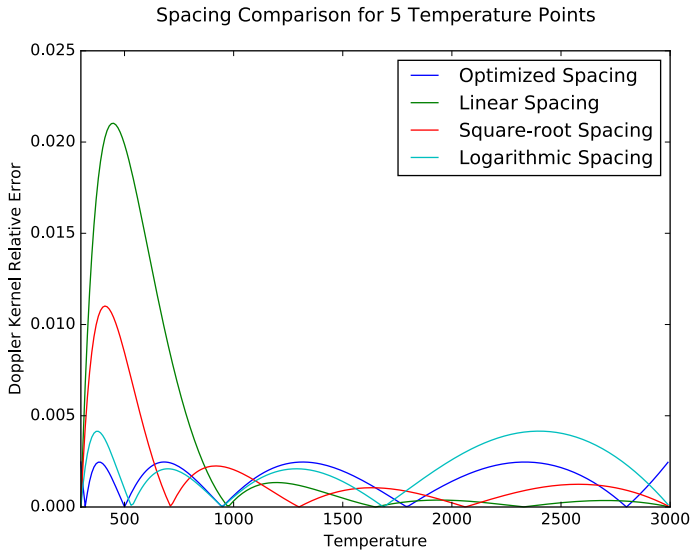

Figure 4-2: Different reference temperature grids. Doppler kernel relative error (F.55) over the range $[300\mathrm{K}, 3000\mathrm{K}]$ for linearly spaced, logarithmic spaced, square-root-spaced, and optimal quadrature temperatures grids.

Doppler kernel reconstruction quadrature temperature grid $\left\{T_j\right\}$ is documented in table 1 (TABLE E.1 of [124]), and depicted in figure -6 (FIG. E.6 of [124]).

Remarkably, it only depends on the number N of reference temperatures, and the

Table 4.1: Optimal temperature grid $\{T_j\}$ for Doppler kernel reconstruction quadrature, as a function of the number N of reference temperatures.

N	Optimized temperature grid $\{T_j\}$ to perform temperature-optimized free Doppler kernel reconstruction temperature interpolation on range [300 K, 3000 K]
1	[948.427]
2	[435.246, 2062.500]
3	[358.012, 948.520, 2512.500]
4	[332.153, 629.087, 1425.806, 2700.000]
5	[320.460, 500.262, 947.380, 1793.691, 2800.000]
6	[314.094, 435.908, 720.689, 1249.489, 2065.967, 2862.500]
7	[310.307, 398.356, 595.912, 949.001, 1511.168, 2259.447, 2893.160]
8	[307.963, 374.068, 519.349, 770.695, 1165.427, 1728.875, 2399.149, 2912.500]
9	[306.145, 359.232, 471.071, 660.047, 950.788, 1369.094, 1917.188, 2513.831, 2937.500]
10	[305.048, 347.608, 436.673, 584.202, 806.228, 1123.081, 1548.951, 2069.173, 2596.590, 2950.000]
11	[304.252, 338.681, 412.408, 530.512, 705.793, 951.890, 1283.538, 1704.703, 2189.430, 2653.095, 2950.000]
12	[303.585, 332.980, 393.688, 492.033, 634.213, 831.825, 1096.021, 1435.603, 1846.909, 2297.375, 2708.445, 2962.500]
13	[303.000, 328.648, 380.443, 462.297, 580.728, 742.398, 956.598, 1232.018, 1571.752, 1966.591, 2380.887, 2744.320, 2962.500]
14	[302.495, 325.278, 370.687, 441.433, 541.558, 677.013, 855.133, 1082.763, 1365.105, 1701.746, 2078.919, 2460.747, 2783.786, 2971.098]
15	[302.0560, 322.886, 362.312, 423.02, 508.989, 624.631, 774.835, 965.193, 1201.262, 1485.613, 1814.241, 2170.679, 2520.285, 2809.074, 2975.000]

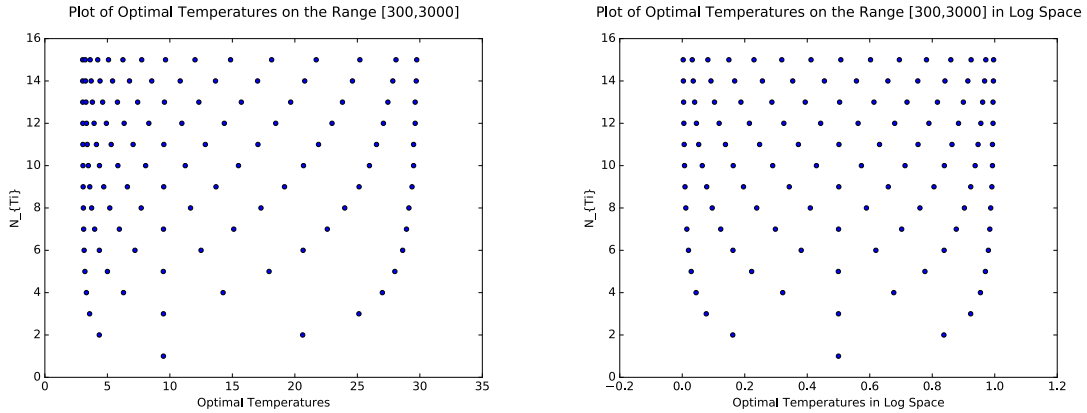

Figure 4-3: Optimal quadrature temperatures grids $\{T_j\}$ for Doppler kernel reconstruction. Reference temperature grids in both linear and log space as a function of the number N of reference temperatures.

dimensionless ratio

$$r \triangleq \ln\left(\frac{T_{max}}{T_{min}}\right) \tag{4.7}$$

which determines the natural variable of the problem (dimensionless temperature):

$$\tau \triangleq \ln\left(\frac{T}{T_{min}}\right) / \ln\left(\frac{T_{max}}{T_{min}}\right) \tag{4.8}$$

The optimal temperature points are then symmetric in τ, centered on 1/2, and determined only by the ratio $r = \left(\frac{T_{max}}{T_{min}}\right)$. For instance, in the particular case of $r = \mathrm{e}$ (the Euler number), the optimal values match exactly those of the Chebyshev quadrature, as shown in figure -5 (FIG. E.5 of [124]), and can range all the way to those of the Legendre quadrature depending on the value of r.

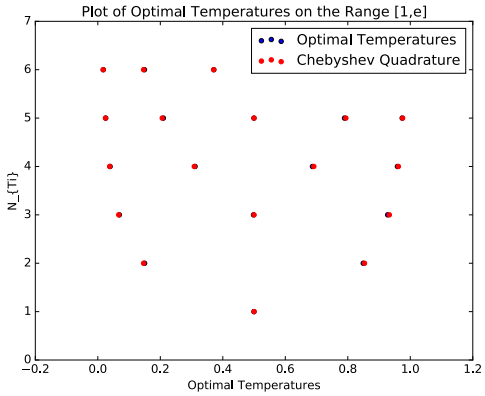

Figure 4-4: Optimal quadrature temperature grids vs. roots of the Chebyshev polynomials. Number of reference temperatures vs optimal temperatures on the range [1,e]. Optimal temperature points line up with Chebyshev quadrature.

4.2 On-the-fly stochastic nuclear cross sections using the windowed multipole representation

To improve the performance of Doppler broadening and facilitate on-the-fly calculations, one must look at the functional form of nuclear cross sections. These cross sections are derived from R-matrix theory, a quantum model of nuclear interactions that parametrizes their energy dependence with resonance parameters called *resonance energies* E_λ (for each level λ) and *resonance widths* $\gamma_{\lambda,c}$ (for each channel c and level λ).

4.2.1 Windowed multipole representation formalism

We have recently established that R-matrix cross sections can be parametrized equivalently with poles and residues and local expansion terms. This is called the *windowed multipole representation of R-matrix cross sections* [130], which is essentially the meromorphic continuation (local Mittag-Leffler expansion) of R-Matrix cross sections to complex wavenumbers. For real wavenumbers (that is energies above threshold), the windowed multipole expansion is exactly equivalent to the R-matrix formalism (though they differ for complex wavenumbers as is the case below threshold). In the case where no threshold reactions are present (we refer to theorem 1 of [130] for the general case), nuclear cross sections admit the following windowed multipole representation:

$$\sigma(z) \underset{\mathcal{W}(E)}{=} \frac{1}{z^2}\Re_{\text{conj}}\left[\sum_{j\geq 1}\frac{r_j}{z-p_j}\right] + \sum_{n\geq -2} a_n z^n \tag{4.9}$$

where $z \triangleq \sqrt{E}$ is the square root of the relative energy of the two interacting bodies (in the center of mass), and where $\Re_{\text{conj}}\left[f(z)\right] \triangleq \frac{f(z)+[f(z^*)]^*}{2}$ designates the analytic continuation of the real part (called conjugate continuation in [130]). The poles $\left\{p_j\right\}$

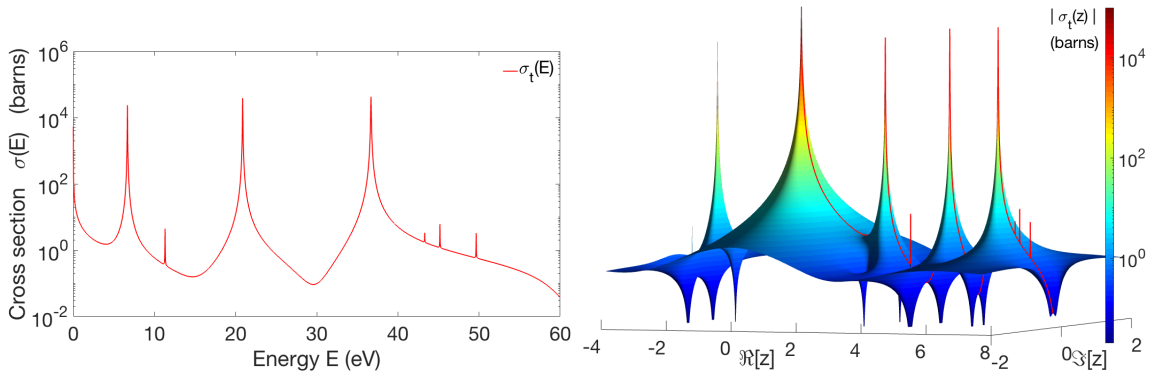

(a) ^{238}U first resonances (3 s-waves and 4 p-waves).

(b) ^{238}U windowed multipole cross section surface.

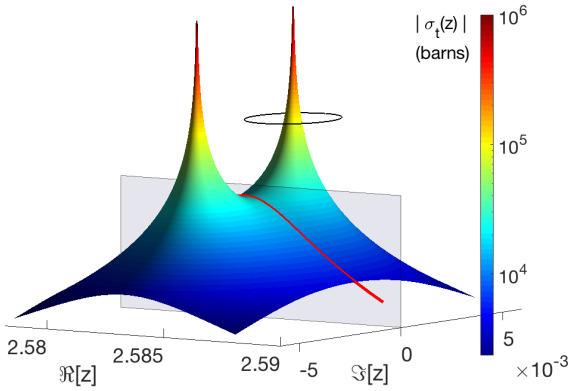

(c) ^{238}U first s-wave resonance peak.

Figure 4-5: Windowed multipole representation of R-matrix cross sections. ^{238}U total cross section (minus potential scattering) meromorphic continuation into the complex z-plane, for $z = \pm\sqrt{E}$ in $(\sqrt{\text{eV}})$. This surface's crest and thalweg line along the real axis is the R-matrix cross section above the zero threshold. FIG. E-1(b) shows the resonance peaks are the saddle points between the complex conjugate poles. Negative z in FIG.E-1(b) are on the shadow branch $\{E, -\}$ of the energy-wavenumber mapping $k_c(E)$. The black circle in FIG.E-1(c) represents the contour integrals around the poles of the complex cross section which enable both conversion to windowed multipole covariances (theorem 2 in [130]) and analytic Doppler broadening (theorem 3 of [130]).

and residues $\{r_j\}$ are global parameters, while the expansion coefficients $\{a_n\}$ are local and depend on each energy window $\mathcal{W}(E)$. Figure E-1 (FIG. 1 of [130]) shows the structure of nuclear resonances in the windowed multipole representation, and how they exactly match R-matrix cross sections along the real axis in wavenumber space (real energies above threshold).

4.2.2 Windowed multipole representation Doppler broadening

This windowed multipole representation (E.96) has the great advantage that angle-integrated cross sections can then be analytically Doppler broadened on-the-fly as follows (theorem 3 of [130]):

$$\begin{aligned}\sigma_T(z) \underset{\mathcal{W}(E)}{=} & \sum_{n\geq -2} a_n \mathrm{D}_\beta^n(z) \\ & + \frac{1}{z^2}\Re\left[\mathrm{i}\sqrt{\pi}\sum_{j\geq 1}\frac{r_j}{\beta}\cdot\left[\mathrm{w}\left(\frac{z-p_j}{\beta}\right) - \mathrm{C}\left(\frac{z}{\beta},\frac{p_j}{\beta}\right)\right]\right]\end{aligned} \tag{4.10}$$

where $\mathrm{C}\left(\frac{z}{\beta},\frac{p_j}{\beta}\right)$ is a correction term defined as:

$$\mathrm{C}\left(\frac{z}{\beta},\frac{p_j}{\beta}\right) \triangleq \frac{2\,p_j}{\mathrm{i}\pi\beta}\int_0^\infty \frac{\mathrm{e}^{-\left(\frac{z}{\beta}+t\right)^2}}{t^2-\left(\frac{p_j}{\beta}\right)^2}\mathrm{d}t \tag{4.11}$$

which is negligible in most physical ranges of temperatures and energies, so that Doppler broadened windowed multipole cross sections can be well approximated as

$$\sigma_T(z) \underset{\mathcal{W}(E)}{\simeq} \frac{1}{z^2}\Re\left[\sqrt{\pi}\sum_{j\geq 1}\frac{r_j}{\mathrm{i}\beta}\cdot\mathrm{w}\left(\frac{z-p_j}{\beta}\right)\right] + \sum_{n\geq -2} a_n \mathrm{D}_\beta^n(z) \tag{4.12}$$

where $\mathrm{D}_\beta^n(z)$ are the Doppler broadened monomials:

$$\mathrm{D}_\beta^n(z) \triangleq \int_0^\infty \frac{x^{n+2}}{z^2}\mathcal{K}_\beta^{\mathbb{D}}(z,x)\mathrm{d}x \tag{4.13}$$

which can be computed from elemental Gaussian and error functions (defined in eq. 7.2.1 of [250]) using the following recurrence formulae [197]:

$$\begin{aligned}\mathrm{D}_\beta^{n+2}(z) \underset{\forall n\geq 1}{=} & \left[\frac{\beta^2}{2}(2n+1)+z^2\right]\mathrm{D}_\beta^n(z) - \left(\frac{\beta^2}{2}\right)^2 n(n-1)\mathrm{D}_\beta^{n-2}(z) \\ \mathrm{D}_\beta^0(z) = & \left[\frac{\beta^2}{2}+z^2\right]\mathrm{D}_\beta^{-2}(z) + \frac{\beta}{z\sqrt{\pi}}\mathrm{e}^{-\left(\frac{z}{\beta}\right)^2} \\ \mathrm{D}_\beta^{-1}(z) = & \frac{1}{z} \\ \mathrm{D}_\beta^{-2}(z) = & \frac{1}{z^2}\mathrm{erf}\left(\frac{z}{\beta}\right)\end{aligned} \tag{4.14}$$

and where $\mathrm{w}(z)$ is the Faddeyeva function (defined in eq. 7.2.3 of [250]),

$$\mathrm{w}(z) \triangleq \mathrm{e}^{-z^2}\Big(1-\mathrm{erf}\left(-\mathrm{i}z\right)\Big) = \mathrm{e}^{-z^2}\left(1+\frac{2\mathrm{i}}{\sqrt{\pi}}\int_0^z e^{t^2}\mathrm{d}t\right) \tag{4.15}$$

called at poles in the complex lower semi-plane, i.e. $\Im\left[\frac{z-p_j}{\beta}\right] > 0$. For all other poles, which satisfy $\Im\left[\frac{z-p_j}{\beta}\right] \leq 0$, we use the fact that the windowed multipole Representation has complex conjugate poles to call the Faddeyeva function at $-\left[\mathrm{w}\left(z^*\right)\right]^* = -\mathrm{w}\left(-z\right)$.

Figure E-6 (FIG.6 of [130]) shows how the windowed multipole cross sections Doppler broadened using (4.12) match perfectly the direct integration of Solbrig's kernel, drastically outperforming the ϕ/χ functions approximation method of traditional approaches, and even the direct implementation of the SIGMA1 method in NJOY [228].

Starting from the approximate form of the Doppler broadening (4.12), and therefore assuming that the temperature partial derivatives of the $\mathrm{C}\left(\frac{z}{\beta}, \frac{p_j}{\beta}\right)$ function are small (which in practice they are), we were also able to establish the k-th temperature derivative as

$$\partial_T^{(k)}\sigma_T(z) \underset{\mathcal{W}(E)}{\simeq} \frac{1}{z^2}\Re\left[\mathrm{i}\sqrt{\pi}\sum_{j\geq 1} r_j \cdot \mathrm{X}_\beta^{(k)}\left(z-p_j\right)\right] + \sum_{n\geq -2} a_n \cdot \partial_T^{(k)}\mathrm{D}_\beta^n(z) \tag{4.16}$$

$\mathrm{X}_\beta^{(k)}\left(z-p_j\right)$ are the k-th temperature derivatives of the Doppler broadened resonances:

$$\begin{aligned}\mathrm{X}_\beta^{(k)}\left(z-p_j\right) &\triangleq \partial_T^{(k)}\left[\theta\cdot\mathrm{w}\Big(\theta\left(z-p_j\right)\Big)\right] \\ &= \sum_{n=1}^{k}\Big(\partial_\theta^{(n)}\theta\cdot\mathrm{w}\Big(\theta(z-p_j)\Big)\Big)\times B_{k,n}\left(\theta^{(1)},\theta^{(2)},\ldots,\theta^{(k-n+1)}\right)\end{aligned} \tag{4.17}$$

where the sum is the Arbogast composite derivatives (Faà di Bruno) formula [61], linking the θ-derivatives

$$\partial_\theta^{(n)}\theta\cdot\mathrm{w}\Big(\theta(z-p_j)\Big) \underset{\forall n\geq 1}{=} -\frac{(z-p_j)^{n-1}}{2}\mathrm{w}^{(n+1)}\Big(\theta(z-p_j)\Big) \tag{4.18}$$

to the $\theta^{(n)}$ temperature derivatives of θ

$$\theta^{(n)} \triangleq \partial_T^{(n)}\theta = \frac{1}{\beta}\left(\frac{-1}{2}\right)^n\frac{(2n-1)!!}{(T-T_0)^n} \tag{4.19}$$

by means of the partial exponential Bell polynomials $B_{k,n}\left(\theta^{(1)},\theta^{(2)},\ldots,\theta^{(k-n+1)}\right)$ [71, 49, 85]. The derivatives of the Faddeyeva function can be computed using recurrence formulae (c.f. 7.10 in [250]):

$$\begin{aligned}\mathrm{w}^{(1)}(z) &= -2z\mathrm{w}(z) + \frac{2\mathrm{i}}{\sqrt{\pi}} \\ \mathrm{w}^{(n+2)}(z) &= -2z\mathrm{w}^{(n+1)}(z) - 2(n+1)\mathrm{w}^{(n)}(z)\end{aligned} \tag{4.20}$$

$\partial_T^{(k)}\mathrm{D}_\beta^n(z)$ are the temperature derivatives of the Doppler broadened monomials, which

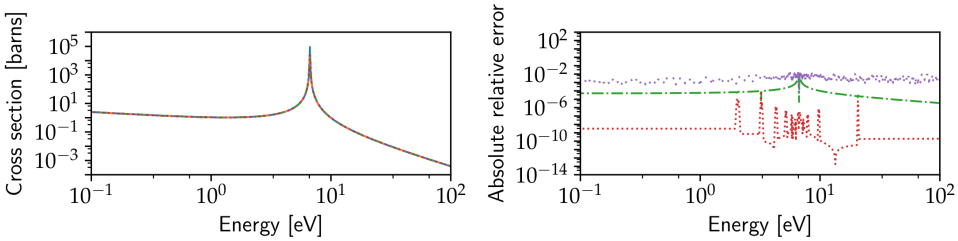

(a) T = 300 Kelvin

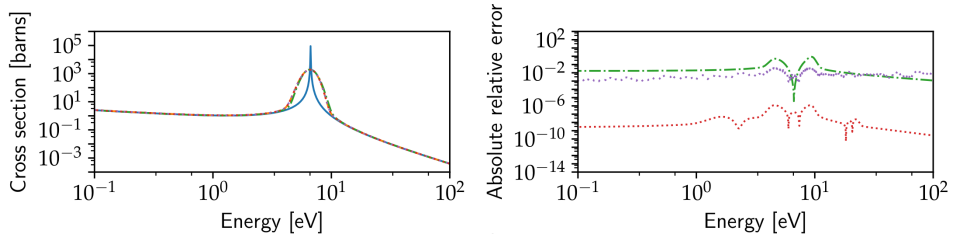

(b) T = 10^5 Kelvin

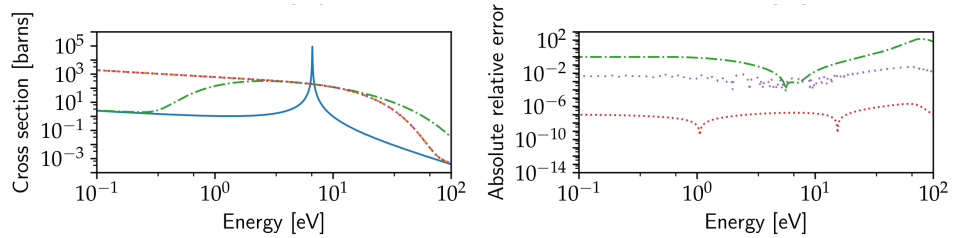

(c) T = 10^7 Kelvin

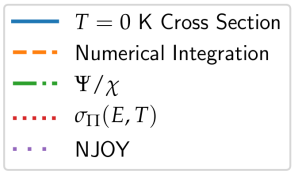

Figure 4-6: Accuracy of different Doppler-broadening methods. Modeling the first resonance of ^{238}U with a Single-Level-Breit-Wigner, the cross section is reconstructed at T=0K. For each temperature $\{300, 10^5, 10^7\}$ Kelvin, the cross section is then broadened using four different methods: (i) numerical integration of the Solbrig Kernel (E.136); (ii) Using the ψ_T/χ_T approximation for SLBW Doppler broadening (classical method described in section IV.B. of [130]); (iii) conversion of the resonance parameters $\{\Gamma\}$ to multipoles $\{\Pi\}$ and analytic Doppler broadening of windowed multipole representation (4.12); (iv) formulation of the parameters in ENDF format and processing using NJOY [228]. For each temperature, the right column shows the absolute relative error for methods (ii), (iii), and (iv) to the direct integration of the Solbrig Kernel (i). Note: NJOY was run with a tolerance parameter of 10^{-2} as higher accuracy required a prohibitively long computation time.

are subject to the following recurrence formulae, defining $a \triangleq \frac{k_{\mathbb{B}}}{A}$:

$$
\begin{aligned}
\partial_T^{(k)}\mathrm{D}_\beta^{n+2}(z) &\underset{\forall n\geq 1}{=} \left[\frac{\beta^2}{2}(2n+1)+z^2\right]\partial_T^{(k)}\mathrm{D}_\beta^{n}(z)+\frac{a}{2}(2n+1)k\;\partial_T^{(k-1)}\mathrm{D}_\beta^{n}(z) \\
&\qquad -\frac{n(n-1)}{4}\left[\beta^4\partial_T^{(k)}\mathrm{D}_\beta^{n-2}(z)+2a\beta k\;\partial_T^{(k-1)}\mathrm{D}_\beta^{n-2}(z)+a^2k(k-1)\partial_T^{(k-2)}\mathrm{D}_\beta^{n-2}(z)\right] \\
\partial_T^{(k)}\mathrm{D}_\beta^{0}(z) &= \left[\frac{\beta^2}{2}+z^2\right]\partial_T^{(k)}\mathrm{D}_\beta^{-2}(z)+\frac{a}{2}k\;\partial_T^{(k-1)}\mathrm{D}_\beta^{-2}(z)+\frac{1}{z\sqrt{\pi}}\Big[\beta^2\partial_T^{(k)}\theta\mathrm{e}^{-(z\theta)^2}+ak\,\partial_T^{(k-1)}\theta\mathrm{e}^{-(z\theta)^2}\Big] \\
\partial_T^{(k)}\mathrm{D}_\beta^{-1}(z) &= \frac{1}{z}\delta_{k,0} \\
\partial_T^{(k)}\mathrm{D}_\beta^{-2}(z) &= \frac{1}{z^2}\partial_T^{(k)}\mathrm{erf}\,(z\theta)
\end{aligned}
\tag{4.21}
$$

In recurrence relations (E.158), the terms $\partial_T^{(k)}\theta\mathrm{e}^{-(z\theta)^2}$ can themselves be computed using Arbogast's formula:

$$
\partial_T^{(k)}\theta\mathrm{e}^{-(z\theta)^2}=\mathrm{e}^{-(z\theta)^2}\sum_{n=1}^{k}F_z^{(n)}(\theta)\times B_{k,n}\left(\theta^{(1)},\theta^{(2)},\ldots,\theta^{(k-n+1)}\right) \tag{4.22}
$$

where $F_z^{(n)}(\theta)$ are polynomials of degree $n+1$ defined as

$$
F_z^{(n)}(\theta)\triangleq\mathrm{e}^{(z\theta)^2}\partial_\theta^{(n)}\theta\mathrm{e}^{-(z\theta)^2}=\sum_{i=0}^{n+1}\alpha_i^{(n)}\theta^i \tag{4.23}
$$

which are recursively constructed from $F_z^{(0)}(\theta)=\theta$ as

$$
F_z^{(n+1)}(\theta)=\partial_\theta F_z^{(n)}(\theta)-2z^2\theta F_z^{(n)}(\theta) \tag{4.24}
$$

entailing these recurrence formulae on their coefficients:

$$
\begin{aligned}
\alpha_0^{(0)} &= 0 & \alpha_1^{(0)} &= 1 \\
\alpha_{n+1}^{(n+1)} &= -2z^2\alpha_n^{(n)} & \alpha_{n+2}^{(n+1)} &= -2z^2\alpha_{n+1}^{(n)} \\
\alpha_i^{(n+1)} &\underset{1\leq i\leq n}{=} (i+1)\alpha_{i+1}^{(n)}-2z^2\alpha_{i-1}^{(n)}
\end{aligned}
\tag{4.25}
$$

Finally, the terms $\partial_T^{(k)}\mathrm{erf}\,(z\theta)$ in recurrence relations (E.158) can also be computed using Arbogast's formula:

$$
\partial_T^{(k)}\mathrm{erf}\,(z\theta)=\sum_{n=1}^{k}\left(\partial_\theta^{(n)}\mathrm{erf}\,(z\theta)\right)\cdot B_{k,n}\left(\theta^{(1)},\ldots,\theta^{(k-n+1)}\right) \tag{4.26}
$$

in which the θ derivatives can be expressed as

$$
\partial_\theta^{(n)}\mathrm{erf}\,(z\theta)\underset{n\geq 1}{=}z^n(-1)^{n-1}\frac{2}{\sqrt{\pi}}\mathrm{H}_{n-1}\left(z\theta\right)\mathrm{e}^{-(z\theta)^2} \tag{4.27}
$$

where the Hermite polynomials $\mathrm{H}_n(z)$ are recursively calculable from $\mathrm{H}_0 = 1$ and $\mathrm{H}_1 = 2z$ as:

$$\mathrm{H}_{n+1} \underset{n\geq 1}{=} 2z\mathrm{H}_n - 2n\mathrm{H}_{n-1} \tag{4.28}$$

We have thus established an efficient method to compute arbitrary-order temperature derivatives of nuclear cross sections on-the-fly, the performance of which is reported in [197, 198] and is roughly as fast as temperature lookup and interpolation (slower than single but faster than double lookup) while requiring 1000 times less memory. This capability could be combined with other codes to achieve advanced and efficient neutronics-theromhydraulics coupling for high-fidelity and high-performance reactor simulations [168, 167, 169].

4.2.3 Converting resonance parameters to windowed multipoles

The detailed theory of the windowed multipole representation, and how to obtain it from R-matrix parameters, is established in our article [130], reproduced in appendix E. For summary, we here recall that general scattering theory expresses the incoming channel c and outgoing channel c' angle-integrated partial cross section $\sigma_{c,c'}(E)$ at energy E as a function of the probability *transmission matrix* $T_{cc'}(E)$, according to eq.(3.2d) VIII.3. p.293 of [214]:

$$\sigma_{cc'}(E) = 4\pi g_{J_c^\pi} \left| \frac{T_{cc'}(E)}{k_c(E)} \right|^2 \tag{4.29}$$

where k_c is the wavenumber of the channel, and the *spin statistical factor* is defined eq.(3.2c) VIII.3. p.293. of [214] as:

$$g_{J_c^\pi} \triangleq \frac{2J_c + 1}{(2I_1 + 1)(2I_2 + 1)} \tag{4.30}$$

where J_c^π is the total angular momentum of the channel (with its parity), I_1 and I_2 the spins of the two interacting bodies. The transmission matrix is itself derived from the *scattering matrix* $\boldsymbol{U}$ of the interaction:

$$\boldsymbol{T} \triangleq \frac{\mathbb{I} - \mathbf{e}^{-\mathrm{i}\boldsymbol{\omega}}\boldsymbol{U}\mathbf{e}^{-\mathrm{i}\boldsymbol{\omega}}}{2} \tag{4.31}$$

where $\boldsymbol{\omega} \triangleq \mathbf{diag}\Big(\omega_c\Big)$ is the diagonal matrix composed of $\omega_c \triangleq \sigma_{\ell_c}(\eta_c) - \sigma_0(\eta_c)$, that is the difference in *Coulomb phase shift*, $\sigma_{\ell_c}(\eta_c)$, which are linked to the phases (argument) of the Gamma function as defined by Ian Thompson in eq.(33.2.10) of [250] for angular momentum ℓ_c

$$\sigma_{\ell_c}(\eta_c) \triangleq \arg\Big(\Gamma\left(1 + \ell_c + \mathrm{i}\eta_c\right)\Big) \tag{4.32}$$

and *dimensionless Coulomb field parameter*:

$$\eta_c \triangleq \frac{Z_1 Z_2 e^2 M_\alpha a_c}{\hbar^2 \rho_c} \tag{4.33}$$

where a_c is the channel radius, e the elementary charge, $\hbar$ the Planck constant, Z_1 and Z_2 the number of charges in the two interacting bodies, M_α the reduced mass of the system, and ρ_c the dimensionless wavenumber:

$$\rho_c \triangleq k_c \, a_c \tag{4.34}$$

Note that transmission matrix (E.7) definition $T_{cc'} \triangleq \frac{\delta_{cc'} - \mathrm{e}^{-\mathrm{i}\omega_c} U_{cc'} \mathrm{e}^{-\mathrm{i}\omega_{c'}}}{2}$ is a scaled rotation of the one defined by Lane and Thomas $T_{cc'}^{\mathrm{L\&T}} \triangleq \delta_{cc'} \mathrm{e}^{2\mathrm{i}\omega_c} - U_{cc'}$ (c.f. eq. (2.3), VIII.2. p.292 and eq.(3.2d) VIII.3. p.293 of [214]). We introduce definition (E.7) for better physical interpretability, algebraic simplicity and numerical stability.

Unitarity of the scattering matrix entails that the total cross section of a given channel is:

$$\sigma_c(E) \triangleq \sum_{c'} \sigma_{cc'}(E) = 4\pi g_{J_c^\pi} \frac{\Re\left[T_{cc}(E)\right]}{\left|k_c(E)\right|^2} \tag{4.35}$$

R-matrix theory parametrizes the scattering matrix $\boldsymbol{U}(E)$ as:

$$\boldsymbol{U} = \boldsymbol{O}^{-1}\boldsymbol{I} + 2\mathrm{i}\boldsymbol{\rho}^{1/2}\boldsymbol{O}^{-1}\boldsymbol{\gamma}^{\mathsf{T}}\boldsymbol{A}\boldsymbol{\gamma}\boldsymbol{O}^{-1}\boldsymbol{\rho}^{1/2} \tag{4.36}$$

where the *level matrix* $\boldsymbol{A}$ (see equations (17) and (18) of section II.C of [127]) is defined as

$$\boldsymbol{A^{-1}} \triangleq \boldsymbol{e} - E\mathbb{I} - \boldsymbol{\gamma}\left(\boldsymbol{L} - \boldsymbol{B}\right)\boldsymbol{\gamma}^{\mathsf{T}} \tag{4.37}$$

This level matrix is parametrized by the *resonance energies* E_λ and the *resonance widths* $\gamma_{\lambda,c}$ – of which we respectively build the diagonal matrix $\boldsymbol{e} = \mathbf{diag}\left(E_\lambda\right)$ of size N_λ, the number of levels (resonances), and the rectangular matrix $\boldsymbol{\gamma} = \mathbf{mat}\left(\gamma_{\lambda,c}\right)$ of size $N_\lambda \times N_c$ where N_c is the number of channels. In exact R-matrix theory, these *resonance parameters* (together symbolically denoted $\left\{\Gamma\right\}$ here) are real, but they become complex in the Reich-Moore formalism. Finally, $\boldsymbol{B} = \mathbf{diag}\left(B_c\right)$ is the diagonal matrix of real arbitrary boundary conditions B_c, and $\boldsymbol{L} = \mathbf{diag}\left(L_c\right)$ where $L_c(\rho_c)$ is the dimensionless reduced logarithmic derivative of the outgoing-wave function at the channel surface:

$$L_c(\rho_c) \triangleq \frac{\rho_c}{O_c}\frac{\partial O_c}{\partial \rho_c} \tag{4.38}$$

where the incoming and outgoing waves, $\boldsymbol{I} = \mathbf{diag}\left(I_c\right)$ and $\boldsymbol{O} = \mathbf{diag}\left(O_c\right)$ — subject to the following Wronksian condition for all channel c, $w_c \triangleq O_c^{(1)} I_c - I_c^{(1)} O_c = 2\mathrm{i}$ — are functions of the dimensionless wavenumber $\rho_c \triangleq a_c k_c$ and are linked to the regular and irregular Coulomb wave functions (or Bessel functions in the case of neutral particle

channels), defined in eq.(2.13a)-(2.13b) III.2.b p.269 [214]:

$$\begin{aligned} O_c &= H_{+_c} \mathrm{e}^{-\mathrm{i}\omega_c} = (G_c + \mathrm{i}F_c)\, \mathrm{e}^{-\mathrm{i}\omega_c} \\ I_c &= H_{-_c} \mathrm{e}^{\mathrm{i}\omega_c} = (G_c - \mathrm{i}F_c)\, \mathrm{e}^{\mathrm{i}\omega_c} \end{aligned} \tag{4.39}$$

and for properties of which we refer to Ian J. Thompson's Chapter 33, eq.(33.2.11) in [250], or Abramowitz & Stegun chapter 14, p.537 [51].

We now seek to convert these R-matrix nuclear cross sections (E.5) and (E.10) into the following corresponding windowed multipole representations:

- Partial cross sections (E.5):

$$\sigma_{cc'}(z) \underset{\mathcal{W}(z)}{\triangleq} \sum_{n\geq -2} \widetilde{a}_n^{cc'} k_c^n(z) + \frac{1}{z^2} \Re_{\text{cont}} \left[\sum_{j\geq 1} \frac{\widetilde{r}_j^{cc'}}{z - p_j} \right] \tag{4.40}$$

- Total cross section (E.10) takes the form:

$$\sigma_c(z) \underset{\mathcal{W}(z)}{\triangleq} \sum_{n\geq -2} a_n^c k_c^n(z) + \frac{1}{z^2} \Re_{\text{cont}} \left[\sum_{j\geq 1} \frac{r_j^c}{z - p_j} \right] \tag{4.41}$$

As explained in theorem 1 of [130] (appendix E), this conversion can be performed in one of two ways:

1. **Resonance parameters conversion**: Convert R-matrix resonance parameters $\left\{\Gamma\right\}$ directly into the poles $\left\{p_j\right\}$ and residues $\left\{r_j\right\}$ of the windowed multipole representation (E.96). As explained in [130], this can be performed in a three-step process:

   (a) Pole finding: First find the *radioactive parameters*, that is the complex *radioactive poles* $\{p_j\}$ and corresponding *level matrix residue widths* $\{\boldsymbol{\alpha_j}\}$ which solve the level-matrix radioactive eigenproblem in $z \triangleq \sqrt{E}$ space:

   $$\boldsymbol{A}^{-1}(z)\Big|_{z=p_j} \boldsymbol{\alpha_j} = \boldsymbol{0} \tag{4.42}$$

   Of which one will find N_L solutions, where for massive (non-photon) neutral particles this number of poles is

   $$N_L = \left(2N_\lambda + \sum_{c=1}^{N_c} \ell_c \right) \times 2^{(N_{E_{T_c} \neq E_{T_{c'}}} - 1)} \tag{4.43}$$

   with $N_{E_{T_c} \neq E_{T_{c'}}}$ denoting the number of channels with different thresholds. Whereas for charged particles, there is an infinite number (countable) of radioactive poles, $N_L = \infty$, because in addition to the nearby ℓ_c poles, the Coulomb functions add an infinity of far-away poles. Establishing the correct number of radioactive poles (E.42) in theorem 1 of [125] is one of our major nuclear physics theoretical findings.

(b) Residue finding: Having found the radioactive poles $\{p_j\}$, there are two ways of computing the corresponding residues of the windowed multipole representation (E.96) of R-matrix cross sections.

i. Constructive way: To each radioactive pole p_j corresponds an eigenvector $\boldsymbol{\alpha_j}$ that is subject to normalization:

$$\boldsymbol{\alpha_j}^{\mathsf{T}} \left(\frac{\partial \boldsymbol{A}^{-1}}{\partial z}\bigg|_{z=p_j} \right) \boldsymbol{\alpha_j} = 1 \tag{4.44}$$

which is readily calculable from

$$\frac{\partial \boldsymbol{A}^{-1}}{\partial z}(p_j) = -2z\mathbb{I} - \boldsymbol{\gamma}\frac{\partial \boldsymbol{L}}{\partial z}(p_j)\boldsymbol{\gamma}^{\mathsf{T}} \tag{4.45}$$

The resonance matrix residue widths are then defined as:

$$\boldsymbol{\zeta_j} = {\boldsymbol{H}_+}^{-1}(p_j)\,\boldsymbol{\rho}^{1/2}(p_j)\;\boldsymbol{\gamma}^{\mathsf{T}}\boldsymbol{\alpha_j} \tag{4.46}$$

from which the partial cross sections residues can be constructed from R-matrix parameters as:

$$\widetilde{r}_j^{cc'} \triangleq -\mathrm{i}\frac{4\pi g_{J_c^\pi} p_j^2}{|k_c(p_j)|^2}\left[2\;\boldsymbol{\zeta_j}\boldsymbol{\zeta_j}^{\mathsf{T}} \circ \boldsymbol{T}\left(p_j^*\right)^*\right]_{cc'} \tag{4.47}$$

and the total residues as

$$r_j^c \triangleq -\mathrm{i}\frac{4\pi g_{J_c^\pi} p_j^2}{|k_c(p_j)|^2}\left[\boldsymbol{\zeta_j}\boldsymbol{\zeta_j}^{\mathsf{T}}\right]_{cc} \tag{4.48}$$

ii. Contour integral way: Perform analytic continuation in $z = \sqrt{E}$ space of R-matrix cross sections (E.5) and (E.10). This can readily be achieved by continuing all R-matrix operators in (E.14), and using, for any function $f(z)$, its *continued conjugate* $f^*(z)$, defined as:

$$f^*(z) \triangleq f(z^*)^* \tag{4.49}$$

so that the continued conjugate real part is defined as

$$\Re_{\text{cont}}\left[f(z)\right] \triangleq \frac{f(z) + f^*(z)}{2} \tag{4.50}$$

and the continued conjugate square modulus as

$$|f|^2_{\text{cont}}(z) \triangleq f(z) \times f^*(z) \tag{4.51}$$

Then, the windowed multipole representation residues can be directly

obtained by numerically performing the contour integrals

$$\widetilde{r}_j^{cc'} = \frac{1}{\mathrm{i}\pi} \oint_{\mathfrak{C}_{p_j}} z^2 \sigma_{cc'}(z) \mathrm{d}z \tag{4.52}$$

where $\mathfrak{C}_{p_j}$ designates a positively oriented simple closed contour containing only pole p_j. For instance, if $\mathfrak{C}_{p_j}$ is a circle of small radius $\epsilon > 0$ around pole p_j, this yields

$$r_j^c = \frac{\epsilon}{\pi} \int_{\theta=0}^{2\pi} \left(p_j + \epsilon \mathrm{e}^{\mathrm{i}\theta}\right)^2 \sigma_c \left(p_j + \epsilon \mathrm{e}^{\mathrm{i}\theta}\right) \mathrm{e}^{\mathrm{i}\theta} \mathrm{d}\theta \tag{4.53}$$

(c) Background windowing fit: Once the global poles and residues are found, the background Laurent expansion $\left\{a_n\right\}$ coefficients, specific to each energy window $\mathcal{W}(E)$, can be found by removing the local poles and residues and curve-fitting the remaining "background" term (as in [197]).

2. **Direct point-wise conversion**: Alternatively, one can directly curve-fit point-wise nuclear cross sections with the windowed multipole representation (E.96) by means of rational approximation algorithms. This approach, undertaken in [262] and [225], has the advantage of being able to deal with cross sections that have discontinuous background terms in standard nuclear data evaluations (for instance file 3 in ENDF-6 format).

Regardless of the approach taken, one can constitute a complete *windowed multipole library*[48] of all evaluated isotopes. Our personal contributions to the windowed multipole library have been to:

- (i) Generalize the windowed multipole representation to encompass all nuclear reactions (Coulomb channels and thresholds), thereby establishing it as a fundamental physics equivalent to R-matrix theory: this is the core purpose of article [130] which built upon [125] and [127].

- (ii) Establish the exact number of poles of the windowed multipole representation (theorem 1 of [125]), when all previous methods suffered from looking for too many poles. In particular, in his initial article on "a rigorous pole representation of multilevel cross sections"[190], Hwang only considered the case of zero-threshold neutron cross sections (no charged particle channels). In this case there is a finite amount of poles, which we establish in equation (34) theorem 1 of [125], and it is possible to represent exactly nuclear cross sections in a closed form multipole representation without the need of windows, though this requires the scattering and total cross section channels to have energy-dependent residues (as we establish in section II.F. of [130]). Also, Hwang (and all subsequent authors who attempted to convert resonance parameters into multipole parameters) confronted serious numerical difficulties as he was looking for too many cross section poles: the discovery of the correct number of poles only came later, with our first proof established in theorem 1 of [125].

Regardless, this original "rigorous pole representation" of Hwang is not computationally efficient as all the poles and resonances have to be explicitly Doppler broadened to call the cross section at any given temperature. In this sense, switching from the "rigorous pole representation" to the "windowed multipole representation" can be seen as a compression algorithm to minimize the cost of Doppler broadening on-the-fly. It is also a generalization, as the windowed multipole representation (E.96) — with energy-independent residues and a Laurent expansion background term for every window — is valid for all cross sections, with or without charged particle channels and thresholds (to correctly represent the thresholds see theorem 1 and section II.E.4. of [130]).

- (iii) Develop the Doppler broadening algorithm for the Laurent expansion curve-fit (E.149) [197]. This was necessary to Doppler broaden cross sections at low energy, where the $\mathrm{C}\left(\frac{z}{\beta}, \frac{p_j}{\beta}\right)$ term from (E.146) is not negligible.

- (iv) Derive the formulae for arbitrary-order temperature derivatives of Doppler broadened windowed multipole cross sections (E.153) [130].

- (v) Introduce a regularized rational approximation algorithm to fit point-wise nuclear cross section with the windowed multipole representation while avoiding over-fitting with spurious poles [262].

- (vi) Establish rigorous methods to directly convert the R-matrix resonance parameters into windowed multipole parameters. These methods are described in detail in theorem 1 of [130]. They require to first solve the *radioactive eigenproblem* to find the poles and residue widths of the *Kapur-Peierls operator*. These poles are also those of the windowed multipole cross sections, and their residues can then be constructed by one of two ways: (a) evaluating the analytic continuation of the complex conjugate (called *conjugate continuation* in section II.D. of [130]) of the transmission matrix at these pole values; (b) using the conjugate continuations of all R-matrix operators to directly perform the analytic continuation of R-matrix cross sections, and then perform contour integrals around each pole to evaluate their residues. Once all the poles and residues are found, a local sub-set of these can be called in the vicinity of any given energy window $\mathcal{W}(E)$ and the rest of the cross section can be curve-fitted with the Laurent expansion background term (this is the approach taken in [197] which is different from the direct curve-fitting of cross sections deployed in [262] and [225]).

- (vii) Establish a method to translate resonance parameters covariances into windowed multipole covariances, which reproduces the uncertainty reported in standard nuclear data libraries [130]. As it is central to nuclear data uncertainty inference and propagation using the windowed multipole representation, this method and its consequences are summarized in the following section 4.2.4.

4.2.4 Translating resonance parameters uncertainties into windowed multipole covariances

We denote $\left\{\Gamma\right\}$ the set of all R-matrix resonance parameters $\left\{\Gamma\right\} \triangleq \left\{E_\lambda, \gamma_{\lambda,c}\right\}$. These are implicitly considered to be the expectation value $\left\{\Gamma\right\} \triangleq \mathbb{E}\left[\Gamma\right]$ of the underlying uncertainty distribution from which they are drawn, assumed to be a multivariate normal distribution $\mathcal{N}\left(\Gamma, \mathbb{V}\mathrm{ar}\left(\Gamma\right)\right)$, where $\mathbb{V}\mathrm{ar}\left(\Gamma\right)$ designates their corresponding joint covariance matrix.

If we are provided with the sensitivities $\frac{\partial\sigma}{\partial\Gamma}(z)$ of R-matrix cross sections (analytically continued) to resonance parameters (these $\frac{\partial\sigma}{\partial\Gamma}(z)$ can readily be obtained analytically or by simple numerical finite differences of the conjugate continuation of R-matrix cross section expressions), then we established in theorem 2 of [130] that the multipole sensitivities (Jacobian matrix) with respect to the resonance parameters, $\left(\frac{\partial\Pi}{\partial\Gamma}\right)$, can be obtained from the following system (4.54) of contour integrals in the complex plane, where $\mathfrak{C}_{p_j}$ designates any positively oriented simple closed contour containing only pole p_j. For instance, $\mathfrak{C}_{p_j}$ can be a circle of radius $\epsilon > 0$ around pole p_j.

$$\begin{aligned}
\frac{1}{2}\frac{r_j}{p_j^2}\cdot\left(\frac{\partial p_j}{\partial\Gamma}\right) &= \frac{1}{2\pi\mathrm{i}}\oint_{\mathfrak{C}_{p_j}}(z-p_j)\frac{\partial\sigma}{\partial\Gamma}(z)\mathrm{d}z \\
&= \frac{\epsilon^2}{2\pi}\int_{\theta=0}^{2\pi}\frac{\partial\sigma}{\partial\Gamma}(p_j+\epsilon\mathrm{e}^{\mathrm{i}\theta})\mathrm{e}^{2\mathrm{i}\theta}\mathrm{d}\theta \\
\frac{1}{2}\frac{1}{p_j^2}\cdot\left(\frac{\partial r_j}{\partial\Gamma}\right) - \frac{r_j}{p_j^3}\cdot\left(\frac{\partial p_j}{\partial\Gamma}\right) &= \frac{1}{2\pi\mathrm{i}}\oint_{\mathfrak{C}_{p_j}}\frac{\partial\sigma}{\partial\Gamma}(z)\mathrm{d}z \\
&= \frac{\epsilon}{2\pi}\int_{\theta=0}^{2\pi}\frac{\partial\sigma}{\partial\Gamma}(p_j+\epsilon\mathrm{e}^{\mathrm{i}\theta})\mathrm{e}^{\mathrm{i}\theta}\mathrm{d}\theta \\
\left(\frac{\partial a_n}{\partial\Gamma}\right) + \delta_{-1,n}\Re_{\mathrm{conj}}\left[\sum_{j=1}^{N_L}\frac{2\left(r_j\cdot\frac{\partial p_j}{\partial\Gamma}\right)-p_j\left(\frac{\partial r_j}{\partial\Gamma}\right)}{p_j^3}\right] & \\
+\delta_{-2,n}\Re_{\mathrm{conj}}\left[\sum_{j=1}^{N_L}\frac{\left(r_j\cdot\frac{\partial p_j}{\partial\Gamma}\right)-p_j\left(\frac{\partial r_j}{\partial\Gamma}\right)}{p_j^2}\right] &= \frac{1}{2\pi\mathrm{i}}\oint_{\mathfrak{C}_0}\frac{1}{z^{n+1}}\frac{\partial\sigma}{\partial\Gamma}(z)\mathrm{d}z \\
&= \frac{1}{2\pi\epsilon^n}\int_{\theta=0}^{2\pi}\frac{\partial\sigma}{\partial\Gamma}(\epsilon\mathrm{e}^{\mathrm{i}\theta})\mathrm{e}^{-\mathrm{i}n\theta}\mathrm{d}\theta
\end{aligned} \tag{4.54}$$

For each energy window $\mathcal{W}(E)$, the multipole sensitivities $\left(\frac{\partial\Pi}{\partial\Gamma}\right)$ from system (4.54) can then be converted to first order into windowed multipole covariances $\mathbb{V}\mathrm{ar}\left(\Pi\right)$ as:

$$\mathbb{V}\mathrm{ar}\left(\Pi\right) = \left(\frac{\partial\Pi}{\partial\Gamma}\right)\mathbb{V}\mathrm{ar}\left(\Gamma\right)\left(\frac{\partial\Pi}{\partial\Gamma}\right)^{\dagger} \tag{4.55}$$

where $[\,\cdot\,]^{\dagger}$ designates the Hermitian conjugate (adjoint).

Assuming R-matrix cross section uncertainty is well represented by the resonance parameters multivariate normal distribution $\mathcal{N}\left(\Gamma, \mathbb{V}\mathrm{ar}\left(\Gamma\right)\right)$ documented in standard

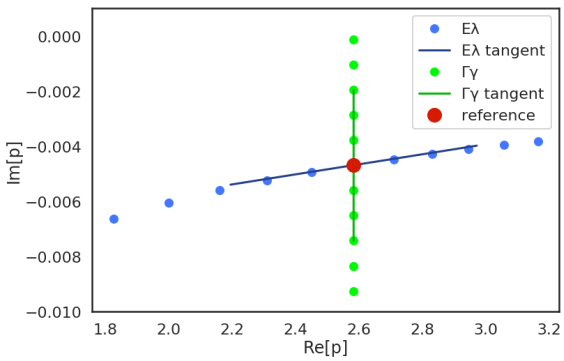

Figure 4-7: Multipole sensitivities to R-matrix parameters $\left(\frac{\partial \Pi}{\partial \Gamma}\right)$. Trajectories of pole p as resonance parameters $\{\Gamma\}$ vary, using the SLBW approximation of the first resonance of ^{238}U (appendix A of [130]). The blue points show how the pole changes as E_λ is varied with equal spacing within 3 standard deviations of the enlarged covariance matrix, while the green points result from equally spaced variations of Γ_γ within their uncertainty range (3 standard deviations of enlarged covariance matrix). The Jacobian $\left(\frac{\partial \Pi}{\partial \Gamma}\right)$ from system (4.54) are the tangents of these trajectories from the mean pole p (red reference point) and are shown in solid lines. Complex pole p units are $(\sqrt{\text{eV}})$.

nuclear data libraries (file 32 in ENDF/B-VIII.0 [87]), there are two ways of translating this into cross section distributions: 1) first-order sensitivity propagation, or; 2) stochastic cross sections.

1. For any given energy E, first-order sensitivity propagation simply considers the R-matrix cross section sensitivities to resonance parameters $\frac{\partial \sigma}{\partial \Gamma}(E)$ and linearly converts the resonance parameter covariance $\mathbb{V}\text{ar}\left(\Gamma\right)$ into a cross section covariance $\mathbb{V}\text{ar}\left(\sigma(E)\right)$ at each energy E, using the chain rule:

$$\mathbb{V}\text{ar}\left(\sigma_\Gamma(E)\right) = \left(\frac{\partial \sigma(E)}{\partial \Gamma}\right) \mathbb{V}\text{ar}\left(\Gamma\right) \left(\frac{\partial \sigma(E)}{\partial \Gamma}\right)^\dagger \tag{4.56}$$

   The same approach can be undertaken using R-matrix cross section sensitivities to windowed multipoles $\frac{\partial \sigma}{\partial \Pi}(E)$, established in equations (126) of lemma 1 in [130], and then propagating to first order the windowed multipole covariances $\mathbb{V}\text{ar}\left(\Pi\right)$, obtained through (4.55), yielding cross section covariances

$$\mathbb{V}\text{ar}\left(\sigma_\Pi(E)\right) = \left(\frac{\partial \sigma(E)}{\partial \Pi}\right) \mathbb{V}\text{ar}\left(\Pi\right) \left(\frac{\partial \sigma(E)}{\partial \Pi}\right)^\dagger \tag{4.57}$$

2. Stochastic cross sections consist of sampling resonance parameters $\left\{\Gamma\right\}$ from their uncertainty distribution – say multivariate normal $\mathcal{N}\left(\Gamma, \mathbb{V}\text{ar}\left(\Gamma\right)\right)$ – and computing the corresponding cross section $\sigma_\Gamma(E)$ as a function of energy

$$\mathrm{d}\mathbb{P}\Big(\sigma_\Gamma(E)\Big) = \sigma_{\mathrm{d}\mathbb{P}(\Gamma)}(E) \tag{4.58}$$

Alternatively, one could sample multipoles $\left\{\Pi\right\}$ from a windowed multipole distribution – say multivariate normal $\mathcal{N}\left(\Pi, \mathbb{V}\mathrm{ar}\left(\Pi\right)\right)$ – and correspondingly generate windowed multipole stochastic cross sections

$$\mathrm{d}\mathbb{P}\Big(\sigma_{\Pi}(E)\Big) = \sigma_{\mathrm{d}\mathbb{P}(\Pi)}(E) \tag{4.59}$$

Stochastic cross sections uncertainties only match first order sensitivity approaches (E.130) and (E.131) for very small covariances. This is because normally distributed resonance parameters do not translate into normally distributed cross sections (E.132): sampling resonance parameters from $\mathcal{N}\left(\Gamma, \mathbb{V}\mathrm{ar}\left(\Gamma\right)\right)$ and then computing the corresponding cross sections through R-matrix equations cannot in general lead to normally distributed cross sections $\sigma_{\Gamma}(E)$ at all energies. However, they do in the linear case, which is a good first-order approximation for small covariances.

Significant work has been carried out to infer parameter distributions that accurately reproduce our uncertainty of nuclear cross sections [149, 70, 101, 205, 206, 173, 281, 54, 282]. By introducing resonance covariances $\mathbb{V}\mathrm{ar}\left(\Gamma\right)$, present standard nuclear data libraries are built with the implicit assumption that sampling resonance parameters from a multivariate normal distribution $\mathcal{N}\left(\Gamma, \mathbb{V}\mathrm{ar}\left(\Gamma\right)\right)$ and computing the corresponding cross sections $\sigma_{\Gamma}(E)$ generates outcome distributions commensurate to our experimental uncertainty. This parameter uncertainty representation is not obvious *in se*, because cross sections are measured at specific energies, with a resolution subject to an exogenous uncertainty distribution (say normal, log-normal, or exponential) dictated by the experiment. Therefore, no parameter distribution (be it resonance parameters multivariate normal $\mathcal{N}\left(\Gamma, \mathbb{V}\mathrm{ar}\left(\Gamma\right)\right)$ or any other) can exactly reproduce the cross section uncertainty for each measurement energy. And yet, these parameters distributions are our best way of balancing all the different uncertainties from disjointed experiments with the underlying R-matrix theory which unifies our understanding of nuclear interactions physics. In other words stochastic cross sections (E.132) are the conceptually correct way of representing nuclear data uncertainty (though sensitivity analysis yields almost identical results when the uncertainty is small): they are at the core of the TENDL library [207, 209], and being able to sample them is a necessary prerequisite to the *Total Monte Carlo* [283, 285, 55] and *Embedded Monte Carlo* [132, 133] uncertainty propagation methods.

Generating stochastic cross sections has been a major computational challenge in practice because of the need of Doppler broadening nuclear cross sections: one must sample resonance parameters from standard nuclear data libraries, reconstruct the corresponding nuclear cross sections at zero Kelvin (0K), and then process each one (with codes such as NJOY [228]) to compute the corresponding Doppler broadened cross sections at temperature T (as explained in section 2.6). The whole comes at significant computational cost and gargantuan memory footprint to store all the pre-processed cross sections. In contrast, the windowed multipole library can generate stochastic cross sections (E.133) on-the-fly, without any pre-processing nor storage, because one can directly compute Doppler-broadened nuclear cross sections from windowed multipole parameters $\left\{\Pi\right\}$ using (4.12): this constitutes a genuine physics-

enabled computational breakthrough.

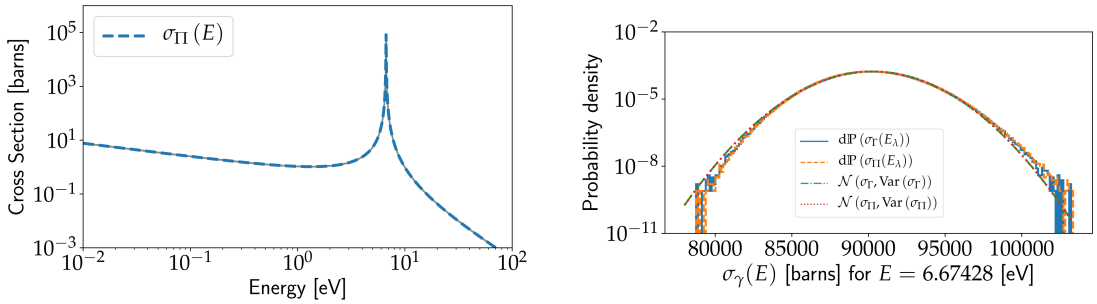

(a) ^{238}U first capture resonance, parameters sampled from ENDF/B-VIII uncertainty. 30 samples shown here.

(b) Cross section histogram at resonance energy $E_\lambda = 6.67428$ eV.

Figure 4-8: Windowed multipole covariances reproduce resonance parameters uncertainty (small covariance case). R-matrix cross sections uncertainty, computed either from the ENDF/B-VIII resonance parameters covariance $\mathbb{V}\mathrm{ar}(\Gamma)$ (from table II in appendix A of [130]), or from the multipoles covariance $\mathbb{V}\mathrm{ar}(\Pi)$, as converted through (4.55), for both the stochastic cross sections (E.132, E.133) and the sensitivities approach (E.130, E.131).

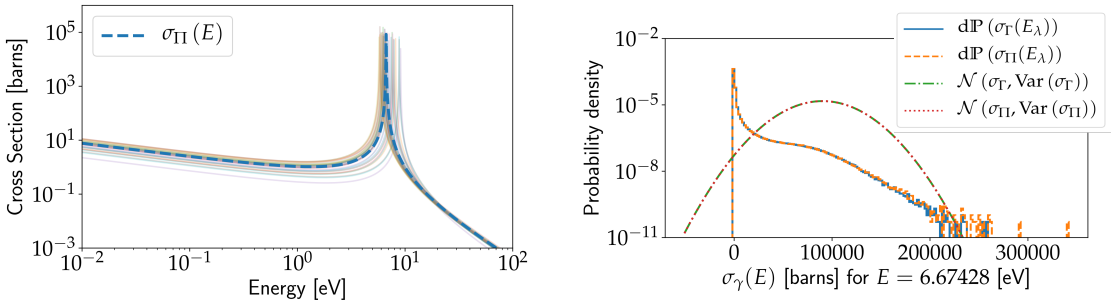

(a) ^{238}U first capture resonance, parameters sampled from an enlarged ENDF/B-VIII uncertainty. 30 samples shown here.

(b) Cross section histogram at resonance energy $E_\lambda = 6.67428$ eV.

Figure 4-9: Windowed multipole covariances reproduce resonance parameters uncertainty (large covariance case). R-matrix cross sections uncertainty, computed either from the enlarged ENDF/B-VIII resonance parameters covariance $\mathbb{V}\mathrm{ar}(\Gamma)$ (from table II in appendix A of [130]), or from the multipoles covariance $\mathbb{V}\mathrm{ar}(\Pi)$, as converted through (4.55), for both the stochastic cross sections (E.132, E.133) and the sensitivities approach (E.130, E.131).

To be fully consistent with standard nuclear data libraries, uncertainties computed using the windowed multipole representation $\{\Pi\}$ must correspond to those computed using resonance parameters $\{\Gamma\}$ (for both sensitivity analysis and stochastic cross sections uncertainty). We showed that the windowed multipole covariances

computed from our direct uncertainty conversion method (4.54) and (4.55) can exactly reproduce the uncertainty stemming from resonance parameters covariances, for both small and large uncertainties. We demonstrated this on a numerical experiment in section III of [130], where the cross section uncertainty distributions were computed by either covariances $\mathbb{V}\mathrm{ar}\,(\Gamma)$ or $\mathbb{V}\mathrm{ar}\,(\Pi)$, for both sensitivity method (E.130) and (E.131), or stochastic cross sections (E.132) and (E.133), and figures E-4 and E-5 show the strong correspondence in generated uncertainty distributions for both small and large uncertainties. In particular, figures 4-8(a) and 4-9(a) show the stochastic cross sections generating by sampling resonance parameters (30 samples) from the multivariate normal uncertainty distributions from the analytic benchmark, respectively with the ENDF and the enlarged covariances. Next to them, in figures 4-8(b) and 4-9(b), we show their respective histograms of cross sections at one energy point — the resonance energy E_λ (near the resonance peak) — on which we overlap the Gaussians from linearized sensitivity analysis, which are identical for both the R-matrix resonance parameters and the windowed multipoles covariances. More remarkably, the histograms of stochastic cross sections also match, computed either from sampling resonance parameters from their multivariate normal uncertainty distribution or from sampling multipoles from their own multivariate normal distribution with a windowed multipole covariances converted from (4.54) and (4.55). This result is not trivial, and tends to show that the linearity regime from Jacobian transformation (4.55) — tangent lines of figure E-3 — is larger than for the cross section (specially at near the resonance peak). We refer to [130] (appendix E) for more details.

4.3 Advances in theoretical nuclear physics achieved along the way

As we established the windowed multipole representation as an alternative formalism to R-matrix theory which enables to compute on-the-fly Doppler broadened stochastic nuclear cross sections, we achieved a few advances in theoretical nuclear physics along the way, which we briefly list here and refer to their corresponding articles for in-depth study:

- We discovered shadow poles in Brune's alternative parametrization of R-matrix theory, as well as associated new properties, which we completely established and proved, in the process generalizing the alternative parametrization to encompass the Reich-Moore formalism and complex resonance parameters [127].

- We identified there exists an ambiguity in the way the nuclear physics community continues R-matrix theory to complex wave numbers, and showed how it is necessary to resolve it in order to propose alternative nuclear data representations of resonance parameters (such as the Brune alternative parameters, or the windowed multipole parameters) [127, 125].

- We proposed a way to solve this ambiguity by arguing in favor of analytic continuation as the new standard way of continuing R-matrix operators (and in particular the shift $S(\rho)$ and penetration $P(\rho)$ functions)[125], against the prevailing legacy of Lane & Thomas [214].

- We showed how the Siegert-Humblet pole expansions in radioactive states are the bridge between R-matrix theory and the scattering matrix wave number pole expansions of Humblet and Rosenfeld [125].

- We established numerous new mathematical physics results, such as: the Mittag-Leffler expansion of the outgoing wave function reduced logarithmic derivative $L(\rho)$ function [127]; all the poles of the scattering matrix are those of the Kapur-Peierls operator (radioactive poles) and all other poles cancel out of the scattering matrix when performing analytic continuation of R-matrix operators while conserving the Wronskian condition [125]; quantum tunneling evanescence could explain channel closure when performing analytic continuation of R-matrix operators to complex wave numbers [125]; the exact number of complex alternative poles [127] and of radioactive poles [125]; etc.

- All these results form a "xenon trilogy on pole parametrizations of R-matrix theory" [127, 125, 130], where all the predictions from these theoretical results were revealed to be true as they were observed in the case of xenon 134. This trilogy of articles is summarized in appendix B, and each article is transcribed *verbatim* in appendices C, D, and E respectively.

- In parallel, we contributed to establishing the *Generalized Reich Moore* formalism, which enables to convert complex Reich-Moore parameters into equivalent real R-matrix parameters, albeit this often comes at the cost of significantly expanding the number of capture levels [60].

- We also developed innovative high-order polynomial root-finding algorithms to search for the radioactive poles [131].

- Finally, we explored other uses of the windowed multipole formalism, from resonance upscattering [222], to Fourier transform Doppler broadening of thermal scattering [130], not withstanding the analytic resolution of transport problems as in the analytic benchmark [298, 53].

Chapter 5

Conclusion

The scientist has a lot of experience with ignorance and doubt and uncertainty, and this experience is of very great importance, I think.
- Richard Feynman

To design future nuclear technologies — from weapons stewardship to medical imaging or zero-carbon power reactors — we need high-fidelity nuclear simulations with trustworthy confidence intervals. Our knowledge of nuclear physics is parametrized by nuclear data, whose values are drawn from experiments which invariably carry uncertainty. Propagating this nuclear data uncertainty across nuclear simulations is thus of paramount importance. It has even been the limiting factor for the design of some new advanced reactor technologies, such as Terrapower's new molten salt fast spectrum nuclear reactor. Such problems would be alleviated by furthering our ability to take real-world measures in integral experiments of nuclear reactors, and from these infer and narrow down our nuclear data uncertainty.

The previous two methods used to perform such propagation and inference of nuclear data uncertainty across Monte Carlo particle transport simulations were: Sensitivity Analysis (SA); and Nested Monte Carlo (NMC) (called Total Monte Carlo (TMC) and Bayesian Monte Carlo (BMC) in the field). The main drawbacks of SA are: it is linear (cannot account for non-linear phenomena); it can only propagate uncertainty to one output at the time (or infer from one observation at the time); and it cannot accurately account for temperature effects (Doppler broadening) on the uncertainty inference and propagation. This is why people have resorted to NMC, the main drawbacks of which are: its immense computational cost; its impractical results in the form of histograms which are difficult to store and sample from; and the gargantuan memory cost of sampling the required stochastic cross sections.

This thesis introduced a series of new tools — both from statistical inference and machine learning (*Embedded Monte Carlo*) as well as from nuclear physics and data models (*windowed multipole stochastic cross sections*) — which, when combined, can

systematically infer and propagate nuclear data uncertainty across nuclear simulations with considerably superior performance and higher fidelity than all previous state-of-the-art methods.

5.1 Achievements

By restricting the inputs and outputs distributions to pre-determined parametric families (outputs must be parametrizable with their moments) Embedded Monte Carlo performs approximate propagation and inference of inputs uncertainty across the Monte Carlo computations.

Compared to sensitivity analysis, Embedded Monte Carlo can propagate uncertainty to all outputs of nuclear simulations at once and with accurate temperature treatment, with 2 to 10 times less neutrons as those needed to compute the sensitivities and adjoint flux. Inference can be performed with the same asymptotic converge rate.

For both the inference and the propagation problems, *Embedded Monte Carlo* requires at least 10 to 100 times less particle simulations than Nested Monte Carlo (or fast-TMC) to achieve the same accuracy (and further gains up to 10,000 times less particles can be achieved in cases of large nuclear data uncertainty and small random walk variance).

Moreover, to solve the major sampling bottleneck due to temperature Doppler broadening, we used a new nuclear data formalism called *windowed multipole* that allows on-the-fly sampling and on-the-fly Doppler broadening of stochastic nuclear cross sections (we contributed to develop the theory and the later on-the-fly capabilities of the windowed multipole representation). This can drastically cut the memory footprint by up to a million times.

Indeed, for the resolved resonance region (RRR), the memory footprint of the windowed multipole library is of 15 MB, and we can assume it to reach 250 MB for stochastic windowed multipoles (adding the multipole covariances). This contrasts with a memory burden of 500 MB for point-wise cross sections, for each reference temperature, and a 100 reference temperatures are necessary to span the range of 300 - 3,000 Kelvin and achieve a 0.1% accuracy in Doppler broadening using the traditional log-log interpolation. In table 5.1, we compare orders of magnitude of memory and runtime for all the methods discussed, for both uncertainty inference and propagation as well as for Doppler broadening. Non-linear inference and propagation to all outputs simultaneously can be achieved by the brute-force Nested Monte Carlo (fast-TMC [285]) with traditional log-log interpolation for Doppler broadening at a cost 50-500 TB of memory for sampling. In the starkest of contrasts, this compares to Embedded Monte Carlo with stochastic windowed multipoles, which has a memory footprint of 250 MB (200,000 - 2,000,000 times less), all the while running 10 - 100 times less particles.

Table 5.1: Uncertainty propagation and inference methods: memory and processing comparisons. Statistical methods: Nested Monte Carlo (NMC) (for $M = 1,000 - 10,000$ nuclear data samples using fast-TMC [285]); Sensitivity Analysis (SA); and Embedded Monte Carlo. Doppler broadening methods for 0.1% interpolation accuracy from 300K to 3000K on the resolved resonance range (RRR) for which point-wise cross sections take 500 MB memory, and the windowed multipole library 15 MB (assuming 250 MB with covariances) [23]: traditional log-log interpolation (100 temperatures) [314]; optimal quadrature Doppler kernel reconstruction (10 temperatures) [124]; rejection sampling [316, 317, 288]; windowed multipole [130, 197].

Statistical method (Doppler broadening)	Characteristics	Memory	Runs (particles)
Nested Monte Carlo (Log-log interpolation)	Exact + All outputs Histogram	ref. 50 - 500 TB	ref.
Nested Monte Carlo (Rejection sampling)	Exact + All outputs Histogram	100 × less	2 × more
Nested Monte Carlo (Kernel reconstruction)	Exact + All outputs Histogram	10 × less	same
Nested Monte Carlo (Stochastic windowed multipole)	Exact + All outputs Histogram	200,000 - 2,000,000 × less 250 MB	same
Sensitivity Analysis (Log-log interpolation)	Linear + One output No Doppler broadening of uncertainty	1,000 - 10,000 × less 50 GB	$100 - 1,000\times$ less
Sensitivity Analysis (Rejection sampling)	Linear + One output No Doppler broadening of uncertainty	100,000 - 1,000,000 × less 500 MB	$50 - 500\times$ less
Sensitivity Analysis (Kernel reconstruction)	Linear + One output No Doppler broadening of uncertainty	10,000 - 100,000 × less 5 GB	$100 - 1,000\times$ less
Sensitivity Analysis (Stochastic windowed multipole)	Linear + One output No Doppler broadening of uncertainty	100,000 - 1,000,000 × less 500 MB	$100 - 1,000\times$ less
Embedded Monte Carlo (Log-log interpolation)	Approximate + All outputs Moments	same 50 - 500 TB	$10 - 100$ × less
Embedded Monte Carlo (Rejection sampling)	Approximate + All outputs Moments	100 × less	$5 - 50$ × less
Embedded Monte Carlo (Kernel reconstruction)	Approximate + All outputs Moments	10 × less	$10 - 100$ × less
Embedded Monte Carlo (Stochastic windowed multipole)	Approximate + All outputs Moments	200,000 - 2,000,000 × less 250MB	$10 - 100$ × less

5.2 New horizons

This thesis established the general theory of Embedded Monte Carlo methods, and of stochastic windowed multipoles. It however only implemented them in small-scale proof-of-concept toy-problems which, though verisimilar, do not present many of the challenges of scale. Scaling up the methods to full-core reactor calculations will require much future implementation work.

For the stochastic windowed multipole library, coding the contour integral method for covariance generation (4.55) in a streamlined program that can process entire nuclear data libraries will be a major undertaking. And there will remain the problems posed by isotopes non represented with resonance parameters, but only point-wise data.

Embedded Monte Carlo methods are but in their infancy. For Embedded Forward Propagation, methods to estimate the optimal trade-off on inner-loop to outer-loop particles to be run as the computation unfolds will be necessary to accelerate convergence. Further research will also have to investigate the convergence of criticality eigenvalue problems, in particular the fission source. Embedded Variational Inference will require a considerable amount of additional work to properly scale. In particular, the study of the learning rates choice and estimation will be crucial. But so will be establishing ways to add constraints to the parameter space. And many trade-offs in convergence between the inner-loop N, the outer-loop M, and the number of iterations T are yet to be understood. Perhaps most fundamentally, Embedded Variational Inference optimizes according to a new standard — that of relative entropy (Kullback–Leibler divergence) rather than the traditional least squares — so we must understand how this affects traditional nuclear data evaluations.

New research grants are being sought to pursue these new horizons.

5.3 Epilogue

Research-wise, we were able to find closure on the windowed multipole front. The physics theory is now fully achieved, and the remaining openings are in possible new applications of the formalism, such as: threshold Doppler broadening; differential Doppler broadening (not angle-integrated); use for other temperature treatments (thermal scattering); analytic method of characteristics; etc.

While we closed a theoretical physics topic, we were privileged enough to open a new statistical learning field. Embedded Monte Carlo is a new, fertile ground. While much more research is needed to engineer and optimize the methods to specific applications (learning rates and algorithmic optimizations), Embedded Monte Carlo holds the promise of breakthrough progress in many fields requiring statistical learning across challenging computations.

In this wake, we hope that the field of nuclear computations will continue to spearhead and lead innovations in the general treatment of information and computation — just as it did when giving birth to the Monte Carlo method — for these lay at the heart of our knowledge economy in the Information Age.

Bibliography

[1] Advanced Simulationand Computing. https://asc.llnl.gov/.

[2] AP1000 Pressurized Water Reactor | Westinghouse Nuclear. https://www.westinghousenuclear.com/new-plants/ap1000-pwr.

[3] Argonne National Laboratory Homepage | Argonne National Laboratory. https://www.anl.gov/.

[4] Brookhaven National Laboratory — a passion for discovery. https://www.bnl.gov/world/.

[5] CASL | The Consortium For Advance Simulation Of Light Water Reactors. https://casl.gov.

[6] CASL, Westinghouse simulate neutron behavior in AP1000 reactor core. https://phys.org/news/2014-02-casl-westinghouse-simulate-neutron-behavior.html.

[7] Department of energy | why the Nuclear Stockpile Needs Supercomputers. https://www.energy.gov/articles/why-nuclear-stockpile-needs-supercomputers.

[8] Home - TerraPower. https://www.terrapower.com/.

[9] HPE and AMD power complex scientific discovery in world's fastest supercomputer for U.S. Department of Energy's (DOE) National Nuclear Security Administration (NNSA). https://www.hpe.com/us/en/newsroom/press-release/2020/03/hpe-and-amd-power-complex-scientific-discovery-in-worlds-fastest-supercomputer-for-us-department-of-energys-doe-national-nuclear-security-administration-nnsa.html.

[10] Is the World Ready for Floating Nuclear Power Stations? - IEEE Spectrum. https://spectrum.ieee.org/energywise/energy/nuclear/is-the-world-ready-for-floating-nuclear-power-stations.

[11] JANIS. https://www.oecd-nea.org/jcms/pl_39910/janis.

[12] Key Nuclear Data Impacting Reactivity in Advanced Reactor | ORNL. https://www.ornl.gov/file/key-nuclear-data-impacting-reactivity-advanced-reactor/display.

[13] Lawrence Livermore National Laboratory. https://www.llnl.gov/.

[14] Lawrence Livermore National Laboratory: Uncertainty Quantification | Weapons and Complex Integration. https://wci.llnl.gov/simulation/computer-codes/uncertainty-quantification.

[15] Limited Test Ban Treaty (LTBT). //2009-2017.state.gov/t/avc/trty/199116.htm.

[16] Los Alamos National Lab: National Security Science. https://www.lanl.gov/.

[17] NASA Technical Reports Server (NTRS): Monte carlo methods in materials science based on fluka and root. https://ntrs.nasa.gov/citations/20030060561.

[18] National Laboratories. https://www.energy.gov/national-laboratories.

[19] Nuclear Test Ban Treaty | JFK Library. https://www.jfklibrary.org/learn/about-jfk/jfk-in-history/nuclear-test-ban-treaty.

[20] Nuclear Testing and Comprehensive Test Ban Treaty (CTBT) Timeline | Arms Control Association. https://www.armscontrol.org/factsheets/NuclearTestingTimeline.

[21] NuScale Power | SMR Nuclear Technology. https://www.nuscalepower.com/.

[22] Oak Ridge National Laboratory | ORNL. https://www.ornl.gov/.

[23] Official Data Libraries | OpenMC.

[24] Rosatom State Atomi Energy Corporation ROSATOM global leader in nuclear technologies nuclear energy. https://www.rosatom.ru/en/press-centre/news/first-of-a-kind-floating-nuclear-power-unit-akademik-lomonosov-leaves-murmansk-for-pevek/.

[25] Russia commissions floating NPP : New Nuclear - World Nuclear News. https://world-nuclear-news.org/Articles/Russia-commissions-floating-NPP.

[26] SAMMY: Nuclear Cross Section Evaluation Tool | ORNL. https://www.ornl.gov/division/rnsd/projects/sammy-nuclear-cross-section-evaluation-tool.

[27] Sandia National Laboratories: Exceptional Service in the National Interest. https://www.sandia.gov/.

[28] SCALE Overview | ORNL. https://www.ornl.gov/scale/overview.

[29] Sierra. https://computing.llnl.gov/computers/sierra.

[30] Sierra | High Performance Computing. https://hpc.llnl.gov/hardware/platforms/sierra.

[31] Simulation of AP1000 first core with VERA - Image455502 - Nuclear Engineering International. https://www.neimagazine.com/features/featuresimulation-of-ap1000-first-core-with-vera-4295660/featuresimulation-of-ap1000-first-core-with-vera-4295660-455502.html.

[32] Southern Company and TerraPower Prep for Testing on Molten Salt Reactor. https://www.energy.gov/ne/articles/southern-company-and-terrapower-prep-testing-molten-salt-reactor.

[33] Summit. https://www.olcf.ornl.gov/summit/.

[34] TerraPower. https://www.terrapower.com/.

[35] TOP500 | supercomputer performance list. https://www.top500.org/.

[36] Trinity. https://www.lanl.gov/projects/trinity/.

[37] U.S. Department of Energy: Advanced Modeling & simulation. https://www.energy.gov/ne/nuclear-reactor-technologies/advanced-modeling-simulation.

[38] U.S. Department of Energy advances nuclear stockpile research and simulations with 4X more powerful supercomputer built by Hewlett Packard Enterprise. https://www.hpe.com/us/en/newsroom/press-release/2020/09/us-department-of-energy-advances-nuclear-stockpile-research-and-simulations-with-4x-more-powerful-supercomputer-built-by-hewlett-packard-enterprise.html.

[39] U.S. Department of State: Nuclear Weapon Computer Simulations. //2009-2017.state.gov/t/avc/rls/202014.htm.

[40] What the First H-Bomb Test Looked Like. https://time.com/4096424/ivy-mike-history/.

[41] Why France is eyeing nuclear power again. https://www.technologyreview.com/2019/10/16/65172/why-france-is-eyeing-nuclear-power-again/.

[42] The World Nuclear Industry Status Report 2019 (HTML). https://www.worldnuclearreport.org/The-World-Nuclear-Industry-Status-Report-2019-HTML.html.

[43] *Quantifying uncertainty in nuclear analytical measurements*. Number 1401 in TECDOC series. INTERNATIONAL ATOMIC ENERGY AGENCY, Vienna, 2004.

[44] Report of the Defense Science Board Task Force on Nuclear Weapon Effects Test, Evaluation, and Simulation. Technical report, OFFICE OF THE UNDER SECRETARY OF DEFENSE FOR ACQUISITION TECHNOLOGY AND LOGISTICS WASHINGTON DC, April 2005. https://dsb.cto.mil/reports/2000s/ADA434656.pdf.

[45] *International Evaluation of Neutron Cross-Section Standards*. Non-Serial Publications. INTERNATIONAL ATOMIC ENERGY AGENCY, Vienna, 2007. https://www-pub.iaea.org/MTCD/Publications/PDF/Pub1291_web.pdf.

[46] Tackling the Challenges of Nuclear Data in the Future. https://www.iaea.org/newscenter/news/tackling-the-challenges-of-nuclear-data-in-the-future, October 2016.

[47] After 28 years, should the U.S. resume testing nuclear weapons?, November 2020. https://www.psr.org/blog/after-28-years-should-the-u-s-resume-testing-nuclear-weapons/.

[48] MIT NSE CRPG . Windowed multipole library, May 2019. https://github.com/mit-crpg/WMP_Library.

[49] Moncef Abbas and Sadek Bouroubi. On new identities for Bell's polynomials. *Discrete Mathematics*, 293(1):5–10, April 2005.

[50] Oliver Aberth. Iteration Methods for Finding all Zeros of a Polynomial Simultaneously. *Mathematics of Computation*, 27(122), 1973. https://www.ams.org/journals/mcom/1973-27-122/S0025-5718-1973-0329236-7/S0025-5718-1973-0329236-7.pdf.

[51] Milton Abramowitz and Irene A. Stegun. United States Department of Commerce. National Bureau of Standards, Applied Mathematics Series, 1964.

[52] Abdulla Alhajri and Benoit Forget. Eigenvalue Sensitivity in Monte Carlo Simulations to Nuclear Data Parameters using the Multipole Formalism. *International Conference on Mathematics and Computational Methods applied to Nuclear Science and Engineering (M&C 2019), Portland, OR, USA.*, August 25-29 2019.

[53] Abdulla Alhajri, Vladimir Sobes, Pablo Ducru, Barry D. Ganapol, and Benoit Forget. An Analytic Benchmark for Neutron Boltzmann Transport with Downscattering. Part II. Flux & eigenvalue sensitivities to nuclear cross sections & resonance parameters. *Nuclear Science and Engineering*, January 2021. submitted.

[54] E. Alhassan, D. Rochman, H. Sjöstrand, A. Vasiliev, A. J. Koning, and H. Ferroukhi. Bayesian updating for data adjustments and multi-level uncertainty propagation within Total Monte Carlo. *Annals of Nuclear Energy*, 139:107239, May 2020.

[55] E Alhassan, H Sjöstrand, P Helgesson, AJ Koning, M Österlund, S Pomp, and D Rochman. Uncertainty and correlation analysis of lead nuclear data on reactor parameters for the european lead cooled training reactor. *Annals of Nuclear Energy*, 75:26–37, 2015.

[56] Grégoire Allaire. A review of adjoint methods for sensitivity analysis, uncertainty quantification and optimization in numerical codes. *Ingenieurs de l'Automobile, SIA*, 836:33–36, December 14 2015. https://hal.archives-ouvertes.fr/hal-01242950.

[57] Grégoire Allaire, Xavier Blanc, Bruno Despres, and FranGolse. *Transport et Diffusion.* École Polytechnique, École Polytechnique, route de Saclay, Palaiseau, France. http://www.cmap.polytechnique.fr/ allaire/map567/M1TranspDiff.pdf.

[58] J. Allison, K. Amako, J. Apostolakis, P. Arce, M. Asai, T. Aso, E. Bagli, A. Bagulya, S. Banerjee, G. Barrand, B. R. Beck, A. G. Bogdanov, D. Brandt, J. M. C. Brown, H. Burkhardt, Ph. Canal, D. Cano-Ott, S. Chauvie, K. Cho, G. A. P. Cirrone, G. Cooperman, M. A. Cortés-Giraldo, G. Cosmo, G. Cuttone, G. Depaola, L. Desorgher, X. Dong, A. Dotti, V. D. Elvira, G. Folger, Z. Francis, A. Galoyan, L. Garnier, M. Gayer, K. L. Genser, V. M. Grichine, S. Guatelli, P. Guèye, P. Gumplinger, A. S. Howard, I. Hřivnáčová, S. Hwang, S. Incerti, A. Ivanchenko, V. N. Ivanchenko, F. W. Jones, S. Y. Jun, P. Kaitaniemi, N. Karakatsanis, M. Karamitros, M. Kelsey, A. Kimura, T. Koi, H. Kurashige, A. Lechner, S. B. Lee, F. Longo, M. Maire, D. Mancusi, A. Mantero, E. Mendoza, B. Morgan, K. Murakami, T. Nikitina, L. Pandola, P. Paprocki, J. Perl, I. Petrović, M. G. Pia, W. Pokorski, J. M. Quesada, M. Raine, M. A. Reis, A. Ribon, A. Ristić Fira, F. Romano, G. Russo, G. Santin, T. Sasaki, D. Sawkey, J. I. Shin, I. I. Strakovsky, A. Taborda, S. Tanaka, B. Tomé, T. Toshito, H. N. Tran, P. R. Truscott, L. Urban, V. Uzhinsky, J. M. Verbeke, M. Verderi, B. L. Wendt, H. Wenzel, D. H. Wright, D. M. Wright, T. Yamashita, J. Yarba, and H. Yoshida. Recent developments in Geant4. *Nuclear Instruments and Methods in Physics Research Section A: Accelerators, Spectrometers, Detectors and Associated Equipment*, 835:186–225, November 2016. https://doi.org/10.1016/j.nima.2016.06.125.

[59] C. Angulo and P. Descouvemont. R-matrix analysis of interference effects in $^{12}\mathrm{C}(\alpha,\alpha)^{12}\mathrm{C}$ and $^{12}\mathrm{C}(\alpha,\gamma)^{16}\mathrm{O}$. *Physical Review C*, 61(6):064611, May 2000. https://link.aps.org/doi/10.1103/PhysRevC.61.064611.

[60] Goran Arbanas, Vladimir Sobes, Andrew Holcomb, Pablo Ducru, Marco Pigni, and Dorothea Wiarda. Generalized Reich-Moore R-matrix approximation. *EPJ Web of Conferences*, 146(12006):1–5, 2017. https://doi.org/10.1051/epjconf/201714612006.

[61] Louis-François-Antoine Arbogast. A Strasbourg, de l'Imprimerie de Levrault, Frères, An VIII (1800). https://docnum.unistra.fr/digital/collection/coll7/id/39933.

[62] R. E. Azuma, E. Uberseder, E. C. Simpson, C. R. Brune, H. Costantini, R. J. de Boer, J. Görres, M. Heil, P. J. LeBlanc, C. Ugalde, and M. Wiescher. AZURE: An R-matrix code for nuclear astrophysics. *Physical Review C*, 81(4):045805, 2010.

[63] R.E. Azuma, E. Uberseder, E.C. Simpson, C.R. Brune, H. Costantini, R. J. de Boer, J. Gorres, M. Heil, P.J. LeBlanc, C. Ugalde, and M. Wiescher. AZURE: An R-matrix code for nuclear astrophysics. *Physical Review C*, 81(045805), 2010. https://doi.org/10.1103/PhysRevC.81.045805.

[64] David H. Bailey and Paul N. Swarztrauber. A Fast Method for the Numerical Evaluation of Continuous Fourier and Laplace Transforms. *SIAM Journal on Scientific Computing*, 15(5):1105–1110, September 1994. Publisher: Society for Industrial and Applied Mathematics.

[65] C. T. Ballinger. The direct S({alpha},{beta}) method for thermal nuetron scattering. *Proceedings of the international conference on mathematics and computations, reactor physics, and environmental analyses, Portland, OR (United States), 30 Apr - 4 May*, April - May 1995. Number: CONF-950420- Publisher: American Nuclear Society, Inc., La Grange Park, IL (United States).

[66] Ilan Bar-On and Victor Ryaboy. Fast Diagonalization of Large and Dense Complex Symmetric Matrices, with applications to Quantum Reaction Dynamics. *SIAM Journal of Scientific Computing*, 18(5):1412–1435, September 1997. https://doi.org/10.1137/S1064827594269056.

[67] F. C. Barker. The Boundary Condition Parameter in R-matrix Theory. *Australian Journal of Physics*, 25:341–348, 1972. https://doi.org/10.1071/PH720341.

[68] J. C. Batchelder, S.-A. Chong, J. Morrell, M. Ayllon Unzueta, P. Adams, J. D. Bauer, T. Bailey, T. A. Becker, L. A. Bernstein, M. Fratoni, A. M. Hurst, J. James, A. M. Lewis, E. F. Matthews, M. Negus, D. Rutte, K. Song, K. Van Bibber, M. Wallace, and C. S. Waltz. Possible evidence of nonstatistical properties in the $\hat{35}\mathrm{Cl}(n, p)\hat{35}\mathrm{S}$ cross section. *Physical Review C*, 99(4):044612, April 2019. https://doi.org/10.1103/PhysRevC.99.044612.

[69] Giuseppe Battistoni, Till Boehlen, Francesco Cerutti, Pik Wai Chin, Luigi Salvatore Esposito, Alberto Fassò, Alfredo Ferrari, Anton Lechner, Anton Empl, Andrea Mairani, Alessio Mereghetti, Pablo Garcia Ortega, Johannes Ranft, Stefan Roesler, Paola R. Sala, Vasilis Vlachoudis, and George Smirnov. Overview of the FLUKA code. *Annals of Nuclear Energy*, 82:10–18, August 2015. https://doi.org/10.1016/j.anucene.2014.11.007.

[70] E. Bauge, S. Hilaire, and P. Dossantos-Uzarralde. Evaluation of the covariance matrix of neutronic cross sections with the Backward-Forward Monte Carlo method. In *International Conference on Nuclear Data for Science and Technology*, pages 259–264. EDP Sciences, 2007.

[71] E. T. Bell. Exponential Polynomials. *Annals of Mathematics*, 35(2):258–277, 1934. Publisher: Annals of Mathematics.

[72] George I. Bell and Samuel Glasstone. *Nuclear Reactor Physics*. Division of Technical Information, United States Atomic Energy Commission, Van Nostrand Reinhold Company, 1970. Library of Congress Catalog Card Number 73-122674.

[73] Mario Berljafa and Stefan GÃŒttel. The RKFIT Algorithm for Nonlinear Rational Approximation. *SIAM Journal on Scientific Computing*, 39(5):A2049–A2071, January 2017. Publisher: Society for Industrial and Applied Mathematics.

[74] Iwo Bialynicki-Birula. On the wave function of the photon. *Acta Physica Polonica A*, 86(1-2):97–116, 1994. http://przyrbwn.icm.edu.pl/APP/PDF/86/a086z1p08.pdf.

[75] Iwo Bialynicki-Birula. On the wave function of the photon. *Progress in Optics*, 36:245–294, 1996. https://doi.org/10.1016/S0079-6638(08)70316-0.

[76] G. Lansing Blackshaw and Raymond L. Murray. Scattering Functions for Low-Energy Neutron Collisions in a Maxwellian Monatomic Gas. *Nuclear Science and Engineering*, 27(3):520–532, March 1967. Publisher: Taylor & Francis _eprint: https://doi.org/10.13182/NSE86-A17617.

[77] John M. Blatt and Victor F. Weisskopf. *Theoretical Nuclear Physics*. Springer-Verlag, Massachusetts Institute of Technology, Cambridge, MA 02139, U.S.A., 1952. DOI: 10.1007/978-1-4612-9959-2.

[78] David M. Blei, Alp Kucukelbir, and Jon D. McAuliffe. Variational Inference: A Review for Statisticians. *Journal of the American Statistical Association*, 112(518):859–877, April 2017. Publisher: Taylor & Francis _eprint: https://doi.org/10.1080/01621459.2017.1285773.

[79] C. Bloch. Une formulation unifiée de la théorie des réactions nucléaires. *Nuclear Physics*, 4:503–528, avril 1957.

[80] A.I. Blokhin, E.V. Gai, A.V. Ignatyuk, I.I. Koba, V.N. Manokhin, and V.G. Pronyaev, 2016. https://www.vant.ippe.ru/en/year2016/2/neutron-constants/1150-5.html,
https://www.vant.ippe.ru/images/pdf/2016/2-5.pdf.

[81] Wesley E. Bolch. The Monte Carlo Method in Nuclear Medicine: Current Uses and Future Potential. *Journal of Nuclear Medicine*, 51(3):337–339, March 2010. https://doi.org/10.2967/jnumed.109.067835.

[82] Ludwig Boltzmann. Weitere Studien über das Wärmegleichgewicht unter Gasmolekülen. *Sitz.-Ber. Akad. Wiss. Wien*, 66:275–370, 1872.

[83] A. Bouloré. Importance of uncertainty quantification in nuclear fuel behaviour modelling and simulation. *Nuclear Engineering and Design*, 355:110311, December 2019.

[84] N. Bourbaki. chapter 9. Hermann, Paris, 1959. N. Bourbaki et Springer-Verlag, Berlin, 2007, 1959. https://link.springer.com/content/pdf/10.1007%2F978-3-540-35339-3.pdf.

[85] Khristo N. Boyadzhiev. Exponential Polynomials, Stirling Numbers, and Evaluation of Some Gamma Integrals. *Abstract and Applied Analysis*, September 2009. ISSN: 1085-3375 Pages: e168672 Publisher: Hindawi Volume: 2009.

[86] G. Breit. Scattering matrix of radioactive states. *Physical Review*, 58:1068–1074, December 1940.

[87] D. A. Brown, M. B. Chadwick, R. Capote, A. C. Kahler, A. Trkov, M. W. Herman, A. A. Sonzogni, Y. Danon, A. D. Carlson, M. Dunn, D. L. Smith, G. M. Hale, G. Arbanas, R. Arcilla, C. R. Bates, B. Beck, B. Becker, F. Brown, R. J. Casperson, J. Conlin, D. E. Cullen, M. A. Descalle, R. Firestone, T. Gaines, K. H. Guber, A. I. Hawari, J. Holmes, T. D. Johnson, T. Kawano, B. C. Kiedrowski, A. J. Koning, S. Kopecky, L. Leal, J. P. Lestone, C. Lubitz, J. I. Márquez Damián, C. M. Mattoon, E. A. McCutchan, S. Mughabghab, P. Navratil, D. Neudecker, G. P. A. Nobre, G. Noguere, M. Paris, M. T. Pigni, A. J. Plompen, B. Pritychenko, V. G. Pronyaev, D. Roubtsov, D. Rochman, P. Romano, P. Schillebeeckx, S. Simakov, M. Sin, I. Sirakov, B. Sleaford, V. Sobes, E. S. Soukhovitskii, I. Stetcu, P. Talou, I. Thompson, S. van der Marck, L. Welser-Sherrill, D. Wiarda, M. White, J. L. Wormald, R. Q. Wright, M. Zerkle, G. Åœerovnik, and Y. Zhu. ENDF/B-VIII.0: The 8th Major Release of the Nuclear Reaction Data Library with CIELO-project Cross Sections, New Standards and Thermal Scattering Data. *Nuclear Data Sheets*, 148:1–142, February 2018.

[88] D.A. Brown, M.B. Chadwick, R. Capote, A.C. Kahler, A. Trkov, M.W. Herman, A.A. Sonzogni, Y. Danon, A.D. Carlson, M. Dunn, D.L. Smith, G.M. Hale, G. Arbanas, R. Arcilla, C.R. Bates, B. Beck, B. Becker, F. Brown, R.J. Casperson, J. Conlin, D.E. Cullen, M.-A. Descalle, R. Firestone, T. Gaines, K.H. Guber, A.I. Hawari, J. Holmes, T.D. Johnson, T. Kawano, B.C. Kiedrowski, A.J. Koning, S. Kopecky, L. Leal, J.P. Lestone, C. Lipitz, J.I. Márquez Damián, C.M. Mattoon, E.A. McCutchan, S. Mughabghab, P. Navratil, D. Neudecker, G.P.A. Nobre, G. Noguere, M. Paris, M.T. Pigni, A.J. Plompen, B. Pritychenko, V.G.

Pronyaev, D. Roubtsov, D. Rochman, P. Romano, P. Schillebeeckx, S. Simakov, M. Sin, I. Sirakov, B. Sleaford, V. Sobes, E.S. Soukhovitskii, I. Stetcu, P. Talou, I. Thompson, S. van der Marck, L. Wesler-Sherrill, D. Wiarda, M. White, J.L. Wormald, R.Q. Wright, M. Zerkle, G. Zeronik, and Y. Zhu. ENDF/B-VIII.0: The 8-th Major Release of the Nuclear Reaction Data Library with CIELO-project Cross Sections, New Standards and Thermal Scattering Data. *Nuclear Data Sheets*, 148:1–142.

[89] F Brown and B Kiedrowski. Continuous-energy sensitivity coefficient capability in mcnp6. *American Nuclear Society Winter Meeting*, 2012.

[90] F Brown and B Kiedrowski. Methodology, verification, and performance of the continuous-energy nuclear data sensitivity capability in mcnp6. *International Conference on Mathematics and Computational Methods Applied to Nuclear Science and Engineering*, 2013.

[91] E. Brun, F. Damian, C. M. Diop, E. Dumonteil, F. X. Hugot, C. Jouanne, Y. K. Lee, F. Malvagi, A. Mazzolo, O. Petit, J. C. Trama, T. Visonneau, and A. Zoia. TRIPOLI-4®, CEA, EDF and AREVA reference Monte Carlo code. *Annals of Nuclear Energy*, 82:151–160, August 2015. https://doi.org/10.1016/j.anucene.2014.07.053.

[92] C. R. Brune. Alternative parametrization of R-matrix theory. *Phys. Rev. C*, 66:044611, Oct 2002.

[93] Carl R. Brune, Gerald M. Hale, and Mark W. Paris. Monotonic properties of the shift and penetration factors. *Phys. Rev. C*, 97:024603, Feb 2018.

[94] Antonio Brusegan, Gilles Noguere, and Frank Gunsing. The Resolution Function in Neutron Time-of-Flight Experiments. *Journal of Nuclear Science and Technology*, 39(sup2):685–688, August 2002.

[95] B. D. Buckley, P. G. Burke, and Vo Ky Lan. R-matrix calculations for electron-molecule scattering. *Computer Physics Communications*, 17:175–179, 1979.

[96] Angelika Bunse-Gerstner and William B. Gragg. Singular value decomposition of complex symmetric matrices. *Journal of Computational and Applied Mathematics*, 21:41–54, 1988.

[97] P. G. Burke. *R-Matrix Theory of Atomistic Collisions*. 2011.

[98] P. G. Burke and W. D. Robb. *The R-Matrix Theory of Atomic Processes*. 2008. https://doi.org/10.1016/S0065-2199(08)60030-5.

[99] Dan Gabriel Cacuci, editor. *Handbook of Nuclear Engineering: Vol. 1: Nuclear Engineering Fundamentals; Vol. 2: Reactor Design; Vol. 3: Reactor Analysis; Vol. 4: Reactors of Generations III and IV; Vol. 5: Fuel Cycles, Decommissioning, Waste Disposal and Safeguards*. Springer US, 2010.

[100] Roberto Capote and Donald L. Smith. An Investigation of the Performance of the Unified Monte Carlo Method of Neutron Cross Section Data Evaluation. *Nuclear Data Sheets*, 109(12):2768–2773, December 2008.

[101] Roberto Capote, Donald L. Smith, Andrej Trkov, and Mehdi Meghzifene. A New Formulation of the Unified Monte Carlo Approach (UMC-B) and Cross-Section Evaluation for the Dosimetry Reaction $^{55}Mn(n,\hat{\imath}^3)^{56}Mn$. *Journal of ASTM International*, 9(3):1–12, March 2012. Publisher: ASTM International.

[102] L. L. Carter and E. D. Cashwell. Particle-transport simulation with the monte carlo method. *ERDA critical review series*, TID-26607, February 1975. https://inis.iaea.org/collection/NCLCollectionStore/_Public/07/227/7227109.pdf.

[103] Bruno CATTANEO. GELINA, the JRC Neutron Time-of-Flight Facility (EUFRAT). https://ec.europa.eu/jrc/en/research-facility/open-access/relevance-driven/2020-1-rd-eufrat-gelina, June 2020.

[104] MB Chadwick, M Herman, P Obložinskỳ, Michael E Dunn, Y Danon, AC Kahler, Donald L Smith, B Pritychenko, Goran Arbanas, R Arcilla, et al. *ENDF/B-VII.1 nuclear data for science and technology: cross sections, covariances, fission product yields and decay data*. National Nuclear Data Center, Brookhaven National Laboratory, Upton, NY 11973-5000, 2010.

[105] Pafnutii Lvovich Chebyshev. *Sur les valeurs limites des intégrales*. Imprimerie de Gauthier-Villars, 1874.

[106] Shengli Chen, Pierre Tamagno, David Bernard, Pascal Archier, and Gilles Noguere. From nuclear physics to displacement damage calculation and uncertainty propagation in CONRAD. *Results in Physics*, 17:103023, June 2020.

[107] Z.-P Chen, Y.-Y Sun, R. Zhang, and T.-J Liu. Covariance propagation in R-matrix model fitting. *High Energy Physics and Nuclear Physics -Beijing-*, 28, 01 2004. https://inis.iaea.org/collection/NCLCollectionStore/_Public/23/077/23077172.pdf.

[108] Go Chiba, Amsashi Tsuji, and Tadashi Narabayashi. Resonance self-shielding effect in uncertainty quantification of fission reactor neutronics parameters. *Nuclear Engineering and Technology*, 46:281–290, June 2014. https://doi.org/10.5516/NET.01.2014.707.

[109] K. A. Cliffe, M. B. Giles, R. Scheichl, and A. L. Teckentrup. Multilevel Monte Carlo methods and applications to elliptic PDEs with random coefficients. *Computing and Visualization in Science*, 14(1):3, August 2011.

[110] H Comisel, C. Hategan, and R. A. Ionescu. Radioactive States in R-matrix Theory. *Romanian Journal Physics*, 57:138–148, 2012.

[111] J.L. Conlin, W. Ji, J.C. Lee, and W.R. Martin. Pseudo Material Construct for Coupled Neutronic-Thermal-Hydraulic Analysis of VHTGR. *Transactions of the American Nuclear Society*, 92:225–227, 2005.

[112] James W. Cooley and John W. Tukey. An algorithm for the machine calculation of complex Fourier series. *Mathematics of Computation*, 19(90):297–301, 1965.

[113] B.D. Craven. Complex symmetric matrices. *Journal of the Australian Mathematical Society*, 10(3-4):341–354, 1969. https://doi.org/10.1017/S1446788700007588.

[114] Ed Crooks. Nuclear power backers push cheaper, smaller plants. https://www.ft.com/content/b4c5ecf6-28a2-11e9-9222-7024d72222bc, March 2019.

[115] Andrés Cruz and Javier Sesma. Zeros of the Hankel Function of Real Order and of Its Derivative. *Mathematics of Computation*, 39(160):639–645, October 1982.

[116] Andrés Cruz and Javier Sesma. Modulus and Phase of the Reduces Logarithmic Derivative of the Hankel Function. *Mathematics of Computation*, 41(164):597–605, October 1983. DOI: 10.2307/2007696.

[117] Attila Csoto and Gerald Hale. S-matrix and R-matrix determination of the low-energy 5-He and 5-Li resonance parameters. *Physical Review C*, 55(1):536–539, 1997.

[118] Dermott E. Cullen and Charles R. Weisbin. Exact Doppler Broadening of Tabulated Cross Sections. *Nuclear Science and Engineering*, 60(3):199–229, July 1976. Publisher: Taylor & Francis _eprint: https://doi.org/10.13182/NSE76-1.

[119] J.K Cullum and R.A. Willoughby. *Nondefective Complex Symmetric Matrices*. Birkhauser Boston (1985), 978-1-4684-9178-4, 1985. https://doi.org/10.1007/978-1-4684-9178-4_7.

[120] Pierre Descouvemont and D. Baye. The R-matrix theory. *Reports on progress in physics*, 73:036301, 2010. http://dx.doi.org/10.1088/0034-4885/73/3/036301.

[121] Laurent Desvillettes, Carl Graham, and Sylvie Méléard. Probabilistic Interpretation and Numerical Approximation of a Kac Equation without Cutoff. *Stochastic Processes and their Applications*, 84(1):115–135, November 1999.

[122] Boro Döring. Complex zeros of cylinder functions. *Math. Comp.*, 20:215–222, 1966. https://doi.org/10.1090/S0025-5718-1966-0192632-1.

[123] P. Ducru, K. Dibert, C. Josey, B. Forget, V. Sobes, and K. Smith. Optimal temperature grid for accurate doppler kernel reconstruction. *Transactions of the American Nuclear Society*, 115:1148–1151, November 2016.

[124] P. Ducru, C. Josey, K. Dibert, V. Sobes, B. Forget, and K. Smith. Kernel reconstruction methods for doppler broadening. *Journal of Computational Physics*, 335:535–557, 2017. http://dx.doi.org/10.1016/j.jcp.2017.01.039.

[125] Pablo Ducru, Gerald Hale, Mark Paris, Vladimir Sobes, and Benoit Forget. Scattering matrix pole expansions for complex wavenumbers in R-matrix theory. *Physical Review C*, December 2020. accepted [CU10668].

[126] Pablo Ducru, Gerald Hale, Mark Paris, Vladimir Sobes, and Benoit Forget. Scattering matrix pole expansions for complex wavenumbers in R-matrix theory. *Physical Review C*, August 2020. submitted.

[127] Pablo Ducru, Gerald Hale, Mark Paris, Vladimir Sobes, and Benoit Forget. Shadow poles in the alternative parametrization of R-matrix theory. *Physical Review C*, September 2020. accepted [CC10651].

[128] Pablo Ducru, Colin Josey, Vladimir Sobes, Benoit Forget, and Kord Smith. Doppler broadening by linear combination of reference temperature cross sections. *Transactions of American Nuclear Society*, 113, 2015.

[129] Pablo Ducru, Jingang Liang, Vladimir Sobes, Abdulla Alhajri, Isaac Meyer, Benoit Forget, and Kord Smith. Embedded Monte Carlo: Neutron Random Walk and Uncertainty in Nuclear Cross Sections. *International Conference on Mathematics and Computational Methods applied to Nuclear Science and Engineering (M&C 2019), Portland, OR, USA.*, August 25-29 2019.

[130] Pablo Ducru, Vladimir Sobes, Abdulla Alhajri, Isaac Meyer, Benoit Forget, Jingang Liang, and Colin Josey. Windowed multipole representation of R-matrix cross sections. *Physical Review C*, 00(0):000–000, December 2020. accepted [CX10702].

[131] Pablo Ducru, Vladimir Sobes, Benoit Forget, and Kord Smith. On methods for conversion of R-matrix resonance parameters to multi-pole formalism. In *Proceedings of PHYSOR 2016*, pages 2138–2150, 555 North Kensington Avenue La Grange Park, Illinois 60526 U.S.A., May 1-5 2016. American Nuclear Society.

[132] Pablo Ducru, Joshua Tenenbaum, Vladimir Sobes, and Benoit Forget. Embedded Monte Carlo. *Journal of Machine Learning Research*, January 2021. submitted.

[133] Pablo Ducru, Joshua Tenenbaum, Vladimir Sobes, and Benoit Forget. Embedded Variational Inference. *International Conference on Machine Learning (ICML)*, January 2021. submitted.

[134] E. Durand. Solutions numériques des équations algébriques, vol. 1. In *Equations du type F(x) = 0 : Racines d'un Polynome*. Mason Paris, 1960.

[135] S. Dyatlov and M. Zworski. *Mathematical Theory of Scattering Resonances*. MIT, Massachusetts Institute of Technology, 77, Massachusetts ave. MA 02139, U.S.A. http://math.mit.edu/ dyatlov/res/res_final.pdf.

[136] James Dyrda, Ian Hill, Luca Fiorito, Oscar Cabellos, and Nicolas Soppera. A comparison of uncertainty propagation techniques using NDaST: Full, half or zero Monte Carlo? *EPJ Nuclear Sciences & Technologies*, 4:14, 2018.

[137] R. J. Eden and J. R. Taylor. Poles and shadow poles in the many-channel s matrix. *Physical Review*, 133:B1575–B1580, Mar 1964.

[138] C.J. Werner (editor). *MCNP Users Manual - Code Version 6.2*. Los Alamos National Laboratory (LANL), 2017. https://laws.lanl.gov/vhosts/mcnp.lanl.gov/pdf_files/la-ur-17-29981.pdf.

[139] Ioannis Z. Emiris and Victor Y. Pan. Improved algorithms for computing determinants and resultants. *Journal of Complexity*, 21(1):43–71, February 2005.

[140] Tomohiro Endo, Akio Yamamoto, and Tomoaki Watanabe. Bias factor method using random sampling technique. *Journal of Nuclear Science and Technology*, 53(10):1494–1501, October 2016. https://doi.org/10.1080/00223131.2015.1126541.

[141] LLC for the U. S. Department of Los Alamos National Laboratory Energy, Operated by Los Alamos National Security. The history of computing from punched cards to petaflops. https://www.lanl.gov/discover/publications/national-security-science/2013-april/punched-cards-to-petaflops.php. http://permalink.lanl.gov/object/tr?what=info:lanl-repo/lareport/LA-UR-17-24329.

[142] LLC for the U. S. Department of Los Alamos National Laboratory Energy, Operated by Los Alamos National Security. Will our nuclear weapons work? https://www.lanl.gov/discover/publications/national-security-science/2013-april/but-will-it-work.php.

[143] J. Esparza, J. L. López, and J. Sesma. Zeroes of the Whittaker function associated to Coulomb waves. *IMA Journal of Applied Mathematics*, 63:71–87, 1999. https://doi.org/10.1093/imamat/63.1.71.

[144] L. Favella and M. T. Reineri. Properties of the s-matrix as a function of the complex angular momentum for the many-channel case for the dirac equation. *Il Nuovo Cimento*, XXIII(3):616–640, Febbraio 1962.

[145] Ghislain Ferran, Wim Haeck, and Michel Gonin. A New Method for the Doppler Broadening of the Solbrig Kernel Using a Fourier Transform. *Nuclear Science and Engineering*, 179(3):285–301, March 2015. Publisher: Taylor & Francis _eprint: https://doi.org/10.13182/NSE14-64.

[146] Benoit Forget, Sheng Xu, and Kord Smith. Direct doppler broadening in monte carlo simulations using the multipole representation. *Annals of Nuclear Energy*, 64:78–85, 2014.

[147] Jean-Baptiste-Joseph Fourier. *Théorie analytique de la chaleur*. Firmin Didot, Imprimeur du Roi, 1822. https://gallica.bnf.fr/ark:/12148/bpt6k1045508v.

[148] Thomas Freiman. *The multipole method for the on-the-fly computation of the temperature dependency of nuclear cross-sections*. phdthesis, UniversitÃ© Paris-Saclay, January 2020. https://tel.archives-ouvertes.fr/tel-02906474.

[149] F. H. Frohner. Evaluation and analysis of nuclear resonance data. Technical Report 18, IAEA, 2000.

[150] Bruno Gabutti and Luigi Gatteschi. New Asymptotics for the Zeros of Whittaker's Functions. *Numerical Algorithms*, 28:159–170, 2001. https://doi.org/10.1023/A:1014094732209.

[151] S.R. Garcia and M. Punitar. Complex symmetric operators and applications. *Transactions of the American Mathematical Society*, 358(3):1285–1315, 2005. S 0002-9947(05)03742-6.

[152] S.R. Garcia and M. Punitar. Complex symmetric operators and applications ii. *Transactions of the American Mathematical Society*, 356(8):3913–3931, 2007. S 0002-9947(07)04213-4.

[153] Zhigang Ge, Haicheng Wu, Guochang Chen, and Ruirui Xu. CENDL project, the chinese evaluated nuclear data library. *EPJ Web of Conferences*, 146:02002, 2017. doi: 10.1051/epjconf/201714602002.

[154] Nathan A. Gibson. *Novel Resonance Self-Shielding Methods for Nuclear Reactor Analysis*. Ph.D. thesis, Massachusetts Institute of Technology, department of Nuclear Science and Engineering, 2016.

[155] Michael B. Giles. Multilevel Monte Carlo methods. *Acta Numerica*, 24:259–328, May 2015.

[156] Takashi Goda. Computing the variance of a conditional expectation via non-nested Monte Carlo. *Operations Research Letters*, 45(1):63–67, January 2017.

[157] I.C. Gohberg and E.I. Sigal. An operator generalization of the logarithmic residue theorem and the theorem of rouché. *Math. USSR Sbornik*, 13(4):603–625, 1971.

[158] Xavier Gourdon. *Combinatoire, Algorithmique et Géométrie des Polynômes*. Ph.D. thesis, École Polytechnique, 27 Juin 1996.

[159] L. Guillopé. Théorie spectrale de quelques variétés à bouts. *Annales scientifiques de l'École Normale Supérieure, Série 4:*, 22(1):137–160, 1989. https://doi.org/10.24033/asens.1580.

[160] B. Gustavsen. Improving the pole relocating properties of vector fitting. *IEEE Transactions on Power Delivery*, 21(3):1587–1592, 2006. DOI: 10.1109/TPWRD.2005.860281.

[161] B. Gustavsen and A. Semlyen. Rational approximation of frequency domain responses by vector fitting. *IEEE Transactions on Power Delivery*, 14(3):1052–1061, 1999. DOI: 10.1109/61.772353.

[162] B. Habert, C. De Saint Jean, G. Noguere, L. Leal, and Y. Rugama. Retroactive Generation of Covariance Matrix of Nuclear Model Parameters Using Marginalization Techniques. *Nuclear Science and Engineering*, 166(3):276–287, November 2010. https://doi.org/10.13182/NSE09-85.

[163] G. M. Hale, R. E. Brown, and N. Jarmie. Pole structure of the j-pi = 3/2+ resonance in he-5. *Physical Review Letters*, 59(7):763–766, August 1987.

[164] Gerald M. Hale. Covariances from Light-Element R-Matrix Analyses. *Nuclear Data Sheets*, 109:2812–2816, 2008. https://doi.org/10.1016/j.nds.2008.11.015.

[165] Gerald M. Hale, Lowell S. Brown, and Mark W. Paris. Effective field theory as a limit of R-matrix theory for light nuclear reactions. *Physical Review C*, 89(014623), January 2014. https://doi.org/10.1103/PhysRevC.89.014623.

[166] Gerald M. Hale and Mark W. Paris. Data Covariances from R-Matrix Analyses of Light Nuclei. *Nuclear Data Sheets*, 123:165–170, January 2015. https://doi.org/10.1016/j.nds.2014.12.029.

[167] Sterling Harper, Kord Smith, and Benoit Forget. Faster Monte Carlo multiphysics using temperature derivatives. *Proceedings of the PHYSOR conference, Cancun, Mexico, Apr. 22-26*, April 2018.

[168] Sterling (Sterling M.) Harper. *Calculating reaction rate derivatives in Monte Carlo neutron transport*. Thesis, Massachusetts Institute of Technology (MIT), 2016. Accepted: 2017-01-30T18:50:47Z.

[169] Sterling(Sterling M.) Harper. *Tally Derivative Based Surrogate Models for Faster Monte Carlo Multiphysics*. Thesis, Massachusetts Institute of Technology, 2020.

[170] W. K. Hastings. Monte Carlo sampling methods using Markov chains and their applications. *Biometrika*, 57(1):97–109, April 1970. https://doi.org/10.1093/biomet/57.1.97.

[171] Alain Hébert. *Applied Reactor Physics*. Presses Internationales Polytechnique, 2009. ISBN 978-2-553-01436-9.

[172] P Helgesson, D Rochman, A Koning, and al. Uo2 vs mox: propagated nuclear data uncertainty for keff, with burnup. Technical report, Nuclear Research and Consultancy Group NGR and Uppsala University, Sweden, 2013.

[173] P. Helgesson, H. Sjöstrand, A. J. Koning, J. Rydén, D. Rochman, E. Alhassan, and S. Pomp. Combining Total Monte Carlo and Unified Monte Carlo: Bayesian nuclear data uncertainty quantification from auto-generated experimental covariances. *Progress in Nuclear Energy*, 96:76–96, April 2017.

[174] Dave M. Higdon, Mark C. Anderson, Salman Habib, Richard Klein, Mark Berliner, Curt Covey, Omar Ghattas, Carlo Graziani, Mark Seager, Joseph Sefcik, Philip Stark, and James Stewart. Uncertainty quantification and error analysis. Technical Report LA-UR-10-00262; LA-UR-10-262, Los Alamos National Lab. (LANL), Los Alamos, NM (United States), January 2010.

[175] A Hoefer, O. Buss, M. Hennebach, M. Schmid, and D. Porsch. MOCABA: A general Monte Carlo-Bayes procedure for improved predictions of integral functions of nuclear data. *Annals of Nuclear Energy*, 77:514–521, March 2015. https://doi.org/10.1016/j.anucene.2014.11.038.

[176] David E. Hoffman. Supercomputers offer tools for nuclear testing — and solving nuclear mysteries. *Washington Post*, 2011-11-01T07:56-500. https://www.washingtonpost.com/national/national-security/supercomputers-offer-tools-for-nuclear-testing–and-solving-nuclear-mysteries/2011/10/03/gIQAjnngdM_story.html.

[177] J. Eduard Hoogenboom, William R. Martin, and Bojan Petrovic. The Monte Carlo performance benchmark test - AIMS, specifications and first results. In *International Conference on Mathematics and Computational Methods Applied to Nuclear Science and Engineering (MC 2011) Rio de Janeiro, RJ, Brazil, May 8-12, 2011, on CD-ROM, Latin American Section (LAS) / American Nuclear Society (ANS) ISBN 978-85-63688-00-2*. https://inis.iaea.org/collection/NCLCollectionStore/_Public/48/022/48022330.pdf?r=1.

[178] J. Eduard Hoogenboom, William R. Martin, and Bojan Petrovic. *MONTE CARLO PERFORMANCE BENCHMARK FOR DETAILED POWER DENSITY CALCULATION IN A FULL SIZE REACTOR CORE Benchmark Specifications*. 2010. http://citeseerx.ist.psu.edu/viewdoc/download?doi=10.1.1.206.321rep=rep1type=pdf.

[179] J. Eduard Hoogenboom, Bojan Petrovic, and William R. Martin. Present Status and Extensions of the Monte Carlo Performance Benchmark. In *SNA + MC 2013 - Joint International Conference on Supercomputing in Nuclear Applications + Monte Carlo*, page 03602. EDP Sciences, 2014. https://doi.org/10.1051/snamc/201403602.

[180] J Humblet. *Definition of virtual levels of atomic nuclei and establishment of the scattering equation*. PhD thesis, 1 1952.

[181] J. Humblet. Theory of Nuclear Reactions, III. Physical Quantities and Channel Radii. *Nuclear Physics*, 31:544–549, 1962.

[182] J. Humblet. Theory of Nuclear Reactions, IV. Coulomb Interactions in the Channels and Penetration Factors. *Nuclear Physics*, 50:1–16, 1964.

[183] J. Humblet. Theory of Nuclear Reactions, VI. Unitarity, Open and Closed Channels. *Nuclear Physics*, 57:386–401, 1964.

[184] J. Humblet. K-matrix analysis of resonance nuclear reactionss. *Physical Review C*, 42(4):1582–1591, 1990.

[185] J. Humblet and L. Rosenfeld. Theory of Nuclear Reactions, I. Resonant States and Collision Matrix. *Nuclear Physics*, 26:529–578, May 1961.

[186] R. N. Hwang. Recent Advances in Utilization of the R-matrix parameters for reactor applications. *Argonne National Laboratory Report ANL/CP–71459*, 111:1–4, 1991.

[187] R. N. Hwang. An Extension of the Rigorous Pole Representation of Cross Sections for Reactor Applications. *Nucl. Sci. Eng.*, 111(2):113–131, 1992.

[188] R. N. Hwang. Recent developments pertinent to processing of endf/b-6 type resonnance cross section data. *International Conference on the Physics of Nuclear Science and Technology*, 1998.

[189] R. N. Hwang. Generalized pole representation revisited. *Transactions of the American Nuclear Society*, 88(Nuclear Data, Noise Analysis, and System Control: Rafael Perez Legacy – II):491–493, 2003.

[190] Richard N Hwang. A rigorous pole representation of multilevel cross sections and its practical applications. *Nucl. Sci. Eng.*, 96:192–209, 1987.

[191] G. W. Inverarity. Fast Computation of Multidimensional Fourier Integrals. *SIAM Journal on Scientific Computing*, 24(2):645–651, January 2002. Publisher: Society for Industrial and Applied Mathematics.

[192] Carlo Jacoboni and Lino Reggiani. The monte carlo method for the solution of charge transport in semiconductors with applications to covalent materials. *Review of Modern Physics*, 55:645–705, July 1983. https://doi.org/10.1103/RevModPhys.55.645.

[193] C. Jammes and R. N. Hwang. Conversion of single- and multilevel breit-wigner resonance parameters to pole representation parameters. *Nuclear Science and Engineering*, 134:37–49, 2000.

[194] Cyrille De Saint Jean, Gilles Noguere, Benoit Habert, and Bertrand Iooss. A Monte Carlo Approach to Nuclear Model Parameter Uncertainties Propagation. *Nuclear Science and Engineering*, 161(3):363–370, March 2009. https://doi.org/10.13182/NSE161-363.

[195] J. P. Jeukenne. Theory of Nuclear Reactions, V. Penetration Factors for Charged Particles in Low Energy Nuclear Reactions. *Nuclear Physics*, 58:1–8, 1965.

[196] Steven G. Johnson. Faddeeva package - AbInitio - MIT License, December 2013. http://ab-initio.mit.edu/wiki/index.php/Faddeeva_Package.

[197] C Josey, P Ducru, B Forget, and K Smith. Windowed multipole for cross section doppler broadening. *Journal of Computational Physics*, 307:715–727, 2016. https://doi.org/10.1016/j.jcp.2015.08.013.

[198] Colin Josey. *Windowed Multipole : An Efficient Doppler Broadening Technique for Monte Carlo*. Thesis, Massachusetts Institute of Technology, 2015.

[199] Colin Josey, Benoit Forget, and Kord Smith. Windowed multipole sensitivity to target accuracy of the optimization procedure. *Journal of Nuclear Science and Technology*, 52(7-8):987–992, August 2015. https://doi.org/10.1080/00223131.2015.1035353.

[200] P. L. Kapur and R. Peierls. The dispersion formula for nuclear reactions. *Proceedings of the Royal Society*, 166:277–295, May 1938. DOI: 10.1098/rspa.1938.0093.

[201] Joseph B. Keller, S. I. Rubinow, and Max Goldstein. Zeros of Hankel Functions and Poles of Scattering Amplitudes. *Journal of Mathematical Physics*, 4(829):829–832, October 1963. https://doi.org/10.1063/1.1724325.

[202] M. K. Kerimov and S. L. Skorokhodov. Calculation of the complex zeros of Hankel functions and their derivatives. *USSR Computational Mathematics and Mathematical Physics*, 35(6):26–36, 1985. https://doi.org/10.1016/0041-5553(85)90005-9.

[203] B Kiedrowski. Mcnp continuous-energy sensitivity and uncertainty progress and application. *DOE/NNSA Nuclear Criticality Safety Program Technical Review*, 2014.

[204] David Warren Kirsch. *The Silent Arms Race: The Role of the Supercomputer During the Cold War, 1947-1963*. Ph.D. thesis, University of Arkansas, FayetteVille, 2012. https://scholarworks.uark.edu/etd/423.

[205] A. J. Koning. Bayesian Monte Carlo method for nuclear data evaluation. *The European Physical Journal A*, 51(12):184, December 2015.

[206] A. J. Koning. Bayesian Monte Carlo Method for Nuclear Data Evaluation. *Nuclear Data Sheets*, 123:207–213, January 2015.

[207] A. J. Koning and D. Rochman. Modern Nuclear Data Evaluation with the TALYS Code System. *Nuclear Data Sheets*, 113(12):2841–2934, December 2012.

[208] A. J. Koning and D. Rochman. Modern Nuclear Data Evaluation with the TALYS Code System. *Nuclear Data Sheets*, 113(12):2841–2934, December 2012.

[209] A. J. Koning, D. Rochman, J. Ch. Sublet, N. Dzysiuk, M. Fleming, and S. van der Marck. TENDL: Complete Nuclear Data Library for Innovative Nuclear Science and Technology. *Nuclear Data Sheets*, 155:1–55, 2019.

[210] Mark Grigorevich Krein and Adol'f Abramovich Nudel'man. *The Markov moment problem and extremal problems: ideas and problems of PL Cebysev and AA Markov and their further development*. American Mathematical Society, 1977.

[211] Dirk P. Kroese, Tim Brereton, Thomas Taimre, and Zdravko I. Botev. Why the Monte Carlo method is so important today. *WIREs Computational Statistics*, 6(6):386–392, 2014.

[212] S. Kullback and R. A. Leibler. On Information and Sufficiency. *Annals of Mathematical Statistics*, 22(1):79–86, March 1951. Publisher: Institute of Mathematical Statistics.

[213] Matthew Gledhill & David Lague. From the Archives: The end of French nuclear testing in South Pacific. https://www.smh.com.au/world/oceania/from-the-archives-the-end-of-french-nuclear-testing-in-south-pacific-20190127-p50tyj.html, January 2019.

[214] A. M. Lane and R. G. Thomas. R-matrix theory of nuclear reactions. *Reviews of Modern Physics*, 30(2):257–353, 1958.

[215] Pierre-Simon de Laplace. *Essai philosophique sur les probabilités ; par M. le marquis de Laplace, pair de France, grand-officier de la Légion-d'honneur ; l'un des quarante de l'Académie française ; de l'Académie des sciences... Cinquième édition, revue et augmentée par l'auteur*. 1825. VIème principe: inférence. p.18, https://gallica.bnf.fr/ark:/12148/bpt6k96200351/f30.item.texteImage.

[216] Coline Larmier, Andrea Zoia, Fausto Malvagi, Eric Dumonteil, and Alain Mazzolo. Monte Carlo particle transport in random media: The effects of mixing statistics. *Journal of Quantitative Spectroscopy and Radiative Transfer*, 196:270–286, July 2017.

[217] Nancy M. Larson. *Updated User's Guide for SAMMY*. ORNL, October 2008. https://info.ornl.gov/sites/publications/files/Pub13056.pdf.

[218] A. Lejeune and C. Mahaux. Wave functions near resonance and R-matrix expansion. *Nuclear Physics A*, 145:613–656, April 1970. https://doi.org/10.1016/0375-9474(70)90445-8.

[219] Jaakko Leppänen, Maria Pusa, Tuomas Viitanen, Ville Valtavirta, and Toni Kaltiaisenaho. The Serpent Monte Carlo code: Status, development and

applications in 2013. *Annals of Nuclear Energy*, 82:142–150, August 2015. https://doi.org/10.1016/j.anucene.2014.08.024.

[220] Jia-Ming Li, Lan Vo Ky, Yi-Zhi Qu, Pei-Hong Zhang, Hsiao-Ling Zhou, and Paul Faucher. Eigenchannel treatment of R-matrix theory. *Physical Review A*, 55(4):3239–3242, 1997.

[221] Jikui Li, Liangzhi Cao, Tiejun Zu, and Hongchun Wu. Resonance self-shielding treatment and analysis of resonance integral tables for Fully Ceramic Micro-encapsulated fuels with the Embedded Self-Shielding Method. *Annals of Nuclear Energy*, 112:450–463, 2018. https://doi.org/10.1016/j.anucene.2017.10.027.

[222] Jingang Liang, Pablo Ducru, and Benoit Forget. Target Velocity Sampling for Resonance Elastic Scattering using Windowed Multipole Cross Section Data. *Transactions of the American Nuclear Society*, 119:1163–1166, November 11-15 2018. http://dx.doi.org/10.1016/j.jcp.2017.01.039.

[223] Jingang Liang, Xingjie Peng, Shichang Liu, Colin Josey, Benoit Forget, and Kord Smith. Processing of a Comprehensive Windowed Multipole Library via Vector Fitting. *Proceedings of the PHYSOR conference, Cancun, Mexico.*, April 22-26 2018.

[224] Ying Liang, Wazir Muhammad, Gregory R. Hart, Bradley J. Nartowt, Zhe J. Chen, James B. Yu, Kenneth B. Roberts, James S. Duncan, and Jun Deng. A general-purpose Monte Carlo particle transport code based on inverse transform sampling for radiotherapy dose calculation. *Nature: Scientific Reports*, 10(1):9808, June 2020. https://doi.org/10.1038/s41598-020-66844-7.

[225] Shichang Liu, Xingjie Peng, Colin Josey, Jingang Liang, Benoit Forget, Kord Smith, and Kan Wang. Generation of the windowed multipole resonance data using Vector Fitting technique. *Annals of Nuclear Energy*, 112:30–41, February 2018.

[226] George K. Loudos. Monte Carlo simulations in Nuclear Medicine. *AIP Conference Proceedings*, 958(1):147–150, November 2007. https://doi.org/10.1063/1.2825768.

[227] Ivan Lux and Laszlo Koblinger. Monte Carlo Particle Transport Methods: Neutron and Photon Calculations. *ECDC Press*, ISBN 0-8493-6074-9, 1990. https://gnssn.iaea.org/NSNI/Shared%20Documents/OPEN%20Shared%20Files/MonteCarloPar

[228] R. E. MacFarlane and A. C. Kahler. Methods for Processing ENDF/B-VII with NJOY. *Nuclear Data Sheets*, 111(12):2739–2890, December 2010.

[229] Donald Mackenzie. The Influence of the Los Alamos and Livermore National Laboratories on the Development of Supercomputing. *IEEE Annals of the History of Computing*, 13(02):179–201, April 1991.

[230] C. Mahaux. Theory of Nuclear Reactions, IX. Few Levels Approximations. *Nuclear Physics*, 68:481–503, 1965.

[231] C. Mahaux. Theory of Nuclear Reactions, IX. Few Levels Approximations. *Nuclear Physics*, 71:241–266, 1965.

[232] G. Malajovich and J. P. Zubelli. A fast and stable algorithm for splitting polynomials. *Computers & Mathematics with Applications*, 33(3):1–23, February 1997.

[233] Vanessa Griffen and Talei Luscia Mangioni. 'Will to fight together': Fiji's has taken another bold step in the battle against nuclear weapons | Vanessa Griffen and Talei Luscia Mangioni. http://www.theguardian.com/world/commentisfree/2020/jul/08/will-to-fight-together-fijis-latest-bold-step-in-battle-against-nuclear-weapons, July 2020.

[234] A. Markoff. Démonstration de certaines inégalités de M. Tchébychef. *Mathematische Annalen*, 24(2):172–180, June 1884.

[235] William R Martin, Scott Wilderman, Forrest B Brown, and Gokhan Yesilyurt. Implementation of on-the-fly doppler broadening in mcnp. In *International Conference on Mathematics and Computational Methods Applied to Nuclear Science and Engineering, Sun Valley, Idaho*, 2013.

[236] F. A. McDonald and J. Nuttall. Complex-Energy Method for Elastic e-H Scattering above the Ionization Threshold. *Physical Review Letters*, 23(3):361–363, 1969.

[237] C. F. McMillain, T. F. Adams, M. G. McCoy, R. B. Christensen, B. S. Pudliner, M. R. Zika, P. S. Brantley, J. S. Vetter, and J. M. May. Computational Challenges in Nuclear Weapons Simulation. Technical Report UCRL-JC-155202, Lawrence Livermore National Lab. (LLNL), Livermore, CA (United States), August 2003.

[238] J. M. McNamee and Victor Y. Pan. Efficient polynomial root-refiners: A survey and new record efficiency estimates. *Computers & Mathematics with Applications*, 63(1):239–254, January 2012.

[239] Nicholas Metropolis. The Beginning of the Monte Carlo Method. *Los Alamos Science*, 15, 1987. https://la-science.lanl.gov/lascience15.shtml.

[240] Nicholas Metropolis, Arianna W. Rosenbluth, Marshall N. Rosenbluth, Augusta H. Teller, and Edward Teller. Equation of State Calculations by Fast Computing Machines. *The Journal of Chemical Physics*, 21(6):1087–1092, June 1953. https://doi.org/10.1063/1.1699114.

[241] Nicholas Metropolis and Stanislaw Ulam. The Monte Carlo Method. *Journal of the American Statistical Association*, 44(247):335–341, 1949. Publisher: [American Statistical Association, Taylor & Francis, Ltd.].

[242] N. Michel. Precise coulomb wave functions for a wide range of complex ℓ, η and z. *Computer Physics Communications*, 176:232–249, November 2006. doi:10.1016/j.cpc.2006.10.004.

[243] N. Michel, W. Nazarewicz, J Okolowicz, and M. Ploszajczak. Radioactive states in R-matrix theory. *Journal of Physics G: Nuclear and Particle Physics*, 37(6):064042, 2010.

[244] G. Mittag-Leffler. Sur la représentation analytique des fonctions monogènes uniformes d'une variable indépendante. *Acta Mathematica*, t.4:1–79, 1884.

[245] D. Morgan and M. R. Pennington. Pole structure in nuclear and particle physics. *Physical Review Letters*, 59(24):2818, December 1987.

[246] Yuji Nakatsukasa, Olivier SÃšte, and Lloyd N. Trefethen. The AAA Algorithm for Rational Approximation. *SIAM Journal on Scientific Computing*, 40(3):A1494–A1522, January 2018. Publisher: Society for Industrial and Applied Mathematics.

[247] John W. Norbury, Tony C. Slaba, Sukesh Aghara, Francis F. Badavi, Steve R. Blattnig, Martha S. Clowdsley, Lawrence H. Heilbronn, Kerry Lee, Khin M. Maung, Christopher J. Mertens, Jack Miller, Ryan B. Norman, Chris A. Sandridge, Robert Singleterry, Nikolai Sobolevsky, Jan L. Spangler, Lawrence W. Townsend, Charles M. Werneth, Kathryn Whitman, John W. Wilson, Sharon Xiaojing Xu, and Cary Zeitlin. Advances in space radiation physics and transport at NASA. *Life Sciences in Space Research*, 22:98–124, August 2019. https://doi.org/10.1016/j.lssr.2019.07.003.

[248] K. Nordlund. Historical review of computer simulation of radiation effects in materials. *Journal of Nuclear Materials*, 520:273–295, July 2019.

[249] J Okolowicz and M. Ploszajczak. Exceptional points in the scattering continuum. *Physical Review C*, 80(034619), 2009.

[250] F. W. J. Olver, A. B. Olde Daalhuis, D. W. Lozier, B. I. Schneider, R. F. Boisvert, C. W. Clark, B. R. Miller, B. V. Saunders, and eds. *NIST Digital Library of Mathematical Functions*. National Institute of Standards and Technology, U.S. Department of Commerce, 2020. https://dlmf.nist.gov.

[251] H. K. Owusu, K. Wagh, and E. A. Yuzbashyan. The link between integrability, level crossings and exact solution in quantum models. *Journal of Physics A: Mathematical and Theoretical*, 42(035206), December 2009. doi: 10.1088/1751-8113/42/3/035206.

[252] V. Y. Pan. Optimal and nearly optimal algorithms for approximating polynomial zeros. *Computers & Mathematics with Applications*, 31(12):97–138, June 1996.

[253] Victor Y. Pan. Solving a Polynomial Equation: Some History and Recent Progress. *SIAM Review*, 39(2):187–220, January 1997. Publisher: Society for Industrial and Applied Mathematics.

[254] Victor Y Pan. Approximating Complex Polynomial Zeros: Modified Weyl's Quadtree Construction and Improved Newton's Iteration. *Journal of Complexity*, 16(1):213–264, March 2000. https://doi.org/10.1006/jcom.1999.0532.

[255] Victor Y. Pan and Elias Tsigaridas. Accelerated approximation of the complex roots and factors of a univariate polynomial. *Theoretical Computer Science*, 681:138–145, June 2017.

[256] Victor Y. Pan and Ai-Long Zheng. New progress in real and complex polynomial root-finding. *Computers & Mathematics with Applications*, 61(5):1305–1334, March 2011.

[257] Tara M. Pandya, Seth R. Johnson, Thomas M. Evans, Gregory G. Davidson, Steven P. Hamilton, and Andrew T. Godfrey. Implementation, capabilities, and benchmarking of Shift, a massively parallel Monte Carlo radiation transport code. *Journal of Computational Physics*, 308:239–272, March 2016. https://doi.org/10.1016/j.jcp.2015.12.037.

[258] Mark Paris and James Richard de Boer. The 2016 R-Matrix Workshop on Methods and Applications, Santa Fe, New Mexico, U.S.A. https://indico.fnal.gov/event/10228/.

[259] Ho Jin Park, Hyung Jin Shim, and Chang Hyo Kim. Uncertainty Propagation in Monte Carlo Depletion Analysis. *Nuclear Science and Engineering*, 167(3):196–208, March 2011.

[260] Sung Y. Park and Anil K. Bera. Maximum entropy autoregressive conditional heteroskedasticity model. *Journal of Econometrics*, 150(2):219–230, June 2009.

[261] Sitao Peng, Allan B. Shaohong Zhang, and Xiaofeng Jiang. Investigations on the point-wise neutron cross-section temperature interpolation methods. *Annals of Nuclear Energy*, 45:155–160, 2012.

[262] XingJie Peng, Pablo Ducru, ShiChang Liu, Benoit Forget, and Jingang Liang. Converting point-wise nuclear cross sections to pole representation using regularized vector fitting. *Computer Physics Communications*, 224:52–62, 2018. https://doi.org/10.1016/j.cpc.2017.12.004.

[263] Xingjie Peng, Jingang Liang, Abdulla Alhajri, Benoit Forget, and Kord Smith. Development of continuous-energy sensitivity analysis capability

in OpenMC. *Annals of Nuclear Energy*, 110:362–383, December 2017. https://doi.org/10.1016/j.anucene.2017.06.061.

[264] Jean-Philippe M. Peraud, Colin D. Landon, and Nicolas G. Hadjiconstantinou. Monte carlo methods for solving the boltzmann transport equation. *ANNUAL REVIEW OF HEAT TRANSFER*, 17, 2014. https://doi.org/10.1615/AnnualRevHeatTransfer.2014007381.

[265] Christopher Michael Perfetti. *Advanced Monte Carlo Methods for Eigenvalue Sensitivity Coefficient Calculation*. PhD Thesis, University of Michigan, 2012.

[266] Miodrag Petkovic. *Iterative Methods for Simultaneous Inclusion of Polynomial Zeros*, volume 1387. Springer-Verlag Berlin Heidelberg, 1 edition, 1989.

[267] A. J. M. Plompen, O. Cabellos, C. De Saint Jean, M. Fleming, A. Algora, M. Angelone, P. Archier, E. Bauge, O. Bersillon, A. Blokhin, F. Cantargi, A. Chebboubi, C. Diez, H. Duarte, E. Dupont, J. Dyrda, B. Erasmus, L. Fiorito, U. Fischer, D. Flammini, D. Foligno, M. R. Gilbert, J. R. Granada, W. Haeck, F.-J. Hambsch, P. Helgesson, S. Hilaire, I. Hill, M. Hursin, R. Ichou, R. Jacqmin, B. Jansky, C. Jouanne, M. A. Kellett, D. H. Kim, H. I. Kim, I. Kodeli, A. J. Koning, A. Yu. Konobeyev, S. Kopecky, B. Kos, A. Krása, L. C. Leal, N. Leclaire, P. Leconte, Y. O. Lee, H. Leeb, O. Litaize, M. Majerle, J. I. Márquez Damián, F. Michel-Sendis, R. W. Mills, B. Morillon, G. Noguère, M. Pecchia, S. Pelloni, P. Pereslavtsev, R. J. Perry, D. Rochman, A. Röhrmoser, P. Romain, P. Romojaro, D. Roubtsov, P. Sauvan, P. Schillebeeckx, K. H. Schmidt, O. Serot, S. Simakov, I. Sirakov, H. Sjöstrand, A. Stankovskiy, J. C. Sublet, P. Tamagno, A. Trkov, S. van der Marck, F. Álvarez-Velarde, R. Villari, T. C. Ware, K. Yokoyama, and G. Žerovnik. The joint evaluated fission and fusion nuclear data library, JEFF-3.3. *The European Physical Journal A*, 56(7):181, July 2020.

[268] Martin Plummer, Jimena D. Gorfinkiel, and Jonathan Tennyson. *Mathematical and computational methods in R-matrix theory*. 2007. http://www.ccp2.ac.uk/R-matrix_booklet_2007.pdf.

[269] Boris Polyak. New stochastic approximation type procedures. *Avtomatica i Telemekhanika*, 7:98–107, 01 1990.

[270] G. P. M. Poppe and C. M. J. Wijers. More efficient computation of the complex error function. *ACM Transactions on Mathematical Software*, 16(1):38–46, March 1990. https://doi.org/10.1145/77626.77629.

[271] John L. Powell. Recurrence formulas for coulomb wave functions. *Phys. Rev.*, 72:626–627, Oct 1947.

[272] Edwin Privas, Cyrille De Saint Jean, and Gilles Noguere. On the use of the BMC to resolve Bayesian inference with nuisance parameters. *EPJ Nuclear Sciences & Technologies*, 4:36, 2018.

[273] Lisa Quigley and Keith Berrington. The qb method: analysing resonances using R-matrix theory. applications to c+, he and li. *Journal of Physics B: Atomic, Molecular, and Optical Physics*, 29:4529–4542, 1996.

[274] Tom Rainforth, Rob Cornish, Hongseok Yang, Andrew Warrington, and Frank Wood. On Nesting Monte Carlo Estimators. In *International Conference on Machine Learning*, pages 4267–4276, 2018.

[275] S. A. Rakityansky and N. Elander. Analyzing the contribution of individual resonance poles of the s-matrix to the two-channel scattering. *International Journal of Quantum Chemistry*, 106, November 2005. https://doi.org/10.1002/qua.20859.

[276] C. W. Reich and M. S. Moore. Multilevel formula for the fission process. *Phys. Rev.*, 111:929–933, Aug 1958.

[277] Human Survivability Research and Development Integrated Program Team. Monte-carlo modeling of the prompt radiation emitted by a nuclear device in the national capital region, revision 1. Technical Report DTRA-TR-13-045 (R1), Defense Threat Reduction Agency, 8725 John J. Kingman Road, MS 6201 Fort Belvoir, VA 22060-6201, USA, 2016. https://apps.dtic.mil/dtic/tr/fulltext/u2/1014428.pdf.

[278] Paul Reuss. A Generalization of the Livolant-Jeanpierre Theory for Resonance Absorption Calculation. *Nuclear Science and Engineering*, 92(2):261–266, 1986. https://doi.org/10.13182/NSE86-A18174.

[279] Paul Reuss. *Précis de Neutronique*. EDP Sciences, 2003. ISBN 2-86883-637-2.

[280] Herbert Robbins and Sutton Monro. A Stochastic Approximation Method. *Annals of Mathematical Statistics*, 22(3):400–407, September 1951. Publisher: Institute of Mathematical Statistics.

[281] D. Rochman, E. Bauge, A. Vasiliev, H. Ferroukhi, S. Pelloni, A. J. Koning, and J. Ch. Sublet. Monte Carlo nuclear data adjustment via integral information. *The European Physical Journal Plus*, 133(12):537, December 2018.

[282] D. Rochman, A. J. Koning, and J. Ch. Sublet. A Statistical Analysis of Evaluated Neutron Resonances with TARES for JEFF-3.3, JENDL-4.0, ENDF/B-VIII.0 and TENDL-2019. *Nuclear Data Sheets*, 163:163–190, January 2020.

[283] D Rochman, A.J Koning, and al. Nuclear data uncertainty propagation: Perturbation vs. monte carlo. *Annals of Nuclear Energy*, 38:942–952, 2011.

[284] D Rochman and S van der Marck. Nuclear data uncertainties for local power densities in the martin-hoogenboom benchmark. In *Joint International Conference of Supercomputing in Nuclear Applications and Monte Carlo, Paris, France, 2013*, 2013. https://doi.org/10.1051/snamc/201402410.

[285] D Rochman, W Zwermann, A Koning, and al. Nuclear data uncertainty propagation: Perturbation vs. monte carlo. *Nuclear Science and Engineering*, 177:337–349, 2014.

[286] Mathew D. Rogers. Partial fraction expansions fo identities for products of Bessel functions. *Journal of Mathematical Physics*, 46:043509, March 2005. https://doi.org/10.1063/1.1866222.

[287] Paul K. Romano, Nicholas E. Horelik, Bryan R. Herman, Adam G. Nelson, Benoit Forget, and Kord Smith. OpenMC: A state-of-the-art Monte Carlo code for research and development. *Annals of Nuclear Energy*, 82:90 – 97, 2015. Joint International Conference on Supercomputing in Nuclear Applications and Monte Carlo 2013, SNA + MC 2013. Pluri- and Trans-disciplinarity, Towards New Modeling and Numerical Simulation Paradigms.

[288] Paul K. Romano and Jonathan A. Walsh. An improved target velocity sampling algorithm for free gas elastic scattering. *Annals of Nuclear Energy*, 114:318–324, April 2018.

[289] L. Rosenfeld. Theory of Nuclear Reactions, II. The Foundation of the Optical Model. *Nuclear Physics*, 26:594–607, May 1961.

[290] L. Rosenfeld. Theory of Nuclear Reactions, VIII. Time Evolution of the Scattering Process. *Nuclear Physics*, 70:1–27, 1965.

[291] Schönhage, Arnold. The Fundamental Theorem of Algebra in Terms of Computational Complexity. Technical report, Mathematisches Institut der Universität Tübingen, 1982. http://citeseerx.ist.psu.edu/viewdoc/download?doi=10.1.1.123.3313&rep=rep1&type=pdf.

[292] N. H. Scott. A new canonical form for complex symmetric matrices. *Proceedings of the Royal Society of London. Series A: Mathematical and Physical Sciences*, 441(1913):625–640, june 1993. https://royalsocietypublishing.org/doi/10.1098/rspa.1993.0083.

[293] Keiichi Shibata, Osamu Iwamoto, Tsuneo Nakagawa, Nobuyuki Iwamoto, Akira Ichihara, Satoshi Kunieda, Satoshi Chiba, Kazuyoshi Furutaka, Naohiko Otuka, Takaaki Ohsawa, Toru Murata, Hiroyuki Matsunobu, Atsushi Zukeran, So Kamada, and Jun-ichi Katakura. JENDL-4.0: A New Library for Nuclear Science and Engineering. *Journal of Nuclear Science and Technology*, 48(1):1–30, January 2011. Publisher: Taylor & Francis _eprint: https://doi.org/10.1080/18811248.2011.9711675.

[294] B. R. L. Siebert. Sensitivity Analysis and Uncertainty Assessment in Applied Monte Carlo Particle Transport. In Andreas Kling, Fernando J. C. Barão, Masayuki Nakagawa, Luis Távora, and Pedro Vaz, editors, *Advanced Monte Carlo for Radiation Physics, Particle Transport Simulation and Applications*, pages 719–724, Berlin, Heidelberg, 2001. Springer.

[295] D. Siefman, M. Hursin, D. Rochman, S. Pelloni, and A. Pautz. Stochastic vs. sensitivity-based integral parameter and nuclear data adjustments. *The European Physical Journal Plus*, 133(10):429, October 2018.

[296] A. J. F. Siegert. On the derivation of the dispersion formula for nuclear reactions. *Physical Review*, 56:750–752, Oct 1939.

[297] Lisa C. Simonsen, Tony C. Slaba, Peter Guida, and Adam Rusek. NASA's first ground-based Galactic Cosmic Ray Simulator: Enabling a new era in space radiobiology research. *PLOS Biology*, 18(5):e3000669, May 2020.

[298] Vladimir Sobes, Pablo Ducru, Abdulla Alhajri, Barry Ganapol, and Benoit Forget. An Analytic Benchmark for Neutron Boltzmann Transport with Downscattering. Part I. Flux & eigenvalue solutions. *Nuclear Science and Engineering*, January 2021. accepted.

[299] Vladimir Sobes, Pablo Ducru, Abdulla Alhajri, Barry D. Ganapol, and Benoit Forget. An Analytic Benchmark for Neutron Boltzmann Transport with Downscattering. Part I. Flux & eigenvalue solutions. *Nuclear Science and Engineering*, January 2021. accepted.

[300] AW Solbrig Jr. Doppler effect in neutron absorption resonances. *American Journal of Physics*, 29:257, 1961.

[301] Andrea D. Steffen. Bill Gates Debuts Mini-Reactor + Energy Storage To Balance Renewables, September 2020.

[302] Thomas Jan Stieltjes. Sur l'évaluation approchée des intégrales. *CR Math. Acad. Sci. Paris, Sér. I*, 97:740–742, 1883.

[303] J. Struckmeier. *Numerical Simulation of the Boltzmann Equation by Particle Methods*. Birkhauser, Boston, MA, 2000. https://doi.org/10.1007/978-1-4612-0513-$5_1$0.

[304] Angus E. Taylor. Mittag-Leffler expansions and spectral theory. *Pacific Journal of Mathematics*, 10(3):1049–1066, 1960. https://projecteuclid.org/euclid.pjm/1103038251.

[305] T. Teichmann and E. P. Wigner. Sum rules in the dispersion theory of nuclear reactions. *Physical Review*, 87(1):123–135, July 1952. DOI: https://doi.org/10.1103/PhysRev.87.123.

[306] Theodor Teichmann. *Some general properties of nuclear reactions cross-sections and level widths*. Phd thesis, Princeton University, Department of Physics, June 1949.

[307] Jonathan Tennyson and Lesley A. Morgan. Electron collisions with polyatomic molecules using the R-matrix method. *Philosophical Transactions of the Royal Society A*, 357:1161–1173, 1999. DOI: 10.1098/rsta.1999.0369.

[308] I. J. Thompson. Coulomb and bessel functions of complex arguments and order. *Journal of Computational Physics*, 64:490–509, 1986.

[309] Ian J. Thompson, R. J. deBoer, P. Dimitriou, S. Kunieda, M. T. Pigni, G. Arbanas, H. Leeb, Th. Srdinko, G. Hale, P. Tamagno, and P. Archier. Verification of R-matrix calculations for charged-particle reactions in the resolved resonance region for the 7Be system. *The European Physical Journal A*, 55(6):92, June 2019.

[310] Shimansky G A Lebedeva E E Lichadeev V V Ryazanov D K Tikhonchev, M Yu and A I Tellin. The role of computer simulation in nuclear technologies development, Jul 2001. https://inis.iaea.org/collection/NCLCollectionStore/_Public/33/011/33011231.pdf.

[311] N. Touran and J. Yang. Sensitivities and uncertainties due to nuclear data in a traveling wave reactor. In *Proceedings of the PHYSOR 2016 Meeting in Sun Valley, ID*, pages 2138–2150, 555 North Kensington Avenue La Grange Park, Illinois 60526 U.S.A., May 1-5 2016. American Nuclear Society.

[312] Nicholas W. Touran, John Gilleland, Graham T. Malmgren, Charles Whitmer, and William H. Gates. Computational Tools for the Integrated Design of Advanced Nuclear Reactors. *Engineering*, 3(4):518–526, August 2017. https://doi.org/10.1016/J.ENG.2017.04.016.

[313] T. H. Trumbull. Treatment of Nuclear Data for Transport Problems Containing Detailed Temperature Distributions. *Nuclear Technology*, 156(1):75–86, October 2006. https://doi.org/10.13182/NT156-75.

[314] T.H. Trumbull. Treatment of nuclear data for transport problems containing detailed temperature distributions. *Nuclear Technology*, 156:75–86, 2006.

[315] C. Vaglio-Gaudard, A. Santamarina, D. Bernard, G. Noguère, J. M. Ruggieri, J. F. Vidal, and A. Lyoussi. New 56Fe Covariances for the JEFF3 File from the Feedback of Integral Benchmark Analysis. *Nuclear Science and Engineering*, 166(3):267–275, November 2010. https://doi.org/10.13182/NSE09-103.

[316] Tuomas Viitanen and Jaakko Leppänen. Explicit Treatment of Thermal Motion in Continuous-Energy Monte Carlo Tracking Routines. *Nuclear Science and Engineering*, 171(2):165–173, June 2012. Publisher: Taylor & Francis _eprint: https://doi.org/10.13182/NSE11-36.

[317] Tuomas Viitanen and Jaakko Leppänen. Target Motion Sampling Temperature Treatment Technique with Elevated Basis Cross-Section Temperatures. *Nuclear Science and Engineering*, 177(1):77–89, May 2014. Publisher: Taylor & Francis _eprint: https://doi.org/10.13182/NSE13-37.

[318] George H. Vineyard. Scattering of Slow Neutrons by a Liquid. *Physical Review*, 110(5):999–1010, June 1958. Publisher: American Physical Society.

[319] Heinrich Voss. chapter 115, pages 1–24. Nonlinear Eigenvalue Problems. Chapman and Hall/CRC, New York, 2014. https://www.mat.tuhh.de/forschung/rep/rep164.pdf.

[320] Wolfgang Wagner. A convergence proof for bird's direct simulation monte carlo method for the boltzmann equation. *Journal of Statistical Physics*, 66(3-4):1011–1044, February 1992. https://doi.org/10.1007/BF01055714.

[321] J. a. C. Weideman. Computation of the Complex Error Function. *SIAM Journal on Numerical Analysis*, 31(5):1497–1518, October 1994. Publisher: Society for Industrial and Applied Mathematics. https://epubs.siam.org/doi/abs/10.1137/0731077.

[322] E. P. Wigner. On the behavior of cross sections near thresholds. *Physical Review*, 73(9):1002–1009, May 1948.

[323] E. P. Wigner and L. Eisenbud. Higher angular momenta and long range interaction in resonance reactions. *Physical Review*, 72(1):29–41, July 1947. DOI: https://doi.org/10.1103/PhysRev.72.29.

[324] James H. Wilkinson. The evaluation of the zeros of ill-conditioned polynomials. *Numerische Mathematik*, 1:150–166, 1959.

[325] Mark L. Williams. Resonance Self-Shielding Methodologies in SCALE 6. *Nuclear Technology*, 174(2):149–168, 2011.

[326] Gokhan Yesilyurt, William R. Martin, and Forrest B. Brown. On-the-Fly Doppler Broadening for Monte Carlo Codes. *Nuclear Science and Engineering*, 171(3):239–257, July 2012. Publisher: Taylor & Francis _eprint: https://doi.org/10.13182/NSE11-67.

[327] Mofreh R. Zaghloul. Algorithm 985: Simple, Efficient, and Relatively Accurate Approximation for the Evaluation of the Faddeyeva Function. *ACM Transactions on Mathematical Software*, 44(2):22:1–22:9.5, 2017. https://doi.org/10.1145/3119904.

[328] Mofreh R. Zaghloul and Ahmed N. Ali. Algorithm 916: Computing the Faddeyeva and Voigt Functions. *ACM Transactions on Mathematical Software*, 38(2):15:1–15:22, January 2012. https://doi.org/10.1145/2049673.2049679.

[329] Kaiyue Zeng, Jason Hou, Kostadin Ivanov, and Matthew Anderson Jessee. Uncertainty Quantification and Propagation of Multiphysics Simulation of the Pressurized Water Reactor Core. *Nuclear Technology*, 205(12):1618–1637, December 2019.

[330] W. Zwermann and al. Aleatoric and epistemic uncertainties in sampling based nuclear data uncertainty and sensitivity analyses. In *Proceedings of PHYSOR 2012*, April 2012.

Appendix A

Appendix of Embedded Monte Carlo: Proofs and explicit solutions

Here are *verbatim* transcribed the appendices from our article [132].

A.1 The polynomial log-likelihood class

This article establishes new methods to infer and propagate uncertainty across intractable stochastic processes when the log-likelihoods – either of the noisy data D (for inference EVI) or of the stochastic process ensemble average Z(X) (for forward propagation EFP) – are polynomial.

To understand the scope of this article, we thus study the polynomial log-likelihood class. Our key result is theorem 4, which establishes that a distribution whose log-likelihood is a polynomial of degree d can be fully reconstructed with the knowledge of its first $2d-1$ moments.

Theorem 4. *Polynomial Log-likelihood class.*
The polynomial log-likelihood class can be fully reconstructed with the knowledge of the raw moments. If X is a random variable with a (real) polynomial log-likelihood of degree d, i.e. $\exists \{a_k\} \in \mathbb{R}^{d+1}$ such that

$$\ell(X) \triangleq \ln p(X) = -Q(X) = -\sum_{k=0}^{d} a_k X^k \tag{A.1}$$

then

- *the degree d is even: i.e. $d \equiv 0 \pmod 2$*
- *the dominant coefficient a_d is positive: $a_d > 0$*

so that there exists $\{\alpha_k, \beta_k\} \in \{\mathbb{R} \times \mathbb{R}\}^d$ *such that*

$$Q(X) = a_d \prod_{k=1}^{d/2} \left[(X - \alpha_k)^2 + \beta_k \right] \tag{A.2}$$

Moreover, the first $2d-1$ *raw moments* $m_n \triangleq \mathbb{E}\left[X^n\right]$ *suffice to fully characterize the distribution of* X*: coefficients* $\{a_k\}_{k=1}^d$ *can be found by solving linear system*

$$\forall n \in [\![0, d]\!] \,, \quad (n+1) \cdot m_n = \sum_{k=1}^{d} k \cdot a_k \cdot m_{n+k} \tag{A.3}$$

after which the constant a_0 *is determined as*

$$a_0 = \ln \int_{\mathbb{R}} \exp\left(- \sum_{k=1}^{d} a_k x^k \right) \mathrm{d}x \tag{A.4}$$

Proof. The zero-th moment of a probability density is unity

$$m_0 \triangleq \int_{\mathbb{R}} \mathrm{e}^{-Q(x)} \mathrm{d}x = 1 \tag{A.5}$$

For this normalization (A.5) to hold, we must have $Q(X) \underset{X \to \pm\infty}{\longrightarrow} +\infty$, which entails that both the degree d is even – i.e. $d \equiv 0 \pmod 2$ – and that the dominant coefficient a_d is positive: $a_d > 0$. Moreover, applying the fundamental theorem of algebra to $Q(X)$, and factoring the even number of roots – which are either real or complex conjugate – yields expression (A.2).

We then proceed to an integration per parts:

$$\int_{\mathbb{R}} x^n \mathrm{e}^{-Q(x)} \mathrm{d}x = \int_{\mathbb{R}} \frac{x^{n+1}}{n+1} Q'(x) \mathrm{e}^{-Q(x)} \mathrm{d}x$$

where $Q'(X) = \sum_{k=1}^{d} k \cdot a_d \cdot X^{k-1}$, which establishes system (A.3). This is a linear system of size d with d unknowns, inverting it therefore yields the coefficients $\{a_k\}_{k=1}^d$.

To find the constant coefficient a_0, we separate a_0 in $Q(X)$ and take e^{-a_0} out of the integral in the right-hand-side of normalization (A.5). Since we now have all the $\{a_k\}_{k=1}^d$, this readily yields the result (A.4). □

Note that polynomials can suffer from numerical instabilities when represented through their coefficients $\{a_k\}$ as in (A.1), rather than their roots or some factorization (A.2).

This polynomial log-likelihood class is somewhat restrictive: it must have infinite support (all of $\mathbb{R}$ rather than restricted to an interval) and few standard distributions belong to it (not even the log-normal distribution, for instance). Yet these exponential of polynomials densities are rapidly falling functions, thus defining a class of tempered distributions in Schwartz space. As such, they are intrinsically local distributions, and cannot capture heavy-tail phenomena. Excluding this, the polynomial log-likelihood

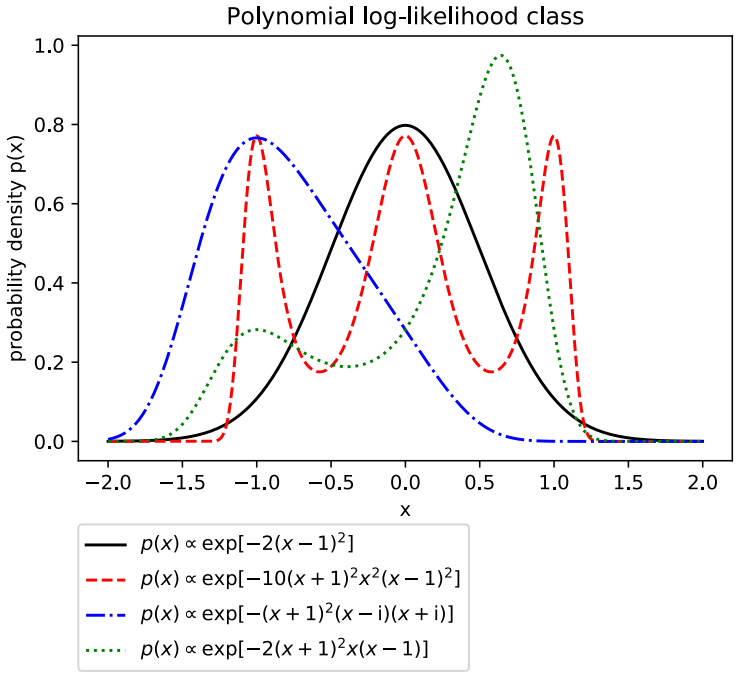

Figure A-1: Polynomial log-likelihood class. Examples of distributions with a polynomial log-likelihood. The distributions can have varied, local shapes, and are evanescent beyond the first and last root (cannot be fat-tailed).

class is quite versatile, generalizing the Gaussian distribution (which belongs to it) through factorization (A.2). Figure A-1 illustrates how polynomial log-likelihood distributions can have a variety of maxima and shapes, all exponentially evanescent past the first and last root.

For instance, for the simple Gaussian $\mathcal{N}(\mu, \sigma)$ case: $m_0 = 1$; $m_1 = \mu$; $m_2 = \mu^2 + \sigma^2$; and $m_3 = \mu^3 + 3\mu\sigma^2$. Upon inversion of system (A.3), this readily yields: $a_1 = -\frac{\mu}{\sigma^2}$, and $a_2 = \frac{1}{2\sigma^2}$. Using the Gauss integral $\int_{\mathbb{R}} \mathrm{e}^{-t^2} \mathrm{d}t = \sqrt{\pi}$ to express (A.4) then begets: $a_0 = \frac{1}{2}\left(\frac{\mu}{\sigma}\right)^2 + \ln\left(\sqrt{2\pi\sigma^2}\right)$, which indeed are the correct coefficients.

A.2 Proof of theorem 2

We here derive the proof of theorem 2, which establishes the mean versus variance convergence trade-off.

Proof. We assume verified the conditions of uniform convergence necessary to apply the Markov theorem (strong law of large numbers for the case of independent non-identically distributed random variables), so that the average of ensemble average estimators converges almost surely to as the average of their expectation values $Z(X) \triangleq \mathbb{E}_Y[Y|X]$ (unbiased estimators), that is $\widehat{\langle Z \rangle} \triangleq \frac{1}{M}\sum_{m=1}^{M} \widehat{Z}(X_m) \xrightarrow[M\to\infty]{\text{a.s.}} \frac{1}{M}\sum_{m=1}^{M} Z(X_m)$,

and the rate of this convergence (in law) is given by the central limit theorem for independent, non-identically distributed random variables (assuming hypotheses for the Lindeberg form):

$$\widehat{\langle Z \rangle} \underset{M\to\infty}{\overset{\mathbb{L}\text{aw}}{\longrightarrow}} \frac{1}{M}\sum_{m=1}^{M} Z(X_m) + \mathcal{N}\left(0, \frac{1}{M}\sum_{m=1}^{M} \frac{\mathbb{V}\text{ar}_Y\left[\widehat{Z}(X_m)\right]}{M}\right)$$

where the variance of the ensemble average estimator is the well-known $\mathbb{V}\text{ar}_Y\left[\widehat{Z}(X_m)\right] = \frac{\Sigma_Y(X_m)}{N}$. Applying the same reasoning again to $\frac{1}{M}\sum_{m=1}^{M} Z(X_m) \underset{M\to\infty}{\overset{\text{a.s.}}{\longrightarrow}} \langle Z \rangle$, this time with independent identically distributed random variables $Z(X_m)$, entails

$$\frac{1}{M}\sum_{m=1}^{M} Z(X_m) \underset{M\to\infty}{\overset{\mathbb{L}\text{aw}}{\longrightarrow}} \langle Z \rangle + \mathcal{N}\left(0, \frac{\langle \Delta^2 Z \rangle}{M}\right)$$

The law of large numbers entails $\sum_{m=1}^{M} \frac{\Sigma_Y(X_m)}{MN} \underset{M\to\infty}{\overset{\text{a.s.}}{\longrightarrow}} \frac{\langle \Sigma_Y \rangle}{N}$, so that the additivity of variances and Slutsky's theorem yield asymptotic convergence rate (3.15), which can be seen as a form of the law of total expectation and the law of total variance.

We are now given a fixed budget T for the total amount of stochastic process $Y|X$ simulations: $T \triangleq M \times N$. We notice that the variance in convergence rate (3.15) can be expressed as $\frac{N\langle \Delta^2 Z \rangle + \langle \Sigma_Y \rangle}{T}$, which is minimized for the smallest possible N value, that is $N_{\text{mean}} = 1$. Nonetheless, if one wants to estimate this convergence rate in (3.15), one must tally at least $N = 2$ stochastic processes in the inner-loop $Y_n|X_m$, and $M = 2$ in the outer-loop, as necessary to construct unbiased estimators (3.39) and (3.11) respectively.

The same reasoning can now be applied to establish the asymptotic convergence rate of unbiased variance estimator $\widehat{\langle \Delta^2 Z \rangle}$, which can be re-written from (3.13) as:

$$\widehat{\langle \Delta^2 Z \rangle} = \frac{1}{M}\sum_{m=1}^{M}\left[\left(\widehat{Z}(X_m) - \langle Z \rangle\right)^2 - \frac{\widehat{\Sigma_Y}(X_m)}{N}\right] - \left(\widehat{\langle Z \rangle} - \langle Z \rangle\right)^2 + \frac{\widehat{\langle \Delta^2 Z \rangle}}{M} + \frac{\widehat{\langle \Sigma_Y \rangle}}{MN}$$

As M increases, the last two terms vanish. Moreover, the law of large numbers guarantees almost sure convergence $\widehat{\langle Z \rangle} \underset{M\to\infty}{\overset{\text{a.s.}}{\longrightarrow}} \langle Z \rangle$, while the just established (3.15) guarantees $\sqrt{M}\left(\widehat{\langle Z \rangle} - \langle Z \rangle\right) \underset{M\to\infty}{\overset{\mathbb{L}\text{aw}}{\longrightarrow}} \mathcal{N}\left(0, \langle \Delta^2 Z \rangle + \frac{\langle \Sigma_Y \rangle}{N}\right)$, so that the unbiased estimator $\widehat{\langle \Delta^2 Z \rangle}$ of the ensemble average variance almost surely converges to:

$$\widehat{\langle \Delta^2 Z \rangle} \underset{M\to\infty}{\overset{\text{a.s.}}{\longrightarrow}} \frac{1}{M}\sum_{m=1}^{M}\left[\left(\widehat{Z}(X_m) - \langle Z \rangle\right)^2 - \frac{\widehat{\Sigma_Y}(X_m)}{N}\right]$$

By developing the inner mean and variance estimator terms from (3.37) and (3.39), one finds:

$$\mathbb{E}_Y\left[\left(\widehat{Z}(X_m) - \langle Z \rangle\right)^2 - \frac{\widehat{\Sigma_Y}(X_m)}{N}\right] = \left(Z(X_m) - \langle Z \rangle\right)^2$$

Using definition (A.6), we again apply the central limit theorem for independent non identically distributed random variables (Lindeberg form) to find:

$$\widehat{\langle \Delta^2 Z \rangle} \xrightarrow[M\to\infty]{\mathbb{L}\text{aw}} \frac{1}{M}\sum_{m=1}^{M}\Big(Z(X_m)-\langle Z\rangle\Big)^2 + \mathcal{N}\left(0, \frac{1}{M}\sum_{m=1}^{M}\frac{W(X_m)}{M}\right)$$

where we defined

$$W_N(X) \triangleq \mathbb{V}\text{ar}_Y\left[\Big(\widehat{Z}(X)-\langle Z\rangle\Big)^2 - \frac{\widehat{\Sigma_Y}(X)}{N}\right] \tag{A.6}$$

Since we now have $\mathbb{E}_X\left[\Big(Z(X_m)-\langle Z\rangle\Big)^2\right] = \langle \Delta^2 Z\rangle$, the well known relation ruizespejoOptimalUnbiasedEstimation2013, ruizespejoErratumOptimalUnbiased2016

$$\mathbb{V}\text{ar}_X\left[\Big(Z(X_m)-\langle Z\rangle\Big)^2\right] = \langle \Delta^4 Z\rangle - \langle \Delta^2 Z\rangle^2$$

entails one can again apply the central limit theorem, now for independent identically distributed random variables, as well as the Markov theorem and the plug-in limit from Slutsky's theorem, yielding (3.17).

To obtain explicit expression (3.17), we will now show that $W_N(X)$ defined in (A.6) satisfies

$$W_N(X) = \frac{4\,\Delta^2 Z(X)\,\Sigma_Y(X) + 2\frac{\Sigma_Y^2(X)}{N-1}}{N} \tag{A.7}$$

which will immediately entail (3.17). This can be achieved by developing all the terms in definition (A.6), yielding

$$\begin{aligned}
W(X_m) &\triangleq \mathbb{V}\text{ar}_Y\left[\Big(\widehat{Z}(X_m)-\langle Z\rangle\Big)^2 - \frac{\widehat{\Sigma_Y}(X_m)}{N}\right] \\
&= \mathbb{E}_Y\left[\left(\Big(\widehat{Z}(X_m)-\langle Z\rangle\Big)^2 - \frac{\widehat{\Sigma_Y}(X_m)}{N} - \Big(Z(X_m)-\langle Z\rangle\Big)^2\right)^2\right] \\
&= \mathbb{E}_Y\left[\widehat{y}_m^4 + \frac{\widehat{\Sigma_Y}^2(X_m)}{N^2} - 2\widehat{y}_m^2\frac{\widehat{\Sigma_Y}(X_m)}{N} + 4\Delta Z(X_m)\left(\widehat{y}_m^3 - \widehat{y}_m\frac{\widehat{\Sigma_Y}(X_m)}{N}\right) + 4\Delta^2 Z(X_m)\widehat{y}_m^2\right]
\end{aligned}$$

where

$$\Delta Z(X_m) \triangleq Z(X_m) - \langle Z \rangle$$

$$\widehat{y}_m \triangleq \widehat{Z}(X_m) - Z(X_m) = \frac{1}{N}\sum_{n=1}^{N}\left(Y_n|X_m - Z(X_m)\right)$$

$$\widehat{\Sigma_Y}(X_m) \triangleq \frac{1}{N-1}\sum_{n=1}^{N}\left(Y_n|X_m - \widehat{Z}(X_m)\right)^2 = \left(\frac{N}{N-1}\right)\left[\frac{1}{N}\sum_{n=1}^{N}\left(Y_n|X_m - Z(X_m)\right)^2 - \widehat{y}_m^2\right]$$

since for any x_i independent identically distributed random variables with raw moments $m_k \triangleq \mathbb{E}\left[x^k\right]$ we have:

$$\mathbb{E}\left[\sum_{n=1}^{N}\sum_{k=1}^{N} x_n x_k\right] = Nm_2 + N(N-1)m_1^2$$

$$\mathbb{E}\left[\sum_{n=1}^{N}\sum_{k=1}^{N}\sum_{i=1}^{N} x_n x_k x_i\right] = Nm_3 + 3N(N-1)m_2 m_1 + N(N-1)(N-2)m_1^3$$

$$\begin{aligned}\mathbb{E}\left[\sum_{n=1}^{N}\sum_{k=1}^{N}\sum_{i=1}^{N}\sum_{j=1}^{N} x_n x_k x_i x_j\right] &= Nm_4 + 3N(N-1)m_2^2 + 4N(N-1)m_3 m_1 \\ &\quad + 6N(N-1)(N-2)m_2 m_1^2 + N(N-1)(N-2)(N-3)m_1^4\end{aligned}$$

it stems that

$$\mathbb{E}_Y\left[\widehat{y}_m\right] = 0$$

$$\mathbb{E}_Y\left[\widehat{y}_m^2\right] = \frac{\Sigma_Y(X_m)}{N}$$

$$\mathbb{E}_Y\left[\widehat{y}_m^3\right] = \frac{\mu_Y^3(X_m)}{N^2}$$

$$\mathbb{E}_Y\left[\widehat{y}_m^4\right] = \frac{\mu_Y^4(X_m)}{N^3} + 3\frac{N-1}{N^3}\Sigma_Y^2(X_m)$$

$$\mathbb{E}_Y\left[\widehat{y}_m\frac{\widehat{\Sigma_Y}(X_m)}{N}\right] = \frac{\mu_Y^3(X_m)}{N^2}$$

$$\mathbb{E}_Y\left[\widehat{y}_m^2\frac{\widehat{\Sigma_Y}(X_m)}{N}\right] = \frac{\mu_Y^4(X_m)}{N^3} + \frac{N-3}{N^3}\Sigma_Y^2(X_m)$$

$$\mathbb{E}_Y\left[\frac{\widehat{\Sigma_Y}^2(X_m)}{N^2}\right] = \frac{\mu_Y^4(X_m)}{N^3} + \frac{\Sigma_Y^2(X_m)}{N^2}\left(1 - \frac{1}{N} + \frac{2}{N(N-1)}\right)$$

where the inner third $\mu_Y^3(X)$ and fourth $\mu_Y^4(X)$ central moments of the stochastic

process $Y|X$ are defined as

$$\mu_Y^3(X) \triangleq \mathbb{E}_Y\left[(Y|X - Z(X))^3\right]$$
$$\mu_Y^4(X) \triangleq \mathbb{E}_Y\left[\Big(Y|X - Z(X)\Big)^4\right]$$

Identifying the terms in the developed expression yields the result (A.7).

Having established convergence rate (3.17), we are now given a budget T of total number of stochastic process $Y|X$ simulation runs, $T \triangleq M \times N$, and we search for the choice of N that will minimize the variance $\frac{N\left(\langle\Delta^4 Z\rangle - \langle\Delta^2 Z\rangle^2\right) + 4\langle\Delta^2 Z\ \Sigma_Y\rangle + 2\frac{\langle\Sigma_Y^2\rangle}{N-1}}{T}$ in (3.17). By differentiating the latter expression, we find the variance is minimized for the closest integer that satisfies (3.19).

Finally, to construct unbiased estimators of this convergence rate (3.17), we can again use the general mean-power property (3.28) to build term-by-term unbiased estimators:

- Outputs (ensemble average) fourth central moment unbiased estimator:

$$\begin{aligned}\widehat{\langle\Delta^4 Z\rangle} = &\frac{1}{M}\sum_{m=1}^{M}\widehat{Z^4}(X_m) \\ &-\frac{4}{M(M-1)}\sum_{m=1}^{M}\sum_{\substack{k=1\\k\neq m}}^{M}\widehat{Z^3}(X_m)\widehat{Z}(X_k) \\ &+\frac{6}{M(M-1)(M-2)}\sum_{m=1}^{M}\sum_{\substack{k=1\\k\neq m}}^{M}\sum_{\substack{j=1\\j\neq m\\j\neq k}}^{M}\widehat{Z^2}(X_m)\widehat{Z}(X_k)\widehat{Z}(X_j) \\ &-\frac{3}{M(M-1)(M-2)(M-3)}\sum_{m=1}^{M}\sum_{\substack{k=1\\k\neq m}}^{M}\sum_{\substack{j=1\\j\neq m\\j\neq k}}^{M}\sum_{\substack{\ell=1\\\ell\neq m\\\ell\neq k\\\ell\neq j}}^{M}\widehat{Z}(X_m)\widehat{Z}(X_k)\widehat{Z}(X_j)\widehat{Z}(X_\ell)\end{aligned} \tag{A.8}$$

where

$$\begin{aligned}\widehat{Z^3}(X_m) &= \frac{1}{N(N-1)(N-2)}\sum_{n=1}^{N}\sum_{\substack{i=1\\i\neq n}}^{N}\sum_{\substack{s=1\\s\neq n\\s\neq i}}^{N}\left(Y_n \cdot Y_i \cdot Y_s\right)|X_m \\ \widehat{Z^4}(X_m) &= \frac{1}{N(N-1)(N-2)(N-3)}\sum_{n=1}^{N}\sum_{\substack{i=1\\i\neq n}}^{N}\sum_{\substack{s=1\\s\neq n\\s\neq i}}^{N}\sum_{\substack{q=1\\q\neq n\\q\neq i\\q\neq s}}^{N}\left(Y_n \cdot Y_i \cdot Y_s \cdot Y_q\right)|X_m\end{aligned} \tag{A.9}$$

- Square of the outer (ensemble average) variance unbiased estimator

$$\begin{aligned}\widehat{\langle\Delta^2 Z\rangle^2}=&\frac{1}{M(M-1)}\sum_{m=1}^{M}\sum_{\substack{k=1\\k\neq m}}^{M}\widehat{Z^2}(X_m)\widehat{Z^2}(X_k)\\&-\frac{2}{M(M-1)(M-2)}\sum_{m=1}^{M}\sum_{\substack{k=1\\k\neq m}}^{M}\sum_{\substack{j=1\\j\neq m\\j\neq k}}^{M}\widehat{Z^2}(X_m)\widehat{Z}(X_k)\widehat{Z}(X_j)\\&+\frac{1}{M(M-1)(M-2)(M-3)}\sum_{m=1}^{M}\sum_{\substack{k=1\\k\neq m}}^{M}\sum_{\substack{j=1\\j\neq m\\j\neq k}}^{M}\sum_{\substack{\ell=1\\\ell\neq m\\\ell\neq k\\\ell\neq j}}^{M}\widehat{Z}(X_m)\widehat{Z}(X_k)\widehat{Z}(X_j)\widehat{Z}(X_\ell)\end{aligned} \tag{A.10}$$

- Inner-loop/outer-loop cross term unbiased estimator:

$$\begin{aligned}\widehat{\langle\Delta^2 Z\ \Sigma_Y\rangle}=&\frac{1}{M(M-1)}\sum_{m=1}^{M}\sum_{\substack{k=1\\k\neq m}}^{M}\widehat{Z^2}(X_m)\widehat{\Sigma_Y}(X_k)\\&+\frac{1}{M(M-1)(M-2)}\sum_{m=1}^{M}\sum_{\substack{k=1\\k\neq m}}^{M}\sum_{\substack{j=1\\j\neq m\\j\neq k}}^{M}\widehat{Z}(X_m)\widehat{Z}(X_k)\widehat{\Sigma_Y}(X_j)\\&-\frac{2}{M(M-1)(M-2)(M-3)}\sum_{m=1}^{M}\sum_{\substack{k=1\\k\neq m}}^{M}\sum_{\substack{j=1\\j\neq m\\j\neq k}}^{M}\sum_{\substack{\ell=1\\\ell\neq m\\\ell\neq k\\\ell\neq j}}^{M}\widehat{Z}(X_m)\widehat{Z}(X_k)\widehat{Z}(X_j)\widehat{\Sigma_Y}(X_\ell)\end{aligned} \tag{A.11}$$

- Square of inner-loop variance unbiased estimator, with fourth centered moment optimal unbiased estimator from ruizespejoOptimalUnbiasedEstimation2013,ruizespejoErratumO

$$\begin{aligned}\widehat{\langle\Sigma_Y^2\rangle}=&\frac{1}{M}\sum_{m=1}^{M}\widehat{\Sigma_Y^2}(X_m)\\\widehat{\Sigma_Y^2}(X_m)=&\left(\frac{N(N-1)}{N(N-2)+3}\right)\left[\widehat{\Sigma_Y}^2(X_m)-\frac{\widehat{\mu_Y^4}(X_m)}{N}\right]\\\frac{\widehat{\mu_Y^4}}{N}=&\frac{(N(N-2)+3)\left[\widehat{m_Y^4}-4\widehat{m_Y^3}\widehat{Z}\right]-3(2N-3)\widehat{m_Y^2}^2+3N^2\left[2\widehat{m_Y^2}\widehat{Z}^2-\widehat{Z}^4\right]}{(N-1)(N-2)(N-3)}\\\widehat{m_Y^k}(X_m)\triangleq&\frac{1}{N}\sum_{n=1}^{N}Y_n^k|X_m\end{aligned} \tag{A.12}$$

Though estimators (A.8), (A.9), (A.10), (A.11), and (A.12) are expressed in a non-computationally efficient way to calculate, they nonetheless show that it is necessary

to have $N \geq 4$ and $M \geq 4$ to construct unbiased estimators of the outer variance convergence rate (3.17). This result is interesting in that the skewness and the kurtosis of the stochastic process $Y|X$ cancel out in the expression of convergence rate (3.17), nonetheless, they to appear in the construction of an unbiased estimator of the square of the variance Σ_Y^2. □

A.3 Analytic toy-problem: Multivariate inputs & Gaussian outputs noise

We here design a simple toy case that is analytically solvable, with the aim of verifying the general Embedded Monte Carlo methods. We choose a multivariate normal prior $X|\theta$, and an affine relation for ensemble average $Z(X)$, so that we can perform Bayesian inference (2.2) analytically, and thus know the exact posterior $X|D$ distribution. We then use Embedded Variational Inference (EVI) to approximate the exact $p(X|D)$ density with $p_\omega(X)$, assuming that $p_\omega(X)$ is itself a multivariate normal distribution, and search for the meta-parameters $\omega_\star$ which solve (3.26). We run the EVI algorithm, and observe that the meta-parameters $\omega_\star$ converge towards the exact $p(X|D)$ solution. We then use Embedded Forward Propagation (EFP) to approximately propagate this inferred parameters uncertainty distribution to $Z(X|D)$, and compare the results to the exact solutions.

A.3.1 Exact Solution: a tractable stochastic process for multivariate Gaussian conjugate priors Bayesian inference

Let $X \triangleq [X_1, X_2, \ldots, X_q]^\mathsf{T}$ be the vector of parameters we are searching to infer. Let $\mathcal{B}_Y(\cdot)$ denote the Bernoulli random Law, $\boldsymbol{\alpha_Y}$ and $\boldsymbol{a}$ two real q-size vectors, and b and β_Y two known scalars, with $0 < \beta_Y < 1$. We consider the stochastic process:

$$Y|X \sim \boldsymbol{a}^\mathsf{T} \cdot X \cdot \frac{\left[1 + \mathrm{e}^{-\boldsymbol{\alpha_Y}^\mathsf{T} \cdot X}\right]}{\beta_Y} \mathcal{B}_Y\left(\frac{\beta_Y}{1 + \mathrm{e}^{-\boldsymbol{\alpha_Y}^\mathsf{T} \cdot X}}\right) + b \tag{A.13}$$

so that the output ensemble average $Z(X) \triangleq \mathbb{E}_Y[Y|X]$ is affine:

$$Z(X) = \boldsymbol{a}^\mathsf{T} \cdot X + b \tag{A.14}$$

and the variance of the stochastic process $\Sigma_Y(X) \triangleq \mathbb{V}\mathrm{ar}_Y[Y|X]$ is:

$$\Sigma_Y(X) = \left(\boldsymbol{a}^\mathsf{T} \cdot X\right)^2 \cdot \left(\frac{1 + \mathrm{e}^{-\boldsymbol{\alpha_Y}^\mathsf{T} \cdot X}}{\beta_Y} - 1\right) \tag{A.15}$$

We generate a data-set of noisy measurements $D = \{Z_i\}$, with heterosckedastic Gaussian noise $Z_i \sim \mathcal{N}(Z(X), \Sigma_i)$, where each Σ_i is different but known (Σ_i is the variance, that is the square of the standard deviation). We consider a multivariate normal prior $X|\theta \sim \mathcal{N}(\boldsymbol{\mu}_0, \boldsymbol{\Sigma}_0)$. Since $Z(X)$ is affine, the (conjugate) posterior Bayesian update

(2.2) is also normal: $X|D \sim \mathcal{N}(\boldsymbol{\mu}_D, \boldsymbol{\Sigma}_D)$, with:

$$\boldsymbol{\Sigma}_D^{-1} = \boldsymbol{\Sigma}_0^{-1} + \boldsymbol{a}\left[\sum_{k=1}^{d} \Sigma_i^{-1}\right]\boldsymbol{a}^{\mathsf{T}} \tag{A.16}$$

$$\boldsymbol{\mu}_D = \boldsymbol{\Sigma}_D\left[\boldsymbol{\Sigma}_0^{-1}\boldsymbol{\mu}_0 + \boldsymbol{a}\left[\sum_{k=1}^{d} \Sigma_i^{-1}(Z_i - b)\right]\right] \tag{A.17}$$

Moreover, affine transform (A.14) entails the forward propagated distribution of ensemble averages is also normal, $Z(X|D) \sim \mathcal{N}(\langle Z\rangle, \langle \Delta^2 Z\rangle)$, with mean and variance:

$$\langle Z\rangle = \boldsymbol{a}^{\mathsf{T}}\boldsymbol{\mu}_D + b \tag{A.18}$$

$$\langle \Delta^2 Z\rangle = \boldsymbol{a}^{\mathsf{T}}\boldsymbol{\Sigma}_D\boldsymbol{a} \tag{A.19}$$

The convergence rates from theorem 2 are therefore given by (A.19) and (A.15) for the mean (3.15), whereas for the variance (3.17), we have the outer loop ensemble average $Z(X)$ following a normal distribution, so that $\langle \Delta^4 Z\rangle - \langle \Delta^2 Z\rangle^2 = 2\langle \Delta^2 Z\rangle^2 = 2\left(\boldsymbol{a}^{\mathsf{T}}\boldsymbol{\Sigma}_D\boldsymbol{a}\right)^2$. Moreover, the cross term and the variance squared integrals can be expressed as:

$$\begin{aligned}
\langle \Sigma_Y\rangle &= \left(\frac{1}{\beta_Y} - 1\right)\mathfrak{M}_2 + \frac{1}{\beta_Y}\mathfrak{L}_2(\alpha_Y)\\
\langle \Sigma_Y^2\rangle &= \left(\frac{1}{\beta_Y} - 1\right)^2\mathfrak{M}_4 + \frac{2}{\beta_Y}\left(\frac{1}{\beta_Y} - 1\right)\mathfrak{L}_4(\alpha_Y) + \frac{1}{\beta_Y^2}\mathfrak{L}_4(2\alpha_Y)\\
\langle \Delta^2 Z\ \Sigma_Y\rangle &= \left(\frac{1}{\beta_Y} - 1\right)\left[\mathfrak{M}_4 - 2\left(\boldsymbol{a}^{\mathsf{T}}\boldsymbol{\mu}_D\right)\mathfrak{M}_3 + \left(\boldsymbol{a}^{\mathsf{T}}\boldsymbol{\mu}_D\right)^2\mathfrak{M}_2\right]\\
&\quad + \frac{1}{\beta_Y}\left[\mathfrak{L}_4(\alpha_Y) - 2\left(\boldsymbol{a}^{\mathsf{T}}\boldsymbol{\mu}_D\right)\mathfrak{L}_3(\alpha_Y) + \left(\boldsymbol{a}^{\mathsf{T}}\boldsymbol{\mu}_D\right)^2\mathfrak{L}_2(\alpha_Y)\right]\\
\mathfrak{M}_k(\boldsymbol{\mu}_D) &\triangleq \int\left(\boldsymbol{a}^{\mathsf{T}}\cdot x\right)^k p_X(x)\mathrm{d}x\\
\mathfrak{M}_2(\boldsymbol{\mu}_D) &= \left(\boldsymbol{a}^{\mathsf{T}}\boldsymbol{\mu}_D\right)^2 + \boldsymbol{a}^{\mathsf{T}}\boldsymbol{\Sigma}_D\boldsymbol{a}\\
\mathfrak{M}_3(\boldsymbol{\mu}_D) &= \left(\boldsymbol{a}^{\mathsf{T}}\boldsymbol{\mu}_D\right)\left[\left(\boldsymbol{a}^{\mathsf{T}}\boldsymbol{\mu}_D\right)^2 + 3\boldsymbol{a}^{\mathsf{T}}\boldsymbol{\Sigma}_D\boldsymbol{a}\right]\\
\mathfrak{M}_4(\boldsymbol{\mu}_D) &= \left(\boldsymbol{a}^{\mathsf{T}}\boldsymbol{\mu}_D\right)^4 + 6\left(\boldsymbol{a}^{\mathsf{T}}\boldsymbol{\mu}_D\right)^2\boldsymbol{a}^{\mathsf{T}}\boldsymbol{\Sigma}_D\boldsymbol{a} + 3\left(\boldsymbol{a}^{\mathsf{T}}\boldsymbol{\Sigma}_D\boldsymbol{a}\right)^2\\
\mathfrak{L}_k(\alpha_Y) &\triangleq \int\left(\boldsymbol{a}^{\mathsf{T}}\cdot x\right)^k \mathrm{e}^{-\boldsymbol{\alpha_Y}^{\mathsf{T}}\cdot x}p_X(x)\mathrm{d}x\\
\mathfrak{L}_k(\alpha_Y) &= \mathrm{e}^{-\boldsymbol{\alpha_Y}^{\mathsf{T}}\cdot\boldsymbol{\mu}_D + \frac{1}{2}\boldsymbol{\alpha_Y}^{\mathsf{T}}\boldsymbol{\Sigma}_D\boldsymbol{\alpha_Y}}\mathfrak{M}_k(\boldsymbol{\mu}_D - \boldsymbol{\Sigma}_D\boldsymbol{\alpha_Y})
\end{aligned} \tag{A.20}$$

These constitute our exact reference toy-problem solutions.

A.3.2 Numerical verification: Embedded Monte Carlo converges to exact solutions

Toy-problem (A.13) was coded with the following characteristics:

- Stochastic process (A.13) meta-parameter values were set at:
  $\boldsymbol{a} = [2, -1]$, $\alpha_Y = \boldsymbol{a}$, $b = -3$, $\beta_Y = 1/3$.

- Five noisy observations were generated at random:
  $D = \{Z_i\} = \{9.18454678, 10.92305208, 7.564019177.16029873, 8.48488501\}$,
  with corresponding variances:
  $\{\Sigma_i\} = \{42.88669551, 3.17228589, 4.10857714, 4.2055173, 19.81653964\}$.

- Learning rate hyper-parameter sequences were set at:
  é $\gamma_t{}^{\boldsymbol{\mu}} = \frac{8\times10^{-3}}{t^{1/2}}$ and $\gamma_t{}^{\boldsymbol{S}} = \frac{5\times10**^{-3}}{t^{7/10}}$.

- The full code is accessible at this link[1].

The Embedded Monte Carlo results of this toy-problem are reported in figures 3-5, 3-1, and 3-4.

[1] https://www.dropbox.com/sh/uwe8h2duee3ztb7/AAAJla7nm0Xl4MlyI9kMzmzwa?dl=0

Appendix B

A xenon trilogy on pole parametrizations of R-matrix theory

Cross sections are of paramount importance in nuclear physics. They quantify the probability that this or that outcome occurs when two bodies collide and interact. Nuclear cross sections vary with the momentum or energy at which the two bodies are swung against each other. A model of two-body quantum interactions called R-matrix theory parametrizes this energy dependence, and campaigns of measurements are conducted to infer the corresponding R-matrix parameters, compiling them into standard evaluated nuclear data libraries (ENDF, JEFF, BROND, JENDL, CENDL, TENDL): these constitute a pillar of our common knowledge of nuclear physics.

In the past, two branches of theoretical physics formalisms emerged to describe and parametrize nuclear cross sections (and their underlying scattering matrix): R-matrix theory (of Kapur-Peierls [200], Wigner [323], and Bloch [79]), and pole expansions (of Humblet and Rosenfeld [185, 289, 181, 182, 195, 183, 230, 290, 231]). The two have been quite isolated from one another. The following three articles [127, 125, 130] bridge these two formalisms, and build upon them to construct a new unified theory to parametrize nuclear cross section: the windowed multipole representation of R-matrix cross sections. We support this new theory with empirical evidence observed in isotope xenon ^{134}Xe spin-parity group $J^\pi = 1/2^{(-)}$. As such, the articles form a xenon trilogy on pole parametrizations of R-matrix cross sections.

Present nuclear data libraries are all based on R-matrix resonance parameters. This has many advantages, but also some drawbacks. For instance, R-matrix theory requires some arbitrary parameters (boundary condition B_c and channel radii a_c). Also, R-matrix nuclear cross sections come in a format that is difficult to subsequently post-process to account for temperature effects. People have thus proposed different cross section parametrizations addressing some of these shortcomings, hoping to establish improved nuclear data libraries with the new parameters.

One such alternative parametrization was recently proposed by Brune [92]. Our first article, *Shadow poles in the alternative parametrization of R-matrix theory* [127], establishes various novel properties of this alternative parametrization, including the

full counting of the number of alternative poles, revealing the existence of shadow poles, and proving that one can choose any subset of these poles to fully parametrize the scattering matrix (and therefore the cross sections) provided the subset maps at least one-to-one to the resonance levels. We also generalize the alternative parametrization to encompass the important Reich-Moore formalism, commonly used for heavy isotopes. This requires we continue R-matrix operators to complex energies (and wavenumbers), in particular the shift $S(E)$ and penetration $P(E)$ functions. However, the nuclear physics community has disagreed as to how to do so, with two competing ways emerging from ambiguous definitions of the shift and penetration functions, $L(E) = S(E) + iP(E)$, dividing the community along the same two branches: following an interpretation from Lane and Thomas [214], R-matrix theory people have traditionally "force closed" channels by setting the penetration functions to zero bellow threshold energies (complex wavenumbers); meanwhile people in mathematical scattering theory perform analytic continuation of all operators into pole expansions. In order to establish new nuclear data libraries with alternative parameters, the nuclear physics community must thus decide what convention to adopt.

In our second article, *Scattering matrix pole expansions for complex wavenumbers in R-matrix theory* [125], we argue in favor of analytical continuation (against the legacy Lane and Thomas "force-closure" approach). We support our claim that analytic continuation is the physically correct way of continuing R-matrix operators to complex wavenumbers (and energies) with a series of mathematical and physics arguments, showing that analytic continuation preserves generalized unitarity, cancels spurious poles introduced by the "forced-closure" approach, and closes channels below threshold with evanescent quantum tunneling. In the process, we prove that the Siegert-Humblet pole expansion in radioactive states constitutes the bridge between R-matrix theory and the wavenumber pole expansions of Humblet and Rosenfeld, and discover various new properties of the radioactive poles and residue widths, including their invariance properties to changes in channel radii a_c.

R-matrix theory, the alternative Brune parameters, or the expansion in radioactive states, all parametrize nuclear cross sections at zero Kelvin. These must then be processed to account for temperature effects, in particular Doppler broadening, which is the averaging of cross sections over the thermal motion of the target atoms. Doppler broadening is of critical importance in neutron transport applications as it ensures the stability of many nuclear reactors (negative thermal reactivity). Yet it has been a considerable bottleneck for nuclear computations. In our third article, *Windowed multipole representation of R-matrix cross sections* [130], we build upon the expansion in radioactive states to establish the windowed multipole representation as an alternative way to parametrize nuclear cross sections and their uncertainties (equivalent to R-matrix theory). Remarkably, one can sample windowed multipole cross sections from their uncertainty distribution and analytically Doppler broaden them, all computed on-the-fly (no need to pre-compute and store). This drastically reduces the memory footprint of nuclear data (over a thousand-fold), without incurring additional computational costs.

These three articles together thus form a new, in-depth study of the parametriza-

tions underpinning our standard nuclear cross section libraries, and propose innovations for the way we document and use this body of nuclear cross sections knowledge. This is of general interest to the nuclear physics community, as it paves the way for alternative nuclear data libraries, whose parametrizations of nuclear cross sections can unlock considerable gains, both for nuclear physics and computations.

Appendix C

Shadow poles in the alternative parametrization of R-matrix theory

Here is *verbatim* transcribed our article [127].

C.1 Abstract

We discover new, hitherto unknown, shadow poles in Brune's alternative parametrization of R-matrix theory [C. R. Brune, Phys. Rev. C 66, 044611 (2002)]. Where these poles are, and how many, depends on how one continues R-matrix operators to complex wavenumbers (specially the shift S and penetration P functions). This has little consequence for the exact R-matrix formalism (past the last energy threshold), as we show one can still always fully reconstruct the scattering matrix with only the previously known alternative parameters (poles and corresponding resonance widths), for which there were as many poles as the number of levels N_λ. However, we generalize the alternative parametrization to the Reich-Moore formalism, and show that the choice of continuation is now critical as it changes the alternative parameters values (poles and residue widths are now complex). In order to establish nuclear libraries with alternative parameters, the nuclear community will thus have to decide what convention to adopt. We argue in favor of analytical continuation (against the legacy Lane and Thomas approach) in a follow-up article [P. Ducru, Phys. Rev. C (2020)]. We observe the first evidence of shadow poles in the alternative parametrization of R-matrix theory in isotope xenon ^{134}Xe spin-parity group $J^\pi = 1/2^{(-)}$, and show how they indeed depend on the choice of continuation to complex wavenumbers.

C.2 Introduction

When two nuclear bodies collide at a given energy – say a neutron and an uranium-235 nucleus ($\mathrm{n} + {}^{235}_{92}\mathrm{U}$), a γ particle (photon) and a beryllium atom ($\gamma + {}^{9}_{4}\mathrm{Be}$), or an alpha particle (${}^{4}_{2}\mathrm{He}$) and a gold atom ($\alpha + {}^{197}_{79}\mathrm{Au}$) – the outcomes of this interaction are expressed as nuclear cross sections. These cross sections are a fundamental component of our nuclear physics knowledge, documented in standard nuclear data libraries (ENDF [87], JEFF[267], JENDL[293], BROND[80], CENDL[153], TENDL[207, 209]).

To constitute nuclear data libraries, an evaluation process fits experimental measurements of reaction rates with a parametric model of nuclear interaction cross sections called R-matrix theory, using evaluation codes such as EDA [164, 166], SAMMY [217], or AZURE [62]. R-matrix theory models nuclear interactions as two incoming bodies yielding two outgoing bodies through the action of a total Hamiltonian. The latter is assumed to be the addition of a short-range, interior Hamiltonian that is null beyond channel radius a_c, and a long-range, exterior Hamiltonian that we know, say Coulomb potential or free moving. This partitioning, along with an orthogonality assumption of channels at the channel boundary, is what we could call the *R-matrix scattering model*, described by Kapur and Peierls in their seminal article [200], unified by Bloch in [79], and reviewed by Lane and Thomas in [214]. The outcomes of the interaction depend on the energy at which the interaction occurs, and R-matrix theory parametrizes, for calculability reasons, this energy dependence. It can do so in several ways: the one that has come to prevail in the nuclear physics community is the Wigner-Eisenbud parametrization [323, 79, 214].

There are good reasons for this: the Wigner-Eisenbud parameters are unconstrained real parameters — i.e. though physically and statistically correlated, any set of real parameters is mathematically acceptable (though not necessarily present in nature) — that parametrize the interior interaction Hamiltonian (usually an intractable many-body nuclear problem) and separate it from the exterior one (usually a well-known free-body or Coulomb Hamiltonian with analytic Harmonic expansions). Thus, Wigner and Eisenbud constructed a parametrization of the scattering matrix for calculability purposes: introducing simple real parameters that help de-correlate what happens in the inner interaction region from the asymptotic outer region. Despite all their advantages, the Wigner-Eisenbud parameters present a drawback for nuclear data evaluators: they require the introduction, for every channel c, of an arbitrary real "boundary condition" parameter, B_c. If this arbitrary parameter is set to different values, the same experimental nuclear data will yield different Wigner-Eisenbud resonance parameters. This poses both a physics interpretability problem, and a standardization problem when edifying the standard nuclear data libraries.

In order to circumvent the need for arbitrary boundary parameters B_c, Brune introduced an alternative parametrization of R-matrix theory in [92]. The alternative parameters are real (like the Wigner-Eisenbud ones) and are independent of the arbitrary boundary condition parameters B_c. However, they do entangle the interior region (function of the total energy E) with the outer region (function of the incoming wavenumber k_c and outgoing wavenumber $k_{c'}$), so that the alternative parameters depend on how the wavenumbers are related to the energy of the system, $k_c(E)$, and this mapping has branch-points and different sheets corresponding to all the choices of sign in the square roots $\pm\sqrt{E - E_{T_c}}$ of mapping (E.2). Using monotonic properties of the shift function $S(E)$ on the physical sheet $\left\{E, +\right\}$ of energy-wavenumber (E.2) mapping (recently proved in [93]), Brune showed a one-to-one correspondence between the number N_λ of resonances (or levels) and the number of alternative resonance energies (or poles) [92]. This would make the conversion of nuclear data libraries from Wigner-Eisenbud to alternative parameters very convenient.

Section C.3 summarizes the Wigner-Eisenbud R-matrix parametrization, reports on the branch-point nature of the energy-wavenumber mapping (E.2) – and its simple relativistic generalisation (E.4) – and, for the first time, establishes in theorem 5 the Mittag-Leffler expansion of the reduced logarithmic derivative of the outgoing wave operator $L_c(\rho_c)$. These results are used in section C.4 to show there exists more alternative poles than previously thought: these *shadow poles* reside below the reaction threshold energies E_{T_c}. We also show that these alternative shadow poles depend on the definition that is chosen to continue the R-matrix operators to complex wavenumbers. If the legacy Lane & Thomas definition (C.41) is chosen, then we call them *alternative branch poles* and establish their properties in theorem 6, amongst which that the shadow poles reside on the nonphysical sheet $\left\{E, -\right\}$ sub-threshold. If, instead, the analytic continuation definition (C.43) is chosen, then we call them *alternative analytic poles*, and we establish their properties in theorem 7, in particular we show alternative analytic poles are in general complex, of which there exists at least N_λ real ones. Moreover, and similarly to the Wigner-Eisenbud parameters, alternative analytic poles only depend on the total energy E and thus no longer present the branches of mapping (E.4). In theorem 8, we also show that, under a proper generalization of the alternative level matrix, one can choose any subset of N_S alternative poles (for both definitions and real or complex) and still fully reconstruct the scattering matrix (and thus the cross section), as long as $N_S \geq N_\lambda$.

In nuclear libraries, many isotopes are evaluated with the Reich-Moore formalism instead of the full R-matrix one. In section C.5, we generalize the alternative parametrization of R-matrix theory to the Reich-Moore formalism, including the newly discovered alternative shadow poles. The first evidence of alternative shadow poles is observed in isotope xenon ^{134}Xe spin-parity group $J^\pi = 1/2^{(-)}$, and reported in section C.6. We also demonstrate how in practice (for Reich-Moore isotopes or when thresholds are present) all alternative parameters depend on the choice of continuation of R-matrix operators to complex wavenumbers. This means that in order to convert nuclear data libraries to alternative parameters, the nuclear physics community must first agree on how to continue the R-matrix operators to complex wavenumbers. We argue in favor of analytic continuation in a follow-up article [125].

C.3 R-matrix Wigner-Eisenbud parametrization

We here recall some fundamental definitions and equations of the Wigner-Eisenbud R-matrix parameters [323, 79, 214]. As described by Bloch and Lane & Thomas, for each channel c, R-matrix theory treats the two-body-in/two-body-out many-body system as a reduced one-body system. All the study is then performed in the reduced system and we consider the wave-number of each channel k_c, which we can render dimensionless using the channel radius a_c and defining $\boldsymbol{\rho} = \mathbf{diag}\left(\rho_c\right)$ with $\rho_c = k_c a_c$.

C.3.1 Energy dependence and wavenumber mapping

All of the channel wavenumbers link back to one unique total system energy E, eigenvalue of the total Hamiltonian. Conservation of energy entails that this energy E must be the total energy of any given channel c (c.f. equation (5.12), p.557 of [185]):

$$E = E_c = E_{c'} = \dots \quad , \forall\, c \tag{C.1}$$

Each channel's total energy E_c is then linked to the wavenumber k_c of the channel by its corresponding relation (E.4), say (C.4) and (C.5).

In the semi-classical model described in Lane & Thomas [214], we can separate on the one hand massive particles, for which the wavenumber k_c is related to the center-of-mass energy E_c of relative motion of channel c particle pair with masses $m_{c,1}$ and $m_{c,2}$ as

$$k_c = \sqrt{\frac{2m_{c,1}m_{c,2}}{(m_{c,1}+m_{c,2})\,\hbar^2}\,(E_c - E_{T_c})} \tag{C.2}$$

where E_{T_c} denotes a threshold energy beyond which the channel c is closed, as energy conservation cannot be respected ($E_{T_c} = 0$ for reactions without threshold). On the other hand, for a photon particle interacting with a massive body of mass $m_{c,1}$ the center-of-mass wavenumber k_c is linked to the total center-of-mass energy E_c of channel c according to:

$$k_c = \frac{(E_c - E_{T_c})}{2\hbar \mathrm{c}}\left[1 + \frac{m_{c,1}\mathrm{c}^2}{(E - E_{T_c}) + m_{c,1}\mathrm{c}^2}\right] \tag{C.3}$$

Alternatively, in a more unified approach, one can perform a relativistic correction and smooth these differences away by means of the special relativity Mandelstam variable $s_c = (p_{c,1}+p_{c,2})$, also known as the square of the center-of-mass energy, where $p_{c,1}$ and $p_{c,2}$ are the Minkowsky metric four-momenta of the two bodies composing channel c, with respective masses $m_{c,1}$ and $m_{c,2}$ (null for photons). The channel wavenumber k_c can then be expressed as:

$$k_c = \sqrt{\frac{[s_c - (m_{c,1}+m_{c,2})^2\mathrm{c}^2]\,[s_c - (m_{c,1}-m_{c,2})^2\mathrm{c}^2]}{4\hbar^2 s_c}} \tag{C.4}$$

and the Mandelstam variable s_c can be linked to the center-of-mass energy of the channel E_c through

$$E_c = \frac{s_c - (m_{c,1}+m_{c,2})^2\mathrm{c}^2}{2(m_{c,1}+m_{c,2})} \tag{C.5}$$

Interestingly, this is identical to the non-relativistic expression for the center-of-mass energy in terms of the lab energy in whichever channel the total mass $(m_{c,1}+m_{c,2})$ is chosen to be the reference for E (but not in any other). This special relativistic correction to the non-relativistic R-matrix theory is the approach taken by the EDA code in use at the Los Alamos National Laboratory [164, 166].

Regardless of the approach taken to link the channel energy E_c to the channel wavenumber k_c, conservation of energy (C.1) entails there exists a complex mapping

linking the total center-of-mass energy E to the wavenumbers k_c, or their associated dimensionless variable $\rho_c = k_c r_c$:

$$\rho_c(E) \quad \longleftrightarrow \quad E \tag{C.6}$$

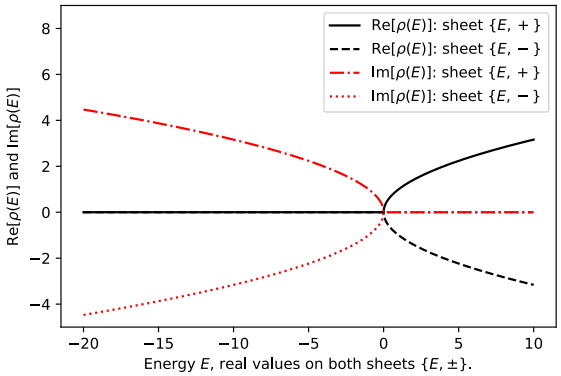

Figure C-1: Riemann surface of energy-wavenumber mapping $\rho(E)$ for massive particles in the semi-classical limit (E.2). The square root $\rho_c(E) = \pm\rho_0\sqrt{E - E_{T_c}}$ gives rise to two sheets: $\{E, +\}$ and $\{E, -\}$. Units such that $\rho_0 = 1$. Threshold set at zero: $E_{T_c} = 0$.

Critical properties throughout this article will stem from the analytic continuation of R-matrix operators. As the outgoing O_c and incoming I_c wave functions are defined according to ρ_c (c.f. section C.3.2 below), the natural variable to perform analytic continuation is thus ρ_c, which is equivalent to extending the wavenumbers into the complex plane $k_c \in \mathbb{C}$. We can see that the mapping (E.4) from complex k_c to complex energies is non-trivial, specially since the wavenumbers are themselves all interconnected. This creates a multi-sheeted Riemann surface, with branch-points at each threshold E_{T_c}, well documented by Eden & Taylor [137] (also c.f. section 8 of [185]). More precisely, when calculating ρ_c from E one has to chose which sign to assign to $\pm\sqrt{E - E_{T_c}}$ in the semi-classical mapping (E.2) of massive particles (i.e. not photons), or to the more general mapping (C.4). Figure C-1 shows mapping (E.2) with zero threshold $E_{T_c} = 0$: one can see that $\rho_c(E)$ has two branches $\rho_c(E) = \pm\rho_0\sqrt{E - E_{T_c}}$ and is purely real above threshold (zero imaginary part), and purely imaginary below threshold (zero real part). Each channel c thus introduces two choices, and hence there are 2^{N_c} sheets to the Riemann surface mapping (C.1) onto (E.4), with the branch points close or equal to the threshold energies E_{T_c}. As we will see, the choice of the sheet will have an impact when finding different R-matrix and alternative parameters.

C.3.2 External region wave functions

In the R-matrix model, the external region is subject to either a Coulomb interaction or a free particle movement. In either case, the solutions form a two-dimensional vector space, a basis of which is composed of the incoming and outgoing wave functions: $\boldsymbol{O}(\boldsymbol{k}) \triangleq \mathbf{diag}\,(O_c(k_c))$, $\boldsymbol{I}(\boldsymbol{k}) \triangleq \mathbf{diag}\,(I_c(k_c))$. These are Whittaker or confluent

Table C.1: Reduced logarithmic derivative $L_\ell(\rho) \triangleq \frac{\rho}{O_\ell}\frac{\partial O_\ell}{\partial r}(\rho)$ of outgoing wavefunction $O_\ell(\rho)$, and $L_\ell^0(\rho) \triangleq L_\ell(\rho) - B_\ell$ using $B_\ell = -\ell$, irreducible forms and Mittag-Leffler pole expansions for neutral particles, for angular momenta $0 \leq \ell \leq 4$.

	$L_\ell(\rho)$ from recurrence (C.11)	$L_\ell^0(\rho) \triangleq L_\ell(\rho) - B_\ell$ using $B_\ell = -\ell$ in (C.11)	$L_\ell(\rho)$ from theorem 5, poles $\left\{\omega_n\right\}$ from table C.2	Outgoing wavef $O_\ell(\rho)$ from (
ℓ	$L_\ell(\rho) = \frac{\rho^2}{\ell - L_{\ell-1}(\rho)} - \ell$	$L_\ell^0(\rho) = \frac{\rho^2}{2\ell - 1 - L_{\ell-1}^0(\rho)}$	$L_\ell(\rho) = -\ell + \mathrm{i}\rho + \sum_{n\geq 1}\frac{\rho}{\rho - \omega_n}$	$O_\ell(\rho) = \mathrm{e}^{\mathrm{i}\left(\rho + \frac{1}{2}\ell\pi\right)}$
0	$\mathrm{i}\rho$	$\mathrm{i}\rho$	$\{\emptyset\}$	$\mathrm{e}^{\mathrm{i}\rho}$
1	$\frac{-1+\mathrm{i}\rho+\rho^2}{1-\mathrm{i}\rho}$	$\frac{\rho^2}{1-\mathrm{i}\rho}$	$\omega_1^{\ell=1} = -\mathrm{i}$	$\mathrm{e}^{\mathrm{i}\rho}\left(\frac{1}{\rho} - \mathrm{i}\right.$
2	$\frac{-6+6\mathrm{i}\rho+3\rho^2-\mathrm{i}\rho^3}{3-3\mathrm{i}\rho-\rho^2}$	$\frac{\rho^2-\mathrm{i}\rho^3}{3-3\mathrm{i}\rho-\rho^2}$	$\omega_{1,2}^{\ell=2} \approx \pm 0.86602 - 1.5\mathrm{i}$	$\mathrm{e}^{\mathrm{i}\rho}\left(\frac{3}{\rho^2} - \frac{3\mathrm{i}}{\rho}\right.$
3	$\frac{-45+45\mathrm{i}\rho+21\rho^2-6\mathrm{i}\rho^3-\rho^4}{15-15\mathrm{i}\rho-6\rho^2+\mathrm{i}\rho^3}$	$\frac{3\rho^2-3\mathrm{i}\rho^3-\rho^4}{15-15\mathrm{i}\rho-6\rho^2+\mathrm{i}\rho^3}$	$\omega_1^{\ell=3} \approx -2.32219\mathrm{i}$ $\omega_{2,3}^{\ell=3} \approx \pm 1.75438 - 1.83891\mathrm{i}$	$\mathrm{e}^{\mathrm{i}\rho}\left(\frac{15}{\rho^3} - \frac{15\mathrm{i}}{\rho^2} - \right.$
4	$\frac{-420+420\mathrm{i}\rho+195\rho^2-55\mathrm{i}\rho^3-10\rho^4+\mathrm{i}\rho^5}{105-105\mathrm{i}\rho-45\rho^2+10\mathrm{i}\rho^3+\rho^4}$	$\frac{15\rho^2-15\mathrm{i}\rho^3-6\rho^4+\mathrm{i}\rho^5}{105-105\mathrm{i}\rho-45\rho^2+10\mathrm{i}\rho^3+\rho^4}$	$\omega_{1,2}^{\ell=4} \approx \pm 2.65742 - 2.10379\mathrm{i}$ $\omega_{3,4}^{\ell=4} \approx \pm 0.867234 - 2.89621\mathrm{i}$	$\mathrm{e}^{\mathrm{i}\rho}\left(\frac{105}{\rho^4} - \frac{105\mathrm{i}}{\rho^3} - \frac{45}{\rho^2}\right.$

hypergeometric function whose analytic continuation is discussed in section II.2.b and the appendix of [214], and for whose elemental properties and calculation we refer to chapter 14 of [51] and chapter 33 of [250], as well as Powell [271], Thompson [308], and Michel [242].

Note that the incoming and outgoing wave functions are only dependent on the wavenumber of the given channel k_c, this is a fundamental hypothesis of the R-matrix model. For clarity of writing, we will not explicitly write the k_c dependence of these operators unless it is of importance for the argument.

Importantly, the Wronksian of the system is constant: $\forall c,\ w_c \triangleq O_c^{(1)} I_c - I_c^{(1)} O_c = 2\mathrm{i}$, or with identity matrix $\mathbb{I}$

$$\begin{aligned} \boldsymbol{w} &\triangleq \boldsymbol{O}^{(1)}\boldsymbol{I} - \boldsymbol{I}^{(1)}\boldsymbol{O} \\ &= 2\mathrm{i}\mathbb{I} \end{aligned} \tag{C.7}$$

Of central importance to R-matrix theory is the *Bloch operator*, $\mathcal{L}$, which Claude Bloch introduced as the *opérateur de conditions aux limites* in equation (35) of [79], and that projects the system radially onto the channel boundaries for each channel, at the channel radius $r_c = a_c$. The Bloch operator $\mathcal{L}$ is then added to the Hamiltonian to form an invertible and diagonalizable (but not Hermitian) operator in the internal region (c.f. equation (34) of [79]). One can then diagonalize or invert this operator using different complete discrete generative eigenbases of the Hilbert space to construct different parameterizations of the solutions of the Schrodinger equation for the R-matrix scattering model (Kapur-Peierls, Wigner-Eisenbud, etc.). This is the essence of R-matrix theory, as best described by Claude Bloch in [79].

When using the Wigner-Eisenbud basis, this projection on the channel boundaries at $r_c = a_c$, gives rise to the as yet unnamed quantity $\boldsymbol{L}^0$, introduced in equation (1.6a), section VII.1. p.289 of [214], and which can be recognized in equation (57) of [79],

defined for each channel as:

$$L_c^0(\rho_c) \triangleq L_c(\rho_c) - B_c \tag{C.8}$$

where $\rho_c = k_c a_c$ has been projected on the channel surface, B_c is the arbitrary outgoing-wave boundary condition parameter, and $L_c(\rho_c)$ is the dimensionless reduced logarithmic derivative of the outgoing-wave function at the channel surface:

$$L_c(\rho_c) \triangleq \frac{\rho_c}{O_c}\frac{\partial O_c}{\partial \rho_c} \tag{C.9}$$

or, equivalently, in matrix notation, and where $[\,\cdot\,]^{(1)}$ designates the derivative with respect to ρ_c:

$$\boldsymbol{L} = \mathbf{diag}\,(L_c) = \boldsymbol{\rho O}^{-1}\boldsymbol{O}^{(1)} \tag{C.10}$$

so that the $\boldsymbol{L^0}$ matrix function is written: $\boldsymbol{L^0} \triangleq \boldsymbol{L} - \boldsymbol{B}$.

Using the Powell recurrence formulae [271], R.G. Thomas established the following scheme to calculate the outgoing-wave reduced logarithmic derivatives L_c for different angular momenta ℓ values in the Coulomb case (c.f. p.350, appendix of [214], eqs.(A.12) and (A.13))

$$L_\ell = \frac{a_\ell}{b_\ell - L_{\ell-1}} - b_\ell \tag{C.11}$$

with

$$a_\ell \triangleq \rho^2 + \left(\frac{\rho\eta}{\ell}\right)^2 \quad , \quad b_\ell \triangleq \ell + \left(\frac{\rho\eta}{\ell}\right) \tag{C.12}$$

In general, both $O_c(\rho)$ and $L_\ell(\rho)$ are meromorphic functions of ρ with *a priori* an infinity of poles, and for whose computation we refer to [271, 308, 242]. In theorem 5, we here establish the Mittag-Leffler expansion of $L_c(\rho)$.

Theorem 5. *Outgoing-wave reduced logarithmic derivative $L_c(\rho)$ Mittag-Leffler Expansion.*
The outgoing-wave reduced logarithmic derivative $L_c(\rho)$, defined in (C.9), admits the following Mittag-Leffler pole expansion:

$$\frac{L_c(\rho)}{\rho} = \frac{-\ell}{\rho} + \mathrm{i} + \sum_{n\geq 1}\frac{1}{\rho - \omega_n} \tag{C.13}$$

where $\{\omega_n\}$ are the roots of the $O_c(\rho)$ outgoing wavefunctions: $\forall n$, $O_c(\omega_n) = 0$. For neutral particles, there are a finite number of such roots, reported in table C.2.

Proof. From definition (C.9), L_c is the reduced logarithmic derivative of the outgoing wavefunction $L_c(\rho) \triangleq \rho\frac{O_c^{(1)}(\rho)}{O_c(\rho)}$. In both the Coulomb and the neutral particle case, the outgoing wavefunction $O_c(\rho)$ is a confluent hypergeometric function with simple roots $\{\omega_n\}$. Moreover, their logarithmic derivative $\frac{O_c^{(1)}(\rho)}{O_c(\rho)}$ is bound at infinity. Thus, the following hypotheses stand:

- $L_\ell(\rho)$ has simple poles $\{\omega_n\}$, zeros of the $O_c(\rho)$,

- $\frac{L_\ell(\rho)}{\rho}$ has residues of 1 at the $\{\omega_n\}$ poles,
- $\exists M \in \mathbb{R}$ such as $|L_\ell(\rho)| < M|z|$ on circles $\mathcal{C}_D$ as $D \longrightarrow \infty$

By removing the pole of $\frac{O_c^{(1)}(\rho)}{O_c(\rho)}$ at zero, these hypotheses ensure Mittag-Leffler expansion (C.14) is verified:

$$\frac{L_c(\rho)}{\rho} = \frac{L_c(0)}{\rho} + L_c^{(1)}(0) + \sum_{n\geq 1}\left[\frac{1}{\rho-\omega_n} + \frac{1}{\omega_n}\right] \tag{C.14}$$

R.G. Thomas' recurrence formula (C.11) implies that $L_c(\rho_c)$ satisfies $L_\ell(0) = -\ell$, for both neutral and charged particles. Moreover, evaluating $\frac{O_c^{(1)}(\rho)}{O_c(\rho)}$ at the limit of infinity yields:

$$L_c^{(1)}(0) + \sum_{k\geq 1}\frac{1}{\omega_k} = \lim_{\rho\to\infty}\left(\frac{L_c(\rho)}{\rho}\right) = \lim_{\rho\to\infty}\left(\frac{O_c^{(1)}(\rho)}{O_c(\rho)}\right) = \mathrm{i} \tag{C.15}$$

so that the Mittag-Leffler expansion (C.14) takes the desired form of (D.7).

□

Theorem 5 establishes, for the first time, the Mittag-Leffler expansion of $L_c^0(\rho_c)$ as a function of the roots $\{\omega_n\}$ of the outgoing wavefunctions $O_c(\rho)$, which are Hankel functions in the neutral particle case, and Whittaker functions in the more general case of charged particles (c.f. equations (2.14b) and (2.17) section III.2.b. p.269 of [214]). Extensive literature covers these functions [51, 250]. In the neutral particles case of Hankel functions [201, 122, 115, 116, 202, 286] the search for their zeros established that the reduced logarithmic derivative of the outgoing wave function is a rational function of k_c of degree ℓ. In the general case, there are indeed ℓ zeros to the Hankel function for $|\Re[\rho]| < \ell$, but for $|\Re[\rho]| > \ell$ there exists an infinity of zeros, on or close to the real axis (c.f. FIG.1&2 of [122]). However, in our particular case of physical (i. e. integer) angular momenta $\ell \in \mathbb{Z}$, the order of the Hankel function happens to be a half-integer: $H_{\ell+1/2}$. Crucially, Hankel functions of half integer order constitute a very special case: they have only a finite number of zeros in the finite complex plane, where all but ℓ of them have migrated to infinity. This behavior is reported in [115], where one can observe how the zeros of H_ν as ν varies between two consecutive integer values. Here, we report in table C.2 all the algebraically solvable cases of up to $\ell = 4$, past which $\{\omega_n\}$ are not guaranteed to be solvable by radicals (c.f. Abel-Ruffini theorem and Galois theory).

Another perspective over this property is that in the neutral particle case, $\eta = 0$ and $L_{\ell=0}(\rho) = \mathrm{i}\rho$, so that recurrence relation (C.11) entails $L_c(\rho_c)$ – and thus the $\boldsymbol{L^0}$ function – is a rational fraction in ρ_c, whose irreducible expressions are reported in table C.1 along with their partial fraction decomposition, established in theorem 5, and whose poles are documented in table C.2. Moreover, since definition (C.9) entails $\frac{\partial O_c}{\partial \rho}(\rho) = \frac{L_c}{\rho}(\rho)O_c(\rho)$, a direct integration of (C.14) yields (with the correct

Table C.2: Roots $\{\omega_n\}$ of the outgoing wave function $O_\ell(\rho)$, algebraic solutions for neutral particles up to $\ell \leq 4$.

$\ell = 0$: s-wave	$\left\{\omega_0^{\ell=0}\right\} = \{\emptyset\}$
$\ell = 1$: p-wave	$\left\{\omega_1^{\ell=1}\right\} = \left\{-\mathrm{i}\right\}$
$\ell = 2$: d-wave	$\left\{\omega_1^{\ell=2}, \omega_2^{\ell=2}\right\} = \left\{\frac{1}{2}\left(-\sqrt{3} - 3\mathrm{i}\right) \quad , \quad \frac{1}{2}\left(\sqrt{3} - 3\mathrm{i}\right)\right\}$
$\ell = 3$: f-wave	$\left\{\omega_1^{\ell=3}, \omega_2^{\ell=3}, \omega_3^{\ell=3}\right\}$
	$\omega_1^{\ell=3} \triangleq -2\mathrm{i} - \frac{1}{2}\left(\sqrt{3} - \mathrm{i}\right)\sqrt[3]{\frac{1}{2}\left(1+\sqrt{5}\right)} - \frac{\sqrt{3}+\mathrm{i}}{2^{2/3}\sqrt[3]{1+\sqrt{5}}}$
	$\omega_2^{\ell=3} \triangleq \mathrm{i}\left(-2 + \sqrt[3]{\frac{2}{1+\sqrt{5}}} - \sqrt[3]{\frac{1}{2}\left(1+\sqrt{5}\right)}\right)$
	$\omega_3^{\ell=3} \triangleq -2\mathrm{i} + \frac{1}{2}\left(\sqrt{3} + \mathrm{i}\right)\sqrt[3]{\frac{1}{2}\left(1+\sqrt{5}\right)} + \frac{\sqrt{3}-\mathrm{i}}{2^{2/3}\sqrt[3]{1+\sqrt{5}}}$
$\ell = 4$: g-wave	$\left\{\omega_1^{\ell=4}, \omega_2^{\ell=4}, \omega_3^{\ell=4}, \omega_4^{\ell=4}\right\}$

$$\omega_1^{\ell=4} \triangleq -\frac{5\mathrm{i}}{2} - \frac{1}{2}\sqrt{5 + \frac{15^{2/3}}{\sqrt[3]{\frac{1}{2}\left(5+\mathrm{i}\sqrt{35}\right)}} + \sqrt[3]{\frac{15}{2}\left(5+\mathrm{i}\sqrt{35}\right)}}$$
$$- \frac{1}{2}\sqrt{10 - \frac{15^{2/3}}{\sqrt[3]{\frac{1}{2}\left(5+\mathrm{i}\sqrt{35}\right)}} - \sqrt[3]{\frac{15}{2}\left(5+\mathrm{i}\sqrt{35}\right)} - \frac{10\mathrm{i}}{\sqrt{5+\frac{15^{2/3}}{\sqrt[3]{\frac{1}{2}\left(5+\mathrm{i}\sqrt{35}\right)}}+\sqrt[3]{\frac{15}{2}\left(5+\mathrm{i}\sqrt{35}\right)}}}}$$

$$\omega_2^{\ell=4} \triangleq -\frac{5\mathrm{i}}{2} - \frac{1}{2}\sqrt{5 + \frac{15^{2/3}}{\sqrt[3]{\frac{1}{2}\left(5+\mathrm{i}\sqrt{35}\right)}} + \sqrt[3]{\frac{15}{2}\left(5+\mathrm{i}\sqrt{35}\right)}}$$
$$+ \frac{1}{2}\sqrt{10 - \frac{15^{2/3}}{\sqrt[3]{\frac{1}{2}\left(5+\mathrm{i}\sqrt{35}\right)}} - \sqrt[3]{\frac{15}{2}\left(5+\mathrm{i}\sqrt{35}\right)} - \frac{10\mathrm{i}}{\sqrt{5+\frac{15^{2/3}}{\sqrt[3]{\frac{1}{2}\left(5+\mathrm{i}\sqrt{35}\right)}}+\sqrt[3]{\frac{15}{2}\left(5+\mathrm{i}\sqrt{35}\right)}}}}$$

$$\omega_3^{\ell=4} \triangleq -\frac{5\mathrm{i}}{2} + \frac{1}{2}\sqrt{5 + \frac{15^{2/3}}{\sqrt[3]{\frac{1}{2}\left(5+\mathrm{i}\sqrt{35}\right)}} + \sqrt[3]{\frac{15}{2}\left(5+\mathrm{i}\sqrt{35}\right)}}$$
$$- \frac{1}{2}\sqrt{10 - \frac{15^{2/3}}{\sqrt[3]{\frac{1}{2}\left(5+\mathrm{i}\sqrt{35}\right)}} - \sqrt[3]{\frac{15}{2}\left(5+\mathrm{i}\sqrt{35}\right)} + \frac{10\mathrm{i}}{\sqrt{5+\frac{15^{2/3}}{\sqrt[3]{\frac{1}{2}\left(5+\mathrm{i}\sqrt{35}\right)}}+\sqrt[3]{\frac{15}{2}\left(5+\mathrm{i}\sqrt{35}\right)}}}}$$

$$\omega_4^{\ell=4} \triangleq -\frac{5\mathrm{i}}{2} + \frac{1}{2}\sqrt{5 + \frac{15^{2/3}}{\sqrt[3]{\frac{1}{2}\left(5+\mathrm{i}\sqrt{35}\right)}} + \sqrt[3]{\frac{15}{2}\left(5+\mathrm{i}\sqrt{35}\right)}}$$
$$+ \frac{1}{2}\sqrt{10 - \frac{15^{2/3}}{\sqrt[3]{\frac{1}{2}\left(5+\mathrm{i}\sqrt{35}\right)}} - \sqrt[3]{\frac{15}{2}\left(5+\mathrm{i}\sqrt{35}\right)} + \frac{10\mathrm{i}}{\sqrt{5+\frac{15^{2/3}}{\sqrt[3]{\frac{1}{2}\left(5+\mathrm{i}\sqrt{35}\right)}}+\sqrt[3]{\frac{15}{2}\left(5+\mathrm{i}\sqrt{35}\right)}}}}$$

multiplicative constant):

$$O_\ell(\rho)=\mathrm{e}^{\mathrm{i}\left(\rho+\frac{1}{2}\ell\pi\right)}\frac{\prod_{n\geq 1}\left(\rho-\omega_n\right)}{\rho^\ell} \tag{C.16}$$

This expression converges for neutral particles as the number of poles is finite, so using Vieta's formulas with the denominator of $L_\ell(\rho)$ enables to construct the developed forms reported in table C.1.

Similar results do not hold for the charged particules case of Whittaker functions, where there always exists an infinity of zeros to the outgoing wavefunction [143, 150], and where a Coulomb phase shift would be present for any Weierstrass expansion in infinite product of type (C.16).

C.3.3 Internal region parameters

Projections upon the orthonormal basis formed by the eigenvectors of the Hamiltonian completed by the Bloch operator $\mathcal{L}$ allow for the parametrization of the interaction Hamiltonian in the internal region by means of the Wigner-Eisenbud *resonance parameters* [79], composed of both the real *resonance energies* $E_\lambda \in \mathbb{R}$, and the real *resonance widths* $\gamma_{\lambda,c} \in \mathbb{R}$. From the latter, and using Brune's notation $\boldsymbol{e} \triangleq \mathbf{diag}\left(E_\lambda\right)$ and $\boldsymbol{\gamma} \triangleq \mathbf{mat}\left(\gamma_{\lambda,c}\right)_{\lambda,c}$, the *Channel R matrix*, $\boldsymbol{R}$, is defined as

$$R_{c,c'} \triangleq \sum_{\lambda=1}^{N_\lambda}\frac{\gamma_{\lambda,c}\gamma_{\lambda,c'}}{E_\lambda-E} \quad \text{i.e.} \quad \boldsymbol{R} \;=\; \boldsymbol{\gamma}^{\mathsf{T}}\left(\boldsymbol{e}-E\mathbb{I}\right)^{-1}\boldsymbol{\gamma} \tag{C.17}$$

and the *Level A matrix*, $\boldsymbol{A}$, is defined through its inverse:

$$\boldsymbol{A^{-1}} \triangleq \boldsymbol{e}-E\mathbb{I}-\boldsymbol{\gamma}\left(\boldsymbol{L}-\boldsymbol{B}\right)\boldsymbol{\gamma}^{\mathsf{T}} \tag{C.18}$$

where $\boldsymbol{B} = \mathbf{diag}\left(B_c\right)$ is the arbitrary outgoing-wave boundary condition, which is arbitrary, constant (non-dependent on the wavenumber), and for which Bloch demonstrated that if it is real (i.e. $B_c \in \mathbb{R}$), then the Wigner-Eisenbud resonance parameters are also real [79]. From this, one can view the Wigner-Eisenbud parameters as the set of channel radii a_c, boundary conditions B_c, resonance widths $\gamma_{\lambda,c}$, resonance energies E_λ and thresholds E_{T_c}. This set of parameters $\{a_c, B_c, \gamma_{\lambda,c}, E_\lambda, E_{T_c}\}$ fully determines the energy (or wavenumber) dependence of the scattering matrix $\boldsymbol{U}$ through equation (E.14).

C.3.4 Scattering matrix and R-matrix parameters

As explained by Claude Bloch, the genius of R-matrix theory stems from it combining the internal region with the external region to simply express the resulting scattering matrix $\boldsymbol{U}$ (also called *collision matrix*, and often noted $\boldsymbol{S}$, though we here stick to

the Lane & Thomas scripture $\boldsymbol{U}$ for the scattering matrix) as:

$$\begin{aligned}\boldsymbol{U} &= \boldsymbol{O}^{-1}\boldsymbol{I} + \boldsymbol{w}\boldsymbol{\rho}^{1/2}\boldsymbol{O}^{-1}\left[\boldsymbol{R}^{-1} + \boldsymbol{B} - \boldsymbol{L}\right]^{-1}\boldsymbol{O}^{-1}\boldsymbol{\rho}^{1/2} \\ &= \boldsymbol{O}^{-1}\boldsymbol{I} + 2\mathrm{i}\boldsymbol{\rho}^{1/2}\boldsymbol{O}^{-1}\boldsymbol{\gamma}^{\mathsf{T}}\boldsymbol{A}\boldsymbol{\gamma}\boldsymbol{O}^{-1}\boldsymbol{\rho}^{1/2} \\ &= \boldsymbol{O}^{-1}\boldsymbol{I} + 2\mathrm{i}\boldsymbol{\rho}^{1/2}\boldsymbol{O}^{-1}\boldsymbol{R}_L\boldsymbol{O}^{-1}\boldsymbol{\rho}^{1/2}\end{aligned} \tag{C.19}$$

The equivalence between these channel and level matrix expressions stems from the identity $\left[\mathbb{I} - \boldsymbol{R}\boldsymbol{L}^{\boldsymbol{0}}\right]^{-1}\boldsymbol{R} = \boldsymbol{\gamma}^{\mathsf{T}}\boldsymbol{A}\boldsymbol{\gamma}$ which defines the *Kapur-Peierls operator*, $\boldsymbol{R}_L$:

$$\boldsymbol{R}_L \triangleq \left[\mathbb{I} - \boldsymbol{R}\boldsymbol{L}^{\boldsymbol{0}}\right]^{-1}\boldsymbol{R} = \boldsymbol{\gamma}^{\mathsf{T}}\boldsymbol{A}\boldsymbol{\gamma} \tag{C.20}$$

Identity (C.20) can be proved by means of the *Woodbury identity*:

$$\left[\boldsymbol{A} + \boldsymbol{B}\boldsymbol{D}^{-1}\boldsymbol{C}\right]^{-1} = \boldsymbol{A}^{-1} - \boldsymbol{A}^{-1}\boldsymbol{B}\left[\boldsymbol{D} + \boldsymbol{C}\boldsymbol{A}^{-1}\boldsymbol{B}\right]^{-1}\boldsymbol{C}\boldsymbol{A}^{-1} \tag{C.21}$$

Indeed, the application of the Woodbury identity (C.21) to equality (C.20), with $\boldsymbol{A}_{\text{Wood}} = \boldsymbol{R}^{-1}$, $\boldsymbol{B}_{\text{Wood}} = \boldsymbol{L}^{\boldsymbol{0}}$, and $\boldsymbol{C}_{\text{Wood}} = \boldsymbol{D}_{\text{Wood}} = \mathbb{I}$ yields

$$\begin{aligned}\left[\mathbb{I} - \boldsymbol{R}\boldsymbol{L}^{\boldsymbol{0}}\right]^{-1}\boldsymbol{R} &= \boldsymbol{R} + \boldsymbol{R}\boldsymbol{L}^{\boldsymbol{0}}\left[\mathbb{I} - \boldsymbol{R}\boldsymbol{L}^{\boldsymbol{0}}\right]^{-1}\boldsymbol{R} \\ &= \boldsymbol{\gamma}^{\mathsf{T}}\left[(\boldsymbol{e} - E\mathbb{I})^{-1} + (\boldsymbol{e} - E\mathbb{I})^{-1}\boldsymbol{\gamma}\boldsymbol{L}^{\boldsymbol{0}}\times\right. \\ &\left.\left[\mathbb{I} - \boldsymbol{\gamma}^{\mathsf{T}}(\boldsymbol{e} - E\mathbb{I})^{-1}\boldsymbol{\gamma}\boldsymbol{L}^{\boldsymbol{0}}\right]^{-1}\boldsymbol{\gamma}^{\mathsf{T}}(\boldsymbol{e} - E\mathbb{I})^{-1}\right]\boldsymbol{\gamma}\end{aligned}$$

and then reversely applying the Woodbury identity with $\boldsymbol{A}_{\text{Wood}} = (\boldsymbol{e} - E\mathbb{I})$, $\boldsymbol{B}_{\text{Wood}} = -\boldsymbol{\gamma}\boldsymbol{L}^{\boldsymbol{0}}$, $\boldsymbol{C}_{\text{Wood}} = \boldsymbol{\gamma}^{\mathsf{T}}$, and $\boldsymbol{D}_{\text{Wood}} = \mathbb{I}$ one now recognizes

$$\begin{aligned}\left[\mathbb{I} - \boldsymbol{R}\boldsymbol{L}^{\boldsymbol{0}}\right]^{-1}\boldsymbol{R} &= \boldsymbol{\gamma}^{\mathsf{T}}\left[(\boldsymbol{e} - E\mathbb{I}) - \boldsymbol{\gamma}\boldsymbol{L}^{\boldsymbol{0}}\boldsymbol{\gamma}^{\mathsf{T}}\right]^{-1}\boldsymbol{\gamma} \\ &= \boldsymbol{\gamma}^{\mathsf{T}}\boldsymbol{A}\boldsymbol{\gamma}\end{aligned}$$

Considering the multi-sheeted Riemann surface stemming from the analytic continuation of mapping (E.4), a truly remarkable and seldom noted property of the Wigner-Eisenbud formalism is that it completely de-entangles the branch points and the multi-sheeted structure — entirely present in the outgoing $\boldsymbol{O}$ and incoming $\boldsymbol{I}$ wave functions in the scattering matrix expression (E.14) — from the resonance parameters — which are the poles and residues of the channel matrix $\boldsymbol{R}$ as of equation (E.16), and these poles and residues live on a simple complex energy E sheet, with no branch points, and furthermore are all real. This de-entanglement of the branch-point structure gives the $\boldsymbol{R}$ matrix all its uniqueness in R-matrix theory. For instance, it does not translate to the level matrix $\boldsymbol{A}$, whose analytic continuation entails a multi-sheeted Riemann surface due to the introduction of the $\boldsymbol{L}^{\boldsymbol{0}}(\boldsymbol{\rho}(E))$ matrix function in its definition (E.18). The same is true for the alternative parameters, as will be discussed throughout this article.

C.3.5 Cross section and scattering matrix

General scattering theory expresses the incoming channel c and outgoing channel c' angle-integrated partial cross section $\sigma_{c,c'}(E)$ at energy E as a function of the scattering matrix $U_{c,c'}(E)$ according to eq.(3.2d) VIII.3. p.293 of [214]:

$$\sigma_{c,c'}(E) = \pi g_{J_c^\pi} \left| \frac{\delta_{c,c'} \mathrm{e}^{2\mathrm{i}\left(\sigma_{\ell_c}(\eta_c) - \sigma_0(\eta_c)\right)} - U_{c,c'}(E)}{k_c(E)} \right|^2 \tag{C.22}$$

where $g_{J_c^\pi} \triangleq \frac{2J+1}{(2I_1+1)(2I_2+1)}$ is the *spin statistical factor* defined eq.(3.2c) VIII.3. p.293, and where the *Coulomb phase shift*, $\sigma_{\ell_c}(\eta_c)$, is defined by Ian Thompson in eq.(33.2.10) of [250] for angular momentum ℓ_c and dimensionless Coulomb field parameter $\eta_c = \frac{Z_1 Z_2 e^2 M_\alpha a_c}{\hbar^2 \rho_c}$.

C.3.6 Invariance to arbiraty boundary parameter B_c

Having recalled essential results from R-matrix theory and the Wigner-Eisenbud parameters $\{a_c, B_c, \gamma_{\lambda,c}, E_\lambda, E_{T_c}\}$, we here focus on the fact that the fundamental physical operator describing the scattering event is the scattering matrix $\boldsymbol{U}$, and while the threshold energies E_{T_c} are intrinsic physical properties of the system, all the other Wigner-Eisenbud parameters a_c, B_c, $\gamma_{\lambda,c}$, and E_λ are interrelated and depend on arbitrary values of the channel radius a_c, or the boundary condition B_c. Though the channel radius a_c can arguably have some physical interpretation, this is not the case of the boundary condition B_c.

The dependence of the Wigner-Eisenbud parameters to the boundary condition B_c can be made explicit by fixing the channel radius a_c and performing a change of boundary condition $\boldsymbol{B} \to \boldsymbol{B'}$. This must entail a change in resonance parameters $E_\lambda \to E'_\lambda$ and $\gamma_{\lambda,c} \to \gamma'_{\lambda,c}$ which leaves the scattering matrix $\boldsymbol{U}$ unchanged.

As described by Barker in [67], such change of variables can be performed by noticing that $\boldsymbol{e} - \boldsymbol{\gamma}\left(\boldsymbol{B'} - \boldsymbol{B}\right)\boldsymbol{\gamma}^\mathsf{T}$ is a real symmetric matrix when both $\boldsymbol{B}$ and $\boldsymbol{B'}$ are real. The spectral theorem thus assures there exists a real orthogonal matrix $\boldsymbol{K}$ and a real diagonal matrix $\boldsymbol{D}$ such that

$$\boldsymbol{e} - \boldsymbol{\gamma}\left(\boldsymbol{B'} - \boldsymbol{B}\right)\boldsymbol{\gamma}^\mathsf{T} = \boldsymbol{K}^\mathsf{T}\boldsymbol{D}\boldsymbol{K} \tag{C.23}$$

The new parameters are then defined as

$$\boldsymbol{e'} \triangleq \boldsymbol{D} \qquad , \qquad \boldsymbol{\gamma'} \triangleq \boldsymbol{K}\boldsymbol{\gamma} \tag{C.24}$$

This change of variables satisfies:

$$\boldsymbol{\gamma'}^\mathsf{T}\boldsymbol{A}_{B'}\boldsymbol{\gamma'} = \boldsymbol{\gamma}^\mathsf{T}\boldsymbol{A}_B\boldsymbol{\gamma} \tag{C.25}$$

and thus leaves the scattering matrix unaltered through equation (E.14). Here $\boldsymbol{A}_{B'}$ designates the level matrix from parameters $\boldsymbol{e'}$, $\boldsymbol{\gamma'}$ and $\boldsymbol{B'}$. Equivalently, using the

Woodbury identity (C.21) shows that this change of variables verifies (c.f. eq.(4) of [67] or eq. (3.27) of [120]):

$$\boldsymbol{R}_B^{-1} + \boldsymbol{B} \;=\; \boldsymbol{R}_{B'}^{-1} + \boldsymbol{B'} \tag{C.26}$$

If the change of variable is infinitesimal, this invariance property translates into the following equivalent differential equations on the Wigner-Eisenbud $\boldsymbol{R}_B$ matrix,

$$\frac{\partial \boldsymbol{R}_B^{-1}}{\partial \boldsymbol{B}} + \mathbb{I} \;=\; \boldsymbol{0} \quad \text{i.e.} \quad \frac{\partial \boldsymbol{R}_B}{\partial \boldsymbol{B}} - \boldsymbol{R}_B^2 \;=\; \boldsymbol{0} \tag{C.27}$$

(c.f. eq (2.5b) section IV.2. p.274 of [214]) where we made use of the following property to prove the equivalence:

$$\frac{\partial \boldsymbol{M^{-1}}}{\partial z}(z) = -\boldsymbol{M^{-1}}(z) \left(\frac{\partial \boldsymbol{M}}{\partial z}(z) \right) \boldsymbol{M^{-1}}(z) \tag{C.28}$$

C.4 The alternative parametrization of R-matrix theory

Since the physics of the system are invariant with the choice of the arbitrary B_c boundary condition, Brune built on the work of Barker [67], Angulo and Descouvemont [59], to propose an alternative parametrization of R-matrix theory in which the alternative parameters, $\widetilde{\boldsymbol{e}}$ and $\widetilde{\boldsymbol{\gamma}}$, are boundary-condition independent [92].

C.4.1 Definition of the alternative $\boldsymbol{R}_S$ parametrization

Key to the alternative parametrization is the splitting of the outgoing-wave reduced logarithmic derivative – and thus the $\boldsymbol{L^0}$ matrix function – into real and imaginary parts, respectively the shift $\boldsymbol{S}$ and penetration $\boldsymbol{P}$ factors:

$$\boldsymbol{L} \;=\; \boldsymbol{S} + i\boldsymbol{P} \tag{C.29}$$

From there, and with slight changes from the notation in [92], the *alternative level matrix* $\widetilde{\boldsymbol{A}}$ is defined as:

$$\widetilde{\boldsymbol{A}}^{-1}(E) \;=\; \widetilde{\boldsymbol{G}} + \widetilde{\boldsymbol{e}} - E\left[\mathbb{I} + \widetilde{\boldsymbol{H}}\right] - \widetilde{\boldsymbol{\gamma}}\boldsymbol{L}(E)\widetilde{\boldsymbol{\gamma}}^{\mathsf{T}} \tag{C.30}$$

with

$$\widetilde{G}_{\lambda\mu} \;=\; \frac{\widetilde{\gamma_\mu}\left(S_\mu \widetilde{E_\lambda} - S_\lambda \widetilde{E_\mu}\right)\widetilde{\gamma_\lambda}}{\widetilde{E_\lambda} - \widetilde{E_\mu}} \tag{C.31}$$

and

$$\widetilde{H}_{\lambda\mu} \;=\; \frac{\widetilde{\gamma_\mu}\left(S_\mu - S_\lambda\right)\widetilde{\gamma_\lambda}}{\widetilde{E_\lambda} - \widetilde{E_\mu}} \tag{C.32}$$

such that with the new *alternative resonance parameters*, $\widetilde{E_i}$ and $\widetilde{\gamma_{i,c}}$, the following

equality stands,

$$\boldsymbol{\gamma}^{\mathsf{T}}\boldsymbol{A}\boldsymbol{\gamma} = \widetilde{\boldsymbol{\gamma}}^{\mathsf{T}}\widetilde{\boldsymbol{A}}\widetilde{\boldsymbol{\gamma}} \tag{C.33}$$

and thus the scattering matrix $\boldsymbol{U}$ is left unchanged.

These alternative parameters $\widetilde{e}$ and $\widetilde{\gamma}$ are no longer $\boldsymbol{B}$ dependent since the arbitrary boundary condition does not appear in the definition of the alternative level matrix, and from there in the parametrization of the scattering matrix.

Brune explains how to compute these alternative parameters from the Wigner-Eisenbud ones by finding the $\left\{\widetilde{E_i}\right\}$ scalars and $\{\boldsymbol{a_i}\}$ vectors that solve the Brune generalized eigenproblem [92]:

$$\left[\boldsymbol{e} - \boldsymbol{\gamma}\left(\boldsymbol{S}(\widetilde{E_i}) - \boldsymbol{B}\right)\boldsymbol{\gamma}^{\mathsf{T}}\right]\boldsymbol{a_i} = \widetilde{E_i}\boldsymbol{a_i} \tag{C.34}$$

where each eigenvector is normalized so that:

$$\boldsymbol{a_i}^{\mathsf{T}}\boldsymbol{a_i} = 1 \tag{C.35}$$

and defining the alternative parameters as:

$$\widetilde{\boldsymbol{e}} \triangleq \mathbf{diag}(\widetilde{E_i}) \qquad , \qquad \widetilde{\boldsymbol{\gamma}} \triangleq \boldsymbol{a}^{\mathsf{T}}\boldsymbol{\gamma} \tag{C.36}$$

where $\boldsymbol{a}$ is the matrix composed of the column eigenvectors: $\boldsymbol{a} \triangleq [\boldsymbol{a_1}, \ldots, \boldsymbol{a_i}, \ldots]$. The alternative level matrix is then defined as (c.f. equation (30), [92]):

$$\widetilde{\boldsymbol{A}}^{-1} \triangleq \boldsymbol{a}^{\mathsf{T}}\boldsymbol{A}^{-1}\boldsymbol{a} \tag{C.37}$$

which guarantees

$$\boldsymbol{A} = \boldsymbol{a}\widetilde{\boldsymbol{A}}\boldsymbol{a}^{\mathsf{T}} \tag{C.38}$$

and thus (D.3.2), and whose explicit expression is (C.30).

Note that searching for the general eigenvalues in (C.34) is equivalent to solving (apply the Sylvester determinant identity theorem, or c.f. eq. (49)-(50) in [92]):

$$\det\left(\boldsymbol{R}_S^{-1}(E)\right)\Big|_{E=\widetilde{E_i}} = 0 \tag{C.39}$$

i.e. solving for the poles of the $\boldsymbol{R}_S$ operator defined as

$$\boldsymbol{R}_S^{-1} \triangleq \boldsymbol{R}^{-1} + \boldsymbol{B} - \boldsymbol{S} \tag{C.40}$$

The key insight is that in equation (22) of [92], Brune builds a square matrix $\boldsymbol{a} \triangleq [\boldsymbol{a_1}, \ldots, \boldsymbol{a_i}, \ldots, \boldsymbol{a_{N_\lambda}}]$, from which he is able to built the inverse alternative level matrix in his equation (30) of [92]. Brune justifies that this matrix is indeed square in the paragraphs between equations (46) and (47) by a three-step monotony argument depicted in FIG. 1 of [92]: 1) he assumes $S_c(E)$ is continuous (i.e. has no real poles); 2) he assumes $\frac{\partial S_c}{\partial E} \geq 0$, which is always true for negative energies and has recently proved to be true for positive energies in the case of repulsive Coulomb interactions [93] (a general proof is lacking for positive energy attractive Coulomb channels but has

always been verified in practice); 3) he invokes the eigenvalue repulsion behavior (no-crossing rule). If these three assumption are true, since the left-hand-side of (C.34) is a real symmetric matrix for any real energy value, then the spectral theorem guarantees there exists N_λ different real eigenvalues to it, and Brune's three assumptions above elegantly guarantee that there exists exactly N_λ real solutions to the generalized eiganvalue problem (C.34).

C.4.2 Ambiguity in shift and penetration factors definition for complex wavenumbers

There is a subtlety, however. A careful analysis reveals that the assumption that $S_c(E)$ is continuous or monotonously increasing is not unequivocal, and points to an open discussion in the field of R-matrix theory and nuclear cross section evaluations: how should we continue the scattering matrix $\boldsymbol{U}$ to complex wavenumbers $k_c \in \mathbb{C}$? Indeed, there is an ambiguity in the definition of the shift $S_c(E)$ and penetration $P_c(E)$ functions: two approaches are possible, and the community is not clear on which one is correct.

The first approach, legacy of Lane & Thomas, is to define the shift and penetration functions as the real and imaginary parts of the the outgoing-wave reduced logarithmic derivative:

$$\forall E \in \mathbb{C}\ , \begin{cases} \boldsymbol{S}(E) \triangleq & \Re\left[\boldsymbol{L}(E)\right] \in \mathbb{R} \\ \boldsymbol{P}(E) \triangleq & \Im\left[\boldsymbol{L}(E)\right] \in \mathbb{R} \end{cases} \tag{C.41}$$

This definition, introduced in [214] III.4.a. from equations (4.4) to (4.7c), finds its justification in the discussion between equations (2.1) and (2.2) of [214] VII.2, as it presents the advantage of automatically closing the sub-threshold channels since:

$$\forall E < E_{T_c}\ , \quad \Im\left[L_c(E)\right] = 0 \tag{C.42}$$

This elegant closure of channels comes at the cost of loosing the mathematical properties of the scattering matrix $\boldsymbol{U}(\boldsymbol{k})$: it is no longer analytic for complex wavenumbers $k_c \in \mathbb{C}$ (we will also show in a follow-up article [125] that this introduces non-physical spurious poles to the scattering matrix and brakes the generalized unitarity of Eden & Taylor [137]). In this Lane & Thomas approach (C.41), the function calculated for $\boldsymbol{S}$ changes from $S(E) \triangleq S_c(E)$ above threshold ($E \geq E_{T_c}$), to $S(E) \triangleq L_c(E)$ below threshold ($E < E_{T_c}$), because of (C.42). Moreover, definition (C.41) induces ramifications for both the shift and the penetration factors, as we show in lemma 1.

Lemma 1. *Branch-point definition of shift $S_c(E)$ and penetration $P_c(E)$ functions.*
Definition (C.41) of the shift $S_c(E)$ and penetration $P_c(E)$ functions, legacy of Lane & Thomas, entails:

- *branch-points for both $S_c(E)$ and $P_c(E)$, induced by the multi-sheeted nature of mapping (E.4),*

- *on the* $\left\{E,-\right\}$ *sheet below threshold* $E < E_{T_c}$*, the shift function* $S_c(E)$ *can present discontinuities and areas where* $\frac{\partial S_c}{\partial E}(E) < 0$*,*

- *in particular, for neutral particles of odd angular momenta* $\ell_c \equiv 1 \pmod 2$*, there is exactly one real sub-threshold pole to* $S_c(E)$ *on the* $\left\{E,-\right\}$ *sheet,*

- *everywhere other than sub-threshold* $\left\{E,-\right\}$ *sheet, and in particular on all of the* $\left\{E,+\right\}$ *sheet, the shift function* $S_c(E)$ *is continuous and monotonously increasing:* $\frac{\partial S_c}{\partial E}(E) \geq 0$*.*

Proof. The proof simply introduces the branch-structure of the $\rho_c(E)$ mapping (E.4), observable in figure C-1, into the Lane & Thomas definition (C.41). Historically, the study of the properties emanating from this definition have neglected the $\left\{E,-\right\}$ sheet. Importantly, it was recently proved that $\frac{\partial S_c}{\partial E}(E) \geq 0$ is true for most cases [93]. This proof did not consider the $\left\{E,-\right\}$ sheet of mapping (E.4). However, their proof of $\frac{\partial S_c}{\partial E}(E) \geq 0$ should still stand on the $\left\{E,+\right\}$ sheet. Moreover, the proof of lemma 2 establishes that all the discontinuity points, i.e. the real-energy poles, happen at sub-threshold energies, and in particular that neutral particles with odd angular moment introduce exactly one such sub-threshold discontinuity. This means that above threshold, both the shift $S_c(E)$ and penetration $P_c(E)$ functions are continuous. These behaviors are depicted in figure C-2. Finally, one will notice that the $\left\{E,+\right\}$ and $\left\{E,-\right\}$ sheets coincide above threshold for the shift function $S_c(E)$, and below threshold for the penetration function $P_c(E)$. For $P_c(E)$, this is because of property (C.42). For $S_c(E)$, this is because for real energies above threshold, both definitions (C.41) and (C.44) coincide, and lemma 2 shows the analytic continuation definition of $S_c(E)$ is function of $\rho_c^2(E)$, which unfolds the sheets of the Riemann mapping (E.4). Hence, for above-threshold energies, this property still stands for the Lane & Thomas definition of the shift factor $S_c(E)$. □

The second approach to defining the shift and penetration functions, $\boldsymbol{S}$ and $\boldsymbol{P}$, consists of performing analytic continuation of the scattering matrix $\boldsymbol{U}$ to complex energies $E \in \mathbb{C}$. This is implicit in the Kapur-Peierls or Siegert-Humblet expansions (c.f. [**?**, 180] and section sections IX.2.c-d-e p.297-298 of [214]), and an abundant literature revolves around the analytic properties of the scattering matrix in the complex plane, including the vast Theory of Nuclear Reaction of Humblet and Rosenfeld [185, 289, 181, 182, 195, 183, 230, 290, 231], or the general unitarity condition on the multi-sheeted Riemann surface introduced by Eden and Taylor in [137]. In this approach, energy dependence of the shift and penetration factors for positive energies are analytically continued into the complex plane, i.e.

$$\boldsymbol{S} : \left\{ \begin{array}{ccc} \mathbb{C} & \mapsto & \mathbb{C} \\ E & \rightarrow & S_c(E) \end{array} \right. \text{ s.t. } S(E) = S_c(E),\ \forall (E - E_{T_c}) \in \mathbb{R}_+ \tag{C.43}$$

so that they can be computed from the outgoing wavefunction reduced logarithmic

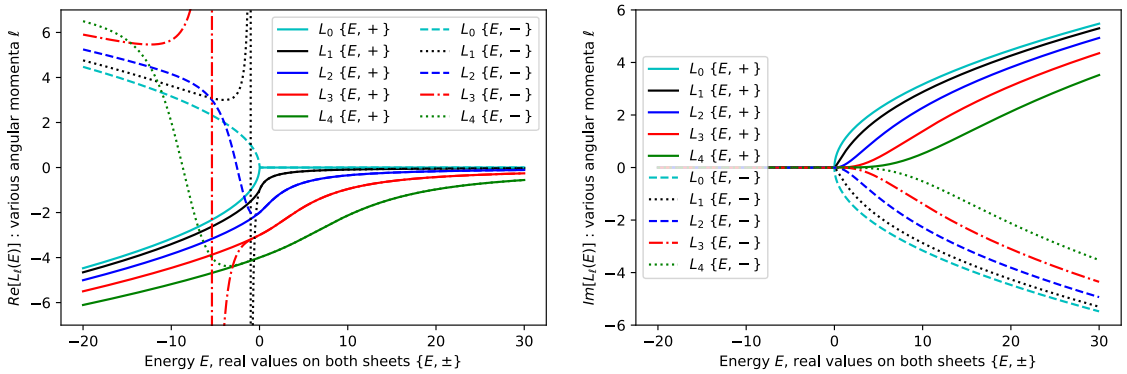

(a) Real part $\Re\big[L_\ell(E)\big]$, on both $\{E, \pm\}$ sheets. (b) Imaginary part $\Im\big[L_\ell(E)\big]$, on both $\{E, \pm\}$ sheets.

Figure C-2: Real and imaginary parts of the reduced logarithmic derivative of the outgoing wavefunction $L_\ell(E)$, for semi-classical massive neutral particles (table C.1) energy-wavenumber mapping (E.2), for different angular momenta $\ell \in [\![1, 4]\!]$. These real and imaginary parts were used by Lane & Thomas to define the shift and penetration functions, $S_\ell(E)$ and $P_\ell(E)$, as (C.41). This definition commands branch points from mapping (E.2) (c.f. figure C-1). $\Re\big[L_\ell(E)\big]$ presents sub-threshold discontinuities (for odd angular momenta ℓ) and non-monotonic behavior (for even angular momenta ℓ) below threshold on the $\{E, -\}$ sheet. Units such that $\rho_0 = 1$. Threshold set at zero: $E_{T_c} = 0$.

derivative $\boldsymbol{L}$ by analytic continuation in wavenumber space $k_c \in \mathbb{C}$:

$$\forall \rho_c \in \mathbb{C}\ , \begin{cases} S_c(\rho_c) \triangleq \frac{L_c(\rho_c)+[L_c(\rho_c^*)]^*}{2} \in \mathbb{C} \\ P_c(\rho_c) \triangleq \frac{L_c(\rho_c)-[L_c(\rho_c^*)]^*}{2\mathrm{i}} \in \mathbb{C} \end{cases} \tag{C.44}$$

From this definition (C.44), and using the recurrence relation (C.11), one readily finds the expressions for the neutral particles shift and penetration factors documented in table C.3. Critically, both definitions (C.41) and (C.44) will yield the same shift $S_c(E)$ and penetration $P_c(E)$ functions for real energies above threshold $E \geq E_{T_c}$. Moreover, definition (C.44) bestows interesting analytic properties onto the shift and penetration functions, here established in lemma 2.

Lemma 2. *Analytic continuation definition of shift $S_c(E)$ and penetration $P_c(E)$ functions.*
When defined by analytic continuation (C.44), the shift function, $S_c(\rho)$, satisfies the Mittag-Leffler expansion:

$$S_c(\rho) = -\ell + \sum_{\substack{n \geq 1 \\ \arg(\omega_n) \in \left[-\frac{\pi}{2}, 0\right]}} \frac{\rho^2}{\rho^2 - \omega_n^2} + \frac{\rho^2}{\rho^2 - \omega_n^{*2}} \tag{C.45}$$

where the poles $\{\omega_n\}$ are only the lower-right-quadrant roots – i.e. such that $\arg(\omega_n) \in [-\frac{\pi}{2}, 0]$ – of the outgoing wave function $O_c(\rho_c)$. In the neutral particles cases, these are reported in table C.2. Given $\rho_c(E)$ mapping (E.4), this entails $S_c(E)$:

Table C.3: Shift $S_\ell(\rho)$, $S_\ell^0(\rho) \triangleq S_\ell(\rho) - B_\ell$ using $B_\ell = -\ell$, and $P_\ell(\rho)$ irreducible forms for neutral particles, for angular momenta $0 \leq \ell \leq 4$, all defined from analytic continuation (C.44).

	$S_\ell(\rho)$	$S_\ell^0(\rho) \triangleq S_\ell(\rho) - B_\ell$ (recurrence for $B_\ell = -\ell$)	$P_\ell(\rho)$
ℓ	$S_\ell(\rho) = \frac{\rho^2(\ell - S_{\ell-1}(\rho))}{(\ell - S_{\ell-1}(\rho))^2 + P_{\ell-1}(\rho)^2} - \ell$	$S_\ell^0(\rho) \triangleq S_\ell(\rho) + \ell = \frac{\rho^2\left(2\ell - 1 - S_{\ell-1}^0(\rho)\right)}{\left(2\ell - 1 - S_{\ell-1}^0(\rho)\right)^2 + P_{\ell-1}(\rho)^2}$	$P_\ell(\rho) = \frac{\rho P_{\ell-1}(\rho)}{(\ell - S_{\ell-1}(\rho))^2 + P_{\ell-1}(\rho)^2}$
0	0	0	ρ
1	$-\frac{1}{1+\rho^2}$	$\frac{\rho^2}{1+\rho^2}$	$\frac{\rho^3}{1+\rho^2}$
2	$-\frac{18+3\rho^2}{9+3\rho^2+\rho^4}$	$\frac{3\rho^2+2\rho^4}{9+3\rho^2+\rho^4}$	$\frac{\rho^5}{9+3\rho^2+\rho^4}$
3	$-\frac{675+90\rho^2+6\rho^4}{225+45\rho^2+6\rho^4+\rho^6}$	$\frac{45\rho^2+12\rho^4+3\rho^6}{225+45\rho^2+6\rho^4+\rho^6}$	$\frac{\rho^7}{225+45\rho^2+6\rho^4+\rho^6}$
4	$-\frac{44100+4725\rho^2+270\rho^4+10\rho^6}{11025+1575\rho^2+135\rho^4+10\rho^6+\rho^8}$	$\frac{1575\rho^2+270\rho^4+30\rho^6+4\rho^8}{11025+1575\rho^2+135\rho^4+10\rho^6+\rho^8}$	$\frac{\rho^9}{11025+1575\rho^2+135\rho^4+10\rho^6+\rho^8}$

- *unfolds the sheets of $\rho_c(E)$ mapping (E.4),*
- *is purely real for real energies: $\forall E \in \mathbb{R},\ S_c(E) \in \mathbb{R}$.*

The penetration function, $P_c(\rho)$, satisfies the Mittag-Leffler expansion:

$$P_c(\rho) = \rho\left[1 - \mathrm{i} \sum_{\substack{n\geq 1 \\ \arg(\omega_n)\in\left[-\frac{\pi}{2},0\right]}} \frac{\omega_n}{\rho^2 - \omega_n^2} - \frac{\omega_n^*}{\rho^2 - \omega_n^{*2}}\right] \tag{C.46}$$

which in turn entails that $P_c(E)$:

- *is purely real for above threshold energies: $\forall E > E_{T_c},\ P_c(E) \in \mathbb{R}$,*
- *is purely imaginary for sub-threshold energies: $\forall E < E_{T_c},\ P_c(E) \in \mathrm{i}\mathbb{R}$,*

In the neutral particles case, Mittag-Leffler expansions (C.45) and (C.46) are the partial fraction decompositions of the rational fractions reported in table C.3, and for all odd angular momenta $\ell_c \equiv 1 \pmod 2$, both have one, shared, real sub-threshold pole.

Proof. The proof uses theorem 5, where we establish the Mittag-Leffler expansion (C.14) of the reduced logarithmic derivative $L_c(\rho_c)$. We recall the conjugacy relations of the outgoing and incoming wavefunctions (eq. (2.12), VI.2.c. in [214]), whereby, for any channel c:

$$\begin{aligned} \left[O_c(k_c^*)\right]^* = I_c(k_c) \quad &, \quad \left[I_c(k_c^*)\right]^* = O_c(k_c) \\ O_c(-k_c) = I_c(k_c) \quad &, \quad I_c(-k_c) = O_c(k_c) \\ -O_c^{(1)}(-k_c) = I_c^{(1)}(k_c) \quad &, \quad -I_c^{(1)}(-k_c) = O_c^{(1)}(k_c) \end{aligned} \tag{C.47}$$

where the third line was obtained by taking the derivative of the second. Properties (D.71) on the poles $\left\{\omega_n\right\}$ mean each pole ω_n on the lower right quadrant of the complex plane – i.e. such that $\arg(\omega_n) \in [-\frac{\pi}{2}, 0]$ – induces a specular pole $-\omega_n^*$. Dividing the poles in specular pairs, we can re-write the Mittag-Leffler expansion (C.14) as:

$$L_c(\rho) = -\ell + \mathrm{i}\rho + \sum_{\substack{n\geq 1 \\ \arg(\omega_n)\in\left[-\frac{\pi}{2},0\right]}} \frac{\rho}{\rho-\omega_n} + \frac{\rho}{\rho+\omega_n^*} \tag{C.48}$$

Plugging-in expression (C.48) into the shift function definition (C.44) readily yields (C.45) and (C.46).

Note that (C.45) unfolds the Riemann surface of mapping (E.4), whereas (C.46) factors-out the branch points so that all its branches are symmetric. In (C.46) we recognize the odd powers of ρ in the neutral particles case of table C.3, which do not unfold the Riemann sheets of mapping (E.4). These behaviors are illustrated in figure C-3.

In the neutral particles case, L_c is a rational fraction in ρ_c, and its denominator is of degree ℓ_c, as can be observed in table C.1, thus inducing ℓ_c poles, reported in table C.2. Since these poles $\left\{\omega_n\right\}$ must respect the specular symmetry: $\omega \longleftrightarrow -\omega_n^*$; it thus entails that these poles come in symmetric pairs. For neutral particles, odd angular momenta mean there is an odd number of poles $\left\{\omega_n\right\}$. For them to come in pairs thus imposes one is exactly imaginary $\omega_n = -\mathrm{i}x_n$, with $x_n \in \mathbb{R}_+$. When squared, this purely imaginary pole will introduce a real energy sub-threshold pole in both (C.45) and (C.46), through: $\frac{1}{\rho^2+x_n^2}$. □

An example to illustrate the difference between definitions (C.41) and (C.44) is depicted in figures C-2 and C-3. Consider the elemental case of a neutron channel with angular momentum $\ell_c = 1$, and let ρ_0 be the proportionality constant so that (E.2) is written $\rho(E) = \pm\rho_0\sqrt{E - E_{T_c}}$. Let us also set a zero threshold $E_{T_c} = 0$, for simplicity.

In this case, the legacy Lane & Thomas definition (C.41) corresponds to taking $S(E) \triangleq S_c(\rho_c(E)) = -\frac{1}{1+\rho_c^2}$ for above-threshold energies $E \geq E_{T_c}$, and switch to $S(E) \triangleq L_c(\rho_c(E)) = \frac{-1+\mathrm{i}\rho_c+\rho_c^2}{1-\mathrm{i}\rho_c}$ for sub-threshold energies $E < E_{T_c}$. Since the (E.2) mapping $\rho(E) = \pm\rho_0\sqrt{E - E_{T_c}}$ has two sheets, this means definition (C.41) entails: $S(E) \triangleq S_c(E) = -\frac{1}{1+\rho_0^2 E}$ for $E \geq E_{T_c}$, and $S(E) \triangleq L_c(E) = \frac{-1\pm\mathrm{i}\rho_0\sqrt{E}+\rho_0^2 E}{1\mp\mathrm{i}\rho_0\sqrt{E}}$ for $E < E_{T_c}$, which is a real quantity. Definition (C.41) thus introduces the ramifications reported in figure C-2. In particular, the full cyan line ($L_0\left\{E,+\right\}$ case) of our $\Re\Big[L_\ell(E)\Big]$ plot (figure C-2) corresponds to the uncharged case for angular momentum $\ell = 0$ reported as a full black curve in FIG.1, p.6 of [93]. Notice that all the $\Big\{E,+\Big\}$ sheet curves are continuous and monotonically increasing ($\frac{\partial S_c}{\partial E} \geq 0$), which is in accordance to the monotonic properties established in [93]. However, on the $\Big\{E,-\Big\}$ sheet below threshold, $\Re\Big[L_c(E)\Big]$ is no longer monotonic for even angular momenta ($\frac{\partial\Re\Big[L_c(E)\Big]}{\partial E} \geq 0$ does not hold), and is discontinuous in the case of odd angular

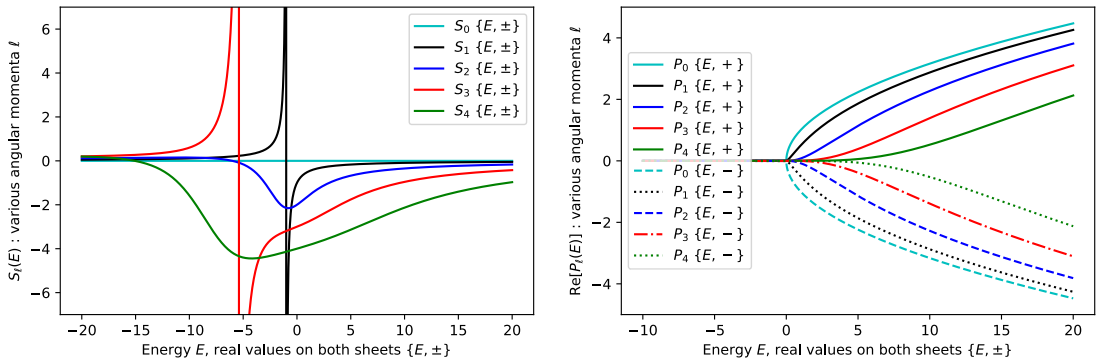

(a) Analytic shift function $S_\ell(E)$, for both $\{E,\pm\}$ sheets.

(b) Analytic penetration function real part $\Re[P_\ell(E)]$.

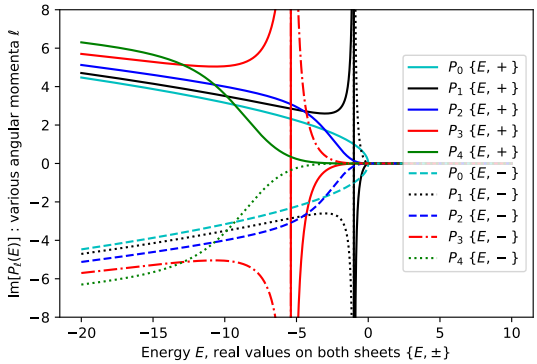

(c) Analytic penetration function imaginary part $\Im[P_\ell(E)]$.

Figure C-3: Analytic shift $S_\ell(E)$ and penetration $P_\ell(E)$ functions, definition (C.44), non-relativistic neutral particles (table C.3) $k_c(E)$ mapping (E.2), angular momenta $\ell \in [\![0,4]\!]$, zero threshold $E_{T_c} = 0$. The shift function $S_c(E)$ has no $\{E,\pm\}$ branches (proof in lemma 2), has discontinuities (odd ℓ) and non-monotonic behavior (even ℓ) below threshold. $P_\ell(E)$ has $\{E,\pm\}$ branches, is purely real above threshold, and purely imaginary below. Units such that $\rho_0 = 1$.

momenta.

In contrast, for our same elemental case, the analytic continuation definition (C.44) simply defines $S(E) \triangleq S_c(\rho_c(E)) = -\frac{1}{1+\rho_c^2}$ for all real or complex energies $E \in \mathbb{C}$, that is $S(E) \triangleq -\frac{1}{1+\rho_0^2 E}$. The later happens to have a real pole, which introduces a discontinuity, at $E_{\text{dis.}} = -\frac{1}{\rho_0^2}$, as can be seen in figure C-3. One can observe that all odd angular momenta are monotonous but have a real sub-threshold pole. For even angular momenta, $S_\ell(E)$ is continuous, monotonically increasing above-threshold, but $\frac{\partial S}{\partial E}(E) \geq 0$ does not hold below-threshold. For the penetration function $P_c(E)$, each ramification is monotonous, but in opposite, mirror direction. In figure C-3, the shift function $S_c(E)$ does not present branch points, as proved in lemma 2: it is a function of ρ^2 so no $\pm\sqrt{\cdot}$ choice is necessary in $\rho_c(E)$ mapping (C.4).

C.4.3 Number of alternative poles: existence of shadow poles

Definitions (C.41) and (C.43) have a major impact on the alternative parameters (C.36): they command that the number N_S of alternative poles $\left\{\widetilde{E_i}\right\}$, solutions to Brune's generalized eigenproblem (C.34), is greater than the N_λ previously found in [92]: i.e. $N_S \geq N_\lambda$. And this is regardless of whether definition (C.41) or (C.43) is chosen for the shift factor $S_c(E)$ when searching for these solutions.

The fundamental reason for this is that Brune's three-step monotony argument, which elegantly proved in [92] that there are exactly N_λ solutions to (C.34) and which we here recall in the last paragraph of section C.4.1, rests on two hypotheses on the shift function $S_c(E)$: 1) it is continuous (i.e. has no real poles), and; 2) it is monotonously increasing, i.e. $\frac{\partial S_c}{\partial E} \geq 0$. In [93], these two hypotheses have just been proved to hold true for energies above threshold $E \geq E_{T_c}$, i.e. for real wavenumbers $k_c \in \mathbb{R}$. Yet, we just established in lemmas 1 and 2 that proper accounting of the multi-sheeted nature of the Riemann surface created by mapping (E.4) shows these two hypotheses do not hold for sub-threshold energies $E < E_{T_c}$, where the wavenumber is purely imaginary from mapping (E.2). This engenders additional solutions to Brune's generalized eigenproblem (C.34), so that the number N_S of alternative poles $\left\{\widetilde{E_i}\right\}$ is in fact greater than the number of channels: $N_S \geq N_\lambda$. So how many N_S solutions are there? This depends on the R-matrix parameters and on the definition chosen for the shift function $S_c(E)$, as we now show in theorems 6 and 7, for definitions (C.41) and (C.43), respectively.

Theorem 6. *Alternative Branch Poles.*
Let the alternative branch poles $\left\{\widetilde{E_i}\right\}$ be the solutions of the Brune generalized eigenproblem (C.34), using the legacy Lane & Thomas definition (C.41) for the shift $S_c(E)$, and let N_S be the number of such solutions, then:

- *all the alternative branch poles are real, and reside on the 2^{N_c} sheets of the Riemann surface from (E.4) mapping: $\left\{\widetilde{E_i}, \underbrace{\pm, \ldots, \pm}_{N_c}\right\} \in \mathbb{R}^{N_S}$,*
- *exactly N_λ alternative branch poles are present on the $\left\{E, \underbrace{+, \ldots, +}_{N_c}\right\}$ sheet of mapping (E.4): these are the principal (or resonant) poles,*
- *additional alternative branch shadow poles can be found below threshold, $E < E_{T_c}$, on the $\left\{E, -\right\}$ sheets of mapping (E.4), depending on the values of the resonance parameters $\left\{E_\lambda, \gamma_{\lambda c}, B_c, E_{T_c}, a_c\right\}$ – though in a way that is invariant under change of boundary-condition B_c,*
- *each neutral particle, odd angular momentum $\ell_c \equiv 1 \pmod 2$, channel adds at least one alternative branch shadow pole below threshold on its $\left\{E, -\right\}$ sheet,*

so that the total number $N_S^{\pm}$ of alternative branch poles on all sheets of mapping (E.4) is greater or equal to the number N_λ of levels: $N_S^{\pm} \geq N_\lambda$.

Proof. Let us go about solving the Brune generalized eigenproblem (C.34), following the three-step argument of Brune (c.f. last paragraph of section C.4.1). We consider the left-hand side of (C.34). According to definition (C.41), the shift function is always real, even for complex wavenumbers $k_c \in \mathbb{C}$. Since by construction the Wigner-Eisenbud R-matrix parameters $\Big\{E_\lambda, \gamma_{\lambda c}, B_c, E_{T_c}, a_c\Big\}$ are also all real, this implies the right-hand side must be real to solve (C.34). Thus, all the alternative branch poles from definition (C.41) are real. To find them, we follow Brune's approach: for any energy E, on any of the 2^{N_c} sheets of mapping (E.4), the left-hand side is a real symmetric matrix, and its eigenvalue decomposition will thus yield N_λ real eigenvalues: $\Big\{\widetilde{E_i}(E)\Big\} \in \mathbb{R}$. We then have to vary the E value until these real eigenvalues cross the $E = E$ identity line in the right-hand side. In general, the full accounting of all the Riemann sheets from mapping (E.4) will entail solutions of the generalized Brune eigenproblem (C.34) on all sheets. These alternative branch poles should thus be reported with the choice of sheet from the mapping (E.4) for each channel: $\Big\{\widetilde{E_i}, +, -, \ldots, +\Big\}$.

We state in lemma 1 than on the $\Big\{E, +\Big\}$ sheet, $S_c(E)$ is indeed continuous and monotonously increasing. We can thus apply Brune's three-step argument: the N_λ eigenvalues of the left-hand side of (C.34) will satisfy $\frac{\partial \widetilde{E_i}}{\partial E}(E) \leq 0$, and thus each and every one of them will eventually cross the $E = E$ identity line exactly once as E varies continuously. On the $\Big\{E, +\Big\}$ sheet for all channels, there are thus exactly N_λ alternative poles: $\left\{\widetilde{E_i}, \underbrace{+, \ldots, +}_{N_c}\right\} \in \mathbb{R}^{N_\lambda}$

However, we showed in lemma 1 that $S_c(E)$ is not monotonous and can be discontinuous for sub-threshold energies $E < E_{T_c}$ on the $\Big\{E, -\Big\}$ sheet. So how many alternative poles are there on all sheets? Unfortunately, the number of solutions to Brune's generalized eigenproblem (C.34) will depend on the values of the resonance parameters $\Big\{E_\lambda, \gamma_{\lambda c}, B_c, E_{T_c}, a_c\Big\}$ – though in a way that is invariant under change of boundary-condition B_c, as made evident in (C.39) when considering invariance (C.26). That the number of solutions to (C.34) depends on the parameters can be observed in figure C-5.

For neutral particles odd momenta $\ell_c \equiv 1 \pmod 2$ channels, lemma 1 also showed there exist exactly one sub-threshold pole to $S_c(E)$ on the $\Big\{E, -\Big\}$ sheet of mapping (E.4). This pole will automatically cross the $E = E$ identity line of Brune's three-step argument twice, once below and once above threshold, adding an additional alternative shadow pole to the N_λ ones Brune found in [92]. This proves that there exists alternative shadow poles, just as shadow poles in the Siegert-Humblet parameters were revealed by G.Hale in [163, 245]. This behavior is illustrated in figure C-4. □

Theorem 6 establishes the existence of sub-threshold alternative shadow poles when the legacy Lane & Thomas definition (C.41) is chosen for the shift function

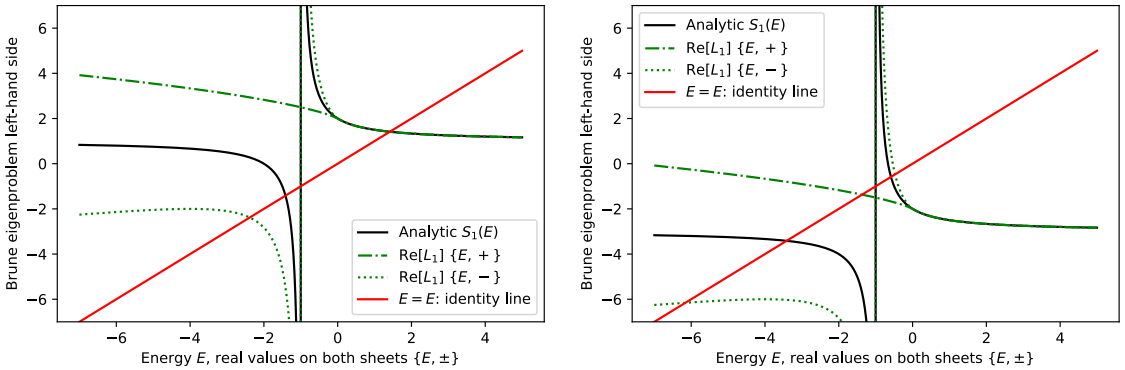

(a) Positive resonance energy $E_\lambda = 2$.

(b) Negative resonance energy $E_\lambda = -2$.

Figure C-4: Brune eigenproblem (C.54) for 1-level 1-channel p-wave: comparison of real solutions from definitions (C.41) versus (C.44), for angular momentum $\ell_c = 1$, neutral particles energy-wavenumber mapping (E.2), resonance width $\gamma_{\lambda,c} = 1$, using $B_c = -\ell_c$ convention and zero threshold $E_{T_c} = 0$. Units such that $\rho_0 = 1$. Since both have a real sub-threshold poles, both will yield two solutions (crossing the E=E diagonal), one above and one below the discontinuity. If at threshold energy E_{T_c} the left hand side of (C.54) is above the E=E diagonal, then the above-threshold solutions from both definitions coincide. In any case, the sub-threshold solutions differ. Behavior is analogous for all odd angular momenta $\ell_c \equiv 1 (\mathrm{mod} 2)$.

$S_c(E)$. If instead the analytic continuation definition (C.43) is chosen, we now show in theorem 7 that this unfolds the Riemann surface for the shift function $S_c(E)$ so that no branch points are required to define the alternative analytic parameters. We argue in a follow-up article that the analytic continuation approach (C.44) is the physically correct one [125], as it conserves the meromorphic properties of the Kapur-Peierls operator, which preserves general unitarity, cancels non-physical poles out of the scattering matrix $\boldsymbol{U}(E)$ otherwise spuriously introduced by the Lane & Thomas approach (C.41), allows for parameters transform under change of channel radius, and still should close cross sections below channel thresholds. Though there is no absolute consensus yet amongst the community as to which approach ought to be valid, both yield identical results for real energies above threshold (real wavenumbers $k_c \in \mathbb{R}$) in the case of exact R-matrix formalism (but not the Reich-Moore approximation as we show in section C.5).

Theorem 7. *Alternative Analytic Poles.*
Let the alternative analytic poles $\left\{\widetilde{E}_i\right\}$ *be the solutions of the Brune generalized eigenproblem (C.34), using the analytic continuation definition (C.44) for the shift* $S_c(E)$*, and let* N_S *be the number of such solutions, then:*

- *the alternative analytic poles are in general complex, and live on the single sheet of the unfolded Riemann surface from (E.4) mapping:* $\left\{\widetilde{E}_i\right\} \in \mathbb{C}^{N_S}$,
- *in the neutral particle case, there are exactly* N_S *complex alternative analytic*

poles with:

$$N_S = N_\lambda + \sum_{c=1}^{N_c} \ell_c \tag{C.49}$$

- *in the charged particles case, there is a countable infinity of complex alternative analytic poles:* $N_S = \infty$,
- *for each level* λ*, there exists a real principal (or resonant) alternative analytic pole. These* N_λ *principal poles are the same as the principal alternative branch poles of theorem 6,*
- *the number* $N_S^{\mathbb{R}}$ *of real alternative analytic poles,* $\left\{\widetilde{E_i}\right\} \in \mathbb{R}^{N_S^{\mathbb{R}}}$*, is greater than the number of levels,* $N_S^{\mathbb{R}} \geq N_\lambda$*, and depends on the values of the resonance parameters* $\left\{E_\lambda, \gamma_{\lambda c}, B_c, E_{T_c}, a_c\right\}$ *– though in a way that is invariant under change of boundary-condition* B_c*,*
- *each neutral particle, odd angular momentum* $\ell_c \equiv 1 \pmod 2$*, channel adds at least one real alternative analytic shadow pole below threshold,*

so that the number N_S *of complex and* $N_S^{\mathbb{R}}$ *of real alternative analytic poles is greater than the number* N_λ *of levels:* $N_S \geq N_S^{\mathbb{R}} \geq N_\lambda$.

Proof. The proof follows the one of theorem 6. However, when considering the left-hand side of (C.34), the shift function is now defined from analytic continuation definition (C.44), which in general entails $S_c(E)$ is a complex number. This entails the left-hand side of (C.34) is now a complex symmetric matrix. In general, a complex symmetric matrix is not diagonalizable, has no special properties on its spectrum, and we refer to reference literature on its Jordan canonical form and other properties [113, 119, 96, 292, 66, 151, 152]. Nonetheless, we know the left-hand side of (C.34) will be real-symmetric, thus diagonalizable, for real energies above threshold, which hints (but does not prove) it is probably a good assumption to assume the complex symmetric matrix to be non-defective in general. Regardless of the eigenvectors, we can search for the alternative poles $\left\{\widetilde{E_i}\right\}$ by solving problem (C.39) directly (c.f. discussion around equation (51) in [92]). Here, the analytic properties of definition (C.44), established in lemma 2, entail the determinant in (C.39) is a meromorphic operator of ρ^2, which unfolds mapping (E.4) so that all the solutions of (C.39) live on one single sheet.

In the case of N_c massive neutral channels, the shift factor $S_c(\rho)$ is a rational fraction in ρ^2 with a degree of ℓ_c (in E space) in the denominator, where ℓ_c is the angular momentum of the channel (c.f. table C.3 and lemma 2 with table C.2). The search for the poles of the $\boldsymbol{R}_S$ operator (C.39) will then yield N_S complex alternative poles $\left\{\widetilde{E_i}\right\} \in \mathbb{C}$ with $N_S = N_\lambda + \sum_{c=1}^{N_c} \ell_c$, as stated in (C.49). The intuition behind this number N_S is that both the R-matrix (E.16) and the diagonal matrix of shift functions, $\boldsymbol{S}(E) \triangleq \boldsymbol{diag}\left(S_c(E)\right)$, will each contribute their number of poles, N_λ and $\sum_c \ell_c$ respectively, adding them up to yield $N_S = N_\lambda + \sum_{c=1}^{N_c} \ell_c$ solutions (C.49) to the determinant problem (C.39). We achieved a formal proof of result (C.49), though

it is somewhat technical. It rests on the diagonal divisibility and capped multiplicities lemma 3, which we apply to the developed rational fraction $\det\left(\boldsymbol{R}_S^{-1}(E)\right)$ in (C.39), or directly to (C.34), depending on whether $N_\lambda \geq N_c$ or $N_c \geq N_\lambda$. In the (most common) case of $N_\lambda \geq N_c$, we develop $\det\left(\boldsymbol{R}_S^{-1}\right)(E) = \det\left(\boldsymbol{R}^{-1} - \boldsymbol{S^0}\right)(E)$ by n-linearity: $\det\left(\boldsymbol{R}^{-1} - \boldsymbol{S^0}\right) = \det\left(\boldsymbol{R}^{-1}\right)\det\left(\mathbb{I} - \boldsymbol{RS^0}\right)$ with $\det\left(\mathbb{I} - \boldsymbol{RS^0}\right) = 1 - \mathrm{Tr}\left(\boldsymbol{RS^0}\right) + \ldots + \mathrm{Tr}\left(\mathbf{Adj}\left(-\boldsymbol{RS^0}\right)\right) + \det\left(-\boldsymbol{RS^0}\right)$, so that: $\det\left(\boldsymbol{R}_S^{-1}\right) = \det\left(\boldsymbol{R}^{-1}\right) - \mathrm{Tr}\left(\mathbf{Adj}\left(\boldsymbol{R}^{-1}\right)\boldsymbol{S^0}\right) + \ldots - \mathrm{Tr}\left(\boldsymbol{R}^{-1}\mathbf{Adj}\left(\boldsymbol{S^0}\right)\right) + (-1)^{N_c}\det\left(\boldsymbol{S^0}\right)$. In the latter expression, $\boldsymbol{R}^{-1}(E) = \boldsymbol{\gamma}^+\left(\boldsymbol{e} - E\mathbb{I}\right)\boldsymbol{\gamma}^{\mathsf{T}^+}$ has no poles, so its determinant is a polynomial $\det\left(\boldsymbol{R}^{-1}\right)(E) \in \mathbb{C}[X]$. The rational fraction with greatest degree in the denominator is $\det\left(\boldsymbol{S^0}\right)(E) \in \mathbb{C}(X)$. For neutral particles $S_c^0(E) = \frac{s_c^0(E)}{d_c(E)}$, where the denominator is of degree $\ell_c = \deg\left(d_c(E)\right)$ in E space (c.f. table C.3), so that to rationalize the rational fraction $\det\left(\boldsymbol{R}_S^{-1}\right)(E) \in \mathbb{C}(X)$, we must multiply it by the denominator of $\det\left(\boldsymbol{S^0}\right)(E)$, which is $\prod_{c=1}^{N_c} d_c(E)$, a polynomial of degree $\sum_c \ell_c$. That is $\left(\prod_{c=1}^{N_c} d_c(E)\right) \times \det\left(\boldsymbol{R}_S^{-1}\right)(E) = \left(\prod_{c=1}^{N_c} d_c(E)\right) \times \det\left(\boldsymbol{R}^{-1}\right)(E) + \ldots + (-1)^{N_c}\prod_{c=1}^{N_c} s_c^0(E) \in \mathbb{C}[X]$. The dominant degree polynomial in this expression is $\left(\prod_{c=1}^{N_c} d_c(E)\right) \times \det\left(\boldsymbol{R}^{-1}\right)(E)$. In this expression, the total degree of the polynomial is the sum of the degrees of the product terms. We readily have $\deg\left(\prod_{c=1}^{N_c} d_c(E)\right) = \sum_c \ell_c$. For the degree of the determinant term $\det\left(\boldsymbol{R}^{-1}\right)(E)$, the application of diagonal divisibility and capped multiplicities lemma 3 stipulates that if $E_{\lambda_1} = E_{\lambda_2} = \ldots = E_{\lambda_{m_\lambda}}$, this multiplicity m_λ of the resonance energy value E_λ will be capped by N_c. In practice, this does not happen because the Wigner-Eisenbud resonance parameters E_λ are defined as different from each other $E_\lambda \neq E_{\mu\neq\lambda}$. This is no longer true in the case $N_c \geq N_\lambda$, where developing the determinant of (C.34) directly will similarly yield by n-linearity, and denoting $\boldsymbol{\Delta} \triangleq \boldsymbol{e} - E\mathbb{I}$ for clarity of scripture: $\det\left(\boldsymbol{\Delta} - \boldsymbol{\gamma S^0 \gamma^{\mathsf{T}}}\right) = \det\left(\boldsymbol{\Delta}\right) - \mathrm{Tr}\left(\mathbf{Adj}\left(\boldsymbol{\Delta}\right)\boldsymbol{\gamma S^0 \gamma^{\mathsf{T}}}\right) + \ldots - \mathrm{Tr}\left(\boldsymbol{\Delta}\ \mathbf{Adj}\left(\boldsymbol{\gamma S^0 \gamma^{\mathsf{T}}}\right)\right) + (-1)^{N_\lambda}\det\left(\boldsymbol{\gamma S^0 \gamma^{\mathsf{T}}}\right)$. Again, in the latter expression the rational fraction with the highest-degree denominator is $\det\left(\boldsymbol{\gamma S^0 \gamma^{\mathsf{T}}}\right)(E) \in \mathbb{C}(X)$. Applying the diagonal divisibility and capped multiplicities lemma 3 to it commands that if there are various channels with the same $S_c(E)$, for instance with the same ℓ_c and ρ_{0c}, their multiplicity of occurrence is capped by N_λ when rationalizing the fraction $\det\left(\boldsymbol{\gamma S^0 \gamma^{\mathsf{T}}}\right)(E) \in \mathbb{C}(X)$, so that $Q(E) \times \det\left(\boldsymbol{\gamma S^0 \gamma^{\mathsf{T}}}\right)(E) \in \mathbb{C}[X]$ is a polynomial, with $Q(E) \triangleq \left(\prod_{\substack{c=1 \\ d_c \neq d_{c\neq c'}}}^{N_c} d_c(E)\right) \times \left(\prod_{\substack{c=1 \\ d_c = d_{c\neq c'}}}^{\min\{N_c, N_\lambda\}} d_c(E)\right)$. In the developed expression of the polynomial $Q(E) \times \det\left(\boldsymbol{\Delta} - \boldsymbol{\gamma S^0 \gamma^{\mathsf{T}}}\right)$, the dominant degree term is now: $Q(E) \times \det\left(\boldsymbol{\Delta}\right)$, the degree of which is the sum of the degree of each term. The degree of $\det\left(\boldsymbol{\Delta}\right)$ is N_λ, whereas the degree of $Q(E)$ is $\deg\left(Q(E)\right) = \sum_{c=1|\ell_c\neq\ell_{c'}}^{N_c} \ell_c + \sum_{c=1|\ell_c=\ell_{c'}}^{\min\{N_\lambda, N_c\}} \ell_c$. Hence, we find back the expression (C.49) to be proved: $N_S = N_\lambda + \sum_{c=1}^{N_c} \ell_c$, but with the additional subtlety that the multiplicities (repeating occurrences) are capped, both

for $\sum_{\substack{E_\lambda \text{ multiplicity} \\ \text{capped at } N_c}} \deg\left(E_\lambda - \rho^2(E)\right)$ and for $\sum_{\substack{S_c \text{ multiplicity} \\ \text{capped at } N_\lambda}} \deg\left(d_c(\rho(E))\right)$, so that the final, exact number of complex eigenvalues to Brune's generalized eigenproblem (C.34) in the neutral channels case is:

$$N_S = N_\lambda + \sum_{\substack{S_c \text{ multiplicity} \\ \text{capped at } N_\lambda}} \ell_c \tag{C.50}$$

This means that if many channels, say m_c, have the same shift function $S_c = S_{c'}$, the resulting $\ell_c = \ell_{c'}$ will only be added $\min\{m_c, N_\lambda\}$ times in the sum (C.50).
A final technical note to state that this number N_S of poles (C.50) is true in E space, as we have showed in lemma 2 that definition (C.44) unfolds the Riemann sheet of (E.4). If we were performing this in ρ space, we would thus simply multiply the degrees by 2. This is not true if we were searching for the poles of the Kapur-Peierls operator $\boldsymbol{R}_L$, as the mapping of $\rho(E)$ is not one-to-one anymore. From table C.1, we would be able to perform the same analysis that yielded (C.50), but it would have to be in ρ space.

In the charged particles case, $S_c(E)$ has an infinity of poles (c.f. lemma 2). Extending our proof of (C.50) from the neutral particles to the charged particles ones would thus yield a countable infinity of complex alternative analytic poles.

A key question is: how many of the N_S complex alternative poles are real? To address it, we come back to the three-step Brune argument and look for real eigenvalues from the left-hand-side of (C.34) that will cross the right-hand side identity line $E = E$ for real values. Here again, Brune's three-step argument will guarantee at least N_λ real solutions. There are in general more solutions however, and as for the alternative shadow poles of theorem 6, the number of real alternative analytic poles, solutions to (C.34), will depend on the R-matrix parameters $\left\{E_\lambda, \gamma_{\lambda c}, B_c, E_{T_c}, a_c\right\}$, in a way that is invariant under change of boundary-condition B_c (plug-in invariance (C.26) into (C.39)). We illustrate various such cases in figure C-5. However, each neutral particle channel with odd angular momentum $\ell_c \equiv 1 \pmod 2$ will add at least one real sub-threshold solution to the N_λ ones, due to the real sub-threshold pole of $S_c(E)$ discovered in lemma 2. This behavior is depicted in figure C-4. □

Lemma 3. *Diagonal divisibility and capped multiplicities.*
Let $\boldsymbol{M} \in \mathbb{C}^{m\times n}$ be a complex matrix and $\boldsymbol{D}(z) \in \mathbf{Diag}_n\left(\mathbb{C}\left(X\right)\right)$ be a diagonal matrix of complex rational functions with simple poles, that is $D_{ij}(z) = \delta_{ij}\frac{R_i(z)\in\mathbb{C}[X]}{P_i(z)\in\mathbb{C}[X]}$, with $\mathbb{C}\left[X\right]$ designating the set of polynomials and $\mathbb{C}\left(X\right)$ the set of rational expressions, and we assume $P_i(z)$ has simple roots.
Let $Q(z) \in \mathbb{C}\left[X\right]$ be the denominator of $\det\left(\boldsymbol{D}\right)(z)$, but with all multiplicities capped by m, i.e.

$$Q(z) \triangleq \prod_{\substack{j=1 \\ P_j \neq P_{i\neq j}}}^{n} P_j(z) \prod_{\substack{i=1 \\ P_i = P_{i\neq j}}}^{\min\{n,m\}} P_i(z) \tag{C.51}$$

then $Q(z)$ is the denominator of $\det\Big(\boldsymbol{M}\boldsymbol{D}(z)\boldsymbol{M}^{\mathsf{T}}\Big)$*, so that:*

$$Q(z)\cdot\det\Big(\boldsymbol{M}\boldsymbol{D}(z)\boldsymbol{M}^{\mathsf{T}}\Big)\in\mathbb{C}\left[X\right] \tag{C.52}$$

Proof. Leibniz's determinant formula yields:

$$\det\Big(\boldsymbol{M}\boldsymbol{D}(z)\boldsymbol{M}^{\mathsf{T}}\Big)=\sum_{\sigma\in S_m}\epsilon(\sigma)\prod_{i=1}^{m}\sum_{j=1}^{n}M_{ij}M_{\sigma ij}\frac{R_j(z)}{P_j(z)}$$

Let us now develop the product using the formula:

$$\prod_{i=1}^{m}\sum_{j=1}^{n}x_{i,j}=\sum_{j_1,\dots,j_m\in[\![1,n]\!]^m}\prod_{i=1}^{m}x_{i,j_i}$$

which leads to:

$$\det\Big(\boldsymbol{M}\boldsymbol{D}\boldsymbol{M}^{\mathsf{T}}\Big)=\sum_{\sigma\in S_m}\epsilon(\sigma)\sum_{\substack{j_1,\dots,j_m\\ \in\,[\![1,\,n]\!]^m}}\prod_{i=1}^{m}M_{ij_i}M_{\sigma ij_i}\frac{R_{j_i}(z)}{P_{j_i}(z)} \tag{C.53}$$

We here have a sum of products of m terms; thus, the $\frac{R_j(z)}{P_j(z)}$ never appear more than m times in each product – nor more than their multiplicity in $\det\left(\boldsymbol{D}\right)(z)$. It thus suffices to account for each $P_j(z)$ a number of times that is the maximum between its multiplicity and m in order to rationalize the $\det\Big(\boldsymbol{M}\boldsymbol{D}(z)\boldsymbol{M}^{\mathsf{T}}\Big)\in\mathbb{C}(X)$ fraction. □

Importantly, since both shift function $S_c(E)$ definitions (C.41) and (C.43) coincide above threshold, the solutions to (C.34) will be the same above thresholds. The discrepancy in the values of the alternative parameters, solutions to (C.34), will only differ when certain channels have to be considered below threshold: $S_c(E)$ with $E<E_{T_c}$.

To illustrate these differences, let us consider the simple example of a one-level, one-channel neutral particle interaction, with a zero-threshold $E_{T_c}=0$, and set about solving the Brune generalized eigenproblem (C.34), which here takes the simple scalar form:

$$E_\lambda-\gamma_{\lambda,c}\Big(S_c(E)-B_c\Big)\gamma_{\lambda,c}=E \tag{C.54}$$

In figures C-4 and C-5, we plotted the left and right hand side of this elemental Brune eigenproblem (C.54), for both definitions (C.41) and (C.44) of the shift function $S_c(E)$, for various values of resonance parameters $\{E_\lambda,\gamma_{\lambda,c}\}$ and the convention $B_c=-\ell_c$, for different angular momenta ℓ_c.

In the case of $\ell_c=1$, depicted in figure C-4, one can observe that the real sub-threshold pole engendered by odd angular momenta (c.f. section C.4.2) introduces a sub-threshold alternative parameter, where the left-hand side of (C.54) crosses the $E=E$ identity line. In the case of the Lane & Thomas legacy definition (C.41),

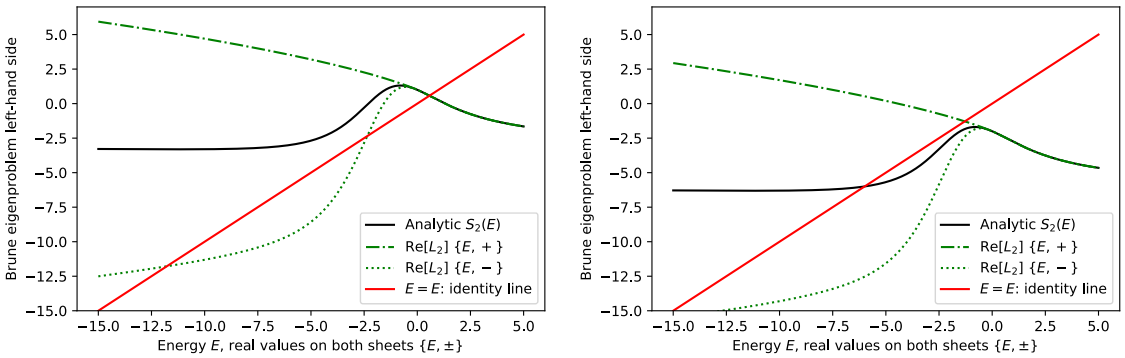

(a) Positive resonance energy $E_\lambda = 1$.

(b) Negative resonance energy $E_\lambda = -2$.

Figure C-5: Brune eigenproblem (C.54) for 1-level 1-channel d-wave: comparison of real solutions from definitions (C.41) versus (C.44), for angular momentum $\ell_c = 2$, neutral particles energy-wavenumber mapping (E.2), resonance width $\gamma_{\lambda,c} = \sqrt{2}$, using $B_c = -\ell_c$ convention and zero threshold $E_{T_c} = 0$. Units such that $\rho_0 = 1$. Since there are no real sub-threshold poles, both can yield one, two, or three solutions (crossing the E=E diagonal), depending on the values of the resonance parameters. If at threshold energy E_{T_c} the left hand side of (C.54) is above the E=E diagonal, then the above-threshold solutions from both definitions coincide. In any case, the sub-threshold solutions differ. Behavior is analogous for all even angular momenta $\ell_c \equiv 0(\text{mod}2)$.

this sub-threshold alternative shadow pole is on the $\left\{E, -\right\}$ sheet of mapping (E.2), whereas for analytic continuation definition (C.44) it is on the same, unique sheet. The same behavior will be observable for all odd angular momenta $\ell_c \equiv 1 \pmod 2$.

In the case $\ell_c = 2$, depicted in figure C-5, the non-purely-imaginary poles $\{\omega_n, \omega_n^*\} \notin \text{i}\mathbb{R}$ (c.f. lemma 2 and table C.2) will impact the shift function $S_c(\rho_c)$ in ways that may or may not produce additional real solutions $\left\{\widetilde{E_i}\right\} \in \mathbb{R}$ to the generalized eigenproblem (C.34). This behavior is reported in figure C-5, where one can observe that, depending on the R-matrix parameter values $\left\{E_\lambda, \gamma_{\lambda,c}, B_c\right\}$, there are either one, two (tangential for the analytic continuation definition), or three solutions to the Brune generalized eigenproblem (C.54). For instance, one can see that definition (C.41) can yield situations with two sub-threshold alternative branch poles – one on the $\left\{E, +\right\}$ branch and one shadow pole (i.e. on the $\left\{E, -\right\}$ branch) – or with two sub-threshold alternative shadow poles – both sub-threshold on the $\left\{E, -\right\}$ branch – or situations where only one, above-threshold solution is produced. On the other hand, analytic continuation definition (C.44) can also yield one, two (tangentially) or three solutions, depending on the sub-threshold behavior and the resonant parameters eigenvalues $\left\{E_\lambda, \gamma_{\lambda,c}, B_c\right\}$. The number of real solutions $\left\{\widetilde{E_i}\right\} \in \mathbb{R}$ to the Brune generalized eigenproblem (C.34) will thus depend on the R-matrix parameters, and is in general comprised between N_λ and N_S.

To verify the number of complex alternative analytic poles (C.49), a trivial example is considering (C.54) in the $\ell_c = 1$ case, where the analytic shift function takes the wavenumber dependence, $S(\rho) = -\frac{1}{1+\rho^2}$, and thus the poles of the $\boldsymbol{R}_S$ operator are

nothing but the solutions to $\frac{E_\lambda - E}{\gamma^2_{\lambda,c}} + B + \frac{1}{1+\rho_0^2(E-E_{T_c})} = 0$. The fundamental theorem of algebra then guarantees this problem has $N_S = 2$ complex solutions, not $N_\lambda = 1$. The surprising part is that both are real poles: one above and one below threshold, which again stems from the fact the number of roots $\{\omega_n\}$ is odd and that their symmetries thus require one pole to be exactly imaginary (in wavenumber space), as explained in section C.4.2. For $\ell_c = 2$, we would have $S_2^0(E) = \frac{3E+2E^2}{\frac{9}{\rho_0^2}+3E+E^2}$, so that the fundamental theorem of algebra commands (C.54) will have $N_S = 3$ solutions, verifying the $N_S = N_\lambda + \sum_{c=1}^{N_c} \ell_c$ complex poles we establish in (C.49). In the general charged-particles case, the shift factor $S_c(\rho)$ is no longer a rational fraction in ρ^2 but is a meromorphic operator in ρ^2 with an infinity of poles (c.f. lemma 2). This illustrates how, in general, there exist $N_\lambda \leq N_S \leq \infty$ complex poles of the $\boldsymbol{R}_S$ operator, and that at least N_λ of them are real.

When the left-hand side of (C.54) crosses the $E = E$ identity line above threshold, the alternative branch poles coincide with the alternative analytic poles, as can be observed in figures C-4 and C-5. Since the shift function $S_c(E)$ is continuous and monotonically increasing above threshold, the question is whether the eigenvalues of the left-hand side of (C.34) are above the $E = E$ identity line at the threshold value: $E = E_{T_c}$. If yes, then it would mean that past the last threshold there will be exactly N_λ solutions to (C.34). However, nothing guarantees *a priori* that all the eigenvalues of the left hand side of (C.34) are above the $E = E$ at the last threshold. From solving the elemental Brune problem (C.54), we observed that it seems to require negative resonance levels $E_\lambda < 0$ to induce the left-hand side of (C.34) to be below the $E = E$ identity line at the threshold value, as illustrated in figures C-4 and C-5. When this happens, the alternative poles will be sub-threshold, and thus depend on the (C.41) or (C.44) definition for the shift function $S_c(E)$. However, the fact that different channels will have different threshold levels $E_{T_c} \neq E_{T_{c'}}$, and that nothing stops R-matrix parameters from displaying negative resonance levels $E_\lambda < 0$, mean no definitive conclusion can be reached as to the number of real alternative parameters (other than there exists at least N_λ of them).

C.4.4 Choice of alternative poles

Brune defined the alternative parameters in (C.36) and (C.37) by building the square matrix $\boldsymbol{a}$, and then inverting it to guarantee (C.38) (c.f. section C.4.1). We just demonstrated in theorems 6 and 7 that there are in general more alternative poles N_S – either alternative branch poles or alternative analytic poles – than the number N_λ of resonance levels: $N_S \geq N_\lambda$. Yet the fact that there are more than N_λ solutions to (C.34) implies the $\boldsymbol{a} \triangleq [\boldsymbol{a_1}, \ldots, \boldsymbol{a_i}, \ldots, \boldsymbol{a_{N_S}}]$ matrix, composed of the N_S solutions to Brune's eigenproblem (C.34), is in general not square, and could even be infinite if $N_S = \infty$ (Coulomb channels). This brings two critical questions: 1) do these additional alternative poles impede us from well defining the alternative parameters? 2) can we still uniquely define the alternative poles?

We here demonstrate in theorem 8 the striking property that choosing any finite set of at least N_λ different solutions from the $N_\lambda \leq N_S \leq \infty$ solutions of Brune's

eigenproblem (C.34), suffices, under our new extended definition (C.55), to properly describe the R-matrix scattering model.

Theorem 8. *Choice of alternative poles*
If we generalize definition (C.37) of the alternative level matrix $\widetilde{\boldsymbol{A}}$ by defining it as the following (Moore-Penrose) pseudo-inverse:

$$\widetilde{\boldsymbol{A}} \triangleq \left[\boldsymbol{a}^{\mathsf{T}}\boldsymbol{A}^{-1}\boldsymbol{a}\right]^{+} \tag{C.55}$$

then the choice of any number N_S of alternative poles, solutions to the Brune generalized eigenproblem (C.34), will reconstruct the scattering matrix $\boldsymbol{U}(E)$, if, and only if, we choose at least N_λ solutions: $N_S \geq N_\lambda$.

Proof. The proof rests on the pseudo-inverse property for independent columns and rows, and applies it to the $\boldsymbol{a} \triangleq [\boldsymbol{a_1}, \ldots, \boldsymbol{a_i}, \ldots, \boldsymbol{a_{N_S}}]$ matrix, constructed by choosing N_S solutions of the generalized eigenproblem (C.34). If $N_S \geq N_\lambda$, then $\boldsymbol{a}$ has independent rows so that its pseudo-inverse will yield: $\widetilde{\boldsymbol{A}} = \boldsymbol{a}^{+}\boldsymbol{A}\boldsymbol{a}^{\mathsf{T}^{+}}$. This property in turn entails (C.38) is satisfied, and thus (D.3.2) stands, leaving unchanged the Kapur-Peierls operator $\boldsymbol{R}_L$, and hence fully representing the scattering matrix $\boldsymbol{U}(E)$. □

Critically, N_λ real solutions to (C.34) can always be found – as shown in theorems 6 and 7 – meaning the alternative parametrization is always capable of fully reconstructing the scattering matrix energy behavior with real parameters through generalized pseudo-inverse definition (C.55). It is well defined.

Yet, if any choice of N_λ alternative poles will yield the same scattering matrix $\boldsymbol{U}(E)$ through definition (C.55), this choice is *a priori* not unique. Can we define some conventions on the choice of alternative parameters to make them unique? Under the legacy Lane & Thomas definition (C.41), this can readily be achieved by neglecting the shadow poles and restraining the search to the principal sheet $\left\{E, +, \ldots, +\right\}$, for all N_c channels, where we have shown in theorem 6 that one will find exactly N_λ poles. Under the analytic continuation definition (C.44), one can still uniquely define the N_λ "first" solutions in the following algorithmic way: one starts the search by diagonalizing, at the last threshold energy (greatest E_{T_c} value), the left-hand side of (C.34). If all the eigenvalues are above the $E = E$ line, then increase the energy until the eigenvalues cross the $E = E$ diagonal, and we will have N_λ uniquely defined real alternative analytic poles. If at the first threshold some eigenvalues are below the $E = E$ identity line (as we saw could happen if some resonance energies are negative $E_\lambda < 0$), then we can decrease the energy values until those cross the $E = E$ identity line for the first time, and stop the search there, thus again uniquely defining N_λ alternative analytic poles. This foray into the algorithmic procedure for solving (C.44) gives us the occasion to point to the vast literature on methods to solve nonlinear eigenvalue problems, in particular [319].

In the end, though we argue that the physically correct definition for the shift function $S_c(E)$ ought to be through analytic continuation (C.44), both approaches enable to set conventions that will uniquely determine N_λ real alternative poles.

C.5 Generalized alternative parameters for Reich-Moore formalism

In this section, we study how the community could convert present nuclear data libraries – featuring both Wigner-Eisenbud parameters and Reich-Moore parameters – to alternative parameters, in order to eliminate the dependence on the arbitrary boundary condition parameters B_c. We generalize the alternative parametrization to encompass the widely used Reich-Moore formalism, with which many evaluations are conducted, and we show that it is necessary for the community to decide on a convention to continue R-matrix operators to complex wavenumbers – that is we must choose between branch-points definition (C.41) and analytic continuation (C.43).

C.5.1 Generalization to Reich-Moore formalism and Teichmann-Wigner eliminated channels

In practice we are only interested in certain outcomes of a nuclear reaction (such as neutron fission, scattering, etc.) and we are sometimes unable to track the vast number of all possible channels (such as every single individual photon interaction) – this is specially true of heavy nuclides for which the interaction becomes a large many-body problem. For these cases, the community has traditionally resorted to Teichmann and Wigner's channel elimination method (c.f. [305] or section X, p.299 of [214]) to not explicitly treat all the channels we are not interested in, but still capture their effects on channels of interest. This yields the Reich-Moore approximation of R-matrix theory [276], which models the effects of all the eliminated channels (usually γ "gamma capture" photon channels) on every level by adding to every level's resonance energy E_λ a partial eliminated capture width $\Gamma_{\lambda,\gamma}$ that shifts the effective resonance energy into the complex plane:

$$\boldsymbol{e}_{\text{R.M.}} \triangleq \mathbf{diag}\left(E_\lambda - \mathrm{i}\frac{\Gamma_{\lambda,\gamma}}{2}\right) \tag{C.56}$$

From this, the Reich-Moore formalism R-matrix (E.16), where all the eliminated capture channels have been collapsed into one γ channel, is now:

$$\begin{aligned} R_{c,c'\notin\gamma_{\text{elim.}}} &\triangleq \sum_{\lambda=1}^{N_\lambda} \frac{\gamma_{\lambda,c}\gamma_{\lambda,c'}}{E_\lambda - \mathrm{i}\frac{\Gamma_{\lambda,\gamma}}{2} - E} \\ \text{i.e.} \quad \boldsymbol{R}_{\text{R.M.}} &= \boldsymbol{\gamma}^{\mathsf{T}}\left(\boldsymbol{e}_{\text{R.M.}} - E\mathbb{I}\right)^{-1}\boldsymbol{\gamma} \end{aligned} \tag{C.57}$$

and, equivalently, the Reich-Moore inverse level matrix (E.18) thereby becomes:

$$\boldsymbol{A^{-1}}_{\text{R.M.}} \triangleq \boldsymbol{e}_{\text{R.M.}} - E\,\mathbb{I} - \boldsymbol{\gamma}\left(\boldsymbol{L} - \boldsymbol{B}\right)\boldsymbol{\gamma}^{\mathsf{T}} \tag{C.58}$$

All the other R-matrix expressions linking these operators to the scattering matrix (E.14), and thereby the cross section (C.22) remain unchanged in the Reich-Moore formalism. In practice, the only effect of this channel elimination is that the Reich-

Moore formalism allows for complex resonance energies (E.19) in the parametrizations of R-matrix theory. In this sense, though initially emerging from the channel elimination approximation, the Reich-Moore formalism can be seen like an actual extension of the exact R-matrix formalism.

This has consequential effects on the alternative parametrization. If one wants to convert the Reich-Moore parameters into alternative parameters, Brune's equations of section C.4 are not valid, since they assume the left hand side of (C.34) is a real symmetric matrix (and thus diagonalizable with real eigenvalues). We here generalize the alternative parametrization of R-matrix theory to encompass the Reich-Moore formalism – which is of great practical importance – and the additional shadow poles previously discovered (in theorems 6 and 7). First, we notice that in the Reich-Moore formalism, Brune's generalized eigenproblem (C.34) becomes:

$$\left[\boldsymbol{e}_{\text{R.M.}} - \boldsymbol{\gamma}\left(\boldsymbol{S}(\widetilde{E_i}) - \boldsymbol{B}\right)\boldsymbol{\gamma}^{\mathsf{T}}\right]\boldsymbol{a_i} = \widetilde{E_i}\boldsymbol{a_i} \tag{C.59}$$

The fact that the left hand side of generalized eigenproblem (C.59) is now a complex symmetric matrix (and not a real symmetric nor a Hermitian matrix) entails the solutions $\widetilde{E_i}$ are no longer real, but complex (we now have complex alternative poles $\widetilde{E_i} \in \mathbb{C}$ and eigenvectors $\boldsymbol{a_i} \in \mathbb{C}^{N_\lambda}$). In order to conserve an euclidean norm on the space of eigenvectors, the normalization condition must now be generalized to vectors by means of the Hermitian conjugate:

$$\boldsymbol{a_i}^{\dagger}\boldsymbol{a_i} = 1 \tag{C.60}$$

We then define the alternative parameters with Hermitian conjugate transformation:

$$\widetilde{\boldsymbol{e}}_{\mathbf{R.M.}} \triangleq \mathbf{diag}(\widetilde{E_i}) \qquad , \qquad \widetilde{\boldsymbol{\gamma}} \triangleq \boldsymbol{a}^{\dagger}\boldsymbol{\gamma} \tag{C.61}$$

where $\boldsymbol{a}$ is the matrix composed of the column eigenvectors: $\boldsymbol{a} \triangleq [\boldsymbol{a_1}, \ldots, \boldsymbol{a_i}, \ldots]$. We then define the generalized alternative level matrix by means of theorem 8, generalized to complex eigenvectors and for an arbitrary number $N_S \geq N_\lambda$ (at least as many generalized alternative poles as the number of levels) of solutions (now complex) to the generalized eigenproblem (C.59):

$$\widetilde{\boldsymbol{A}}_{\text{R.M.}} \triangleq \left[\boldsymbol{a}^{\dagger}\boldsymbol{A}_{\text{R.M.}}^{-1}\boldsymbol{a}\right]^{+} \tag{C.62}$$

This generalized definition will guarantee that the Kapur-Peierls operator (C.20) will we conserved through the following generalization of Brune's relation (D.3.2):

$$\boldsymbol{R}_{L\text{R.M.}} = \boldsymbol{\gamma}^{\mathbf{T}}\boldsymbol{A}_{\mathbf{R.M.}}\boldsymbol{\gamma} = \widetilde{\boldsymbol{\gamma}}^{\dagger}\widetilde{\boldsymbol{A}}_{\mathbf{R.M.}}\widetilde{\boldsymbol{\gamma}} \tag{C.63}$$

thus preserving the scattering matrix (E.14) and ultimately the cross section (C.22), as long as we choose more (or equal) solutions to (C.59) than there are levels: $N_S \geq N_\lambda$.

Note that our generalization (C.63) does not make the Kapur-Peierls operator Hermitian, since the generalized alternative level $\widetilde{\boldsymbol{A}}_{\text{R.M.}}$ matrix (C.62) is still not

Hermitian, but complex symmetric.

C.5.2 Necessary choice: how to continue R-matrix operators into the complex plane?

The fact that $\widetilde{\boldsymbol{e}}_{\mathbf{R.M.}}$ is now complex – complex alternative poles $\widetilde{E_i} \in \mathbb{C}$ and eigenvectors $\boldsymbol{a_i} \in \mathbb{C}^{N_\lambda}$ solve (C.59) – has profound consequences on the Reich-Moore alternative parameters (C.61), because it breaks Brune's three-step monotony argument (last paragraph of section C.4.1) to prove that here are exactly N_λ real solutions on the physical sheet above threshold (we showed there are shadow poles below threshold or in the complex plane in both theorem 6 and 7). Indeed, nothing guarantees the three-step monotony argument still stands in the complex plane, when calling the shift operator $\boldsymbol{S}(\widetilde{E_i})$ at complex values $\widetilde{E_i} \in \mathbb{C}$. Actually, the choice of convention to continue the R-matrix operators into the complex plane – that is branch-point definition (C.41) or analytic continuation (C.44) – is now of critical importance, since it will change $\boldsymbol{S}(\widetilde{E_i})$ (for $\widetilde{E_i} \in \mathbb{C}$) and thus the values of the all the Reich-Moore alternative parameters (C.61), including the principal poles. If we choose analytic continuation definition (C.44), then theorem 7 still stands and there are $N_S \geq N_\lambda$ (complex) alternative poles as in (C.49). However, if we choose branch-point definition (C.41), then Brune's three-step monotony argument does not stand and we have no guarantee on the number of alternative poles anymore, nor on which sheet of mapping (E.4) the alternative poles reside.

The only workaround to this is to use the *Generalized Reich-Moore* framework to convert the Reich-Moore parameters into real R-matrix parameters as described in [60]; but this would incur a great computational and memory cost as we will have to expand a few eliminated channels R-matrix ($N_c \times N_c$ with $c \notin \gamma_{\text{elim.}}$) into a square R-matrix of the size of the levels ($N_\lambda \times N_\lambda$), when for large nuclides we often have $N_\lambda \gg N_c$. And even in the case of Generalized Reich-Moore (which is equivalent to exact R-matrix in that it yields real resonance parameters), the values of the alternative parameters will still depend on the choice of continuation in the complex plane – branch-point definition (C.41) versus analytic continuation definition (C.43) – when there are many different thresholds for different channels, and the $\boldsymbol{S}(E)$ operator must be called below threshold for certain channels when solving (C.59). In fact, the only case where the choice of continuation – definition (C.41) versus definition (C.43) – has no consequence on the values of the principal alternative poles (the Shadow poles always differ) is when we are using the exact R-matrix equations (or the generalized Reich-Moore ones [60]) and all the alternative poles are above the thresholds of all the channels.

In practice, this means that the choice of continuation matters because it changes the values of all the alternative parameters: for Reich-Moore alternative parameters (C.61) we need to call the external R-matrix operators $(\boldsymbol{O}, \boldsymbol{I}, \boldsymbol{P}, \boldsymbol{S})$ into the complex plane; and for real R-matrix alternative parameters (C.36) the many thresholds will mix up in the sub-threshold (shadow) values of the $S_c(E)$ operator (unless we are only solving past the last threshold). Thus, in order to convert nuclear data libraries from

Wigner-Eisenbud to alternative parameters, the nuclear scientists community must convene on a convention – either branch-point definition (C.41) or analytic continuation definition (C.43) – to compute R-matrix operators for complex wavenumbers. The authors are publishing a follow-up article arguing in favor of analytic continuation [125].

C.6 Evidence of shadow alternative poles in xenon ^{134}Xe

We here report the first evidence of the existence of shadow poles in the alternative parametrization of R-matrix theory, observed in isotope xenon ^{134}Xe for neutron reactions: $\mathrm{n} + {}^{134}\mathrm{Xe}$. In doing so, we also demonstrate that all alternative parameters depend on the convention used for continuation into the complex plane of R-matrix operators.

We chose xenon ^{134}Xe because it has only a few resonances per spin group, this makes it a clear case that is simple to solve numerically. Xenon ^{134}Xe is stable and the fourth most abundant isotope of xenon (10.436% of natural content, most abundant is ^{132}Xe with 26.909%). The isotope spin is $0^{(+)}$, and the neutron's $1/2^{(+)}$. There are three spin groups: $J^\pi = 1/2^{(+)}$ with 3 s-wave resonances; $J^\pi = 1/2^{(-)}$ with 2 p-wave resonances; and $J^\pi = 3/2^{(-)}$ with 1 p-wave resonance. The R-matrix parameters of xenon ^{134}Xe, here reported in table C.4, were taken from ENDF/B-VIII.0 nuclear data library [87], where we observe the two p-waves in the $J^\pi = 1/2^{(-)}$ spin group. The xenon ^{134}Xe ENDF/B-VIII.0 evaluation is listed as a MLBW (Multi-Level Breit-Wigner) with B=S approximation, which means that the exact R-matrix equations are not used (neither the Reich-Moore ones), but instead the physically incorrect approximation that $S_c(E) = B_c$ is constant is made (i.e. the shift function is forced onto the boundary parameters, to simplify the evaluation process). All ENDF/B-VIII.0 evaluations with only a few resonances are carried out with this B=S approximation. Though this has no incidence on s-waves ($S_{\ell=0} = 0$) for neutral channels, and in general the B=S approximation has only small effects in practice on the evaluation, these equations cannot rigorously match the R-matrix-equivalent formalisms we here derive.

To validate theorems 6 and 7, we first create a verisimilar fictitious single-channel xenon ^{134}Xe isotope in R-matrix formalism (instead of MLBW), by setting all the capture widths (explicit γ or eliminated capture) to zero, and treating the resulting purely scattering system with R-matrix equations – i.e. (E.14) and (E.16). We then convert these Wigner-Eisenbud R-matrix parameters into alternative parameters by solving the generalized eigenvalue system (C.34), and report the results in table C.5. The alternative poles reported in table C.5 exhibit all the behaviors proved in theorems 6 and 7. As in theorem 6, the alternative branch poles – i.e. found using the Lane & Thomas definition (C.41) – are all real and count $N_\lambda = 2$ principal poles on the $\{E, +\}$ sheet of mapping (C-1), near the resonances, as well as one shadow alternative branch pole on the $\{E, -\}$ sheet bellow threshold. Meanwhile, as proved in

theorem 7, there are three (from (C.49) we have $N_S = 2+1$) alternative analytic poles – i.e. using the analytic continuation definition (C.43). Two (the 'principal' ones) are real (because $N_\lambda = 2$), and the last one (the 'shadow alternative analytic pole') is sub-threshold and also happens to be real because $\ell_c = 1$ is an odd number (c.f. theorem 7). Again, since definition (C.44) unfolds mapping (E.4), the alternative analytic poles have no multi-sheeted structure (which we made explicit by stating both $\{E, \pm\}$ sheets).

To validate our generalization to Reich-Moore, established in section C.5.1, we proceed just as we did with the fictitious R-matrix single-channel xenon ^{134}Xe isotope, and convert the ENDF/B-VIII.0 resonance parameters into alternative parameters by solving the Brune-generalized-to-Reich-Moore eigenproblem (C.59). The results are reported in table C.6. The Reich-Moore generalized alternative parameters in table C.6 also inherit most of the results from theorems 6 and 7. There are some notable differences however. Generalizing to Reich-Moore entails all the alternative poles are now complex, regardless of which definition (C.41) or (C.43) is chosen to continue the shift function $S_c(k_c)$ to complex wavenumbers $k \in \mathbb{C}$.
This has major consequences when choosing the Lane & Thomas definition (C.41): unlike in the R-matrix case, in Reich-Moore the N_λ principal poles are no longer on the physical sheet $\{E, +\}$. Indeed, we observe in table C.6 that in our case all the alternative branch poles are now on the non-physical sheet $\{E, -\}$. In the general case, the alternative branch poles could be on the physical or the non-physical sheet (we have no proof for either), and one could thus say that all alternative poles are shadow poles in the Reich-Moore formalism. This lack of knowledge of on what sheet to find the alternative branch poles comes atop the fact, discussed in section C.5.2, that Brune's three-step monotony argument (which proved the existence of exactly N_λ real alternative poles above threshold) is only valid for real-symmetric matrices. When generalized to Reich-Moore, eigenproblem (C.59) counts a complex-symmetric matrix, entailing Brune's three-step monotony argument at the core of theorem 6 is no longer valid, and we actually do not have proof of the number of alternative branch poles (theorem 6 proof only stands for R-matrix, or generalized Reich-Moore).
This is not the case for the alternative analytic poles, which generalize quite naturally to Reich-Moore formalism. In fact, the only difference to theorem 7 is that the three-step monotony argument can no longer be used to prove that N_λ of the $N_S = N_\lambda + \sum_c \ell_c$ alternative analytic poles (C.49) are real – and indeed they are not, as shown in table C.6. Apart from that, theorem 7 remains intact for our generalization to Reich-Moore established in section C.5.1: there are still $N_S = N_\lambda + \sum_c \ell_c$ alternative analytic poles (C.49), and there is no need to specify on which $\{E, \pm\}$ sheet of mapping (E.4) they reside since the analytic continuation of the shift function $S_c(\rho_c)$ unfolds the mapping (c.f. lemma 2 and theorem 7).

Take a closer observation at the results in tables C.5 and C.6. Notice that the imaginary part of the alternative branch poles are all equal to -0.039, which is exactly the opposite of half the eliminated channel width: convenient. This can readily be explained by splitting the generalized-to-Reich-Moore Brune-eigenproblem (C.59) into real and imaginary parts, and noticing that if all the eliminated channel widths

are the same, then the eigenvalue's (alternative pole) imaginary part is exactly opposite to the eliminated channel width divided by two, i.e. if $\forall \lambda, \lambda' \in J^\pi,\ \Gamma_{\lambda,\gamma} = \Gamma_{\lambda',\gamma}$ then $\forall j\,,\ \Im\left[\widetilde{E_j}\right] = -\frac{\Gamma_{\lambda,\gamma}}{2}$, from (E.19). It so happens that in our particular case of xenon ^{134}Xe this is indeed true, all eliminated capture widths are equal to 0.078 (c.f. table C.4). Looking at the ENDF/B-VIII.0 library it is surprisingly common to have the same eliminated capture widths within the same spin group (both xenon-132 and xenon ^{134}Xe are such examples). But this is of course not true in general, and a quick look at uranium-238 will show that different levels have different eliminated capture widths (i.e. $\exists \lambda, \lambda' \in J^\pi,\quad \Gamma_{\lambda,\gamma} \neq \Gamma_{\lambda',\gamma}$). So when the Lane & Thomas convention (C.41) is chosen, the alternative branch poles imaginary part will in general not coincide with the eliminated capture widths: $\Im\left[\widetilde{E_j}\right] \neq -\frac{\Gamma_{\lambda,\gamma}}{2}$. Similarly, neither will the alternative branch eigenvectors be real in general.

Note that the eigenvectors in tables C.5 and C.6 are close, but differ when going to higher digits precision, and those small differences have strong impact on the cross section calculation. This leads us to discuss the numerical methods employed to solve the generalized eigenproblem (C.59), which need to be solved in wavenumber space k_c (we here use the variable $z = \sqrt{E}$) to properly describe the multi-sheeted nature of mapping (E.4). For the fictitious R-matrix problem (dealing with only one channel and real values), we coded the analytic continuation of the $S_c(\rho_c)$ shift function (c.f. table C.3), and used the built-in MATLAB polynomial rootfinder to solve (C.59), verifying that the results were indeed roots. For the branch-point definition (C.41), we used a built-in MATLAB numerical solver for equations of the type $f(x) = 0$ on the determinant of the left-hand side of (C.34), and solved the roots one-by-one. For the generalized Reich-Moore Brune eigenproblem (C.59), the alternative analytic poles are readily found in the complex plane with the same polynomial rootfinder (we discuss methods to solve for all the roots of a polynomial simultaneously in [131] and [**?**]). Finding the alternative branch poles is much more complicated: the built-in $f(x) = 0$ MATLAB solver finds the two principal poles (on the non-physical sheet $\{E, -\}$ this time), but to find the shadow pole we had to devise a procedure manually: from the solution when the eliminated capture width is zero (R-matrix case), we zoom-in in the region around that solution and build a convex bowl around it and then slowly increase the eliminated capture width from zero. For each capture width value we did a minimization on the norm of the determinant to find the updated alternative pole for an in-between value of the eliminated capture width. We then iteratively re-solve, re-do a new complex bowl, augment the eliminated capture width, until we converge on the shadow alternative branch pole. This cumbersome procedure points to the mathematical advantages of analytic continuation definition (C.44) as it conserves smooth analytic properties of the Kapur-Peierls operator into the complex plane, which greatly simplifies the conversion to alternative poles for Reich-Moore evaluations.

Finally, to validate theorem 8, as well as the entire generalization to Reich-Moore formalism we establish in section C.5.1, we construct the corresponding cross sections

using the xenon ^{134}Xe resonance parameters from ENDF/B-VIII.0 with the exact R-matrix and Reich-Moore equations – i.e. (E.14) and (E.16) to compute (C.22). The resulting point-wise cross section values are plotted in figure E-2, and their peak resonance values are provided for reference in table C.7. These cross sections do not exactly coincide with the point-wise evaluation values from ENDF/B-VIII.0, since ENDF uses the (coarser) MLBW equations instead of the Reich-Moore (or R-matrix) ones.

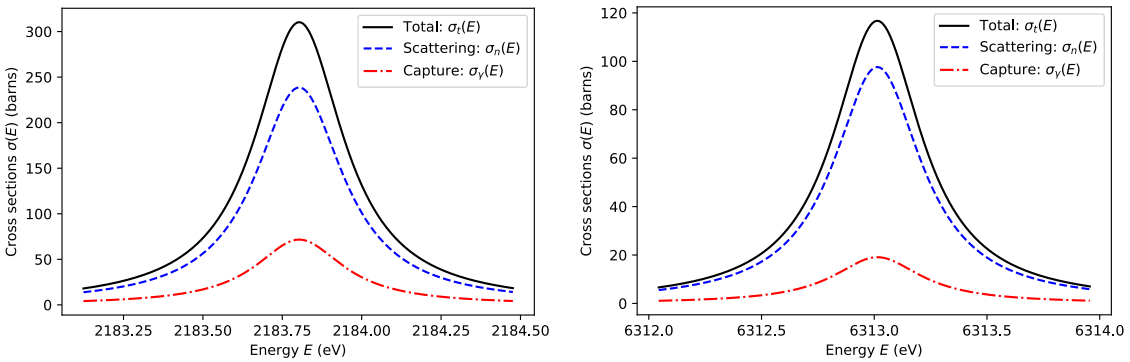

(a) First p-wave resonance.

(b) Second p-wave resonance.

Figure C-6: Xenon ^{134}Xe Reich-Moore cross sections for spin-parity group $J^\pi = 1/2^{(-)}$ p-wave resonances: the cross sections are generated using the ENDF/B-VIII.0 resonance parameters (a MLBW evaluation) into the Reich-Moore formalism equations. Similarly, the R-matrix cross section is generated by setting all capture (including eliminated) widths to zero. For reference, the exact cross section values at the resonance peaks are reported in table C.7.

We then compute the cross section using the alternative parameters reported in tables C.5 and C.6 and following the procedure established in section C.5.1 to reconstruct the Kapur-Peierls operator (C.63), necessary for computing the scattering matrix (E.14), and ultimately the cross section (C.22). We can now observe the alternative parametrization yield the exact same cross section as the R-matrix (or the Reich-Moore) parametrizaton, for both the Lane & Thomas (C.41) or the analytic continuation (C.43) conventions, and by choosing any subset of at least N_λ alternative poles: including discarding the principal poles and instead using the shadow poles. This result validates theorem 8 and its generalization to Reich-Moore (C.62), and will come as quite striking to some evaluators: for p-waves (or higher angular momentum) one can choose to discard the principal alternative pole directly close to the resonance and instead use the shadow pole, which is far below the threshold and into the complex plane, or even use both principal and shadow alternative poles (using the generalized inverse definition (C.62) and the procedure detailed in section C.5.1), to produce the exact same cross section resonance behavior.

C.7 Conclusion

This article establishes the existence of shadow poles in the alternative parametrization of R-matrix theory. This parametrization is being considered as an alternative to the traditional Wigner-Eisenbud resonance parameters to document nuclear cross section values in the nuclear data libraries.

The Wigner-Eisenbud parameters are the poles $\left\{E_\lambda\right\}$ and residue widths $\left\{\gamma_{\lambda,c}\right\}$ of the $\boldsymbol{R}$ matrix (E.16). They are $N_\lambda \in \mathbb{N}$ real poles, which are independent from one another (meaning any choice of real parameters are physically acceptable), and deentangle the energy dependence of the $\boldsymbol{R}$ matrix from the branch-points the thresholds $\{E_{T_c}\}$ introduce in the multi-sheeted Riemann surface of mapping (E.4). Both $\left\{E_\lambda\right\}$ and $\left\{\gamma_{\lambda,c}\right\}$ are dependent on both the channel radii $\left\{a_c\right\}$ and the boundary conditions $\left\{B_c\right\}$. The set of Wigner-Eisenbud parameters $\left\{E_{T_c}, a_c, B_c, E_\lambda, \gamma_{\lambda,c}\right\}$ is sufficient to fully describe the scattering matrix $\boldsymbol{U}(E)$ energy dependence (E.14).

The alternative parameters are the poles $\left\{\widetilde{E_i}\right\}$ of the $\boldsymbol{R}_S$ matrix (C.39) and the widths $\{\widetilde{\gamma_{i,c}}\}$, transformed by (C.36) from the residue widths of the alternative level matrix $\widetilde{\boldsymbol{A}}$ in (C.30) and (C.34). They are $N_S^\pm \geq N_\lambda$ poles, and are intimately interdependent in that not any set of real parameters is physically acceptable (they must be solutions of (C.34)). If the legacy Lane & Thomas definition (C.41) is chosen for the shift function $\boldsymbol{S}$, the alternative branch poles live on the multi-sheeted Riemann surface of mapping (E.4): they have branch shadow poles $\left\{\widetilde{E_i}\right\}$ on the unphysical sheets $\{E, -\}$ below threshold $E < E_{T_c}$, though there are only N_λ real poles on the physical sheet (theorem 6). If analytic continuation definition (C.43) is chosen, then the shift factor $\boldsymbol{S}$ is a function of ρ_c^2, which unfolds the sheets in mapping (E.4): there are then $N_S^{\mathbb{C}} \geq N_\lambda$ analytic poles $\left\{\widetilde{E_i}\right\}$, in general complex (though for R-matrix at least N_λ of them are real), all living on the same sheet with no branch points (theorem 7). Both $\left\{\widetilde{E_i}\right\}$ and $\{\widetilde{\gamma_{i,c}}\}$ are invariant to change in boundary conditions $\left\{B_c\right\}$, though both depend on the channel radii $\left\{a_c\right\}$. Any subset of N_λ or more alternative parameters $\left\{E_{T_c}, a_c, \widetilde{E_i}, \widetilde{\gamma_{i,c}}\right\}$ is sufficient to entirely determine the energy behavior of the scattering matrix $\boldsymbol{U}$ through (D.3.2) and (E.14) (theorem 8).

The first shadow alternative poles are observed in xenon isotope ${}^{134}_{54}\mathrm{Xe}$ spin-parity group $J^\pi = 1/2^{(-)}$, which has two p-wave resonance. We show how the shadow alternative poles can be chosen instead of the traditional principal alternative poles to compute the cross sections. We also demonstrate that any subset of N_λ alternative poles will also reconstruct the cross section. Since there are N_λ principal (resonant) alternative poles, this means that the shadow poles can be discarded from future nuclear data libraries without compromising their capability to fully reconstruct R-matrix cross sections (i.e. entirely describe their energy dependence).

In order to convert the xenon resonance parameters, we generalize the alternative parameters to deal with the Reich-Moore approximation and the additional shadow poles. The Reich-Moore approximation – widely used in nuclear data libraries – introduces complex Reich Moore alternative parameters (C.61), and their values depend on

which convention – analytic continuation definition (C.43) versus branch-point definition (C.41) – is chosen to continue the R-matrix operators to complex wavenumbers. Deciding on this convention is thus a necessary prerequisite to converting nuclear data libraries to alternative parameters. For mathematical and physical reasons, we argue in favor of analytic continuation in a follow-up article [125].

C.8 Acknowledgments

This work was partly funded by the Los Alamos National Laboratory (summer 2017 research position in T-2 division with G. Hale and M. Paris), as well as by the Consortium for Advanced Simulation of Light Water Reactors (CASL), an Energy Innovation Hub for Modeling and Simulation of Nuclear Reactors under U.S. Department of Energy Contract No. DE-AC05-00OR22725. In addition to a Research Assistantship from the Massachusetts Institute of Technology, U.S.A., the first author was also supported as AXA Fellow of the Schwarzman Scholars Program, Tsinghua University, Beijing, China.

We would like to thank and acknowledge Dr. Yoann Desmouceaux, author of the proof of diagonal divisibility and capped multiplicities lemma 3, who's help and inputs were key on technical algebraic points. Our genuine gratitude to Dr. Andrew Holcomb, from Oak-Ridge National Laboratory, who helped us numerically test the veracity of Mittag-Leffler expansion (D.7). We would also like to thank Prof. Javier Sesma, from Universidad de Zaragoza, for his invaluable guidance on the properties of the Hankel functions, as well as Haile Owusu for his insight into Hamiltonian degeneracy. Finally, we are grateful towards the organizers of the R-matrix workshop of summer 2016 in Santa Fe, New Mexico [258], which was genuinely catalytic to these findings.

Table C.4: Xenon ^{134}Xe resonance parameters for the two p-waves of spin group $J^\pi = 1/2^{(-)}$, from ENDF/B-VIII.0 evaluation

$z = \sqrt{E}$ with E in (eV)
$A = 132.760$
$a_c = 5.80$: channel radius (Fermis)
$\rho(z) = \frac{Aa_c\sqrt{\frac{2m_n}{h}}}{A+1}z$
with $\sqrt{\frac{2m_n}{h}} = 0.002196807122623$ in units $(1/(10^{-14}\mathrm{m}\sqrt{\mathrm{eV}}))$
$E_1 = 2186.0$: first resonance energy (eV)
$\Gamma_{1,n} = 0.2600$: neutron width of first resonance
(not reduced width), i.e. $\Gamma_{\lambda,c} = 2P_c(E_\lambda)\gamma^2_{\lambda,c}$
$\Gamma_{1,\gamma} = 0.0780$: eliminated capture width (eV)
$E_2 = 6315.0$: second resonance energy (eV)
$\Gamma_{2,n} = 0.4000$ (eV)
$\Gamma_{2,\gamma} = 0.0780$ (eV)
$g_{J^\pi} = 1/3$: spin statistical factor
$B_c = -1$

Table C.5: Xenon ^{134}Xe alternative parameters for spin-parity group $J^\pi = 1/2^{(-)}$. For a verisimilar fictitious isotope, all capture widths (including eliminated channels) are set to zero, and the p-waves are converted using ENDF/B-VIII.0 resonance parameters into R-matrix equations, and solving the Brune eigenproblem (C.34) as detailed in section C.4.1, for both conventions to continue the shift function to complex wavenumbers: Lane & Thomas (C.41) versus analytic continuation (C.43). (Results to two significant digits of discrepancy)

R-matrix alternative parameters (C.34) (verisimilar fictitious isotope)
Lane & Thomas definition (C.41)
Alternative branch poles (eV) and their sheet of mapping (C-1):
$\left\{\widetilde{E_1}, -\right\} = -626,938 \quad ; \quad \widetilde{z_1} = -791.794\,\mathrm{i}$
$\left\{\widetilde{E_2}, +\right\} = 2,183 \quad ; \quad \widetilde{z_2} = 46.73$
$\left\{\widetilde{E_3}, +\right\} = 6,313 \quad ; \quad \widetilde{z_3} = 79.454$
Corresponding eigenvectors:
$\boldsymbol{a_1} = [0.8732734 \;\; , \;\; 0.4872304]^\mathsf{T}$
$\boldsymbol{a_2} = [1.0 \;\; , \;\; 2.9864 \times 10^{-4}]^\mathsf{T}$
$\boldsymbol{a_3} = [-8.5708 \times 10^{-4} \;\; , \;\; 1.0]^\mathsf{T}$
Analytic continuation definition (C.43)
Alternative analytic poles (eV) and their sheet of mapping (C-1):
$\left\{\widetilde{E_1}, \pm\right\} = -626,111 \quad ; \quad \widetilde{z_1} = 791.271\,\mathrm{i}$
$\left\{\widetilde{E_2}, \pm\right\} = 2,183 \quad ; \quad \widetilde{z_2} = 46.73$
$\left\{\widetilde{E_3}, \pm\right\} = 6,313 \quad ; \quad \widetilde{z_3} = 79.454$
Corresponding eigenvectors:
$\boldsymbol{a_1} = [0.8732752 \;\; , \;\; 0.4872272]^\mathsf{T}$
$\boldsymbol{a_2} = [1.0 \;\; , \;\; 2.9864 \times 10^{-4}]^\mathsf{T}$
$\boldsymbol{a_3} = [-8.5708 \times 10^{-4} \;\; , \;\; 1.0]^\mathsf{T}$

Table C.6: Xenon ^{134}Xe alternative parameters for spin-parity group $J^\pi = 1/2^{(-)}$. The p-waves are converted using ENDF/B-VIII.0 resonance parameters into Reich-Moore equations, and solving the generalized eigenproblem (C.59) as detailed in section C.5.1, for both conventions to continue the shift function to complex wavenumbers: Lane & Thomas (C.41) versus analytic continuation (C.43). (Results to two significant digits of discrepancy)

Reich-Moore alternative parameters (C.59)
Lane & Thomas definition (C.41)
Alternative branch poles (eV) and their sheet of mapping (C-1):
$\left\{\widetilde{E_1}, -\right\} = -626938 - 0.039\,\mathrm{i}$
$\widetilde{z_1} = 2.462 \times 10^{-5} - 791.794\,\mathrm{i}$
$\left\{\widetilde{E_2}, -\right\} = 2183.8031735 - 0.039\,\mathrm{i}$
$\widetilde{z_2} = 46.73117988 - 4.172 \times 10^{-4}\,\mathrm{i}$
$\left\{\widetilde{E_3}, -\right\} = 6313.013519 - 0.039\,\mathrm{i}$
$\widetilde{z_3} = 79.454474511 - 2.4542 \times 10^{-4}\,\mathrm{i}$
Corresponding eigenvectors:
$\boldsymbol{a_1} = [0.8732734\ ,\ 0.487230]^\mathsf{T}$
$\boldsymbol{a_2} = [1.0\ ,\ 2.9863794 \times 10^{-4}]^\mathsf{T}$
$\boldsymbol{a_3} = [-8.570833 \times 10^{-4}\ ,\ 1.0]^\mathsf{T}$
Analytic continuation definition (C.43)
Alternative analytic poles (eV) and their sheet of mapping (C-1):
$\left\{\widetilde{E_1}, \pm\right\} = -626111 - 5.119 \times 10^{-5}\,\mathrm{i}$
$\widetilde{z_1} = 3.234 \times 10^{-8} - 791.271\,\mathrm{i}$
$\left\{\widetilde{E_2}, \pm\right\} = 2183.8031770 - 0.03896\,\mathrm{i}$
$\widetilde{z_2} = 46.73117992 - 4.168 \times 10^{-4}\,\mathrm{i}$
$\left\{\widetilde{E_3}, \pm\right\} = 6313.013521 - 0.03898\,\mathrm{i}$
$\widetilde{z_3} = 79.454474522 - 2.4534 \times 10^{-4}\,\mathrm{i}$
Corresponding eigenvectors:
$\boldsymbol{a_1} = [0.8732752 + 3.5344 \times 10^{-10}\,\mathrm{i}\ ,\ 0.487227]^\mathsf{T}$
$\boldsymbol{a_2} = [1.0 + 1.7772 \times 10^{-5}\,\mathrm{i}\ ,\ 2.9863747 \times 10^{-4}]^\mathsf{T}$
$\boldsymbol{a_3} = [-8.570825 \times 10^{-4} + 5.2348 \times 10^{-9}\,\mathrm{i}\ ,\ 1.0]^\mathsf{T}$

Table C.7: Resonance peaks: Xenon ^{134}Xe spin-parity group $J^\pi = 1/2^{(-)}$ two p-waves cross section values at the peak of the resonances (truncated to 4 digits accuracy). The cross sections are generated using the ENDF/B-VIII.0 resonance parameters (a MLBW evaluation) into the Reich-Moore formalism equations. Similarly, the R-matrix cross section is generated by setting all capture (including eliminated) widths to zero.

Energy (eV)	2183.8030	6313.0138
Total cross-section (barns)	310.2761	116.7259
Scattering cross-section (barns)	238.6095	97.6224
Capture cross-section (barns)	71.6666	19.1035
R-matrix cross-section (barns)	403.4677	139.5677

Appendix D

Scattering matrix pole expansions for complex wavenumbers in R-matrix theory

Here is *verbatim* transcribed our article [125].

D.1 Abstract

In this follow-up article to [Ducru, Phys. Rev. C 004600 [CC10651] (2020)], we establish new results on scattering matrix pole expansions for complex wavenumbers in R-matrix theory. In the past, two branches of theoretical formalisms emerged to describe the scattering matrix in nuclear physics: R-matrix theory, and pole expansions. The two have been quite isolated from one another. Recently, our study of Brune's alternative parametrization of R-matrix theory has shown the need to extend the scattering matrix (and the underlying R-matrix operators) to complex wavenumbers. Two competing ways of doing so have emerged from a historical ambiguity in the definitions of the shift $\boldsymbol{S}$ and penetration $\boldsymbol{P}$ functions: the legacy Lane & Thomas "force closure" approach, versus analytic continuation (which is the standard in mathematical physics). The R-matrix community has not yet come to a consensus as to which to adopt for evaluations in standard nuclear data libraries, such as ENDF.

In this article, we argue in favor of analytic continuation of R-matrix operators. We bridge R-matrix theory with the Humblet-Rosenfeld pole expansions, and discover new properties of the Siegert-Humblet radioactive poles and widths, including their invariance properties to changes in channel radii a_c. We then show that analytic continuation of R-matrix operators preserves important physical and mathematical properties of the scattering matrix – cancelling spurious poles and guaranteeing generalized unitarity – while still being able to close channels below thresholds.

D.2 Introduction

Myriad nuclear interactions have been modeled with R-matrix theory, with applications to many branches of nuclear physics, from nuclear simulation, radiation trans-

port, astrophysics and cosmology, and extending to particle physics or atomistic and molecular simulation [77][214][97][268, 307, 98, 95, 273]. Our current nuclear data libraries are based on R-matrix evaluations (ENDF[87], JEFF[267], BROND[80], JENDL[293], CENDL[153], TENDL[207, 209]). The R-matrix scattering model takes different incoming particle-waves and lets them interact through a given Hamiltonian to produce different possible outcomes. R-matrix theory studies the particular two-body-in/two-body-out model of this scattering event, with the fundamental assumption that the total Hamiltonian is the superposition of a short-range, interior Hamiltonian, which is null after a given channel radius a_c, and a long-range, exterior Hamiltonian which is well known (free particles or Coulomb potential, for instance)[200, 323, 79, 214]. R-matrix theory can then parametrize the energy dependence of the scattering matrix in different ways. The Wigner-Eisenbud parametrization is the historical standard, because its parameters are real and well defined, though some are arbitrary (the channel radius a_c and the boundary condition B_c). To remove this dependence on an arbitrary boundary condition B_c, the nuclear community has recently been considering shifting nuclear data libraries to an alternative parametrization of R-matrix theory [67, 92, 59, 127].

In parallel, a vast literature in mathematical physics and nuclear physics has studied pole expansions of the scattering matrix [135, 159, 117, 144, 236], starting with the well-known developments by Humblet and Rosenfeld [185, 289, 181, 182, 195, 183, 230, 290].

In this article, which builds upon our previous [127], we show in section D.3 how the Siegert-Humblet expansion into radioactive states is the link between R-matrix theory and the scattering matrix pole expansions of Humblet & Rosenfeld. In the process, we unveil new relations between the radioactive poles and residues and the alternative parametrization of R-matrix theory, and establish for the first time the number of radioactive poles in wavenumber space (theorem 9) along with their branch-structure. Section D.4 investigates the invariance properties of Siegert-Humblet radioactive parameters to a change in channel radius a_c. We demonstrate in theorem 10 that invariance of the scattering matrix to a_c sets a partial differential equation on the Kapur-Peierls operator $\boldsymbol{R}_L$, which in turn enables us to derive explicit transformations of the Siegert-Humblet radioactive widths $\{r_{j,c}\}$ under a change of channel radius a_c. Section D.5 considers the continuation of the scattering matrix to complex wavenumbers in R-matrix theory. We establish several new results. We show that the legacy of Lane & Thomas to force-close channels below threshold not only breaks the analytic properties of the scattering matrix, but also introduces nonphysical spurious poles. Yet we prove that these spurious poles are cancelled-out if one performs analytic continuation of R-matrix operators instead (theorem 11). We also show that this analytic continuation of R-matrix operators enforces the generalized unitarity conditions described by Eden & Taylor [137] (theorem 12). Finally, in the case of massive particles, we propose a solution to the conundrum of how to close the channels below thresholds, by invoking both a quantum tunneling argument, whereby the transmission matrix is evanescent below threshold (theorem 13), and a physical argument based on the definition of the cross section as the ratio of probability currents (theorem 14). All these results make us argue that, contrary

to what Lane & Thomas prescribed [214], the R-matrix parametrization should be analytically continued to complex wave-numbers $k_c \in \mathbb{C}$. These considerations have practical implications on R-matrix evaluation codes, such as EDA [164, 166], SAMMY [217], or AZURE [62], used to build our nuclear data libraries: ENDF[87]; JEFF[267]; BROND[80]; JENDL[293]; CENDL[153]; TENDL[207, 209]). We thus call for analytic continuation of R-matrix operators to become the new standard for nuclear cross section evaluations.

D.3 Siegert-Humblet pole expansion in radioactive states

We here establish new R-matrix theory results concerning the Siegert-Humblet expansion into radioactive states (c.f. sections IX.2.c-d-e p.297-298 in [214]). These *radioactive parameters* express the energy dependence of the scattering matrix into a simple sum of poles and residues. We show this constitutes the link between R-matrix theory and the scattering matrix pole expansions of Humblet and Rosenfeld [185, 289, 181, 182, 195, 183, 230, 290] (section D.3.6). In the wake, we show how to obtain the radioactive parameters (section D.3.1), link them to the Brune alternative parametrization (section D.3.2), reveal their branch structure (theorem 9 section D.3.3), which emerges from the wavenumber-energy mapping (E.4):

$$\rho_c(E) \quad \longleftrightarrow \quad E \tag{D.1}$$

where $\rho_c \triangleq a_c k_c$ is the dimensionless wavenumber variable $\boldsymbol{\rho} \triangleq \mathbf{diag}\,(\rho_c)$, a_c is the arbitrary channel radius, and $k_c(E)$ is the wavenumber of channel c, which is linked to the energy E of the system (eigenvalue of the Hamiltonian of the Schödinger equation) as explained in section II.A. of [127].

D.3.1 Definition of Siegert & Humblet parametrization

Following the notation of [127] (to which we refer for further explanations), we here recall the essential relation expressing the scattering matrix $\boldsymbol{U}$ as a function of R-matrix operators:

$$\boldsymbol{U} = \boldsymbol{O}^{-1}\boldsymbol{I} + 2\mathrm{i}\boldsymbol{\rho}^{1/2}\boldsymbol{O}^{-1}\boldsymbol{R}_L\boldsymbol{O}^{-1}\boldsymbol{\rho}^{1/2} \tag{D.2}$$

$\boldsymbol{I}$ and $\boldsymbol{O}$ are the incoming and outgoing wavefunctions, which are subject to the following Wronksian condition: for all channel c, $w_c \triangleq O_c^{(1)} I_c - I_c^{(1)} O_c = 2\mathrm{i}$, or with identity matrix $\mathbb{I}$ (expression (7) in [127]) and denoting $[\,\cdot\,]^{(1)}$ the diagonal channel c derivative with respect to ρ_c

$$\boldsymbol{w} \triangleq \boldsymbol{O}^{(1)}\boldsymbol{I} - \boldsymbol{I}^{(1)}\boldsymbol{O} = 2\mathrm{i}\mathbb{I} \tag{D.3}$$

and where $\boldsymbol{R}_L$ is the *Kapur-Peierls operator*, defined as (see equation (20) section II.D of [127]):

$$\boldsymbol{R}_L \triangleq \left[\mathbb{I} - \boldsymbol{R}\,(\boldsymbol{L} - \boldsymbol{B})\right]^{-1}\boldsymbol{R} = \boldsymbol{\gamma}^{\mathsf{T}}\boldsymbol{A}\boldsymbol{\gamma} \tag{D.4}$$

This Kapur-Peierls $\boldsymbol{R}_L$ operator is at the heart of the Siegert-Humblet parametrization, and its study composes a core part of this article. The Kapur-Peierls operator $\boldsymbol{R}_L$ is a function of the Wigner-Eisenbud R-matrix $\boldsymbol{R}$, parametrized by the *resonance parameters* (energies $\boldsymbol{e} \triangleq \mathbf{diag}\,(E_\lambda)$ and widths $\boldsymbol{\gamma} \triangleq \mathbf{mat}\,(\gamma_{\lambda,c})$)

$$\boldsymbol{R}(E) \triangleq \boldsymbol{\gamma}^{\mathsf{T}}\,(\boldsymbol{e} - E\,\mathbb{I})^{-1}\,\boldsymbol{\gamma} \tag{D.5}$$

as well as the arbitrary boundary condition $\boldsymbol{B} \triangleq \mathbf{diag}\,(B_c)$, and the reduced logarithmic derivative of the outgoing wavefunction $\boldsymbol{L} \triangleq \mathbf{diag}\,(L_c)$, defined as (c.f. section II.B of [127])

$$L_c(\rho_c) \triangleq \frac{\rho_c}{O_c}\frac{\partial O_c}{\partial \rho_c} \tag{D.6}$$

and which admits the following Mittag-Leffler pole expansion (theorem 1 section II.B of [127]):

$$\frac{L_c(\rho)}{\rho} = \frac{-\ell}{\rho} + \mathrm{i} + \sum_{n\geq 1}\frac{1}{\rho - \omega_n} \tag{D.7}$$

where $\{\omega_n\}$ are the roots of the $O_c(\rho)$ outgoing wavefunctions: $\forall n,\ O_c(\omega_n) = 0$ (reported in TABLE II of [127] for neutral particles).
Equivalently, the Kapur-Peierls operator $\boldsymbol{R}_L$ can be expressed with the level matrix $\boldsymbol{A}$ (see equations (17) and (18) of section II.C of [127]):

$$\boldsymbol{A^{-1}} \triangleq \boldsymbol{e} - E\mathbb{I} - \boldsymbol{\gamma}\,(\boldsymbol{L} - \boldsymbol{B})\,\boldsymbol{\gamma}^{\mathsf{T}} \tag{D.8}$$

All these R-matrix operators are functions of the wavenumbers $k_c(E)$ (or their corresponding dimensionless wavenumber variable $\boldsymbol{\rho} \triangleq \mathbf{diag}\,(\rho_c)$). The Siegert-Humblet pole expansion in radioactive states consists of analytically continuing the Kapur-Peierls $\boldsymbol{R}_L$ operator to complex wavenumbers $k_c \in \mathbb{C}$, thereby becoming a locally meromorphic operator. The poles of this meromorphic operator can be assumed to have a Laurent expansion of order one (i.e. simple poles), as we will discuss in section D.5.3. Since the Kapur-Peierls $\boldsymbol{R}_L$ operator is complex-symmetric, its residues at any given pole value $\mathcal{E}_j \in \mathbb{C}$ are also complex-symmetric. For non-degenerate eigenvalues $\mathcal{E}_j \in \mathbb{C}$, the corresponding residues are rank-one and expressed as $\boldsymbol{r_j}\boldsymbol{r_j}^{\mathsf{T}}$, while for degenerate eigenvalues $\mathcal{E}_j \in \mathbb{C}$ of multiplicity M_j, the corresponding residues are rank-M_j and expressed as $\sum_{m=1}^{M_j}\boldsymbol{r_j^m}\boldsymbol{r_j^{m\mathsf{T}}}$. On a given domain, the Mittag-Leffler theorem [244, 304] then states that $\boldsymbol{R}_L$ locally takes the form, in the vicinity $\mathcal{W}(E)$ (neighborhood) of any complex energy $E \in \mathbb{C}$ away from the branch points (threshold energies E_{T_c}) of mapping (E.4), of a sum of poles and residues and a holomorphic entire part $\mathbf{Hol}_{\boldsymbol{R}_L}(E)$:

$$\boldsymbol{R}_L(E) \underset{\mathcal{W}(E)}{=} \sum_{j\geq 1}\frac{\sum_{m=1}^{M_j}\boldsymbol{r_j^m}\boldsymbol{r_j^{m\mathsf{T}}}}{E - \mathcal{E}_j} + \mathbf{Hol}_{\boldsymbol{R}_L}(E) \tag{D.9}$$

or, in the particular (but most common) case where $\mathcal{E}_j$ is a non-degenerate eigenvalue

(with multiplicity $M_j = 1$),

$$\boldsymbol{R}_L(E) \underset{\mathcal{W}(E)}{=} \sum_{j\geq 1} \frac{\boldsymbol{r_j}\boldsymbol{r_j}^{\mathsf{T}}}{E - \mathcal{E}_j} + \mathbf{Hol}_{\boldsymbol{R}_L}(E) \tag{D.10}$$

This is the Siegert-Humblet expansion into so-called *radioactive states* [296, 86, 218, 220, 110] — equivalent to equation (2.16) of section IX.2.c. in [214] where we have modified the notation for greater consistency ($\mathcal{E}_j$ corresponds to H_λ of [214] and $\boldsymbol{r_j}$ corresponds to $\boldsymbol{\omega_\lambda}$) since there are more complex poles $\mathcal{E}_j$ than real energy levels E_λ. The Siegert-Humblet parameters are then the poles $\{\mathcal{E}_j\}$ and residue widths $\{\boldsymbol{r_j}\}$ of this complex resonance expansion of the Kapur-Peierls operator $\boldsymbol{R}_L$.

The Gohberg-Sigal theory [157] provides a method for calculating these poles and residues by solving the following generalized eigenvalue problem — which we call *radioactive problem*:

$$\boldsymbol{R}_L^{-1}(E)\Big|_{E=\mathcal{E}_j} \boldsymbol{q_j} = \mathbf{0} \tag{D.11}$$

that is finding the poles $\left\{\mathcal{E}_j\right\}$ of the Kapur-Peierls operator, $\boldsymbol{R}_L$, and their associated eigenvectors $\{\boldsymbol{q_j}\}$. The poles are complex and usually decomposed as:

$$\mathcal{E}_j \triangleq E_j - \mathrm{i}\frac{\Gamma_j}{2} \tag{D.12}$$

It can be shown (c.f. discussion section IX.2.d pp.297–298 in [214], or section 9.2 eq. (9.11) in [185]) that fundamental physical properties (conservation of probability, causality and time reversal) ensure that the poles reside either on the positive semi-axis of purely-imaginary $k_c \in \mathrm{i}\mathbb{R}_+$ – corresponding to bound states for real sub-threshold energies, i.e. $E_j < E_{T_c}$ and $\Gamma_j = 0$ – or that all the other poles are on the lower-half k_c plane, with $\Gamma_j > 0$, corresponding to "resonance" or "radioactively decaying" states. All poles enjoy the specular symmetry property: if $k_c \in \mathbb{C}$ is a pole of the Kapur-Peierls operator, then $-k_c^*$ is too.

Let $M_j = \dim\left(\mathrm{Ker}\left(\boldsymbol{R}_L^{-1}(\mathcal{E}_j)\right)\right)$ be the dimension of the nullspace of the inverse of the Kapur-Peierls operator at pole value $\mathcal{E}_j$ – that is M_j is the geometric multiplicity. We can thus write $\mathrm{Ker}\left(\boldsymbol{R}_L^{-1}(\mathcal{E}_j)\right) = \mathrm{Span}\left(\boldsymbol{q_j^1}, \ldots, \boldsymbol{q_j^m}, \ldots, \boldsymbol{q_j^{M_j}}\right)$. As we discuss in section D.5.3, it is physically reasonable to assume that the geometric and algebraic multiplicities are equal (semi-simplicity condition), which entails a Laurent development of order one for the poles – i.e. no higher powers of $\frac{1}{E-\mathcal{E}_j}$ in expansion (D.9). Since $\boldsymbol{R}_L$ is complex-symmetric, if we assume we can find non-quasi-null eigenvectors solutions to (E.32) – that is $\forall\ (j,m)\ ,\ \boldsymbol{q_j^m}^{\mathsf{T}}\boldsymbol{q_j^m} \neq 0$ so it is non-defective [113, 119, 96, 292, 66, 151, 152] – then Gohberg-Sigal theory can be adapted to the case of complex-symmetric matrices to normalize the rank-M_j residues of $\boldsymbol{R}_L$ matrix as:

$$\sum_{m=1}^{M_j} \boldsymbol{r_j^m}\boldsymbol{r_j^m}^{\mathsf{T}} = \sum_{m=1}^{M_j} \frac{\boldsymbol{q_j^m}\boldsymbol{q_j^m}^{\mathsf{T}}}{\boldsymbol{q_j^m}^{\mathsf{T}}\left(\frac{\partial \boldsymbol{R}_L^{-1}}{\partial E}\Big|_{E=\mathcal{E}_j}\right)\boldsymbol{q_j^m}} \tag{D.13}$$

The residue widths $\left\{\boldsymbol{r_j^m}\right\}$, here called *radioactive widths*, can thus directly be expressed as:

$$\boldsymbol{r_j^m} = \frac{\boldsymbol{q_j^m}}{\sqrt{\boldsymbol{q_j^{m\mathsf{T}}}\left(\frac{\partial \boldsymbol{R_L^{-1}}}{\partial E}\Big|_{E=\mathcal{E}_j}\right)\boldsymbol{q_j^m}}} \tag{D.14}$$

where $\frac{\partial \boldsymbol{R_L^{-1}}}{\partial E}\Big|_{E=\mathcal{E}_j}$ can readily be calculated by means of the following property:

$$\frac{\partial \boldsymbol{R_L^{-1}}}{\partial E}\Big|_{E=\mathcal{E}_j} = \frac{\partial \boldsymbol{R}^{-1}}{\partial E}(\mathcal{E}_j) - \frac{\partial \boldsymbol{L}}{\partial E}(\mathcal{E}_j) \tag{D.15}$$

where the R-matrix $\boldsymbol{R}$ is invertible at the radioactive poles $\{\mathcal{E}_j\}$, with

$$\frac{\partial \boldsymbol{R}^{-1}}{\partial E}(E) = -\boldsymbol{R}^{-1}\boldsymbol{\gamma}^{\mathsf{T}}\left(\boldsymbol{e} - E\mathbb{I}\right)^{-2}\boldsymbol{\gamma}\boldsymbol{R}^{-1} \tag{D.16}$$

In practice, we are most often presented with non-degenerate states where $M_j = 1$, meaning the kernel is an eigenline $\mathrm{Ker}\left(\boldsymbol{R_L^{-1}}(\mathcal{E}_j)\right) = \mathrm{Span}\left(\boldsymbol{q_j}\right)$, which entails rank-one residues normalized as:

$$\boldsymbol{r_j}\boldsymbol{r_j}^{\mathsf{T}} = \frac{\boldsymbol{q_j}\boldsymbol{q_j}^{\mathsf{T}}}{\boldsymbol{q_j}^{\mathsf{T}}\left(\frac{\partial \boldsymbol{R_L^{-1}}}{\partial E}\Big|_{E=\mathcal{E}_j}\right)\boldsymbol{q_j}} \tag{D.17}$$

or equivalently

$$\boldsymbol{r_j}^{\mathsf{T}}\left(\frac{\partial \boldsymbol{R_L^{-1}}}{\partial E}\Big|_{E=\mathcal{E}_j}\right)\boldsymbol{r_j} = 1 \tag{D.18}$$

thus for clarity of reading and without loss of generality, we henceforth drop the superscript "m" and summation over the multiplicity, unless it is of specific interest.

The *radioactive poles*, $\{\mathcal{E}_j\}$, and *radioactive widths*, $\left\{\boldsymbol{r_j^m} = \left[r^m_{j,c_1}, \ldots, r^m_{j,c}, \ldots, r^m_{j,c_{N_c}}\right]^{\mathsf{T}}\right\}$, are the Siegert-Humblet parameters. They are complex and locally untangle the energy dependence into an expansion sum of poles and residues (D.9). Additional discussion on these poles and residues can be found in [214], sections IX.2.c-d-e p.297-298, or in [296, 86, 218, 110].

The Kapur-Peierls matrix $\boldsymbol{R}_L$ is invariant to a change in boundary conditions B_c — c.f. equations (25) and (26) of section II.F of [127] — this entails the radioactive poles $\{\mathcal{E}_j\}$ and widths $\{\boldsymbol{r_j}\}$ are independent of the boundary condition B_c.

D.3.2 Level matrix $\boldsymbol{A}(E)$ approach to Siegert & Humblet expansion

An alternative approach to calculating the Siegert-Humblet parameters $\left\{a_c, \mathcal{E}_j, r^m_{j,c}, E_{T_c}\right\}$ from the Wigner-Eisenbud ones $\{a_c, B_c, \gamma_{\lambda,c}, E_\lambda, E_{T_c}\}$ is through the level matrix $\boldsymbol{A}$.

We search for the poles and eigenvectors of the level matrix operator $\boldsymbol{A}$:

$$\boldsymbol{A}^{-1}(E)\Big|_{E=\mathcal{E}_j}\boldsymbol{b_j}=\boldsymbol{0} \tag{D.19}$$

from (E.18), this means solving for the eigenvalues $\{\mathcal{E}_j\}$ and associated eigenvectors $\{\boldsymbol{b_j}\}$ that satisfy:

$$\left[\boldsymbol{e}-\boldsymbol{\gamma}\left(\boldsymbol{L}(\mathcal{E}_j)-\boldsymbol{B}\right)\boldsymbol{\gamma}^{\mathsf{T}}\right]\boldsymbol{b_j}=\mathcal{E}_j\boldsymbol{b_j} \tag{D.20}$$

This problem is analogous to the alternative parametrization of R-matrix theory, but replacing the shift factor $\boldsymbol{S}$ with the outgoing-wave reduced logarithmic derivative $\boldsymbol{L}$ (c.f. [127]).

Again, the same hypotheses as for the Kapur-Peierls operator $\boldsymbol{R}_L$ in section D.3.1 allow us to adapt the Gohberg-Sigal theory to the case of complex-symmetric operators to yield the following local Mittag-Leffler expansion of the level matrix (with normalized residues):

$$\boldsymbol{A}(E)\underset{\mathcal{W}(E)}{=}\sum_{j\geq 1}\frac{\sum_{m=1}^{M_j}\boldsymbol{a_j^m}\boldsymbol{a_j^{m\mathsf{T}}}}{E-\mathcal{E}_j}+\mathbf{Hol}_{\boldsymbol{A}}(E) \tag{D.21}$$

In the most frequent case of non-degenerate eigenvalues to (E.36), this yields rank-one residues as:

$$\boldsymbol{A}(E)\underset{\mathcal{W}(E)}{=}\sum_{j\geq 1}\frac{\boldsymbol{a_j}\boldsymbol{a_j}^{\mathsf{T}}}{E-\mathcal{E}_j}+\mathbf{Hol}_{\boldsymbol{A}}(E) \tag{D.22}$$

Again, under non-quasi-null eigenvectors assumption $\boldsymbol{b_j^{m\mathsf{T}}}\boldsymbol{b_j^m}\neq 0$, Gohberg-Sigal theory ensures the residues are normalized as:

$$\boldsymbol{a_j^m}\boldsymbol{a_j^{m\mathsf{T}}}=\frac{\boldsymbol{b_j^m}\boldsymbol{b_j^{m\mathsf{T}}}}{\boldsymbol{b_j^{m\mathsf{T}}}\left(\frac{\partial\boldsymbol{A}^{-1}}{\partial E}\Big|_{E=\mathcal{E}_j}\right)\boldsymbol{b_j^m}} \tag{D.23}$$

which is readily calculable from

$$\frac{\partial\boldsymbol{A}^{-1}}{\partial E}(\mathcal{E}_j)=-\mathbb{I}-\boldsymbol{\gamma}\frac{\partial\boldsymbol{L}}{\partial E}(\mathcal{E}_j)\boldsymbol{\gamma}^{\mathsf{T}} \tag{D.24}$$

Plugging (D.21) into (E.15), and invoking the unicity of the complex residues, implies the radioactive widths (D.14) can be obtained as

$$\boldsymbol{r_j^m}=\boldsymbol{\gamma}^{\mathsf{T}}\boldsymbol{a_j^m} \tag{D.25}$$

This is an interesting and novel way to define the Siegert-Humblet parameters, which is similar to the alternative parameters definition of [127]. From this perspective, the alternative parameters appear as a special case that leave the Siegert-Humblet level-matrix parameters invariant to boundary condition B_c. Indeed, one could search for the Siegert-Humblet expansion of the alternative parametrization of R-matrix theory, by simply proceeding as in equation (34) section III.A of [127], but

replacing the level matrix $\boldsymbol{A}$ with the alternative level matrix $\widetilde{\boldsymbol{A}}$ (defined in equations (30) and (33) section III.A of [127]):

$$\widetilde{\boldsymbol{A}}^{-1}(E)\Big|_{E=\mathcal{E}_j}\widetilde{\boldsymbol{b}_j}=\boldsymbol{0} \tag{D.26}$$

The exact same Gohberg-Sigal procedure can then be applied to the Mittag-Leffler expansion of the alternative level matrix $\widetilde{\boldsymbol{A}}$, in the vicinity $\mathcal{W}(E)$ of $E\in\mathbb{C}$ away from branch points $\{E_{T_c}\}$,

$$\widetilde{\boldsymbol{A}}(E)\underset{\mathcal{W}(E)}{=}\sum_{j\geq 1}\frac{\sum_{m=1}^{M_j}\widetilde{\boldsymbol{a}_j^m}\widetilde{\boldsymbol{a}_j^m}^{\mathsf{T}}}{E-\mathcal{E}_j}+\mathbf{Hol}_{\widetilde{\boldsymbol{A}}}(E) \tag{D.27}$$

yielding the normalized residue widths:

$$\widetilde{\boldsymbol{a}_j^m}\widetilde{\boldsymbol{a}_j^m}^{\mathsf{T}}=\frac{\widetilde{\boldsymbol{b}_j^m}\widetilde{\boldsymbol{b}_j^m}^{\mathsf{T}}}{\widetilde{\boldsymbol{b}_j^m}^{\mathsf{T}}\left(\frac{\partial\widetilde{\boldsymbol{A}}^{-1}}{\partial E}\Big|_{E=\mathcal{E}_j}\right)\widetilde{\boldsymbol{b}_j^m}} \tag{D.28}$$

where (E.38) can be combined to equation (33) of [127]:

$$\boldsymbol{\gamma}^{\mathsf{T}}\boldsymbol{A}\boldsymbol{\gamma}=\widetilde{\boldsymbol{\gamma}}^{\mathsf{T}}\widetilde{\boldsymbol{A}}\widetilde{\boldsymbol{\gamma}}$$

to calculate the energy derivative. Then, plugging (D.28) into the same equation (33) of [127], we obtain the relation between the alternative R-matrix parameters and the Siegert-Humblet radioactive parameters:

$$\boldsymbol{r_j^m}=\widetilde{\boldsymbol{\gamma}}^{\mathsf{T}}\widetilde{\boldsymbol{a}_j^m} \tag{D.29}$$

This relation (D.29) is especially enlightening when compared to (E.39) from the viewpoint of invariance to boundary condition B_c. Indeed, we explained that the Siegert-Humblet parameters $\left\{\mathcal{E}_j,\boldsymbol{r_j^m}\right\}$ are invariant with a change of boundary condition $B_c\to B_c'$. This is however not true of the level matrix residue widths $\left\{\boldsymbol{a_j^m}\right\}$ from (D.23). Thus, we can formally write this invariance by differentiating (E.39) with respect to B_c and noting that $\frac{\partial\boldsymbol{r_j^m}}{\partial\boldsymbol{B}}=\boldsymbol{0}$, yielding:

$$\boldsymbol{0}=\frac{\partial\boldsymbol{\gamma}^{\mathsf{T}}}{\partial\boldsymbol{B}}\boldsymbol{a_j^m}+\boldsymbol{\gamma}^{\mathsf{T}}\frac{\partial\boldsymbol{a_j^m}}{\partial\boldsymbol{B}} \tag{D.30}$$

This new relation links the variation of the Wigner-Eisenbud resonance widths $\gamma_{\lambda,c}$ at level values E_λ (resonance energies) under a change of boundary conditions $B_{c'}$, to the variation of the level matrix residue widths $a_{j,c}^m$ at pole values $\mathcal{E}_j$ under change of boundary condition $B_{c'}$. Since transformations (26) and (27) of section II.F in [127] detail how to perform $\frac{\partial\boldsymbol{\gamma}^{\mathsf{T}}}{\partial\boldsymbol{B}}$, equation (D.30) could be used to update $\boldsymbol{a_j^m}$ under a change $B_c\to B_{c'}$.

Another telling insight from relation (D.30) is when we apply it to the relation between the alternative parameters and the Siegert-Humblet radioactive widths (D.29). Since the alternative parameters $\widetilde{\boldsymbol{\gamma}}$ are invariant to B_c (that is their main purpose), the same differentiation as in (D.30) now yields zero derivatives,

$$\mathbf{0} = \widetilde{\boldsymbol{\gamma}}^{\mathsf{T}} \frac{\partial \widetilde{\boldsymbol{a}_j^m}}{\partial \boldsymbol{B}} \tag{D.31}$$

This is obvious from the fact that the alternative level matrix $\widetilde{\boldsymbol{A}}$ is invariant under change of boundary condition. Yet invariance (D.31) is insightful at it presents the alternative parameters $\left\{\widetilde{E_i}, \widetilde{\gamma}\right\}$ as the ones which, when transformed to Siegert-Humblet radioactive parameters $\{\mathcal{E}_j, \boldsymbol{r_j}\}$ though (D.29), leave the level residue widths $\{\widetilde{\boldsymbol{a_j}}\}$ invariant to B_c.

Conversely, the Kapur-Peierls pole expansion (E.41) extends the alternative parametrization in that it generates boundary condition B_c independent poles $\{\mathcal{E}_j\}$ and radioactive widths $\{\boldsymbol{r_j}\}$ that explicitly invert the alternative level matrix $\widetilde{\boldsymbol{A}}$ to yield (D.27).

D.3.3 Siegert-Humblet Radioactive Pole Expansion Branch Structure

Section D.3.1 introduced the Siegert-Humblet parametrization as the solutions of radioactive problem (E.32), where the $\boldsymbol{R}(E)$ matrix (E.16) is a function of the energy E, while $\boldsymbol{L}(\boldsymbol{\rho})$ is a function of the dimensionless wavenumber $\rho_c \triangleq a_c k_c(E)$. Thus, radioactive problem (E.32) can be solved either in energy space or in momentum space, both of which are linked by the $\rho(E)$ mapping (E.4). This mapping induces a multi-sheeted Riemann surface, which introduces branch-points and sheets we now unveil in theorem 9.

Theorem 9. *Siegert-Humblet Radioactive Pole Expansion Branch Structure.*
Let the radioactive poles $\{\mathcal{E}_j\}$ be the solutions of the radioactive problem (E.32), and $\{E_{T_c}\}$ denote the threshold energies, branch-points of the $\rho_c(E)$ wavenumber-energy mapping (E.4), then:

- *in the neighborhood $\mathcal{W}(E)$ of any complex energy E away from branch-points $\{E_{T_c}\}$, there exists a series of complex matrices $\{\mathbf{c}_n\}$ such that the Mittag-Leffler expansion (E.41) takes the analytic form:*

$$\boldsymbol{R}_L(E) \underset{\mathcal{W}(E)}{=} \sum_{j\geq 1} \frac{\boldsymbol{r_j}\boldsymbol{r_j}^{\mathsf{T}}}{E - \mathcal{E}_j} + \sum_{n\geq 0} \mathbf{c}_n E^n \tag{D.32}$$

- *the radioactive poles $\{\mathcal{E}_j\}$ are complex, and live on the multi-sheeted Riemann surface of $k_c(E)$ wavenumber-energy mapping (E.4):*

$$\left\{\mathcal{E}_j, +, +, -, \ldots, +, -\right\} \tag{D.33}$$

- *Let N_L be the number of solutions to the radioactive problem (E.32) in wavenumber $\boldsymbol{\rho}$ space. For every sheet of the of the wavenumber-energy mapping (E.4), each pole of the R-matrix (resonance energy E_λ level) yields two radioactive poles, and each pole of the outgoing wavefunction reduced logarithmic derivative operator $L_c(\rho_c)$ (the ω_n of Mittag-Leffler expansion (D.7) established in theorem 1 section II.B and documented in TABLES I & II of [127]) yields another additional pole.*

- *For neutral particles, denoting $N_{E_{T_c} \neq E_{T_{c'}}}$ the number of channels with different thresholds, this entails the number N_L of radioactive poles is:*

$$N_L = \left(2N_\lambda + \sum_{c=1}^{N_c} \ell_c \right) \times 2^{\left(N_{E_{T_c} \neq E_{T_{c'}}} - 1\right)} \tag{D.34}$$

- *For charged particles, this entails an infinite number (countable) of radioactive poles: $N_L = \infty$.*

Proof. Away from the branch points $\{E_{T_c}\}$, the holomorphic part of Mittag-Leffler expansion (E.41) can be analytically expanded in series as (D.32) – we here assumed the non-degenerate case of rank-one residues (multiplicity $M_j = 1$) though it is readily generalizable to (D.9).

When solving radioactive problem (E.32), or (D.20), to obtain the Siegert-Humblet poles $\{\mathcal{E}_j\}$ and residues $\{\boldsymbol{r_j}\}$, or $\{\boldsymbol{a_j}\}$, it is necessary to compute the $\boldsymbol{L^0}$ matrix function $\boldsymbol{L^0}(E) \triangleq \boldsymbol{L^0}(\boldsymbol{\rho}(E))$ for complex energies $E \in \mathbb{C}$. As discussed in [127] (c.f. sections II.A, B, III. B. and C. of [127]), mapping (E.4) generates a multi-sheeted Riemann surface with 2^{N_c} branches (with the threshold values E_{T_c} as branch points), corresponding to the choice for each channel c, of the sign of the square root in $\boldsymbol{\rho}(E)$. This means that when searching for the poles, one has to keep track of these choices and specify for each pole $\mathcal{E}_j$ on what sheet it is found. Every pole $\mathcal{E}_j$ must thus come with the full reporting of these N_c signs, i.e. $\{\mathcal{E}_j, -, +, +, \ldots, -, +\}$ as (D.33).

When searching for these radioactive poles in wavenumber space, the $\boldsymbol{R}_L$ Kapur-Peierls operator (E.15) is continued to complex wavenumbers by meromorphic continuation of $\boldsymbol{L}(\boldsymbol{\rho})$, where the reduced logarithmic derivative of the outgoing wavefunction (E.17) takes the Mittag-Leffler expansion described in equation (13) of theorem 1 section II.B. of [127]. There are more radioactive poles $\{\mathcal{E}_j\}$ than Wigner-Eisenbud levels $\{E_\lambda\}$ — as was the case for the alternative parameters (c.f. theorems 2 and 3 III.C of [127]). For massive neutral particles, we can proceed in an analogous fashion as for the proof of theorem 3 section III.C of [127], and apply the diagonal divisibility and capped multiplicities lemma (lemma 3 section III.C. of [127]) to the determinant of the Kapur-Peierls operator $\boldsymbol{R}_L$ in (E.32) – but this time in ρ_c space – and then look at the order of the resulting rational fractions in ρ_c and the number of times one must square the polynomials to unfold all $\rho_c = \mp\sqrt{\cdot}$ sheets of mapping (E.4). We were thus able to establish that the number N_L of poles in wavenumber ρ-space is $2N_\lambda + \sum_{c=1}^{N_c} \ell_c$ poles per sheet, capped by the level multiplicities (c.f. eq. (50) of

[127]):

$$N_L/2^{\left(N_{E_{T_c}\neq E_{T_{c'}}}-1\right)} = N_\lambda + \sum_{\substack{L_c \text{ multiplicity} \\ \text{capped at } N_\lambda}} \ell_c \tag{D.35}$$

which in practice falls back to (E.42) over all sheets (there are rarely fewer levels than the number of different channels that have the exact same $L_c(\rho_c)$ function), where $N_{E_{T_c}\neq E_{T_{c'}}}$ designates the number of different thresholds (including the obvious $E_{T_c} = 0$ zero threshold) and thus the number of sheets.

In the charged particles case, $L_c(\rho_c)$ has a countably infinite number of poles, which in turn induces an infinite number (countable) of solutions to the radioactive problem (E.32), though the discussion after the proof of theorem 1 in section II.B of [127] shows most of these poles are far-away poles, and only ℓ_c ones are within a closer range. □

It is important to grasp the meaning of the Mittag-Leffler expansion (E.41) — or (D.21) and (D.27). These are local expressions: they do not hold for all complex energies $E \in \mathbb{C}$ because of the branch-point structure of the Riemann sheet. However, in the neighborhood $\mathcal{W}(E)$ of any complex energy point $E \in \mathbb{C}$ away from the branch-points (thresholds $\{E_{T_c}\}$), the Mittag-Leffler expansion (E.41) is true, and its holomorphic part admits an analytic expansion $\mathbf{Hol}_{\boldsymbol{R}_L}(E) \triangleq \sum_{n\geq 0} \boldsymbol{c}_n E^n$. This has two major consequences for the Siegert-Humblet expansion. First, contrarily to the alternative parameters $\left\{\widetilde{E_i}, \widetilde{\gamma_{i,c}}\right\}$ discussed in [127], the Siegert-Humblet set of radioactive poles and widths $\{\mathcal{E}_j, r_{j,c}\}$ do not suffice to uniquely determine the energy behavior of the scattering matrix $\boldsymbol{U}(E)$: one needs to locally add the expansion coefficients $[\boldsymbol{c}_n]_{c,c'}$ of the entire part $\mathbf{Hol}_{\boldsymbol{R}_L}(E) \triangleq \sum_{n\geq 0} \boldsymbol{c}_n E^n$. Second, since the set of coefficients $\{\boldsymbol{c}_n\}$ is *a priori* infinite (and so is the set of poles in the Coulomb case), this means that numerically the Siegert-Humblet expansion can only be used to compute local approximations of the scattering matrix, which can nonetheless reach any target accuracy by increasing the number of $\{\mathcal{E}_j\}_{j\in[\![1,N_L]\!]}$ poles included and the order of the truncation $N_{\mathcal{W}(E)}$ in $\{\boldsymbol{c}_n\}_{n\in[\![1,N_{\mathcal{W}(E)}]\!]}$. In practice, this means that to compute the scattering matrix one needs to provide the Siegert-Humblet parameters $\{\mathcal{E}_j, r_{j,c}\}$, cut the energy domain of interest into local windows $\mathcal{W}(E)$ away from threshold branch-points $\{E_{T_c}\}$, and provide a set of local coefficients $\{\boldsymbol{c}_n\}_{n\in[\![1,N_{\mathcal{W}(E)}]\!]}$ for each window.

As discussed in [127] (c.f. lemmas 1 and 2 section III.B and theorems 2 and 3 of section III.C of [127]), the definition of the shift and penetration functions for complex wavenumbers is ambiguous (in particular purely imaginary wavenumbers yield negative or sub-threshold energies), which in turn entail various possible alternative parameters. When solving radioactive problem (E.32) to find the Siegert-Humblet radioactive poles and residues $\{\mathcal{E}_j, r_{j,c}\}$ – or (D.20) equivalently – there are no such ambiguities on the definition of $\boldsymbol{L}$: the Kapur-Peierls operator is simply analytically continued to complex wavenumbers. The unicity of analytic continuation thus entails that the Siegert-Humblet parameters are uniquely defined, as long as we specify for each channel c what sheet of the Riemann surface from mapping (E.4) was chosen,

as in (D.33).

The $\{\mathcal{E}_j, +, +, \ldots, +, +\}$ sheet is called the *physical sheet*, and we here call the poles on that sheet the *principal poles*. All other sheets are called *nonphysical* and the poles laying on these sheets are called *shadow poles*. Often, the principal poles are responsible for the resonant behavior, with shadow poles only contributing to background behavior, but cases have emerged where the shadow poles contribute significantly to the resonance structure, as reported in [163], and G. Hale there introduced a quantity called *strength* of a pole (c.f. eq. (7) in [163], or paragraph after eq. (2.11) XI.2.b, p.306, and section XI.4, p.312 in [214]) to quantify the impact a pole $\mathcal{E}_j$ will have on resonance behavior, by comparing the residue $r_{j,c}$ to the Wigner-Eisenbud widths $\gamma_{\lambda,c}$.

Result (E.42) is quite instructive: one can observe that the number N_L of Siegert-Humblet poles adds-up the number of levels N_λ and the number of poles of $\boldsymbol{L}$ (which is $\sum_{c=1}^{N_c} \ell_c$ for neutral massive particles, and is infinite in the Coulomb case, c.f. discussion after theorem 1 in section II.B of [127]. Moreover, N_L is duplicated with each new sheet of the Riemann surface from mapping (E.4) — that is associated to a new threshold, hence the $N_{E_{T_c} \neq E_{T_{c'}}}$. Interestingly, comparing N_L from (E.42) with the number N_S of alternative analytic poles from equation (49) in theorem 3 section III.C of [127] — which are in E-space and must thus be doubled to obtain the number of ρ-space poles — we note that the analytic continuation of the shift factor $\boldsymbol{S}$ (c.f. lemma 2 III.B of [127]) adds a virtual pole for each pole of $\boldsymbol{L}$ when unfolding the sheets of mapping (E.4), because it is a function of $\rho_c^2(E)$. This can readily be observed in the trivial case of a p-wave ($\ell = 1$) channel with one resonance (one level $N_\lambda = 1$), where $S(E) = -\frac{1}{1+\rho^2(E)}$ introduces two poles at $\rho(E) = \pm \mathrm{i}$, while $L(E) = \frac{-1+\mathrm{i}\rho(E)+\rho^2(E)}{1-\mathrm{i}\rho(E)}$ only counts one pole, at $\rho(E) = \mathrm{i}$.

As for equation (50) of theorem 3 section III.C. of [127], one should add the precision that in the sum over the channels in (E.42), the multiplicity of possible $L_c(\rho_c)$ repeated over many different channels $L_c(\rho_c) = L_{c' \neq c}(\rho_{c'})$ is capped by N_λ, which in practice would only occur in the rare cases where only one or two levels occurs for many channels with same angular momenta (and, of course, total angular momenta and parity J^π).

Numerically, solving the generalized eigenvalue problems (E.32) or (D.20) falls into the well-known class of nonlinear eigenvalue problems, for which algorithms we direct the reader to Heinrich Voss's chapter 115 in the Handbook of Linear Algebra [319]. We will just state that instead of the Rayleigh-quotient type of methods expressed in [319], it can sometimes be computationally advantageous to first find the poles $\{\mathcal{E}_j\}$ by solving the channel determinant problem, $\det\left(\boldsymbol{R}_L^{-1}(E)\Big|_{E=\mathcal{E}_j}\right) = 0$, or the corresponding level determinant one, $\det\left(\boldsymbol{A}^{-1}(E)\Big|_{E=\mathcal{E}_j}\right) = 0$, and then solve the associated linear eigenvalue problem. Methods tailored to find all the roots of this problem where introduced in [131], or in equations (200) and (204) of [149]. Notwithstanding, from a numerical standpoint, having the two approaches is beneficial in that solving (E.32) will be advantageous over solving (D.20) when the number of

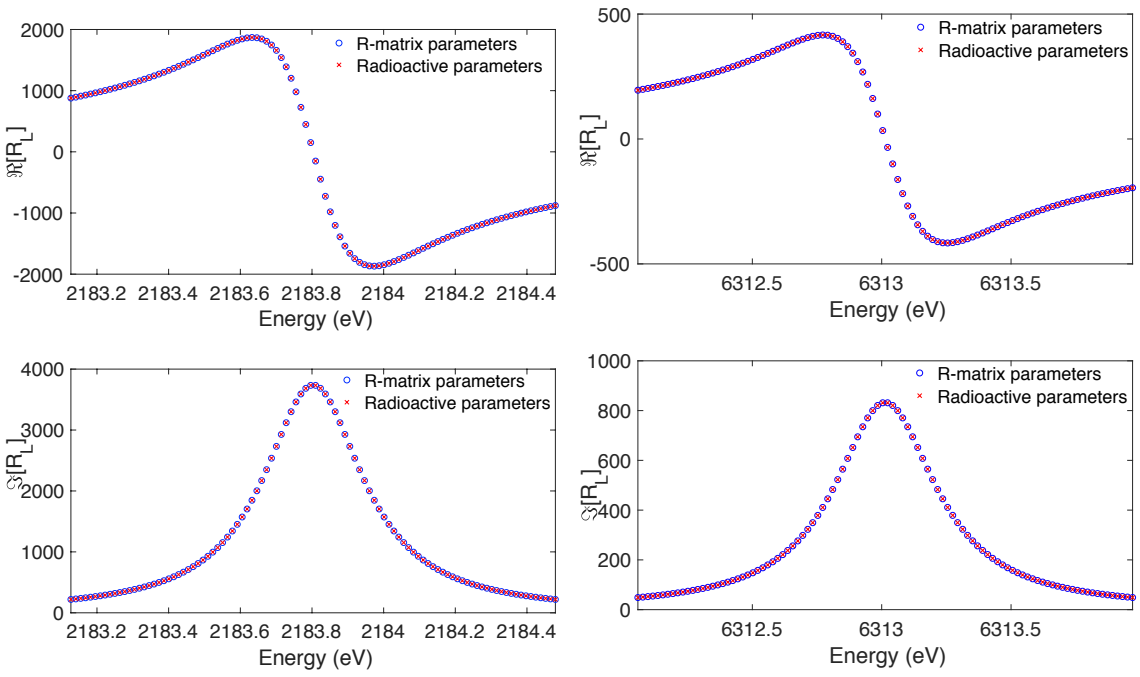

(a) First p-wave resonance.

(b) Second p-wave resonance.

Figure D-1: Kapur-Peierls $\boldsymbol{R}_L(E)$ operator (E.15) of xenon ^{134}Xe two p-wave resonances in spin-parity group $J^\pi = 1/2^{(-)}$. Dimensionless $\boldsymbol{R}_L(E)$ is computed using radioactive parameters from TABLE D.1 in expression (D.40), or using the R-matrix parameters from TABLE D.1 in Reich-Moore level-matrix (E.18) – that is definition (58) of [127] – yielding identical real and imaginary parts.

levels N_λ far exceeds the number of channels N_c, and conversely. Nonetheless, the multi-sheeted nature of the radioactive problem makes it harder to solve, as one must search each sheet of mapping (E.4) to find all the poles.

D.3.4 Xenon ^{134}Xe evidence of radioactive parameters

In our previous article [127], we observed the first evidence of shadow poles in the alternative parametrization of R-matrix theory in isotope xenon ^{134}Xe spin-parity group $J^\pi = 1/2^{(-)}$, showing how they depend on the choice of continuation to complex wavenumbers. We here document in TABLE D.1 the Siegert-Humblet radioactive parameters (poles and residues of the Kapur-Peierls $\boldsymbol{R}_L$ operator), for these same p-wave resonances of ^{134}Xe spin-parity group $J^\pi = 1/2^{(-)}$. As shown in FIG.D-1, both the radioactive parameters and the R-matrix parameters yield an identical Kapur-Peierls $\boldsymbol{R}_L(E)$ operator, and therefore exactly reconstruct the scattering matrix $\boldsymbol{U}(E)$ of the nuclear interactions, as reported in FIG. D-2. Note there are $N_L = 5$ radioactive poles, as predicted by (E.42) in theorem 9: two for each resonance energy E_λ level, and ℓ_c for each $L_c(\rho_c)$ channel. Indeed, we here have only one threshold (at zero) so that $N_{E_{T_c} \neq E_{T_{c'}}} = 1$, and there is only one channel, for which $\ell_c = 1$ (p-wave). As such, we observe in TABLE D.1 that for each resonance energy E_λ, there are two nearby

radioactive poles, each on one sheet of the Riemann surface energy-wavenumber mapping (E.4), and both close to (but not exactly) complex conjugates of one another. Also, the additional radioactive pole (the first in TABLE D.1) is close to the corresponding pole of the reduced logarithmic derivative of the outgoing operator $L_c(\rho_c)$: for neutral particles p-waves we have $\omega_1^{\ell=1} = -\mathrm{i}$ (see TABLE I of [127]), which entails a radioactive pole close to $\left(\frac{\mathrm{i}}{\rho_0}\right)^2 \approx -6.0673 \times 10^{+5}$. Incidentally, note that if there were only one level $N_\lambda = 1$, but two channels $N_c = 2$, both with the same angular momentum (say p-waves) and the same $\rho_c(E)$ mapping, then we would need to cap the multiplicity of the number of poles induced by these identical $L_c(\rho_c)$ to $N_\lambda = 1$, according to equation (D.35). This is rare in practice.

The exact reconstruction of the scattering matrix $\boldsymbol{U}(E)$ shown in FIG. D-2 is made possible because ^{134}Xe spin-parity group $J^\pi = 1/2^{(-)}$ has only a neutron channel with zero threshold ($E_{T_c} = 0$). In the particular case of neutral particles with zero threshold, the outgoing wavefunction reduced logarithmic derivative operator $\boldsymbol{L}(\boldsymbol{\rho})$ is a rational function in $\sqrt{E}$: this can be seen from Mittag-Leffler expansion (D.7) with a finite amount of poles $\{\omega_n\}$ (reported in theorem 1 section II.B and TABLE II of [127]). Therefore, the transformation $z \triangleq \sqrt{E}$ unfolds the Riemann surface of mapping (E.4): that is that searching for solutions to the radioactive problem (E.32) in z-space is equivalent to searching on both sheets of the $\pm\sqrt{E}$ Riemann surface from mapping (E.4). Moreover, a study of the numerator and denominator of the inverse level matrix $\boldsymbol{A^{-1}}(z)$ from (E.18) then shows that the level matrix $\boldsymbol{A}(z)$ is rational function of degree -2 in z-space, with N_L poles from (E.42) with only one sheet (no other thresholds than zero), so that its Mittag-Leffler expansion (D.22) is actually a partial fraction decomposition in simple z poles, without constant nor holomorphic part (c.f. section II.F. of [130] for more in depth discussion of this process):

$$\boldsymbol{A}(E) = \sum_{j=1}^{N_L} \frac{\frac{\boldsymbol{a_j}\boldsymbol{a_j}^\mathsf{T}}{2\sqrt{\mathcal{E}_j}}}{\sqrt{E} - \sqrt{\mathcal{E}_j}} \tag{D.36}$$

Note that the nullity of the constant term entails the following remarkable property:

$$\sum_{j=1}^{N_L} \frac{\boldsymbol{a_j}\boldsymbol{a_j}^\mathsf{T}}{2\sqrt{\mathcal{E}_j}} = \boldsymbol{0} \tag{D.37}$$

Since from (E.39) we have $\boldsymbol{r_j} = \boldsymbol{\gamma}^\mathsf{T}\boldsymbol{a_j}$ (assuming non-degenerate states), the latter properties on the level-matrix can be transcribed into the following exact pole expansion for the Kapur-Peierls operator (E.15):

$$\boldsymbol{R}_L(E) = \sum_{j=1}^{N_L} \frac{\frac{\boldsymbol{r_j}\boldsymbol{r_j}^\mathsf{T}}{2\sqrt{\mathcal{E}_j}}}{\sqrt{E} - \sqrt{\mathcal{E}_j}} \tag{D.38}$$

which is equivalent to eq. (106) of [130], and the null constant relations (D.37) entails

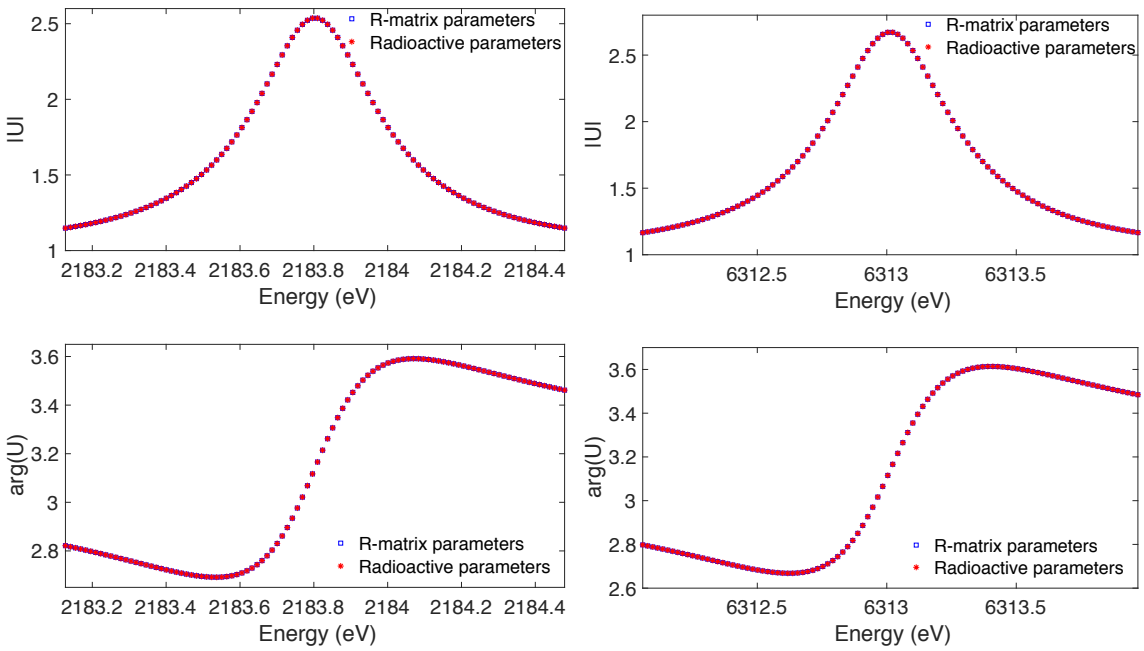

(a) First p-wave resonance. (b) Second p-wave resonance.

Figure D-2: Scattering matrix $\boldsymbol{U}(E)$ of xenon ^{134}Xe two p-wave resonances in spin-parity group $J^\pi = 1/2^{(-)}$, from equation (E.14). Dimensionless $\boldsymbol{U}(E)$ is computed using outgoing waves $\boldsymbol{O}(E)$ from TABLE I of [127] and conjugacy relations (D.71), combined with radioactive parameters from TABLE D.1 in expression (D.40), or R-matrix parameters from TABLE D.1 in Reich-Moore level-matrix (E.18) – that is definition (58) of [127] – yielding identical moduli and arguments.

the remarkable property on the radioactive parameters (c.f. eq. (108) of [130]):

$$\sum_{j=1}^{N_L} \frac{\boldsymbol{r_j}\boldsymbol{r_j}^\mathsf{T}}{2\sqrt{\mathcal{E}_j}} = \boldsymbol{0} \tag{D.39}$$

By setting a choice of sheet in $z = \pm\sqrt{E}$, the latter equations can be written as:

$$\boldsymbol{R}_L(E) = \sum_{j=1}^{N_L} \frac{\boldsymbol{r_j}\boldsymbol{r_j}^\mathsf{T}}{E - \mathcal{E}_j} + \underbrace{\sum_{j=1}^{N_L} \frac{\frac{\boldsymbol{r_j}\boldsymbol{r_j}^\mathsf{T}}{2\sqrt{\mathcal{E}_j}}}{\sqrt{E} + \sqrt{\mathcal{E}_j}}}_{\mathbf{Hol}_{\boldsymbol{R}_L}(E)} \tag{D.40}$$

where $-\sqrt{\mathcal{E}_j}$ is not a pole, and therefore the second term is the exact holomorphic part $\mathbf{Hol}_{\boldsymbol{R}_L}(E)$ from (E.41).

D.3.5 Comparing radioactive, traditional, and alternative R-matrix parameters

This case of xenon ^{134}Xe shows the general merits of the radioactive parameters: in contrast with the R-matrix resonance parameters, the radioactive poles $\mathcal{E}_j$ are independent of both the arbitrary boundary parameter B_c and the channel radius a_c, while the radioactive widths $\boldsymbol{r_j}$ are independent of the boundary parameters B_c and depend on the channel radius in a systematic way (provided by theorem 10 bellow). Moreover, in this specific neutral particles with zero-threshold case, the Kapur-Peierls $\boldsymbol{R}_L(E)$ operator pole expansions (D.38) and (D.40) are exact (c.f. FIG.D-1), and therefore can fully reconstruct the R-matrix model scattering matrix, as can be seen in FIG.D-2.

Nonetheless, this example also shows the limitations of the radioactive parameters pole expansion approach (D.32) of theorem 9. Just as the alternative parameters of Brune in [127], the radioactive parameters entangle the energy dimension with the wavenumber one, meaning one now has to specify with each radioactive pole $\mathcal{E}_j$ its sheet (D.33) on the Riemann surface of mapping (E.4), for each threshold branch, as specified in theorem 9. In contrast, though they depend on the arbitrary boundary parameters B_c and channel radii a_c, the traditional Wigner-Eisenbud R-matrix parameters have the truly remarkable (and seldom appreciated) property of de-entangling the energy dimension from the wavenumber one. The Wigner-Eisenbud resonance parameters are real and well defined in energy space, without any need to map to the wavenumber and therefore specify where the resonance energies E_λ dwell on the multi-sheeted Riemann surface of mapping (E.4).

Another significant limitation of the radioactive parameters is that they are in general incomplete, meaning that the knowledge of the radioactive poles and residues is not sufficient to fully parametrize the $\boldsymbol{R}_L(E)$ Kapur-Peierls operator: one also needs to parametrize the holomorphic part $\mathbf{Hol}_{\boldsymbol{R}_L}(E)$ in Mittag-Leffler expansion (D.32). In the general case of charged particles or thresholds, there is no simple way of parametrizing this holomorphic part (though it is known exactly for zero-threshold neutral particles as equation (D.40) specifies). Moreover, even if the holomorphic part were known, in the general case of charged particles and thresholds there is an infinite number of radioactive poles ($N_L = \infty$), all of which are necessary to exactly reconstruct the scattering matrix. This means the radioactive parameters alone are not very well suited for evaluations in standard nuclear data libraries. Nonetheless, the radioactive poles have recently been used to constitute an alternative nuclear data library — the *windowed multipole library* — with the goal of achieving significant computational performance gains in nuclear simulations, as we explain in our follow-up article [130]: the final in the xenon trilogy on pole parametrizations of R-matrix theory [127, 126, 130].

For comparison, the alternative parameters proposed by Brune in [92] combine some merits and drawbacks of both the radioactive and the traditional (Wigner-Eisenbud) parameters. Like the radioactive parameters, the alternative parameters are independent of the arbitrary boundary condition B_c, though they still depend on arbitrary channel radii a_c. Like the Wigner-Eisenbud resonance parameters, the

alternative parameters are always complete: with the knowledge of N_λ alternative poles, one can fully reconstruct the scattering matrix (c.f. theorem 4 of [127]). On the other hand, unlike the Wigner-Eisenbud resonance parameters, the alternative parameters entangle the energy dimension with the wavenumber one: as for the radioactive poles, one must specify on which sheet of the Riemann surface (E.4) are the alternative poles (c.f. theorems 2 of [127]). However, proper analytic continuation will unfold the sheets of Riemann surface (E.4) and thus render such specification useless, as we show in theorem 3 of [127] — this is another strong argument in favor of analytic continuation of R-matrix operators, in particular the shift $S_c(\rho_c)$ and penetration $P_c(\rho_c)$ functions (contrarily to "force-closure" legacy of Lane & Thomas). Moreover, in practice this is not as much of a limitation, as we showed in theorem 4 of [127] that we can always choose the first N_λ resonant alternative poles of the physical sheet $\{E, +\}$. Nonetheless, all Reich-Moore and sub-threshold alternative parameters still change depending on whether the shift $S_c(E)$ and penetration $P_c(E)$ functions are analytically continued (theorem 3 of [127]) or "forced-closed" as defined by Lane & Thomas (theorem 2 of [127]): we here argue that the physically and mathematically correct way is to perform analytic continuation of the shift $S_c(\rho_c)$ and penetration $P_c(\rho_c)$ functions, and provide many more arguments for this in section D.5.

Note that a commonly alleged advantage of the alternative poles $\widetilde{E_\lambda}$ is that they correspond to the peak of the resonances – actually of the Kapur-Peierls operator $\boldsymbol{R}_L(E)$ since the cross section has an additional $\frac{1}{|k_c(E)|^2}$ modulating term (see [130] for more discussion on this). Though this is true in the case of full R-matrix equations (where the resonance energies are real) for resonant poles above threshold (not the shadow poles discovered in [127]), this ceases to be true for channel-eliminated Reich-Moore evaluations (where the resonance energies are in effect complex $E_\lambda - \mathrm{i}\frac{\Gamma_{\lambda,\gamma}}{2}$ as explained in section II.A.4. of [130]). Indeed, the alternative poles $\widetilde{E_\lambda}$ are then complex (c.f. section IV.A of [127]), and neither analytic continuation nor Lane & Thomas force-closure will entail their real parts exactly correspond to the Kapur-Peierls operator $\boldsymbol{R}_L(E)$ resonance peaks. The exact peaks of the $\boldsymbol{R}_L(E)$ resonances are actually the real parts of the radioactive poles $\Re[\mathcal{E}_j]$, and the widths are the imaginary parts $\Im[\mathcal{E}_j]$, which we here document in TABLE D.1 and shown in FIG.D-1 for the two p-wave resonances of xenon ^{134}Xe spin-parity group $J^\pi = 1/2^{(-)}$. In practice, though, the real part of the alternative poles $\Re\left[\widetilde{E_\lambda}\right]$ are close (but not identical) to the real part of the radioactive poles $\Re[\mathcal{E}_j]$ (one needs to go to more digits to see the discrepancy between values of TABLE VI in [127] to our TABLE D.1 here), and as such are much closer to the peak of the resonances than are the Wigner-Eisenbud resonance energies E_λ.

Another important characteristic of the radioactive parameters is that they are the bridge between the R-matrix theory parametrizations of nuclear reactions, and the scattering matrix pole expansions of Humblet and Rosenfeld, as we now explain in section D.3.6.

D.3.6 Radioactive parameters link R-matrix theory to the scattering matrix pole expansions

So far, we have started from the R-matrix Wigner-Eisenbud parameters $\{E_\lambda, \gamma_{\lambda,c}\}$ to construct the poles and residues of the Kapur-Peierls operator $\boldsymbol{R}_L$, through (E.32) and (D.14). We here show that these Siegert-Humblet radioactive parameters are the link between R-matrix theory (c.f. [323, 79, 214]) and the scattering matrix pole expansions of Humblet-Rosenfeld and others (c.f. [135, 159, 117, 185, 289, 181, 182, 195, 183, 230, 290]).

Indeed, plugging-in the Kapur-Peierls $\boldsymbol{R}_L$ operator expansion (E.41) into the expression of the scattering matrix (E.14) then yields the Mittag-Leffler expansion of the scattering matrix:

$$\boldsymbol{U}(E) \underset{\mathcal{W}(E)}{=} \boldsymbol{w} \sum_{j\geq 1} \frac{\boldsymbol{u_j}\boldsymbol{u_j}^\mathsf{T}}{E-\mathcal{E}_j} + \mathbf{Hol}_{\boldsymbol{U}}(E) \tag{D.41}$$

where $\boldsymbol{w} \triangleq 2\mathrm{i}\mathbb{I}$ is the Wronskian (D.3), and the scattering residue widths $\boldsymbol{u_j}$ are defined as:

$$\boldsymbol{u_j} \triangleq \left[\boldsymbol{\rho}^{1/2}\boldsymbol{O}^{-1}\right]_{E=\mathcal{E}_j} \boldsymbol{r_j} \tag{D.42}$$

In writing (D.41), we have used the fact that all the resonances of the scattering matrix $\boldsymbol{U}(E)$ come from the Kapur-Peierls radioactive poles $\{\mathcal{E}_j\}$ – indeed, we demonstrate in theorem 11, section D.5.4, that the poles $\{\omega_n\}$ of the outgoing wave function $\boldsymbol{O}(E)$ cancel out in (E.14) and are thus not present in the scattering matrix. Cauchy's residues theorem then allows us to evaluate the residues at the pole value to obtain (D.42). As for (E.41), if a resonance were to be degenerate with multiplicity M_j, the residues would no longer be rank-one, but instead the scattering matrix residue associated to pole $\mathcal{E}_j$ would be $\sum_{m=1}^{M_j} \boldsymbol{u_j^m}\boldsymbol{u_j^m}^\mathsf{T}$, with $\boldsymbol{u_j^m} \triangleq \left[\boldsymbol{\rho}^{1/2}\boldsymbol{O}^{-1}\right]_{E=\mathcal{E}_j} \boldsymbol{r_j^m}$.

Expression (D.41) exhibits the advantage that the energy dependence of the scattering matrix $\boldsymbol{U}(E)$ is untangled in a simple sum. All the resonance behavior stems from the complex poles and residue widths $\{\mathcal{E}_j, u_{j,c}\}$, which yield the familiar Breit-Wigner profiles (Cauchy-Lorentz distributions) for the cross section. Conversely, all the threshold behavior and the background are described by the holomorphic part $\mathbf{Hol}_{\boldsymbol{U}}(E)$, which can be expanded in various forms, for instance analytically (D.43).

This establishes the important bridge between the R-matrix parametrizations and the Humblet-Rosenfeld expansions of the scattering matrix. More precisely, Mittag-Leffler expansion (D.41) is identical to the Humblet-Rosenfeld expansions (10.22a)-(10.22b) in [185] for the neutral particles case, and (5.4a)-(5.4b) in [182] for the Coulomb case. We thus here directly connect the R-matrix parameters with the Humblet-Rosenfeld resonances, parametrized by their partial widths and real and imaginary poles, as described in [181]. In particular, the poles $\{\mathcal{E}_j\}$ from (E.40), found by solving (E.32), are exactly the ones defined by equations (9.5) and (9.8) in [185]. The scattering residue widths $\{u_{j,c}\}$, calculated from (D.42), then correspond to the Humblet-Rosenfeld complex residues (10.12) in [185], from which they build their quantities $\{G_{c,n}\}$ appearing in expansions (10.22a)-(10.22b) in [185], or (5.4a)-

(5.4b) in [182]. Finally, the holomorphic part $\mathbf{Hol}_U(E)$ corresponds to the regular function $Q_{c,c'}(E)$ defined between (10.14a) and (10.14b) in [185].

Just as Humblet and Rosenfeld did with $Q_{c,c'}(E)$ in section 10.2 of [185] and section 4 of [182], we do not give here an explicit way of calculating this holomorphic contribution $\mathbf{Hol}_U(E)$ other than stating that it is possible to expand it in various ways. Far from a threshold, an analytic series in energy space E can stand:

$$\mathbf{Hol}_U(E) \underset{\mathcal{W}(E)}{=} \sum_{n\geq 0} \boldsymbol{s}_n E^n \tag{D.43}$$

In the immediate vicinity of a threshold, the asymptotic threshold behavior will prevail (for massive particles, $U_{c,c'} \sim k_c^{\ell_c+1} k_{c'}^{\ell_{c'}}$, c.f. eq.(10.5) in [185], or [322]), yielding an expansion in wavenumber space of the form:

$$\mathbf{Hol}_U(E) \underset{\mathcal{W}(E_{T_c})}{=} \sum_{n\geq 0} \boldsymbol{s}_n k_c^n(E) \tag{D.44}$$

Though there is no explicit way of linking these expansions (D.44) or (D.43) to the R-matrix Wigner-Eisenbud parameters $\{E_\lambda, \gamma_{\lambda,c}\}$, this means that the same approach as that discussed in the paragraph following theorem 9 can be taken: one can provide a local set of coefficients $\{\boldsymbol{s}_n\}_{\mathcal{W}(E)}$ to expand the holomorphic part of the scattering matrix $\mathbf{Hol}_U(E)$, and then calculate the scattering matrix from the Mittag-Leffler expansion (D.41). This is at the core of the windowed multipole representation of R-matrix cross sections established in [130].

An important question is that of the radius of convergence of the Mittag-Leffler expansion (D.41), in other terms how big can the vicinity $\mathcal{W}(E)$ be? Humblet and Rosenfeld analyze this problem in section 1.4 of [185], and perform the Mittag-Leffler expansion (1.50). In the first paragraph of p.538 it is stated that Humblet demonstrated in his Ph.D. thesis that the Mittag-Leffler series will converge for $M \geq 1$ for $U(k)$, though this does not investigate the multi-channel case, and thus the multi-sheeted nature of the Riemann surface stemming from mapping (E.4). They assume at the beginning of section 10.2 that this property stands in the multi-channel case and yet continue their discussion with a choice of $M = 0$ that would leave the residues diverging according to their expansion (1.50). This is one reason why we chose in this article to start from a local Mittag-Leffler expansion, and then search for its domain of convergence. General mathematical scattering theory shows that the Mittag-Leffler expansion holds at least on the whole physical sheet (c.f. theorem 0.2 p.139 of [159]). Moreover, in his article on "threshold behaviour in quantum field theory"[**?**], Eden proves that "between the threshold values [...] the [Scattering] matrix elements are analytic functions of the energies and momenta of the incident particles", though it does not specify in which form the Mittag-Leffler expansion will converge separately on each sheet. In practice this requirement is not needed since it is often computationally more advantageous to break down an energy region between two consecutive thresholds $\left[E_{T_c}, E_{T_{c+1}}\right]$ into smaller vicinities (a compression method for efficient computation used in the windowed multipole library [130]).

As we see, by performing the Mittag-Leffler expansion (D.41), we have traded-

off a finite set of real, unwound, Wigner-Eisenbud parameters $\{E_\lambda, \gamma_{\lambda,c}\}$ that completely parametrize the energy dependence of the scattering matrix through (E.14), with an infinite set of complex Siegert-Humblet radioactive parameters $\{\mathcal{E}_j, r_{j,c}\}$ plus some local coefficients $\{\boldsymbol{s_n}\}_{\mathcal{W}(E)}$ for the holomorphic part, all intricately intertwined through radioactive problem (E.32), which makes them dwell on a sub-manifold of the multi-sheeted Riemann surface of mapping (E.4). This additional complexity of the Siegert-Humblet parameters comes at the gain of a simple parametrization of the energy dependence for the scattering matrix: the poles and residues expansion (D.41). For computational purposes, this may sometimes be a trade-off worth doing: this is the basis for the windowed multipole representation of R-matrix cross sections [130].

D.4 Radioactive parameters invariance to channel radii

Section D.3 provided new insights into the link between the Humblet-Rosenfeld scattering matrix pole expansions, and both the Wigner-Eisenbud, and the Siegert-Humblet parametrizations of R-matrix theory. Concerning invariance to arbitrary parameters, we saw that the Siegert-Humblet parameters are invariant under change of boundary condition B_c, but not under change of channel radius a_c — this is also true for the alternative parameters discussed in [127]. This section is dedicated to invariance properties of the Siegert-Humblet radioactive parameters to a change in channel radius a_c. This problem is less studied than that of the invariance to the boundary conditions B_c. To the best of our knowledge, the only previous results on this topic are the partial differential equations on the Wigner-Eisenbud $\{E_\lambda, \gamma_{\lambda,c}\}$ parameters Teichmann derived in his Ph.D. thesis (c.f. eq. (2.29) and (2.31) sections III.2. p.27 of [306]), a recent study of the limit case $a_c \to 0$ in [165], as well as the general results of the variations of the R-matrix to any arbitrary parameter by Mockel and Perez (c.f equations (71) and (75) [**?**]). We here focus on the Siegert-Humblet parameters $\left\{\mathcal{E}_j, r_{j,c}\right\}$. Our main result of this section resides in theorem 10, which establishes a way of converting the Siegert-Humblet radioactive parameters under a change of channel radius a_c.

Theorem 10. *Radioactive parameters transformation under change of channel radius a_c.*
Let the radioactive poles $\{\mathcal{E}_j\}$ be the solutions of the radioactive problem (E.32). Under a change of channel radius $a_c^{(0)} \to a_c$ (or infinitesimal $\frac{\partial \cdot}{\partial a_c}$):

- *the Kapur-Peierls operator $\boldsymbol{R}_L$, defined in (E.15), is subject to the following partial differential equations: for the diagonal elements,*

$$a_c \frac{\partial R_{Lcc}}{\partial a_c} + (1 - 2L_c) R_{Lcc} - 1 = 0 \tag{D.45}$$

and for off-diagonal ones,

$$a_c \frac{\partial R_{Lcc'}}{\partial a_c} + (\frac{1}{2} - L_c) R_{Lcc'} = 0 \tag{D.46}$$

- *the radioactive poles* $\{\mathcal{E}_j\}$ *are invariant:*

$$\frac{\partial \mathcal{E}_j}{\partial a_c} = 0 \tag{D.47}$$

- *the radioactive widths* $\{r_{j,c}\}$ *(widths of the Kapur-Peierls* $\boldsymbol{R}_L$ *operator residues (D.13)), are subject to the following first-order linear partial differential equation:*

$$a_c \frac{\partial r_{j,c}}{\partial a_c} + (\frac{1}{2} - L_c) r_{j,c} = 0 \tag{D.48}$$

- *which can be formally solved as,*

$$r_{j,c}(a_c) = r_{j,c}(a_c^{(0)}) \sqrt{\frac{a_c^{(0)}}{a_c}} \exp\left(\int_{a_c^{(0)}}^{a_c} \frac{L_c(k_c x)}{x} \mathrm{d}x \right) \tag{D.49}$$

- *and explicitly integrates to:*

$$\frac{r_{j,c}(a_c)}{r_{j,c}(a_c^{(0)})} = \frac{O_c(\rho_c(a_c))}{O_c(\rho_c(a_c^{(0)}))} \sqrt{\frac{a_c^{(0)}}{a_c}} \tag{D.50}$$

- *Moreover, letting* $\{\omega_n\}$ *be the roots of the outgoing wave function* $\Big\{ \omega_n \mid O_c(\omega_n) = 0 \Big\}$*, the latter (D.50) can take the following elemental product expansion:*

$$\frac{r_{j,c}(a_c)}{r_{j,c}(a_c^{(0)})} = \sqrt{\frac{a_c^{(0)}}{a_c}} \left(\frac{a_c^{(0)}}{a_c} \right)^{\ell} \mathrm{e}^{\mathrm{i}k_c \left(a_c - a_c^{(0)} \right)} \prod_{n \geq 1} \left(\frac{k_c a_c - \omega_n}{k_c a_c^{(0)} - \omega_n} \right) \tag{D.51}$$

where there are an infinite number of such roots $\{\omega_n\}$ *in the Coulomb case, while for neutral particle channel* c *with angular momentum* ℓ*, there exists exactly* ℓ *roots* $\{\omega_n\}_{n \in [\![1,\ell]\!]}$*, the exact and algebraically solvable values of which are reported, up to angular momentum* $\ell = 4$*, in TABLE II of [127].*

Proof. We start by bringing forth the observation that the scattering matrix $\boldsymbol{U}$ is invariant under change of channel radius a_c, i.e. for any channel c we have:

$$\frac{\partial \boldsymbol{U}}{\partial a_c} = \boldsymbol{0} \tag{D.52}$$

Since theorem 11 will show that the poles of the scattering matrix are exactly the ones of the Kapur-Peierls operator $\boldsymbol{R}_L$, which are the Siegert-Humblet poles $\{\mathcal{E}_j\}$,

invariance (D.52) entails that the radioactive poles are invariant under change of channel radius a_c, i.e. (D.47).

This is not the case for the radioactive widths $\{r_{j,c}\}$. However, one can use invariance (D.52) to differentiate the scattering matrix $\boldsymbol{U}$ expression (E.14). The $\boldsymbol{L}$ operator definition (E.17), and $\rho_c = k_c a_c$, entail

$$\frac{\partial \rho_c^{1/2} O_c^{-1}}{\partial a_c} = \frac{1}{a_c} \rho_c^{1/2} O_c^{-1} \left[\frac{1}{2} - L_c \right] \tag{D.53}$$

this enables us to establish the partial differential equations (D.45) and (D.46) on the Kapur-Peierls matrix operator $\boldsymbol{R}_L$ elements, which can be synthesized into expression,

$$\boldsymbol{a} \frac{\partial \boldsymbol{R}_L}{\partial \boldsymbol{a}} + (\frac{1}{2}\mathbb{I} - \boldsymbol{L})\boldsymbol{R}_L + \mathbb{I} \circ \left[(\frac{1}{2}\mathbb{I} - \boldsymbol{L})\boldsymbol{R}_L - \mathbb{I} \right] = \boldsymbol{0} \tag{D.54}$$

where $\circ$ designates the Hadamard matrix product, and where we used the notation:

$$\left[\frac{\partial \boldsymbol{R}_L}{\partial \boldsymbol{a}} \right]_{cc'} \triangleq \frac{\partial R_{Lcc'}}{\partial a_c} \tag{D.55}$$

Equivalently, inverting the Kapur-Peierls operator in differential equation (D.55) yields the following Riccati equation:

$$\boldsymbol{a} \frac{\partial \boldsymbol{R}_L^{-1}}{\partial \boldsymbol{a}} - \boldsymbol{R}_L^{-1}(\frac{1}{2}\mathbb{I} - \boldsymbol{L}) - \mathbb{I} \circ \left[\boldsymbol{R}_L^{-1}(\frac{1}{2}\mathbb{I} - \boldsymbol{L}) - \boldsymbol{R}_L^{-2} \right] = \boldsymbol{0} \tag{D.56}$$

These first order partial differential equations on the Kapur-Peierls operator $\boldsymbol{R}_L$ are equivalent to relations (71) and (75) Mockel and Perez established for the $\boldsymbol{R}$ matrix in [**?**]. They are quite inconvenient to solve in that they are channel-dependent, and thus give rise to equations for each cross term. Remarkably, this is not the case for the radioactive residues.

Having demonstrated the radioactive poles invariance (D.47), Mittag-Leffler expansion (D.41) entails that $\boldsymbol{u_j}$ from (D.42) satisfies invariance: $\frac{\partial \boldsymbol{u_j}}{\partial a_c} = \boldsymbol{0}$. Applying result (D.53) to the latter then yields partial differential equation (D.48), the direct integration of which readily yields (D.49). Since $L_c(\rho_c) \triangleq \frac{\rho_c}{O_c(\rho_c)} \frac{\partial O_c(\rho_c)}{\partial \rho_c}$, (D.49) integrates explicitly to (D.50). This result also stands for any degenerate state of multiplicity M_j, where for each radioactive width $\boldsymbol{r_j^m}$ we have:

$$\frac{r_{j,c}^m(a_c)}{r_{j,c}^m(a_c^{(0)})} = \frac{O_c(\rho_c(a_c))}{O_c(\rho_c(a_c^{(0)}))} \sqrt{\frac{a_c^{(0)}}{a_c}} \tag{D.57}$$

Finally, the proof of (D.51) is the element-wise integration of (D.49) using the Mittag-Leffler pole expansion (D.7) of $L_c(\rho)$, which we established in theorem 1 of [127] – invoking Fubini's theorem to permute sum and integral. In the case of neutral particles, there is a finite number of roots $\{\omega_n\}$ so that the product in (D.51) is finite. Note that in the charged particles case, there is an infinite number (countable) of roots

$\{\omega_n\}$, and the Weierstrass factorization theorem would thus usually require (D.51) to be cast in a Hadamard canonical representation with Weierstrass elementary factors. However, in (D.51), the product elements tend towards unity as n goes to infinity $\left(\frac{k_c a_c - \omega_n}{k_c a_c^{(0)} - \omega_n}\right) \underset{n\to\infty}{\longrightarrow} 1$, so that the infinite product in (D.51) should still converge.

□

Note that for neutral particles (massive or massless) s-waves ($\ell = 0$), the outgoing wave function is $O_c(\rho(a_c)) = \mathrm{e}^{\mathrm{i}k_c a_c}$ (c.f. TABLE I of [127]), so that (D.50) yields $r_{j,c}(a_c) = r_{j,c}(a_c^{(0)}) \sqrt{\frac{a_c^{(0)}}{a_c}} \mathrm{e}^{\mathrm{i}k_c\left(a_c - a_c^{(0)}\right)}$. Alternatively, directly integrating (D.49) with the outgoing-wave reduced logarithmic derivative expression $L_c(\rho(a_c)) = \mathrm{i}k_c a_c$ yields back the same result. Thus for s-wave neutral channels subject to a change of channel radius, the modulus of the radioactive widths decreases proportionally to the inverse square root of the channel radius a_c, at least for real wavenumbers $k_c \in \mathbb{R}$, i.e. real energies above the channel threshold. Since the transition probability rates partial widths can be defined as the square of the modulus of the radioactive width (c.f. eq. (6) in [163]), this means these transition partial widths decrease inversely to the channel radius: $\left|\frac{r_{j,c}(a_c)}{r_{j,c}(a_c^{(0)})}\right|^2 = \frac{a_c^{(0)}}{a_c}$.

A striking property of the R-matrix parametrizations is that they separate the channel contribution to each resonance, meaning that to compute, for instance, the $R_{c,c'}$ element in (E.16), one only requires the widths for each level of each channel, $\gamma_{\lambda,c}$, and not some new parameter for each specific channel pair c, c' combination. In this spirit, we show in theorem 10 that the Siegert-Humblet radioactive widths $r_{j,c}$ play a similar role in that their transformation under a change of channel radius only depends on that given channel.

Theorem 10 makes explicit the behavior of the radioactive widths $\left\{r_{j,c}\right\}$ under a change of channel radius a_c. Strikingly, only the Kapur-Peierls matrix $\boldsymbol{R}_L$ appears in this change of variable. This means that the R-matrix $\boldsymbol{R}$ and the $\boldsymbol{L^0}$ matrix function suffice to both compute the Siegert-Humblet parameters $\left\{\mathcal{E}_j, r_{j,c}\right\}$ from (E.32), and to change the radioactive widths $\left\{r_{j,c}\right\}$ under a change of channel radius a_c. This novel result portrays the Siegert-Humblet parameters as allowing a simple energy dependence to the scattering matrix (D.41) — albeit locally and needing the expansion coefficients (D.43) — all the while being boundary condition B_c independent and easy to transform under a change of channel radius a_c.

D.5 Scattering matrix continuation to complex energies

In section 5.2 of [185], Humblet and Rosenfeld continue the scattering matrix to complex wave numbers $k_c \in \mathbb{C}$, and define corresponding open and closed channels. They however never point to the conundrum that this entails: in their approach, the scattering matrix seemingly does not annul itself below threshold. This is contrary to the approach taken by Lane & Thomas, where they explicitly annul the elements of

the scattering matrix below thresholds, as stated in the paragraph between equations (2.1) and (2.2) of section VII.1. p.289 [214]. Claude Bloch ingeniously circumvents the problem by explicitly stating after eq. (50) in [79] that the scattering matrix is a matrix of the open channels only, meaning its dimensions change as more channels open when energy E increases past new thresholds $E > E_{T_c}$. In his approach, sub-threshold elements of the scattering matrix need not be annulled, one simply does not consider them.

We dedicate this section to this question of how to extend the scattering matrix to complex wavenumbers $k_c \in \mathbb{C}$, while closing the channels below threshold. We argue that analytic continuation of R-matrix operators (lemma 2 section III.B of [127]) is the physically correct way of constructing the scattering matrix for complex wavenumbers. To support this, we advance and demonstrate three new arguments: analytic continuation cancels out spurious poles otherwise introduced by the outgoing wavefunctions O_c (theorem 11); analytic continuation respects generalized unitarity (theorem 12); and, for massive particles (not photons), analytic continuation of real wavenumber expressions to sub-threshold energies naturally sees the transmission matrix evanesce on the physical sheet (theorem 13), while always closing the channels by annulling the cross section (theorem 14).

D.5.1 Forcing sub-threshold elements to zero: the legacy of Lane & Thomas

To close the channels for real energies below threshold, the simplest approach is the one proposed by Lane & Thomas in [214]. The scattering matrix expressions (E.14) can be re-written, for real energies above threshold, according to section VII.1 equation (1.6b) in [214]:

$$\boldsymbol{U} = \boldsymbol{\Omega}\left(\mathbb{I} + \boldsymbol{w}\boldsymbol{\mathfrak{P}}^{1/2}\boldsymbol{R}_L\boldsymbol{\mathfrak{P}}^{1/2}\right)\boldsymbol{\Omega} \tag{D.58}$$

with Wronskian $\boldsymbol{w}$ from (D.3) and the values defined for energies above the thresholds in III.3.a. p.271 of [214]:

$$\begin{aligned} \boldsymbol{\Omega} &\triangleq \boldsymbol{O}^{-1}\boldsymbol{I} \\ \boldsymbol{\mathfrak{P}} &\triangleq \boldsymbol{\rho}\boldsymbol{O}^{-1}\boldsymbol{I}^{-1} \end{aligned} \tag{D.59}$$

Let us note that the Mittag-Leffler expansion (E.41) of the Kapur-Peierls matrix $\boldsymbol{R}_L$ operator can still be performed.

The Lane & Thomas "sub-threshold channel force-closure" approach exploits the ambiguity in the definition of the shift $\boldsymbol{S}(E)$ and penetration $\boldsymbol{P}(E)$ factors:

$$\boldsymbol{L} \;=\; \boldsymbol{S} + i\boldsymbol{P} \tag{D.60}$$

for complex energies $E \in \mathbb{C}$, as discussed in section III.B of [127] (of which we follow the notation). Lane & Thomas choose the branch-point definitions for the shift $\boldsymbol{S}$ and penetration $\boldsymbol{P}$ functions, made explicit in lemma 1 section III.B of [127]. Lane & Thomas do not specify how they would continue the quantities (D.59) for negative

energies, as they state "we need not be concerned with stating similar relations for the negative energy channels" (c.f. paragraph after equation (4.7c), p.271.), but they do specify that $\boldsymbol{P} = \mathbf{0}$ below threshold energies and $\boldsymbol{P} = \boldsymbol{\mathfrak{P}}$ above. This means that plugging-in $\boldsymbol{P}$ in place of $\boldsymbol{\mathfrak{P}}$ in (D.59) has the convenient property of automatically closing the reaction channels below threshold, since in that case $U_{c,c'} = \Omega_c \Omega_{c'}$, which annuls the off-diagonal terms of the cross section (the reaction channels $c \neq c'$) when plugged into equation (1.10) in [214] VIII.1. p.291. Note that this approach only annuls the off-diagonal terms of the scattering cross section, leaving non-zero cross sections for the diagonal $\sigma_{cc}(E)$, even below threshold. Indeed, equation (4.5a) section III.4.a., p.271 of [214] gives $\Omega_c = \mathrm{e}^{\mathrm{i}(\omega_c - \phi_c)}$, whilst the cross section is begotten by the amplitudes of the *transmission matrix* $\boldsymbol{T}(E)$, defined as $T_{cc'} \triangleq \delta_{cc'} \mathrm{e}^{2\mathrm{i}\omega_c} - U_{cc'}$ in (2.3), section VIII.2., p.292. For sub-threshold real energies, the diagonal term of the transmission matrix is thus equal to $T_{cc} = \mathrm{e}^{2\mathrm{i}\omega_c}\left(1 - \mathrm{e}^{-2\mathrm{i}\phi_c}\right)$. This means that in the Lane & Thomas approach, all channels $c' \neq c$ are force-closed to zero below the incoming channel threshold $E < E_{T_c}$, except for the $c \to c$ reaction, which is tactfully overlooked as non-physical.

Of course, this approach comes at the cost of sacrificing the analytic properties of the scattering matrix $\boldsymbol{U}$: since $P_c = \Im[L_c]$, the penetration factor is no longer meromorphic and thus neither is $\boldsymbol{U}$. This entails that in decomposition (D.58) of the scattering matrix, if one "force-closes" the channels using the branch-point definition of Lane & Thomas — instead of analytically continuing both $\boldsymbol{\mathfrak{P}}$ and $\boldsymbol{\Omega}$ to complex wavenumbers $\boldsymbol{\rho} \in \mathbb{C}$ — the scattering matrix $\boldsymbol{U}(E)$ cannot have poles, as there is then no mathematical meaning to such notion. This goes directly against a vast amount of literature on the analytic properties of the scattering matrix [137, 185, 289, 181, 182, 195, 183, 230, 290, 231, 184, 304, 159, 135]. This is the approach presently taken by the SAMMY code at Oak Ridge National Laboratory [217], and upon which rest numerous ENDF evaluations [87].

We would like to note that under careful reading, this might not actually have been the approach intended by Lane & Thomas in [214]. Indeed, Lane & Thomas never specify how to prolong the $\boldsymbol{\mathfrak{P}}$ to sub-threshold energies, and in equation (D.58) it is $\boldsymbol{\mathfrak{P}}$ that is present and not $\boldsymbol{P}$. They do however note in the paragraph between equations (2.1) and (2.2) of section VII.1. p.289, that "as there are no physical situations in which the I_c^- occur, the components of the [scattering matrix] are not physically significant and one might as well set them equal to zero as can be seen from (1.6b). This may be accomplished without affecting the [positive energy channels] by setting the negative energy components of the Wronskian matrix to zero; $w_c^- = 0$. (This means that the O_c^- and I_c^- are not linearly independent.)". The choice of wording is here important. Indeed, it says that it is possible to set the Wronskian to zero to close channels below the threshold, though it is not necessary. This is yet another way of closing sub-threshold channels that would allow to keep the analytic properties of the scattering matrix, with $\boldsymbol{\mathfrak{P}} \triangleq \boldsymbol{\rho O}^{-1}\boldsymbol{I}^{-1}$ still analytically continued, albeit at the cost of not knowing when in the complex plane should the Wronskian w_c be set to zero — perhaps only on $\mathbb{R}_-$, which would then become a branch line.
We show in theorem 11 (section D.5.4) that as long as the Wronskian relation (D.3)

is guaranteed, the poles of the outgoing scattering wave function O_c cancel out of the scattering expressions (E.14) and (D.58). The Wronskian condition (D.3) is conserved when keeping $\boldsymbol{\mathfrak{P}}$ from (D.59) analytically continued — instead of the definition $P_c \triangleq \Im[L_c]$, which cannot respect the Wronskian relation (D.3) — so that this approach of setting the Wronskian to zero below threshold while analytically continuing the penetration and shift factors would indeed cancel out the spurious poles of the outgoing wave functions O_c.

D.5.2 Analytic continuation of the scattering matrix

In opposition to the Lane & Thomas approach, an entire field of physics and mathematics has studied the analytic continuation of the scattering matrix to complex wavenumbers $k_c \in \mathbb{C}$ [135, 159, 117, 144, 236, 185, 289, 181, 182, 195, 183, 230, 290].

As we saw, there is no ambiguity as to how to continue the $\boldsymbol{L}(\boldsymbol{\rho})$ matrix function to complex wave numbers (c.f. theorem 1 section II.B of [127]), and thus the $\boldsymbol{R}_L$ Kapur-Peierls operator (E.15). Indeed, the incoming $I_c(\rho_c)$ and outgoing $O_c(\rho_c)$ wave functions can be analytically continued to complex wavenumbers $k_c \in \mathbb{C}$ (c.f. theorem 1 section II.B of [127]), and through the multi-sheeted mapping (E.4) to complex energies $E \in \mathbb{C}$. This naturally yields the meromorphic continuation of the scattering matrix to complex energies (D.41). Since many evaluations are performed using decomposition (D.58), in practice performing analytic continuation of R-matrix operators thus means continuing (D.59) operators $\boldsymbol{\Omega}$ and $\boldsymbol{\mathfrak{P}}$, setting $\boldsymbol{\mathfrak{P}} \triangleq \boldsymbol{P}$, and defining the shift $S_c(\rho_c)$ and penetration $P_c(\rho_c)$ functions as analytically continued complex meromorphic functions (that is definition (44) and lemma 2 of [127] as opposed to the Lane & Thomas "force closure" definition (41) and lemma 1 of [127]).

The shortcoming of this analytic continuation approach is that it does not evidently annul the channel elements of the scattering matrix for sub-threshold energies $E < E_{T_c}$. Indeed, analytic continuation (D.41) means the scattering matrix $\boldsymbol{U}$ is a meromorphic operator from $\mathbb{C}$ to $\mathbb{C}$ on the multi-sheeted Riemann surface of mapping (E.4). Unicity of the analytic continuation then means that if the scattering matrix elements are zero below their threshold, $U_{c,c'}(E) = 0 \ , \ \forall E - E_{T_c} \in \mathbb{R}_-$, then it is identically zero for all energies on that sheet of the manifold: $U_{c,c'}(E) = 0 \ , \ \forall E \in \mathbb{C}$. Thus, the analytic continuation formalism cannot set elements of the scattering matrix to be identically zero below thresholds $\{E_{T_c}\}$.

This apparent inability to close channels below thresholds is the principal reason why the nuclear data community has stuck to the legacy approach of Lane & Thomas (lemma 1 section III.B of [127]), when computing the scattering matrix in equation (E.14). This has been the subject of an ongoing controversy in the field on how to continue the scattering matrix to complex wave numbers.

D.5.3 Assuming semi-simple poles in R-matrix theory

Before advancing our analytic continuation arguments of channel closure (section D.5.6) and generalized unitarity (section D.5.5), let us first start with a general note on high-order poles in R-matrix theory (see the consequences for analytic continuation

in section D.5.4). Being a high-order pole, as opposed to a simple pole, can bear various meanings. In our context, the three following definitions are of interest: a) *Laurent order*: the order of the polar expansion in the Laurent development in the vicinity of a pole; b) *Algebraic multiplicity*: the multiplicity of the root of the resolvant at a pole value; c) *Geometric multiplicity*: the dimension of the associated nullspace.

From equation (D.9) and throughout the article, we have treated the case of degenerate states where the geometric multiplicity $M_j > 1$ was higher than one, leading to rank-M_j residues. We have however always assumed the Laurent order to be one: in equation (D.9), the residues might be rank-M_j, but the Laurent order is still unity (no $\frac{1}{(E-\mathcal{E}_j)^2}$ or higher Laurent orders).

In the general case, the Laurent order is greater than one but it does not equal geometric or algebraic multiplicity. In terms of Jordan normal form, if the Jordan cells had sizes $n_1, ..., n_{m_g}$, then the geometric multiplicity is equal to m_g, the algebraic multiplicity m_a is the sum $m_a = n_1 + ... + n_{m_g}$, and the Laurent order is the maximum $\max\{n_1, ..., n_m\}$.

Alternatively, these can be defined as follows: Let $\boldsymbol{M}(z)$ be a complex-symmetric meromorphic matrix operator, with a root at $z = z_0$ (i.e. $\boldsymbol{M}(z_0)$ is non-invertible). The algebraic multiplicity m_a is the first non-zero derivative of the determinant, i.e. the first integer $m_a \in \mathbb{N}$ such that $\frac{\mathrm{d}^{m_a}}{\mathrm{d}z^{m_a}}\det\Big(\boldsymbol{M}(z)\Big)\Big|_{z=z_0} \neq 0$; alternatively, using Cauchy's theorem, the first integer m_a such that $\oint_{\mathcal{C}_{z_0}} \frac{\boldsymbol{M}(z)}{(z-z_0)^{m_a}}\mathrm{d}z = \boldsymbol{0}$. The geometric multiplicity m_g is the dimension of the kernel (nullspace), i.e. $m_g = \dim\left(\mathrm{Ker}\left(\boldsymbol{M}(z_0)\right)\right)$. In general the algebraic multiplicity is greater than the geometric one: $m_a \geq m_g$.

$\boldsymbol{M}(z_0)$ is said to be *semi-simple* if its geometric and algebraic multiplicities are equal, i.e. $m_a = m_g$ (c.f. theorem 2, p.120 in [84]). Semi-simplicity can be established using the following result: $\boldsymbol{M}(z_0)$ is semi-simple if, and only if, for each nonzero $v \in \mathrm{Ker}\left(\boldsymbol{M}(z_0)\right)$, there exists $w \in \mathrm{Ker}\left(\boldsymbol{M}(z_0)\right)$ such that:

$$v^{\mathsf{T}}\left(\left.\frac{\mathrm{d}\boldsymbol{M}}{\mathrm{d}z}\right|_{z=z_0}\right)w \neq 0 \tag{D.61}$$

If an operator $\boldsymbol{M}(z_0)$ is semi-simple at a root z_0, then z_0 is a pole of Laurent order one for the inverse operator $\boldsymbol{M}^{-1}(z) \underset{\mathcal{W}(z_0)}{\sim} \frac{\widetilde{\boldsymbol{M}}}{z-z_0}$. For Hermitian operators, the semi-simplicity property is guaranteed. However, resonances seldom correspond to Hermitian operators. In our case, the resonances correspond to the poles of the scattering matrix $\boldsymbol{U}(E)$, which is not self-adjoint but complex-symmetric $\boldsymbol{U}^{\mathsf{T}} = \boldsymbol{U}$ (c.f. equation (2.15) section VI.2.c p.287 in [214]). For complex-symmetric operators, semi-simplicity is not guaranteed in general, even when discarding the complex case of quasi-null vectors.

In the case of R-matrix theory, we were able to find cases where the geometric multiplicity of the scattering matrix does not match the algebraic one, thus R-matrix theory does not always yield semi-simple scattering matrices, and the Laurent development orders of the resonance poles can be higher. For instance, we can devise

examples of non-semi-simple inverse level matrices from definition (E.18) by choosing resonance parameters such that the algebraic multiplicity is strictly greater than the geometric one.

However, one can also observe in these simple cases that the space of parameters for which semi-simplicity is broken is a hyper-plane of the space of R-matrix parameters. This gives credit to the traditional physics arguments that the probability of this occurring is quasi-null: R-matrix theory can yield scattering matrices with Laurent orders higher than one, but this is extremely unlikely; a mathematical approach of generic simplicity of resonances can be found in chapter 4 "Black Box Scattering in $\mathbb{R}^{n}$" of [135], in particular theorem 4.4 (Meromorphic continuation for black box Hamiltonians), theorem 4.5 (Spectrum of black box Hamiltonians), theorem 4.7 (Singular part of RV(λ) for black box Hamiltonians), and theorem 4.39 (Generic simplicity of resonances for higher dimensional black box with potential perturbation). In other terms, we assume semi-simplicity is almost always guaranteed through R-matrix parametrizations.

Henceforth, we use this argument to continue assuming the Kapur-Peierls matrix $\boldsymbol{R}_L$ is usually semi-simple, and thus the Laurent order of the radioactive poles $\left\{\mathcal{E}_j\right\}$ in (D.9) is, in practice, one.

But let us be aware that in general scattering theory, the scattering operator may exhibit high-order poles [135, 159, 251], and efforts are being made to have these "exceptional points" of second order arise in the specific case of nuclear interactions [249, 243]. The traditional R-matrix assumption where the poles of the scattering matrix are almost-always of Laurent-order one is unable to describe these physical phenomena.

D.5.4 Scattering matrix poles are the Siegert-Humblet radioactive poles

This section is dedicated to a remarkable property of the Siegert-Humblet radioactive poles $\{\mathcal{E}_j\}$: in R-matrix theory, these are exactly the poles of the scattering matrix (theorem 11).

Theorem 11. *Scattering matrix poles are the Siegert-Humblet radioactive poles.*
In R-matrix theory, when the R-matrix operators (Kapur-Peierls $\boldsymbol{R}_L$ and incoming and outgoing wavefunctions $\boldsymbol{I}$ and $\boldsymbol{O}$) are analytically continued to complex energies $E \in \mathbb{C}$ such as to respect the Wronskian condition (D.3), then the poles of the scattering matrix $\boldsymbol{U}$ are exactly the poles of the Kapur-Peierls operator $\boldsymbol{R}_L$, i.e. the Siegert-Humblet radioactive poles $\left\{\mathcal{E}_j\right\}$ from (E.32) and (E.40). These poles are almost always of Laurent-order of one.

Section D.5.3 gives the reasons to assume that the poles of the Kapur-Peierls matrix $\boldsymbol{R}_L$ are simple (i.e. or Laurent order one). For the rest of this theorem, we here give two proofs: a first by *reductio ad absurdum*, and a second constructive proof.

Proof. Reductio ad absurdum: Since the radioactive poles $\mathcal{E}_j$ are not poles of the outgoing wavefunction, i.e. $\boldsymbol{O}^{-1}\boldsymbol{\rho}^{1/2}(\mathcal{E}_j) \neq \mathbf{0}$, expression (E.14) implies that all the poles $\mathcal{E}_j$ of the Kapur-Peierls $\boldsymbol{R}_L(E)$ operator are poles of the scattering matrix $\boldsymbol{U}(E)$. As first sight, expression (E.14) would suggest the roots $\{\omega_n\}$ of the outgoing wavefunctions (i.e. all such that there exists a channel c for which $O_c(\omega_n) = 0$) are also poles of the scattering matrix. However, when performing analytic continuation of R-matrix operators while conserving the Wronskian condition (D.3), expression (E.14) is equivalent to expression eq. (1.5) of section VII.1 of [214], for which it is evident that the roots $\{\omega_n\}$ of the outgoing wavefunction $O_c(\rho_c)$ are not poles of the scattering matrix $\boldsymbol{U}$ (that is because in both the Coulomb and the neutral particle case the outgoing wavefunctions $O_c(\rho_c)$ are confluent hypergeometric functions with simple roots $\{\omega_n\}$ entailing that $O_c^{(1)}(\omega_n) \neq 0$). Hence the poles of the scattering matrix $\boldsymbol{U}(E)$ must be exactly all the radioactive poles $\mathcal{E}_j$. □

Though this latter proof is correct, it does not explain how the roots $\{\omega_n\}$ of the outgoing wavefunction $O_c(\rho_c)$ cancel out of the scattering matrix in expression (E.14). Yet it is important to understand this because expression (E.14) defines the potential cross section in standard nuclear data libraries, which taken as is should thus count the $\{\omega_n\}$ as poles. We use this explicit cancellation of these spurious poles at the residues level to establish the windowed multipole representation in our follow-up article [130]. Moreover, if one uses the Lane & Thomas "force closure" definitions, then expression (E.14) and eq. (1.5) of section VII.1 of [214] are no longer equivalent in the complex plane. In this case, not only is the scattering matrix $\boldsymbol{U}(E)$ no longer meromorphic, but it also diverges at the $\{\omega_n\}$ outgoing wavefunction roots. Also, a constructive proof requires a closer look at the behavior of specific poles and residues, and gives us an opportunity to explain in detail different non-trivial assumptions usually made in nuclear physics about radioactive states and other states degeneracy. For all these reasons, we believe it of interest to here provide a second, constructive proof of theorem 11. It rests on the following lemma 4.

Lemma 4. *Diagonal Semi-Simplicity – If a diagonal matrix $\boldsymbol{D}^{-1}(z)$ is composed of elements with simple roots $\left\{\omega_n\right\}$, then its inverse is semi-simple, i.e. when a pole ω_n of a diagonal matrix $\boldsymbol{D}(z)$ has an algebraic multiplicity $M_n > 1$ the Laurent development order of the pole remains 1 while the associated residue matrix is of rank M_n, and can be expressed as:*

$$\begin{aligned} \boldsymbol{D}(z) &\underset{\mathcal{W}(z=\omega_n)}{=} \boldsymbol{D}_0 + \frac{\boldsymbol{D}_n}{z-\omega_n} \\ \boldsymbol{D}_n &\triangleq \sum_{m=1}^{M_n} \frac{\boldsymbol{v_n}\boldsymbol{v_n}^{\intercal}}{\boldsymbol{v_n}^{\intercal}\boldsymbol{D_0^{-1}}^{(1)}\boldsymbol{v_n}} \end{aligned} \tag{D.62}$$

Proof. Without loss of generality, a change of variables can be performed so as to set $\omega_n = 0$. Let $\boldsymbol{D}(z) = \mathbf{diag}\left(d_1(z), d_2(z), \ldots, d_1(z), d_j(z), d_n(z)\right)$ be a diagonal meromorphic complex-valued operator, which admits a pole at $z = 0$. $\boldsymbol{D^{-1}}(z) = \mathbf{diag}\left(d_1^{-1}(z), d_2^{-1}(z), \ldots, d_1^{-1}(z), d_j^{-1}(z), d_n^{-1}(z)\right)$ is well known, and $\det\left(\boldsymbol{D^{-1}}\right)(z =$

$0) = d_1^{-1}(z)^2 \prod_{j\neq 1} d_j^{-1}(z)$. Let us assume only $d_1^{-1}(z=0) = 0$, with a simple root, so that $d_1(z) \underset{\mathcal{W}(z=0)}{=} d0_1 + \frac{R_1}{z}$. Then $\det\left(\boldsymbol{D^{-1}}(z)\right)(z=0) = d_1^{-1}(z)^2 \prod_{j\neq 1} d_j^{-1}(z)$ has a double root: the algebraic multiplicity is thus 2. However, it is immediate to notice that:

$$\begin{aligned}\boldsymbol{D}(z) &= \mathbf{diag}\left(d_1(z), d_2(z), \ldots, d_1(z), d_j(z), d_n(z)\right) \\ &\underset{\mathcal{W}(z=0)}{=} \mathbf{diag}\left(d0_1, d_2(z), \ldots, d0_1(z), d_j(z), d_n(z)\right) \\ &\quad + \frac{1}{z}\mathbf{diag}\left(R_1, 0, \ldots, R_1, 0, 0\right)\end{aligned}$$

This means the Laurent development order remains 1, albeit the algebraic multiplicity of the pole is 2 (or higher M_n). It can thus be written that: $\boldsymbol{D}(z) \underset{\mathcal{W}(z=0)}{=} \boldsymbol{D}_0 + \frac{\boldsymbol{D}_1}{z}$. When solving for the non-linear eigenproblem $\boldsymbol{D^{-1}}(z)\boldsymbol{v} = \mathbf{0}$, the kernel is no longer an eigenline, but instead spans $(\boldsymbol{v_1}, \boldsymbol{v_2})$, i.e. $\mathrm{Ker}\left(\boldsymbol{D^{-1}}_0\right) = \mathrm{Span}\left(\boldsymbol{v_1}, \boldsymbol{v_2}\right)$, with $\boldsymbol{v_1} = a_1\left[1, 0, \ldots, 0, 0, 0\right]^\mathsf{T}$ and $\boldsymbol{v_2} = a_2\left[0, 0, \ldots, 1, 0, 0\right]^\mathsf{T}$. Then, following Gohberg-Sigal's theory [157], the fundamental property:

$$\boldsymbol{D^{-1}}\boldsymbol{D} = \mathbb{I}$$

and the Laurent development around the pole:

$$\boldsymbol{D^{-1}}(z) \underset{\mathcal{W}(z=0)}{=} \boldsymbol{D^{-1}}_0 + z\boldsymbol{D^{-1}}_0^{(1)} + \mathcal{O}\left(z^2\right)$$

yield the relations:

$$\begin{aligned}\boldsymbol{D^{-1}}_0\boldsymbol{D}_0 + \boldsymbol{D^{-1}}_0^{(1)}\boldsymbol{D}_1 &= \mathbb{I} \\ \boldsymbol{D^{-1}}_0\boldsymbol{D}_1 &= \mathbf{0}\end{aligned}$$

Constructing $\boldsymbol{D}_1$ to satisfy the latter then entails

$$\boldsymbol{D}_1 = \frac{\boldsymbol{v_1}\boldsymbol{v_1}^\mathsf{T}}{\boldsymbol{v_1}^\mathsf{T}\boldsymbol{D_0^{-1}}^{(1)}\boldsymbol{v_1}} + \frac{\boldsymbol{v_2}\boldsymbol{v_2}^\mathsf{T}}{\boldsymbol{v_2}^\mathsf{T}\boldsymbol{D_0^{-1}}^{(1)}\boldsymbol{v_2}}$$

where the transpose is used because the matrix is complex-symmetric. This reasoning immediately generalizes to expression (D.62). □

Let $\{\omega_n\}$ be all the roots of the outgoing-wave functions (i.e. the poles of inverse outgoing wave $\boldsymbol{O}^{-1}$), which we can find by solving the non-linear Eigenvalue problem:

$$\boldsymbol{O}(\omega_n)\boldsymbol{w_{n}}_m = \mathbf{0} \tag{D.63}$$

Looking at (E.14) shows that the roots of the outgoing wave functions $\boldsymbol{O}$ could endow the scattering matrix with additional poles, through $\boldsymbol{O}^{-1}$, and that these poles could potentially have higher Laurent orders, since $\boldsymbol{O}^{-1}$ appears twice in expression (E.14). Yet, because $\boldsymbol{O}$ is diagonal with simple roots, lemma 4 entails $\boldsymbol{O}^{-1}$ is semi-simple: the algebraic multiplicities are equal to the geometric multiplicities, and thus the poles $\{\omega_n\}$ all have Laurent order one. Situations can arise where same-charge channels within the same total angular momentum J^π will carry same angular momenta $\ell_c = \ell_{c'}$

and equal channel radii $a_c = a_{c'}$. In that case, the geometric multiplicity M_n of pole ω_n will be equal to the number of channels sharing the same functional outgoing waves $O_c = O_{c'}$. Diagonal semi-simplicity lemma 4 then establishes that the residue of $\boldsymbol{O}^{-1}$ associated to pole ω_n is now a diagonal rank-M_n matrix, $\boldsymbol{D_n}$, expressed as:

$$\boldsymbol{D_n} = \sum_{m=1}^{M_n} \frac{\boldsymbol{w_{n}}_m \boldsymbol{w_{n}}_m^{\mathsf{T}}}{\boldsymbol{w_{n}}_m^{\mathsf{T}} \boldsymbol{O}^{(1)}(\omega_n) \boldsymbol{w_{n}}_m} \tag{D.64}$$

where $\boldsymbol{O}^{(1)}(\omega_n)$ designates the first derivative of $\boldsymbol{O}$, evaluated at the pole value ω_n. This establishes the existence of higher-rank residues associated to the inverse outgoing wave function $\boldsymbol{O}^{-1}$. Notice that if the channel radii $\left\{a_c\right\}$ where chosen at random, these high-rank residues would almost never emerge (null probability). However, since a_c is chosen arbitrarily in the context of R-matrix theory, it is often the case that evaluators set a_c to a fixed value for multiple different channels, and even across isotopes. This is because the scattering radius is determined early on by the evaluator (an not varied afterwards) based on the amount of potential scattering observed in the experimental data, which is very similar for isotopes of the same element. Therefore, in practice these high-rank residues are not uncommon. Our constructive proof now establishes how analytic continuation annuls these high-rank residues.

Proof. Constructive: Consider the scattering matrix expression $\boldsymbol{U} = \boldsymbol{O}^{-1}\left[\boldsymbol{I} + 2i\boldsymbol{\rho}^{1/2}\boldsymbol{R}_L\boldsymbol{O}^{-1}\boldsymbol{\rho}^{1/2}\right]$ from (E.14). Result (D.64) entails that, in the vicinity of ω_n (root of the outgoing wave-function $\boldsymbol{O}$) the residue is locally given by:

$$\boldsymbol{U}(z) \underset{\mathcal{W}(E=\omega_n)}{=} \boldsymbol{U}_0(\omega_n) + \frac{\boldsymbol{D}_n\left[\boldsymbol{I} + 2i\boldsymbol{\rho}^{1/2}\boldsymbol{R}_L\boldsymbol{O}^{-1}\boldsymbol{\rho}^{1/2}\right]_{E=\omega_n}}{E - \omega_n} \tag{D.65}$$

We now notice that evaluating the Kapur-Peierls $\boldsymbol{R}_L$ operator (E.15) at the pole value ω_n yields the following equality:

$$\boldsymbol{R}_L\boldsymbol{O}^{-1}(\omega_n)\boldsymbol{w_{n}}_m = -\left[\boldsymbol{\rho}\boldsymbol{O}^{(1)}\right]^{-1}(\omega_n)\boldsymbol{w_{n}}_m \tag{D.66}$$

Plugging (D.66) into the residue of (D.65), and using the fact that (D.64) guarantees $\boldsymbol{D_n}$ is a linear combination of $\boldsymbol{w_{n}}_m\boldsymbol{w_{n}}_m^{\mathsf{T}}$, we then have the following equality on the residues at poles ω_n:

$$\boldsymbol{D}_n\left[\boldsymbol{I} + 2i\boldsymbol{\rho}^{1/2}\boldsymbol{R}_L\boldsymbol{O}^{-1}\boldsymbol{\rho}^{1/2}\right]_{E=\omega_n} = \boldsymbol{D}_n\left[\boldsymbol{I} - 2i{\boldsymbol{O}^{(1)}}^{-1}\right]_{E=\omega_n} \tag{D.67}$$

The rightmost term is diagonal and independent from the resonance parameters. Since the Wronskian matrix $\boldsymbol{w}$ of the external region interaction (for Coulomb or free particles) is constant (D.3), $\boldsymbol{w} = \boldsymbol{O}^{(1)}\boldsymbol{I} - \boldsymbol{I}^{(1)}\boldsymbol{O} = 2i\mathbb{I}$, evaluating at outgoing wave-function root ω_n, one finds $2i\mathbb{I} = \boldsymbol{O}^{(1)}\boldsymbol{I}(\omega_n)$. Plugging this result into (D.67) annuls the corresponding residue from the scattering matrix, i.e.:

$$\boldsymbol{D}_n\left[\boldsymbol{I} + 2i\boldsymbol{\rho}^{1/2}\boldsymbol{R}_L\boldsymbol{O}^{-1}\boldsymbol{\rho}^{1/2}\right]_{E=\omega_n} = \boldsymbol{0} \tag{D.68}$$

Thus, if the Wronskian condition (D.3) is respected, the $\left\{\omega_n\right\}$ poles cancel out of the scattering matrix $\boldsymbol{U}$ □

Importantly, both the Lane & Thomas force-closing of sub-threshold channels D.5.1 or the analytic continuation D.5.2 will yield the same cross section values for real energies above thresholds. However, theorem 11 demonstrates that the choice of analytic continuation in equation (E.14), respecting the Wronskian condition (D.3), leads to the cancellation from the scattering matrix $\boldsymbol{U}$ of the $\left\{\omega_n\right\}$ spurious poles, which have nothing to do with the resonant states of the scattering system. This cancellation is thus physically accurate, and would not take place had the choice of $\mathfrak{P} = \boldsymbol{P}$ been made in equation (D.58) with the Lane & Thomas "force closure" definition $\boldsymbol{P} = \Im\left[\boldsymbol{L}(z)\right] \in \mathbb{R}$ (c.f. lemma 1 section III.B of [127]), under which the scattering matrix diverges at $\left\{\omega_n\right\}$. Conversely, analytically continuing the penetration function as $\boldsymbol{P}(z) \triangleq \frac{1}{2\mathrm{i}}\left(\boldsymbol{L}(z) - \left[\boldsymbol{L}(z^*)\right]^*\right) \in \mathbb{C}$ (c.f. lemma 2 section III.B of [127]) will guarantee the cancellation of the $\left\{\omega_n\right\}$ poles from the scattering matrix $\boldsymbol{U}$ when using (D.58). Notice this is almost the definition (D.74) of $\boldsymbol{\Delta L}(\rho)$ we hereafter use in the proof of the generalized unitarity. Then, to force-close sub-threshold channels, one could set the Wronskian to zero, as proposed by Lane & Thomas in the paragraph between equation (2.1) and (2.2) of section VII.1. p.289. This shifts the problem to how to maintain the Wronskian condition (D.3) while setting the Wronskian to zero below thresholds. Alternatively, we here argue in section D.5.6 that this might not be necessary, as analytic continuation can naturally close sub-threshold channels.

D.5.5 Generalized unitarity for analytically continued scattering matrix

One of the authors, G. Hale, proved a somewhat more esoteric argument in favor of analytic continuation of the scattering matrix, showing it satisfies generalized unitarity.

Eden & Taylor established a generalized unitarity condition, eq. (2.16) in [137], which extents the one described by Lane & Thomas, eq. (2.13), VI.2.c. p.287, in that the subset of open channels is unitary (thus conserving probability), but the scattering matrix can still be continued to sub-threshold channels and be non-zero, that is the full scattering matrix of open and closed channels is not unitary but satisfies the generalized unitarity condition. This is also consistent with approaches other than R-matrix to modeling nuclear interactions (c.f. commentary above eq. (3) p.4 in [243], [236], or[117]).

The premises of the problem lies again in the multi-sheeted Riemann surface spawning from mapping (E.4): when considering the scattering matrix $\boldsymbol{U}(E)$ at a given energy E, there are multiple possibilities for the choice of wavenumber k_c at each channel. Following Eden & Taylor eq. (2.14a) and eq. (2.14b) [137], we consider the case of momenta being continued along the following paths in the multi-sheeted Riemann surface: one subset of channels c, denoted by $\widehat{\mathfrak{C}}$, is continued as $k_{c\in\widehat{\mathfrak{C}}} \to k^*_{c\in\widehat{\mathfrak{C}}}$, while all the others are continued as $k_{c\notin\widehat{\mathfrak{C}}} \to -k^*_{c\notin\widehat{\mathfrak{C}}}$, and we collectively denote this

continuation $\boldsymbol{k} \to \widetilde{\boldsymbol{k}}$:

$$\boldsymbol{k} \to \widetilde{\boldsymbol{k}} : \begin{cases} \forall c \in \widehat{\mathfrak{C}}\,, & k_c \;\to\; k_c^* \\ \forall c \notin \widehat{\mathfrak{C}}\,, & k_c \;\to\; -k_c^* \end{cases} \tag{D.69}$$

We then seek to reproduce the generalized unitarity property eq. (2.16) of [137], which states that the submatrix $\widehat{\boldsymbol{U}}$ composed of the channels $c \in \widehat{\mathfrak{C}}$, verifies the generalized unitarity condition:

$$\widehat{\boldsymbol{U}}(\boldsymbol{k})\Big[\widehat{\boldsymbol{U}}(\widetilde{\boldsymbol{k}})\Big]^\dagger = \mathbb{I} \tag{D.70}$$

We now show that analytically continuing the R-matrix expression (E.14) ensures the scattering matrix respects Eden & Taylor generalized unitarity condition.

Theorem 12. *Analytic continuation of the R-matrix expression for the scattering matrix ensures generalized unitarity.*
By performing the analytic continuation of the R-matrix expression (E.14), the scattering matrix $\boldsymbol{U}$ satisfies Eden & Taylor's generalized unitarity condition (D.70).

Proof. The proof is based on the conjugacy relations of the outgoing and incoming wavefunctions eq. (2.12), VI.2.c. in [214], whereby, for any channel c:

$$\begin{array}{rcrcr} \Big[O_c(k_c^*)\Big]^* = I_c(k_c) & , & \Big[I_c(k_c^*)\Big]^* = O_c(k_c) \\ O_c(-k_c) = I_c(k_c) & , & I_c(-k_c) = O_c(k_c) \\ -O_c^{(1)}(-k_c) = I_c^{(1)}(k_c) & , & -I_c^{(1)}(-k_c) = O_c^{(1)}(k_c) \end{array} \tag{D.71}$$

where the third line was obtained by taking the derivative of the second. Conjugacy relations (D.71) entail the following relations on the outgoing-wave reduced logarithmic derivative $\boldsymbol{L}$:

$$\Big[L_c(k_c^*)\Big]^* = L_c(-k_c) \quad , \quad \Big[L_c(-k_c^*)\Big]^* = L_c(k_c) \tag{D.72}$$

We also notice that the Wronskian condition (D.3) is equivalent to:

$$\frac{2\mathrm{i}\rho_c}{O_c I_c} = \rho_c \left[\frac{O_c^{(1)}}{O_c} - \frac{I_c^{(1)}}{I_c}\right] \tag{D.73}$$

Recognizing the definition (E.17) of $\boldsymbol{L}$, and using conjugacy relations (D.72), this Wronskian condition (D.73) can be expressed as a difference of the reduced logarithmic L_c derivatives:

$$\Delta L_c(k_c) \triangleq L_c(k_c) - L_c(-k_c) \;=\; \frac{2\mathrm{i}\rho_c}{O_c I_c}(k_c) \tag{D.74}$$

Defining the diagonal matrix $\boldsymbol{\Delta L} \triangleq \mathbf{diag}\Big(\Delta L_c(k_c)\Big)$, we can then re-write, similarly to (D.58), the R-matrix expression (E.14) of the scattering matrix $\boldsymbol{U}$ as a function of

$\Delta L_c(k_c)$, so that:

$$\begin{aligned} \boldsymbol{U} &= \boldsymbol{O}^{-1}\left[\mathbb{I} + \left[\boldsymbol{\rho}^{1/2}\boldsymbol{R}_L\boldsymbol{\rho}^{-1/2}\right]\boldsymbol{\Delta L}\right]\boldsymbol{I} \\ &= \boldsymbol{I}\left[\mathbb{I} + \boldsymbol{\Delta L}\left[\boldsymbol{\rho}^{-1/2}\boldsymbol{R}_L\boldsymbol{\rho}^{1/2}\right]\right]\boldsymbol{O}^{-1} \end{aligned} \tag{D.75}$$

Notice again how this expression is closely related to the analytic continuation of expression (D.58).

Coming back to the Eden & Taylor continuation (D.69), let us now establish a relation between the Kapur-Peierls operator $\boldsymbol{R}_L$ and $\boldsymbol{\Delta L}$. From the definition (E.15) of the Kapur-Peierls operator $\boldsymbol{R}_L$, recalling that under Eden & Taylor continuations (D.69) the energy E from mapping (E.4) remains unaltered, and given that the boundary-condition B_c in the $\boldsymbol{L^0}$ matrix function is real and thus the R-matrix parameters (E.16) are too, it follows that:

$$\left[\boldsymbol{R}_L^{-1}(\widetilde{\boldsymbol{k}})\right]^* - \boldsymbol{R}_L^{-1}(\boldsymbol{k}) \;=\; \begin{pmatrix} \widehat{\boldsymbol{\Delta L}}(\boldsymbol{k}) & 0 \\ 0 & 0 \end{pmatrix} \tag{D.76}$$

where we have used the $\boldsymbol{L}$ conjugacy relations (D.72) to establish that all channels $c \notin \widehat{\mathfrak{C}}$ cancel out, and the rest yield $\Delta L_{c\in\widehat{\mathfrak{C}}}(k_c)$. The $\widehat{\boldsymbol{\Delta L}}$ thus designates the sub-matrix composed of all the channels $c \in \widehat{\mathfrak{C}}$. Multiplying both left and right, and considering the sub-matrices on the channels $c \in \widehat{\mathfrak{C}}$ thus yields:

$$\widehat{\boldsymbol{R}}_L(\boldsymbol{k}) - \left[\widehat{\boldsymbol{R}}_L(\widetilde{\boldsymbol{k}})\right]^* = \widehat{\boldsymbol{R}}_L(\boldsymbol{k})\widehat{\boldsymbol{\Delta L}}(\boldsymbol{k})\left[\widehat{\boldsymbol{R}}_L(\widetilde{\boldsymbol{k}})\right]^* \tag{D.77}$$

This relation is what guarantees the scattering matrix $\boldsymbol{U}$ satisfies generalized unitarity condition (D.70). Indeed, let us develop the left-hand side of (D.70), using expressions (D.75) on the sub-matrices of the channels $c \in \widehat{\mathfrak{C}}$:

$$\begin{aligned} &\widehat{\boldsymbol{U}}(\boldsymbol{k})\left[\widehat{\boldsymbol{U}}(\widetilde{\boldsymbol{k}})\right]^\dagger \;= \\ &\widehat{\boldsymbol{O}}^{-1}(\boldsymbol{k})\left[\mathbb{I} + \left[\boldsymbol{\rho}^{\frac{1}{2}}\widehat{\boldsymbol{R}_L\boldsymbol{\rho}^{-\frac{1}{2}}}\right](\boldsymbol{k})\widehat{\boldsymbol{\Delta L}}(\boldsymbol{k})\right]\widehat{\boldsymbol{I}}(\boldsymbol{k}) \\ &\quad\times\left[\widehat{\boldsymbol{I}}(\widetilde{\boldsymbol{k}})\left[\mathbb{I} + \widehat{\boldsymbol{\Delta L}}(\widetilde{\boldsymbol{k}})\left[\boldsymbol{\rho}^{-\frac{1}{2}}\widehat{\boldsymbol{R}_L\boldsymbol{\rho}^{\frac{1}{2}}}\right](\widetilde{\boldsymbol{k}})\right]\widehat{\boldsymbol{O}}^{-1}(\widetilde{\boldsymbol{k}})\right]^\dagger \\ &=\; \widehat{\boldsymbol{O}}^{-1}(\boldsymbol{k})\left[\mathbb{I} + \left[\boldsymbol{\rho}^{\frac{1}{2}}\widehat{\boldsymbol{R}_L\boldsymbol{\rho}^{-\frac{1}{2}}}\right](\boldsymbol{k})\widehat{\boldsymbol{\Delta L}}(\boldsymbol{k})\right]\widehat{\boldsymbol{I}}(\boldsymbol{k})\times \\ &\left[\widehat{\boldsymbol{O}}^{-1}(\widehat{\boldsymbol{k}}^*)\right]^*\left[\mathbb{I} + \left[\boldsymbol{\rho}^{-\frac{1}{2}}\widehat{\boldsymbol{R}_L\boldsymbol{\rho}^{\frac{1}{2}}}\right](\widehat{\boldsymbol{k}}^*)\left[\widehat{\boldsymbol{\Delta L}}(\widehat{\boldsymbol{k}}^*)\right]^*\right]\left[\widehat{\boldsymbol{I}}(\widehat{\boldsymbol{k}}^*)\right]^* \end{aligned} \tag{D.78}$$

Noticing that conjugacy relation (D.72) entail the following $\boldsymbol{\Delta L}$ symmetry from definition (D.74), $\left[\widehat{\boldsymbol{\Delta L}}(\widehat{\boldsymbol{k}}^*)\right]^* = -\widehat{\boldsymbol{\Delta L}}(\boldsymbol{k})$, and making use of the conjugacy relations for

the wave functions (D.71), we can further simplify (D.78) to:

$$\begin{aligned}\widehat{\boldsymbol{U}}(\boldsymbol{k})\Big[\widehat{\boldsymbol{U}}(\widetilde{\boldsymbol{k}})\Big]^{\dagger} \;=\; \mathbb{I} \;+\; \widehat{\boldsymbol{O}}^{-1}(\boldsymbol{k})\Big[\widehat{\boldsymbol{\rho}^{\frac{1}{2}}\boldsymbol{R}_L\boldsymbol{\rho}^{-\frac{1}{2}}}\Big](\boldsymbol{k}) \times \Bigg[\\ \Bigg[\Big[\widehat{\boldsymbol{\rho}^{\frac{1}{2}}\boldsymbol{R}_L\boldsymbol{\rho}^{-\frac{1}{2}}}\Big]^{-1}(\boldsymbol{k}^*)\Bigg]^{\dagger} - \Big[\widehat{\boldsymbol{\rho}^{\frac{1}{2}}\boldsymbol{R}_L\boldsymbol{\rho}^{-\frac{1}{2}}}\Big]^{-1}(\boldsymbol{k}) - \widehat{\boldsymbol{\Delta L}}(\boldsymbol{k}) \\ \Bigg] \times \Big[\widehat{\boldsymbol{\rho}^{-\frac{1}{2}}\boldsymbol{R}_L\boldsymbol{\rho}^{\frac{1}{2}}}\Big](\widehat{\boldsymbol{k}}^*)\Bigg]^{\dagger} \widehat{\boldsymbol{\Delta L}}(\boldsymbol{k})\widehat{\boldsymbol{O}}(\boldsymbol{k})\end{aligned} \tag{D.79}$$

In the middle, we recognize property (D.76), where the $\boldsymbol{\rho}^{\pm 1/2}$ cancel out by commuting with the diagonal matrix. Property (D.76) thus annuls all non-identity terms, leaving Eden & Taylor's generalized unitarity condition (D.70) satisfied. □

Let us also note that the proof required real boundary conditions $B_c \in \mathbb{R}$. Thus, in R-matrix parametrization (E.14), real boundary conditions $B_c \in \mathbb{R}$ are necessary for the scattering matrix $\boldsymbol{U}$ to be unitarity (and by extension generalized unitary).

Theorem 12 beholds a strong argument in favor of performing analytic continuation of the R-matrix operators as the physically correct way of prolonging the scattering matrix to complex wavenumbers $k_c \in \mathbb{C}$.

D.5.6 Closure of sub-threshold cross sections through analytic continuation

We finish this article with the key question of how to close sub-threshold channels. Analytically continuing the scattering matrix below thresholds entails it cannot be identically zero there, since this would entail it is the null function on the entire sheet of the maniforld (unicity of analytic continuation). However, we here show that for massive particles subject to $\rho(E)$ mappings (2) or (4) section II.A of [127], adequate definitions and careful consideration will both make the transmission matrix evanescent sub-threshold (in a classical case of quantum tunnelling), and annul the sub-threshold cross-section — the physically measurable quantity.

The equations linking the scattering matrix $\boldsymbol{U}$ to the cross section — equations (1.9), (1.10) and (2.4) section VIII.1. of [214] pp.291-293 — were only derived for real positive wavenumbers. Yet, when performing analytic continuation of them to sub-threshold energies, the quantum tunneling effect will naturally make the transmission matrix infinitesimal on the physical sheet of mapping (E.4). Indeed, the *transmission matrix*, $\boldsymbol{T}$, is defined in [214] after eq. (2.3), VIII.2. p.292, as:

$$T_{cc'} \triangleq \delta_{cc'}\mathrm{e}^{2\mathrm{i}\omega_c} - U_{cc'} \tag{D.80}$$

where ω_c is defined by Lane & Thomas in eq.(2.13c) III.2.b. p.269, and used in eq.(4.5a) III.4.a. p.271 in [214], and is the difference $\omega_c = \sigma_{\ell_c}(\eta_c) - \sigma_0(\eta_c)$, where the *Coulomb phase shift*, $\sigma_{\ell_c}(\eta_c)$ is defined by Ian Thompson in eq.(33.2.10) of [250]. Defining the diagonal matrix $\boldsymbol{\omega} \triangleq \mathbf{diag}\big(\omega_c\big)$, and using the R-matrix expression

(E.14) for the scattering matrix, the Lane & Thomas transmission matrix (D.80) can be expressed with R-matrix parameters as:

$$\boldsymbol{T}_{\mathrm{L\&T}} \triangleq -2\mathrm{i}\boldsymbol{O}^{-1}\left[\underbrace{\left(\frac{\boldsymbol{I}-\boldsymbol{O}\mathrm{e}^{2\mathrm{i}\boldsymbol{\omega}}}{2\mathrm{i}}\right)}_{\boldsymbol{\Theta}}+\boldsymbol{\rho}^{1/2}\boldsymbol{R}_L\boldsymbol{O}^{-1}\boldsymbol{\rho}^{1/2}\right] \tag{D.81}$$

The angle-integrated partial cross sections $\sigma_{cc'}(E)$ can then be expressed as eq.(3.2d) VIII.3. p.293 of [214]:

$$\sigma_{cc'}(E) = \pi g_{J_c^\pi}\left|\frac{T^{cc'}_{\mathrm{L\&T}}(E)}{k_c(E)}\right|^2 \tag{D.82}$$

where $g_{J_c^\pi} \triangleq \frac{2J+1}{(2I_1+1)(2I_2+1)}$ is the *spin statistical factor* defined eq.(3.2c) VIII.3. p.293. Plugging-in the transmission matrix R-matrix parametrization (D.81) into cross-section expression (D.82) then yields: [214]:

$$\sigma_{cc'} = 4\pi g_{J_c^\pi}\left|\frac{1}{O_c k_c}\right|^2\left|\boldsymbol{\Theta}+\boldsymbol{\rho}^{1/2}\boldsymbol{R}_L\boldsymbol{O}^{-1}\boldsymbol{\rho}^{1/2}\right|^2_{cc'} \tag{D.83}$$

An alternative, more numerically stable, way of computing the cross section is used at Los Alamos National Laboratory, where one of the authors, G. Hale, introduced the following rotated transmission matrix, defined as:

$$\boldsymbol{T}_{\mathrm{H}} \triangleq -\frac{\mathbf{e}^{-\mathrm{i}\boldsymbol{\omega}}\boldsymbol{T}_{\mathrm{L\&T}}\mathbf{e}^{-\mathrm{i}\boldsymbol{\omega}}}{2\mathrm{i}} \tag{D.84}$$

and whose R-matrix parametrization is thus

$$\boldsymbol{T}_{\mathrm{H}} = {\boldsymbol{H}_+}^{-1}\left[\boldsymbol{\rho}^{1/2}\boldsymbol{R}_L\boldsymbol{\rho}^{1/2}{\boldsymbol{H}_+}^{-1}-\underbrace{\left(\frac{\boldsymbol{H}_+-\boldsymbol{H}_-}{2\mathrm{i}}\right)}_{\boldsymbol{F}}\right] \tag{D.85}$$

where $\boldsymbol{H}_\pm$ are defined as in eq.(2.13a)-(2.13b) III.2.b p.269 [214]:

$$\begin{aligned} H_{+c} &= O_c\mathrm{e}^{\mathrm{i}\omega_c} = G_c+\mathrm{i}F_c \\ H_{-c} &= I_c\mathrm{e}^{-\mathrm{i}\omega_c} = G_c-\mathrm{i}F_c \end{aligned} \tag{D.86}$$

and for which we refer to Ian J. Thompson's Chapter 33, eq.(33.2.11) in [250], or Abramowitz & Stegun chapter 14, p.537 [51]. The partial cross section is then directly related to the $\boldsymbol{T}_{\mathrm{H}}$ rotated transmission matrix (D.84) as:

$$\sigma_{cc'}(E) = 4\pi g_{J_c^\pi}\left|\frac{T_H^{cc'}(E)}{k_c(E)}\right|^2 \tag{D.87}$$

Theorem 13. *Evanescence of sub-threshold transmission matrix.*

For massive particles, analytic continuation of R-matrix parametrization (E.14) makes the sub-threshold transmission matrix $\boldsymbol{T}$, defined as (D.81), evanescent on the physical sheets of wavenumber-energy $\rho(E)$ mappings (2) or (4) section II.A of [127]. In turn, this quantum tunnelling entails the partial cross sections $\sigma_{cc'}(E)$ become infinitesimal below threshold.

Proof. The proof is based on noticing that both transmission matrix expressions (D.81) and (D.84) entail their modulus square is proportional to:

$$|\boldsymbol{T}_{cc'}|^2(E) \propto \left|\frac{1}{H_+(E)}\right|^2 \tag{D.88}$$

This is because $\boldsymbol{R}_L\boldsymbol{O}^{-1} = \left[\boldsymbol{O}\left[\boldsymbol{R}^{-1} - \boldsymbol{B}\right] - \boldsymbol{\rho}\boldsymbol{O}^{(1)}\right]^{-1}$, which does not diverge below threshold. Asymptotic expressions for the behavior of $H_+(\rho)$ then yield, for small ρ values:

$$H_+(\rho) \underset{\rho\to 0}{\sim} \frac{\rho^{-\ell}}{(2\ell+1)C_\ell(\eta)} - \mathrm{i}C_\ell(\eta)\rho^{\ell+1} \tag{D.89}$$

and asymptotic large-ρ behavior:

$$H_+(\rho) \underset{\rho\to\infty}{\sim} \mathrm{e}^{\mathrm{i}(\rho-\eta\ln(2\rho)-\frac{1}{2}\ell\pi+\sigma_\ell(\eta))} \tag{D.90}$$

Above the threshold, $\rho \in \mathbb{R}$ is real and thus equation (D.90) shows how $|H_+(\rho)| \underset{\rho\to\infty}{\longrightarrow} 1$. In other terms, the $|H_+(\rho)|$ term cancels out of the cross section expressions (D.83) and (D.87) for open-channels above threshold.

Yet, in both wavenumber-energy $\rho(E)$ mappings (2) or (4) section II.A of [127], the sub-threshold dimensionless wavenumber is purely imaginary: $\rho \in \mathrm{i}\mathbb{R}$. Since asymptotic form (D.90) is dominated in modulus by: $|H_+(\rho)| \underset{\rho\to\infty}{\sim} |\mathrm{e}^{\mathrm{i}\rho}|$. Depending on which sheet ρ is continued sub-threshold, we can have $\rho = \pm\mathrm{i}x$, with $x \in \mathbb{R}$. Thus, on the non-physical sheet $\left\{E, \ldots, -_c, \ldots\right\}$ for the given channel c of ρ_c, the transmission matrix (D.88) experiences exponential decay of $1/|H_+(\rho)|$ leading to the evanescence of the cross section (D.82), or (D.87). In effect, this means that the $|O_c(\rho_c)|$ term in (D.83) asymptotically acts like a Heaviside function, being unity for open channels, but closing the channels below threshold. Since $\rho_c = k_c r_c$ for the outgoing scattered wave $O_c(\rho_c)$, the exponential closure depends on two factors: the distance r_c from the nucleus, and how far from the threshold one is $|E - E_{T_c}|$. This is a classical evanescence behavior of quantum tunneling.

What happens when continuing on the physical sheet $\left\{E, \ldots, +_c, \ldots\right\}$, as $|H_+(\rho)|$ will now tend to diverge as a "divide by zero"? The authors have no rigorous answer, but point to the fact that since E is left unchanged by the choice of the k_c sheet, the evanescence result ought to also stand, despite the apparent divergence.

Note that for photon channels, the semi-classic wavenumber-energy $\rho(E)$ mappings (3) of section II.A of [127] does not yield this behavior, only the relativistic mapping (4) does.

□

We can estimate the orders of magnitude required to experimentally observe this evanescent quantum tunneling closure of the cross sections below threshold. At distance r_c from the center of mass of the nucleus, and at wavenumber k_c, distant from the threshold as $|E - E_{T_c}|$, the asymptotic behavior or the cross-section below threshold is:

$$\ln\left(\sigma_{cc'}(k_c, r_c)\right) \underset{\substack{E_c \leq E_{T_c} \\ k_c \to -\infty}}{\sim} -2r_c|k_c| \tag{D.91}$$

Assuming a detector is placed at a distance r_c of the nucleus, the cross section would decay exponentially below threshold as the distance $\Delta E_c = |E - E_{T_c}|$ of E to the threshold E_{T_c} increases. For instance, for a threshold of ^{238}U target reacting with neutron n channel, evanescence (D.91) would be of the rate of $\log_{10}\left(\sigma_{cc'}(k_c, r_c)\right) \sim -3 \times 10^{16} r_{c\mathrm{m}} \sqrt{\Delta E_{c\mathrm{eV}}}$. For a detector placed at a millimeter $r_c \sim 10^{-3}$m, this means one order of magnitude is lost for the cross section in $\Delta E_c \sim 10^{-27}$eV, evanescent indeed. Conversely, detecting this quantum tunneling with a detector sensitive to micro-electronvolts $\Delta E_c \sim 10^{-6}$eV $\sim 1\mu$eV (200 times more sensitive than the thermal energy of the cosmic microwave background) would see the cross section drop of one order of magnitude for a move of less than 10^{-13}m, or a tenth of a pico-meter. We are at sub-atomic level of quantum tunneling: the outgoing wave evanesces into oblivion way before reaching the electron cloud...

Regardless of the evanescence of the transmission matrix, a more general argument on the cross section shows that analytic continuation of the above-threshold expressions will automatically close the channels below the threshold.

Theorem 14. *Analytic continuation annuls sub-threshold cross sections.*
For massive particles, analytic continuation of above-threshold cross-section expressions to complex wavenumbers $k_c \in \mathbb{C}$ will automatically close channels for real energies $E \in \mathbb{R}$ below thresholds $E - E_{T_c} < 0$

Proof. The proof is based on the fact that massive particles are subject to mappings (2) or (4) section II.A of [127], which entail wavenumbers are real above threshold, and purely imaginary sub-threshold: $\forall E < E_{T_c}, k_c \in \mathrm{i}\mathbb{R}$. Let $\psi(\vec{r})$ be a general wave function, so that the probability density is $|\psi|^2(\vec{r})$.

For a massive particle subject to a real potential, the de Broglie non-relativistic Schrödinger equation applies, so that writing the conservation of probability on a control volume, and applying the Green-Ostrogradsky theorem, will yield the following expression for the probability current vector:

$$\vec{j}_\psi \triangleq \frac{\hbar}{\mu} \Im\left[\psi^* \vec{\nabla} \psi\right] \tag{D.92}$$

where μ is the reduced mass of the two-particle system (c.f. equations (2.10) and (2.12) section VIII.2.A, p.312 in [77]). By definition, the differential cross section $\frac{\mathrm{d}\sigma_{cc'}}{\mathrm{d}\Omega}$ is the ratio of the outgoing current in channel c' by the incoming current from

channel c, by unit of solid angle $\mathrm{d}\Omega$.

Consider the incoming channel c, classically modeled as a plane wave, $\psi_c(\vec{r}_c) \propto \mathrm{e}^{\mathrm{i}\vec{k}_c\cdot\vec{r}_c}$; and the outgoing channel c', classically modeled as radial wave, $\psi_{c'}(r_{c'}) \propto \frac{\mathrm{e}^{\mathrm{i}k_{c'}r_{c'}}}{r_{c'}}$. For arbitrary complex wavenumbers, $k_c, k_{c'} \in \mathbb{C}$, definition (D.92) will yield the following probability currents respectively:

$$\begin{aligned} \vec{j}_{\psi_c} &\propto \frac{\hbar}{\mu}\Im\left[\mathrm{i}\vec{k}_c\mathrm{e}^{-2\Im[\vec{k}_c]\cdot\vec{r}_c}\right] \\ \vec{j}_{\psi_{c'}} &\propto \frac{\hbar}{\mu}\Im\left[\left(\mathrm{i}k_{c'} - \frac{1}{r_{c'}}\right)\frac{\mathrm{e}^{-2\Im[k_{c'}]\cdot r_c}}{r_{c'}^2}\right]\vec{e}_r \end{aligned} \tag{D.93}$$

One will note these expressions are not the imaginary part of an analytic function in the wavenumber, because of the imaginary part $\Im[k_c]$. If however we look at real wavenumbers $k_c, k_{c'} \in \mathbb{R}$, that is at above-threshold energies $E \geq E_{T_c}$, the probability currents (D.93) readily simplify to:

$$\vec{j}_{\psi_c} \propto \frac{\hbar}{\mu}\Re\left[\vec{k}_c\right] \quad , \quad \vec{j}_{\psi_{c'}} \propto \frac{\hbar}{\mu}\Re\left[k_{c'}\right]\vec{e}_r \tag{D.94}$$

These expressions are the real part of analytic functions of the wavenumbers. If we analytically continue them to complex wavenumbers, and consider the cases of sub-threshold reactions $E < E_{T_c}$, for either the incoming or the outgoing channel, the wavenumbers are then exactly imaginary, $k_c, k_{c'} \in \mathrm{i}\mathbb{R}$. The real parts in (D.94) become zero, thereby annulling the cross section $\sigma_{c,c'}(E)$. This means that for massive particles (not massless photons) subject to real potentials, analytic continuation of the probability currents expressions above threshold (D.94) will automatically close the sub-threshold channels. This is true regardless of whether the transmission matrix (D.80) is or is not evanescent below threshold. This constitutes another major argument in favor of analytic continuation of open-channels expressions to describe the closed channels. □

Note that for photon channels, the derivations for the probability current vector (D.92) do not stand, and the wavenumber k_c is not imaginary below threshold using mapping (2) nor using the relativistic-correction (4) of section II.A of [127]. The fundamental reason why photon treatment is not straightforward is that R-matrix theory was constructed on the semi-classical formalism of quantum physics, with wavefunctions instead of state vectors. Though not incorrect, this wave function approach of quantum mechanics does not translate directly for photons, though some work has been done to describe photons through wave functions [74, 75]. This is another open area in the field of R-matrix theory, beyond the scope of this article.

D.6 Conclusion

In this article, we conduct a study and establish novel properties of the Siegert-Humblet pole expansion in radioactive states, which we show links R-matrix theory

to the Humblet-Rosenfeld pole expansions of the scattering matrix. The Siegert-Humblet parameters are the poles $\left\{\mathcal{E}_j\right\}$ and residue widths $\{r_{j,c}\}$ of the Kapur-Peierls $\boldsymbol{R}_L$ operator (E.15). They are $N_L \geq N_\lambda$ complex, (almost always) simple poles, that reside on the Riemann surface of mapping (E.4), comprised of 2^{N_c} branches, and for which one must specify on which sheet they reside, as shown in theorem 9. They are intimately interwoven in that not any set of complex parameters is physically acceptable: they must be solution to (E.32). Both $\left\{\mathcal{E}_j\right\}$ and $\left\{r_{j,c}\right\}$ are invariant to changes in boundary conditions $\{B_c\}$. Furthermore, $\left\{\mathcal{E}_j\right\}$ is invariant to a change in channel radii $\{a_c\}$, and we established in theorem 10 a simple way of transforming the radioactive widths $\left\{r_{j,c}\right\}$ under a change of channel radius a_c. Since the Siegert-Humblet parameters are the poles and residues of the local Mittag-Leffler expansion (E.41) of the Kapur-Peierls operator $\boldsymbol{R}_L$, the set of Siegert-Humblet parameters $\left\{E_{T_c}, a_c, \mathcal{E}_j, r_{i,c}\right\}$ is insufficient to entirely determine the energy behavior of the scattering matrix $\boldsymbol{U}$ through (D.42) and (D.41). The latter expressions directly link the R-matrix parameters to the poles and residues of the Humblet-Rosenfeld expansion of the scattering matrix, and can be complemented by local coefficients $\{\boldsymbol{s}_n\}_{\mathcal{W}(E)}$ of the entire part (D.43), to untangle the energy dependence of the scattering matrix into a simple sum of poles and residues (D.41), which is the full Humblet-Rosenfeld expansion of the scattering matrix. Theorem 11 establishes that under analytic continuation of the R-matrix operators, the poles of the Kapur-Peierls $\boldsymbol{R}_L$ operator (i.e. the Siegert-Humblet radioactive poles) are exactly the poles of the scattering matrix $\boldsymbol{U}$.

The latter is one of three results we advance to argue that, contrary to the legacy force-closure of sub-threshold channels presented in Lane & Thomas [214], R-matrix operators ought to be analytically continued for complex momenta. Such analytic continuation is necessary to cancel the spurious poles which would otherwise be introduced by the outgoing wavefunctions, as we establish in theorem 11. Moreover, we show in theorem 12 that the analytic continuation of R-matrix operators in scattering matrix parametrization (E.14) enforces Eden & Taylor's generalized unitarity condition (D.70). Finally, we argue in theorems 13 and 14 that analytic continuation will still close cross sections for massive particle channels (not massless photon channels) below threshold.

We thus conclude that the R-matrix community should henceforth come to consensus and agree to set the analytic continuation as the standard way of computing R-matrix operators (in particular the shift $S_c(E)$ and penetration $P_c(E)$ functions) when performing nuclear data evaluations.

D.7 Acknowledgments

This work was partly funded by the Los Alamos National Laboratory (research position in T-2 division during summer 2017), as well as by the Consortium for Advanced Simulation of Light Water Reactors (CASL), an Energy Innovation Hub for Modeling and Simulation of Nuclear Reactors under U.S. Department of Energy Contract No.

DE-AC05-00OR22725.

The first author is profoundly grateful to Prof. Semyon Dyatlov, from MIT and U.C. Berkeley, for his critical contribution in pointing to us towards the Gohberg-Sigal theory and providing important insights within it. He would also like to thank Haile Owusu for his time in discussing Hamiltonian degeneracy; as well as Grégoire Allaire for his important guidance on the Fredholm alternative and the Perron-Frobenius theorem. Finally, this work could not have come to fruition without the leadership of Vladimir Sobes at Oak Ridge National Laboratory during the summers of 2015, 2016, and 2018, and to Los Alamos National Laboratory Gerald Hale (author of theorem 12) and Mark Paris, who organized the R-matrix summer workshops (2016 and 2021), which have been platforms to spark and share these findings.

Table D.1: Radioactive parameters (Siegert-Humblet poles and residue widths of the Kapur-Peierls $\boldsymbol{R}_L(E)$ operator) of the two p-wave resonances of ^{134}Xe, spin-parity group $J^\pi = 1/2^{(-)}$, converted from ENDF/B-VIII.0 evaluation (MLBW) to multipole representation using Reich-Moore level matrix (E.18), that is definition (58) of [127].

$z = \sqrt{E}$ with E in (eV)
$A = 132.7600$
$a_c = 5.80$: channel radius (Fermis)
$\rho_0 = \frac{Aa_c\sqrt{\frac{2m_n}{h}}}{A+1}$ in $(\sqrt{\text{eV}}^{-1})$, so that $\rho(z) \triangleq \rho_0 z$
with $\sqrt{\frac{2m_n}{h}} = 0.002196807122623$ in units $(1/(10^{-14}\text{m}\sqrt{\text{eV}}))$

Radioactive parameters (rounded to 5 digits):

Radioactive poles $\{\mathcal{E}_j, \pm\}$ from (D.20) (eV), sheet of (E.4)	Radioactive residue widths $\boldsymbol{r_j}$ from (E.39) $(\sqrt{\text{eV}})$	Level-matrix residue widths $\boldsymbol{a_j}$ from (D.22) (dimensionless)
$\left\{\begin{matrix}-6.2694\times10^{+5}\\ -\text{i}1.0238\times10^{-4}\end{matrix},+\right\}$	$\begin{matrix}9.1193\times10^{-8}\\ -\text{i}1.4762\times10^{+0}\end{matrix}$	$\left[\begin{matrix}2.7683\times10^{-9}\\ -\text{i}4.4744\times10^{-2}\\ \hline 1.5345\times10^{-9}\\ -\text{i}2.4964\times10^{-2}\end{matrix}\right]$
$\left\{\begin{matrix}2.1838\times10^{+3}\\ +\text{i}9.0757\times10^{-2}\end{matrix},-\right\}$	$\begin{matrix}8.6799\times10^{-4}\\ -\text{i}2.5113\times10^{+1}\end{matrix}$	$\left[\begin{matrix}4.444\times10^{-5}\\ -\text{i}9.995\times10^{-1}\\ \hline -1.7608\times10^{-5}\\ -\text{i}2.9849\times10^{-4}\end{matrix}\right]$
$\left\{\begin{matrix}2.1838\times10^{+3}\\ -\text{i}1.6868\times10^{-1}\end{matrix},+\right\}$	$\begin{matrix}8.6814\times10^{-4}\\ +\text{i}2.5113\times10^{+1}\end{matrix}$	$\left[\begin{matrix}4.444\times10^{-5}\\ +\text{i}9.995\times10^{-1}\\ \hline -1.7597\times10^{-5}\\ +\text{i}2.9849\times10^{-4}\end{matrix}\right]$
$\left\{\begin{matrix}6.3130\times10^{+3}\\ +\text{i}1.6025\times10^{-1}\end{matrix},-\right\}$	$\begin{matrix}2.4919\times10^{-3}\\ -\text{i}1.4085\times10^{+1}\end{matrix}$	$\left[\begin{matrix}8.5974\times10^{-5}\\ +\text{i}8.5696\times10^{-4}\\ \hline 2.3534\times10^{-5}\\ -\text{i}9.9984\times10^{-1}\end{matrix}\right]$
$\left\{\begin{matrix}6.3130\times10^{+3}\\ -\text{i}2.3822\times10^{-1}\end{matrix},+\right\}$	$\begin{matrix}2.4916\times10^{-3}\\ +\text{i}1.4085\times10^{+1}\end{matrix}$	$\left[\begin{matrix}8.5964\times10^{-5}\\ -\text{i}8.5697\times10^{-4}\\ \hline 2.3534\times10^{-5}\\ +\text{i}9.9984\times10^{-1}\end{matrix}\right]$

R-matrix parameters:

$E_1 = 2186.0$: first resonance energy (eV)
$\Gamma_{1,n} = 0.2600$: neutron width of first resonance
(not reduced width), i.e. $\Gamma_{\lambda,c} = 2P_c(E_\lambda)\gamma^2_{\lambda,c}$
$\Gamma_{1,\gamma} = 0.0780$: eliminated capture width (eV)
$E_2 = 6315.0$: second resonance energy (eV)
$\Gamma_{2,n} = 0.4000$ (eV)
$\Gamma_{2,\gamma} = 0.0780$ (eV)
$g_{J^\pi} = 1/3$: spin statistical factor
$B_c = -1$

Appendix E

Windowed multipole representation of R-matrix cross sections

Here is *verbatim* transcribed our article [130].

E.1 Abstract

Nuclear cross sections are basic inputs to any nuclear computation. Campaigns of experiments are fitted with the parametric R-matrix model of quantum nuclear interactions, and the resulting cross sections are documented – both point-wise and as resonance parameters (with uncertainties) – in standard evaluated nuclear data libraries (ENDF, JEFF, BROND, JENDL, CENDL, TENDL): these constitute our common knowledge of fundamental low-energy nuclear cross sections. In the past decade, a collaborative effort has been deployed to establish a new nuclear cross section library format — the *Windowed Multipole Library* — with the goal of considerably reducing the computational cost of cross section calculations in nuclear transport simulations.

This article lays the theoretical foundations underpinning these efforts. From general R-matrix scattering theory, we derive the *windowed multipole representation* of nuclear cross sections. Though physically and mathematically equivalent to R-matrix cross sections, the windowed multipole representation is particularly well suited for subsequent temperature treatment of angle-integrated cross sections, in particular Doppler broadening, which is the averaging of cross sections over the thermal motion of the target atoms. Doppler broadening is of critical importance in neutron transport applications, as it ensures the stability of many nuclear reactors (negative thermal reactivity). Yet, Doppler broadening of nuclear cross sections has been a considerable bottleneck for nuclear transport computations, often requiring memory-costly pre-tabulations. We show that the Windowed Multipole Representation can perform accurate Doppler broadening analytically (up to the first reaction threshold), from which we derive cross sections temperature derivatives to any order — all computable on-the-fly (without pre-calculations stored in memory). Furthermore, we here establish a way of converting the R-matrix resonance parameters uncertainty (covariance matrices) into windowed multipole parameters uncertainty. We show that generating stochastic nuclear cross sections by sampling from the resulting windowed multipole covari-

ance matrix can reproduce the cross section uncertainty in the original nuclear data file. The Windowed Multipole Representation is therefore a novel nuclear physics formalism able to generate Doppler broadened stochastic nuclear cross sections on-the-fly, unlocking breakthrough computational gains for nuclear computations.

Through this foundational article, we hope to make the Windowed Multipole Representation accessible, reproducible, and usable for the nuclear physics community, as well as provide the theoretical basis for future research on expanding its capabilities.

E.2 Introduction

Our knowledge of nuclear reactions is progressively built-up by undertaking experiments and analyzing their outcomes through the prism of a quantum model of nuclear collisions called R-matrix theory [200, 323, 79, 214]. This is known as the nuclear data evaluation process. Evaluators conduct campaigns to measure nuclear cross sections and fit them with R-matrix parameters. To account for the epistemic uncertainty introduced, evaluators generate nuclear resonance parameters covariance matrices to reproduce the variance observed in the measurements.

Other parametrizations of nuclear cross sections exist – such as the Humblet-Rosenfeld pole expansions in wavenumber space [185, 289, 181, 182, 195, 183, 230, 290, 231] – but none have proven as practical to document or use as R-matrix theory, which is why our standard evaluated nuclear data libraries (ENDF[87], JEFF[267], BROND[80], JENDL[293], CENDL[153], TENDL[207, 209]) are constituted of R-matrix parameters (and their covariance uncertainties).
At the end of the 20^{th} century, R. Hwang from Argonne National Laboratory found a way to calculate from R-matrix parameters the Humblet-Rosenfeld pole expansion of neutron cross sections without thresholds, where the wavenumber is proportional to the square root of energy $k_c(E) \propto \sqrt{E}$. He also showed that this *pole representation* in $z \triangleq \sqrt{E}$ space presents a major advantage for subsequent temperature treatment: integral Doppler broadening can be accurately computed with analytic expressions [190, 186, 187, 188, 189]. This formalism was further developed into the *windowed multipole representation* in order to perform efficient on-the-fly computations of no-threshold neutron cross sections with a lesser computational memory footprint [146, 199, 197, 131, 262]. In this article, we extend the windowed multipole representation to all cross sections in the context of R-matrix theory: be they Coulomb, photon, neutrons, with or without thresholds. We also provide means of converting resonance parameters uncertainties into windowed multipole uncertainties. We thus lay the foundations to constitute a full *Windowed Multipole Library*, encompassing all present nuclear data [48].

In section E.3, we derive the windowed multipole representation from general R-matrix theory, showing it is the meromorphic continuation of cross sections to complex energies, and discuss numerical ways of computing the mutipoles, either from resonance parameters or point-wise cross section data. In section E.4, we expand the windowed multipole representation to account for the epistemic uncertainty of the nuclear cross sections [129, 52]. We establish the analytic sensitivities of the windowed

multipole parameters to the Wigner-Eisenbud R-matrix resonance parameters. This enables us to convert to first-order the standard resonance parameters covariance matrix into a windowed multipoles covariance matrix, and show the latter reproduces the statistical properties of nuclear cross section uncertainties. Having done so, we consider temperature effects in section E.5, showing how to analytically Doppler broaden windowed multipole angle-integrated cross sections, and how to compute arbitrary-order temperature derivatives that can prove useful in multiphysics simulations [168, 167].

By deriving conversion methods of R-matrix resonance parameters and their uncertainties (covariance matrices) to windowed multipoles, and showing how to account for temperature effects, we thus establish the windowed multipole representation as a general, physically equivalent parametrization of R-matrix cross sections. By its efficient on-the-fly treatment of uncertainty and Doppler broadening, the windowed multipole representation can achieve considerable computational gains, and has already found several new nuclear reactor physics applications, from the establishment of a new analytic benchmark for neutron slowing down that resolves nuclear resonances overlap [299], or explicit resonance treatment for thermal up-scattering of angular cross sections [222], to differential temperature tallies for higher-order neutronics-thermohydraulics coupling schemes in nuclear transport solvers [168, 167], or enabling new uncertainty inference and propagation methods across intractable nuclear systems [129].

E.3 From R-matrix to Windowed Multipole

We here establish the *Windowed Multipole Representation*, deriving it from general R-matrix scattering theory. In doing so, we show that R-matrix cross sections are the sum of two phenomena: thresholds and resonances. Thresholds have a behavior in the wavenumber k_c space of the channel c, so that in the vicinity of a threshold the cross section admits a Laurent expansion in powers of k_c (starting at k_c^{-2}). Resonances have a behavior in the energy space E, and can thus be locally expressed as a sum of Single-Level Breit-Wigner (SLBW) resonances, with both symmetric and anti-symmetric Lorenztian functions. In [125], we linked the R-matrix parametrization of the scattering matrix $\boldsymbol{U}(E)$ to its wavenumber k_c expansion, established by Humblet and Rosenfeld in their *Theory of Nuclear Reactions* [185, 289, 181, 182, 195, 183, 230, 290, 231]. In this article, we use this connection to establish the Windowed Multipole Representation, which is the meromorphic continuation of R-matrix cross sections in $z \triangleq \sqrt{E}$ space, locally expressing open channels as pole expansions. We build upon our previous work on such expansions [127, 125], using the same consistent notation as reference.

E.3.1 R-matrix cross section parametrization

R-matrix theory models two-body-in/two-body-out scattering events interacting with a "black-box" Hamiltonian [200, 323, 79, 214]. Each pair of possible two-body-inputs/two-body-outputs, along with all the corresponding quantum numbers that describe then, constitutes a channel c. It is assumed that for each channel, the Hamiltonian can be partitioned into two regions: within an "inner region" sphere of channel radius a_c, the many bodies interacting through the strong nuclear forces are considered an intractable "black-box" Hamiltonian; past the channel radius a_c, the "outer region" Hamiltonian is well known (say Coulomb potential or free-wave). For each channel c, R-matrix theory studies the many-body scattering event into the reduced one-body system, where the solution of the Schrödinger equation is a superposition of an incoming wavefunction I_c and an outgoing wavefunction O_c, both function of the wavenumber k_c. The latter can be multiplied by the arbitrary (but fixed) channel radius a_c to yield the *dimensionless wavenumber*

$$\rho_c \triangleq k_c a_c \tag{E.1}$$

and we define the corresponding diagonal matrix over all the channels $\boldsymbol{\rho} = \mathbf{diag}\left(\rho_c\right)$.

Wavenumber-Energy mapping

Each wavenumber is related to the total energy E of the system, which is an eigenvalue of the Hamiltonian in the reduced center-of-mass frame. In the semi-classical limit, a two massive particles channel (i.e. not photons) of respective masses $m_{c,1}$ and $m_{c,2}$ will have a wavenumber k_c of:

$$k_c(E) = \sqrt{\frac{2m_{c,1}m_{c,2}}{\left(m_{c,1}+m_{c,2}\right)\hbar^2}\left(E - E_{T_c}\right)} \tag{E.2}$$

where E_{T_c} denotes a threshold energy below which the channel c is closed, as energy conservation cannot be respected ($E_{T_c} = 0$ for reactions without threshold). In the same semi-classical limit, a photon particle interacting with a massive body of mass $m_{c,1}$, the center-of-mass wavenumber k_c is linked to the total center-of-mass energy E according to:

$$k_c(E) = \frac{\left(E - E_{T_c}\right)}{2\hbar \mathrm{c}}\left[1 + \frac{m_{c,1}\mathrm{c}^2}{\left(E - E_{T_c}\right) + m_{c,1}\mathrm{c}^2}\right] \tag{E.3}$$

These two semi-classical limits can be encompassed within a single relativistic framework as discussed in equations (4) and (5), section II.A. of [127]. Because one must choose the sign of the square root $\pm\sqrt{\cdot}$ in (E.2), these $k_c(E)$ relations engender a wavenumber-energy mapping

$$\rho_c(E) \quad \longleftrightarrow \quad E \tag{E.4}$$

which forms a complex multi-sheeted Riemann surface with branch-points at (or close to) the threshold energies E_{T_c}, as discussed in section II.A. p.2 of [127].

Transmission matrix and cross section expressions

General scattering theory expresses the incoming channel c and outgoing channel c' angle-integrated partial cross section $\sigma_{c,c'}(E)$ at energy E as a function of the probability *transmission matrix* $T_{cc'}(E)$, according to eq.(3.2d) VIII.3. p.293 of [214]:

$$\sigma_{cc'}(E) = 4\pi g_{J_c^\pi} \left| \frac{T_{cc'}(E)}{k_c(E)} \right|^2 \tag{E.5}$$

where the *spin statistical factor* is defined eq.(3.2c) VIII.3. p.293. of [214] as:

$$g_{J_c^\pi} \triangleq \frac{2J+1}{(2I_1+1)(2I_2+1)} \tag{E.6}$$

The transmission matrix is itself derived from the *scattering matrix* $\boldsymbol{U}$ of the interaction:

$$\boldsymbol{T} \triangleq \frac{\mathbb{I} - \mathbf{e}^{-\mathrm{i}\boldsymbol{\omega}}\boldsymbol{U}\mathbf{e}^{-\mathrm{i}\boldsymbol{\omega}}}{2} \tag{E.7}$$

where $\boldsymbol{\omega} \triangleq \mathbf{diag}\Big(\omega_c\Big)$ is the diagonal matrix composed of $\omega_c \triangleq \sigma_{\ell_c}(\eta_c) - \sigma_0(\eta_c)$, that is the difference in *Coulomb phase shift*, $\sigma_{\ell_c}(\eta_c)$, which are linked to the phases (argument) of the Gamma function as defined by Ian Thompson in eq.(33.2.10) of [250] for angular momentum ℓ_c

$$\sigma_{\ell_c}(\eta_c) \triangleq \arg\Big(\Gamma\left(1 + \ell_c + \mathrm{i}\eta_c\right)\Big) \tag{E.8}$$

and *dimensionless Coulomb field parameter*:

$$\eta_c \triangleq \frac{Z_1 Z_2 e^2 M_\alpha a_c}{\hbar^2 \rho_c} \tag{E.9}$$

Note that this transmission matrix (E.7) definition $T_{cc'} \triangleq \frac{\delta_{cc'} - \mathrm{e}^{-\mathrm{i}\omega_c} U_{cc'} \mathrm{e}^{-\mathrm{i}\omega_{c'}}}{2}$ is a scaled rotation of the one defined by Lane and Thomas $T_{cc'}^{\mathrm{L\&T}} \triangleq \delta_{cc'}\mathrm{e}^{2\mathrm{i}\omega_c} - U_{cc'}$ (c.f. eq. (2.3), VIII.2. p.292 and eq.(3.2d) VIII.3. p.293 of [214]). We introduce definition (E.7) for better physical interpretability, algebraic simplicity and numerical stability.

Unitarity of the scattering matrix entails that $\sum_{c'} \left|\delta_{cc'} - \mathrm{e}^{-\mathrm{i}\omega_c} U_{cc'} \mathrm{e}^{-\mathrm{i}\omega_{c'}}\right|^2 = 2\left(1 - \Re\left[\mathrm{e}^{-2\mathrm{i}\omega_c} U_{cc}\right]\right)$, which in turn leads to the following expression for the total cross section of a given channel:

$$\sigma_c(E) \triangleq \sum_{c'} \sigma_{cc'}(E) = 4\pi g_{J_c^\pi} \frac{\Re\left[T_{cc}(E)\right]}{\left|k_c(E)\right|^2} \tag{E.10}$$

In both cross section expressions (E.5) and (E.10), the $1/\left|k_c\right|^2$ term links the cross section to the probability of interaction, and expresses the channel reversibility equiv-

alence:

$$\frac{k_c^2 \sigma_{cc'}}{g_{J_c^\pi}} = \frac{k_{c'}^2 \sigma_{c'c}}{g_{J_{c'}^\pi}} \tag{E.11}$$

The incoming I_c and outgoing O_c waves are functions of the dimensionless wavenumber $\rho_c \triangleq a_c k_c$ and are linked to the regular and irregular Coulomb wave functions (or Bessel functions in the case of neutral particle channels), defined in eq.(2.13a)-(2.13b) III.2.b p.269 [214]:

$$\begin{aligned} O_c &= H_{+c} \mathrm{e}^{-\mathrm{i}\omega_c} = (G_c + \mathrm{i}F_c)\, \mathrm{e}^{-\mathrm{i}\omega_c} \\ I_c &= H_{-c} \mathrm{e}^{\mathrm{i}\omega_c} = (G_c - \mathrm{i}F_c)\, \mathrm{e}^{\mathrm{i}\omega_c} \end{aligned} \tag{E.12}$$

and for properties of which we refer to Ian J. Thompson's Chapter 33, eq.(33.2.11) in [250], or Abramowitz & Stegun chapter 14, p.537 [51]. In polar notation:

$$\begin{aligned} H_{+c} &= |H_{+c}|\, \mathrm{e}^{\mathrm{i}\phi_c} \\ |H_{+c}| &= \left| \sqrt{|G_c|^2 + |F_c|^2} \right| \\ \phi_c &\triangleq \arg(H_{+c}) = 2 \arctan\left(\frac{|F_c|}{|H_{+c}| + |F_c|} \right) \end{aligned} \tag{E.13}$$

R-matrix scattering matrix parametrization

R-matrix theory parametrizes the energy dependence of the scattering matrix $\boldsymbol{U}(E)$ as:

$$\boldsymbol{U} = \boldsymbol{O}^{-1}\boldsymbol{I} + 2\mathrm{i}\boldsymbol{\rho}^{1/2}\boldsymbol{O}^{-1}\boldsymbol{R}_L\boldsymbol{O}^{-1}\boldsymbol{\rho}^{1/2} \tag{E.14}$$

where the incoming and outgoing wavefunctions, $\boldsymbol{I} = \mathbf{diag}(I_c)$ and $\boldsymbol{O} = \mathbf{diag}(O_c)$, are subject to the following Wronksian condition for all channel c, $w_c \triangleq O_c^{(1)} I_c - I_c^{(1)} O_c = 2\mathrm{i}$, and where $\boldsymbol{R}_L$ is the *Kapur-Peierls operator*, defined as (see equation (20) section II.D of [127]):

$$\boldsymbol{R}_L \triangleq \left[\mathbb{I} - \boldsymbol{R}\boldsymbol{L}^{\boldsymbol{0}}\right]^{-1} \boldsymbol{R} = \boldsymbol{\gamma}^{\mathsf{T}} \boldsymbol{A} \boldsymbol{\gamma} \tag{E.15}$$

where $\boldsymbol{R}$ is the Wigner-Eisenbud *R-matrix* [323]:

$$R_{cc'}(E) \triangleq \sum_{\lambda=1}^{N_\lambda} \frac{\gamma_{\lambda,c}\gamma_{\lambda,c'}}{E_\lambda - E} \tag{E.16}$$

parametrized by the real *resonance energies* $E_\lambda \in \mathbb{R}$ and the real *resonance widths* $\gamma_{\lambda,c} \in \mathbb{R}$ – of which we respectively build the diagonal matrix $\boldsymbol{e} = \mathbf{diag}(E_\lambda)$ of size the number of levels (resonances) N_λ, and the rectangular matrix $\boldsymbol{\gamma} = \mathbf{mat}(\gamma_{\lambda,c})$ of size $N_\lambda \times N_c$ where N_c is the number of channels. The Kapur-Peierls operator (E.15) is thus a function of $\boldsymbol{R}$ and $\boldsymbol{L^0} \triangleq \boldsymbol{L} - \boldsymbol{B}$, where $\boldsymbol{B} = \mathbf{diag}(B_c)$ is the diagonal matrix of real arbitrary boundary conditions B_c, and $\boldsymbol{L} = \mathbf{diag}(L_c)$ where $L_c(\rho_c)$ is the dimensionless reduced logarithmic derivative of the outgoing-wave function at the channel surface:

$$L_c(\rho_c) \triangleq \frac{\rho_c}{O_c} \frac{\partial O_c}{\partial \rho_c} \tag{E.17}$$

An equivalent definition (E.15) of the Kapur-Peierls operator $\boldsymbol{R}_L$ can be expressed with the *level matrix* $\boldsymbol{A}$ (see equations (17) and (18) of section II.C of [127]):

$$\boldsymbol{A^{-1}} \triangleq \boldsymbol{e} - E\mathbb{I} - \boldsymbol{\gamma}\,(\boldsymbol{L} - \boldsymbol{B})\,\boldsymbol{\gamma}^{\mathsf{T}} \tag{E.18}$$

As such, provided with the threshold energies, the channel radius, boundary conditions, and Wigner-Eisenbud resonance energies and widths, which we can collectively call the set of R-matrix parameters $\left\{E_{T_c}, a_c, B_c, E_\lambda, \gamma_{\lambda,c}\right\}$, one can entirely determine the energy behavior of the scattering matrix $\boldsymbol{U}$ through (E.14), and therefore the cross sections through (E.5) and (E.10).

Reich-Moore and Breit-Wigner approximations to R-matrix theory

In practice, many evaluations in standard nuclear data libraries are carried out with approximations of R-matrix theory. The most important and common is the *Reich-Moore* approximation. It reduces the R-matrix to only the channels of interest, and accounts for the effect of all the other channels not explicitly treated by means of the Teichmann and Wigner channel elimination method (c.f. [305] or section X, p.299 of [214]). This approximation is most useful when many channels are eliminated, such that the effect on the off-diagonal elements of the level matrix is small, a scenario often encountered in heavy nuclei. Usually, photon channels (γ "gamma capture") are eliminated, so that in practice the Reich-Moore approximation of R-matrix theory [276] consists of adding a partial eliminated capture width $\Gamma_{\lambda,\gamma}$ to every resonance energy E_λ, shifting the latter into the complex plane (c.f. section IV.A of [127]):

$$\boldsymbol{e}_{\text{R.M.}} \triangleq \mathbf{diag}\left(E_\lambda - \mathrm{i}\frac{\Gamma_{\lambda,\gamma}}{2}\right) \tag{E.19}$$

The R-matrix (E.16) without the eliminated photon channels becomes:

$$\begin{aligned} R_{c,c'\notin\gamma_{\text{elim.}}} &\triangleq \sum_{\lambda=1}^{N_\lambda} \frac{\gamma_{\lambda,c}\gamma_{\lambda,c'}}{E_\lambda - \mathrm{i}\frac{\Gamma_{\lambda,\gamma}}{2} - E} \\ \text{i.e.}\quad \boldsymbol{R}_{\text{R.M.}} &= \boldsymbol{\gamma}^{\mathsf{T}}\left(\boldsymbol{e}_{\text{R.M.}} - E\mathbb{I}\right)^{-1}\boldsymbol{\gamma} \end{aligned} \tag{E.20}$$

and the Reich-Moore inverse level matrix (E.18) becomes:

$$\boldsymbol{A^{-1}}_{\text{R.M.}} \triangleq \boldsymbol{e}_{\text{R.M.}} - E\,\mathbb{I} - \boldsymbol{\gamma}\,(\boldsymbol{L} - \boldsymbol{B})\,\boldsymbol{\gamma}^{\mathsf{T}} \tag{E.21}$$

All the other R-matrix expressions linking these operators to the scattering matrix (E.14), and therefore the cross sections, remain unchanged. Practically, the only consequence of the Reich-Moore formalism is to introduce complex resonance energies (E.19). In this sense, one can consider the Reich-Moore formalism as a generalization of R-matrix theory, even though it finds its source in the elimination of intractable channels. It can thus also be seen as a compression algorithm. Indeed, it is possible to convert Reich-Moore parameters into standard R-matrix ones (not complex resonance

energies) by means of the *Generalized Reich-Moore* formalism, as established in [60]. Yet this comes at the cost of introducing many more parameters, thereby considerably increasing memory requirements. This is because Generalized Reich-Moore converts the eliminated channels R-matrix ($N_c \times N_c$ with $c \notin \gamma_{\text{elim.}}$) into a square R-matrix of the size of the levels ($N_\lambda \times N_\lambda$), and we often have $N_\lambda \gg N_c$, specially for large nuclides (c.f. [60]).

Also, note that some older evaluations are made in the *Multi-Level Breit-Wigner* approximation, which simply consists of assuming the level matrix (E.18) is diagonal. This can be expressed using the Hadamard product " $\circ$ " with the identity matrix as:

$$\boldsymbol{A^{-1}}_{\text{MLBW}} \triangleq \boldsymbol{A^{-1}} \circ \mathbb{I} \tag{E.22}$$

Apart from these modified expressions of the level matrix, neither the Reich-Moore nor the Multi-Level Breit-Wigner approximations have any further incidence on how to convert R-matrix cross sections to Windowed Multipole Representation: it suffices to take the corresponding level matrix and proceed as follows.

Parametrizing R-matrix cross sections

By substituting the R-matrix parametrization (E.14) of the scattering matrix $\boldsymbol{U}$ into the transmission matrix $\boldsymbol{T}$ definition (E.7), and noticing that wavefunction relations (E.12) entail $\frac{\boldsymbol{H_+}-\boldsymbol{H_-}}{2\mathrm{i}} = \boldsymbol{F}$, one finds the transmission matrix can be decomposed into the rotated (by a factor of imaginary i) difference between a diagonal *potential matrix* $\boldsymbol{D}$ and a full *resonance matrix* $\boldsymbol{Z}$:

$$\begin{aligned}
\boldsymbol{T} &= \mathrm{i}\,(\boldsymbol{D} - \boldsymbol{Z}) \\
\boldsymbol{Z} &\triangleq \boldsymbol{H_+}^{-1}\boldsymbol{\rho}^{1/2}\boldsymbol{R}_L\boldsymbol{\rho}^{1/2}\boldsymbol{H_+}^{-1} \\
\boldsymbol{D} &\triangleq \boldsymbol{H_+}^{-1}\boldsymbol{F} = \frac{\mathbb{I} - \boldsymbol{Y}}{2\mathrm{i}} \\
\boldsymbol{Y} &\triangleq \boldsymbol{H_+}^{-1}\boldsymbol{H_-}
\end{aligned} \tag{E.23}$$

From cross section expression (E.5), the transmission probabilities from channel c to channel c' are then the square-modulus $|T_{cc'}|^2$. Decomposition (E.23) expresses this as:

$$|T_{cc'}|^2 = |Z_{cc'}|^2 + |D_c|^2\,\delta_{cc'} - 2\Re\left[Z_{cc'}D_c^*\right]\delta_{cc'} \tag{E.24}$$

where $[\,\cdot\,]^*$ designates the complex conjugate. For the total cross section (E.10), it is the real part of the transmission matrix that appears: $\Re\left[T_{cc}\right] = \Re\left[\mathrm{i}D_c\right] - \Re\left[\mathrm{i}Z_{cc}\right]$. Note that $\boldsymbol{D}$ definition (E.23) entails $2\boldsymbol{D}^* = \mathrm{i}\,(\mathbb{I} - \boldsymbol{Y}^*)$ and $|\boldsymbol{D}|^2 = \Re\left[\mathrm{i}\boldsymbol{D}\right]$, since definition (E.13) yields

$$\Re\left[\mathrm{i}D_c\right] = \frac{|F_c|^2}{|G_c|^2 + |F_c|^2} = |D_c|^2 = \sin^2(\phi_c) \tag{E.25}$$

We can thus decompose the cross sections into the following components, all expressed as the real part of some matrix elements calculable from R-matrix theory:

- Potential cross section (of channel c):

$$\sigma_c^{\text{pot}}(E) \triangleq 4\pi g_{J_c^\pi} \left|\frac{D_c}{k_c}\right|^2 = 4\pi g_{J_c^\pi} \frac{\Re\left[\mathrm{i}D_c\right]}{|k_c|^2} \tag{E.26}$$

- Total cross section (of channel c):

$$\sigma_c(E) \triangleq \sigma_c^{\text{pot}}(E) + 4\pi g_{J_c^\pi} \frac{\Re\left[-\mathrm{i}Z_{cc}\right]}{|k_c|^2} \tag{E.27}$$

- Self-scattering cross section (of channel c):

$$\sigma_c^{\text{scat}}(E) \triangleq 4\pi g_{J_c^\pi} \frac{\Re\left[-2Z_{cc}D_c^*\right]}{|k_c|^2} \tag{E.28}$$

- Interference cross section (of channel c):

$$\sigma_c^{\text{int}}(E) \triangleq 4\pi g_{J_c^\pi} \frac{\Re\left[-\mathrm{i}Z_{cc}Y_c^*\right]}{|k_c|^2} \tag{E.29}$$

- Reaction cross section (from channel c to c'):

$$\sigma_{cc'}^{\text{react}}(E) \triangleq 4\pi g_{J_c^\pi} \left|\frac{Z_{cc'}}{k_c}\right|^2 \tag{E.30}$$

- Partial (angle-integrated) cross section (from channel c to c'):

$$\begin{aligned}\sigma_{cc'}(E) &\triangleq \Big(\sigma_c^{\text{pot}}(E) + \sigma_c^{\text{scat}}(E)\Big)\delta_{cc'} + \sigma_{cc'}^{\text{react}}(E) \\ &= \Big(\sigma_c^{\text{tot}}(E) - \sigma_c^{\text{int}}(E)\Big)\delta_{cc'} + \sigma_{cc'}^{\text{react}}(E)\end{aligned} \tag{E.31}$$

Writing these expressions as functions of the dimensionless wavenumbers of each channel, $\rho_c \triangleq k_c a_c$, cross sections appear as proportional to the area of the channel radius disc $\sigma_c(E) \propto 4\pi a_c^2$, and the modulation of this area is linked to both the transmission matrix amplitudes $|T_{cc'}(E)|^2$ – which exhibit the resonance behavior – and the $1/k_c^2$ wavenumber effect that dominates the total cross section close to the zero-energy threshold.

E.3.2 Kapur-Peierls operator pole expansion in Siegert-Humblet radioactive states

The first step towards the Windowed Multipole Representation consists of performing the pole expansion of the Kapur-Peierls operator $\boldsymbol{R}_L$ into what are called the Siegert-Humblet radioactive states [296, 86, 218, 220, 110]. We here summarize this process

for the usual case of non-degenerate solutions, and we refer to sections II and IV of [125] for a detailed study.

The *radioactive states problem* consists of finding the poles $\left\{\mathcal{E}_j\right\}$ and residue widths vectors $\{\boldsymbol{r_j}\}$ of the Kapur-Peierls operator $\boldsymbol{R}_L$, that is solving the following generalized eigenvalue problem [296, 86, 218, 220, 110]:

$$\boldsymbol{R}_L^{-1}(E)\Big|_{E=\mathcal{E}_j}\boldsymbol{r_j} = \boldsymbol{0} \tag{E.32}$$

where the residue widths vectors $\{\boldsymbol{r_j}\}$ are subject to the following normalization:

$$\boldsymbol{r_j}^{\mathsf{T}}\left(\frac{\partial \boldsymbol{R}_L^{-1}}{\partial E}\bigg|_{E=\mathcal{E}_j}\right)\boldsymbol{r_j} = 1 \tag{E.33}$$

which can be calculated using

$$\frac{\partial \boldsymbol{R}_L^{-1}}{\partial E}\bigg|_{E=\mathcal{E}_j} = \frac{\partial \boldsymbol{R}^{-1}}{\partial E}(\mathcal{E}_j) - \frac{\partial \boldsymbol{L}}{\partial E}(\mathcal{E}_j) \tag{E.34}$$

if the R-matrix $\boldsymbol{R}$ is invertible at $\mathcal{E}_j$, whence

$$\frac{\partial \boldsymbol{R}^{-1}}{\partial E}(E) = -\boldsymbol{R}^{-1}\boldsymbol{\gamma}^{\mathsf{T}}\left(\boldsymbol{e} - E\mathbb{I}\right)^{-2}\boldsymbol{\gamma}\boldsymbol{R}^{-1} \tag{E.35}$$

If the R-matrix $\boldsymbol{R}$ is not invertible at $\mathcal{E}_j$, these *radioactive poles* $\{\mathcal{E}_j\}$ and *radioactive widths* $\left\{\boldsymbol{r_j} = \left[r_{j,c_1}, \ldots, r_{j,c}, \ldots, r_{j,c_{N_c}}\right]^{\mathsf{T}}\right\}$, jointly called the Siegert-Humblet parameters, can be obtained by solving the level matrix $\boldsymbol{A}$ radioactive eigenproblem:

$$\boldsymbol{A}^{-1}(E)\Big|_{E=\mathcal{E}_j}\boldsymbol{a_j} = \boldsymbol{0} \tag{E.36}$$

where the eigenvectors $\boldsymbol{a_j}$ are subject to normalization:

$$\boldsymbol{a_j}^{\mathsf{T}}\left(\frac{\partial \boldsymbol{A}^{-1}}{\partial E}\bigg|_{E=\mathcal{E}_j}\right)\boldsymbol{a_j} = 1 \tag{E.37}$$

which is readily calculable from

$$\frac{\partial \boldsymbol{A}^{-1}}{\partial E}(\mathcal{E}_j) = -\mathbb{I} - \boldsymbol{\gamma}\frac{\partial \boldsymbol{L}}{\partial E}(\mathcal{E}_j)\boldsymbol{\gamma}^{\mathsf{T}} \tag{E.38}$$

The level-matrix residues widths vectors are then linked to the radioactive widths by the following relation:

$$\boldsymbol{r_j} = \boldsymbol{\gamma}^{\mathsf{T}}\boldsymbol{a_j} \tag{E.39}$$

The radioactive energy poles are complex and usually decomposed as:

$$\mathcal{E}_j \triangleq E_j - \mathrm{i}\frac{\Gamma_j}{2} \tag{E.40}$$

It can be shown (c.f. discussion section IX.2.d pp.297–298 in [214], or section 9.2 eq. (9.11) in [185]) that fundamental physical properties (conservation of probability, causality and time reversal) ensure that the poles reside either on the positive semi-axis of purely-imaginary $k_c \in \mathrm{i}\mathbb{R}_+$ – corresponding to bound states for real sub-threshold energies, i.e. $E_j < E_{T_c}$ and $\Gamma_j = 0$ – or that all the other poles are on the lower-half k_c plane, with $\Gamma_j > 0$, corresponding to "resonance" or "radioactively decaying" states. All poles enjoy the specular symmetry property: if $k_c \in \mathbb{C}$ is a pole of the Kapur-Peierls operator, then $-k_c^*$ is too. Additional discussion on these radioactive poles and residues can be found in [214], sections IX.2.c-d-e p.297-298, or in [296, 86, 218, 220, 110].

For our purpose of constructing the Windowed Multipole Representation for R-matrix cross sections, the key property of the radioactive states is that they allow, by virtue of the Mittag-Leffler theorem [244, 304], to locally decompose the Kapur-Peierls operator into a sum of poles and residues and a holomorphic entire part $\mathbf{Hol}_{\boldsymbol{R}_L}(E)$, in the neighborhood $\mathcal{W}(E)$ (vicinity) of any complex energy $E \in \mathbb{C}$ away from the branch points (threshold energies E_{T_c}) of mapping (E.4):

$$\boldsymbol{R}_L(E) \underset{\mathcal{W}(E)}{=} \sum_{j\geq 1} \frac{\boldsymbol{r_j}\boldsymbol{r_j}^\mathsf{T}}{E - \mathcal{E}_j} + \mathbf{Hol}_{\boldsymbol{R}_L}(E) \tag{E.41}$$

Theorem 1 of [125] presents the branch structure of the radioactive poles $\mathcal{E}_j$ on the Riemann surface of the energy-wavenumber mapping (E.4). We also show that when solving in dimensionless wavenumber space ρ_c, there are N_L number of solutions to the radioactive problem (E.32). In the case of massive neutral particles (neutrons and neutrinos) we have

$$N_L = \left(2N_\lambda + \sum_{c=1}^{N_c} \ell_c\right) \times 2^{(N_{E_{T_c}\neq E_{T_{c'}}} - 1)} \tag{E.42}$$

where $N_{E_{T_c}\neq E_{T_{c'}}}$ denotes the number of channels with different thresholds. For charged particles, there is an infinite number (countable) of radioactive poles: $N_L = \infty$. In essence, this is because for each different sheet of the energy-wavenumber mapping (E.4), of which there are $2^{(N_{E_{T_c}\neq E_{T_{c'}}} - 1)}$, the R-matrix contributes $2N_\lambda$ poles in wavenumber space (each resonance energy E_λ yielding two $\rho_c(E)$ space poles), and in addition each pole of the reduced logarithmic derivative $L_c(\rho_c)$ yields another radioactive pole in ρ_c space (c.f. theorem 1 of [125] for more detailed discussion).

Be that as it may, radioactive poles usually have the following characteristics (as can be observed in table E.1 for the case of xenon ^{134}Xe as well as in TABLE I of [125]): for each resonance energy E_λ there are two radioactive poles nearby, usually on opposite sheets, close to but not exactly the specular symmetric of one another across

the imaginary axis in wavenumber ρ_c space (i.e. near opposite complex conjugates); moreover, for each root ω_n of the outgoing function $O_c(\rho_c)$, there is a radioactive pole nearby. Often, only one of the two radioactive poles $\mathcal{E}_j$ close to the E_λ is responsible for most of the cross section resonance behavior, while all the other radioactive poles are more akin to non-resonant "background levels", though they are still necessary to fully describe the cross section.

A critical property of the radioactive poles $\mathcal{E}_j$ is that these are exactly all the poles of the scattering matrix $\boldsymbol{U}(E)$ (proof in theorem 3 of [125]). From decomposition (E.23), this entails that the transmission matrix readily admits the following Mittag-Leffler expansion:

$$\boldsymbol{T}(E) \underset{\mathcal{W}(E)}{=} -\mathrm{i}\sum_{j\geq 1}\frac{\boldsymbol{\tau_j}\boldsymbol{\tau_j}^{\mathsf{T}}}{E-\mathcal{E}_j} + \mathbf{Hol}_{\boldsymbol{T}}(E) \tag{E.43}$$

where the residue width vectors are obtained by evaluating the functions in (E.23) at the pole values:

$$\boldsymbol{\tau_j} = \boldsymbol{H}_+{}^{-1}(\mathcal{E}_j)\,\boldsymbol{\rho}^{1/2}(\mathcal{E}_j)\;\;\boldsymbol{r_j} \tag{E.44}$$

E.3.3 Transmission matrix T and resonance matrix Z expansions in square root of energy z-space

Though energy E-space expansion (E.43) is correct, we will nonetheless also introduce expansions in the square root of energy z-space:

$$z \triangleq \sqrt{E} \tag{E.45}$$

We do this to better express the behavior of massive particles (not massless photons) near the zero-energy threshold, and in order to perform analytic Doppler broadening of massive particles. Indeed, for the zero threshold $E_{T_c} = 0$, the wavenumber of massive particles is simply proportional to the square root of energy: $k \propto z$. Hwang noticed this entails a remarkable property: for neutral particles without threshold, the Kapur-Peierls operator $R_L(z)$ is a rational function of z (c.f. [190]), and therefore the radioactive problem (E.32) can be completely solved using polynomial root finders (c.f. section E.3.6).

The general Mittag-Leffler expansion (E.41) of the Kapur-Peierls operator in z-space is

$$\boldsymbol{R}_L(z) \underset{\mathcal{W}(z)}{=} \sum_{j\geq 1}\frac{\boldsymbol{\kappa_j}\boldsymbol{\kappa_j}^{\mathsf{T}}}{z-p_j} + \mathbf{Hol}_{\boldsymbol{R}_L}(z) \tag{E.46}$$

where square root of energy z-space poles are

$$p_j \triangleq \sqrt{\mathcal{E}_j} \tag{E.47}$$

and the residue widths are connected to the poles as:

$$\boldsymbol{\kappa_j} \triangleq \frac{\boldsymbol{r_j}}{\sqrt{2p_j}} \tag{E.48}$$

This is readily obtained from previous E-space expressions using partial fraction decomposition of simple poles:

$$\frac{\boldsymbol{r_j}\boldsymbol{r_j}^\mathsf{T}}{E-\mathcal{E}_j} = \frac{\frac{\boldsymbol{r_j}\boldsymbol{r_j}^\mathsf{T}}{2\sqrt{\mathcal{E}_j}}}{\sqrt{E}-\sqrt{\mathcal{E}_j}} + \frac{-\frac{\boldsymbol{r_j}\boldsymbol{r_j}^\mathsf{T}}{2\sqrt{\mathcal{E}_j}}}{\sqrt{E}+\sqrt{\mathcal{E}_j}}$$

The poles p_j come in opposite pairs ($p_j^+ = +\sqrt{\mathcal{E}_j}$ and $p_j^- = -\sqrt{\mathcal{E}_j}$), and the corresponding residue widths are thus rotated by $\pm\pi/2$ (multiplication by $\pm\mathrm{i}$): $\boldsymbol{\kappa_j}^- \triangleq \boldsymbol{r_j}/\sqrt{2p_j^-} = -\mathrm{i}\boldsymbol{r_j}/\sqrt{2p_j^+}$. The same $\boldsymbol{r_j}$ is shared by both poles p_j^+ and p_j^-, so that $\boldsymbol{\kappa_j}^-\boldsymbol{\kappa_j}^{-\mathsf{T}} = -\boldsymbol{\kappa_j}^+\boldsymbol{\kappa_j}^{+\mathsf{T}}$.

Alternatively, Mittag Leffler expansion (E.46) can also be directly obtained by solving the radioactive problem in square-root-of-energy z space:

$$\boldsymbol{R}_L^{-1}(z)\Big|_{z=p_j}\boldsymbol{\kappa_j} = \boldsymbol{0} \tag{E.49}$$

where the residue widths vectors $\{\boldsymbol{\kappa_j}\}$ are subject to the following normalization:

$$\boldsymbol{\kappa_j}^\mathsf{T}\left(\frac{\partial \boldsymbol{R}_L^{-1}}{\partial z}\bigg|_{z=p_j}\right)\boldsymbol{\kappa_j} = 1 \tag{E.50}$$

which yields relationship (E.48) (from $z=\sqrt{E}$), and can be calculated directly using

$$\frac{\partial \boldsymbol{R}_L^{-1}}{\partial z}\bigg|_{z=p_j} = \frac{\partial \boldsymbol{R}^{-1}}{\partial z}(p_j) - \frac{\partial \boldsymbol{L}}{\partial z}(p_j) \tag{E.51}$$

where $\boldsymbol{R}$ is invertible at z-space radioactive poles $\{p_j\}$ as

$$\frac{\partial \boldsymbol{R}^{-1}}{\partial z}(z) = -2z\boldsymbol{R}^{-1}\boldsymbol{\gamma}^\mathsf{T}\left(\boldsymbol{e}-z^2\mathbb{I}\right)^{-2}\boldsymbol{\gamma}\boldsymbol{R}^{-1} \tag{E.52}$$

and where the partial derivatives $\frac{\partial \boldsymbol{L}}{\partial z}(p_j)$ can be derived from the Mittag-Leffler expansion of $\boldsymbol{L}(\rho)$ established in theorem 1 of [127]:

$$\frac{\partial \boldsymbol{L}}{\partial z} = \left[\mathrm{i} + \sum_{n\geq 1}\frac{1}{\rho-\omega_n} + \frac{\rho}{(\rho-\omega_n)^2}\right]\frac{\partial \rho}{\partial z} \tag{E.53}$$

where $\{\omega_n\}$ are the roots of the $O_c(\rho)$ outgoing wavefunctions, also roots of $H_{+c}(\rho)$ from (E.12): $\forall n,\ H_{+c}(\omega_n) = 0$. For neutral particles, there are a finite number of such roots, reported in TABLE I of [127].

Equivalently, we can solve for the level matrix $\boldsymbol{A}$ radioactive problem in z-space:

$$\boldsymbol{A}^{-1}(z)\Big|_{z=p_j}\boldsymbol{\alpha_j} = \boldsymbol{0} \tag{E.54}$$

with eigenvectors $\boldsymbol{\alpha_j} \triangleq \frac{\boldsymbol{a_j}}{\sqrt{2p_j}}$ subject to normalization:

$$\boldsymbol{\alpha_j}^{\mathsf{T}} \left(\frac{\partial \boldsymbol{A}^{-1}}{\partial z}\bigg|_{z=p_j} \right) \boldsymbol{\alpha_j} = 1 \tag{E.55}$$

which is readily calculable from

$$\frac{\partial \boldsymbol{A}^{-1}}{\partial z}(p_j) = -2z\mathbb{I} - \boldsymbol{\gamma}\frac{\partial \boldsymbol{L}}{\partial z}(p_j)\boldsymbol{\gamma}^{\mathsf{T}} \tag{E.56}$$

The level-matrix residues widths vectors are then linked to the radioactive widths by the following relation:

$$\boldsymbol{\kappa_j} = \boldsymbol{\gamma}^{\mathsf{T}}\boldsymbol{\alpha_j} \tag{E.57}$$

Regardless of the method deployed to obtain (E.46), the latter entails the following Mittag Leffler expansion for resonance matrix $\boldsymbol{Z}$

$$\boldsymbol{Z}(z) \underset{\mathcal{W}(z)}{=} \sum_{j\geq 1} \frac{\boldsymbol{\zeta_j}\boldsymbol{\zeta_j}^{\mathsf{T}}}{z-p_j} + \mathbf{Hol}_{\boldsymbol{Z}}(z) \tag{E.58}$$

Where the residue widths are connected to the poles as:

$$\begin{aligned} \boldsymbol{\zeta_j} &= \frac{\boldsymbol{\tau_j}}{\sqrt{2p_j}} \\ &= \boldsymbol{H_+}^{-1}(p_j)\,\boldsymbol{\rho}^{1/2}(p_j)\;\;\boldsymbol{\kappa_j} \\ &= \boldsymbol{H_+}^{-1}(p_j)\,\boldsymbol{\rho}^{1/2}(p_j)\;\;\frac{\boldsymbol{r_j}}{\sqrt{2p_j}} \end{aligned} \tag{E.59}$$

This links back to the transmission matrix Mittag Leffler expansion (E.43), which in z-space entails:

$$\boldsymbol{T}(z) \underset{\mathcal{W}(z)}{=} -\mathrm{i}\sum_{j\geq 1} \frac{\boldsymbol{\zeta_j}\boldsymbol{\zeta_j}^{\mathsf{T}}}{z-p_j} + \mathbf{Hol}_{\boldsymbol{T}}(z) \tag{E.60}$$

This transmission matrix Mittag Leffler expansion (E.60) corresponds to the Humblet-Rosenfeld scattering matrix expansion in equation (1.54) section I.1.4, p.538, of [185], where they denote the holomorphic (entire) part $\mathbf{Hol}_{\boldsymbol{T}}(z)$ as $Q_\ell(k)$. As they discuss, the natural variable for this non-resonant part is indeed the wavenumber k_c. Equations (E.60) and (E.59) thus explicitly link the residues of the Humblet-Rosenfeld expansions to the Wigner-Eisenbud R-matrix parameters. Unfortunately, there exists no simple general method to express the expansion coefficients of this entire part directly from R-matrix parameters.

E.3.4 Hwang's conjugate continuation

The Windowed Multipole Representation is essentially an analytic continuation of R-matrix cross sections into the complex plane, in z-space. R-matrix cross sections (E.5)

and (E.10) are the square moduli and real parts of the transmission matrix $T_{cc'}(E)$ and the wavenumber $k_c(E)$, yielding real cross sections. Yet one can analytically continue these cross sections by performing the *conjugate continuation* of all R-matrix operators, which consists of taking the value of the modulus and real parts on the real axis $z \in \mathbb{R}$, and continuing them to the complex plane. This was the key insight introduced by Hwang in [190].

For any meromorphic function $f(z)$, we define its *continued conjugate* $f^*(z)$ as:

$$f^*(z) \triangleq f(z^*)^* \tag{E.61}$$

As such, the continued conjugate real part is defined as

$$\Re_{\text{cont}}\left[f(z)\right] \triangleq \frac{f(z) + f^*(z)}{2} \tag{E.62}$$

and the continued conjugate square modulus as

$$|f|^2_{\text{cont}}(z) \triangleq f(z) \times f^*(z) \tag{E.63}$$

These are meromorphic complex functions: $\Re_{\text{cont}}\left[f(z)\right] \in \mathbb{C}$ and $|f|^2_{\text{cont}}(z) \in \mathbb{C}$. They are the analytic continuation to complex $z \in \mathbb{C}$ of the real part and the square modulus, which they match on the real axis $z \in \mathbb{R}$. Consider a meromorphic function $f(z)$ with simple poles and Mittag-Leffler expansion

$$f(z) \underset{\mathcal{W}(z)}{=} \sum_{j\geq 1} \frac{r_j}{z - p_j} + \sum_{n\geq 0} a_n z^n \tag{E.64}$$

Its continued conjugate square modulus is thus

$$\begin{aligned} |f|^2_{\text{cont}}(z) \underset{\mathcal{W}(z)}{=} & \left(\sum_{j\geq 1} \frac{r_j}{z - p_j} + \sum_{n\geq 0} a_n z^n\right) \\ & \times \left(\sum_{j\geq 1} \frac{r_j^*}{z - p_j^*} + \sum_{n\geq 0} a_n^* z^n\right) \end{aligned} \tag{E.65}$$

The unicity of poles and residues entails all the poles of $|f|^2_{\text{cont}}(z)$ are the poles p_j of $f(z)$ and their complex conjugate p_j^*. By evaluating the corresponding residues, one finds the following Mittag-Leffler expansion for the conjugate continuation:

$$|f|^2_{\text{cont}}(z) \underset{\mathcal{W}(z)}{=} \sum_{j\geq 1} \frac{r_j\ f(p_j^*)^*}{z - p_j} + \frac{r_j^*\ f(p_j^*)}{z - p_j^*} + \sum_{n\geq 0} c_n z^n \tag{E.66}$$

where

$$c_n \triangleq \Re\left[\sum_{k=0}^{n} a_{n-k} a_k^* + 2\sum_{j\geq 1} \frac{r_j\ \left[f(p_j^*)^* - a_n^*\right]}{p_j}\right] \tag{E.67}$$

which can be obtained by developing (E.65) and applying Cauchy's residues theorem

to (E.66) with contour integrations of $\frac{|f|^2(z)}{z^{n+1}}$. In (E.66), one recognizes the remarkable property that the continued square modulus can be expressed as a continued conjugate real part

$$|f|^2_{\text{cont}}(z) \underset{\mathcal{W}(z)}{=} \Re_{\text{cont}}\left[\sum_{j\geq 1}\frac{\widetilde{r}_j}{z-p_j}+\sum_{n\geq 0}c_n z^n\right] \tag{E.68}$$

with

$$\widetilde{r}_j \triangleq 2\ r_j\ f(p_j^*)^* \tag{E.69}$$

Therefore, by using Hwang's conjugate continuation, one can express all R-matrix cross sections as the continued conjugate real part of conjugate continued R-matrix operators: this is the key to converting R-matrix cross sections to Windowed Multipole Representation.

E.3.5 Windowed Multipole Representation

The Windowed Multipole Representation is the analytic continuation of the pole expansion of R-matrix cross sections. For open channels (energies above thresholds $E > E_{T_c}$), the energy dependence of R-matrix cross sections – described by equations (E.5) and (E.10) – is expanded along the real energy axis $E \in R$, and the corresponding expressions are analytically continued to all complex energies $E \in C$. The Windowed Multipole Representation can thus be seen as a generalization of R-matrix cross sections to the complex plane, for open channels, as shown in figure E-1. As such, windowed multipole cross sections only match R-matrix cross sections for real energies above the channel threshold: $E > E_{T_c}$.

Windowed Pole Representation: Transmission matrix approach

The most straightforward approach is to consider the transmission matrix $\boldsymbol{T}(E)$ Mittag-Leffler expansion (E.43), and apply Hwang's conjugate continuation in energy space, which yields:

$$|\boldsymbol{T}|^2_{\text{cont}}(E) \underset{\mathcal{W}(E)}{=} \Re_{\text{cont}}\left[\sum_{j\geq 1}\frac{-\mathrm{i}\widetilde{\boldsymbol{\tau}}_{\boldsymbol{j}}}{E-\mathcal{E}_j}+\mathbf{Hol}_{|\boldsymbol{T}|^2}(E)\right] \tag{E.70}$$

where we use the Hadamard product " $\circ$ " to express the residues as:

$$\widetilde{\boldsymbol{\tau}}_{\boldsymbol{j}} \triangleq 2\ \boldsymbol{\tau}_{\boldsymbol{j}}\boldsymbol{\tau}_{\boldsymbol{j}}{}^{\mathsf{T}} \circ \boldsymbol{T}\left(\mathcal{E}_j^*\right)^* \tag{E.71}$$

Thus, for real energies with open channels, the partial and total cross sections can be expressed respectively as

$$\sigma_{cc'}(E) \underset{\mathcal{W}(E)}{=} \frac{4\pi g_{J_c^\pi}}{|k_c(E)|^2}\Re_{\text{cont}}\left[\sum_{j\geq 1}\frac{-\mathrm{i}\,[\widetilde{\boldsymbol{\tau}}_{\boldsymbol{j}}]_{cc'}}{E-\mathcal{E}_j}+\mathbf{Hol}_{|\boldsymbol{T}|^2}(E)\right] \tag{E.72}$$

and

$$\sigma_c(E) \underset{\mathcal{W}(E)}{=} \frac{4\pi g_{J_c^\pi}}{|k_c(E)|^2} \Re_{\text{cont}} \left[\sum_{j \geq 1} \frac{-\mathrm{i} \left[\boldsymbol{\tau_j} \boldsymbol{\tau_j}^{\mathsf{T}} \right]_{cc}}{E - \mathcal{E}_j} + \mathbf{Hol}_{\boldsymbol{T}}(E) \right] \tag{E.73}$$

Expressions (E.72) and (E.73) are general, they apply to any cross section described by R-matrix theory (be it massless photons or massive charged or neutral particle channels). They are local expressions, only valid on the neighborhood $\mathcal{W}(E)$ of any given energy E away from the thresholds (branch points E_{T_c} of (E.4) mapping), though this neighborhood can be as large as the distance between thresholds (for more discussion on this point, we refer to the penultimate paragraph of section II.D in [125]). They reflect the fact that two physical phenomena dictate the behavior of R-matrix cross sections: resonances and thresholds.

Away from threshold energies E_{T_c} – the branch-points of wavenumber-energy mapping (E.4) – each resonance can be accurately represented by a Single-Level Breit-Wigner (SLBW) profile in energy space E, that is the combination of symmetric and anti-symmetric Lorenztian functions. These are made evident by recalling definition (E.40), which splits the radioactive poles into real and imaginary components $\mathcal{E}_j \triangleq E_j - \mathrm{i}\frac{\Gamma_j}{2}$, and noticing that each resonance of the Windowed Multipole Representation (E.72) can be expressed as:

$$\Re \left[\frac{a + \mathrm{i}b}{E - \mathcal{E}_j} \right] = a \frac{(E - E_j)}{(E - E_j)^2 + \frac{\Gamma_j^2}{4}} + b \frac{\frac{\Gamma_j}{2}}{(E - E_j)^2 + \frac{\Gamma_j^2}{4}} \tag{E.74}$$

The sum of resonances is complemented by the holomorphic background term $\mathbf{Hol}_{\boldsymbol{T}}$, and modulated by the $\frac{1}{|k_c(E)|^2}$ term. This illustrates the fact that the wavenumber k_c dominates the behavior of R-matrix cross sections near thresholds E_{T_c}, where $k_c \to 0$. Moreover, the holomorphic (entire) part is itself more naturally described as a function of the wavenumber k_c rather then the energy: $\mathbf{Hol}_{\boldsymbol{T}}(\boldsymbol{k})$, as explained by Humblet and Rosenfeld through equations (1.64) and (1.67) section I.1.4, p.539-540, of [185]. The threshold behavior of R-matrix cross sections was detailed by Wigner in [322]. Depending on the angular momenta ℓ and ℓ' and the charges of the particles, reaction and scattering cross sections either: a) have threshold behaviors in powers of $k_c^{N(\ell,\ell')}$, where $N(\ell, \ell') \in \mathbb{Z}$ is some integer depending on the different angular momenta, but never smaller than negative two ($N(\ell, \ell') \geq -2$); or b) in some cases of Coulomb repulsion, modulate this with an exponential decay $\propto \exp(-a/k_c)$ with some real positive $a > 0$ (see section III of [322] for more details). This means we can represent in all generality the threshold behavior as a Laurent expansion around the threshold: $\sigma_{cc'} \underset{k_c \to 0}{\sim} \sum_{n \geq -2} a_n k_c^n$.

By thus expressing the threshold behavior explicitly, we can constitute the *Windowed Multipole Representation* of R-matrix cross sections:

$$\sigma_{cc'}(E) \underset{\mathcal{W}(E)}{\triangleq} \sum_{n \geq -2} \widetilde{a}_n^{cc'} k_c^n(E) + \frac{1}{E} \Re_{\text{cont}} \left[\sum_{j \geq 1} \frac{\widetilde{R}_j^{cc'}}{E - \mathcal{E}_j} \right] \tag{E.75}$$

and

$$\sigma_c(E) \underset{\mathcal{W}(E)}{\triangleq} \sum_{n\geq -2} a_n^c k_c^n(E) + \frac{1}{E}\Re_{\text{cont}}\left[\sum_{j\geq 1}\frac{R_j^c}{E-\mathcal{E}_j}\right] \tag{E.76}$$

where the residues are obtained by evaluating at the pole values as:

$$\widetilde{R}_j^{cc'} \triangleq -\mathrm{i}\frac{4\pi g_{J_c^\pi}\mathcal{E}_j}{|k_c(\mathcal{E}_j)|^2}\left[\widetilde{\boldsymbol{\tau}}_{\boldsymbol{j}}\right]_{cc'} \tag{E.77}$$

and

$$R_j^c \triangleq -\mathrm{i}\frac{4\pi g_{J_c^\pi}\mathcal{E}_j}{|k_c(\mathcal{E}_j)|^2}\left[\boldsymbol{\tau}_{\boldsymbol{j}}\boldsymbol{\tau}_{\boldsymbol{j}}{}^{\mathsf{T}}\right]_{cc} \tag{E.78}$$

Equivalently, the Windowed Multipoles Representation can be carried out in square root of energy z-space, in what constitutes theorem 15.

Theorem 15. *Windowed Multipole Formalism*
Let $\mathcal{E}_j$ be the energy-space poles of the Kapur-Peierls operator $\boldsymbol{R}_L$, defined in (E.15), and let $z \triangleq \sqrt{E}$ be the square root of energy. The energy dependence of R-matrix cross sections can be exactly expressed as a Laurent expansion in wavenumber k_c, of order no less than k_c^{-2}, plus the conjugate continuation real part (E.62) of a sum of energy-space resonances with poles $\mathcal{E}_j$, which in z-space yield pairs of opposite poles $p_j = \pm\sqrt{\mathcal{E}_j}$, so that partial cross sections (E.5) take the Windowed Multipole Representation:

$$\sigma_{cc'}(z) \underset{\mathcal{W}(z)}{\triangleq} \sum_{n\geq -2} \widetilde{a}_n^{cc'} k_c^n(z) + \frac{1}{z^2}\Re_{\text{cont}}\left[\sum_{j\geq 1}\frac{\widetilde{r}_j^{cc'}}{z-p_j}\right] \tag{E.79}$$

and the total cross section (E.10) takes the form:

$$\sigma_c(z) \underset{\mathcal{W}(z)}{\triangleq} \sum_{n\geq -2} a_n^c k_c^n(z) + \frac{1}{z^2}\Re_{\text{cont}}\left[\sum_{j\geq 1}\frac{r_j^c}{z-p_j}\right] \tag{E.80}$$

where the partial residues can be constructed from R-matrix parameters as:

$$\widetilde{r}_j^{cc'} \triangleq -\mathrm{i}\frac{4\pi g_{J_c^\pi} p_j^2}{|k_c(p_j)|^2}\left[2\ \boldsymbol{\zeta}_j\boldsymbol{\zeta}_j{}^{\mathsf{T}} \circ \boldsymbol{T}\left(p_j^*\right)^*\right]_{cc'} \tag{E.81}$$

and the total residues as

$$r_j^c \triangleq -\mathrm{i}\frac{4\pi g_{J_c^\pi} p_j^2}{|k_c(p_j)|^2}\left[\boldsymbol{\zeta}_j\boldsymbol{\zeta}_j{}^{\mathsf{T}}\right]_{cc} \tag{E.82}$$

where the $\boldsymbol{\zeta}_j$ residue widths vectors are linked to the Kapur-Peierls operator $\boldsymbol{R}_L$ poles and residues through relations (E.59).

Alternatively, the residues can be numerically obtained through Cauchy's residues theorem contour integrals

$$\widetilde{r}_j^{cc'} = \frac{1}{\mathrm{i}\pi}\oint_{\mathfrak{C}_{p_j}} z^2\sigma_{cc'}(z)\mathrm{d}z \tag{E.83}$$

where $\mathfrak{C}_{p_j}$ designates a positively oriented simple closed contour containing only pole p_j. For instance, if $\mathfrak{C}_{p_j}$ is a circle of small radius $\epsilon > 0$ around pole p_j, this yields

$$r_j^c = \frac{\epsilon}{\pi} \int_{\theta=0}^{2\pi} \left(p_j + \epsilon \mathrm{e}^{\mathrm{i}\theta}\right)^2 \sigma_c \left(p_j + \epsilon \mathrm{e}^{\mathrm{i}\theta}\right) \mathrm{e}^{\mathrm{i}\theta} \mathrm{d}\theta \tag{E.84}$$

In order to perform these contour integrals, R-matrix cross sections (E.5) and (E.10) must have been meromorphically continued to complex energies by means of conjugate continuations (E.63) and (E.62) respectively.

Therefore, by solving the radioactive problem (E.32) – or level-matrix one (E.36) – to find the poles $\mathcal{E}_j$ and residues $\boldsymbol{r_j}$ of the Kapur-Peierls operator (respectively p_j and $\boldsymbol{\kappa_j}$ from (E.50) or level-matrix equivalent (E.54) in z-space), we can compute the transmission matrix residues $\boldsymbol{\tau_j}$ from (E.44) and the conjugate continuation ones $\widetilde{\boldsymbol{\tau}}_{\boldsymbol{j}}$ from (E.71) (respectively $\boldsymbol{\zeta_j}$ from (E.59) in z-space), to find the poles and residues of the Windowed Multipole Representation of R-matrix cross sections, through equations (E.75), (E.76), (E.77), and (E.78); or respectively equations (E.79), (E.80), (E.81), and (E.82) for z-space.

Windowed Pole Representation: potential and resonance matrices approach

The transmission matrix approach is exact, but it has three drawbacks: 1) it is not simple to interpret physically; 2) it does not give us information on the "background" behavior (non-resonant Laurent expansion $\sum_{n\geq -2} a_n k_c^n$); 3) it can be numerically unstable. Decomposition (E.23) of the transmission matrix helps us separate the cross sections into parts we can interpret physically: the potential cross section σ_c^{pot} has no resonances (E.26); the reaction cross section $\sigma_{cc'}^{\mathrm{react}}$ has all the resonances (E.30); and both the partial cross section $\sigma_{cc'}$ from (E.31) and the total cross section σ_c from (E.86) also have interference resonances from the real part of the resonance matrix $\boldsymbol{Z}$. This means all the resonances of R-matrix cross sections can be recovered from the resonance matrix $\boldsymbol{Z}$ Mittag Leffler expansion (E.58). Applying Hwang's conjugate continuation method to construct the Windowed Multipole Representation then yields:

- Potential scattering cross section (of channel c):

$$\sigma_c^{\mathrm{pot}}(E) \underset{\mathcal{W}(z)}{=} 4\pi g_{J_c^\pi} \frac{\Re\left[\mathrm{i}D_c\right]}{\left|k_c\right|^2} \tag{E.85}$$

- Total cross section (of channel c):

$$\sigma_c(z) \underset{\mathcal{W}(z)}{\triangleq} \sigma_c^{\mathrm{pot}}(z) + \frac{1}{z^2} \Re_{\mathrm{cont}} \left[\sum_{j\geq 1} \frac{r_j^c}{z - p_j}\right] + \sum_{n\geq -2} b_n^c k_c^n(z) \tag{E.86}$$

  where the total residues r_j^c are defined in (E.82).

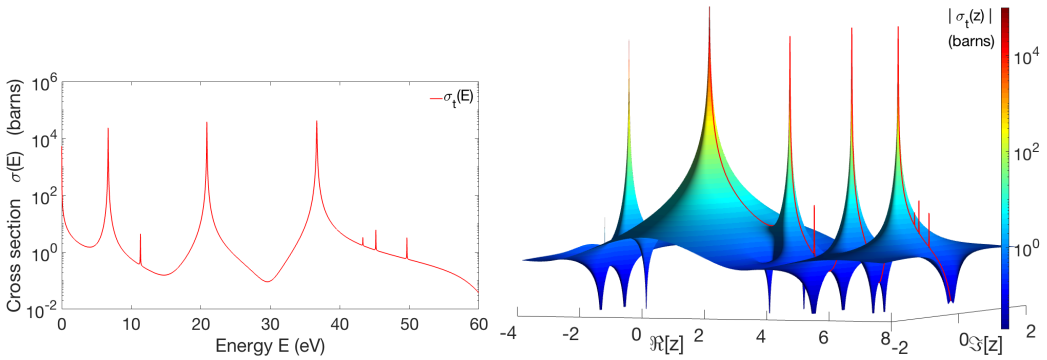

(a) ^{238}U first resonances (3 s-waves and 4 p-waves).

(b) ^{238}U windowed multipole cross section surface.

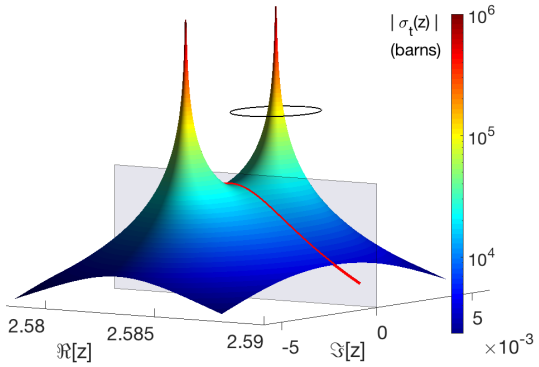

(c) ^{238}U first s-wave resonance peak.

Figure E-1: Windowed multipole representation of R-matrix cross sections: ^{238}U total cross section (minus potential scattering) meromorphic continuation into the complex z-plane, for $z = \pm\sqrt{E}$ in $(\sqrt{\text{eV}})$. This surface's crest and thalweg line along the real axis is the R-matrix cross section above the zero threshold. FIG. E-1(b) shows the resonance peaks are the saddle points between the complex conjugate poles. Negative z in FIG.E-1(b) are on the shadow branch $\{E, -\}$ of mapping (E.2). The black circle in FIG.E-1(c) represents the contour integrals around the poles of the complex cross section which enable both conversion to windowed multipole covariances (theorem 16) and analytic Doppler broadening (theorem 17).

- Self-scattering cross section (of channel c):

$$\sigma_c^{\text{scat}}(E) \underset{\mathcal{W}(z)}{=} \frac{1}{z^2}\Re_{\text{cont}}\left[\sum_{j\geq 1}\frac{{}^{\text{scat}}r_j^c}{z-p_j}\right] + \sum_{n\geq -2} c_n^c k_c^n(z)\delta_{cc'} \tag{E.87}$$

with scattering residues:

$${}^{\text{scat}}r_j^c \triangleq -\frac{4\pi g_{J_c^\pi} p_j^2}{|k_c(p_j)|^2}\left[2\ \boldsymbol{\zeta_j}\boldsymbol{\zeta_j}^{\mathsf{T}} \circ \boldsymbol{D}\left(p_j^*\right)^*\right]_{cc'}\delta_{cc'} \tag{E.88}$$

- Interference cross section (of channel c):

$$\sigma_c^{\text{int}}(E) \underset{\mathcal{W}(z)}{=} \frac{1}{z^2}\Re_{\text{cont}}\left[\sum_{j\geq 1}\frac{{}^{\text{int}}r_j^c}{z-p_j}\right] + \sum_{n\geq -2} d_n^c k_c^n(z)\delta_{cc'} \tag{E.89}$$

with interference residues:

$${}^{\text{int}}r_j^c \triangleq -\mathrm{i}\frac{4\pi g_{J_c^\pi} p_j^2}{|k_c(p_j)|^2}\left[\boldsymbol{\zeta_j}\boldsymbol{\zeta_j}^\mathsf{T} \circ \boldsymbol{Y}\left(p_j^*\right)^*\right]_{cc'}\delta_{cc'} \tag{E.90}$$

- Reaction cross section (from channel c to c'):

$$\sigma_{cc'}^{\text{react}}(z) \underset{\mathcal{W}(z)}{=} \frac{1}{z^2}\Re_{\text{cont}}\left[\sum_{j\geq 1}\frac{{}^{\text{react}}r_j^{cc'}}{z-p_j}\right] + \sum_{n\geq -2} \widetilde{b}_n^{cc'} k_c^n(z) \tag{E.91}$$

with reaction residues:

$${}^{\text{react}}r_j^{cc'} \triangleq \frac{4\pi g_{J_c^\pi} p_j^2}{|k_c(p_j)|^2}\left[2\ \boldsymbol{\zeta_j}\boldsymbol{\zeta_j}^\mathsf{T} \circ \boldsymbol{Z}\left(p_j^*\right)^*\right]_{cc'} \tag{E.92}$$

- Partial (angle-integrated) cross section (E.31) (from channel c to c'):

$$\begin{aligned}\sigma_{cc'}(E) &= \Big(\sigma_c^{\text{pot}}(E) + \sigma_c^{\text{scat}}(E)\Big)\delta_{cc'} + \sigma_{cc'}^{\text{react}}(E)\\ &= \Big(\sigma_c^{\text{tot}}(E) - \sigma_c^{\text{int}}(E)\Big)\delta_{cc'} + \sigma_{cc'}^{\text{react}}(E)\end{aligned}$$

Noticing that $-\mathrm{i}\boldsymbol{T}^* = \boldsymbol{Z}^* - \boldsymbol{D}^*$, this entails the partial residues $\widetilde{r}_j^{cc'}$ from (E.81) are connected to the total residues r_j^c from (E.82), the reaction residues ${}^{\text{react}}r_j^{cc'}$ from (E.92), the scattering residues ${}^{\text{scat}}r_j^c$ from (E.88), and the interference residues ${}^{\text{int}}r_j^c$ from (E.90), according to:

$$\begin{aligned}\widetilde{r}_j^{cc'} &= {}^{\text{react}}r_j^{cc'} + {}^{\text{scat}}\, r_j^c\\ &= {}^{\text{react}}r_j^{cc'} + r_j^c - {}^{\text{int}}\, r_j^c\end{aligned} \tag{E.93}$$

Total cross section decomposition (E.86) is simpler to interpret physically than expression (E.82) directly derived from the transmission matrix, because the potential cross section σ_c^{pot} is extracted from the background Laurent expansion: $\sum_{n\geq -2} a_n^c z^n$. The same holds for the partial cross section (E.79), where the residues decomposition (E.93) untangles the direct expression (E.81) from the transmission matrix approach. Though mathematically equivalent, some of these approaches may be more numerically stable than others.

Importantly, we do not need the poles of the potential matrix $\boldsymbol{D}$ to express the partial and total cross sections. This is because any such poles (the zeros of $\boldsymbol{H}_+$) cancel out of the scattering matrix (E.14), and therefore of the cross sections. Before

we proved this result in theorem 3 of [125], Hwang had to explicitly decompose the potential cross section σ_c^{pot} into poles and residues in eq. (1) and (2) of [188] (also in eq. (3) and (4) of [189]), with severe numerical instability implications which he attempted to remedy by introducing pseudo-poles in [187]. We now known that under proper analytic continuation, these spurious poles have zero residues in the transmission matrix, and thus cancel out of the partial and total cross sections.

Pole expansion: R-matrix construct or rational fit

So far, we have constructed the transmission matrix Mittag-Leffler expansion (E.60) by first solving the radioactive states problem (E.49) and then obtaining the transmission matrix residues from those of the Kapur-Peierls operator, through (E.59). One could dispense of the intermediary steps and find the radioactive poles $\{p_j\}$ directly through the transmission matrix by solving the generalized eigenvalue problem

$$\boldsymbol{T}^{-1}(z)\Big|_{z=p_j} \boldsymbol{\zeta_j} = \boldsymbol{0} \tag{E.94}$$

and subjecting the residue widths vectors $\{\boldsymbol{\zeta_j}\}$ to the following normalization:

$$\boldsymbol{\zeta_j}^{\mathsf{T}} \left(\frac{\partial \boldsymbol{T}^{-1}}{\partial z}\bigg|_{z=p_j} \right) \boldsymbol{\zeta_j} = \mathrm{i} \tag{E.95}$$

Though mathematically equivalent, this all-in-one approach can nonetheless be prone to numerical instabilities. Which leads us to the question of how to numerically solve the generalized eigenproblems - either the radioactive ones (E.49) or directly (E.94). On this issue, we direct the reader to the section of theorem 1 in [125] for a more detailed discussion, in particular on the multi-sheeted nature of the Riemann mapping (E.4), which can complicate the search for solutions. We will here simply state that these are nonlinear eigenvalue problems, and general algorithms to solve them can be found in the Handbook of Linear Algebra [319], chapter 115. One such algorithm is the Rayleigh-quotient method, used by Brune to find alternative parameters in [92]. Alternatively, it is sometimes more computationally advantageous to first find the radioactive poles $\{p_j\}$ directly by solving the channel determinant problem, $\det\left(\boldsymbol{R}_L^{-1}(z)\Big|_{z=p_j} \right) = 0$, or the corresponding level determinant one, $\det\left(\boldsymbol{A}^{-1}(z)\Big|_{z=p_j} \right) = 0$, and to second solve the associated eigenvalue problem (which is now linear), or even to directly evaluate the residues at the found poles by contour integrals (E.83) and (E.84). Such methods tailored to find all the roots of the radioactive problem where introduced in [131], in section 5 of [299], or in equations (200) and (204) of [149]. Also, solving the Kapur Peierls radioactive problem (E.49) will be advantageous over solving the level matrix one (E.54) when the number of levels N_λ far exceeds the number of channels N_c, and conversely.

Rather than starting from the Wigner-Eisenbud R-matrix resonance parameters $\left\{E_{T_c}, a_c, B_c, E_\lambda, \gamma_{\lambda,c}\right\}$ to construct the Windowed Multipole Representation poles p_j

and residues $\widetilde{r}_j^{cc'}$ and r_j^c as (E.81) and (E.82), an alternative approach is to simply curve-fit the point-wise energy-dependence of nuclear cross sections $\sigma_{cc}(E)$ with the corresponding Windowed Multipole Representation forms (E.79) and (E.80). For instance, this approach was successfully deployed in [222] and in [262], where using the "black-box" rational function approximating algorithm called "vector-fitting" [161, 160] led to finding the exact resonant radioactive poles $\{p_j\}$ of ^{16}O, for which no resonance parameters were published [262]. This conversion of point-wise R-matrix cross sections into windowed multipoles representation approach was generalized to most of the nuclides found in the ENDF/B-VII.1 nuclear data library [225, 223], and could potentially be facilitated by recent advances in rational approximation algorithms – such as RKFIT [73] or AAA [246].

Windowing process: Laurent background fit

Regardless of the method deployed to find the poles $\left\{p_j\right\}$ and their corresponding residues, there exists no general way to construct the thresholds Laurent expansions, $\sum_{n\geq -2} a_n k_c(z)^n$, from the R-matrix parameters. One must thus select an energy window $\mathcal{W}(E)$ and curve fit the background Laurent expansion $\sum_{n\geq -2} a_n k_c(z)^n$ by subtracting the resonances, that is the poles contribution $\sum_{j\in\mathcal{W}(E)} \frac{r_j^c}{z-p_j}$. Nonetheless, there is a difficulty as to which such poles one should include explicitly into the window. It is not necessary to explicitly call all the poles $\left\{p_j\right\}$ for each window $\mathcal{W}(E)$, rather the contribution of far-away poles is best curve-fitted and included in the Laurent expansion $\sum_{n\geq -2} a_n k_c(z)^n$. The criterion used to decide which poles $\{p_j\}$ to include within each window is to select an accuracy bound for the Doppler broadened cross section, and include in window $\mathcal{W}(E)$ all the poles whose Doppler broadened resonances have a significant impact on the cross section within that window. Thus, the greater the maximum temperature, the more far-away poles have to be included to compute the cross section within window $\mathcal{W}(E)$. Once the contributing poles (after Doppler broadening) have been found, we subtract them from the zero-kelvin cross sections and curve-fit the difference with a Laurent-expansion $\sum_{n\geq -2} a_n k_c(z)^n$. More detailed explanations on this windowing process can be found in [146, 199, 197].

Though the background Laurent expansion must be numerically fitted, and that the resonant poles themselves may be accurately found using rational approximation "black-box" algorithms, it is critical to understand that the Windowed Multipole Representation (E.79) and (E.80) is not a curve-fitting approximation: this is a rigorous representation, mathematically and physically equivalent to the exact R-matrix theory cross sections (for real energies in open channels), or the Humblet-Rosenfeld pole expansions in wavenumber space. This can be tested by curve-fitting in E and k_c space, both the resonances and the background Laurent expansions. One will notice that the E-space Breit-Wigner profiles (E.74) capture exactly one-for-one the resonance behavior. However, the threshold behaviors are not well represented by the E variable: while few coefficients suffice to reach high accuracy using Laurent expansions in k_c (usually no more than a_{-2}, a_{-1}, a_0, and a_1), many more expansion coefficients are necessary when fitting the background with Laurent expansions with powers of E.

Finally, remember that for non-massless particles, wavenumber-energy mapping (E.2) entails that: $k_c^2 \propto z^2 - E_{T_c}$. Thus, for zero-threshold reactions ($E_{T_c} = 0$), we have a direct proportionality $k_c \propto z$. In order to achieve closed-form Doppler-broadening expressions, we may be willing to sacrifice the physically accurate Laurent expansion in k_c, and replace it with an approximation in powers of z – that is a Laurent expansion $\sum_{n\geq -2} a_n z^n$ – plus rational Padé-type approximations with simple poles – that is adding non-physical pseudo-poles – so as to approximate the exact threshold behavior $\sum_{n\geq -2} a_n k_c(z)^n$ with powers of z and pseudo-poles $\sum_{n\geq -2} \widetilde{a}_n z^n + \sum_{n\geq 1} \frac{\widetilde{r}_n}{z-\widetilde{p}_n}$. Runge's theorem guarantees such approximation can always be performed to high-accuracy, though this is often costly, as many more pseudo-poles and Laurent expansion coefficients have to be introduced. Nonetheless, this approximation will have advantages when Doppler-broadening massive (not massless photons) particles (both charged and neutral), and it also provides a unified Windowed Multipole formalism:

$$\sigma(z) \underset{\mathcal{W}(E)}{=} \sum_{n\geq -2} a_n z^n + \frac{1}{z^2} \Re_{\text{cont}} \left[\sum_{j\geq 1} \frac{r_j}{z - p_j} \right] \tag{E.96}$$

In addition to the residues (E.83) and (E.84) of theorem 15, one can now also obtain the Laurent expansion coefficients by means of contour integrals:

$$\begin{aligned} a_{-2} &= \Re_{\text{cont}} \left[\sum_{j\geq 1} \frac{r_j}{p_j} \right] + \frac{1}{2\mathrm{i}\pi} \oint_{\mathfrak{C}_0} z\ \sigma(z) \mathrm{d}z \\ a_{-1} &= \Re_{\text{cont}} \left[\sum_{j\geq 1} \frac{r_j}{p_j^2} \right] + \frac{1}{2\mathrm{i}\pi} \oint_{\mathfrak{C}_0} \sigma(z) \mathrm{d}z \\ a_n &\underset{n\geq 0}{=} \frac{1}{2\mathrm{i}\pi} \oint_{\mathfrak{C}_0} \frac{\sigma(z)}{z^{n+1}} \mathrm{d}z = \frac{1}{2\pi\epsilon^n} \int_{\theta=0}^{2\pi} \sigma\left(\epsilon \mathrm{e}^{\mathrm{i}\theta}\right) \mathrm{e}^{-\mathrm{i}n\theta} \mathrm{d}\theta \end{aligned} \tag{E.97}$$

where $\mathfrak{C}_0$ designates a positively oriented simple closed contour containing only pole 0, for instance a circle centered at zero with small radius $\epsilon > 0$. Relations (E.97) are obtained by performing partial fraction decomposition:

$$\frac{1}{z^2} \frac{r_j/2}{z - p_j} = \frac{r_j/2}{p_j^2} \left[\frac{1}{z - p_j} - \frac{1}{z} - \frac{p_j}{z^2} \right]$$

Therefore, converting R-matrix cross sections to the unified Windowed Multipole Representation formalism (E.96) is conceptually simple: it suffices to solve for the z-space poles $\{p_j\}$ of the $\boldsymbol{A}$ level matrix (E.18) – that is radioactive problem (E.54) – and then perform contour integrals (E.84), (E.83) and (E.97) on the continued conjugate (E.61) R-matrix cross sections (E.10) and (E.5) to find their residues and Laurent expansion coefficients.

Henceforth, we will only treat this unified Windowed Multipole Representation formalism (E.96): it is physically exact for any R-matrix cross section of zero-threshold, and an approximation of the exact Windowed Multipole representations (E.79) and (E.80) only in windows that include non-zero thresholds.

E.3.6 Hwang's special case: zero-threshold neutron cross sections

There is one special case where it is possible to fully and explicitly convert R-matrix parameters into their exact windowed multipole representation (E.96), without any need of curve-fitting or truncating the Laurent expansion: this is the case of neutron cross sections with no thresholds, which Hwang first investigated in [190]. In this case, because all channels have zero energy threshold ($E_{T_c} = 0$), every channel's wavenumber is proportional to the square root of energy, $k_c \propto z$, we can therefore write the dimensionless wavenumber as:

$$\begin{aligned} \rho_c &= \rho_{0c}\, z \\ \rho_{0c} &\triangleq a_c \sqrt{\frac{2 m_{c,1} m_{c,2}}{(m_{c,1} + m_{c,2})\,\hbar^2}} \end{aligned} \tag{E.98}$$

Moreover, there are no branch-points to mapping (E.2) other than zero, so that the Windowed Multipole Representation (E.96) is exact and valid everywhere for positive energies $E > 0$: the Laurent development $\sum_{n \geq -2} a_n z^n$ at zero accurately describes the threshold behavior (as there is no exponential dampening from charges). Because there are no charges, the dimensionless Coulomb field parameter (E.9) is null, $\eta_c = 0$, so that the difference $\omega_c \triangleq \sigma_{\ell_c}(\eta_c) - \sigma_0(\eta_c)$ in Coulomb phase shift (E.8) is such that we always have $\mathrm{e}^{\mathrm{i}\omega_c} = 1$. From this, definitions (E.12) entail that the incoming and outgoing wavefunctions are then simply the H_- and H_+ combination of regular and irregular Bessel functions:

$$\begin{aligned} O(\rho) = H_+(\rho) &= G(\rho) + \mathrm{i}F(\rho) = \rho\,(-y_\ell(\rho) + \mathrm{i}j_\ell(\rho)) \\ I(\rho) = H_-(\rho) &= G(\rho) - \mathrm{i}F(\rho) = \rho\,(-y_\ell(\rho) - \mathrm{i}j_\ell(\rho)) \end{aligned} \tag{E.99}$$

where $j_\ell(\rho)$ is the spherical Bessel function of the first kind, and $y_\ell(\rho)$ is the spherical Bessel function of the second kind, respectively defined in chapter 10, eq.(10.47.3) and eq.(10.47.4) of [250], or in chapter 10, eq.(10.1.1) of Abramowitz & Stegun [51]. This in turn entails the remarkable property that the reduced logarithmic derivative (E.17) of the outgoing-wave function $L(\rho)$ is now a rational function (that is the ratio of polynomials) in ρ, whose expressions, along with those of $O(\rho)$, are reported in TABLE I of [127], and we refer to section II.B of [127] for a more detailed description of these functions.

Solving the radioactive states problem: polynomial rootfinding

Crucially, in this special case of only neutron channels without threshold, the fact that $L(\rho)$ is now a rational function in z entails that (E.15), the Kapur-Peierls operator $\boldsymbol{R}_L$, is also a rational function in z-space. Therefore, the radioactive problem (E.49) itself becomes that of finding the roots of a rational function. We solve the radioactive problem through the level matrix approach (E.54), where the residue width vectors are normalized as (E.55), which we can calculate through (E.56) where the partial

derivative (E.53) is now simply $\frac{\partial \rho}{\partial z} = \rho_{0c}$ from (E.98). The key is now to find the radioactive poles $\left\{p_j\right\}$ in z-space. We can do so by solving for the roots of the inverse level matrix (E.18) determinant: $\det\left(\boldsymbol{A}^{-1}(z)\Big|_{z=p_j}\right) = 0$. Since this determinant is a rational function in z, one can find all its zeros by expressing it in irreducible form, and solve for all the roots of the numerator polynomial. This can be accomplished by developing the determinant and applying lemma 3 of [127] on *diagonal divisibility and capped multiplicities*, in an analogous fashion as in the proof of theorem 3 in [127], to which we point for more detailed explanations. More precisely, one can see in TABLE I of [127] that $L_\ell(\rho) = \frac{u_{\ell+1}(\rho)}{q_\ell(\rho)}$ is a proper rational function with simple poles, with a denominator $q_\ell(\rho)$ of degree ℓ and a numerator $u_{\ell+1}(\rho)$ of degree $\ell+1$. The polynomial factor $Q(z)$ that makes the denominator of the $\det\left(\boldsymbol{A}^{-1}\right)(z)$ rational function irreducible can then be found by applying lemma 3 of [127] on diagonal divisibility and capped multiplicities, yielding

$$Q(z) \triangleq \prod_{c=1}^{N_c} q_{\ell_c}(z) \tag{E.100}$$

so that for only neutron channels without thresholds, finding all the radioactive poles $\left\{p_j\right\}$ is akin to solving for all the roots of the following polynomial:

$$Q(z)\ \det\left(\boldsymbol{e} - z^2\mathbb{I} - \boldsymbol{\gamma}\left(\boldsymbol{L}(z) - \boldsymbol{B}\right)\boldsymbol{\gamma}^{\mathsf{T}}\right)\Big|_{z=p_j} = 0 \tag{E.101}$$

The degree of this polynomial, and thus the number of (complex) roots $\left\{p_j\right\}$, is:

$$N_L = 2N_\lambda + \sum_{c=1}^{N_c} \ell_c \tag{E.102}$$

which is a particular case of the general number of radioactive poles N_L we stated in (E.42) (and proved in theorem 1 of [125]), but with only one threshold, $E_{T_c} = 0$, so that the number of different thresholds is one: $N_{E_{T_c} \neq E_{T_{c'}}} = 1$.

In the simple case of Multi-Level Breit-Wigner approximation (E.22), the diagonal level matrix $\boldsymbol{A^{-1}}_{\text{MLBW}}$ greatly simplifies the radioactive states eigenproblem (E.54): it is now diagonal and the poles $\{p_j\}$ are the roots of:

$$E_\lambda - p_j^2 - \sum_{c=1}^{N_c} \gamma_{\lambda,c}^2 \left(L_c(p_j) - B_c\right) = 0 \tag{E.103}$$

We then have $\left[\boldsymbol{\kappa_j}\boldsymbol{\kappa_j}^{\mathsf{T}}\right]_{\text{MLBW}} = \boldsymbol{\gamma}^{\mathsf{T}}\left[\boldsymbol{\alpha_j}\boldsymbol{\alpha_j}^{\mathsf{T}}\right]_{\text{MLBW}}\boldsymbol{\gamma}$ where normalization (E.55) entails

$$\left[\boldsymbol{\alpha_j}\boldsymbol{\alpha_j}^{\mathsf{T}}\right]_{\text{MLBW}} = \mathbf{diag}_{N_\lambda}\left(\frac{-1}{2p_j + \sum_{c=1}^{N_c}\gamma_{\lambda,c}^2 \frac{\partial L_c}{\partial z}(p_j)}\right) \tag{E.104}$$

This approach will yield the same results as those in [193].

Interestingly, besides adding the spurious poles $\left\{\omega_n\right\}$ of the potential cross section $\sigma_c^{\rm pot}$ (eq. (1) and (2) of [188] or eq. (3) and (4) of [189]), Hwang also accounted for too many $\left\{p_j\right\}$ poles, in eq. (35a) section III.A, p.197 of [190]. This is for two fundamental reasons: 1) lemma 3 of [127] on diagonal divisibility and capped multiplicities means Hwang's $q_\ell(\sqrt{E})$ functions can be taken out of his product in equation (36) of [190]; 2) these same $q_\ell(\sqrt{E})$ functions are not the same as our $q_\ell(\rho)$ functions, which are the denominator of $L_\ell(\rho)$. Instead, Hwang's $q_\ell(\sqrt{E})$ functions are the denominator of the penetration $P_\ell(\rho)$ and shift $S_\ell(\rho)$ functions – defined as $L_\ell(\rho) = S_\ell(\rho) + \mathrm{i}P_\ell(\rho)$ in (29) of [127] where a thorough and in-depth study of these functions is undertaken – and these denominators are different from the denominator of $L_\ell(\rho)$, as we show in table III of [127]. In essence, this is because by writing $L_\ell(\rho) = S_\ell(\rho) + \mathrm{i}P_\ell(\rho)$, the denominator is brought to its squared modulus: $L_\ell(\rho) = \frac{u_{\ell+1}(\rho)\ q_\ell^*(\rho)}{q_\ell(\rho)\ q_\ell^*(\rho)}$, which is no longer its irreducible form, and which therefore doubles the number of $L_\ell(\rho)$ poles by introducing superfluous complex conjugate poles from $q_\ell^*(\rho)$. These superfluous poles have always been overlooked until now, recent examples are eq. (9) and (10) of [193], eq. (I.7.28) of [**?**], or eq. (2.29) p.75 of [148], where they count them to find $N_L = 2N_\lambda + 2\sum_{c=1}^{N_c} \ell_c$, which is actually the number of alternative analytic poles N_S we establish in eq. (49) theorem 3 of [127], instead of the correct number (E.102) of radioactive poles $N_L = 2N_\lambda + \sum_{c=1}^{N_c} \ell_c$ we demonstrated in theorem 1 of [125].

Because polynomial root-finding is no simple endeavor – see [131] or [148] for methods applied to the radioactive problem (E.101) and see [324, 134, 50, 266, 291, 158, 252, 253, 232, 254, 139, 256, 238, 255] for more general methods – searching for the wrong number of poles (in particular too many) can have dire numerical consequences. For instance, Hwang explains in [190] how he had to go to quadruple precision in this code "WHOPPER". He was finding the poles one by one using a Newton-Raphson method, and then removing them to search for the next pole. But once he had eliminated all the true poles, he was still searching for additional ones which did not actually exist. Numerically, though, one can never fully cancel out a pole, and thus will always find fictitious poles in the immediate vicinity of the cancelled ones. This is exactly what happened to Hwang, and why he had many spurious poles clustered around the non-resonant N_λ ones. Hence knowing the correct number N_L of poles (E.102) – and more generally (E.42) – is crucial in practice.

Exact multipole representations

Hwang also spent a lot of subsequent work performing a pole expansion of the potential cross section $\sigma_c^{\rm pot}$ as well as of the energy dependence he found in his scattering residues, in eq. (1) and (2) of [188] or eq. (3) and (4) of [189]. We recall that though the potential cross section does have poles – roots $\left\{\omega_n\right\}$ of the $H_+(\rho)$ function reported in TABLE I of [127] or expressed by radicals in table II of [127] – these poles actually have zero residues in the scattering matrix, and thus cancel out of the partial and total cross sections, as we prove in theorem 3 of [125]. It will thus suffice to write that for the case of neutron cross sections with zero threshold, (E.25) and

(E.26) entail the potential cross section takes the form:

$$\begin{aligned}\sigma_c^{\text{pot}}(z) &= 4\pi a_c^2 \frac{g_{J_c^\pi}}{{\rho_0}_c^2} \frac{\sin^2\phi_c(z)}{z^2} \\ &= 4\pi a_c^2 \frac{g_{J_c^\pi}}{{\rho_0}_c^2} \frac{1}{z^2} \Re_{\text{cont}} \left[\frac{1-\mathrm{e}^{-2\mathrm{i}\phi_c(z)}}{2}\right]\end{aligned} \tag{E.105}$$

With all this in mind, we can now finish the explicit Windowed Multipole Representation of no-threshold neutral particles cross sections. Upon finding the N_L roots $\left\{p_j\right\}$ of the polynomial radioactive problem (E.101), we can then solve for the nullspace of the inverse level matrix (which we here assume is an eigenline and we refer to [125] for the degenerate cases), and notice that that the degrees of the level matrix components $\boldsymbol{A}$ is at most -2, which leads to the the following, exact, partial fraction decomposition of the level matrix and of the Kapur-Peierls operator:

$$\begin{aligned}\boldsymbol{A}(z) &= \sum_{j=1}^{N_L} \frac{\boldsymbol{\alpha_j}\boldsymbol{\alpha_j}^{\mathsf{T}}}{z-p_j} \\ \boldsymbol{\kappa_j} &\triangleq \boldsymbol{\gamma}^{\mathsf{T}}\boldsymbol{\alpha_j} \\ \boldsymbol{R}_L(z) &= \sum_{j=1}^{N_L} \frac{\boldsymbol{\kappa_j}\boldsymbol{\kappa_j}^{\mathsf{T}}}{z-p_j}\end{aligned} \tag{E.106}$$

We can then build a pole expansion of the resonance matrix $\boldsymbol{Z}$ from (E.23) by noticing that the $\boldsymbol{\rho}^{1/2}(z) = \sqrt{z}{\boldsymbol{\rho}_{\boldsymbol{0}}}^{1/2}$ lead to an additional z term for each residue, and that the degrees of the numerator and denominator of z times the level matrix, $z\boldsymbol{A}(z)$, is still negative (degree of at most -1), guaranteeing the level matrix is a proper rational fraction with simple poles in z-space:

$$\boldsymbol{\rho}^{\frac{1}{2}}\boldsymbol{R}_L\boldsymbol{\rho}^{\frac{1}{2}}(z) = \sum_{j=1}^{N_L} \frac{p_j{\boldsymbol{\rho}_{\boldsymbol{0}}}^{\frac{1}{2}}\boldsymbol{\kappa_j}\boldsymbol{\kappa_j}^{\mathsf{T}}{\boldsymbol{\rho}_{\boldsymbol{0}}}^{\frac{1}{2}}}{z-p_j} \tag{E.107}$$

This has as consequence the remarkable property that for zero-threshold neutral cross sections, the z-space radioactive squared widths $\boldsymbol{\kappa_j}\boldsymbol{\kappa_j}^{\mathsf{T}}$ (rank-one residues of the Kapur-Peierls operator at poles p_j) add up to nullity:

$$\sum_{j=1}^{N_L} \boldsymbol{\kappa_j}\boldsymbol{\kappa_j}^{\mathsf{T}} = \boldsymbol{0} \tag{E.108}$$

From (E.23), we therefore obtain the following expression for the resonance matrix:

$$\boldsymbol{Z}(z) = {\boldsymbol{H}_+}^{-1}(z) \sum_{j=1}^{N_L} \frac{p_j{\boldsymbol{\rho}_{\boldsymbol{0}}}^{\frac{1}{2}}\boldsymbol{\kappa_j}\boldsymbol{\kappa_j}^{\mathsf{T}}{\boldsymbol{\rho}_{\boldsymbol{0}}}^{\frac{1}{2}}}{z-p_j} {\boldsymbol{H}_+}^{-1}(z) \tag{E.109}$$

Where we deliberately left the energy dependence of ${\boldsymbol{H}_+}^{-1}(z)$, and recall that for neutral particles $H_+(\rho) = O(\rho)$. Polar decomposition (E.13) entails:$H_{+\ell}^{-1}(\rho) =$

$\left|d_\ell^{-1}(\rho)\right| \mathrm{e}^{-\mathrm{i}\phi_\ell(\rho)} = \mathrm{e}^{-\mathrm{i}\rho}\ d_\ell^{-1}(\rho)$, which is Hwang's notation in eq (3) of [189]. A closer look at the last column of TABLE I of [127] shows that $d_\ell^{-1}(\rho)$ is the rational function of degree zero (that is a proper rational fraction plus a constant) with ℓ poles – the roots $\left\{\omega_n\right\}$ – that is the square root of that which Hwang identified in eq. (1) of [188]. Careful analysis of this functions, using TABLE I of [127] and conjugate continuation definitions (E.66), yields the following expressions:

$$\begin{aligned}
\mathrm{e}^{-2\mathrm{i}\phi_c(z)} &= \mathrm{e}^{-2\mathrm{i}\rho_c(z)} \frac{d_{\ell_c}^{-1}(z)}{d_{\ell_c}^{-1*}(z)} = Y_c(\rho_c(z)) \\
d_\ell(\rho) &= \mathrm{e}^{\mathrm{i}\ell\frac{\pi}{2}} \frac{\rho^\ell}{\prod_{n=1}^{\ell}(\rho-\omega_n)} \\
\frac{d_\ell^{-1}(\rho)}{d_\ell^{-1*}(\rho)} &= (-1)^\ell \prod_{n=1}^{\ell}\left(\frac{\rho-\omega_n^*}{\rho-\omega_n}\right) \\
|d_\ell|_{\text{cont}}^{-2}(\rho) &= \frac{\rho^{2\ell}}{\prod_{n=1}^{\ell}(\rho-\omega_n)(\rho-\omega_n^*)}
\end{aligned} \tag{E.110}$$

The diagonal elements of (E.109) are therefore exactly:

$$Z_{cc}(z) = |d_{\ell_c}|_{\text{cont}}^{-2}(z) \mathrm{e}^{-2\mathrm{i}\phi_c(z)} \sum_{j=1}^{N_L} \frac{\rho_{0c} p_j \left[\boldsymbol{\kappa_j}\boldsymbol{\kappa_j}^{\mathsf{T}}\right]_{cc}}{z-p_j} \tag{E.111}$$

which, upon partial fraction decomposition, yields the Hwang multipole representation [190]:

$$\begin{aligned}
\sigma_c(z) &= \sigma_c^{\text{pot}}(z) + \sigma_c^{\text{Hwang}}(z) \\
&\quad + \frac{1}{z^2}\Re_{\text{cont}}\left[-\mathrm{i}\ \mathrm{e}^{-2\mathrm{i}\phi_c(z)} \sum_{j=1}^{N_L} \frac{{}^{\text{Hwang}}r_j^c}{z-p_j}\right] \\
{}^{\text{Hwang}}r_j^c &\triangleq 4\pi a_c^2 \frac{g_{J_c^\pi}}{{\rho_0}_c^2} |d_{\ell_c}|_{\text{cont}}^{-2}(p_j)\ \rho_{0c} p_j \left[\boldsymbol{\kappa_j}\boldsymbol{\kappa_j}^{\mathsf{T}}\right]_{cc} \\
\sigma_c^{\text{Hwang}}(z) &\triangleq 4\pi a_c^2 \frac{g_{J_c^\pi}}{{\rho_0}_c^2} \frac{1}{z^2} \Re\left[-\mathrm{i}\ \mathrm{e}^{-2\mathrm{i}\phi_c(z)} \Delta(z)\right] \\
\Delta(z) &\triangleq \sum_{n=1}^{\ell_c}\left[\frac{\Delta_n \left[\boldsymbol{\rho}^{\frac{1}{2}}\boldsymbol{R}_L\boldsymbol{\rho}^{\frac{1}{2}}\right]_{cc}\left(\frac{\omega_n}{\rho_0}\right)}{\rho-\omega_n}\right. \\
&\quad \left. + \frac{\Delta_n^* \left[\boldsymbol{\rho}^{\frac{1}{2}}\boldsymbol{R}_L\boldsymbol{\rho}^{\frac{1}{2}}\right]_{cc}\left(\frac{\omega_n^*}{\rho_0}\right)}{\rho-\omega_n^*}\right] \\
\Delta_n &\triangleq \frac{\omega_n^{2\ell_c}}{\prod_{k=1}^{\ell_c}(\omega_n-\omega_k^*)\prod_{k\neq n}^{\ell_c}(\omega_n-\omega_k)}
\end{aligned} \tag{E.112}$$

where the Hwang residues in (E.112) are identical to eq. (2) of [189]. This scripture is the conjugate continuation real part of $N_L + \ell_c$ poles, as identified in [148]: the N_L radioactive poles (E.102), poles of the Kapur-Peierls operator (E.49), plus the roots $\left\{\omega_n\right\}$ of the outgoing wavefunction $\boldsymbol{O}(\boldsymbol{\rho})$. However, we have proved the latter

cancel out of the transmission matrix, and thus of the cross section (theorem 3 of [125]). Therefore, there must exist a multipole representation with only the N_L Kapur-Peierls poles. This can be achieved by developing the potential cross section (E.105) into poles and residues, factoring the $\mathrm{e}^{-2\mathrm{i}\rho_c}$ component (which has no poles) using expressions (E.110), and performing a partial fraction decomposition of the rational terms. Upon careful consideration, one will notice that this rational function is of degree zero, that its poles are the radioactive poles (and only those), and that the constant (obtained by evaluating at infinity $|\rho_c| \to \infty$) is $(-1)^{\ell_c}$. This shifts the potential cross section, so that the total cross section (E.27) can be expressed as the sum of a background cross section (with no poles),

$$\sigma_c^{\text{back}}(z) \triangleq 4\pi a_c^2 \frac{g_{J_c^\pi}}{\rho_{0_c}^2} \frac{\sin^2\left(\rho_c(z) + \ell_c \frac{\pi}{2}\right)}{z^2} \tag{E.113}$$

plus a resonant cross section with the N_L radioactive poles:

$$\begin{aligned}
\sigma_c(z) &= \sigma_c^{\text{back}}(z) + \frac{1}{z^2} \Re_{\text{cont}} \left[-\mathrm{i}\, \mathrm{e}^{-2\mathrm{i}\rho_c(z)} \sum_{j=1}^{N_L} \frac{{}^{\text{tot}}r_j^c}{z - p_j} \right] \\
{}^{\text{tot}}r_j^c &\triangleq 4\pi a_c^2 \frac{g_{J_c^\pi}}{\rho_{0_c}^2} d_{\ell_c}^{-2}(p_j)\ \rho_{0_c} p_j \left[\boldsymbol{\kappa_j} \boldsymbol{\kappa_j}^{\mathsf{T}} \right]_{cc} \\
&= 4\pi a_c^2 \frac{g_{J_c^\pi}}{\rho_{0_c}^2} (-1)^\ell \frac{(\rho_{0_c} p_j)^{2\ell+1} \left[\boldsymbol{\kappa_j} \boldsymbol{\kappa_j}^{\mathsf{T}} \right]_{cc}}{\prod_{n=1}^{\ell} (\rho_0 p_j - \omega_n)^2}
\end{aligned} \tag{E.114}$$

To the best of our knowledge, expression (E.114) is the first time the exact multipole representation of no-threshold neutron cross sections is derived with the proper number of poles. It is exact and complete, in the sense that no window-by-window Laurent expansions are needed. This is only made possible in this specific case of neutron cross sections with zero threshold (no charged particles nor thresholds): though quite restrictive, it is still a case of great practical importance for nuclear reactor physics, as most heavy isotopes are evaluated with only two channels (neutron and fission) with all the other channels being eliminated under the Reich-Moore approximation. This significant difference with light isotopes (in which many more channels are explicitly treated) is partly due to the fact that for heavy isotopes the number of photon channels is large enough that one can average their contribution out, and also because the resonance region starts at lower energies for heavy isotopes, with many resonances before the first non-zero threshold.

Note that the advantage of not needing local Laurent developments in (E.114) comes at the computational cost of having to sum all the radioactive poles for each energy call, instead of accounting for the contributions of far-away poles in the Laurent expansion of each window – in this sense, the windowing process is a form of local compression algorithm for improved efficiency [187, 146].

To compute the partial cross sections (E.31), we can calculate the reaction cross section (E.30) and the interference one (E.29). For the reaction cross section, we use the square modulus conjugate continuation (E.66), and notice that $\left| {\boldsymbol{H}_+}^{-1} \right|_{\text{cont}}^{-2}(z) =$

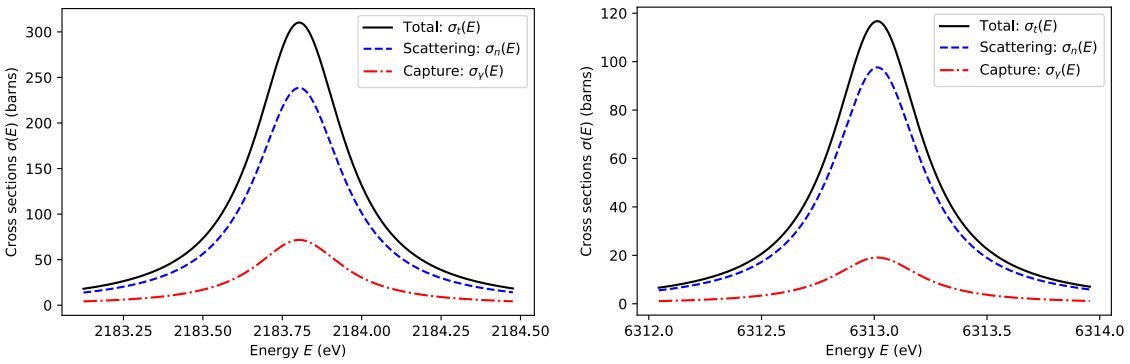

(a) First p-wave resonance.

(b) Second p-wave resonance.

Figure E-2: Xenon ^{134}Xe Reich-Moore cross sections for spin-parity group $J^\pi = 1/2^{(-)}$ p-wave resonances: the cross sections are generated using the multipole parameters from table E.1 in the multipole representation total cross section (E.114), as well as the reaction cross section (E.117) and interference one (E.119) to compute the scattering cross section as (E.31), while the capture cross section is the difference between the total and the scattering. All cross sections are identical to those computed using the Reich-Moore approximation R-matrix equations with the ENDF/B-VIII.0 resonance parameters.

$|\boldsymbol{d}|^{-2}_{\text{cont}}(z) \triangleq \mathbf{diag}\left(d_{\ell_c}(\rho)\ d_{\ell_c}(\rho^*)^*\right)^{-2}$ is now a rational function (the $\mathrm{e}^{-\mathrm{i}\rho}$ terms cancel out). Therefore, evaluating at the pole values yields the partial fraction decomposition of the square modulus of the resonance matrix:

$$|\boldsymbol{Z}|^2_{\text{cont}}(z) = \Re_{\text{cont}}\left[\sum_{j=1}^{N_L} \frac{\boldsymbol{\aleph_j}}{z - p_j}\right] \tag{E.115}$$

where the residues $\boldsymbol{\aleph_j}$ are explicitly constructed as

$$\boldsymbol{\aleph_j} \triangleq 2|\boldsymbol{d}|^{-2}_{\text{cont}}(p_j)\boldsymbol{\rho_0}\left(p_j^2 \boldsymbol{\kappa_j}\boldsymbol{\kappa_j}^{\mathsf{T}} \circ \left[\boldsymbol{R}_L(p_j^*)\right]^*\right)\boldsymbol{\rho_0}\,|\boldsymbol{d}|^{-2}_{\text{cont}}(p_j) \tag{E.116}$$

In summary, the energy dependence of the residues in (E.109) cancels out of the reaction residues, hence the reaction cross section (from channel c to c') is exactly

$$\sigma^{\text{react}}_{cc'}(z) = \frac{1}{z^2}\Re_{\text{cont}}\left[\sum_{j\geq 1} \frac{{}^{\text{react}}r_j^{cc'}}{z - p_j}\right] \tag{E.117}$$

where the residues can either simply be evaluated as (E.92) or constructed as:

$${}^{\text{react}}r_j^{cc'} \triangleq \frac{4\pi a_c^2}{\rho_{0_c}^2} g_{J_c^\pi}\left[\boldsymbol{\aleph_j}\right]_{cc'} \tag{E.118}$$

For the interference cross section (E.29), we notice using expressions (E.110) that the phase behavior also cancels out of $\Re\left[-\mathrm{i}Z_{cc}Y_c^*\right]$, so that plugging the resonance matrix

partial fraction decomposition (E.111) into interference cross section expression (E.29) yields rational fraction

$$\sigma_c^{\rm int}(z) = \frac{1}{z^2}\Re_{\rm cont}\left[\sum_{j=1}^{N_L}\frac{{}^{\rm int}r_j^c}{z-p_j}\right] \tag{E.119}$$

where the interference residues can simply be evaluated as (E.89), or explicitly constructed as

$$\begin{aligned}{}^{\rm int}r_j^c &\triangleq -{\rm i}4\pi a_c^2\frac{g_{J_c^\pi}}{{\rho_{0_c}}^2}\left|d_{\ell_c}\right|^{-2}_{\rm cont}(p_j)\;\rho_{0_c}p_j\left[\boldsymbol{\kappa_j}\boldsymbol{\kappa_j}^{\mathsf{T}}\right]_{cc}\\ &= -{\rm i}4\pi a_c^2\frac{g_{J_c^\pi}}{{\rho_{0_c}}^2}\frac{\left(\rho_{0_c}p_j\right)^{2\ell_c+1}\left[\boldsymbol{\kappa_j}\boldsymbol{\kappa_j}^{\mathsf{T}}\right]_{cc}}{\prod_{n=1}^{\ell}\left(\rho_{0_c}p_j-\omega_n\right)\left(\rho_{0_c}p_j-\omega_n^*\right)}\end{aligned} \tag{E.120}$$

Having explicitly constructed the total, potential, reaction, and interference cross sections, we can thus calculate the partial cross sections explicitly through (E.31).

Evidence for exact multipole representation in ^{134}Xe

We discovered shadow alternative poles of ^{134}Xe spin-parity group $J^\pi = 1/2^{(-)}$ two p-wave resonances in [127], and found the radioactive parameters poles and residues in [125]. We now complete this xenon trilogy by here providing the exact multipole representation of ^{134}Xe spin-parity group $J^\pi = 1/2^{(-)}$ cross section. The multipole parameters are documented in table E.1, and the corresponding cross sections are plotted in figure E-2. In ENDF/B-VIII.0, ^{134}Xe is a MLBW evaluation with only one explicit (neutron) channel, all other channels are eliminated using Wigner-Teichmann and Reich-Moore approximations. One can thus compute the total cross section using mutlipole representation (E.114), and the scattering cross section as the partial cross section for $\sigma_{nn}(E)$ from (E.31), using reaction cross section (E.117) and interference one (E.119). The capture cross section is then computed as the difference between the total and the scattering cross section. The p-waves ($\ell_c = 1$) entail there are $N_L = 5$ radioactive poles – validating (E.102) – and the corresponding residues are documented in table E.1. As we see in this xenon example, the multipole representation is an exact alternative formalism to compute R-matrix cross sections. Nonetheless, if we want to treat charged particle channels and thresholds, we need to use local Laurent developments in energy windows, which makes the windowed multipole representation cumbersome and somewhat unsuited for standard nuclear data libraries.

Exact to windowed multipole representations

Note that we can convert the exact multipole total cross section expression (E.114) – which has energy-dependent residues due to $\mathrm{e}^{-2{\rm i}\rho_c(z)}$ – into the general windowed multipole representation (E.96), with energy-independent residues plus a Laurent expansion of order no less than -2. It suffices to evaluate the residues at the pole values, and note that the Laurent expansion part $\underset{\rm tot}{\rm Laur}(z)$ is then the difference of the

Table E.1: Windowed multipole parameters of the two p-wave resonances of ^{134}Xe, spin-parity group $J^\pi = 1/2^{(-)}$, converted from ENDF/B-VIII.0 evaluation (MLBW) to multipole representation using Reich-Moore level matrix (E.21).

$z = \sqrt{E}$ with E in (eV)
$A = 132.7600$
$a_c = 5.80$: channel radius (Fermis)
$\rho_0 = \frac{Aa_c\sqrt{\frac{2m_n}{\hbar}}}{A+1}$ in $(\sqrt{\text{eV}}^{-1})$, so that $\rho(z) \triangleq \rho_0 z$
with $\sqrt{\frac{2m_n}{\hbar}} = 0.002196807122623$ in units $(1/(10^{-14}\text{m}\sqrt{\text{eV}}))$

Multipole parameters (rounded to 5 digits): converted from R-matrix parameters using Reich-Mo

Radioactive poles p_j ($\sqrt{\text{eV}}$) from (E.101)	Total residues ${}^{\text{tot}}r_j^c$ (barns$\sqrt{\text{eV}^3}$) from (E.114)	Reaction residues ${}^{\text{react}}r_j^{cc'}$ (barns$\sqrt{\text{eV}^3}$) from (E.118)	Interference residue (barns$\sqrt{\text{eV}^3}$) from (
6.4652×10^{-8}	$6.9766 \times 10^{+8}$	2.8519×10^{-2}	-2.8446×10^{-2}
$-\text{i}7.9179 \times 10^{+2}$	$-\text{i}5.5825 \times 10^{-2}$	$+\text{i}4.6048 \times 10^{+5}$	$+\text{i}4.6048 \times 10^{+5}$
$-4.6731 \times 10^{+1}$	$-1.2144 \times 10^{+3}$	-1.5693×10^{-1}	-1.3518×10^{-1}
$-\text{i}9.7105 \times 10^{-4}$	$+\text{i}1.4390 \times 10^{+2}$	$+\text{i}1.7479 \times 10^{+3}$	$+\text{i}1.2229 \times 10^{+3}$
$4.6731 \times 10^{+1}$	$-1.2144 \times 10^{+3}$	1.5693×10^{-1}	1.7868×10^{-1}
$-\text{i}1.8048 \times 10^{-3}$	$-\text{i}1.4386 \times 10^{+2}$	$+\text{i}9.4043 \times 10^{+2}$	$+\text{i}1.2229 \times 10^{+3}$
$-7.9454 \times 10^{+1}$	$-1.0827 \times 10^{+3}$	-4.2538×10^{-1}	-4.1864×10^{-1}
$-\text{i}1.0084 \times 10^{-3}$	$+\text{i}2.1937 \times 10^{+2}$	$+\text{i}1.3735 \times 10^{+3}$	$+\text{i}1.1047 \times 10^{+3}$
$7.9454 \times 10^{+1}$	$-1.0827 \times 10^{+3}$	4.2538×10^{-1}	4.3211×10^{-1}
$-\text{i}1.4991 \times 10^{-3}$	$-\text{i}2.1936 \times 10^{+2}$	$+\text{i}9.2389 \times 10^{+2}$	$+\text{i}1.1047 \times 10^{+3}$

R-matrix parameters: reference ENDF/B-VIII.0 evaluation (MLBW) used with Reich-Moore leve

$E_1 = 2186.0$: first resonance energy (eV)
$\Gamma_{1,n} = 0.2600$: neutron width of first resonance
(not reduced width), i.e. $\Gamma_{\lambda,c} = 2P_c(E_\lambda)\gamma_{\lambda,c}^2$
$\Gamma_{1,\gamma} = 0.0780$: eliminated capture width (eV)
$E_2 = 6315.0$: second resonance energy (eV)
$\Gamma_{2,n} = 0.4000$ (eV)
$\Gamma_{2,\gamma} = 0.0780$ (eV)
$g_{J^\pi} = 1/3$: spin statistical factor
$B_c = -1$

two remaining components, that is:

$$\begin{aligned}
\underset{\text{tot}}{\text{Laur}}(z) &= \frac{1}{z^2}\Re_{\text{cont}}\left[\sum_{j=1}^{N_L}\frac{-\text{i}\,{}^{\text{tot}}r_j^c}{z-p_j}\left(\text{e}^{-2\text{i}\rho_{0_c}z} - \text{e}^{-2\text{i}\rho_{0_c}p_j}\right)\right] \\
&= \Re_{\text{cont}}\left[\sum_{j=1}^{N_L}\frac{{}^{\text{tot}}r_j^c}{\text{i}z^2}\left(\sum_{n\geq 0}\frac{(-2\text{i}\rho_{0_c})^n}{n!}\frac{z^n - p_j^n}{z-p_j}\right)\right] \\
&= \sum_{n\geq 1}\sum_{m=1}^{n}\frac{z^m}{z^3}\Re_{\text{cont}}\left[\sum_{j=1}^{N_L}\frac{{}^{\text{tot}}r_j^c}{\text{i}}p_j^{n-m}\frac{(-2\text{i}\rho_{0_c})^n}{n!}\right] \\
&= \sum_{n\geq -2} a_n z^n
\end{aligned} \tag{E.121}$$

so that the total cross section (E.112) can be expanded as

$$\sigma_c(z) = \sigma_c^{\text{back}}(z) + \frac{1}{z^2}\Re_{\text{cont}}\left[\sum_{j=1}^{N_L}\frac{-\mathrm{i}\ \mathrm{e}^{-2\mathrm{i}\rho_{0_c}p_j\ \text{tot}}r_j^c}{z-p_j}\right] + \underset{\text{tot}}{\text{Laur}}(z) \tag{E.122}$$

where the residues are now independent of energy. By further performing the analytic expansion of the background cross section (E.113)

$$\sigma_c^{\text{back}}(z) \triangleq 4\pi a_c^2 \frac{g_{J_c^\pi}}{\rho_{0_c}^2}\left[\frac{1-(-1)^\ell}{2\ z^2} + \sum_{n\geq 1}\frac{(-1)^n}{2}\frac{(2\rho_{0_c})^{2n}}{(2n)!}\frac{z^{2n}}{z^2}\right] \tag{E.123}$$

one recovers the general windowed multipole representation (E.96).

As we see, in this special case of neutron channels without threshold, we can explicitly construct the full windowed multipole representation (E.122) without the need of local expansions for each energy window $\mathcal{W}(E)$. Somewhat ironically, it is also much more cumbersome to explicitly construct both the Laurent expansion and the residues, compared to the more general approaches of theorem 15. Alternatively, one can solve for the radioactive poles $\left\{p_j\right\}$ through polynomial root-finding (E.101), and then revert to the general methods of theorem 15 to compute the corresponding residues, after what the Laurent expansions can be locally curve-fitted.

E.4 Windowed Multipole Covariances

In section E.3, we established the windowed multipole representation as a general alternative way to parametrize the energy dependence of R-matrix cross sections (theorem 15). In this section, we consider how the Windowed Multipole Representation can account for R-matrix cross section epistemic uncertainties. Such uncertainties exist because nuclear cross sections are known from experiments, and experimental measurements always come with error-bars. Therefore, in addition to evaluating R-matrix parameter values, evaluators add resonance parameters covariance matrices to standard nuclear data libraries (File 32 in the ENDF/B-VIII.0 library [87]), aimed at reproducing the empirical uncertainty observed in nuclear cross sections.

E.4.1 Converting R-matrix parameters covariances

If it exists, the covariance matrix $\mathbb{V}\text{ar}\,(X)$ of a random vector X with expectation value $\mathbb{E}\,[X]$ is a defined as:

$$\mathbb{V}\text{ar}\,(X) \triangleq \mathbb{E}\left[XX^\dagger\right] - \mathbb{E}\,[X]\,\mathbb{E}\,[X]^\dagger \tag{E.124}$$

We denote $\left\{\Gamma\right\}$ the set of R-matrix resonance parameters $\left\{\Gamma\right\} \triangleq \left\{E_\lambda, \gamma_{\lambda,c}\right\}$, which are implicitly considered to be the expectation value of the underlying distribution,

$\left\{\Gamma\right\} \triangleq \mathbb{E}\left[\Gamma\right]$, and $\mathbb{V}\mathrm{ar}\left(\Gamma\right)$ their corresponding covariance matrices. These represent the resonance parameters epistemic uncertainty, which is accounted for by assuming the parameters are drawn from the multivariate normal distribution: $\mathcal{N}\left(\Gamma, \mathbb{V}\mathrm{ar}\left(\Gamma\right)\right)$. Recall that both the channel radii a_c and the boundary conditions B_c are arbitrarily set constants, and therefore have no uncertainty. Also, we here do not explicitly treat the uncertainty on threshold energies E_{T_c}, but our approach could readily be extended to them.

We consider the unified Windowed Multipole Representation of R-matrix cross sections (E.96), which we proved is an exact representation of R-matrix cross sections everywhere but for windows containing a non-zero threshold $E_{T_c} \in \mathcal{W}(E)$ – in these threshold windows, form (E.96) is only an approximation of exact R-matrix cross sections of theorem 15, yet this approximation (E.96) can be made to reach any target accuracy. For each energy window $\mathcal{W}(E)$, we denote $\left\{\Pi\right\}$ the windowed multipole parameters – that is the set of poles $\left\{p_j\right\}$, residues $\left\{\widetilde{r}_j^{cc'}, r_j^c\right\}$, and Laurent expansion coefficients $\left\{a_n\right\}$ that parametrize cross section (E.96) in that energy window: $\left\{\Pi\right\} \triangleq \left\{p_j, \widetilde{r}_j^{cc'}, r_j^c, a_n\right\}$.

The main result of this section – theorem 16 – establishes a framework to convert R-matrix resonance parameters covariance matrices $\mathbb{V}\mathrm{ar}\left(\Gamma\right)$ into *Windowed Multipole Covariances* $\mathbb{V}\mathrm{ar}\left(\Pi\right)$. It is based on the following lemma 5, which derives sensitivities of R-matrix cross sections $\sigma(E)$ to both resonance parameters $\left\{\Gamma\right\}$ and multipoles $\left\{\Pi\right\}$.

Lemma 5. *Cross sections parameter sensitives*
Let $z \in \mathbb{C}$ be the complex, analytically continued square-root-of-energy: $z = \sqrt{E}$. Consider Windowed Multipole cross section (E.96), i.e. locally of the form:

$$\sigma(z) \underset{\mathcal{W}(E)}{=} \sum_{n\geq -2} a_n z^n + \frac{1}{z^2}\Re_{\text{cont}}\left[\sum_{j\geq 1}\frac{r_j}{z-p_j}\right]$$

We recall the Cauchy-Poincaré-Wirtinger holomorphic complex differential definition for $z = x + \mathrm{i}y$, $x, y \in \mathbb{R}$

$$\partial_z \triangleq \frac{1}{2}\left(\partial_x - \mathrm{i}\partial_y\right) \tag{E.125}$$

so that $\partial_z z = 1$, and $\partial_z z^* = 0$, where $z^* \triangleq x - \mathrm{i}y$.

The cross section sensitivities to multipoles $\frac{\partial\sigma}{\partial\Pi}(z)$ (i.e. the partial differentials of the cross section with respect to multipoles) are then given, for each window $\mathcal{W}(E)$,

by:

$$\begin{aligned}
&\frac{\partial\sigma}{\partial p_j}(z)=\frac{1}{z^2}\frac{\frac{r_j}{2}}{(z-p_j)^2} \qquad ,\frac{\partial\sigma}{\partial p_j^*}(z)=\frac{1}{z^2}\frac{\frac{r_j^*}{2}}{\left(z-p_j^*\right)^2}\\
&\frac{\partial\sigma(z)}{\partial\Re\left[p_j\right]}=\frac{1}{z^2}\Re_{\text{cont}}\left[\frac{r_j}{(z-p_j)^2}\right],\frac{\partial\sigma(z)}{\partial\Im\left[p_j\right]}=\frac{1}{z^2}\Re_{\text{cont}}\left[\frac{\mathrm{i}\,r_j}{(z-p_j)^2}\right]\\
&\frac{\partial\sigma}{\partial r_j}(z)=\frac{1}{z^2}\frac{\frac{1}{2}}{z-p_j} \qquad ,\frac{\partial\sigma}{\partial r_j^*}(z)=\frac{1}{z^2}\frac{\frac{1}{2}}{z-p_j^*}\\
&\frac{\partial\sigma(z)}{\partial\Re\left[r_j\right]}=\frac{1}{z^2}\Re_{\text{cont}}\left[\frac{1}{z-p_j}\right] \quad ,\frac{\partial\sigma(z)}{\partial\Im\left[r_j\right]}=\frac{1}{z^2}\Re_{\text{cont}}\left[\frac{\mathrm{i}}{z-p_j}\right]\\
&\frac{\partial\sigma}{\partial a_n}(z)=z^n
\end{aligned} \tag{E.126}$$

Moreover, the cross section sensitivities to resonance parameters $\frac{\partial\sigma}{\partial\Gamma}(z)$ *(i.e. the partial differentials of the cross section with respect to resonance parameters) are subject to the following multipole representation:*

$$\begin{aligned}
\frac{\partial\sigma}{\partial\Gamma}(z) \underset{\mathcal{W}(E)}{=} &\frac{1}{z^2}\Re_{\text{cont}}\left[\sum_{j\geq 1}\frac{\left(\frac{\partial r_j}{\partial\Gamma}\right)}{z-p_j}+\frac{\left(r_j\ \frac{\partial p_j}{\partial\Gamma}\right)}{(z-p_j)^2}\right]\\
&+\sum_{n\geq -2}\left(\frac{\partial a_n}{\partial\Gamma}\right)z^n
\end{aligned} \tag{E.127}$$

We seek to convert R-matrix resonance parameters covariances $\mathbb{V}\mathrm{ar}\left(\Gamma\right)$ into Windowed Multipole covariances $\mathbb{V}\mathrm{ar}\left(\Pi\right)$. Yet obtaining multipoles $\left\{\Pi\right\}$ from resonance parameters $\left\{\Gamma\right\}$ is not a simple transformation: one must solve the radioactive problem (E.49) for the poles $\left\{p_j\right\}$ and then compute the corresponding residues $\left\{\widehat{r}_j^{cc'},r_j^c\right\}$ (theorem 15). We therefore take an implicit functions approach, and locally invert the $\Gamma\rightarrow\Pi$ transformation by means of the Jacobian matrix $\left(\frac{\partial\Pi}{\partial\Gamma}\right)$, that is the sensitivities of windowed multipole coefficients to the R-matrix resonance parameters (Cauchy-Dini implicit functions theorem). Under the assumption of small deviations from the mean (small relative uncertainties), this yields a first-order linear relation from multipoles $\left\{\Pi\right\}$ to resonance parameters $\left\{\Gamma\right\}$. In which case, the chain rule entails the multipoles $\left\{\Pi\right\}$ are also subject to a multivariate normal distribution $\mathcal{N}\left(\Pi,\mathbb{V}\mathrm{ar}\left(\Pi\right)\right)$, the covariance of which is given by (E.129) (sometimes called "sandwich rule"). Therefore, the key to converting resonance covariances $\mathbb{V}\mathrm{ar}\left(\Gamma\right)$ into multipole covariances $\mathbb{V}\mathrm{ar}\left(\Pi\right)$ lies in the sensitivities $\left(\frac{\partial\Pi}{\partial\Gamma}\right)$. Theorem 16 establishes a contour-integrals method to calculate these sensitivities $\left(\frac{\partial\Pi}{\partial\Gamma}\right)$, provided R-matrix cross sections sensitivities $\frac{\partial\sigma}{\partial\Gamma}(E)$ from lemma 5.

Theorem 16. *Windowed Multipole Covariances*
Let us be provided with the sensitivities $\frac{\partial\sigma}{\partial\Gamma}(z)$ *of R-matrix cross sections (analytically continued) to resonance parameters (E.127). Then the multipole sensitivities (Jaco-*

bian matrix) with respect to the resonance parameters, $\left(\frac{\partial \Pi}{\partial \Gamma}\right)$*, can be obtained from the following system (E.128) of contour integrals in the complex plane, where* $\mathfrak{C}_{p_j}$ *designates any positively oriented simple closed contour containing only pole* p_j*. For instance,* $\mathfrak{C}_{p_j}$ *can be a circle of radius* $\epsilon > 0$ *around pole* p_j*.*

$$
\begin{aligned}
\frac{1}{2}\frac{r_j}{p_j^2}\ \left(\frac{\partial p_j}{\partial \Gamma}\right) &= \frac{1}{2\pi \mathrm{i}} \oint_{\mathfrak{C}_{p_j}} (z-p_j)\frac{\partial \sigma}{\partial \Gamma}(z)\mathrm{d}z = \frac{\epsilon^2}{2\pi}\int_{\theta=0}^{2\pi}\frac{\partial \sigma}{\partial \Gamma}(p_j+\epsilon \mathrm{e}^{\mathrm{i}\theta})\mathrm{e}^{2\mathrm{i}\theta}\mathrm{d} \\
\frac{1}{2}\frac{1}{p_j^2}\ \left(\frac{\partial r_j}{\partial \Gamma}\right) - \frac{r_j}{p_j^3}\ \left(\frac{\partial p_j}{\partial \Gamma}\right) &= \frac{1}{2\pi \mathrm{i}} \oint_{\mathfrak{C}_{p_j}} \frac{\partial \sigma}{\partial \Gamma}(z)\mathrm{d}z = \frac{\epsilon}{2\pi}\int_{\theta=0}^{2\pi}\frac{\partial \sigma}{\partial \Gamma}(p_j+\epsilon \mathrm{e}^{\mathrm{i}\theta})\mathrm{e}^{\mathrm{i}\theta}\mathrm{d}\theta \\
\left(\frac{\partial a_n}{\partial \Gamma}\right) + \delta_{-1,n}\Re_{\mathrm{cont}}\left[\sum_{j=1}^{N_L}\frac{2\left(r_j\ \frac{\partial p_j}{\partial \Gamma}\right) - p_j\left(\frac{\partial r_j}{\partial \Gamma}\right)}{p_j^3}\right] &+ \delta_{-2,n}\Re_{\mathrm{cont}}\left[\sum_{j=1}^{N_L}\frac{\left(r_j\ \frac{\partial p_j}{\partial \Gamma}\right) - p_j\left(\frac{\partial r_j}{\partial \Gamma}\right)}{p_j^2}\right] \\
&= \frac{1}{2\pi \mathrm{i}} \oint_{\mathfrak{C}_0} \frac{1}{z^{n+1}}\frac{\partial \sigma}{\partial \Gamma}(z)\mathrm{d}z = \frac{1}{2\pi\epsilon^n}\int_{\theta=0}^{2\pi}\frac{\partial \sigma}{\partial \Gamma}(\epsilon \mathrm{e}^{\mathrm{i}\theta})\mathrm{e}^{-\mathrm{i}n\theta}\mathrm{d}\theta
\end{aligned}
\tag{E.128}
$$

For each energy window $\mathcal{W}(E)$*, the multipole sensitivities* $\left(\frac{\partial \Pi}{\partial \Gamma}\right)$ *from system (E.128) can then be converted to first order into Windowed Multipole covariances* $\mathbb{V}\mathrm{ar}\,(\Pi)$ *as:*

$$
\mathbb{V}\mathrm{ar}\,(\Pi) = \left(\frac{\partial \Pi}{\partial \Gamma}\right)\mathbb{V}\mathrm{ar}\,(\Gamma)\left(\frac{\partial \Pi}{\partial \Gamma}\right)^{\dagger} \tag{E.129}
$$

where $[\,\cdot\,]^{\dagger}$ *designates the Hermitian conjugate (adjoint).*

Proof. Partial fraction expansion of (E.127) lemma 5 yields

$$
\begin{aligned}
\frac{\partial \sigma}{\partial \Gamma}(z) \underset{\mathcal{W}(E)}{=} \quad & \Re_{\mathrm{cont}}\left[\sum_{j=1}^{N_L}\frac{\left(r_j\ \frac{\partial p_j}{\partial \Gamma}\right) - p_j\left(\frac{\partial r_j}{\partial \Gamma}\right)}{p_j^2 z^2}\right. \\
& + \frac{\left(r_j\ \frac{\partial p_j}{\partial \Gamma}\right)}{p_j^2(z-p_j)^2} + \frac{2\left(r_j\ \frac{\partial p_j}{\partial \Gamma}\right) - p_j\left(\frac{\partial r_j}{\partial \Gamma}\right)}{p_j^3 z} \\
& \left. + \frac{p_j\left(\frac{\partial r_j}{\partial \Gamma}\right) - 2\left(r_j\ \frac{\partial p_j}{\partial \Gamma}\right)}{p_j^3(z-p_j)}\right] \\
& + \sum_{n\geq -2}\left(\frac{\partial a_n}{\partial \Gamma}\right) z^n
\end{aligned}
$$

The different residues associated with poles 0 or p_j are then obtained by invoking Cauchy's residue theorem and multiplying correspondingly by z^n or $(z-p_j)$, yielding (E.128). Importantly, these contour integrals cannot be performed without having an analytic representation of the partial derivatives of the cross section at complex energies, $\frac{\partial \sigma}{\partial \Gamma}(z)$, which is made possible for open channels by Hwang's conjugate continuations (E.66) and (E.62). Finally, (E.129) is a direct application of the well-known chain-rule first-order perturbation covariance formula. □

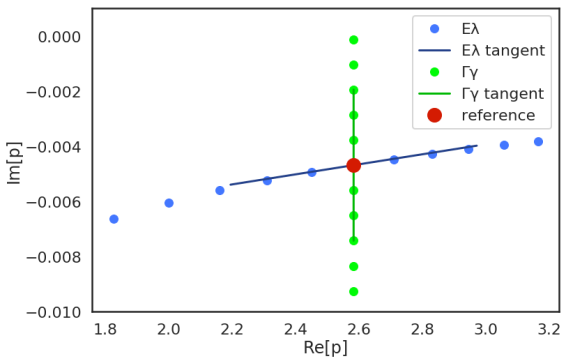

Figure E-3: Multipole sensitivities to R-matrix parameters $\left(\frac{\partial \Pi}{\partial \Gamma}\right)$. Trajectories of pole p as resonance parameters $\{\Gamma\}$ vary, using the SLBW approximation of the first resonance of ^{238}U (appendix E.8). The blue points show how the pole changes as E_λ is varied with equal spacing within 3 standard deviations of the enlarged covariance matrix, while the green points result from equally spaced variations of Γ_γ within their uncertainty range (3 standard deviations of enlarged covariance matrix). The Jacobian $\left(\frac{\partial \Pi}{\partial \Gamma}\right)$ from system (E.128) are the tangents of these trajectories from the mean pole p (red reference point) and are shown in solid lines. Complex pole p units are $(\sqrt{\text{eV}})$.

E.4.2 Cross section uncertainties and parameter covariances

By introducing resonance covariances $\mathbb{V}\text{ar}\,(\Gamma)$, present standard nuclear data libraries are built with the implicit assumption that sampling resonance parameters from a multivariate normal distribution $\mathcal{N}\,(\Gamma, \mathbb{V}\text{ar}\,(\Gamma))$ and computing the corresponding cross sections $\sigma_\Gamma(E)$ generates outcome distributions commensurate to our experimental uncertainty. Note that this parameter uncertainty representation is not obvious *in se*, because cross sections are measured at specific energies, and the measured cross section uncertainty is usually described with a given exogenous distribution (say normal, log-normal, or exponential), dictated by the experiment. Therefore, no parameter distribution (be it resonance parameters multivariate normal $\mathcal{N}\,(\Gamma, \mathbb{V}\text{ar}\,(\Gamma))$ or any other) can exactly reproduce the cross section uncertainty for each measurement energy. And yet, these parameters distributions are our best way of balancing all the different uncertainties from disjointed experiments with the underlying R-matrix theory which unifies our understanding of nuclear interactions physics.

Significant work has been carried out to infer parameter distributions that accurately reproduce our uncertainty of nuclear cross sections [149, 70, 101, 205, 206, 173, 281, 54, 282]. Assuming R-matrix cross section uncertainty is well represented by the resonance parameters multivariate normal distribution $\mathcal{N}\,(\Gamma, \mathbb{V}\text{ar}\,(\Gamma))$ documented in standard nuclear data libraries (file 32 in ENDF/B-VIII.0 [87]), there are two ways of translating this into cross section distributions: 1) first-order sensitivity propagation, or; 2) stochastic cross sections.

1. For any given energy E, first-order sensitivity propagation simply considers the R-matrix cross section sensitivities to resonance parameters $\frac{\partial \sigma}{\partial \Gamma}(E)$ and linearly converts the resonance parameter covariance $\mathbb{V}\text{ar}\,(\Gamma)$ into a cross section covari-

ance $\mathbb{V}\mathrm{ar}\left(\sigma(E)\right)$ at each energy E, using the chain rule:

$$\mathbb{V}\mathrm{ar}\left(\sigma_{\Gamma}(E)\right) = \left(\frac{\partial\sigma(E)}{\partial\Gamma}\right)\mathbb{V}\mathrm{ar}\left(\Gamma\right)\left(\frac{\partial\sigma(E)}{\partial\Gamma}\right)^{\dagger} \tag{E.130}$$

The same approach can be undertaken using R-matrix cross section sensitivities to windowed multipoles $\frac{\partial\sigma}{\partial\Pi}(E)$, established in equations (E.126) of lemma 5, and then propagating the windowed multipole covariances $\mathbb{V}\mathrm{ar}\left(\Pi\right)$ to first order, yielding cross section covariances

$$\mathbb{V}\mathrm{ar}\left(\sigma_{\Pi}(E)\right) = \left(\frac{\partial\sigma(E)}{\partial\Pi}\right)\mathbb{V}\mathrm{ar}\left(\Pi\right)\left(\frac{\partial\sigma(E)}{\partial\Pi}\right)^{\dagger} \tag{E.131}$$

2. Stochastic cross sections consist of sampling resonance parameters $\left\{\Gamma\right\}$ from their uncertainty distribution – say multivariate normal $\mathcal{N}\left(\Gamma, \mathbb{V}\mathrm{ar}\left(\Gamma\right)\right)$ – and computing the corresponding cross section $\sigma_{\Gamma}(E)$ as a function of energy

$$\mathrm{d}\mathbb{P}\Big(\sigma_{\Gamma}(E)\Big) = \sigma_{\mathrm{d}\mathbb{P}(\Gamma)}(E) \tag{E.132}$$

Alternatively, one could sample multipoles $\left\{\Pi\right\}$ from a windowed multipole distribution – say multivariate normal $\mathcal{N}\left(\Pi, \mathbb{V}\mathrm{ar}\left(\Pi\right)\right)$ – and correspondingly generate Windowed Multipole stochastic cross sections

$$\mathrm{d}\mathbb{P}\Big(\sigma_{\Pi}(E)\Big) = \sigma_{\mathrm{d}\mathbb{P}(\Pi)}(E) \tag{E.133}$$

Stochastic cross sections uncertainties only match first order sensitivity approaches (E.130) and (E.131) for very small covariances. This is because normally distributed resonance parameters do not translate into normally distributed cross sections (E.132): sampling resonance parameters from $\mathcal{N}\left(\Gamma, \mathbb{V}\mathrm{ar}\left(\Gamma\right)\right)$ and then computing the corresponding cross sections (E.5) and (E.10) through R-matrix equations (E.7), (E.14), (E.15), (E.16), and (E.17), cannot in general lead to normally distributed cross sections $\sigma_{\Gamma}(E)$ at all energies. However, they do in the linear case, which is a good first-order approximation for small covariances.

Stochastic cross sections (E.132) are at the core of the TENDL library [207, 209], and being able to sample them is a necessary prerequisite to the *Total Monte Carlo* uncertainty propagation method [283, 285, 55]. In practice, this has been a major computational challenge, requiring to sample resonance parameters from standard nuclear data libraries, reconstruct the corresponding nuclear cross sections at zero Kelvin (0K), and then process each one (with codes such as NJOY [228]) to compute the corresponding cross sections at temperature T (c.f. discussion of Doppler broadening and thermal scattering in section E.5). All this is costly, and storing the pre-processed cross sections consumes vasts amount of memory. Because one can directly compute Doppler-broadened nuclear cross sections from Windowed Multipole

parameters $\left\{\Pi\right\}$ (c.f. theorem 17 section E.5), the Windowed Multipole Library can generate stochastic cross sections (E.133) on-the-fly, without any pre-processing nor storage, a true physics-enabled computational breakthrough.

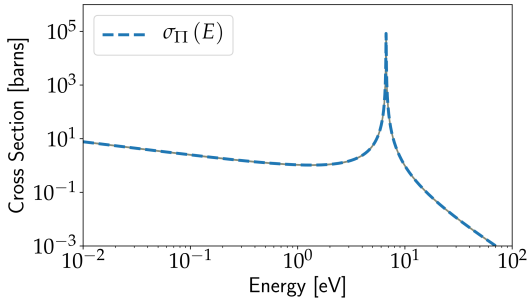

(a) ^{238}U first capture resonance, parameters sampled from ENDF/B-VIII uncertainty. 30 samples shown here.

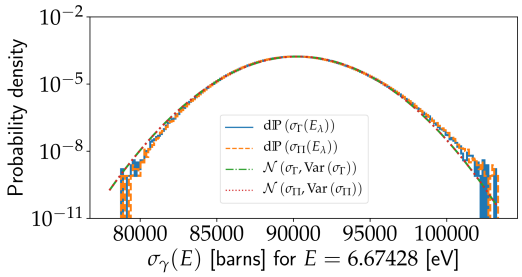

(b) Cross section histogram at resonance energy $E_\lambda = 6.67428$ eV.

Figure E-4: R-matrix cross sections uncertainty, computed either from the ENDF/B-VIII resonance parameters covariance $\mathbb{V}\mathrm{ar}(\Gamma)$ (table E.2 in appendix E.8), or from the multipoles covariance $\mathbb{V}\mathrm{ar}(\Pi)$, as converted through (E.129), for both the stochastic cross sections (E.132, E.133) and the sensitivities approach (E.130, E.131).

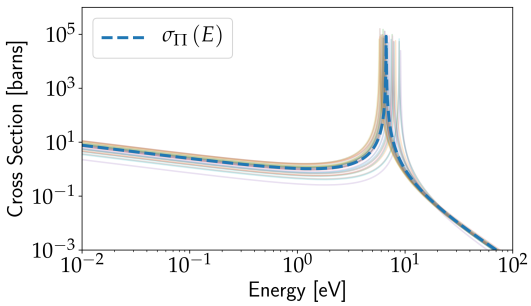

(a) ^{238}U first capture resonance, parameters sampled from an enlarged ENDF/B-VIII uncertainty. 30 samples shown here.

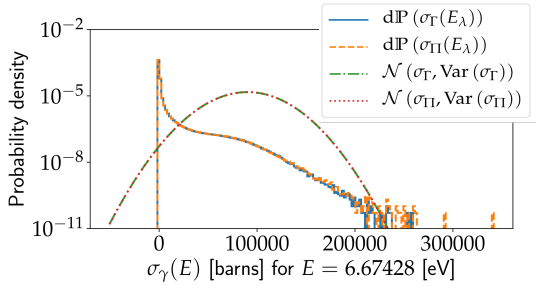

(b) Cross section histogram at resonance energy $E_\lambda = 6.67428$ eV.

Figure E-5: R-matrix cross sections uncertainty, computed either from the enlarged ENDF/B-VIII resonance parameters covariance $\mathbb{V}\mathrm{ar}(\Gamma)$ (table E.2 in appendix E.8), or from the multipoles covariance $\mathbb{V}\mathrm{ar}(\Pi)$, as converted through (E.129), for both the stochastic cross sections (E.132, E.133) and the sensitivities approach (E.130, E.131).

Regardless of the method employed to represent nuclear cross section uncertainty, it would be desirable that the uncertainties stemming from a windowed multipole representation $\left\{\Pi\right\}$ are consistent with those stemming from resonance parameters $\left\{\Gamma\right\}$ upon converting their covariances as indicated in equation (E.129) of theorem 16. We undertook numerical experiments to measure the cross section uncertainty distributions generated by either covariances $\mathbb{V}\mathrm{ar}(\Gamma)$ or $\mathbb{V}\mathrm{ar}(\Pi)$, for both sensitivity method

(E.130) and (E.131), or stochastic cross sections (E.132) and (E.133). We treated the simple case of the first single-level Breit-Wigner capture resonance of uranium isotope ^{238}U, which admits closed form explicit expressions for the multipoles, the cross sections, and the sensitivities, all documented in appendix E.8. We compared the methods for both the ENDF/B-VIII.0 resonance parameters covariance (which is small as this is a very well known resonance), and an enlarged covariance matrix which conserves the same correlations but brings the cross section dependency past the linear regime. Both covariances are documented in table E.2 (appendix E.8), and figures E-4 and E-5 show the following trends:

- For the sensitivity method (E.130) or (E.131), the cross section uncertainty is identical for either the resonance parameter covariance $\mathbb{V}\mathrm{ar}(\Gamma)$ or the windowed multipole covariance $\mathbb{V}\mathrm{ar}(\Pi)$, which is the immediate consequence of conversion (E.129).

- For the stochastic cross section method (E.132) or (E.133), sampling parameters from $\mathcal{N}(\Gamma, \mathbb{V}\mathrm{ar}(\Gamma))$ or $\mathcal{N}(\Pi, \mathbb{V}\mathrm{ar}(\Pi))$ generates similar cross section distributions.

In the small covariance case of figure E-4, the stochastic cross section distributions (E.132) and (E.133) are very close to the normal distributions from the sensitivity approach (E.131), though at the tails they start differing. In the large covariance case of figure E-5, the stochastic cross sections distributions are radically different from the normal distribution of the sensitivity method. This discrepancy is made more blatant because the cross section distribution is recorded at resonance peak energy $E_\lambda = 6.67428$ eV, hence a small shift in resonance energy E_λ can dramatically lower the cross section value. This illustrates the fact that in theorem 16, when converting the resonance parameters covariances $\mathbb{V}\mathrm{ar}(\Gamma)$ into Windowed Multipoles covariances $\mathbb{V}\mathrm{ar}(\Pi)$ through (E.129), the linear assumption used for the local inversion using Jacobians $\left(\frac{\partial \Pi}{\partial \Gamma}\right)$ from (E.128) holds for a wider range of resonance parameters than the liner assumption for the cross section sensitivity method (E.131). This can be seen in figure E-3, where the tangent lines from Jacobians $\left(\frac{\partial \Pi}{\partial \Gamma}\right)$ are close to the conversion surface, trajectories of $\Pi(\Gamma)$, even after three standard deviations of the large covariance matrix, something clearly not true of the cross section linear behavior at peak energy from figure E-5.

Therefore, whichever method is chosen to represent the nuclear cross sections uncertainty, the Windowed Multipoles covariances $\mathbb{V}\mathrm{ar}(\Pi)$ from theorem 16 faithfully reproduce the uncertainty from the resonance parameters covariances $\mathbb{V}\mathrm{ar}(\Gamma)$.

E.5 Doppler broadening of Windowed Multipole cross sections

Hitherto, we have established that the zero Kelvin (0 K) windowed multipole representation of cross sections is equivalent to the traditional Wigner-Eisenbud R-matrix

parametrization, in both cross section values and their uncertainties. We henceforth study how temperature affects R-matrix cross sections at the nuclear level through *Doppler broadening* (we do not address thermal neutron scattering at the crystalline level), and derive how the windowed multipole representation exhibits a major advantage: in its form (E.96) – exact for zero-threshold channels or windows without thresholds, and otherwise an accurate approximation – the window multipole representation of R-matrix cross sections can be Doppler broadened precisely by means of closed-form formulae (theorem 17). This enables the long sought-after computational capability of on-the-fly Doppler broadening of nuclear cross sections [300, 76, 118, 190, 313, 326, 146, 145, 124].

E.5.1 Doppler broadening of nuclear cross sections: Solbrig's Kernel

As temperature rises, nuclei vibrate, so that the effective cross section for a beam of particles sent upon a target at a given energy and wavenumber is the statistical result of the zero Kelvin cross sections averaged out on all the possible relative energies at which the target and the beam interact. For non-relativistic, non-massless particles (not photons) in the semi-classical representation, Doppler broadening of nuclear cross section is the process of integration over the target velocity distribution, assuming the latter is an isotropic Maxwellian (that is a Boltzmann distribution of energies). Solbrig derived this Doppler broadening integral in eq. (3) p. 259 of [300], where the cross section $\sigma_T(E)$ at temperature T and energy E (in the laboratory coordinates) is related to the cross section $\sigma(E)$ at temperature T_0 as:

$$E\sigma_T(E) = \int_0^\infty \frac{\sigma(E')E'^{\frac{1}{2}}}{2\beta\sqrt{\pi}} \left[\mathrm{e}^{-\left(\frac{\sqrt{E'}-\sqrt{E}}{\beta}\right)^2} - \mathrm{e}^{-\left(\frac{\sqrt{E'}+\sqrt{E}}{\beta}\right)^2} \right] \mathrm{d}E' \tag{E.134}$$

where β is the square root temperature energy parameter:

$$\beta \triangleq \sqrt{\frac{k_{\mathbb{B}}(T-T_0)}{A}} \tag{E.135}$$

where A designates the atomic mass number, and $k_{\mathbb{B}}$ the universal Boltzmann constant.
Upon change of variable to $z = \sqrt{E}$, the Doppler broadening operation (E.134) becomes Solbrig's kernel:

$$\begin{aligned} z^2\sigma_T(z) &= \int_0^\infty x^2\sigma_{T_0}(x)\ \mathcal{K}_\beta^{\mathbb{D}}(z,x)\mathrm{d}x \\ \text{where: } \mathcal{K}_\beta^{\mathbb{D}}(z,x) &\triangleq \frac{1}{\beta\sqrt{\pi}} \left[\mathrm{e}^{-\left(\frac{z-x}{\beta}\right)^2} - \mathrm{e}^{-\left(\frac{z+x}{\beta}\right)^2} \right] \end{aligned} \tag{E.136}$$

Note that for zero-threshold channels, where $z \propto k_c(E)$, Solbrig kernel (E.136) is an integral operator acting on $k_c^2(E)\ \sigma_c(E)$, which is the transmission matrix square

amplitudes from cross section definition (E.5). The Solbrig kernel (E.136) thus acts directly on the interaction probabilities, rather than the actual cross section, just as the channel reversibility equivalence (E.11).

Solbrig kernel integral (E.136) has presented major computational challenges in nuclear reactor physics. When no information is provided as to the functional form of the zero Kelvin cross section $\sigma(E)$ – i.e. it is considered a point-wise input – the traditional way of computing the Doppler broadened cross section at any temperature $\sigma_T(E)$ has been to pre-tabulate exact cross sections $\sigma_{T_i}(E)$ (usually using the SIGMA1 algorithm of [118]) for a grid of reference temperatures $\left\{T_i\right\}$, and then interpolate between these points to obtain $\sigma_T(E)$ [111, 313, 261]. However, storing all these pre-computed cross sections at reference temperatures $\left\{T_i\right\}$ represents a considerable memory burden, which is why methods to minimize the memory footprint and perform Doppler broadening (E.136) on-the-fly have been actively sought after [326]. The most state-of-the-art approaches are either optimal temperature Doppler kernel reconstruction quadratures [124] (which only require 10 reference temperatures $\left\{T_i\right\}$ for standard nuclear reactor codes), new Fourier transform methods [145], or Monte Carlo target motion sampling rejection schemes [316, 317, 288].

To do better, one must look at the functional form of the cross section. When the reference temperature is zero Kelvin $T_0 = 0\text{K}$, we have shown in section E.3 that R-matrix cross sections are the sum of threshold behavior and resonances. Resonances have traditionally been Doppler broadened approximately, using Voigt profiles [300], as we here recall in section E.5.2.

E.5.2 Approximate Doppler broadening of Breit-Wigner resonances: Voigt profiles

The traditional approach to Doppler broadening nuclear cross sections has been to consider individual Single-Level Breit-Wigner resonances (E.74) at zero Kelvin, with both symmetric (Cauchy-Lorentz distributions) and anti-symmetric components, assuming it has a zero-energy threshold where it behaves as an s-wave neutron channel (angular momentum $\ell = 0$), so that we can multiply the resonance (E.74) by the threshold behavior $\frac{1}{\sqrt{E}}$, as described by Wigner in III.A.2 [322]:

$$\begin{aligned}\sigma_0^{\text{SLBW}}(E) &\triangleq \frac{1}{\sqrt{E}}\Re\left[\frac{a+\mathrm{i}b}{E-\mathcal{E}_j}\right] \\ &= \frac{1}{\sqrt{E}}\left[\left(\frac{a}{\Gamma_j/2}\right)\chi_0(x) + \left(\frac{b}{\Gamma_j/2}\right)\psi_0(x)\right]\end{aligned} \tag{E.137}$$

where $x \triangleq \left(\frac{E-E_j}{\Gamma_j/2}\right)$ with $\mathcal{E}_j \triangleq E_j - \mathrm{i}\frac{\Gamma_j}{2}$ from (E.40), and

$$\begin{aligned}\psi_0(x) &\triangleq \frac{1}{x^2+1} = \frac{\Gamma_j^2/4}{(E-E_j)^2+\frac{\Gamma_j^2}{4}} \\ \chi_0(x) &\triangleq \frac{x}{x^2+1} = \frac{(E-E_j)\,\frac{\Gamma_j}{2}}{(E-E_j)^2+\frac{\Gamma_j^2}{4}}\end{aligned} \tag{E.138}$$

Upon Doppler broadening (E.134), Single-Level Breit-Wigner resonance (E.137) becomes:

$$\sigma_T^{\mathrm{SLBW}}(E) = \frac{1}{\sqrt{E}}\left[\left(\frac{a}{\Gamma_j/2}\right)\chi_T(E) + \left(\frac{b}{\Gamma_j/2}\right)\psi_T(E)\right] \tag{E.139}$$

where χ_T and ψ_T are defined using $x' \triangleq \left(\frac{E'-E_j}{\Gamma_j/2}\right)$ as

$$\begin{aligned}\chi_T(E) &\triangleq \frac{E^{-\frac{1}{2}}}{2\beta\sqrt{\pi}}\int_0^\infty \chi_0(x')\left[\mathrm{e}^{-\left(\frac{\sqrt{E'}-\sqrt{E}}{\beta}\right)^2} - \mathrm{e}^{-\left(\frac{\sqrt{E'}+\sqrt{E}}{\beta}\right)^2}\right]\mathrm{d}E' \\ \psi_T(E) &\triangleq \frac{E^{-\frac{1}{2}}}{2\beta\sqrt{\pi}}\int_0^\infty \psi_0(x')\left[\mathrm{e}^{-\left(\frac{\sqrt{E'}-\sqrt{E}}{\beta}\right)^2} - \mathrm{e}^{-\left(\frac{\sqrt{E'}+\sqrt{E}}{\beta}\right)^2}\right]\mathrm{d}E'\end{aligned} \tag{E.140}$$

To compute these functions, the following approximations are then traditionally introduced (c.f. [300], or section 3.3.3 chapter 4, volume 1 of [99]):

1. the Maxwell approximation, whereby we assume the second exponential term is vanishingly small: $\mathrm{e}^{-\left(\frac{\sqrt{E'}+\sqrt{E}}{\beta}\right)^2} \ll 1$. This is valid for $E \gg \beta^2$, but fails at low energies or high temperatures,

2. a Taylor expansion around the energy of Doppler broadening: $E' = E + \epsilon$, with $\epsilon \ll 1$. This leads to $\sqrt{E'} - \sqrt{E} = \frac{\epsilon}{2\sqrt{E}} + \mathcal{O}(\epsilon^2)$, so that we approximate $\mathrm{e}^{-\left(\frac{\sqrt{E'}-\sqrt{E}}{\beta}\right)^2} \approx \mathrm{e}^{-\left(\frac{E'-E}{2\sqrt{E}\beta}\right)^2}$ in the integrals, which under change of variable $E' \to x'$ become

$$\begin{aligned}\psi_T(x) &\simeq \frac{1}{2\beta\sqrt{\pi E}}\frac{\Gamma_j}{2}\int_{-2E_j/\Gamma_j}^\infty \psi_0(x')\mathrm{e}^{-\frac{(x'-x)^2}{4\tau}}\mathrm{d}x' \\ \chi_T(x) &\simeq \frac{1}{2\beta\sqrt{\pi E}}\frac{\Gamma_j}{2}\int_{-2E_j/\Gamma_j}^\infty \chi_0(x')\mathrm{e}^{-\frac{(x'-x)^2}{4\tau}}\mathrm{d}x'\end{aligned}$$

   where we defined

$$\tau \triangleq 4E\left(\frac{\beta}{\Gamma_j}\right)^2 = 4E\frac{k_{\mathbb{B}}(T-T_0)}{A\Gamma_j^2} \tag{E.141}$$

3. we furthermore assume $2E_j \gg \Gamma_j$, so that we approximate the integral lower

limit to $-\infty$, yielding

$$\begin{aligned}\psi_T(x) &\simeq \frac{1}{\sqrt{4\pi\tau}}\int_{-\infty}^{+\infty}\frac{1}{1+x'^2}\mathrm{e}^{-\frac{(x'-x)^2}{4\tau}}\mathrm{d}x' \\ \chi_T(x) &\simeq \frac{1}{\sqrt{4\pi\tau}}\int_{-\infty}^{+\infty}\frac{x'}{1+x'^2}\mathrm{e}^{-\frac{(x'-x)^2}{4\tau}}\mathrm{d}x'\end{aligned} \tag{E.142}$$

The latter are the standard Voigt functions, $\mathrm{U}(x,\tau)$ and $\mathrm{V}(x,\tau)$, defined in section 7.19 of [250], which are related to the Faddeyeva function (E.150) defined in 7.2.3 [250], by:

$$\sqrt{\frac{\pi}{4\tau}}\mathrm{w}\left(\frac{x+\mathrm{i}}{2\sqrt{\tau}}\right) = \mathrm{U}(x,\tau)+\mathrm{i}\mathrm{V}(x,\tau)$$

for $\Im\left[\frac{x+\mathrm{i}}{2\sqrt{\tau}}\right] > 0$. In the case $\Im\left[\frac{x+\mathrm{i}}{2\sqrt{\tau}}\right] < 0$, we use $-\left[\mathrm{w}\left(z^*\right)\right]^*$ to calculate the integral. So that the $\psi_T(E)$ and $\chi_T(E)$ functions can approximately be related to the Faddeyeva function as:

$$\begin{aligned}\psi_T(E) &\simeq \sqrt{\frac{\pi}{4\tau}}\Re\left[\mathrm{w}\left(\frac{x+\mathrm{i}}{2\sqrt{\tau}}\right)\right] \\ \chi_T(E) &\simeq \sqrt{\frac{\pi}{4\tau}}\Im\left[\mathrm{w}\left(\frac{x+\mathrm{i}}{2\sqrt{\tau}}\right)\right]\end{aligned} \tag{E.143}$$

So that the Doppler broadened Breit-Wigner resonance, under these approximations, can be expressed as:

$$\begin{aligned}\sigma_T^{\mathrm{SLBW}}(E) &\simeq \frac{1}{\sqrt{E}}\Re\left[\frac{a+\mathrm{i}b}{\mathrm{i}\Gamma_j/2}\sqrt{\frac{\pi}{4\tau}}\mathrm{w}\left(\frac{x+\mathrm{i}}{2\sqrt{\tau}}\right)\right] \\ &= \frac{1}{E}\Re\left[\sqrt{\pi}\frac{a+\mathrm{i}b}{\mathrm{i}2\beta}\mathrm{w}\left(\frac{E-\mathcal{E}_j}{2\beta\sqrt{E}}\right)\right]\end{aligned} \tag{E.144}$$

This has been the traditional "psi-chi" method to perform approximate Doppler broadening of nuclear resonances, though some improvements have been proposed (c.f. eq. (65) in [190]).

Note that the single-level Breit-Wigner profile (E.137) does not represent higher-order angular momenta for neutron channels, nor does it represent charged particles or photon channels (of any angular momenta), neither does it consider non-zero-threshold behaviors.

E.5.3 Analytic Doppler broadening of Windowed Multipole cross sections

Theorem 15 establishes the Windowed Multipole Representation as an equivalent formalism to parametrize R-matrix cross sections. Windowed Multipole cross sections take the form (E.96) for zero-threshold cross sections of any kind (photons, charged, higher angular momenta), and other thresholds can be approximated with this form (E.96), though not exactly. Theorem 17 shows how these Windowed Multipole cross

sections (E.96) can be Doppler broadened analytically to high accuracy, without having to assume an energy dependence of the Single-Level Breit-Wigner cross section form $\sigma_0^{\mathrm{SLBW}}(E)$ as in (E.137).

Theorem 17. *Doppler broadening of Windowed Multipole cross sections*
Consider the Windowed Multipole Representation of R-matrix cross sections (E.96), i.e. locally of the form:

$$\sigma(z) \underset{\mathcal{W}(E)}{=} \frac{1}{z^2}\Re_{\mathrm{cont}}\left[\sum_{j\geq 1}\frac{r_j}{z-p_j}\right] + \sum_{n\geq -2} a_n z^n$$

Upon integration against the Solbrig kernel (E.136), the Doppler broadened cross section at temperature T takes the following analytic expression:

$$\begin{aligned}\sigma_T(z) \underset{\mathcal{W}(E)}{=} & \sum_{n\geq -2} a_n \mathrm{D}_\beta^n(z) \\ & + \frac{1}{z^2}\Re\left[\mathrm{i}\sqrt{\pi}\sum_{j\geq 1}\frac{r_j}{\beta}\ \mathrm{w}\left(\frac{z-p_j}{\beta}\right)\right] \\ & - \frac{1}{z^2}\Re\left[\mathrm{i}\sqrt{\pi}\sum_{j\geq 1}\frac{r_j}{\beta}\ \mathrm{C}\left(\frac{z}{\beta},\frac{p_j}{\beta}\right)\right]\end{aligned} \tag{E.145}$$

where $\mathrm{C}\left(\frac{z}{\beta},\frac{p_j}{\beta}\right)$ *is a correction term defined as:*

$$\mathrm{C}\left(\frac{z}{\beta},\frac{p_j}{\beta}\right) \triangleq \frac{2\,p_j}{\mathrm{i}\pi\beta}\int_0^\infty \frac{\mathrm{e}^{-\left(\frac{z}{\beta}+t\right)^2}}{t^2-\left(\frac{p_j}{\beta}\right)^2}\mathrm{d}t \tag{E.146}$$

which is negligible in most physical ranges of temperatures and energies, so that Doppler broadened Windowed Multipole cross sections can be well approximated as

$$\begin{aligned}\sigma_T(z) \underset{\mathcal{W}(E)}{\simeq} & \frac{1}{z^2}\Re\left[\sqrt{\pi}\sum_{j\geq 1}\frac{r_j}{\mathrm{i}\beta}\ \mathrm{w}\left(\frac{z-p_j}{\beta}\right)\right] \\ & + \sum_{n\geq -2} a_n \mathrm{D}_\beta^n(z)\end{aligned} \tag{E.147}$$

where $\mathrm{D}_\beta^n(z)$ *are the Doppler broadened monomials:*

$$\mathrm{D}_\beta^n(z) \triangleq \int_0^\infty \frac{x^{n+2}}{z^2}\mathcal{K}_\beta^{\mathbb{D}}(z,x)\mathrm{d}x \tag{E.148}$$

which are subject to the following recurrence formulae from elemental Gaussian and

error functions (defined in eq. 7.2.1 of [250]) [197]:

$$\begin{aligned}
\mathrm{D}_\beta^{n+2}(z) &\underset{\forall n\geq 1}{=} \left[\frac{\beta^2}{2}(2n+1)+z^2\right]\mathrm{D}_\beta^n(z) \\
&\quad -\left(\frac{\beta^2}{2}\right)^2 n(n-1)\mathrm{D}_\beta^{n-2}(z) \\
\mathrm{D}_\beta^0(z) &= \left[\frac{\beta^2}{2}+z^2\right]\mathrm{D}_\beta^{-2}(z)+\frac{\beta}{z\sqrt{\pi}}\mathrm{e}^{-\left(\frac{z}{\beta}\right)^2} \\
\mathrm{D}_\beta^{-1}(z) &= \frac{1}{z} \\
\mathrm{D}_\beta^{-2}(z) &= \frac{1}{z^2}\mathrm{erf}\left(\frac{z}{\beta}\right)
\end{aligned} \tag{E.149}$$

and where $\mathrm{w}(z)$ *is the Faddeyeva function (defined in eq. 7.2.3 of [250]),*

$$\mathrm{w}(z) \triangleq \mathrm{e}^{-z^2}\Big(1-\mathrm{erf}\left(-\mathrm{i}z\right)\Big) = \mathrm{e}^{-z^2}\left(1+\frac{2\mathrm{i}}{\sqrt{\pi}}\int_0^z e^{t^2}\mathrm{d}t\right) \tag{E.150}$$

called at poles in the complex lower semi-plane, i.e. $\Im\left[\frac{z-p_j}{\beta}\right] > 0$*. For all other poles, which satisfy* $\Im\left[\frac{z-p_j}{\beta}\right] \leq 0$*, we use the fact that the Windowed Multipole Representation has complex conjugate poles to call the Faddeyeva function at* $-\left[\mathrm{w}\left(z^*\right)\right]^* = -\mathrm{w}\left(-z\right)$*.*

Proof. This analytic Doppler broadening comes from:

$$\begin{aligned}
\sigma_T(z) &\underset{\mathcal{W}(E)}{=} \frac{1}{z^2}\Re\left[\sum_{j\geq 1} r_j \int_0^\infty \frac{\mathcal{K}_\beta^{\mathbb{D}}(z,x)}{x-p_j}\mathrm{d}x\right] \\
&\quad + \sum_{n\geq -2} a_n \mathrm{D}_\beta^n(z)
\end{aligned}$$

Doppler broadening of the Laurent expansion part (E.148), which describes the threshold behavior, was established in [124] (eq. (14) to (16)), and the recurrence formulae (E.149) are obtained through integration by parts.
The resonances Doppler broadening was established in [190] (eq. (70) to (75)), which

we here recall

$$\begin{aligned}
&\beta\sqrt{\pi}\int_0^\infty \frac{\mathcal{K}_\beta^{\mathbb{D}}(z,x)}{x-p_j}\mathrm{d}x \triangleq \int_0^\infty \frac{\mathrm{d}x}{x-p_j}\left[\mathrm{e}^{-\left(\frac{z-x}{\beta}\right)^2} - \mathrm{e}^{-\left(\frac{z+x}{\beta}\right)^2}\right] \\
&= \int_{-\infty}^\infty \frac{\mathrm{e}^{-\left(\frac{z-x}{\beta}\right)^2}}{x-p_j}\mathrm{d}x - \int_{-\infty}^0 \frac{\mathrm{e}^{-\left(\frac{z-x}{\beta}\right)^2}}{x-p_j}\mathrm{d}x - \int_0^\infty \frac{\mathrm{e}^{-\left(\frac{z+x}{\beta}\right)^2}}{x-p_j}\mathrm{d}x \\
&= \int_{-\infty}^\infty \frac{\mathrm{e}^{-t^2}}{t-\left(\frac{z-p_j}{\beta}\right)}\mathrm{d}t + \int_0^\infty \mathrm{e}^{-\left(\frac{z+x}{\beta}\right)^2}\left[\frac{1}{x+p_j} - \frac{1}{x-p_j}\right]\mathrm{d}x \\
&= \mathrm{i}\pi\ \mathrm{w}\left(\frac{z-p_j}{\beta}\right) - 2p_j\int_0^\infty \frac{\mathrm{e}^{-\left(\frac{z+x}{\beta}\right)^2}}{x^2-p_j^2}\mathrm{d}x
\end{aligned}$$

where in the last line we introduced the Faddeyeva function (E.150), defined in eq. 7.2.3 of [250], which admits the following integral representation for $\Im[z] > 0$:

$$\mathrm{w}(z) \underset{\Im[z]>0}{=} \frac{1}{\mathrm{i}\pi}\int_{-\infty}^\infty \frac{\mathrm{e}^{-t^2}}{t-z}\mathrm{d}t = \frac{2z}{\mathrm{i}\pi}\int_0^\infty \frac{\mathrm{e}^{-t^2}}{t^2-z^2}\mathrm{d}t \tag{E.151}$$

In the case $\Im[z] < 0$, we then use the following integral representation:

$$-\left[\mathrm{w}(z^*)\right]^* = -\mathrm{w}(-z) \underset{\Im[z]<0}{=} \frac{1}{\mathrm{i}\pi}\int_{-\infty}^\infty \frac{\mathrm{e}^{-t^2}}{t-z}\mathrm{d}t \tag{E.152}$$

So that, calling the Faddeyeva function directly for the poles in the complex lower semi-plane, $\Im\left[\frac{z-p_j}{\beta}\right] > 0$, while for the others we use $-\left[\mathrm{w}\left(z^*\right)\right]^* = -\mathrm{w}\left(-z\right)$ to calculate the integral representation (the pole representation has complex conjugate poles), the Solbrig kernel Doppler broadening operation yields (E.145). Hwang undertook an in-depth study of the correction term $\mathrm{C}\left(\frac{z}{\beta}, \frac{p_j}{\beta}\right)$ in section IV.D of [190], showing it is negligible in most physical applications. Therefore, approximation (E.147) is effectively faithful, in particular at high energies-to-temperature ratios $z/\beta \gg 1$. □

Compared to the traditional "psi-chi" method (E.144), theorem 17 gives a much more general way to Doppler broaden nuclear cross sections, applicable to charged or uncharged particles of any angular momentum. Theorem 17 also motivates why we decomposed the resonances in $z = \sqrt{E}$ space: it enables more accurate analytic Doppler broadening, since the latter happens in wavenumber space as Hwang showed in eq. (65) of [190].

Note that Hwang derived equations to analytically Doppler broaden his pole representation (E.112), with energy-dependent residues, showing that the $\mathrm{e}^{-2\mathrm{i}\rho}$ component shifts the Faddeyeva function evaluation, adding a purely imaginary offset in eq. (6) of [189]. Nonetheless, this approach is not generalizable to Coulomb channels nor to thresholds, while theorem 17 is.

To compare these different Doppler broadening methods, we conducted numerical calculations on the first capture resonance of ^{238}U, in the simple Single-Level Breit-Wigner resonance case of appendix E.8, reporting the results in figure E-6.

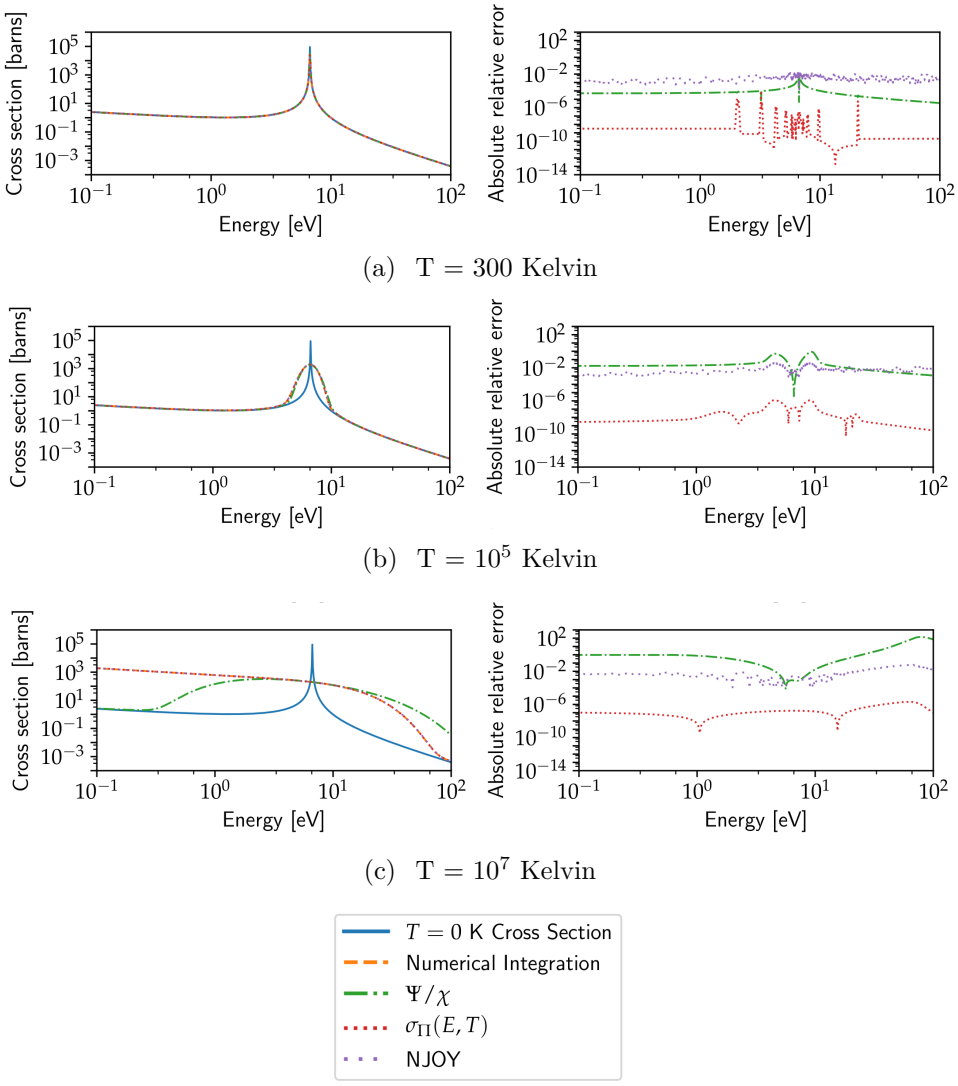

Figure E-6: Accuracy of different Doppler-broadening methods. Using the SLBW resonance description given in appendix E.8, the cross section (E.183) is reconstructed at T=0K. For each temperature $\{300, 10^5, 10^7\}$ Kelvin, the cross section is broadened using four different methods: (i) numerical integration of the Solbrig Kernel (E.136); (ii) Using the ψ_T/χ_T approximation (E.143) for SLBW Doppler broadening (E.144); (iii) conversion (E.187) of the resonance parameters $\{\Gamma\}$ to multipoles $\{\Pi\}$ and analytic Doppler broadening of Windowed Multipole Representation (E.186) from theorem 17 equation (E.147); (iv) formulation of the parameters in ENDF format and processing using NJOY [228]. For each temperature, the right column shows the absolute relative error for methods (ii), (iii), and (iv) to the direct integration of the Solbrig Kernel (i). Note: NJOY was run with a tolerance parameter of 10^{-2} as higher accuracy required a prohibitively long computation time.

They show the analytic Windowed Multipole Doppler broadening exactly matches the direct piece-wise integration of Solbrig's kernel (E.136) to 10^{-6} relative error, significantly outperforming the SIGMA1 method [118] of NYOJ [228], while the tra-

ditional ψ_T/χ_T approximation (E.144) breaks down at high temperatures. Note than in this particular SLBW case of appendix E.8, the poles are exact opposites of one another, while the residues are the same, so that they cancel out of the C-function correction (E.146), hence the analytic Doppler broadening of the Windowed Multipole Representation (E.147) is exact. This cancelling out of C-function correction (E.146) is also true in general of zero threshold neutral particles s-wave cross sections, which behave as $1/z$ at low energies, thereby yielding identical residues $r_j^+ = r_j^-$ for opposite z-poles pairs $p_j^+ = -p_j^-$.

E.5.4 Temperature derivatives of Doppler broadened Windowed Multipole cross sections

The analytic Doppler broadening of Windowed Multipole cross sections (theorem 17) has the additional advantage that one can compute all its temperature derivatives by means of simple recurrence formulae, as we here establish in theorem 18.

Theorem 18. *Temperature derivatives of Windowed Multipole cross sections*
Consider the approximate Doppler broadened Windowed Multipole Representation of R-matrix cross sections (E.147) from theorem 17, upon change of variables $\theta \triangleq \frac{1}{\beta}$

$$\sigma_T(z) \underset{\mathcal{W}(E)}{\simeq} \frac{1}{z^2}\Re\left[\mathrm{i}\sqrt{\pi}\sum_{j\geq 1} r_j\ \theta\ \mathrm{w}\Big(\theta\,(z-p_j)\Big)\right] + \sum_{n\geq -2} a_n \mathrm{D}_\beta^n(z)$$

Then its k-th temperature derivative can be computed as

$$\partial_T^{(k)}\sigma_T(z) \underset{\mathcal{W}(E)}{\simeq} \frac{1}{z^2}\Re\left[\mathrm{i}\sqrt{\pi}\sum_{j\geq 1} r_j\ \mathrm{X}_\beta^{(k)}\,(z-p_j)\right] + \sum_{n\geq -2} a_n\ \partial_T^{(k)}\mathrm{D}_\beta^n(z) \tag{E.153}$$

$\mathrm{X}_\beta^{(k)}\,(z-p_j)$ *are the k-th temperature derivatives of the Doppler broadened resonances:*

$$\begin{aligned}\mathrm{X}_\beta^{(k)}\,(z-p_j) &\triangleq \partial_T^{(k)}\left[\theta\ \mathrm{w}\Big(\theta\,(z-p_j)\Big)\right] \\ &= \sum_{n=1}^{k}\Bigg[\Big(\partial_\theta^{(n)}\theta\ \mathrm{w}\Big(\theta(z-p_j)\Big)\Big) \quad \times \\ &\qquad B_{k,n}\left(\theta^{(1)},\theta^{(2)},\ldots,\theta^{(k-n+1)}\right)\Bigg]\end{aligned} \tag{E.154}$$

where the sum is the Arbogast composite derivatives (Faà di Bruno) formula [61],

linking the θ-derivatives

$$\partial_\theta^{(n)}\theta\ \mathrm{w}\Big(\theta(z-p_j)\Big) \underset{\forall n\geq 1}{=} -\frac{(z-p_j)^{n-1}}{2}\mathrm{w}^{(n+1)}\Big(\theta(z-p_j)\Big) \tag{E.155}$$

to the $\theta^{(n)}$ temperature derivatives of θ

$$\theta^{(n)} \triangleq \partial_T^{(n)}\theta = \frac{1}{\beta}\left(\frac{-1}{2}\right)^n \frac{(2n-1)!!}{(T-T_0)^n} \tag{E.156}$$

by means of the partial exponential Bell polynomials $B_{k,n}\left(\theta^{(1)},\theta^{(2)},\ldots,\theta^{(k-n+1)}\right)$ [71, 49, 85].
The derivatives of the Faddeyeva function can be computed using recurrence formulae (c.f. 7.10 in [250]):

$$\begin{aligned}\mathrm{w}^{(1)}(z) &= -2z\mathrm{w}(z) + \frac{2\mathrm{i}}{\sqrt{\pi}}\\ \mathrm{w}^{(n+2)}(z) &= -2z\mathrm{w}^{(n+1)}(z) - 2(n+1)\mathrm{w}^{(n)}(z)\end{aligned} \tag{E.157}$$

$\partial_T^{(k)}\mathrm{D}_\beta^n(z)$ are the temperature derivatives of the Doppler broadened monomials, which are subject to the following recurrence formulae, defining $a \triangleq \frac{k_{\mathbb{B}}}{A}$:

$$\begin{aligned}\partial_T^{(k)}\mathrm{D}_\beta^{n+2}(z) \underset{\forall n\geq 1}{=} &\left[\frac{\beta^2}{2}(2n+1)+z^2\right]\partial_T^{(k)}\mathrm{D}_\beta^n(z)\\ &+\frac{a}{2}(2n+1)k\ \partial_T^{(k-1)}\mathrm{D}_\beta^n(z)\\ &-\frac{n(n-1)}{4}\Bigg[\beta^4\partial_T^{(k)}\mathrm{D}_\beta^{n-2}(z)\\ &\qquad + \quad 2a\beta k\ \partial_T^{(k-1)}\mathrm{D}_\beta^{n-2}(z)\\ &\qquad + \quad a^2k(k-1)\partial_T^{(k-2)}\mathrm{D}_\beta^{n-2}(z)\Bigg]\end{aligned} \tag{E.158}$$

$$\begin{aligned}\partial_T^{(k)}\mathrm{D}_\beta^0(z) &= \left[\frac{\beta^2}{2}+z^2\right]\partial_T^{(k)}\mathrm{D}_\beta^{-2}(z) + \frac{a}{2}k\ \partial_T^{(k-1)}\mathrm{D}_\beta^{-2}(z)\\ &\quad +\frac{1}{z\sqrt{\pi}}\Big[\beta^2\partial_T^{(k)}\theta\mathrm{e}^{-(z\theta)^2} + ak\,\partial_T^{(k-1)}\theta\mathrm{e}^{-(z\theta)^2}\Big]\\ \partial_T^{(k)}\mathrm{D}_\beta^{-1}(z) &= \frac{1}{z}\delta_{k,0}\\ \partial_T^{(k)}\mathrm{D}_\beta^{-2}(z) &= \frac{1}{z^2}\partial_T^{(k)}\mathrm{erf}\,(z\theta)\end{aligned}$$

In recurrence relations (E.158), the terms $\partial_T^{(k)}\theta\mathrm{e}^{-(z\theta)^2}$ can themselves be computed

using Arbogast's formula:

$$\partial_T^{(k)}\theta \mathrm{e}^{-(z\theta)^2} = \mathrm{e}^{-(z\theta)^2}\sum_{n=1}^{k}\Bigg[F_z^{(n)}(\theta) \quad \times \\ B_{k,n}\left(\theta^{(1)},\theta^{(2)},\ldots,\theta^{(k-n+1)}\right)\Bigg] \tag{E.159}$$

where $F_z^{(n)}(\theta)$ *are polynomials of degree* $n+1$ *defined as*

$$F_z^{(n)}(\theta) \triangleq \mathrm{e}^{(z\theta)^2}\partial_\theta^{(n)}\theta \mathrm{e}^{-(z\theta)^2} = \sum_{i=0}^{n+1}\alpha_i^{(n)}\theta^i \tag{E.160}$$

which are recursively constructed from $F_z^{(0)}(\theta) = \theta$ *as*

$$F_z^{(n+1)}(\theta) = \partial_\theta F_z^{(n)}(\theta) - 2z^2\theta F_z^{(n)}(\theta) \tag{E.161}$$

entailing these recurrence formulae on their coefficients:

$$\begin{array}{rclrcl} \alpha_0^{(0)} & = & 0 & \alpha_1^{(0)} & = & 1 \\ \alpha_{n+1}^{(n+1)} & = & -2z^2\alpha_n^{(n)} & \alpha_{n+2}^{(n+1)} & = & -2z^2\alpha_{n+1}^{(n)} \\ \alpha_i^{(n+1)} & \underset{1\leq i\leq n}{=} & (i+1)\alpha_{i+1}^{(n)} - 2z^2\alpha_{i-1}^{(n)} & & & \end{array} \tag{E.162}$$

Finally, the terms $\partial_T^{(k)}\mathrm{erf}\,(z\theta)$ *in recurrence relations (E.158) can also be computed using Arbogast's formula:*

$$\partial_T^{(k)}\mathrm{erf}\,(z\theta) = \sum_{n=1}^{k}\left(\partial_\theta^{(n)}\mathrm{erf}\,(z\theta)\right)\; B_{k,n}\left(\theta^{(1)},\ldots,\theta^{(k-n+1)}\right) \tag{E.163}$$

in which the θ *derivatives can be expressed as*

$$\partial_\theta^{(n)}\mathrm{erf}\,(z\theta) \underset{n\geq 1}{=} z^n(-1)^{n-1}\frac{2}{\sqrt{\pi}}\mathrm{H}_{n-1}\left(z\theta\right)\mathrm{e}^{-(z\theta)^2} \tag{E.164}$$

where the Hermite polynomials $\mathrm{H}_n(z)$ *are recursively calculable from* $\mathrm{H}_0 = 1$ *and* $\mathrm{H}_1 = 2z$ *as:*

$$\mathrm{H}_{n+1} \underset{n\geq 1}{=} 2z\mathrm{H}_n - 2n\mathrm{H}_{n-1} \tag{E.165}$$

Proof. The underlying assumption of the proof is that one can neglect the derivatives of the correction term (E.146). The proof consists of a series of derivatives expanded using the general Leibniz rule and the Arbogast formula for composite derivatives (Faà di Bruno) (c.f. p.43 of [61]), in which the Bell polynomials can be computed as referenced in [71, 49, 85]. Direct differentiation yields the temperature derivatives of θ (E.156). Expression (E.155) is obtained using the Faddeyeva function recurrence formula (E.157), documented in 7.10 of [250]. The $F_z^{(n)}(\theta)$ polynomials (E.160) are defined from $\partial_\theta^{(n)}\theta\mathrm{e}^{-(z\theta)^2} = F_z^{(n)}(\theta)\mathrm{e}^{-(z\theta)^2}$ and their degree $n+1$ stems from the recur-

sive derivatives (E.161) initialized at $F_z^{(0)}(\theta) = \theta$, entailing the recurrence formula for the coefficients (E.162). Similarly, expression (E.164) is derived from change of variable $z \to \theta z$, and using the derivative formula for the error function (c.f. Abramowitz & Stegun, p.298, eq. 7.1.19 [51], or 7.10.1 in [250]):

$$\mathrm{erf}^{(n+1)}(z) = (-1)^n \frac{2}{\sqrt{\pi}} \mathrm{H}_n(z) \mathrm{e}^{-z^2}$$

while the Hermite polynomials recurrence relation (E.165) is well known and documented (c.f. 18.9 of [250]). □

Underpinning this direct differentiation approach is the assumption that the C-function correction term (E.146), itself negligible, also has negligible temperature derivatives. It is nonetheless possible to extend this method to explicitly include thermal derivatives of the correction term (E.146), by noticing that these derivatives follow a similar polynomial structure as (E.160) and are subject to a recurrence relation similar to (E.161).

E.5.5 Fourier transform approach to temperature treatment

Ferran developed a more general approach, based on Fourier transforms, to Doppler broaden nuclear nuclear cross sections (we here only discussed Doppler broadening of angle-integrated cross sections)[145]. In theorem 19, we generalize Ferran's method, begetting arbitrary-order temperature derivatives of Doppler broadened cross sections, while setting a more general framework for temperature treatments such as low-energy thermal neutrons scattering with the phonons of the target's crystalline structure. Moreover, when applied to the Windowed Multipole Representation of R-matrix cross sections, this Fourier transform approach exactly accounts for the entire nuclear cross section, without neglecting the C-function correction term (E.146). This generality comes at the additional cost of having to compute Fourier transforms on-the-fly. Also, Fourier transforms can be numerically sensitive to the tails of distributions, meaning one has to be careful as to how the cross sections are extended beyond the treated windows (c.f. Ferran's discussion in section IV.B.2 of [145]).

We here recall Ferran's general Fourier transform method from [145]. The function $f \star g$ designates the convolution product between functions f and g, defined as:

$$f \star g\,(x) \underset{\forall x \in \mathbb{R}}{\triangleq} \int_{\mathbb{R}} f(t) g(x-t) \mathrm{d}t \tag{E.166}$$

Ferran expressed Solbrig's kernel (E.136) Doppler broadening operation as a convolution product by introducing the *Ferran representation* odd-parity function [145]:

$$s_T : z \in \mathbb{R} \mapsto \begin{cases} z^2 \sigma_T(z) & \forall z \in \mathbb{R}_+^* \\ 0 & \text{if } z = 0 \\ -z^2 \sigma_T(-z) & \forall z \in \mathbb{R}_-^* \end{cases} \tag{E.167}$$

Applying Solbrig's Kernel to s_T yields a linear convolution product operator that transforms the Ferran representation s_0 of the cross section at temperature T_0, to s_T at temperature $T > T_0$ as follows [145]:

$$s_T = s_0 \star \mathcal{K}_T^{\mathbb{B}} \tag{E.168}$$

where $\mathcal{K}_T^{\mathbb{B}}$ is the Maxwell-Bolztmann distribution of energies of the target

$$\mathcal{K}_T^{\mathbb{B}}(z) \underset{\forall z \in \mathbb{R}}{\triangleq} \frac{1}{\beta\sqrt{\pi}} \mathrm{e}^{-\left(\frac{z}{\beta}\right)^2} \tag{E.169}$$

The Fourier transform of a function f is defined as (unitary, ordinary frequency convention)[147]:

$$\widehat{f}(\nu) \triangleq \int_{\mathbb{R}} f(t)\ e^{-\mathrm{i}2\pi\nu t} \mathrm{d}t \tag{E.170}$$

for which the inverse Fourier transform is:

$$f(x) = \int_{\mathbb{R}} \widehat{f}(\nu)\ e^{i2\pi\nu x} \mathrm{d}\nu \tag{E.171}$$

The Fourier transform of any odd-parity function g can be expressed as

$$\widehat{g}(\nu) = -2i \int_{\mathbb{R}_+} g(t) \sin(2\pi\nu t)\, \mathrm{d}t \tag{E.172}$$

Fourier transforms satisfy the convolution property:

$$\widehat{f \star g} = \widehat{f}\ \widehat{g} \tag{E.173}$$

The Doppler broadening operation can therefore be performed by calculating the inverse Fourier transform of

$$\widehat{s_T} = \widehat{s_0 \star \mathcal{K}_T^{\mathbb{B}}} = \widehat{s_0}\ \widehat{\mathcal{K}_T^{\mathbb{B}}} \tag{E.174}$$

Since the Fourier transform of Boltzmann kernel $\mathcal{K}_T^{\mathbb{B}}$ is well-known

$$\widehat{\mathcal{K}_T^{\mathbb{B}}}(\nu) = \mathrm{e}^{-(\pi\beta\nu)^2} \tag{E.175}$$

given $\widehat{s_0}$, Doppler broadening can therefore be performed as the inverse Fourier transform of $\widehat{s_0}\ \mathrm{e}^{-(\pi\beta\nu)^2}$.

In theorem 19, we derive the Fourier transform of windowed multipole cross sections, and generalize Ferran's method to account for arbitrary order temperature derivatives, as an alternative to theorem 18.

Theorem 19. *Fourier transform Doppler broadening of Windowed Multipole cross sections*
*Consider the zero Kelvin (*0 K*) Ferran representation of Windowed Multipole R-matrix*

cross sections (E.96), i.e. the odd-parity function $s_0(z) = -s_0(-z)$ *locally of the form:*

$$s_0(z) \underset{z>0}{\triangleq} z^2\ \sigma_0(z) \underset{\mathcal{W}(E)}{=} \Re_{\text{cont}}\left[\sum_{j\geq 1} \frac{r_j}{z-p_j}\right] + \sum_{n\geq 0} a_{n-2} z^n \tag{E.176}$$

Then its Fourier transform (E.170) can be expressed as

$$\widehat{s_0}(\nu) \underset{\mathcal{W}(E)}{=} \Re_{\text{cont}}\left[\sum_{j\geq 1} r_j \widehat{\mathrm{V}}_{p_j}(\nu)\right] + \sum_{n\geq 0} a_{n-2} \widehat{\mathrm{F}}_n(\nu) \tag{E.177}$$

where the Fourier transforms of the Laurent expansions $\widehat{\mathrm{F}}_n(\nu)$ *can be expressed for either even or odd positive integers* $n \geq 0$ *as (*$\delta^{(n)}(\nu)$ *designates the n-th derivative of Dirac's Delta distribution):*

$$\begin{aligned} \widehat{\mathrm{F}}_{2n}(\nu) &\triangleq (-1)^{n+1} \frac{2\mathrm{i}(2n)!}{(2\pi\nu)^{2n+1}} \\ \widehat{\mathrm{F}}_{2n+1}(\nu) &\triangleq \frac{(-1)^n \mathrm{i}}{(2\pi)^{2n+1}} \delta^{(n)}(\nu) \end{aligned} \tag{E.178}$$

and the Fourier transforms of the resonances at pole p_j $\widehat{\mathrm{V}}_{p_j}(\nu)$ *can be expressed as*

$$\widehat{\mathrm{V}}_{p_j}(\nu) \underset{|\mathrm{ph}(p_j)|<\pi}{\triangleq} -2\mathrm{i}\ \mathrm{sgn}(\nu)\ f\left(-2\pi|\nu|p_j\right) \tag{E.179}$$

where $\mathrm{sgn}(z)$ *designates the sign function, and* f *is the auxiliary function defined in 6.2.17 of [250].*

The k^{th}*-order temperature derivative of Windowed Multipole R-matrix cross sections is the convolution:*

$$\partial_T^{(k)} s_T = s_0 \star \partial_T^{(k)} \mathcal{K}_T^{\mathbb{B}} \tag{E.180}$$

which is the inverse Fourier transform (E.171) of product

$$\widehat{\partial_T^{(k)} s_T} = \widehat{s_0}\ \partial_T^{(k)} \widehat{\mathcal{K}_T^{\mathbb{B}}} \tag{E.181}$$

whose expressions are (E.177) for $\widehat{s_0}$ *and, defining* $a \triangleq \frac{k_{\mathbb{B}}}{A}$*,*

$$\partial_T^{(k)} \widehat{\mathcal{K}_T^{\mathbb{B}}} = a^k (i\pi\nu)^{2k} \widehat{\mathcal{K}_T^{\mathbb{B}}} = a^k (i\pi\nu)^{2k} \mathrm{e}^{-(\pi\beta\nu)^2} \tag{E.182}$$

Proof. The proof consists of directly calculating the corresponding Fourier transforms by developing the linear operators. Equation (E.181) stems from the Fourier transform linear property $\widehat{\partial_T^{(k)} \mathcal{K}_T^{\mathbb{B}}} = \partial_T^{(k)} \widehat{\mathcal{K}_T^{\mathbb{B}}}$ applied to (E.180). Expression (E.182) is obtained by direct differentiation of (E.175). In key expression (E.177), the Fourier transforms of the Laurent development part (E.178) are obtained by noticing that odd parity polynomials are already odd functions, while the even parity ones must be written as the difference of (E.176) multiplied by the Heaviside function for domains

$\mathbb{R}_-$ and $\mathbb{R}_+$, and then applying standard Fourier transform properties. The Fourier transforms of resonance terms (E.179) are obtained by identifying the integral representation 6.7.13 in [250], and using identity $f\left(z\mathrm{e}^{\pm\mathrm{i}\pi}\right) = \pi\mathrm{e}^{\mp\mathrm{i}z} - f(z)$ (c.f. 6.4.6 [250]) if the phase of the pole p_j does not respect $|\mathrm{ph}\left(p_j\right)| < \pi$. □

The Fourier transform approach of theorem 19 to arbitrary order temperature derivatives is conceptually more elegant than the direct differentiations of theorem 18: there is no need for Arbogast - Faà di Bruno composition expansions nor recurrences. It is also more general, as the correction C-function term (E.146) is not neglected in the Doppler broadening, and that the Fourier transform approach could potentially be expanded to treat thermal scattering with the phonon distributions of targets: one would then need to replace the Boltzmann distributions $\widehat{\mathcal{K}_T^{\mathbb{B}}}$ (E.175) with the corresponding phonon Fourier spectra (c.f. "Neutron Slowing Down and Thermalization" chapter in [99] or [65, 318]). In practice, theorem 19 also runs into its own hurdles: nothing guarantees that numerically performing the on-the-fly Fourier transforms of theorem 19 – using the Fast Fourier Transform FFT and subsequent algorithms [112, 64, 191] – is more computationally efficient than calling the Faddeyeva functions – which also have benefited of great algorithmic and computational performance gains [321, 270, 328, 327, 196] – and the recursive formulae of theorem 18. This is all the more so true than theorem 19 requires the computation of the f auxiliary function (E.179), which could be more costly than calling the Faddeyava function. Also, Fourier transforms are global integrals, so the windowing process complicates this approach, and the windows have now to be selected according to the method Ferran discussed in IV.B.2 of [145], considering that the Doppler broadening only affects the cross section $\sigma(E)$ at a given energy E for a convolution over an interval commensurate to the temperature energy β^2, say four times $E \pm 4\beta^2$ [300, 118, 190, 145]. Note that this locality problem already exists in the direct Doppler broadening of theorem 17 and by extension theorem 18, and even in the windowing process itself, when selecting which poles p_j to include in window $\mathcal{W}(E)$ as discussed in section E.3.5 and established in [146, 197]. Though in theory the Mittag-Leffler expansion converges on the entire energy domain between two thresholds $[E_{T_c}, E_{T_c+1}]$, in practice it is too costly to compute the Faddeyeva functions for all poles, the essence of the windowing process is therefore to only account for the poles which affect the cross section in window $\mathcal{W}(E)$ upon Doppler broadening, in practice extending the domain ("external window" in [146, 197]) for a couple of temperature energy variances in the Boltzmann distribution ($\left[\mathcal{W}(E_{\min} - 4\beta^2_{\max(T)}), \mathcal{W}(E_{\max} + 4\beta^2_{\max(T)})\right]$): this is a very similar process than Ferran's continuation of the function for the Fourier transform, discussed in section IV.B.2 of [145]. Therefore, if the windowing process is well performed, the expression of theorem 19 will be valid within each window. Otherwise, one would need to truncate the Fourier transforms at the boundary of each energy window, and laboriously concatenate the Ferran representation window by window in the Fourier transforms.

Finally, note that Ferran's Doppler broadening method presents similarities with the optimal temperature kernel reconstruction quadratures developed in [124]: both are kernel methods operating on the cross sections, in particular the Boltzmann kernel

eq. (6) of [124]. Appendix D of [124] studies the consequences the Windowed Multipole Representation of R-matrix cross sections on the Fourier transforms involved in theorem 19. In particular are discussed the general shapes of the Fourier transforms of the nuclear resonances, compared to the $\mathcal{K}_T^{\mathbb{B}}$ Boltzmann kernel (E.175), and how this can entail properties of interest, such as frequency separation in L_2 norm (c.f. eq. (D.9) and sections D.2 and D.3 of appendix D in [124]).

E.6 Conclusion

This article establishes the theoretical foundations for the Windowed Multipole Library.

We derive how the Windowed Multipole Representation of R-matrix cross sections can be constructed by finding the poles of the Kapur-Peierls operator and performing Hwang's albebraic continuation (theorem 15). In the process, we connect the Windowed Multipole Representation to both the Bloch and Wigner-Eisenbud R-matrix theory and to the Humblet-Rosenfeld pole expansions in wavenumber space.

We establish a method to convert R-matrix resonance parameters covariance matrices into Windowed Multipole covariances (theorem 16), and show they generate the same uncertainty distribution on nuclear cross sections, either through the sensitivity approach or by sampling stochastic cross sections.

We recall Windowed Multipole cross sections can be Doppler broadened analytically to high accuracy (theorem 17), and expand this on-the-fly capability to arbitrary-order temperature derivatives (theorem 18), whist deriving new capabilities for temperature treatment by means of Fourier transforms of Windowed Multipole cross sections (theorem 19).

The Windowed Multipole Representation of R-matrix cross sections has already proved its efficacy on a vast range of nuclear physics applications. We hope the foundational results of this article will allow for the widespread adoption of the Windowed Multipole Library, and underpin new research efforts to expand its capabilities.

E.7 Acknowledgments

This work was partly funded by the Consortium for Advanced Simulation of Light Water Reactors (CASL), an Energy Innovation Hub for Modeling and Simulation of Nuclear Reactors under U.S. Department of Energy Contract No. DE-AC05-00OR22725.

The first author was also partly funded by: the 2019-2020 AXA Fellowship of the Schwarzman Scholars Program at Tsinghua University. We would like to thank: Mark Paris and Gerald Hale from Los Alamos National Laboratory for their help on R-matrix theory and the R-matrix 2016 summer workshop in Santa Fe; Grégoire Allaire from École Polytechnique for his help on Fredholm's alternative and Perron-Frobenius theory; Semyon Dyatlov from MIT and U.C. Berkeley for his help on Gohberg-Sigal theory; Javier Sesma from Universidad de Zaragoza for his help on properties of the Hankel functions; Yoann Desmouceaux for his help in proving the

diagonal divisibility and capped multiplicities lemma 3 of [127]; Andrew Holcomb for his help in testing theorem 1 of [127]; and Haile Owusu for his help on Hamiltonian degeneracy.

E.8 Appendix: Single Breit-Wigner capture resonance

In order to derive a simple reference case that is tractable analytically, we here study the multipole representation of the first radiative capture s-wave resonance of uranium ^{238}U. We neglect the energy dependence of the widths in the resonance (this constitutes the B=S approximation), and denote $\Gamma_\lambda \triangleq \Gamma_\gamma + \Gamma_n$, so that the γ-channel cross section takes the form:

$$\sigma_\gamma(E) = \pi g_{J^\pi} a_c^2 \frac{\Gamma_\gamma \Gamma_n}{\rho_0^2 \sqrt{E_\lambda}} \frac{1}{\sqrt{E}} \frac{1}{(E_\lambda - E)^2 + \Gamma_\lambda^2/4} \tag{E.183}$$

which is a Single-Level Breit-Wigner resonance (E.137) with $\mathcal{E}_\lambda \triangleq E_\lambda - \mathrm{i}\frac{\Gamma_\lambda}{2}$, $a = 0$, and $b \triangleq 2\pi \frac{\Gamma_\gamma \Gamma_n}{\rho_0^2 \sqrt{E_\lambda} \Gamma_\lambda}$, i.e.

$$\sigma_\gamma(E) = \frac{1}{\sqrt{E}} \Re \left[\frac{\mathrm{i}b}{E - \mathcal{E}_\lambda} \right] \tag{E.184}$$

Let us now cast (E.183) into the multipole representation (E.96). We perform this by change of variables $z^2 = E$, and $p^2 = \mathcal{E}_\lambda$, and partial fraction decomposition:

$$\frac{1}{\sqrt{E}} \Re \left[\frac{\mathrm{i}b}{E - \mathcal{E}_\lambda} \right] = \frac{1}{z^2} \Re \left[\frac{\mathrm{i}b/2}{z - p} + \frac{\mathrm{i}b/2}{z + p} \right] \tag{E.185}$$

So that the multipole cross section in z-space is then:

$$\sigma_\gamma(z) = \frac{1}{z^2} \Re_{\text{cont}} \left[\frac{r}{z - p} + \frac{r}{z + p} \right] \tag{E.186}$$

with

$$\begin{aligned} r &\triangleq \mathrm{i}\pi \frac{\Gamma_\gamma \Gamma_n}{\rho_0^2 \sqrt{E_\lambda}\, \Gamma_\lambda} \\ p &\triangleq \sqrt{E_\lambda - \mathrm{i}\frac{\Gamma_\lambda}{2}} \end{aligned} \tag{E.187}$$

One can then verify the results of theorem 15 with these explicit formulae.

In theorem 16, we develop a method to compute the Jacobian matrix $\left(\frac{\partial \Pi}{\partial \Gamma}\right)$, using the sensitivities $\frac{\partial \sigma}{\partial \Gamma}(E)$ of the cross section $\sigma(E)$ to resonance parameters $\left\{\Gamma\right\}$. These can here be derived by direct differentiation of (E.183), yielding the relative

sensitivities (derivatives):

$$\begin{aligned}
\frac{1}{\sigma_\gamma}\frac{\partial\sigma_\gamma}{\partial E_\lambda} &= \frac{-1}{2E_\lambda} + 2(E-E_\lambda)\sigma_\gamma\frac{\rho_0^2\sqrt{E}\sqrt{E_\lambda}}{\pi\Gamma_n\Gamma_\gamma} \\
\frac{1}{\sigma_\gamma}\frac{\partial\sigma_\gamma}{\partial\Gamma_n} &= \frac{1}{\Gamma_n} - \frac{\Gamma_\lambda}{2}\sigma_\gamma\frac{\rho_0^2\sqrt{E}\sqrt{E_\lambda}}{\pi\Gamma_n\Gamma_\gamma} \\
\frac{1}{\sigma_\gamma}\frac{\partial\sigma_\gamma}{\partial\Gamma_\gamma} &= \frac{1}{\Gamma_\gamma} - \frac{\Gamma_\lambda}{2}\sigma_\gamma\frac{\rho_0^2\sqrt{E}\sqrt{E_\lambda}}{\pi\Gamma_n\Gamma_\gamma}
\end{aligned} \tag{E.188}$$

Alternatively, these same cross section sensitivities $\frac{\partial\sigma}{\partial\Gamma}(E)$ can be computed using (E.184). For real $b \in \mathbb{R}$, the partial derivatives to any real coefficient $\Lambda \in \mathbb{R}$ follow

$$\frac{1}{\sigma_\gamma}\frac{\partial\sigma_\gamma}{\partial\Lambda} = \frac{1}{b}\frac{\partial b}{\partial\Lambda} + \frac{\Re\left[\frac{\mathrm{i}}{(E-\mathcal{E}_\lambda)^2}\frac{\partial\mathcal{E}_\lambda}{\partial\Lambda}\right]}{\Re\left[\frac{\mathrm{i}}{E-\mathcal{E}_\lambda}\right]}$$

Since we have:

$$\begin{aligned}
\frac{\partial\mathcal{E}_\lambda}{\partial E_\lambda} = 1 \quad &, \quad \frac{1}{b}\frac{\partial b}{\partial E_\lambda} = -\frac{1}{2E_\lambda} \\
\frac{\partial\mathcal{E}_\lambda}{\partial\Gamma_n} = \frac{\partial\mathcal{E}_\lambda}{\partial\Gamma_\gamma} = -\frac{\mathrm{i}}{2} \quad &, \quad \frac{1}{b}\frac{\partial b}{\partial\Gamma_n} = \frac{1}{\Gamma_n} - \frac{1}{\Gamma_\lambda} \\
&, \quad \frac{1}{b}\frac{\partial b}{\partial\Gamma_\gamma} = \frac{1}{\Gamma_\gamma} - \frac{1}{\Gamma_\lambda}
\end{aligned} \tag{E.189}$$

the cross section sensitivities $\frac{\partial\sigma}{\partial\Gamma}(E)$ to resonance energy E_λ, neutron scattering width Γ_n, and radiative capture width Γ_γ are thus respectively

$$\begin{aligned}
\frac{1}{\sigma_\gamma}\frac{\partial\sigma_\gamma}{\partial E_\lambda} &= \frac{-1}{2E_\lambda} + \frac{\Re\left[\frac{\mathrm{i}}{(E-\mathcal{E}_\lambda)^2}\right]}{\Re\left[\frac{\mathrm{i}}{E-\mathcal{E}_\lambda}\right]} \\
\frac{1}{\sigma_\gamma}\frac{\partial\sigma_\gamma}{\partial\Gamma_n} &= \frac{1}{\Gamma_n} - \frac{1}{\Gamma_\lambda} + \frac{1}{2}\frac{\Re\left[\frac{1}{(E-\mathcal{E}_\lambda)^2}\right]}{\Re\left[\frac{\mathrm{i}}{E-\mathcal{E}_\lambda}\right]} \\
\frac{1}{\sigma_\gamma}\frac{\partial\sigma_\gamma}{\partial\Gamma_\gamma} &= \frac{1}{\Gamma_\gamma} - \frac{1}{\Gamma_\lambda} + \frac{1}{2}\frac{\Re\left[\frac{1}{(E-\mathcal{E}_\lambda)^2}\right]}{\Re\left[\frac{\mathrm{i}}{E-\mathcal{E}_\lambda}\right]}
\end{aligned} \tag{E.190}$$

where the derivatives could be taken within the real part because all the parameters were real. Using the cross section sensitivities $\frac{\partial\sigma}{\partial\Gamma}(E)$ – either from (E.188) or (E.190) – and performing the corresponding Hwang's conjugate continuation (section E.3.4), one can therefore compute the multipole sensitivities $\left(\frac{\partial\Pi}{\partial\Gamma}\right)$ of theorem 16 using the contour integrals system (E.128).

In this simple case of a Single-Level Breit-Wigner resonance in multipole representation (E.186), we are also able to explicitly calculate the multipole sensitivities to resonance parameters – i.e. Jacobian $\left(\frac{\partial\Pi}{\partial\Gamma}\right)$ – by direct differentiation of the explicit

formulae (E.187), yielding:

$$\begin{aligned}
\frac{\partial p_+}{\partial E_\lambda} &= -\frac{\partial p_-}{\partial E_\lambda} = \frac{1}{2p_+} \\
\frac{\partial r_+}{\partial E_\lambda} &= \frac{\partial r_-}{\partial E_\lambda} = -\frac{r_+}{2E_\lambda} \\
\text{and} & \\
\frac{\partial p_+}{\partial \Gamma_n} &= -\frac{\partial p_-}{\partial \Gamma_n} = \frac{-\mathrm{i}}{4p_+} \\
\frac{\partial r_+}{\partial \Gamma_n} &= \frac{\partial r_-}{\partial \Gamma_n} = r_+\left(\frac{1}{\Gamma_n} - \frac{1}{\Gamma_\lambda}\right) \\
\text{and} & \\
\frac{\partial p_+}{\partial \Gamma_\gamma} &= -\frac{\partial p_-}{\partial \Gamma_\gamma} = \frac{-\mathrm{i}}{4p_+} \\
\frac{\partial r_+}{\partial \Gamma_\gamma} &= \frac{\partial r_-}{\partial \Gamma_\gamma} = r_+\left(\frac{1}{\Gamma_\gamma} - \frac{1}{\Gamma_\lambda}\right)
\end{aligned} \tag{E.191}$$

The latter multipole sensitivities (E.191) can then be used to validate theorem 16.

For verification and reproducibility purposes, we generated figures E-4, E-5, and E-6 using cross section (E.183) with the parameters from the neutron slowdown analytic benchmark [299], which we here report in table E.2. These parameters are similar (but not identical) to those of ENDF/B-VIII.0 evaluations, yielding the same cross section to a multiplicative constant. The resonance energies and widths are those of ENDF/B-VIII.0, as well as their covariance matrix. The enlarged covariance matrix in table E.2 is that of the analytic benchmark [299], and was designed to bring the neutron slowdown problem past the linear regime in resonance sensitivity.

Table E.2: Resonance parameters of the first s-wave radiative γ-capture resonance of ^{238}U used for generating temperature tolerance plot (FIG. E-6) and sensitivities demonstration (FIG.E-4 and FIG.E-5). The resonance energies and widths, as well as their covariance matrix, are those of ENDF/B-VIII.0 evaluation [87]. The enlarged covariance matrix, as well as the channel radius a_c, the atomic weight A, and ρ_0, are those of the analytic neutron slowdown benchmark [299]

$z = \sqrt{E}$ with E in (eV)
$A = 238$
$a_c = 0.000948$: channel radius, in Fermis
$\rho_0/a_c = 0.002196807122623/2$ $(\sqrt{\text{eV}}^{-1})$
$E_\lambda = 6.674280$: first resonance energy (eV)
$\Gamma_n = 0.00149230$: neutron width of first resonance
$\Gamma_\gamma = 0.0227110$: eliminated capture width (eV)
$g_{J^\pi} = 1$: spin statistical factor
ENDF/B-VIII.0 covariance matrix:
$\mathbb{V}\text{ar}\left([E_0, \Gamma_n, \Gamma_\gamma]\right) =$

$$\begin{bmatrix} 1.1637690 \times 10^{-7} & -2.7442070 \times 10^{-10} & 1.8617500 \times 10^{-8} \\ -2.7442070 \times 10^{-10} & 3.9366000 \times 10^{-10} & -6.5102670 \times 10^{-9} \\ 1.8617500 \times 10^{-8} & -6.5102670 \times 10^{-9} & 1.6255630 \times 10^{-7} \end{bmatrix}$$

Enlarged covariance matrix (same correlation):
$\mathbb{V}\text{ar}\left([E_0, \Gamma_n, \Gamma_\gamma]\right) =$

$$\begin{bmatrix} 1.2373892 & -1.1217107 \times 10^{-5} & 5.6993358 \times 10^{-4} \\ -1.1217107 \times 10^{-5} & 6.1859980 \times 10^{-8} & -7.6617177 \times 10^{-7} \\ 5.6993358 \times 10^{-4} & -7.6617177 \times 10^{-7} & 1.4327486 \times 10^{-5} \end{bmatrix}$$

Appendix F

— Kernel reconstruction methods for Doppler broadening — *temperature interpolation by linear combination of reference cross sections at optimally chosen temperatures*

Here is *verbatim* transcribed our article [124] on optimal quadrature kernel reconstruction methods for Doppler broadening interpolation.

F.1 Abstract

This article establishes a new family of methods to perform temperature interpolation of nuclear interactions cross sections, reaction rates, or cross sections times the energy. One of these quantities at temperature T is approximated as a linear combination of quantities at reference temperatures (T_j). The problem is formalized in a cross section independent fashion by considering the kernels of the different operators that convert cross section related quantities from a temperature T_0 to a higher temperature T – namely the Doppler broadening operation. Doppler broadening interpolation of nuclear cross sections is thus here performed by reconstructing the kernel of the operation at a given temperature T by means of linear combination of kernels at reference temperatures (T_j). The choice of the L_2 metric yields optimal linear interpolation coefficients in the form of the solutions of a linear algebraic system inversion. The optimization of the choice of reference temperatures (T_j) is then undertaken so as to best reconstruct, in the L_∞ sense, the kernels over a given temperature range $[T_{min}, T_{max}]$. The performance of these kernel reconstruction methods is then assessed in light of previous temperature interpolation methods by testing them upon isotope ^{238}U. Temperature-optimized free Doppler kernel reconstruction significantly outperforms all previous interpolation-based methods, achieving 0.1% relative error on temperature interpolation of ^{238}U total cross section over the temperature range [300K, 3000K]

with only 9 reference temperatures.

F.2 Introduction

Temperature effects play a crucial role in nuclear reactor physics. One such effect – Doppler broadening – is for instance responsible for important feedback mechanisms that can ensure the stability of a critical reactor.

In both deterministic and Monte Carlo neutron transport calculations, the temperature dependence of nuclear cross sections is often dealt with by pre-tabulating N Doppler-broadened cross sections, $\sigma_{T_j}(E)$, at a sequence of given temperatures, $(T_j)_{j\in[\![1;N]\!]}$, and then interpolating those values through some interpolation scheme to find the cross section, $\sigma_T(E)$, at the desired temperature T [314]. Such an interpolation is necessary in practice due to the difficulty of calculating the exact Doppler broadening on-the-fly. So far, Doppler broadening temperature interpolation has been traditionally performed by *ad hoc* methods that were not the result of a rigorous optimization problem, and which were selected on best-performance criteria.

In this article, a new family of linear interpolation methods is developed: kernel reconstruction methods. They rest on the mathematical concept of minimizing the distance between the kernels of the linear operators that transform a cross section, a reaction rate, or energy times the cross section, from one temperature to another.

As a physical interpretation, these kernel reconstructions seek to recreate the velocity (or energy) distribution of the target particle at a given temperature, T, with a linear combination of the distributions at the reference temperatures, (T_j). This idea had been introduced, though not systematically formalized, in [**?**], for a particular case of reaction rates.

In section F.3, this article presents the principle of linear kernel reconstruction methods for Doppler broadening, and presents four natural kernel reconstruction methods: Doppler kernel reconstruction; Maxwellian kernel reconstruction; Maxwellian-over-velocity kernel reconstruction; and Boltzmann kernel reconstruction. In each case, the linear reconstruction can be performed as a free optimization problem or as a constrained one, for a total of eight methods. For each method, the optimal coefficients – in the L_2 norm sense – for linear interpolation are exhibited as the solution to an inversion of a cross section independent system. Thus, provided a set of reference temperatures (T_j) and a target temperature T to which to interpolate, the kernel reconstruction methods provide optimally chosen interpolation coefficients.

Section F.4 further temperature-optimizes these kernel reconstruction methods by finding the set of reference temperatures $(T_j)_{j\in[\![1;N]\!]}$ that minimize the kernel reconstruction relative error over the entire temperature range $[T_{min}, T_{max}]$ on which the quantities are to be interpolated. An algorithm specifically devised to solve the min-max problem of such a temperature-optimization is introduced. Each kernel reconstruction method is tested with its own optimized reference temperatures grid to assess kernel reconstruction performance.

Finally, section F.5 studies the performance of the kernel reconstruction methods, with their respective optimal $(T_j)_{j\in[\![1;N]\!]}$ reference temperature distributions, on nu-

clide ^{238}U. Temperature-optimized constrained Doppler kernel reconstruction is shown to have the best accuracy amongst all eight kernel reconstruction methods. However, the free Doppler kernel reconstruction method was preferred due to its close accuracy and higher algorithmic and computational performance. Free Doppler kernel is then compared to previous Doppler broadening interpolation methods commonly in use in nuclear reactor physics calculations.

F.3 Kernel reconstruction linear combination temperature interpolation methods

This section defines and establishes the various kernel reconstruction methods to perform Doppler broadening temperature interpolation by means of linear combination of reference cross sections, reaction rates, or energy-times-cross sections.

F.3.1 Dopper broadening operation

Assuming Maxwell-Boltzmann's free-gas model for the target nuclei distributions of velocities $\overrightarrow{v_t}$ and energies, the Doppler broadening effect of temperature on the reaction rates can be modeled as follows [**?**]:

$$v\sigma_T(v) = \int_{v_t|v_r>0} v_r \sigma_{T_0}(v_r) \mathcal{M}_T\left(\overrightarrow{v_t}\right) d\overrightarrow{v_t} \tag{F.1}$$

where T is the temperature of the target nuclei; T_0 a given reference temperature which will henceforth be, without loss of generality, assumed to be zero; v_r is the relative speed between the neutron hitting at speed v the target that has a Maxwell-Boltzmann velocity distribution $\mathcal{M}_T\left(\overrightarrow{v_t}\right)$; and $\sigma_T(v)$ designates the interaction cross section at temperature T for incoming neutron speed v (respectively temperature T_0 and relative speed v_r for $\sigma_{T_0}(v_r)$). The assumption of isotropic velocity distribution yields the following Doppler broadening of the reaction rates operator:

$$v\sigma_T(v) = \frac{1}{2}\int_{-1}^{1} d\mu \int_{v_t|v_r>0} v_r \sigma_{T_0}(v_r) \mathcal{M}_T\left(v_t\right) dv_t \tag{F.2}$$

where $\mu = \overrightarrow{v_t} \cdot \overrightarrow{v_r}$ and $\mathcal{M}_T\left(v_t\right)$ is the Maxwellian distribution of speeds v_t of the target particle at temperature T:

$$\mathcal{M}_T\left(v_t\right) dv_t = \sqrt{\frac{2}{\pi}} \left(\frac{m_n A}{4\xi}\right)^{3/2} v_t^2 \exp\left(-\frac{\frac{1}{2} m_n A v_t^2}{4\xi}\right) dv_t \tag{F.3}$$

m_n designates the neutron mass, and $4\xi = \frac{k_b(T-T_0)}{A}$, where A is the atomic weight ratio of the target nuclei with respect to the incoming neutron, and k_b is the Boltzmann constant. Further developing the classical energy transformation

$$\frac{1}{2}mv_r^2 = \frac{1}{2}m\left(v^2 - 2\mu v_t v + v_t^2\right) \tag{F.4}$$

yields Solbrig's kernel for Doppler broadening as a function of $u = \sqrt{E}$, with $E = \frac{1}{2}m_n v^2$ is the kinetic energy of the incoming neutron [**?**]:

$$\begin{aligned} u^2\sigma_T(u) &= \int_0^\infty x^2\sigma_{T_0}(x)S(u,x)dx \\ S(u,x) &= \frac{1}{2\sqrt{\pi\xi}}\left[e^{-\frac{(u-x)^2}{4\xi}} - e^{-\frac{(u+x)^2}{4\xi}}\right] \end{aligned} \tag{F.5}$$

F.3.2 Kernel operators definitions

From the latter, it stems that Doppler broadening is a kernel linear operation that transforms a quantity at temperature T_0 to its value at temperature T. Depending on which of the following three quantities is being transformed, four kernels $\mathcal{K}$ can be observed:

1. The $E \cdot \sigma(E)$ quantity relates to the $\mathcal{K}_T^{\mathbb{B}}$ kernel – here called the Boltzmann kernel since it is the Boltzmann distribution of the target particles energies:

$$u^2\sigma_T(u) = \int x^2\sigma_{T_0}(x)\mathcal{K}_T^{\mathbb{B}}(u,x)dx \tag{F.6}$$

2. The $v \cdot \sigma(v)$ quantity can relate to two kernels, according to how the integration is interpreted: $\mathcal{K}_T^{\mathbb{M}}$ – here called the Maxwell kernel as it is the Maxwell velocity distribution of the target particles; or $\mathcal{K}_T^{\frac{\mathbb{M}}{v}}$ – here called the Maxwell-over-velocity kernel since that is the ratio that springs from the integration.

$$v\sigma_T(v) = \int x\sigma_{T_0}(x)\mathcal{K}_T^{\mathbb{M}}(v,x)dx \tag{F.7}$$

$$v\sigma_T(v) = \int x\sigma_{T_0}(x)\mathcal{K}_T^{\frac{\mathbb{M}}{v}}(v,x)dx \tag{F.8}$$

3. The $\sigma(u)$ quantity relates to the kernel $\mathcal{K}_T^{\mathbb{D}}$ – here called the Doppler kernel as it is the kernel of the Doppler broadening operation acting on the cross section:

$$\sigma_T(u) = \int \sigma_{T_0}(x)\mathcal{K}_T^{\mathbb{D}}(u,x)dx \tag{F.9}$$

For clarity purposes, the integrals in the latter definitions are so-far willfully left vague, and formal derivations are expressed to present the structure of the reasoning. The details of all derivations are relegated to the appendixes for reproducibility purposes.

F.3.3 Kernel reconstruction

Hereafter is presented the general method of kernel reconstruction, and the kernel reconstruction problem is formally solved in the general case for both free and constrained reconstruction problems.

Temperature interpolation by linear combination of pre-tabulated cross sections

Let us consider the cross section temperature interpolation problem and search for solutions that are linear combinations of the pre-tabulated values, such that we approximate the exact value of the cross section, $\sigma_T^{(exact)}$ by:

$$\sigma_T^{(exact)} \approx \sigma_T^{(approx)} = \sum_{j=1}^{N} c_j \sigma_{T_j} \tag{F.10}$$

where the σ_{T_j} are assumed to be also exactly calculated. Our goal is to formulate the problem so as to find the optimal choice of (c_j) coefficients to perform this linear interpolation.

The linearity of the kernel operators entails that the difference between the exact and the interpolated quantity translates into an integral difference between kernels. In the case of the Doppler kernel, this means:

$$\left(\sigma_T^{(exact)} - \sigma_T^{(approx)}\right)(u) = \int \sigma_{T_0}(x) \left[\mathcal{K}_T^{\mathbb{D}} - \sum_j c_j \mathcal{K}_{T_j}^{\mathbb{D}}\right](u,x)dx \tag{F.11}$$

Free kernel reconstruction & algebraic solution

Regardless of the metrics chosen, the minimization of the latter expression will be cross section dependent. However, to develop a cross section independent interpolation method, a weak formulation can be used to search the (c_j) that minimize, for all σ_{T_0}, the quantity:

$$\int \left(\sigma_T^{(exact)} - \sigma_T^{(approx)}\right)(u)du = \iint \sigma_{T_0}(x) \left[\mathcal{K}_T^{\mathbb{D}} - \sum_j c_j \mathcal{K}_{T_j}^{\mathbb{D}}\right](u,x)dxdu \tag{F.12}$$

In particular, if for all u, the cross section is arbitrarily chosen as:

$$\forall x, \;\; \sigma_{T_0}(x) \;\; = \;\; \left[\mathcal{K}_T^{\mathbb{D}} - \sum_j c_j \mathcal{K}_{T_j}^{\mathbb{D}}\right](u,x) \tag{F.13}$$

this entails the following L_2 minimization problem:

Find the (c_j) *coefficients that minimize in the* L_2 *sense the difference between the exact Doppler kernel at temperature* T *and a linear combination of kernels at temperatures* (T_j)

$$c_j = \underset{c_j}{\operatorname{argmin}} \left\| \mathcal{K}_T^{\mathbb{D}} - \sum_j c_j \mathcal{K}_{T_j}^{\mathbb{D}} \right\|_{\mathrm{L}_2} \tag{F.14}$$

Solving this problem is here called L_2 free Doppler kernel reconstruction, and the same approach on $v \cdot \sigma_T(v)$ and $E \cdot \sigma_T(E)$ yields analog minimization problems and free kernel reconstructions for the Maxwell, Maxwell-over-velocity and Boltzmann kernels.

An important characteristic of these kernel reconstruction schemes is that the choice of the L_2 norm provides an Hilbert space structure in which the latter optimization problems become algebraically solvable. Indeed, let (c_j) be the coefficients we are searching for, and $\langle f|g\rangle$ denote the scalar product acting upon our Hilbert functional space, then developing $\left\|\mathcal{K}_T - \sum_{j=1}^N c_j \mathcal{K}_{T_j}\right\|_{\mathrm{L}_2}^2 = \langle \mathcal{K}_T|\mathcal{K}_T\rangle - 2\sum_{j\in[\![1;N]\!]} c_j \langle \mathcal{K}_{T_j}|\mathcal{K}_T\rangle + \sum_{j,k} c_k c_j \langle \mathcal{K}_{T_j}|\mathcal{K}_{T_k}\rangle$, and searching for the local minima $\forall j \in [\![1;N]\!]$ $\frac{\partial}{\partial c_j}\left\|\mathcal{K}_T - \sum_{j=1}^N c_j \mathcal{K}_{T_j}\right\|_{\mathrm{L}_2}^2 = 0$, yields the following system:

$$\forall j \in [\![1;N]\!], \quad \sum_{k\neq j} c_k \langle \mathcal{K}_{T_j}|\mathcal{K}_{T_k}\rangle + c_j \langle \mathcal{K}_{T_j}|\mathcal{K}_{T_j}\rangle = \langle \mathcal{K}_{T_j}|\mathcal{K}_T\rangle \tag{F.15}$$

Thus, if our problem has an interior solution, it must satisfy the above system, which can be written in matrix form as follows:

$$\mathbb{G}\cdot C \;=\; Y \tag{F.16}$$

where C is the array of coefficients we are searching for:

$$C = \operatorname{vect}\left(\langle \mathcal{K}_{T_i}|\mathcal{K}_T\rangle\right) = \left[\; c_1 \quad , \ldots , \quad c_N \;\right]^\top \tag{F.17}$$

$\mathbb{G}$ is the Gram matrix of the kernels:

$$\mathbb{G} \;=\; \operatorname{mat}\left(\langle \mathcal{K}_{T_i}|\mathcal{K}_{T_j}\rangle\right) \tag{F.18}$$

and Y is the target vector:

$$Y = \left[\; \langle \mathcal{K}_{T_1}|\mathcal{K}_T\rangle \quad , \ldots , \quad \langle \mathcal{K}_{T_N}|\mathcal{K}_T\rangle \;\right]^\top \tag{F.19}$$

Constrained kernel reconstruction & Algebraic solution

Both Boltzmann and Maxwell kernels are the respective densities of the Boltzmann and Maxwell probability distribution functions, which means that their L_1 norm is equal to one.

When performing the kernel reconstruction, it can be advantageous to conserve this physical property, which guarantees the volume of the kernel is unchanged. This implies making sure that the linear combination of Boltzmann or Maxwell distributions integrates to one so that it can still be considered a probability density function for the target nuclei, or, equivalently, imposing that the linear interpolation coefficients c_j sum up to 1.

This leads us to consider the L_2 constrained kernel reconstruction problems:

Find the (c_j) *coefficients that minimize in the* L_2 *sense the difference between the exact kernel at temperature* T *and a linear combination of kernels at temperatures* (T_j)

$$c_j = \underset{c_j}{\operatorname{argmin}} \left\| \mathcal{K}_T - \sum_j c_j \mathcal{K}_{T_j} \right\|_{\mathrm{L}_2}$$

under the unity constraint of conserving probability densities:

$$\sum_{j=1}^{N} c_j = 1 \tag{F.20}$$

In the constrained kernel reconstruction case, injecting the condition $\sum_j c_j = 1$ into $\left\| \mathcal{K}_T - \sum_{j=1}^{N} c_j \mathcal{K}_{T_j} \right\|_{\mathrm{L}_2}$ yields the following system:

$$\begin{cases} \displaystyle\sum_{k \neq j}^{N-1} c_k \langle \widetilde{\mathcal{K}_{T_j}} | \widetilde{\mathcal{K}_{T_k}} \rangle + c_j \langle \widetilde{\mathcal{K}_{T_j}} | \widetilde{\mathcal{K}_{T_j}} \rangle = \langle \widetilde{\mathcal{K}_{T_j}} | \widetilde{\mathcal{K}_T} \rangle \\ \qquad \forall j \in [\![1; N-1]\!], \;\; \widetilde{\mathcal{K}_{T_j}} = \mathcal{K}_{T_j} - \mathcal{K}_{T_N} \\ \qquad\qquad \displaystyle\sum_{j=1}^{N} c_j = 1 \end{cases} \tag{F.21}$$

by noticing that

$$\langle \widetilde{\mathcal{K}_{T_j}} | \widetilde{\mathcal{K}_{T_k}} \rangle = \langle \mathcal{K}_{T_j} | \mathcal{K}_{T_k} \rangle - \langle \mathcal{K}_{T_j} | \mathcal{K}_{T_N} \rangle - \langle \mathcal{K}_{T_N} | \mathcal{K}_{T_k} \rangle + \langle \mathcal{K}_{T_N} | \mathcal{K}_{T_N} \rangle \tag{F.22}$$

the constrained problem is thus reduced to inverting the following matrix system:

$$\widetilde{\mathbb{G}} \cdot C = \widetilde{Y} \tag{F.23}$$

where

$$\begin{bmatrix} \widetilde{g_{1,1}} & \dots & \widetilde{g_{1,N-1}} & 0 \\ \vdots & \ddots & \vdots & \vdots \\ \widetilde{g_{N-1,1}} & \dots & \widetilde{g_{N-1,N-1}} & 0 \\ 1 & \dots & 1 & 1 \end{bmatrix} \tag{F.24}$$

and

$$\widetilde{Y} = \begin{bmatrix} \langle \widetilde{\mathcal{K}_{T_1}} | \widetilde{\mathcal{K}_T} \rangle & , \dots , & \langle \widetilde{\mathcal{K}_{T_{N-1}}} | \widetilde{\mathcal{K}_T} \rangle & , 1 \end{bmatrix}^\top \tag{F.25}$$

The actual expressions of these Gram matrices will now depend on the particular

kernel being reconstructed and the scalar product considered.

F.3.4 Dopper kernel reconstruction

In the case of Doppler kernel reconstruction, the scalar products diverge. However, the algebraic solutions can still be derived with the help of a continuity argument exposed in appendix A. This yields the following temperature-dependent systems.

Free Doppler reconstruction system

The free Doppler kernel reconstruction system is:

$$\mathbb{D} \cdot C = Y \tag{F.26}$$

with

$$\begin{bmatrix} \frac{\sqrt{T_1 T_1}}{\left(\frac{T_1+T_1}{2}\right)} & \cdots & \frac{\sqrt{T_1 T_N}}{\left(\frac{T_1+T_N}{2}\right)} \\ \vdots & \ddots & \vdots \\ \frac{\sqrt{T_1 T_N}}{\left(\frac{T_1+T_N}{2}\right)} & \cdots & \frac{\sqrt{T_N T_N}}{\left(\frac{T_N+T_N}{2}\right)} \end{bmatrix} \cdot \begin{bmatrix} c_1 \\ \vdots \\ c_N \end{bmatrix} = \begin{bmatrix} \frac{\sqrt{T_1 T}}{\left(\frac{T_1+T}{2}\right)} \\ \vdots \\ \frac{\sqrt{T_N T}}{\left(\frac{T_N+T}{2}\right)} \end{bmatrix} \tag{F.27}$$

Constrained Doppler reconstruction system

The constrained Doppler kernel reconstruction system is:

$$\widetilde{\mathbb{D}} \cdot C = \widetilde{A} \tag{F.28}$$

where

$$\begin{bmatrix} \widetilde{d_{1,1}} & \cdots & \widetilde{d_{1,N-1}} & 0 \\ \vdots & \ddots & \vdots & \vdots \\ \widetilde{d_{N-1,1}} & \cdots & \widetilde{d_{N-1,N-1}} & 0 \\ 1 & \cdots & 1 & 1 \end{bmatrix} \cdot \begin{bmatrix} c_1 \\ \vdots \\ c_{N-1} \\ c_N \end{bmatrix} = \begin{bmatrix} \widetilde{y_1} \\ \vdots \\ \widetilde{y_{N-1}} \\ 1 \end{bmatrix} \tag{F.29}$$

with

$$\widetilde{d_{ij}} = \frac{\sqrt{T_i T_j}}{\left(\frac{T_i+T_j}{2}\right)} - \frac{\sqrt{T_i T_N}}{\left(\frac{T_i+T_N}{2}\right)} - \frac{\sqrt{T_N T_j}}{\left(\frac{T_N+T_j}{2}\right)} + \frac{\sqrt{T_N T_N}}{\left(\frac{T_N+T_N}{2}\right)} \tag{F.30}$$

and

$$\widetilde{y_i} = \frac{\sqrt{T_i T}}{\left(\frac{T_i+T}{2}\right)} - \frac{\sqrt{T_i T_N}}{\left(\frac{T_i+T_N}{2}\right)} - \frac{\sqrt{T_N T}}{\left(\frac{T_N+T}{2}\right)} + \frac{\sqrt{T_N T_N}}{\left(\frac{T_N+T_N}{2}\right)} \tag{F.31}$$

Free Doppler reconstruction analytical solution

Further algebraic manipulations, developed in appendix A, have also enabled to exhibit the analytical solution to the free Doppler kernel reconstruction system (i.e. equation F.27). The explicit formulae for the solution coefficients are:

$$c_j = \frac{\sqrt{T_j T}}{\left(\frac{T_j+T}{2}\right)} \prod_{i \neq j} \left(\frac{T - T_i}{T + T_i}\right) \left(\frac{T_j + T_i}{T_j - T_i}\right) \tag{F.32}$$

F.3.5 Maxwell kernel reconstruction

In the case of Maxwell kernel reconstruction, the algebraic solutions stem from the Gauss integrals. These are derived in appendix B, and yield the following temperature-dependent systems:

Free Maxwell reconstruction system

The free Mawell kernel reconstruction system is:

$$\mathbb{M} \cdot C = Y \tag{F.33}$$

with

$$\begin{bmatrix} \frac{T_1 T_1}{(T_1+T_1)^{5/2}} & \cdots & \frac{T_1 T_N}{(T_1+T_N)^{5/2}} \\ \vdots & \ddots & \vdots \\ \frac{T_N T_1}{(T_N+T_1)^{5/2}} & \cdots & \frac{T_N T_N}{(T_N+T_N)^{5/2}} \end{bmatrix} \cdot \begin{bmatrix} c_1 \\ \vdots \\ c_N \end{bmatrix} = \begin{bmatrix} \frac{T_1 T}{(T_1+T)^{5/2}} \\ \vdots \\ \frac{T_N T}{(T_N+T)^{5/2}} \end{bmatrix} \tag{F.34}$$

Constrained Maxwell reconstruction system

The constrained Maxwell kernel reconstruction system is:

$$\widetilde{\mathbb{M}} \cdot C = \widetilde{Y} \tag{F.35}$$

where

$$\begin{bmatrix} \widetilde{m_{1,1}} & \cdots & \widetilde{m_{1,N-1}} & 0 \\ \vdots & \ddots & \vdots & \vdots \\ \widetilde{m_{N-1,1}} & \cdots & \widetilde{m_{N-1,N-1}} & 0 \\ 1 & \cdots & 1 & 1 \end{bmatrix} \cdot \begin{bmatrix} c_1 \\ \vdots \\ c_{N-1} \\ c_N \end{bmatrix} = \begin{bmatrix} \widetilde{y_1} \\ \vdots \\ \widetilde{y_{N-1}} \\ 1 \end{bmatrix} \tag{F.36}$$

with

$$\widetilde{m_{ij}} = \frac{T_i T_j}{(T_i + T_j)^{5/2}} - \frac{T_i T_N}{(T_i + T_N)^{5/2}} - \frac{T_N T_j}{(T_N + T_j)^{5/2}} + \frac{T_N T_N}{(T_N + T_N)^{5/2}} \tag{F.37}$$

and

$$\widetilde{y_i} = \frac{T_i T}{(T_i + T)^{5/2}} - \frac{T_i T_N}{(T_i + T_N)^{5/2}} - \frac{T_N T}{(T_N + T)^{5/2}} + \frac{T_N T_N}{(T_N + T_N)^{5/2}} \tag{F.38}$$

F.3.6 Maxwell-over-velocity kernel reconstruction

In the case of Maxwell-over-velocity kernel reconstruction, the algebraic solutions also stem from the Gauss integrals, but are of a different order due to a different interpretation of the integral domains. Derivations are found in appendix B, and yield the following temperature-dependent systems:

Free Maxwell-over-velocity reconstruction system

The free Maxwell-over-velocity kernel reconstruction system is:

$$\frac{\mathbb{M}}{\boldsymbol{v}} \cdot C = Y \tag{F.39}$$

with

$$\begin{bmatrix} \frac{1}{\sqrt{T_1+T_1}^3} & \cdots & \frac{1}{\sqrt{T_1+T_N}^3} \\ \vdots & \ddots & \vdots \\ \frac{1}{\sqrt{T_N+T_1}^3} & \cdots & \frac{1}{\sqrt{T_N+T_N}^3} \end{bmatrix} \cdot \begin{bmatrix} c_1 \\ \vdots \\ c_N \end{bmatrix} = \begin{bmatrix} \frac{1}{\sqrt{T+T_1}^3} \\ \vdots \\ \frac{1}{\sqrt{T+T_N}^3} \end{bmatrix} \tag{F.40}$$

It should be noted that this system is the Hadamard product 3^{rd} power of the Boltzmann kernel reconstruction problem that will be described below. This has the implication that the condition number of the system is essentially risen to the 3^{rd} power, significantly hindering the numerical stability of this system over the Boltzmann reconstruction one.

Constrained Maxwell-over-velocity reconstruction system

The constrained Maxwell-over-velocity kernel reconstruction system is:

$$\frac{\widetilde{\mathbb{M}}}{\boldsymbol{v}} \cdot C = \widetilde{Y} \tag{F.41}$$

where

$$\begin{bmatrix} \widetilde{mv_{1,1}} & \dots & \widetilde{mv_{1,N-1}} & 0 \\ \vdots & \ddots & \vdots & \vdots \\ \widetilde{mv_{N-1,1}} & \dots & \widetilde{mv_{N-1,N-1}} & 0 \\ 1 & \dots & 1 & 1 \end{bmatrix} \cdot \begin{bmatrix} c_1 \\ \vdots \\ c_{N-1} \\ c_N \end{bmatrix} = \begin{bmatrix} \widetilde{y_1} \\ \vdots \\ \widetilde{y_{N-1}} \\ 1 \end{bmatrix} \tag{F.42}$$

with

$$\widetilde{mv_{ij}} = \frac{1}{\sqrt{T_i+T_j}^3} - \frac{1}{\sqrt{T_i+T_N}^3} - \frac{1}{\sqrt{T_N+T_j}^3} + \frac{1}{\sqrt{T_N+T_N}^3} \tag{F.43}$$

and

$$\widetilde{y_i} = \frac{1}{\sqrt{T_i+T}^3} - \frac{1}{\sqrt{T_i+T_N}^3} - \frac{1}{\sqrt{T_N+T}^3} + \frac{1}{\sqrt{T_N+T_N}^3} \tag{F.44}$$

F.3.7 Boltzmann kernel reconstruction

Boltzmann kernel reconstruction is rooted into Ferran's convolution formalization of the Doppler broadening operation [**?**]. Its Fourier analysis can help to physically justify the arbitrary choice of L_2 norm reconstruction using a frequency separation argument, as reported in appendix D. The algebraic solutions for the Boltzmann kernel reconstruction are derived in appendix C, and yield the following temperature-dependent systems:

Free Boltzmann reconstruction system

The free Boltzmann kernel reconstruction system is:

$$\mathbb{B} \cdot C = Y \tag{F.45}$$

with

$$\begin{bmatrix} \frac{1}{\sqrt{T_1+T_1}} & \cdots & \frac{1}{\sqrt{T_1+T_N}} \\ \vdots & \ddots & \vdots \\ \frac{1}{\sqrt{T_N+T_1}} & \cdots & \frac{1}{\sqrt{T_N+T_N}} \end{bmatrix} \cdot \begin{bmatrix} c_1 \\ \vdots \\ c_N \end{bmatrix} = \begin{bmatrix} \frac{1}{\sqrt{T+T_1}} \\ \vdots \\ \frac{1}{\sqrt{T+T_N}} \end{bmatrix} \tag{F.46}$$

Constrained Boltzmann reconstruction system

The constrained Boltzmann kernel reconstruction system is:

$$\widetilde{\mathbb{B}} \cdot C = \widetilde{Y} \tag{F.47}$$

where

$$\begin{bmatrix} \widetilde{b_{1,1}} & \cdots & \widetilde{b_{1,N-1}} & 0 \\ \vdots & \ddots & \vdots & \vdots \\ \widetilde{b_{N-1,1}} & \cdots & \widetilde{b_{N-1,N-1}} & 0 \\ 1 & \cdots & 1 & 1 \end{bmatrix} \cdot \begin{bmatrix} c_1 \\ \vdots \\ c_{N-1} \\ c_N \end{bmatrix} = \begin{bmatrix} \widetilde{y_1} \\ \vdots \\ \widetilde{y_{N-1}} \\ 1 \end{bmatrix} \tag{F.48}$$

with

$$\widetilde{b_{ij}} = \frac{1}{\sqrt{T_i+T_j}} - \frac{1}{\sqrt{T_i+T_N}} - \frac{1}{\sqrt{T_N+T_j}} + \frac{1}{\sqrt{T_N+T_N}} \tag{F.49}$$

and

$$\widetilde{y_i} = \frac{1}{\sqrt{T_i+T}} - \frac{1}{\sqrt{T_i+T_N}} - \frac{1}{\sqrt{T_N+T}} + \frac{1}{\sqrt{T_N+T_N}} \tag{F.50}$$

F.4 Temperature-Optimized Kernel Reconstruction Doppler Broadening

It has so far been demonstrated that provided the reference temperatures (T_j) and a temperature of interest T to which one wishes to interpolate the value of a Doppler

broadened quantity by linear combination of the values at reference temperatures, then the choice of the (c_j) interpolation coefficients can be optimally approximated in a cross section independent way by solving a kernel reconstruction problem. In other words, given (T_j) and T, optimal choices (in L_2 sense) for (c_j) have been established.

The purpose of this section is to address the optimal choice of reference temperatures (T_j) that will minimize the interpolation error over a given temperature range $T \in [T_{min}, T_{max}]$. This error is dependent on the cross section values. However, appendix D justifies why it is a good approximation to solve the interpolation problem in a cross section independent fashion by minimizing the distance amongst the kernels. From this it stems that the optimal choice of reference temperatures $(T_j)_{j\in[\![1;N]\!]}$ can also be chosen in a cross section independent way by solving for the optimal set of reference temperatures $(T_j)_{j\in[\![1;N]\!]}$ that minimizes the distance, in both energy and temperature spaces, and in a sense yet to be determined, amongst the kernels.

F.4.1 L_2 kernel reconstruction relative error

Another advantage of having defined our problem with a Hilbert space structure is that the relative distances between the kernels also become analytically expressible as functions of the Gram matrix coefficients as follows:

$$\left(\frac{\Delta\epsilon}{\epsilon}\right)_{\mathbb{G}} \equiv \frac{\left\|\mathcal{K}_T - \sum_{j=1}^{N} c_j \mathcal{K}_{T_j}\right\|_{\mathrm{L}_2}}{\|\mathcal{K}_T\|_{\mathrm{L}_2}} = \sqrt{1 - 2\sum_j c_j \frac{\langle \mathcal{K}_{T_i} | \mathcal{K}_T \rangle}{\langle \mathcal{K}_T^{\mathbb{G}} | \mathcal{K}_T \rangle} + \sum_i \sum_j c_i c_j \frac{\langle \mathcal{K}_{T_i} | \mathcal{K}_{T_j} \rangle}{\langle \mathcal{K}_T | \mathcal{K}_T \rangle}} \tag{F.51}$$

Thus, for the various kernel reconstruction problems, one finds the following relative L_2 distances among kernels by reporting the (c_j), which are the solutions of either the constrained or free problem, into:

Boltzmann kernel relative error

$$\left(\frac{\Delta\epsilon}{\epsilon}\right)_{\mathbb{B}} \equiv \frac{\left\|\mathcal{K}_T^{\mathbb{B}} - \sum_{j=1}^{N} c_j \mathcal{K}_{T_j}^{\mathbb{B}}\right\|_{\mathrm{L}_2}}{\|\mathcal{K}_T^{\mathbb{B}}\|_{\mathrm{L}_2}} = \sqrt{1 - 2\sum_j c_j \frac{\sqrt{2T}}{\sqrt{T_j + T}} + \sum_i \sum_j c_i c_j \frac{\sqrt{2T}}{\sqrt{T_i + T_j}}} \tag{F.52}$$

Maxwell kernel relative error

$$\left(\frac{\Delta\epsilon}{\epsilon}\right)_{\mathbb{M}} \equiv \frac{\left\|\mathcal{K}_T^{\mathbb{M}} - \sum_{j=1}^{N} c_j \mathcal{K}_{T_j}^{\mathbb{M}}\right\|_{\mathrm{L}_2}}{\|\mathcal{K}_T^{\mathbb{M}}\|_{\mathrm{L}_2}} = \sqrt{1 - 2\sum_j c_j \frac{T_j 2^{5/2} T^{3/2}}{(T_j + T)^{5/2}} + \sum_i \sum_j c_i c_j \frac{T_i T_j 2^{5/2} T^{1/2}}{(T_i + T_j)^{5/2}}} \tag{F.53}$$

Maxwell-over-velocity kernel relative error

$$\left(\frac{\Delta\epsilon}{\epsilon}\right)_{\frac{\mathbb{M}}{v}} \equiv \frac{\left\|\mathcal{K}_T^{\frac{\mathbb{M}}{v}} - \sum_{j=1}^{N} c_j \mathcal{K}_{T_j}^{\frac{\mathbb{M}}{v}}\right\|_{\mathrm{L}_2}}{\left\|\mathcal{K}_T^{\frac{\mathbb{M}}{v}}\right\|_{\mathrm{L}_2}} = \sqrt{1 - 2\sum_j c_j \frac{\sqrt{2T}^3}{\sqrt{T_j + T}^3} + \sum_i \sum_j c_i c_j \frac{\sqrt{2T}^3}{\sqrt{T_i + T_j}^3}} \tag{F.54}$$

Doppler kernel relative error

$$\left(\frac{\Delta\epsilon}{\epsilon}\right)_{\mathbb{D}} \equiv \frac{\left\|\mathcal{K}_T^{\mathbb{D}} - \sum_{j=1}^{N} c_j \mathcal{K}_{T_j}^{\mathbb{D}}\right\|_{\mathrm{L}_2}}{\|\mathcal{K}_T^{\mathbb{D}}\|_{\mathrm{L}_2}} = \sqrt{1 - 2\sum_i c_i \frac{\sqrt{T_i T}}{\left(\frac{T_i+T}{2}\right)} + \sum_i \sum_j c_i c_j \frac{\sqrt{T_i T_j}}{\left(\frac{T_i+T_j}{2}\right)}} \tag{F.55}$$

F.4.2 L_∞ Temperature Optimization: Min-max problem

These kernel reconstruction errors can now be optimized so as to find the reference temperatures (T_j) that best reconstruct the kernel over a given temperature range. If the L_∞ metric is now chosen to represent what it means to minimize the distance among kernels over all of the temperature range, the optimization can be cast as solving for the following min-max problem:

$$\begin{gathered}
\textit{Find the } (T_j) \textit{ reference temperatures that minimize} \\
\textit{the relative distance between exact and interpolated kernels} \\
(T_j) = \underset{(T_j)}{\operatorname{argmin}} \left(\max_{T\in[T_{min},T_{max}]} \left(\frac{\Delta\epsilon}{\epsilon}\right)_{\mathbb{G}} \right) \\
\textit{over a range of temperatures of interest } T \in [T_{min}, T_{max}]
\end{gathered} \tag{F.56}$$

F.4.3 Solving the min-max problem: Temperature Optimization Algorithm

For a given number N of reference temperatures (T_j), solving this min-max problem for any of the four kernels (and the respective eight solutions of optimal coefficients (c_j) for free and constrained problems) is a highly non-linear (nor convex) high-dimensionality problem. Differential evolution and basin-hopping optimization algorithms were tested in an attempt to minimize the maximum relative error (i.e. $\max\left(\frac{\Delta\epsilon}{\epsilon}\right)_{\mathbb{G}}$) over the temperature range $[T_{min}, T_{max}]$. However, the high dimensionality of the optimization problem coupled with the stochastic nature of these algorithms led to the algorithms converging in many cases to local rather than global minimae, and with very long running times that were prohibitive past $N = 6$. This issue inspired the creation of a non-stochastic optimization algorithm specifically tailored to the needs of solving the min-max problem on $(\frac{\Delta\epsilon}{\epsilon})_{\mathbb{G}}$.

This algorithm works by choosing values for the reference temperatures such that the maximum relative error on the interval between any pair of adjacent reference temperatures is equal to within some tolerance to the maximum relative error between neighboring adjacent reference temperature pairs. In other words, given some number N of reference temperatures, the algorithm chooses reference temperature values so that:

$$\forall (i,j) \in [\![1, N-1]\!]^2 \ , \quad \left(\max_{T\in[T_i,T_{i+1}]} \left(\frac{\Delta\epsilon}{\epsilon}\right)_{\mathbb{G}} \right) \approx \left(\max_{T\in[T_j,T_{j+1}]} \left(\frac{\Delta\epsilon}{\epsilon}\right)_{\mathbb{G}} \right) \tag{F.57}$$

The algorithm begins with an initial linear guess in (T_j), then iterates through sets of three adjacent reference temperatures, equalizing the maximum relative errors on the intervals between the first two and last two temperatures in each set. This is accomplished by moving the center temperature in a binary search fashion until the difference in the maximum errors on each of the two intervals is below some threshold.

The use of this algorithm allowed reference temperature placement to be optimized more accurately and in a much faster manner than either of the previously tried algorithms. The result of the algorithm on six reference temperatures with an initial guess of linear spacing is shown in figure (F-1). A thorough analysis of the optimal reference temperature grid for Doppler kernel reconstruction can be found in appendix E.

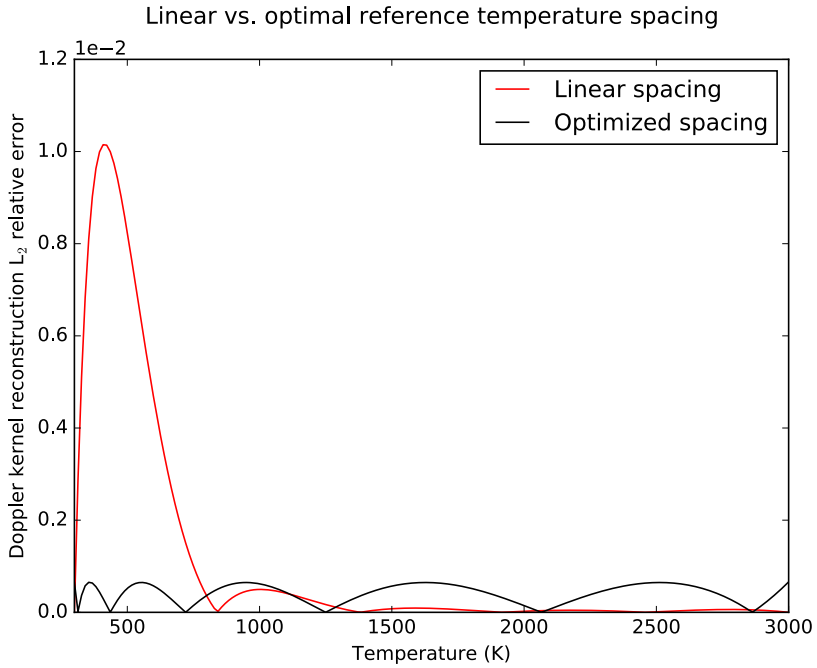

Figure F-1: Free Doppler kernel reconstruction L_2 relative error over the temperature range $[300, 3000]$ for both linearly spaced and optimized spacing of $N = 6$ reference temperatures. Optimization of the reference temperature grid was performed through the presented algorithm with tolerance 10^{-6}, and yields an order of magnitude on kernel reconstruction L_2 relative error.

The high condition numbers of the matrices, specially the one stemming from equation (F.40), necessitated the use of the preconditioned conjugate gradients method for numerically stable inversion. For the free Doppler Kernel method in particular, numerical instability in the calculation of (c_j) values was essentially eliminated through use of the analytical expression for these values shown in equation (F.32).

Another source of numerical instability was the truncation of calculated relative errors due to machine precision when the number of reference temperatures used was sufficiently large. This issue was addressed by calculating both relative errors

and optimal temperature points in arbitrary precision. For any given N number of reference temperatures, $10^{-(N+4)}$ precision was used to compute $\left(\frac{\Delta\epsilon}{\epsilon}\right)^2_{\mathbb{G}}$.

F.4.4 Optimal reference (T_j) distributions kernel reconstruction performance

Once the optimal temperature grid (T_j) has been found for each one of the eight methods, a way of gauging the performance of the various kernel reconstruction methods is to compare, given N reference temperatures, which method is better at reconstructing its own kernel. The results of such an analysis are pictured in figure (F-2).

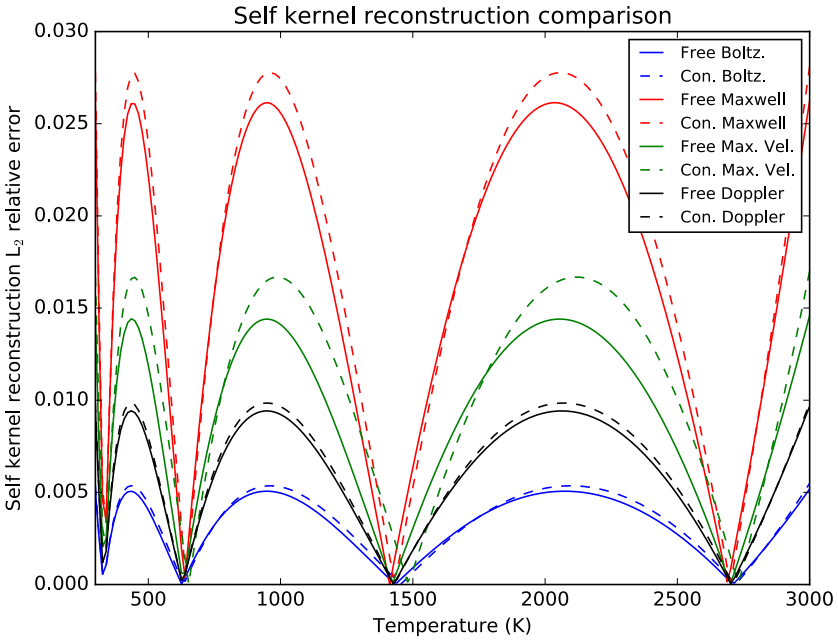

Figure F-2: Comparison of self reconstruction ability: $\left(\frac{\Delta\epsilon}{\epsilon}\right)_{\mathbb{G}}(T)$ for each of the eight kernel reconstruction methods (free and constrained Boltzmann, Maxwell, Maxwell-over-velocity, and Doppler), with there respective optimal reference temperature grids (T_j) for $N = 4$ optimal reference temperatures over the temperature range $[300, 3000]$. The temperature-optimized free Boltzmann kernel reconstruction is the best at reconstructing itself.

It can be observed that the temperature-optimized free Boltzmann kernel reconstruction was the best at reconstructing itself. This, however, did not mean it would fair better on actual isotopes.

F.5 Performance & comparison of temperature interpolation methods

Of the eight Doppler broadening temperature interpolation methods here introduced, only one – the constrained Maxwell kernel reconstruction method – has been previously attempted [**?**]. The other linear interpolation methods traditionally used in the field are provided below, as well as the reference logarithmic interpolation method for comparison purposes [314].

F.5.1 Previous temperature interpolation methods

Traditional temperature interpolation methods have been either linear interpolations in temperature, or linear in logarithmic space, while a recent curve-fit method was introduced in MCNP.

Linear interpolation methods

Linear combination interpolation methods are defined by:

$$\sigma_T \approx \sum_{j=1}^{N} c_j \sigma_{T_j} \tag{F.58}$$

The choices for finding the (c_j) have been [**?**]:

- The "Lin-Lin" interpolation scheme:

$$c_j = \frac{\prod_{i \neq j} (T - T_i)}{\prod_{i \neq j} (T_j - T_i)} \tag{F.59}$$

- The "Lin-Sqrt" interpolation scheme:

$$c_j = \frac{\prod_{i \neq j} \left(\sqrt{T} - \sqrt{T_i}\right)}{\prod_{i \neq j} \left(\sqrt{T_j} - \sqrt{T_i}\right)} \tag{F.60}$$

- The "Lin-Log" interpolation scheme:

$$c_j = \frac{\prod_{i \neq j} (\ln T - \ln T_i)}{\prod_{i \neq j} (\ln T_j - \ln T_i)} \tag{F.61}$$

Logarithmic-Logarithmic method

The "Log-Log" interpolation scheme is defined as:

$$\begin{aligned} \sigma_T &\approx \prod_{j=1}^{N} \left(\sigma_{T_j}\right)^{c_j} \\ c_j &= \frac{\prod_{i\neq j} \left(\ln T - \ln T_i\right)}{\prod_{i\neq j} \left(\ln T_j - \ln T_i\right)} \end{aligned} \tag{F.62}$$

Though they are here defined with general expressions, these interpolation methods as such would suffer from Runge phenomena, and are thus in practice always computed piecewise, using the two closest reference temperature points and ignoring the information provided by all other temperatures. The following comparisons use this two-points interpolation definition.

MCNP curve fit method

One other way to perform temperature interpolation of nuclear data is to curve fit the temperature dimension. This is the method recently adopted by MCNP [235]. For a given reaction, the cross section is Doppler broadened to a large number of temperatures on an union energy mesh. Then, for each energy, the coefficients, $a_{g,i}$, $b_{g,i}$ and c_g are calculated for the following equation using least-squares minimization:

$$\sigma_\gamma(T, E_g) \approx \sum_{i=1}^{N} \frac{a_{g,i}}{T^{i/2}} + \sum_{i=1}^{N} b_{g,i} T^{i/2} + c_g \tag{F.63}$$

The MCNP method is thus a symmetrically truncated Laurent development curve-fit, and the coefficients are entirely cross section and energy dependent.

F.5.2 Performance of the temperature-optimized kernel reconstruction methods

The performance of an interpolation method is assessed on the L_∞ maximum relative error criterium as defined below:.

$$\left|\frac{\Delta\sigma}{\sigma}\right|_{\mathrm{L}_\infty}(T) = \max_{E\in[E_{min},E_{max}]} \left|\frac{\sigma_T^{(exact)}(E) - \sigma_T^{(approx)}(E)}{\sigma_T^{(exact)}(E)}\right| \tag{F.64}$$

and

$$\left\|\frac{\Delta\sigma}{\sigma}\right\|_{\mathrm{L}_\infty} = \max_{T\in[T_{min},T_{max}]} \left\{\left|\frac{\Delta\sigma}{\sigma}\right|_{\mathrm{L}_\infty}(T)\right\} \tag{F.65}$$

The performance of the kernel reconstruction methods here introduced was tested upon isotope ^{238}U, over the energy range $[E_{min} = 10^{-5}\mathrm{eV}, E_{max} = 20\,\mathrm{keV}]$. The pointwise ENDF/B-VII.1 data was Doppler broadened using the SIGMA1 algorithm [**?**], to a sequence of fixed reference temperatures (T_j), providing the exact reference $\sigma_{T_j}(E)$, as well as to calculate all $\sigma_T^{(exact)}(E)$ of the temperature grid. The L_∞ norm of the

relative difference between the exact cross section, $\sigma_T^{(exact)}(E)$, and the interpolated cross section, $\sigma_T^{(approx)}(E)$, was then computed for a range of temperatures.

Best performer amongst kernel reconstruction methods

Each of the eight temperature-optimized kernel reconstruction methods was run using one to six reference temperatures on ^{238}U isotope data. The result of this test for $N = 6$ is displayed in figure (F-3). It can be noticed that the constrained interpolations slightly outperform the free ones in this case. This could presumably be attributed to the fact that constraining the coefficients to summing to unity enforced the essential property of probability distribution, yielding better results overall, specially at the tails of the distributions. Thus, though the free $\frac{\mathbb{M}}{v}$ method does not appear in figure (F-3) due to numerical instability issues, the constrained version of this method can be viewed as its lower bound.

From figure (F-3), it can readily be observed that the two Doppler reconstruction methods outperform all other methods over the entire range of temperatures. Though the temperature-optimized constrained Doppler kernel reconstruction method narrowly outperforms the temperature-optimized free Doppler kernel reconstruction one, the difference in performance is quite slight. The ease with which the free Doppler kernel reconstruction coefficients can be computed using the analytical expression of equation (F.32), as opposed to the matrix inversion required to compute the constrained Doppler coefficients, was felt to make up for the small performance difference between the two methods. Thus the temperature-optimized free Doppler kernel reconstruction method was reckoned to be the best performer amongst temperature-optimized kernel reconstruction methods, and was thus tested on ^{238}U isotope and compared against currently used Doppler broadening interpolation methods.

Performance of temperature-optimized free Doppler kernel reconstruction against previous methods

The temperature-optimized free Doppler kernel reconstruction method was tested on ^{238}U isotope data against linear interpolation, logarithmic interpolation, and the MCNP curve fit method discussed in section F.5.1 for $N = 2$ through 15 reference temperatures. The results of this are displayed in figure (F-4). The free Doppler kernel reconstruction method was found to beat the other methods up to $N = 12$, at which point the maximum relative errors of the kernel reconstruction and the MCNP curve fit methods fell below the level of accuracy from the SIGMA1 Doppler broadening of the ^{238}U isotope data itself, rendering comparison meaningless. From figure (F-4), it can be observed that in order to obtain 0.1% accuracy on a reconstructed ^{238}U kernel using the temperature-optimized free Doppler kernel reconstruction method, nine reference temperatures would be required. The ^{238}U isotope was chosen because the complexity of its resonance structure makes it a difficult isotope to Doppler broaden. Therefore it is likely that using the free Doppler kernel reconstruction method with $N = 10$ reference temperatures would be sufficient to ensure 0.1% precision on all other isotopes.

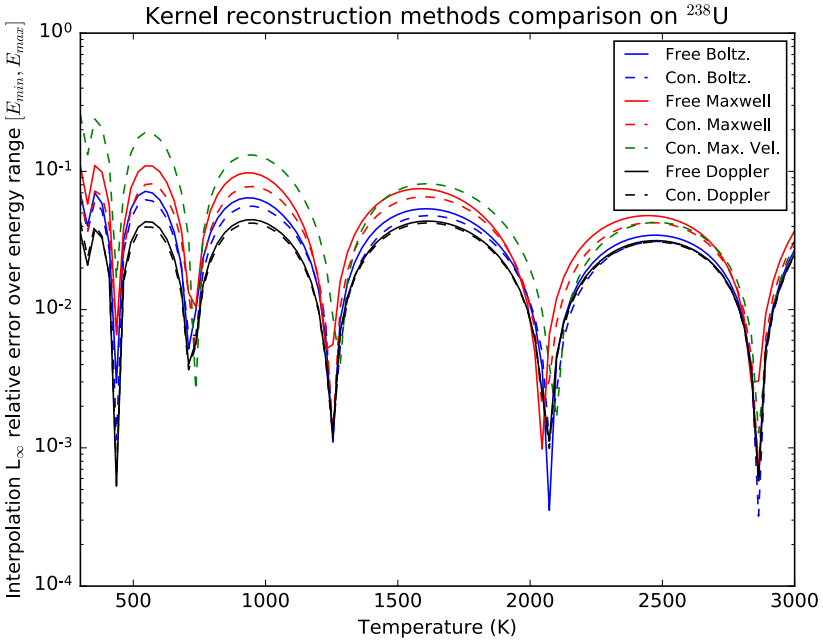

Figure F-3: $\left|\frac{\Delta\sigma}{\sigma}\right|_{L_\infty}(T)$ is computed for $N = 6$ optimal reference temperatures on the temperature range $[300, 3000]$, for each kernel reconstruction method. The two Doppler kernel reconstruction methods outperform all other kernel reconstruction methods on ^{238}U isotope. The ease of computing the free Doppler kernel reconstruction coefficients led to its choice over the constrained Doppler method as a candidate for further testing.

Considerations on performance

Apart from the MCNP curve fit method, which is an *ad hoc* Laurent development curve-fit which kernel reconstruction outperforms by one order of magnitude on precision of interpolation for the same number of reference temperatures, previous methods all consisted of a local interpolation between the two closest temperatures. For a small-enough temperature difference ($T_{j+1} - T_j \to 0$), lin-lin interpolation is sure to converge as a 1^{st} order Taylor expansion, with convergence in $\mathcal{O}(N)$. In contrast, the kernel reconstruction methods here introduced are global methods. They converge as $\mathcal{O}(C^N)$ to the true solution as the number of reference temperatures increases ($N \to \infty$), because the physics of the system at temperature T are increasingly well reconstructed through linear combinations of distributions at reference temperatures T_j.

Analyses have shown that to achieve 0.1% accuracy on temperature interpolation of ^{238}U, previous methods require a temperature mesh of about 30K intervals, thus requiring roughly 100 temperature points to cover nuclear reactor analysis range [314]. The need to use the cross section information for all 10 reference temperatures in the kernel reconstruction methods, instead of only the 2 closest for the older methods (except the MCNP curve fit which needs 12 points for the same precision), invariably requires more cross section lookups. However, the same accuracy can be achieved

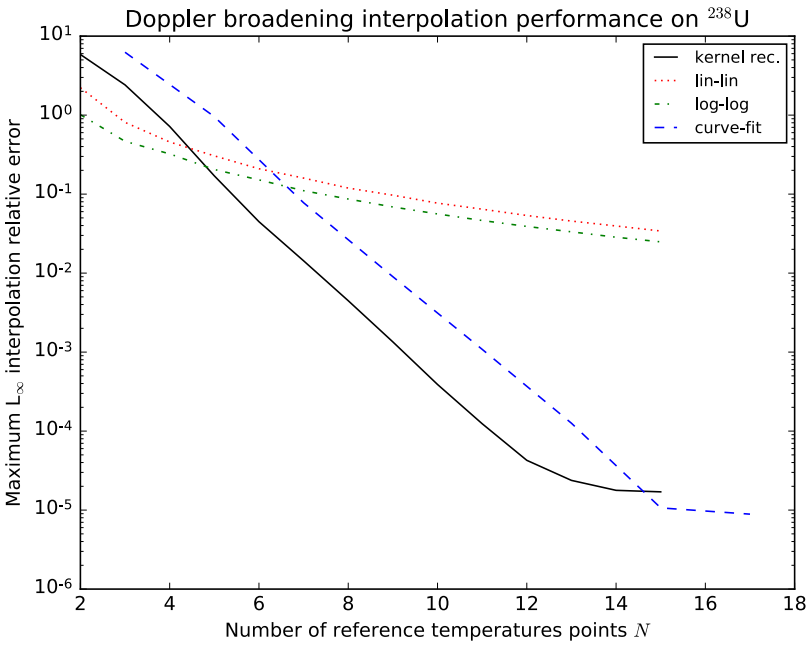

Figure F-4: Maximum relative errors over energy $[10^{-5}\text{eV}, 20\,\text{keV}]$ and temperature $[300\,\text{K}, 3000\,\text{K}]$ ranges. Performance of temperature-optimized free Doppler kernel reconstruction method (kernel rec.) compared to linear interpolation (lin-lin), logarithmic interpolation (log-log), and the MCNP curve fit (curve-fit) method. Temperature-optimized free Doppler kernel reconstruction is one order of magnitude more accurate than the MCNP curve-fit method. $N = 10$ optimal reference temperatures suffice to achieve 0.1% relative error.

with roughly one order of magnitude less temperature points. Additionally, better efficiency can be obtained if each nuclide utilizes a uniform energy grid in temperature and proper ordering.

F.6 Conclusions

A new family of methods has here been established for performing cross section, reaction rates, or energy times cross section, temperature interpolation by linear combination of reference cross sections (or their respective quantity). The methods rely on the L_2-norm difference minimization of operator kernels, representing the physical idea that the optimal way of interpolating is by best reconstructing the conditions of the interaction, that is the kernel of the operation. For instance, this can mean reconstructing the energy (or velocity) distribution for the target nuclei as close as possible to the real one at temperature T. Furthermore, isotope-independent optimal reference temperatures grids have been calculated to fine-tune the performance of kernel reconstruction methods over a given temperature range $[T_{min}, T_{max}]$. Though these methods require higher runtime due to multiple cross section lookups,

the temperature-optimized free Doppler kernel reconstruction method was shown to achieve 0.1% accuracy on isotope ^{238}U cross section temperature interpolation over the entire temperature range $T \in [300K,\ 3000K]$ with only $N = 10$ optimally spaced reference temperatures (T_j), reducing the memory requirements for Doppler broadening interpolation by an order of magnitude.

F.7 Acknowledgments

The first author was supported by the Consortium for Advanced Simulation of Light Water Reactors (CASL), an Energy Innovation Hub for Modeling and Simulation of Nuclear Reactors under U.S. Department of Energy Contract No. DE-AC05-00OR22725. The second author was partially supported under U.S. Department of Energy Nuclear Energy University Programs Graduate Fellowship. The third author was partially supported by the Massachusetts Institute of Technology Undergraduate Research Opportunity Program.

A Appendix A: Doppler kernel reconstruction derivations

A.1 Dopper kernel reconstruction divergence issue

The cross section is extended as an odd function over the entire energy range as:

$$s_T : E \mapsto \begin{cases} \sigma_T(E), & \forall E \in \mathbb{R}_+ \\ s_T(E) = -s_T(-E) & \forall E \in \mathbb{R}_- \end{cases} \tag{66}$$

which transforms Solbrig's kernel into the following Doppler broadening operation:

$$s_T(u) = \int_{-\infty}^{\infty} s_{T_0}(x)\mathcal{K}_T^{\mathbb{D}}(u,x)dx \tag{67}$$

with $u = \sqrt{E}$ and where the Doppler Kernel $\mathcal{K}_T^{\mathbb{D}}$ is here defined as

$$\mathcal{K}_T^{\mathbb{D}}(u,x) \equiv \frac{x^2}{u^2}\mathcal{K}_T^{\mathbb{B}}(u-x) = \frac{1}{2\sqrt{\pi\xi}}\frac{x^2}{u^2}\mathrm{e}^{-\frac{(u-x)^2}{4\xi}} \tag{68}$$

The functional Hilbert space is provided with the following scalar product

$$\langle f|g\rangle \equiv \iint_{\mathbb{R}^2} f \cdot g \tag{69}$$

With this notation, it can be shown that

$$\langle \mathcal{K}_{T_i}^{\mathbb{D}}|\mathcal{K}_{T_j}^{\mathbb{D}}\rangle = \frac{1}{2\pi}\frac{\sqrt{\xi_i\xi_j}}{\xi_i+\xi_j}\Theta \tag{70}$$

where:

$$\Theta = \int_{\theta=0}^{2\pi} \frac{\cos^4\theta}{\sin^4\theta(\cos-\sin)^2} d\theta \tag{71}$$

One can observe that Θ diverges: it is defined everywhere but for the line ($\theta = 0$). The problem thus seems to be ill-defined.

Free Doppler kernel reconstruction

It is however still possible to find an optimal solution to the problem by means of a continuity argument. Defining Θ_ϵ as:

$$\Theta_\epsilon = \int_{\epsilon}^{2\pi} \frac{\cos^4\theta}{\sin^4\theta(\cos-\sin)^2} d\theta \tag{72}$$

For all value of epsilon $\epsilon > 0$, the optimal inversion of the system becomes:

$$\mathbb{D}_\epsilon \cdot C = Y_\epsilon \tag{73}$$

with

$$\begin{bmatrix} \frac{\sqrt{T_1T_1}}{\left(\frac{T_1+T_1}{2}\right)} & \cdots & \frac{\sqrt{T_1T_N}}{\left(\frac{T_1+T_N}{2}\right)} \\ \vdots & \ddots & \vdots \\ \frac{\sqrt{T_1T_N}}{\left(\frac{T_1+T_N}{2}\right)} & \cdots & \frac{\sqrt{T_NT_N}}{\left(\frac{T_N+T_N}{2}\right)} \end{bmatrix} \cdot \begin{bmatrix} c_1 \\ \vdots \\ c_N \end{bmatrix} = \begin{bmatrix} \frac{\sqrt{T_1T}}{\left(\frac{T_1+T}{2}\right)} \\ \vdots \\ \frac{\sqrt{T_NT}}{\left(\frac{T_N+T}{2}\right)} \end{bmatrix} \tag{74}$$

where the definition of $\xi_j = \frac{k_b(T_j - T_0)}{4A}$ was used to show the explicit temperature dependence of the Gram coefficients, and also making the problem nuclide independent. Since the system is invariant in ϵ, by continuity of the property with respect to the value of ϵ, this system still represents the optimal solution in the limit of $\epsilon = 0$.

Constrained Doppler kernel reconstruction

As done above, the constrained problem becomes

$$\widetilde{\mathbb{D}} \cdot C = \widetilde{A} \tag{75}$$

where

$$\begin{bmatrix} \widetilde{d_{1,1}} & \cdots & \widetilde{d_{1,N-1}} & 0 \\ \vdots & \ddots & \vdots & \vdots \\ \widetilde{d_{N-1,1}} & \cdots & \widetilde{d_{N-1,N-1}} & 0 \\ 1 & \cdots & 1 & 1 \end{bmatrix} \cdot \begin{bmatrix} c_1 \\ \vdots \\ c_{N-1} \\ c_N \end{bmatrix} = \begin{bmatrix} \widetilde{y_1} \\ \vdots \\ \widetilde{y_{N-1}} \\ 1 \end{bmatrix} \tag{76}$$

with

$$\widetilde{d_{ij}} = \frac{\sqrt{T_iT_j}}{\left(\frac{T_i+T_j}{2}\right)} - \frac{\sqrt{T_iT_N}}{\left(\frac{T_i+T_N}{2}\right)} - \frac{\sqrt{T_NT_j}}{\left(\frac{T_N+T_j}{2}\right)} + \frac{\sqrt{T_NT_N}}{\left(\frac{T_N+T_N}{2}\right)} \tag{77}$$

and

$$\widetilde{y_i} = \frac{\sqrt{T_i T}}{\left(\frac{T_i+T}{2}\right)} - \frac{\sqrt{T_i T_N}}{\left(\frac{T_i+T_N}{2}\right)} - \frac{\sqrt{T_N T}}{\left(\frac{T_N+T}{2}\right)} + \frac{\sqrt{T_N T_N}}{\left(\frac{T_N+T_N}{2}\right)} \tag{78}$$

A.2 Analytical Solutions

The free Doppler kernel reconstruction system has stunningly remarkable properties:

1. Since $\mathbb{D}$ is a Gram matrix, it is a strictly symmetric positive definite matrix: $\mathbb{D} \in \mathcal{S}_N^{++}$

2. Moreover, the elements of the matrix $\mathbb{D}$ are ratios of the geometric mean to the arithmetic mean of the reference temperature pairs, which only yields values between 0 and 1, with 1's on the diagonal: $\frac{\sqrt{T_i T_j}}{\left(\frac{T_i+T_j}{2}\right)} \in [0,1]$. This quantity is very rich in physical meaning and has links to the information entropy of the system.

3. The matrix $\mathbb{D}$ also exhibits a particular symmetry in that it can be written as:

$$\mathbb{D} \;=\; 2 \cdot \mathbb{T}^{1/2} \cdot \mathbb{C} \cdot \mathbb{T}^{1/2} \tag{79}$$

   where $\mathbb{T} = \text{diag}\,(T_i)$ and $\mathbb{C} = \text{mat}\left(\frac{1}{T_i+T_j}\right)$. The latter is a Cauchy matrix, which enables us to derive the algebraic solution to this system.

Cramer's inversion formula on the free Doppler kernel reconstruction system yields:

$$c_k = \frac{\det\left(\mathbb{D}_{(k)}\right)}{\det\left(\mathbb{D}\right)} \tag{80}$$

where $\mathbb{D}_{(k)}$ is the matrix formed by replacing the k-th column of $\mathbb{D}$ by the column vector Y.

Let us note that $\mathbb{D}_{(k)}$ also exhibits a particular symmetry in that it can be written:

$$\mathbb{D}_{(k)} \;=\; 2 \cdot \mathbb{T}_{(k)}^{1/2} \cdot \mathbb{C}_{(k)} \cdot \mathbb{T}^{1/2} \tag{81}$$

where the sub-index (k) signifies that T_k is replaced by T in the k-th column:
$\mathbb{T}_{(k)} = \text{diag}\,(T_1\,,\,\ldots\,,\,T_{k-1}\,,\,T\,,\,T_{k+1}\,,\,\ldots\,,\,T_N)$ and
$\mathbb{C}_{(k)} = \text{mat}\left(\mathbb{C}_1\,,\,\ldots\,,\,\mathbb{C}_{k-1}\,,\,\left(\frac{1}{T_i+T}\right)_i\,,\,\mathbb{C}_{k+1}\,,\,\ldots\,,\,\mathbb{C}_N\right)$.

Both $\mathbb{C}$ and $\mathbb{C}_{(k)}$ are Cauchy matrices of the type $\left(\frac{1}{a_i+b_j}\right)$, the determinant of which is given by the well-known formula:

$$|\mathbb{C}|_N = \frac{\prod_{i<j}(a_j - a_i)\prod_{i<j}(b_j - b_i)}{\prod_{i,j}(a_i + b_j)} \tag{82}$$

By analyzing the ratio of determinants in Cramer's formula $c_k = \frac{\sqrt{T}\det(\mathbb{C}_k)}{\sqrt{T_k}\det(\mathbb{C})}$, one finds the explicit solution of the kernel-minimizing coefficients:

$$c_k = \frac{\sqrt{T_k T}}{\left(\frac{T_k+T}{2}\right)} \prod_{i \neq k} \left(\frac{T - T_i}{T + T_i}\right) \left(\frac{T_k + T_i}{T_k - T_i}\right) \tag{83}$$

It is noteworthy that $c_k(\sqrt{T})$ is a proper rational fraction in $\sqrt{T}$ of degree -1, and on which it is thus possible to perform partial fraction decomposition, with poles $\pm i\sqrt{T_i}$ and roots $\pm\sqrt{T_i}$ and 0.

Thus, provided a set of reference temperatures (T_j) and given a temperature T, the (c_k) coefficients in equation 83 are the ones that algebraically minimize the L_2 norm between the Doppler kernels.

B Appendix B: Maxwell kernel & Maxwell-over-velocity reconstruction derivations

B.1 Maxwell & Maxwell-over-velocity kernels definition

Physically, the Doppler broadening operation is defined through the conservation of the reaction rate in equation (F.1) as the relative energies span the Maxwellian distribution of velocities of the ideal gaz model for the target nucleus. When interpolating by linear combination of reference temperatures, this yields:

$$\left(v\sigma_T^{(True)} - v\sigma_T^{(approx)}\right)(v) \;=\; \int_{v_t|v_r>0} v_r \sigma_{T_0}(v_r) \left[\mathcal{M}_T\left(\overrightarrow{v_t}\right) - \sum_j c_j \mathcal{M}_{T_j}\left(\overrightarrow{v_t}\right)\right] d\overrightarrow{v_t} \tag{84}$$

Upon change of variables from vectorial velocity to scalar speeds, the Maxwell distribution is recovered:

$$v\sigma_T(v) = \frac{1}{2}\int_0^\infty \left[v_r \sigma_{T_0}(v_r)\right] \frac{v_r}{v} dv_r \int_{|v-v_r|}^{|v+v_r|} \frac{\mathcal{M}_T(v_t)}{v_t} dv_t \tag{85}$$

From this, we define the Maxwell kernel as:

$$\mathcal{K}_T^{\mathbb{M}} \;:\; u \;\mapsto\; \frac{u^2}{\xi}\mathcal{K}_T^{\mathbb{B}} = \frac{1}{2\sqrt{\pi}\sqrt{\xi}^3} u^2 \mathrm{e}^{-\frac{u^2}{4\xi}} \tag{86}$$

The coefficients of the Gram matrix are then readily calculated

$$\langle \mathcal{K}_{T_i}^{\mathbb{M}} | \mathcal{K}_{T_j}^{\mathbb{M}} \rangle = \frac{1}{4\pi} \frac{1}{\sqrt{\xi_i \xi_j}^3} \int_0^\infty u^4 e^{-u^2\left(\frac{1}{4\xi_i} + \frac{1}{4\xi_j}\right)} du \tag{87}$$

Defining the Gauss integrals of order n

$$G_n = \int_0^\infty x^n e^{-x^2} dx \tag{88}$$

and using the following recurrence formula

$$\begin{aligned} G_n &= \frac{n-1}{2} G_{n-2} \\ G_1 &= \frac{1}{2} \\ G_0 &= \frac{\sqrt{\pi}}{2} \end{aligned} \tag{89}$$

one finds

$$\langle \mathcal{K}_{T_i}^{\mathbb{M}} | \mathcal{K}_{T_j}^{\mathbb{M}} \rangle = \frac{3}{\sqrt{\pi}} \frac{\xi_i \xi_j}{(\xi_i + \xi_j)^{5/2}} \tag{90}$$

Let us note that equation (85) leaves the choice of reconstructing the $\frac{\mathcal{M}}{v}$ kernel instead of $\mathcal{M}$. In that particular case, the recurrence formula would have yielded the following Gram matrix coefficients:

$$\langle \frac{\mathcal{K}_{T_i}^{\mathbb{M}}}{v} | \frac{\mathcal{K}_{T_j}^{\mathbb{M}}}{v} \rangle = \frac{1}{2\sqrt{\pi}} \frac{1}{\sqrt{\xi_i + \xi_j}^3} \tag{91}$$

Free Maxwell & Maxwell-over-velocity kernels reconstruction

From the latter, the free Maxwell kernel reconstruction system is:

$$\mathbb{M} \cdot C = Y \tag{92}$$

with

$$\begin{bmatrix} \frac{T_1 T_1}{(T_1+T_1)^{5/2}} & \cdots & \frac{T_1 T_N}{(T_1+T_N)^{5/2}} \\ \vdots & \ddots & \vdots \\ \frac{T_N T_1}{(T_N+T_1)^{5/2}} & \cdots & \frac{T_N T_N}{(T_N+T_N)^{5/2}} \end{bmatrix} \cdot \begin{bmatrix} c_1 \\ \vdots \\ c_N \end{bmatrix} = \begin{bmatrix} \frac{T_1 T}{(T_1+T)^{5/2}} \\ \vdots \\ \frac{T_N T}{(T_N+T)^{5/2}} \end{bmatrix} \tag{93}$$

If instead the choice of reconstructing $\frac{\mathcal{M}}{v}$ is made, then the L_2 minimization solution is given by

$$\frac{\mathbb{M}}{\boldsymbol{v}} \cdot C = Y \tag{94}$$

with

$$\begin{bmatrix} \frac{1}{\sqrt{T_1+T_1}^3} & \cdots & \frac{1}{\sqrt{T_1+T_N}^3} \\ \vdots & \ddots & \vdots \\ \frac{1}{\sqrt{T_N+T_1}^3} & \cdots & \frac{1}{\sqrt{T_N+T_N}^3} \end{bmatrix} \cdot \begin{bmatrix} c_1 \\ \vdots \\ c_N \end{bmatrix} = \begin{bmatrix} \frac{1}{\sqrt{T+T_1}^3} \\ \vdots \\ \frac{1}{\sqrt{T+T_N}^3} \end{bmatrix} \tag{95}$$

which is the Hadamard product 3^{rd} power of the Boltzmann kernel reconstruction problem.

Constrained Maxwell & Maxwell-over-velocity kernels reconstruction

The constrained Maxwell kernel reconstruction problem is then

$$\widetilde{\mathbb{M}} \cdot C = \widetilde{Y} \tag{96}$$

where

$$\begin{bmatrix} \widetilde{m_{1,1}} & \dots & \widetilde{m_{1,N-1}} & 0 \\ \vdots & \ddots & \vdots & \vdots \\ \widetilde{m_{N-1,1}} & \dots & \widetilde{m_{N-1,N-1}} & 0 \\ 1 & \dots & 1 & 1 \end{bmatrix} \cdot \begin{bmatrix} c_1 \\ \vdots \\ c_{N-1} \\ c_N \end{bmatrix} = \begin{bmatrix} \widetilde{y_1} \\ \vdots \\ \widetilde{y_{N-1}} \\ 1 \end{bmatrix} \tag{97}$$

with

$$\widetilde{m_{ij}} = \frac{T_i T_j}{(T_i + T_j)^{5/2}} - \frac{T_i T_N}{(T_i + T_N)^{5/2}} - \frac{T_N T_j}{(T_N + T_j)^{5/2}} + \frac{T_N T_N}{(T_N + T_N)^{5/2}} \tag{98}$$

and

$$\widetilde{y_i} = \frac{T_i T}{(T_i + T)^{5/2}} - \frac{T_i T_N}{(T_i + T_N)^{5/2}} - \frac{T_N T}{(T_N + T)^{5/2}} + \frac{T_N T_N}{(T_N + T_N)^{5/2}} \tag{99}$$

Again, the same considerations are true for the $\frac{\mathcal{M}}{v}$ reconstruction by replacing $\frac{T_i T_j}{(T_i+T_j)^{5/2}}$ by $\frac{1}{\sqrt{T_i+T_j}^3}$.

C Appendix C: Boltzmann kernel reconstruction derivations

C.1 Casting the Doppler broadening operation as a convolution with the Boltzmann distribution

G. Ferran et al. [**?**] recently introduced a generalized, odd parity, function s_T linked to the cross section as:

$$s_T : E \mapsto \begin{cases} E \cdot \sigma_T(E), & \forall E \in \mathbb{R}_+ \\ s_T(E) = -s_T(-E) & \forall E \in \mathbb{R}_- \end{cases} \tag{100}$$

Applying the Doppler broadening operation to s_T yields a linear convolution product operator that transforms the generalized function s_0 from temperature T_0 to temperature $T > T_0$ as follows [**?**]:

$$s_T = s_0 \star \mathcal{K}_T^{\mathbb{B}} \tag{101}$$

where the convolution product is defined as:

$$\forall x \in \mathbb{R},\ f \star g(x) = \int_{-\infty}^{\infty} f(t) g(x - t) dt \tag{102}$$

and with $\mathcal{K}_T^{\mathbb{B}}$ representing the Boltzmann distribution of energies of the target nuclei.

$$\mathcal{K}_T^{\mathbb{B}} : \left\{ \begin{array}{rl} \mathbb{R} & \rightarrow \mathbb{R}_+ \\ t & \mapsto \frac{1}{2\sqrt{\pi\xi}} \mathrm{e}^{-\frac{t^2}{4\xi}} \end{array} \right. \tag{103}$$

The problem provides a Hilbert space structure through the L_2 norm and its associated scalar product:

$$\langle f|g\rangle = \int_{-\infty}^{\infty} f(t)g(t)dt \tag{104}$$

From which it stems that the Gram matrix coefficients are:

$$\langle \mathcal{K}_{T_i}^{\mathbb{B}} | \mathcal{K}_{T_j}^{\mathbb{B}} \rangle = \frac{1}{4\pi\sqrt{\xi_i \cdot \xi_j}} \int_{-\infty}^{+\infty} \mathrm{e}^{-t^2\left[\frac{1}{4\xi_i}+\frac{1}{4\xi_j}\right]} dt \tag{105}$$

and using the recurrence formula for the Gauss integrals (equations 89), one finds:

$$\langle \mathcal{K}_{T_i}^{\mathbb{B}} | \mathcal{K}_{T_j}^{\mathbb{B}} \rangle = \frac{1}{2\sqrt{\pi\left(\xi_i + \xi_j\right)}} \tag{106}$$

C.2 Free Boltzmann kernel reconstruction

The free Boltzmann kernel reconstruction solution for the L_2 norm is thus found by inverting the system:

$$\mathbb{B} \cdot C = Y \tag{107}$$

with

$$\begin{bmatrix} \frac{1}{\sqrt{T_1+T_1}} & \cdots & \frac{1}{\sqrt{T_1+T_N}} \\ \vdots & \ddots & \vdots \\ \frac{1}{\sqrt{T_N+T_1}} & \cdots & \frac{1}{\sqrt{T_N+T_N}} \end{bmatrix} \cdot \begin{bmatrix} c_1 \\ \vdots \\ c_N \end{bmatrix} = \begin{bmatrix} \frac{1}{\sqrt{T+T_1}} \\ \vdots \\ \frac{1}{\sqrt{T+T_N}} \end{bmatrix} \tag{108}$$

Constrained Boltzmann kernel reconstruction

Similarly, the constrained Boltzmann kernel reconstruction problem is:

$$\widetilde{\mathbb{B}} \cdot C = \widetilde{Y} \tag{109}$$

where

$$\begin{bmatrix} \widetilde{b_{1,1}} & \cdots & \widetilde{b_{1,N-1}} & 0 \\ \vdots & \ddots & \vdots & \vdots \\ \widetilde{b_{N-1,1}} & \cdots & \widetilde{b_{N-1,N-1}} & 0 \\ 1 & \cdots & 1 & 1 \end{bmatrix} \cdot \begin{bmatrix} c_1 \\ \vdots \\ c_{N-1} \\ c_N \end{bmatrix} = \begin{bmatrix} \widetilde{y_1} \\ \vdots \\ \widetilde{y_{N-1}} \\ 1 \end{bmatrix} \tag{110}$$

with

$$\widetilde{b_{ij}} = \frac{1}{\sqrt{T_i + T_j}} - \frac{1}{\sqrt{T_i + T_N}} - \frac{1}{\sqrt{T_N + T_j}} + \frac{1}{\sqrt{T_N + T_N}} \tag{111}$$

and

$$\widetilde{y_i} = \frac{1}{\sqrt{T_i + T}} - \frac{1}{\sqrt{T_i + T_N}} - \frac{1}{\sqrt{T_N + T}} + \frac{1}{\sqrt{T_N + T_N}} \tag{112}$$

D Appendix D: Physical justification of the choice of L_2 norm for kernel reconstruction

The performance of all these kernel reconstruction methods will be nuclide dependent, hence the choice in equation (F.13) of posing the problems as L_2 norm minimizations may seem somewhat arbitrary. However, the general physical properties of cross sections tend to support the latter choice in the following way.

D.1 L_2 norm interpolation error for Boltzmann convolution Kernel

When considering the linear combination temperature interpolation problem in the light of Ferran's convolution product approach, the difference between the exact generalized odd function s_T and the interpolated one is given by:

$$s_T^{(True)} - s_T^{(approx)} = s_0 \star \left(\mathcal{K}_T^{\mathbb{B}} - \sum_{j=1}^{N} c_j \mathcal{K}_{T_j}^{\mathbb{B}} \right) \tag{113}$$

Having the approximate temperature-interpolated cross section equating the true value (in a simple convergence sense) $\left(s_T^{(True)} - s_T^{(approx)} = 0 \right)$ is thus equivalent to verifying the condition:

$$s_0 \star \left(\mathcal{K}_T^{\mathbb{B}} - \sum_{j=1}^{N} c_j \mathcal{K}_{T_j}^{\mathbb{B}} \right) = 0 \tag{114}$$

However, considerations hereafter exposed on s_0 show that s_0 is not of a compact support, which means the latter condition can be met if, and only if:

$$\left(\mathcal{K}_T^{\mathbb{B}} - \sum_{j=1}^{N} c_j \mathcal{K}_{T_j}^{\mathbb{B}} \right) = 0 \tag{115}$$

It is however not possible to fully satisfy such condition by interpolation, and thus a metric has to be chosen so as to minimize the distance among kernels to approach this condition. The L_2 metric is a good choice in tune with the properties of s_0. Indeed, if it is sought to minimize the L_2-distance between the two, this means finding the (c_j) such as to minimize:

$$\left\| s_T^{(True)} - s_T^{(approx)} \right\|_{L_2} = \left\| s_0 \star \left(\mathcal{K}_T^{\mathbb{B}} - \sum_{j=1}^{N} c_j \mathcal{K}_{T_j}^{\mathbb{B}} \right) \right\|_{\mathrm{L}_2} \tag{116}$$

Recalling the Fourier transform property on the convolution product,

$$\widehat{f \star g} = \widehat{f} \cdot \widehat{g} \tag{117}$$

one can invoke the theorem of Parseval to establish that:

$$\left\| s_T^{(True)} - s_T^{(approx)} \right\|_{L_2} = \left\| \widehat{s_0} \cdot \left(\widehat{\mathcal{K}_T^{\mathbb{B}}} - \sum_{j=1}^{N} c_j \widehat{\mathcal{K}_{T_j}^{\mathbb{B}}} \right) \right\|_{\mathrm{L}_2} \tag{118}$$

D.2 Pole representation properties of nuclear cross sections

To infer additional information, a careful analysis of the $\widehat{s_0}$ function is required. Angle-integrated nuclear cross sections can be cast into a sum of poles and residues according to the Pole Representation formalism [190] [**?**]. From which s_0 takes the general form:

$$s_0(u) = s_{pot} + \sum_j \Re \left[\frac{r_j}{p_j - u} \right] \tag{119}$$

and thus the Fourier transform verify

$$\widehat{s_0}(\nu) = \widehat{s_{pot}} + \sum_j \Re \left[\frac{r_j}{p_j - u} \right](\nu) \tag{120}$$

The first term can be close to an inverse function or a sign function, the Fourier transform which are Fourier transforms of one-another. The poles will correspond to wide, flat, Fourier transforms, which are known analytically [**?**]. On the contrary, the Boltzmann distributions will have Gaussian Fourier transforms. Frequency separation is thus a physically good approximation and one can treat $\widehat{s_0}$ as slowly varying in comparison to the Boltzmann kernels.

$$\left\| \widehat{s_0} \cdot \left(\widehat{\mathcal{K}_T^{\mathbb{B}}} - \sum_{j=1}^{N} c_j \widehat{\mathcal{K}_{T_j}^{\mathbb{B}}} \right) \right\|_{\mathrm{L}_2} \approx \left\| \widehat{s_0} \right\|_{\mathrm{L}_2} \cdot \left\| \left(\widehat{\mathcal{K}_T^{\mathbb{B}}} - \sum_{j=1}^{N} c_j \widehat{\mathcal{K}_{T_j}^{\mathbb{B}}} \right) \right\|_{\mathrm{L}_2} \tag{121}$$

Thus, minimizing the L_2 norm $\left\| s_T^{(True)} - s_T^{(approx)} \right\|_{\mathrm{L}_2}$ is close to minimizing the L_2 distance between the Boltzmann energy distributions of the target particles.

D.3 Quantifying cross section independent kernel reconstruction error

How good an approximation the former is can be more accurately captured by further analysis, where the isotope specificity of each s_0 appears. Let $\mathcal{K}_c^{\mathbb{B}} = \left(\mathcal{K}_T^{\mathbb{B}} - \sum_{j=1}^{N} c_j \mathcal{K}_{T_j}^{\mathbb{B}} \right)$. The distribution theory property: $\langle f \star g | u \cdot v \rangle = \langle f | u \rangle \cdot \langle g | v \rangle$ is used to establish

$$\frac{\partial}{\partial c_j}\langle s_0 \star \mathcal{K}_c^{\mathbb{B}} | \mathcal{K}_c^{\mathbb{B}} \cdot s_0 \rangle \;=\; \|s_0\|_{\mathrm{L}_2}^2 \, 2\Re\left[\langle \mathcal{K}_c^{\mathbb{B}} | \frac{\partial}{\partial c_j} \mathcal{K}_c^{\mathbb{B}} \rangle\right] \tag{122}$$

Bi-linearity of the hermitian product combined with the Plancherel-Parseval theorem then yield

$$\begin{aligned} \frac{\partial}{\partial c_j}\left\|s_0 \star \mathcal{K}_c^{\mathbb{B}}\right\|_{\mathrm{L}_2}^2 \;&=\; \frac{\partial}{\partial C}\left\|\widehat{s_0} \cdot \widehat{\mathcal{K}_c^{\mathbb{B}}}\right\|_{\mathrm{L}_2}^2 \;=\; 2\Re\left[\langle \widehat{s_0} \cdot \widehat{\mathcal{K}_c^{\mathbb{B}}} | \widehat{s_0} \cdot \frac{\partial}{\partial c_j}\widehat{\mathcal{K}_c^{\mathbb{B}}} \rangle\right] \\ &=\; 2\Re\left[\langle |\widehat{s_0}|^2 \cdot \widehat{\mathcal{K}_c^{\mathbb{B}}} | \frac{\partial}{\partial c_j}\widehat{\mathcal{K}_c^{\mathbb{B}}} \rangle\right] \end{aligned} \tag{123}$$

Thus, the difference among the two is:

$$\frac{\partial}{\partial c_j}\left\|s_0 \star \mathcal{K}_c^{\mathbb{B}}\right\|_{L_2}^2 - \frac{\partial}{\partial c_j}\langle s_0 \star \mathcal{K}_c^{\mathbb{B}} | \mathcal{K}_c^{\mathbb{B}} \cdot s_0 \rangle \;=\; 2\Re\left[\langle \left(|\widehat{s_0}|^2 - \|\widehat{s_0}\|_{\mathrm{L}_2}^2\right) \cdot \widehat{\mathcal{K}_c^{\mathbb{B}}} | \frac{\partial}{\partial c_j}\widehat{\mathcal{K}_c^{\mathbb{B}}} \rangle\right] \tag{124}$$

Yet, when only minimizing the distance amongst the kernels, one solved for:

$$\frac{\partial}{\partial c_j}\left\|\mathcal{K}_c^{\mathbb{B}}\right\|_{L_2}^2 \;=\; 0 \;=\; 2\Re\left[\langle \mathcal{K}_c^{\mathbb{B}} | \frac{\partial}{\partial c_j}\mathcal{K}_c^{\mathbb{B}} \rangle\right] \tag{125}$$

Thus, that at the (c_j) coefficients solution to the L_2 kernel reconstruction problem, the L_2 minimization of s_T interpolation is off from its optimal point by as much as $\left(|\widehat{s_0}|^2 - \|s_0\|_{\mathrm{L}_2}^2\right) \cdot \widehat{\mathcal{K}_c^{\mathbb{B}}}$ is non collinear to $\widehat{\mathcal{K}_c^{\mathbb{B}}}$. More specifically, equation (124) enables us to estimate how close to the s_0 cross section dependent optimal linear interpolation coefficients $(c_j)^{(s_0)}$ are the cross section independent coefficients (c_j) found by L_2 kernel reconstruction. Indeed, at kernel reconstruction optimal (c_j), equation (124) gives the value of $\frac{\partial}{\partial c_j}\left\|s_0 \star \mathcal{K}_c^{\mathbb{B}}\right\|_{L_2}^2$, which should be zero if at cross section optimal $(c_j)^{(g_0)}$. Thus, one can calculate for various cross sections the value of equation (124) at their kernel reconstruction optimal (c_j) and compare: the bigger the value, the most has been lost with respect to isotope-dependent optimality $(c_j)^{(g_0)}$ for this isotope (though how much is not quantified). This quantifies the dependency in s_0 and reinforces the validity of the approximation provided the general mathematical properties of the Pole Representation of angle-integrated nuclear cross sections.

E Appendix E: Temperature optimized free Doppler kernel reconstruction reference temperatures (T_j) distribution study

Here are analyzed important properties of the temperature-optimized free Doppler kernel reconstruction reference temperature grid (T_j).

E.1 Structure of optimal temperature grid (T_j) & scaling properties

The study of the optimal reference temperatures as a function of N shows that the entire problem is scaled according to the dimensionless variable:

$$\tau = \ln\left(\frac{T}{T_{min}}\right) / \ln\left(\frac{T_{max}}{T_{min}}\right) \tag{126}$$

and the entire system is determined only by the ratio $r = \left(\frac{T_{max}}{T_{min}}\right)$, i.e. for any $[T_{min}, T_{max}]$ with the same ratio $r = \left(\frac{T_{max}}{T_{min}}\right)$, the L_2 relative error $\left(\frac{\Delta\epsilon}{\epsilon}\right)$ is left unchanged. Also, the optimal distribution is symmetric, centered on 1/2. Thus,

$$\left(\frac{\Delta\epsilon}{\epsilon}\right)_{(\tau_i)}(1-\tau) \;=\; \left(\frac{\Delta\epsilon}{\epsilon}\right)_{(\tau_i)}(\tau) \;=\; \left(\frac{\Delta\epsilon}{\epsilon}\right)_{(T_i)}(T)\,. \tag{127}$$

A noteworthy property is that for the particular choice of $r = e$, where e designates the Euler number, the optimal values match exactly those of the Chebyshev quadrature, as seen in figure (-5). This hints that the optimization problem is some super-set quadrature, that can range from Chebyshev to Legendre according to the value of r. Indeed, the kernel reconstruction methods can be seen as a form of extended quadrature operation with separation of variables where the coefficients bear all the T dependence and the energy E dependence is carried out by the cross sections.

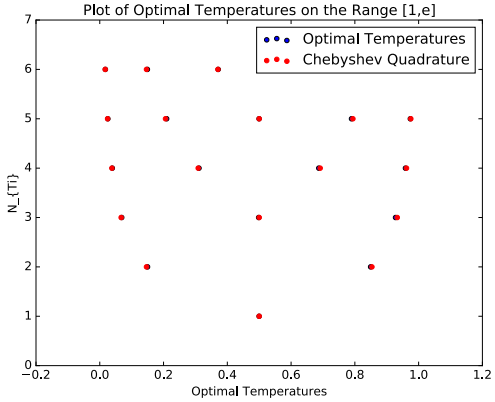

Figure -5: Number of reference temperatures vs optimal temperatures on the range [1,e]. Optimal temperature points line up with Chebyshev quadrature.

E.2 Optimal temperature grid for Doppler kernel reconstruction

For the purpose of reactor analysis, the dimensionless τ_i solutions to the min-max optimization problem with ratio $r = 10$ (which corresponds to the usual values used in nuclear reactor analysis) are hereafter reported in figure (-6), and their scaled

N	Optimized temperature grid (T_j) to perform temperature-optimized free Doppler kernel reconstruction temperature interpolation
1	[948.427]
2	[435.246, 2062.500]
3	[358.012, 948.520, 2512.500]
4	[332.153, 629.087, 1425.806, 2700.000]
5	[320.460, 500.262, 947.380, 1793.691, 2800.000]
6	[314.094, 435.908, 720.689, 1249.489, 2065.967, 2862.500]
7	[310.307, 398.356, 595.912, 949.001, 1511.168, 2259.447, 2893.160]
8	[307.963, 374.068, 519.349, 770.695, 1165.427, 1728.875, 2399.149, 2912.500]
9	[306.145, 359.232, 471.071, 660.047, 950.788, 1369.094, 1917.188, 2513.831, 2937.500]
10	[305.048, 347.608, 436.673, 584.202, 806.228, 1123.081, 1548.951, 2069.173, 2596.590, 2950.000]
11	[304.252, 338.681, 412.408, 530.512, 705.793, 951.890, 1283.538, 1704.703, 2189.430, 2653.095, 2950.000]
12	[303.585, 332.980, 393.688, 492.033, 634.213, 831.825, 1096.021, 1435.603, 1846.909, 2297.375, 2708.445, 2962.500]
13	[303.000, 328.648, 380.443, 462.297, 580.728, 742.398, 956.598, 1232.018, 1571.752, 1966.591, 2380.887, 2744.320, 2962.500]
14	[302.495, 325.278, 370.687, 441.433, 541.558, 677.013, 855.133, 1082.763, 1365.105, 1701.746, 2078.919, 2460.747, 2783.786, 2971.098]
15	[302.0560, 322.886, 362.312, 423.02, 508.989, 624.631, 774.835, 965.193, 1201.262, 1485.613, 1814.241, 2170.679, 2520.285, 2809.074, 2975.000]

Table 1: Optimal temperature grid for cross section interpolation using the free Doppler kernel reconstruction method on the range of temperatures $[300, 3000]$, for a given number N of reference temperatures.

optimal values for $T_{min} = 300$ to $T_{max} = 3000$ reference temperatures corresponding values are recorded in table (1).

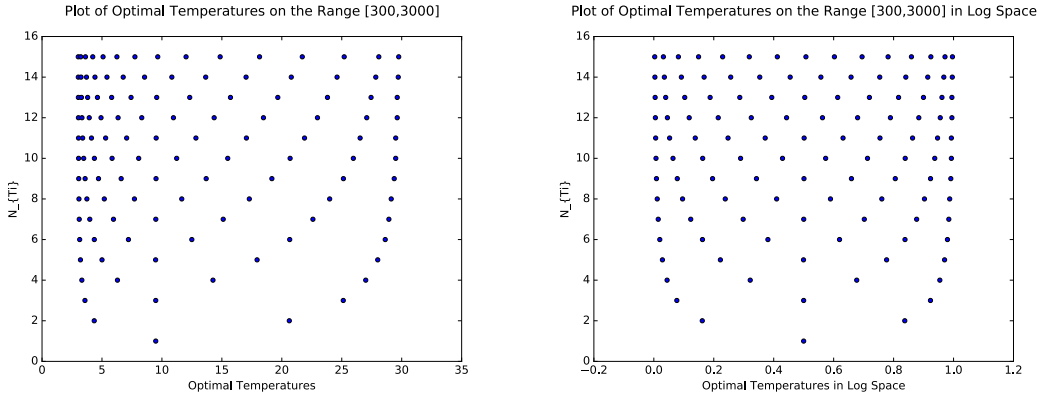

Figure -6: Plots of number of reference temperatures vs optimal reference temperature grid for Doppler kernel reconstruction, in both linear and log space. In Linear space, the scaling properties are such that $[3, 30]$ is equivalent to $[300, 3000]$, as the ratio $r = \left(\frac{T_{max}}{T_{min}}\right)$ is left unchanged.

E.3 Temperature-optimized Doppler kernel reconstruction performance

Here are assessed the efficiency gains in reconstructing the Doppler kernel as the grid of reference temperatures (T_j) varies. These are quantified by comparing the maximum kernel reconstruction relative error $\left(\frac{\Delta\epsilon}{\epsilon}\right)_{\mathbb{D}}$ over the temperature range of interest $[T_{min}, T_{max}]$. The optimized temperature grid outperforms linear, square-root, and logarithmic spacing for any number of reference temperatures. As the number

of reference temperatures increases, optimized spacing yields greater gains over other methods. This is illustrated in figure (-7) and results are recorded in table (E.2) and plotted in (-8).

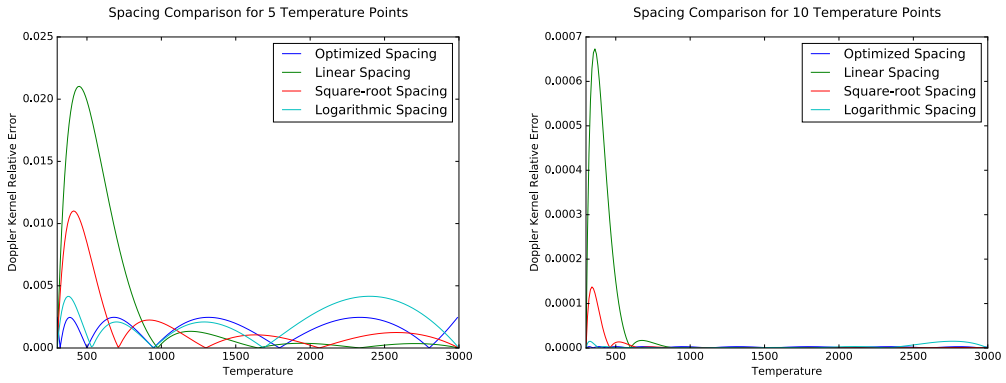

Figure -7: Doppler kernel relative error over the range $[300, 3000]$ for both linearly spaced and optimized temperatures.

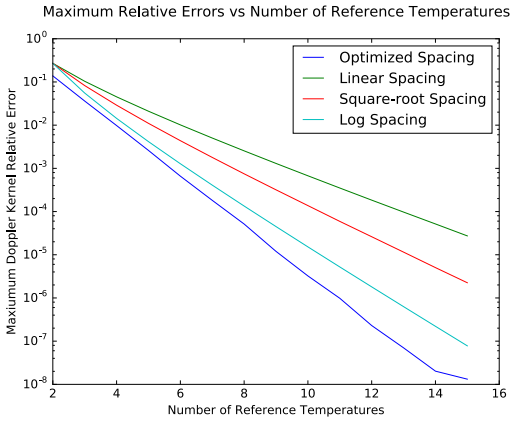

N	Optimized	Linear	Square-root	Logarithmic
2	1.382×10^{-1}	2.698×10^{-1}	2.698×10^{-1}	2.698×10^{-1}
3	3.614×10^{-2}	1.037×10^{-1}	8.241×10^{-2}	5.532×10^{-2}
4	9.791×10^{-3}	4.524×10^{-2}	2.900×10^{-2}	1.435×10^{-2}
5	2.600×10^{-3}	2.102×10^{-2}	1.101×10^{-2}	4.157×10^{-3}
6	6.600×10^{-4}	1.015×10^{-2}	4.372×10^{-3}	1.279×10^{-3}
7	1.819×10^{-4}	5.034×10^{-3}	1.791×10^{-3}	4.091×10^{-4}
8	5.146×10^{-5}	2.542×10^{-3}	7.477×10^{-4}	1.342×10^{-4}
9	1.197×10^{-5}	1.300×10^{-3}	3.184×10^{-4}	4.490×10^{-5}
10	3.236×10^{-6}	6.731×10^{-4}	1.374×10^{-4}	1.522×10^{-5}
11	9.833×10^{-7}	3.508×10^{-4}	5.923×10^{-5}	5.222×10^{-6}
12	2.300×10^{-7}	1.839×10^{-4}	2.614×10^{-5}	1.807×10^{-6}
13	7.005×10^{-8}	9.725×10^{-5}	1.151×10^{-5}	6.296×10^{-7}
14	2.021×10^{-8}	5.166×10^{-5}	5.041×10^{-6}	2.208×10^{-7}
15	1.319×10^{-8}	2.732×10^{-5}	2.247×10^{-6}	7.780×10^{-8}

Figure -8 & Table 2: Maximum relative error in reconstructing the Doppler kernel for a given number of reference temperatures N, for various temperature spacings. The optimal reference temperatures grid (T_j) significantly outperforms all other reference temperature grid spacing.